

DISSERTATION

Search for heavy lepton resonances decaying to a Z boson and a lepton in proton–proton collisions at $\sqrt{s} = 8$ TeV with the ATLAS detector and investigations of radiation tolerant silicon-strip detectors for the high-luminosity LHC upgrade of the ATLAS inner detector

Liv Wiik-Fuchs



Fakultät für Mathematik und Physik
Albert-Ludwigs-Universität Freiburg

**Search for heavy lepton resonances
decaying to a Z boson and a lepton in
proton–proton collisions at $\sqrt{s} = 8$ TeV
with the ATLAS detector and
investigations of radiation tolerant
silicon-strip detectors for the
high-luminosity LHC upgrade of the
ATLAS inner detector**

DISSERTATION

vorgelegt von
Liv Wiik-Fuchs

Fakultät für Mathematik und Physik

ALBERT-LUDWIGS-UNIVERSITÄT

Freiburg im Breisgau

30.11.2016

Dekan: Prof. Dr. Gregor Herten
Betreuer der Arbeit: Prof.Dr.Jochen Dingfelder
Prof. Dr. Karl Jakobs
Referent: Prof. Dr. Karl Jakobs
Koreferent: Prof. Dr. Markus Schumacher
Prüfer: Prof. Dr. Harald Ita
Prof. Dr. Gregor Herten
Prof. Dr. Karl Jakobs

Datum der mündlichen Prüfung:
9. März 2017

Contents

1	Introduction	1
2	Theoretical Context	5
2.1	The Standard Model of Particle Physics	5
2.1.1	Particles and Interactions	6
2.1.2	Quantum Electrodynamics	8
2.1.3	Quantum Chromodynamics	9
2.1.4	Perturbation Theory and Renormalisation	9
2.1.5	Electroweak Unification	11
2.1.6	Electroweak theory and the Higgs mechanism	13
2.1.7	Limitations of the Standard Model	15
2.2	Neutrino Mass	17
2.2.1	The Seesaw Mechanism	18
2.2.2	Type-I Seesaw Model	20
2.2.3	Type-II Seesaw Model	21
2.2.4	Type-III Seesaw Model	22
2.3	Phenomenological Overview of Heavy Lepton Production and Decay at the LHC . . .	23
2.3.1	Simplified Type-III Seesaw Model	23
2.3.2	Production and Cross Section	24
2.3.3	Triplet Decays	25
2.3.4	Bounds on the Mixing Angles	27
2.4	Physics of Proton Proton Collisions	28
2.4.1	Monte Carlo Generation	29
2.4.2	Pile-up	34
2.4.3	Monte Carlo Generators	34
3	The Experimental Setup	37
3.1	An Introduction to the LHC	37
3.1.1	Accelerator Parameters	39
3.2	The ATLAS Experiment	40
3.2.1	The ATLAS Coordinate System	41
3.2.2	The Inner Detector	42
3.2.3	The Calorimeter System	44
3.2.4	The Muon Spectrometer	47
3.2.5	The Magnet System	48

3.2.6	Forward detectors	49
3.3	The ATLAS Trigger System	49
3.4	LHC Operation and ATLAS Data-Taking	51
4	Object Reconstruction	55
4.1	ATLAS Simulation	55
4.2	Track Reconstruction	56
4.3	Vertex Reconstruction	57
4.4	Leptons	58
4.4.1	Electron Trigger	59
4.4.2	Electron Reconstruction	60
4.4.3	Electron Energy Scale and Resolution	64
4.4.4	Muon Trigger	65
4.4.5	Muon Reconstruction	67
4.5	Jet Reconstruction	69
4.6	Missing Transverse Momentum Reconstruction	71
5	Search for a Narrow Heavy Lepton Resonance	73
5.1	Signal Models	73
5.2	Signal Monte Carlo Samples	74
5.2.1	Type-III Seesaw	74
5.2.2	Vector-Like Lepton	76
5.3	Background Processes and Event Samples	79
5.3.1	Diboson Background	79
5.3.2	Triboson Background	81
5.3.3	$t\bar{t} + \mathbf{V}$ Background	83
5.3.4	$\mathbf{Z} + \mathbf{jets}$ Background	83
5.3.5	Photon Conversion	84
5.3.6	$t\bar{t}$ Background	84
5.3.7	Pile-up Reweighting	85
5.4	Data Sample	86
5.4.1	Data Quality Cuts	87
5.5	Object Selection	87
5.5.1	Electrons	87
5.5.2	Muons	88
5.5.3	Jet Definition	89
5.5.4	Resolving Overlapping Objects	90
5.6	Preliminary Result of the Type-III Seesaw Analysis	90
5.7	Signal Selection and Heavy Lepton Resonance Reconstruction	92
5.7.1	Performance on Fiducial Signal Events	95
6	Background Estimation and Validation Regions	99
6.1	Reducible Background Estimation	99
6.1.1	Electron Fake Factors	101
6.1.2	Muon Fake Factors	101
6.1.3	$\mathbf{Z} + \gamma$ Background	103

6.2	Validation Regions	104
6.2.1	High- ΔR Validation Region	104
6.2.2	Off- Z Validation Region	104
6.2.3	ZZ Validation Region	106
6.2.4	WZ Validation Region	106
6.2.5	Summary of the Validation Regions	107
7	Systematic Uncertainties	111
7.1	Luminosity	112
7.2	Trigger Efficiency	112
7.3	Cross sections	112
7.4	Signal PDF	113
7.5	Lepton Efficiencies	113
7.6	Lepton Energy Scale and Resolution	113
7.7	Jet Energy Scale and Resolution	114
7.8	Reducible Background Estimate	115
7.8.1	Electrons	115
7.8.2	Muons	115
7.9	Charge-Flip Scale Factors	116
7.10	Diboson Shape Uncertainty	117
7.11	Summary of Systematic Effects	117
8	Results	123
8.1	Comparison of Data and expected Background Yield	123
9	Statistical Analysis of the Results of the Heavy Lepton Search	133
9.1	Likelihood Fit Model	133
9.1.1	Nuisance Parameters	134
9.1.2	Hypothesis Test	135
9.1.3	Calculation of Exclusion Limit	137
9.2	Signal and Background Parametrisation	137
9.2.1	Signal Parametrisation	138
9.2.2	Background Parametrisation	141
9.3	Combined Fit Model	150
9.3.1	Reduction of free Parameters	152
9.3.2	Validation of Combined Fit Model	152
9.3.3	Comparison of Results Obtained from Pseudo Experiments	154
9.3.4	Fit to Data	154
9.4	Statistical Evaluation of the Results	157
9.4.1	Calculation of the Discovery Significance	162
9.4.2	Calculation of the Exclusion Limit on the Production Cross-Section of Type-III Seesaw and Vector-Like Lepton Model	162
9.4.3	Calculation of the Exclusion Limit on the Production of a Generic Heavy Lepton Resonance	163
9.4.4	Calculation of Fiducial Acceptance and Fiducial Efficiencies	165

10 Introduction to Silicon Detectors	171
10.1 Fundamental Properties of Silicon and Silicon Detectors	172
10.1.1 Intrinsic and Extrinsic Semiconductors	172
10.1.2 Sensor Grade Silicon Material	172
10.1.3 pn-junction	173
10.1.4 Capacitance	176
10.1.5 Charge Motion and Signal Collection	177
10.1.6 Signal Formation and Charge Collection	179
10.1.7 Position Sensitive Measurement	180
10.1.8 Detector Readout and Noise	180
10.2 Radiation damage in Silicon Sensors	181
10.2.1 NIEL Scaling Hypothesis	182
10.2.2 Annealing	183
10.2.3 Leakage Current	184
10.2.4 Effective Doping	185
10.2.5 Charge Trapping	186
10.2.6 Charge Multiplication	188
10.3 Improving Radiation Hardness	188
10.3.1 Change of Operating Conditions	188
10.3.2 Material Engineering	188
10.3.3 Device Engineering	189
11 High Luminosity LHC	191
11.1 The High-Luminosity Upgrade of the LHC	191
11.2 Physics Motivation for the HL-LHC	193
11.3 ATLAS Upgrade	194
11.3.1 Inner Detector Upgrade for the HL-LHC	195
11.4 Silicon Microstrip Detector	197
11.4.1 Petal Concept	202
11.4.2 Super-Module Concept	202
11.5 ATLAS HPK 07 Sensors	203
11.5.1 Irradiations	205
11.5.2 Measurements performed in the Laboratory	207
12 Beam Test Measurement	209
12.1 Devices under Test	209
12.2 Experimental Setup	210
12.3 Data Preparation	212
12.3.1 Alignment	212
12.3.2 Pedestal and Common Mode Reduction	214
12.3.3 Calibration	215
12.3.4 Cluster Finding	217
12.4 Results	218
12.4.1 Measured Signal	218
12.4.2 Efficiency	221
12.4.3 Charge Sharing	223
12.4.4 Space Resolved Signal	225

12.4.5 Single Strip Signal	230
12.5 Spatial Resolution	231
13 ATLAS Inner Tracker Upgrade: B180 Infrastructure	235
13.1 Upgrade Testing Facility B180	235
13.2 Data Acquisition System	237
13.3 Front-end calibration and Electrical Tests	237
13.4 Performance Comparisons of Single and Double-sided Modules	243
14 Conclusion	249
A Auxiliary Information for the Validation Regions	253
A.1 High $\Delta - R$	253
A.2 Off-Z Validation Region	254
A.3 ZZ Validation Region	255
A.3.1 WZ Validation Region	256
B Auxiliary Information for the Signal Region	263
C Appendix Interpretation	269
C.1 Nuisance Parameters	269
C.2 Signal Fit Model	270
Bibliography	275

Introduction

The Standard Model of elementary particles and their interactions has provided a remarkably accurate description of experiments in particle physics over the past 50 years. This has established our understanding of the physics ranging from a few electron Volt (eV) up to energy scales of beyond 100 GeV. Even though the experimental frontier has advanced into the TeV range, no additional particles or interactions beyond the Standard Model have emerged.

The Standard Model describes the strong, weak and electromagnetic forces between the fundamental particles known as quarks and leptons. The Standard Model includes a theory for the origin of particle masses, which goes by the name of *Brout-Englert-Higgs* mechanism, with a newly discovered particle called the *Higgs boson*. In 2012, almost 50 years after it was first predicted, a Higgs-boson-like particle was discovered by the ATLAS and CMS collaborations at the Large Hadron Collider (LHC) at CERN [1, 2]. The discovery of a Higgs-boson was recognised with the awarding of the Nobel Prize to Francois Englert and Peter Higgs in 2013, emphasising its tremendous importance as the last missing building block of the Standard Model.

Despite the remarkable success of the Standard Model in describing all the existing accelerator data with high precision, it fails to answer a number of fundamental questions. Among these are the lack of a dark matter candidate, the relevance of the observed numbers of lepton and quark generations and a possible unification of the electroweak and strong interactions at a high energy scale (GUT scale). Furthermore, the hierarchy problem of fundamental energy scales to differ by many orders of magnitude, the baryon-antibaryon asymmetry in the universe, as well as the missing incorporation of the gravitational force are compelling indicators for physics beyond the Standard Model.

An extension to the Standard Model is also needed to accommodate massive neutrinos, given the compelling evidence from the observation of oscillations in atmospheric, reactor and solar neutrino experiments. These indicate that neutrinos have a small, but non-negligible mass. A number of models, such as seesaw models, have been put forward to explain the neutrino masses and their smallness. However, currently there is insufficient experimental evidence to refute or confirm many of these models. Such a model must not only explain how neutrinos acquire mass but also why their mass is so much smaller than the mass of the other fundamental particles. In fact neutrinos have masses at least a million times smaller than that of the electron, which is the lightest charged fundamental particle. All these problems hint at new physics beyond the Standard Model. There are strong theoretical expectations for new physics to show signatures at the TeV energy scales.

The LHC is the most energetic particle collider and largest scientific experiment ever constructed by

mankind colliding proton beams at a centre-of-mass energy of up to $\sqrt{s} = 14$ TeV to potentially unravel new phenomena up to the TeV scale. During the first data-taking run spanning from 2010 to 2012 the LHC was able to deliver an integrated luminosity of $L = 5.36 \text{ fb}^{-1}$ at $\sqrt{s} = 7$ TeV and $\mathcal{L} = 22.8 \text{ fb}^{-1}$ at $\sqrt{s} = 8$ TeV to the ATLAS experiment. Four large experiments are installed at the LHC. One of them is the omni-purpose detector ATLAS, designed to reconstruct a large variety of different particles over a broad range of energies, thus enabling measurements for a wide range of possible signals.

Searches for new particle resonances often utilise purely leptonic decays to electrons or muons, which allow for the full four-momentum reconstruction with a mass resolution superior to that achievable with hadronic or semileptonic decay modes. Dilepton resonance searches led to the discovery of the J/ψ [3, 4], the Υ [5], and the Z boson [6, 7]. These have been used at the CERN Large Hadron Collider (LHC) to place strong constraints on a variety of new particles such as additional gauge bosons [8, 9]. Much less attention has been paid to trilepton resonances with masses at or above the weak scale. These arise in several extensions of the Standard Model predicting new heavy leptons. This search is spurred on by trilepton resonances arising in the type-III seesaw mechanism [10]. This model explains the origin of small neutrino masses through the introduction of heavy SU(2) triplets with zero hypercharge. Trilepton resonances also arise in vector-like lepton models, which are invoked to explain the mass hierarchy between the different lepton generations [11], but are also contained in certain Higgs models [12, 13] and models of warped extra dimensions [14, 15].

The first part of this thesis is dedicated to the search for high-mass trilepton resonances with the ATLAS detector, using a data sample corresponding to 20.3 fb^{-1} of integrated luminosity collected in proton–proton collisions at $\sqrt{s} = 8$ TeV at the LHC. In this search events are selected if they contain three charged electrons or muons, two of which are consistent with originating from a Z -boson decay. The results are interpreted in the context of vector-like leptons and type-III seesaw models [16] and thus allow to advance our understanding of the neutrino mass generation. The search for the type-III seesaw heavy lepton was a novel analysis idea brought to the ATLAS experiment by the author of this thesis. Hence the fundamental strategy for the analysis was defined, optimised, implemented and executed by the author herself.

In order to search for new physics with low cross sections and to further study mass generation mechanisms a large amount of data is required. The LHC is expected to accumulate $300 - 500 \text{ fb}^{-1}$ of data over its data-taking period. However, to study low cross-section processes and rare decay channels, much higher luminosities are desirable. Therefore upgrades to the existing accelerator complex and to the detectors are planned, to extend the vast physics potential of the LHC. For the so-called Phase-2 upgrade, also called the High Luminosity LHC (HL-LHC), the average luminosity will be five to ten times higher than the design luminosity of the LHC, leading to a total amount of 3000 fb^{-1} of data within 10-12 years of data-taking. This will lead to an increased track density, which requires finer granularity detector components in order to maintain the performance, and hence allowing to fully exploit the physics potential given by the upgrade. Since radiation damages scale with integrated luminosity it is expected that over the project lifetime of the HL-LHC radiation doses of up to $1 - 2 \times 10^{16} \text{ n}_{\text{eq}}/\text{cm}^2$ in the innermost pixel detector layer will be prevalent. The radiation damage induced by fast hadrons leads to bulk damage and constitutes the main cause of a deterioration in performance of silicon detectors at the LHC. Bulk damage leads to an increase in depletion voltage, trapping of free charge carriers, an increase in leakage current and changes to the electric field distribution in silicon sensors. This leads to a significant degradation of the detection efficiency of the silicon sensors, making them inoperable under HL-LHC conditions. Therefore radiation harder sensors are of fundamental importance for a successful operation of silicon tracking detectors at the HL-LHC. Novel silicon detector concepts are being studied in the framework of the RD50 collaboration and the upgrade projects of the experiments. Promising

candidates for radiation hard options are planar sensors with n-type readout and silicon sensors in 3D technology. Here columnar electrodes are etched into the silicon substrate.

Hence, the most significant upgrade of the ATLAS detector for the Phase-II data collection will be the replacement of the entire inner detector, used for tracking of charged particles, with a detector made entirely of silicon. In the envisaged layout the upgraded inner detector will consist of four pixel layers, two short and three long strip layers, and end caps at both sides.

The second part of this thesis is dedicated to research and development projects of radiation hard silicon detectors for the upgrade of the LHC to the HL-LHC. This includes both a comparative beam test between competing radiation hard detector geometries, as well as projects dedicated to the prototyping of the new module design for the strip layers of the new inner detector.

The thesis is structured as follows: Chapter 2 provides the reader with a brief overview of the Standard Model of particle physics together with an outline of the seesaw mechanisms and the phenomenological aspects of the three lepton final state search at the LHC. An introduction to the LHC and the ATLAS detector are given in Chapter 3 before introducing particle and object reconstruction in Chapter 4. The heavy lepton search strategy is presented in Chapter 5, which also includes the signal generation process, an introduction to the event selection to separate signal from background events, and the reconstruction of the heavy lepton resonance. Chapter 6 describes the background estimation techniques and their validation followed by the evaluation of the uncertainties in Chapter 7. The results of the search for a heavy lepton resonance in three-lepton final states are presented in Chapter 8. The analysis is concluded by Chapter 9, which describes the statistical methods used to interpret the results of the search for a heavy leptons.

The second part of this thesis, dedicated to the upgrades of the silicon strip detector, commences in Chapter 10, with an introduction to the basic physics of semiconductors and their radiation damage arising from their application in high energy physics experiments. An introduction to the HL-LHC upgrade project with an emphasis on the ATLAS inner detector upgrade is given Chapter 11. A beam test measurement of highly irradiated silicon sensors is presented in Chapter 12. A summary on the installation of a centralised test facility for the ATLAS upgrade of the silicon strip detector including dedicated measurements is given in Chapter 13. The final conclusion of this thesis is provided in Chapter 14.

Theoretical Context

This chapter intends to provide the reader with a basic overview of the theoretical concepts of particle physics relevant for this thesis. An introduction to the *Standard Model* of Particle Physics is given in Section 2.1. The Standard Model is a coherent quantum mechanical description of the fundamental particles and their interactions. Whilst it has proven to be remarkably successful and is experimentally verified with high precision over energies ranging from a few eV to the TeV scale, there are several indications, discussed in Section 2.1.7, pointing to a more extended theory beyond the Standard Model. One of these is the observation of neutrino oscillations, which indicates that neutrinos are not massless as predicted by the Standard Model. Possible extensions to the Standard Model to accommodate neutrino masses are given in Section 2.2. Additionally, a brief overview of vector-like leptons is given in Section 2.3. This Chapter is concluded with an introduction to the phenomenology of proton–proton interactions 2.4.

2.1 The Standard Model of Particle Physics

The Standard Model of Particle Physics is a widely accepted theoretical framework, which evolved during the second half of the past century. According to the Standard Model *quarks* (q) and *leptons* (ℓ) are the fundamental constituents of matter. They are described as spin-1/2 fermions and are further classified by quantum numbers such as electric charge, isospin or colour charge. Interactions between the fermions are mediated by the exchange of force carriers, which are elementary particles of spin-1, called bosons. These interactions include both the transfer of energy and momentum and the alteration of the different quantum numbers. The Standard Model incorporates three of the four known forces, namely the *electromagnetic*, the *weak* and the *strong interaction*.

Mathematically, the Standard Model is a quantum field theory using special relativity and quantum mechanics to describe the interactions of fundamental particles in a unified way. Fermions are represented as states of the quantised spinor fields, bosons are states of the quantised vector fields, whereas the Higgs boson is defined through a scalar field. The kinematics and dynamics of the system are formulated by a *Lagrangian density* \mathcal{L} , called Lagrangian in the remainder of this thesis. The Euler-Lagrange equations, the equations of motions for the fields, are found through the principle of least action, $\delta A = 0$, where A is defined as $A = \int dt \mathcal{L}$ and t denotes time. This results in the *Klein-Gordon* equation for bosons and in the *Dirac* equation for fermions. The interactions between the fermions and bosons are found on the basis of gauge transformations, which leave the Lagrangian locally invariant under certain

unitary transformations.

The Standard Model has been enormously successful in the prediction of a wide range of phenomena, such as the discovery of the beauty- [5, 17] and top quark [18, 19], the W and Z boson [6, 7, 20, 21], the τ neutrino [22] and more recently the discovery of the Higgs boson [1, 2] by the ATLAS and CMS collaborations at the Large Hadron Collider (LHC) in 2012. In the following a short overview of the particle content of the Standard Model is given followed by a brief introduction of the theories describing the particle interactions. This section follows several textbooks that offer a more pedagogical and exhaustive introduction to the matter [23–26].

2.1.1 Particles and Interactions

The Standard Model incorporates 12 fermions which are divided into six leptons and six quarks, shown in Table 2.1. Each fermion has a corresponding antiparticle, which is identical to the particle except for the sign of the additive quantum numbers. Throughout this thesis, the particle name refers to both the particle and its antiparticle, if not stated otherwise. Both, leptons and quarks are grouped into three generations, where the second and third generation are heavier copies of the first generation. However, the fermions of the second and third generation are unstable and subsequently decay into the stable fermions of the first generation. The first generation of fermions consists of the electrically charged electron (e), the electrically neutral electron neutrino (ν_e) and the up- (u) and down (d) quarks, which carry fractional charges of $+2/3$ and $-1/3$, respectively. Ordinary matter is exclusively built from first-generation fermions, where protons and neutrons can be regarded as compounds of u and d quarks, and the electrons form the atomic shell. The leptons of the second and third generation are the muon (μ) and tauon (τ) with their corresponding neutrinos. The quarks of the heavier generations are the charm (c) and strange (s), for the second, and beauty (b) and top (t) for the third generation. The masses of the leptons range from 0.511 eV for the electron to 1776 MeV for the tau lepton [27]. While the Standard Model assumes neutrinos to be massless, the observation of neutrino oscillations [28–31] requires the neutrinos to have non-vanishing masses. Several mechanisms exist to alter the Standard Model such that non-vanishing neutrino masses are included. The quark masses range from a few MeV for the lightest quarks to 4.2 GeV for the beauty and 173 ± 0.6 (stat) ± 0.8 (syst) GeV for the top quark, which is the most massive particle within the Standard Model [27]. This large mass hierarchy between the Standard Model fermions is one of the intriguing questions yet to be understood.

The spin-1 gauge bosons mediate interactions between the fermions and are summarised in Table 2.2. The electromagnetic interaction is described by the theory of *Quantum Electrodynamics* (QED), which was established in the 1950s. It describes the interactions between electrically charged particles through the exchange of electrically neutral photons, which are the quanta of the electromagnetic field. Since the photons are massless, electromagnetic interactions have an infinite range, the potential falls off $\propto 1/r^2$, where r is the distance between the charges. QED proved to be a valid theory to describe a large range of phenomena in the binding processes of atoms and molecules, such as the fine-structure splitting of atomic energy levels.

The strong force is described by *Quantum Chromodynamics* (QCD). It characterises the interactions between *partons*, i.e. all fundamental particles that carry *colour charge*. These are the quarks and gluons (g_{ij}), which are the massless mediators of the strong force itself. There exist three independent colour states, usually named red (r), green (g) and blue (b), and their respective anticolours. The motivation for colour arose from the discovery of particles like the Δ^{++} and the Ω^- , which are bound states of three quarks with the same spin and flavour [32, 33]. Therefore a further degree of freedom was needed to obey the Pauli exclusion principle of fermions. Equivalent to chromatics, colour neutral states, called *hadrons*, are built from combinations of red, green and blue and their anti-colours anti-red,

	Generation			Charge Units of e	Feels force of		
	1 st	2 nd	3 rd		Strong	EM	Weak
up - type quarks (x 3 colours)	u	c	t	+2/3	Y	Y	Y
down - type quarks (x 3 colours)	d	s	b	-1/3	Y	Y	Y
charged leptons	e	μ	τ	1	N	Y	Y
neutral leptons	ν_e	ν_μ	ν_τ	0	N	N	Y

Table 2.1: The matter particles, spin-1/2.

anti-green and anti-blue. There are two kinds of hadrons: the *mesons* consisting of a quark-antiquark pair carrying colour and the respective anti-colour ($q_1\bar{q}_2$) or *baryons* consisting of three quarks or anti-quarks of different colour ($q_1q_2q_3$ or $\bar{q}_1\bar{q}_2\bar{q}_3$). A further fundamental difference between QED and QCD is the scaling behaviour. Due to the self interaction of gluons and the number of colour states, the potential of the strong force actually increases with increasing distance between the partons. Consequently, when separating a quark from other quarks, new quark pairs will be generated using the energy from the gluon field, such that quarks are always bound into hadrons and no quarks can exist freely. This phenomenon is called *confinement* and leads to the typical dimensions of hadrons of about 10^{-15} m. At small distances, however, the partons can be considered as free with respect to the strong force, called *asymptotic freedom*, as Gross, Politzer, and Wilczek proved in 1973 [34, 35]. The first observation of three-jet events in 1979 by the PETRA experiments at DESY [36] was the experimental evidence for the existence of gluons. QCD has subsequently been probed in great detail for example in deep-inelastic scattering experiments at the HERA collider [37] at DESY.

The third force incorporated in the Standard Model is the *weak interaction*. All Standard Model fermions carry *weak charge*. The weak interaction is mediated by three massive gauge bosons, the electrically charged W^\pm bosons and the electrically neutral Z boson. The W^\pm bosons have a mass of (80.399 ± 0.023) GeV [27] and the neutral Z boson has a mass of about (91.1876 ± 0.0021) GeV [27]. This results in the weak force being suppressed compared to the electromagnetic force at scales below the W/Z -mass. There are two distinct types of weak interaction: First, the neutral current interaction mediated by the Z boson, which behaves similarly to the photon. Second, the charged current interaction, mediated by the W bosons. In this interaction the flavour type of the fermion is altered. In the weak interaction the flavour eigenstates do not correspond to the mass eigenstates. Due to the very small neutrino masses the charged current in the lepton sector occurs to a first approximation only within one generation. Hence a lepton ℓ is converted into the corresponding lepton neutrino under the emission of a W or vice versa. In the quark sector an up-type quark is converted into a down-type quark. The relative strength of the different transition probabilities are given by the Cabibbo-Kobayashi-Maskawa matrix (CKM matrix) [17, 38]. As the W^\pm carry electrical and weak charges, self-couplings of the vector bosons and couplings to the Z and photons are allowed. A further specific characteristic of the weak interaction is that it violates parity maximally. This means that the weak interaction does not behave symmetric under spatial point reflections. This was experimentally verified in the Wu experiment, through the decay of $^{60}_{27}\text{Co}$ isotopes [39].

A remarkable success of the LHC physics programme was the discovery of the Higgs boson in 2012 by the ATLAS and CMS experiments [1, 2], which is the final building block of the Standard Model. The Higgs particle is the only scalar (spin-0) boson. In the Standard Model the particles acquire their mass through their coupling to the Higgs field. The Higgs mass has been measured to be $125.09 \pm 0.21(\text{syst}) \pm 0.11(\text{stat})$ GeV [27].

Force	Name	Symbol	Number	Mass [GeV]	Associated Charge
Electromagnetic	Photon	γ	1	$< 1 \cdot 10^{-25}$ eV	electric
Strong	Gluons	g_{ij}	8	$< 1 \cdot 10^{-18}$ eV & colour	
Weak	W	W^\pm	2	80.385 ± 0.015 GeV	weak isospin
	Z	Z^0	1	91.187 ± 0.002 GeV	weak isospin

Table 2.2: The interactions of the SM and their mediating gauge bosons. Masses are taken from [27].

2.1.2 Quantum Electrodynamics

Quantum Electrodynamics (QED) was the first quantum field theory. It is based on a coherent relativistic and quantum mechanical description of the electrons and the transformation of classical Maxwell equations into the relativistic description. The Lagrangian of the Dirac equation, describing free spin-1/2 particles with mass m , is given by

$$\mathcal{L} = (i\bar{\psi}\gamma^\mu\partial_\mu - m)\psi \quad (2.1)$$

The upper and lower greek indices run from 0 to 3 and are summed over according to the Minkowski metric. The γ^μ are known as the *Dirac* or *Gamma* matrices and are four linearly-independent, traceless Hermitian 4×4 matrices and ∂_μ denotes the space-time derivative. Equation 2.1 is invariant under global gauge transformations

$$\psi(x) \rightarrow \psi'(x) = e^{i\alpha}\psi(x), \quad \bar{\psi}(x) \rightarrow \bar{\psi}'(x) = e^{i\alpha}\bar{\psi}(x), \quad (2.2)$$

where the phase $i\alpha$ is independent of the spacetime x . In contrast, the local gauge invariance corresponds to demanding invariance for phases $i\alpha(x)$ which are chosen independently at each spacetime point. In this case the partial derivative, $\partial_\mu\alpha(x)$ violates the local gauge invariance. The solution is found by replacing the ordinary derivative ∂_μ by the covariant derivative D_μ ,

$$D_\mu \equiv \partial_\mu + ieA_\mu, \quad (2.3)$$

where a local gauge field A_μ couples to the Dirac fermions of charge e . To arrive at the complete QED Lagrangian, a free term for the gauge field of the form $F_{\mu\nu}F^{\mu\nu}$ must be introduced, with $F_{\mu\nu} \equiv \partial_\mu A_\nu - \partial_\nu A_\mu$. This free field can be interpreted as the photon field. It must be massless, as otherwise local gauge invariance would not hold. The QED Lagrangian is thus given by

$$\mathcal{L} = -\frac{1}{4}F_{\mu\nu}F^{\mu\nu} + i\bar{\psi}\gamma^\mu D_\mu\psi - m\bar{\psi}\psi = -\frac{1}{4}F_{\mu\nu}F^{\mu\nu} + i\bar{\psi}\gamma^\mu\partial_\mu\psi - e\bar{\psi}\gamma^\mu\psi A_\mu - m\bar{\psi}\psi. \quad (2.4)$$

The components can be identified as the free Lagrangian of the Dirac field, the free Lagrangian of the massless photon field and an interaction term between the photon and the Dirac field. Since the phase transformations $e^{i\alpha}$ belong to the group of unitary 1×1 matrices, the underlying symmetry of the QED is denoted as U(1) gauge invariant.

The relativistic Maxwell equations are found as the equations of motions, derived from Eq. 2.4 using the Euler-Lagrange equation with respect to A_μ . Furthermore applying Noether's theorem to Eq. 2.4 one finds the continuity equation, i.e. the conservation of local charges expressed as: $j_\mu(x) \propto -\psi\gamma_\mu\psi$. Hence the conservation of the electric charge is the conserved quantity of the U(1) symmetry of QED.

2.1.3 Quantum Chromodynamics

The interactions between quarks and gluons are described by a non-Abelian gauge theory called *Quantum Chromodynamics* (QCD). It follows from the invariance under the $SU(3)_C$ transformation between the colour states. Each quark comes in three experimentally equivalent colours denoted red, green and blue, each anti-quark comes in the the anti-colours, anti-red, anti-green, anti-blue. They are represented as spinors

$$\psi_q = \begin{pmatrix} \psi_{q_r} \\ \psi_{q_g} \\ \psi_{q_b} \end{pmatrix}, \quad (2.5)$$

with $q \in [u, c, t, d, s, b]$. The underlying $SU(3)_C$ gauge group implies the existence of eight gluons, which mediate the colour charge interactions between the quarks. The gluon fields are expressed by G_μ^j , where the colour index j runs from 1...8. Each of these gluon fields acts on the quark colour through one of the generator matrices of the $SU(3)_C$. These are expressed as $T_j = \lambda_j/2$, where λ_j are the 3×3 Gell-Mann matrices, and j is the colour index. They are non-commuting (non-Abelian) and satisfy the Lie-algebra, such that

$$[T_i, T_j] = i f_{ijk} T_k, \quad (2.6)$$

where f_{ijk} are the totally antisymmetric structure constants. Equivalent to QED, the Lagrangian for QCD is derived by requiring local gauge invariance under $SU(3)_C$ transformations, i.e.

$$\psi_q(x) \rightarrow \psi'_q(x) \rightarrow e^{igs\alpha^j(x)T^j} \psi_q(x), \quad (2.7)$$

where g_s is the coupling constant and $\alpha_j(x)$ ($j = 1...8$) are real differentiable functions of x . The QCD Lagrangian can be written as

$$\mathcal{L}_{\text{QCD}} = i\bar{\psi}_q \gamma^\mu D_\mu \psi_q - m\bar{\psi}_q \psi_q - \frac{1}{4} G_{\mu\nu}^j G^{\mu\nu,j}, \quad (2.8)$$

where D^μ is the covariant derivative and $G^{\mu\nu,j}$ is the field strength tensor, given by:

$$D_\mu \equiv \partial^\mu + i \frac{g_s}{2} \lambda_j G_\mu^j, \quad (2.9)$$

$$G^{\mu\nu,j} \equiv \partial^\mu G_\nu^j - \partial^\nu G_\mu^j - g_s f^{jkl} G_\mu^k G_\nu^l. \quad (2.10)$$

Unlike in QED the non-commutativity of the group leads to an additional term $-g_s f^{jkl} G_\mu^k G_\nu^l$, which incorporates the interaction of two gluon fields. These are responsible for the three- and four-point self-interactions of the gluon and lead to the unusual energy scaling behaviour discussed in the introduction.

2.1.4 Perturbation Theory and Renormalisation

Most equations of motions derived from the Standard Model Lagrangian cannot be solved analytically, but depend on perturbation theory. Consequently the solution is represented as an expansion in the order of the coupling constants. A simple scattering process S of the initial state $|\psi_i\rangle$ of a system into the state $|\psi_f\rangle$ is given by

$$|\psi_f\rangle = S \psi_i = \left(\sum_{n=0}^{\infty} g^n C_n \right) \phi_i. \quad (2.11)$$

For demonstration purposes, it is assumed that only one interaction between charges g exist, which is chosen to have a coupling constant $\alpha \propto g^2$. The different coefficients C_n in the perturbation series can be identified with a particular physical process contributing to the total interaction. While C_0 describes no interaction, C_1 is zero, to conserve energy and momentum. Hence, the leading-order (LO) interaction arises from C_2 and is related to a $2 \rightarrow 2$ process, containing two vertices with coupling $\sqrt{\alpha}$. The next-to-leading order (NLO) describes processes with three vertices, such as initial- or final-state radiation, given by the coefficient C_3 . The physical observables for a final state ψ_f are calculated from the matrix element

$$\mathcal{M}_{fi} = \langle \psi_f | \psi \rangle = \langle \psi_f | S | \psi_i \rangle. \quad (2.12)$$

For instance the total cross section is proportional to the matrix element squared $|\mathcal{M}_{fi}|^2$ and the constant term contains the available phase space of the transition. The terms C_n of the perturbation series can be displayed as Feynman diagrams. Due to the rapidly increasing number of diagrams per additional order, usually only the first few orders are calculated. In general the order of the expansion coefficient reflects the current precision of the experimental result, such that the first few orders are sufficient. Problems arise in higher order diagrams, which contain virtual loops, as these virtual particles are not constrained, such that all possible energy-momentum combinations in the loop are to be integrated over, ultimately leading to infinite cross sections when using finite orders in the expansion (ultra-violet divergencies). These can be circumvented by dimensional regularisation and a renormalisation mechanism, in which the divergencies are absorbed by the redefinition of the fields, coupling constants and masses, using renormalisation constants at an arbitrary energy scale μ_R , the renormalisation scale. Through the introduction of μ_R , the coupling constant α itself becomes a function of μ_R and is divergent. Since μ_R is an arbitrary parameter, physical observables depending on α must remain independent of it. Therefore α must satisfy the renormalisation group equation

$$\frac{d\alpha(\mu^2)}{d \ln \mu^2} = \beta(\alpha(\mu^2)), \quad \beta(\alpha) = \alpha^2(b_0 + b_1\alpha + b_2\alpha^2 + \dots). \quad (2.13)$$

The function $\beta(\alpha)$ is the so-called *beta-function*, which relates α to μ_R at some reference scale μ . It can be expanded perturbatively in terms of α . The value of $\alpha(\mu^2)$ has to be measured experimentally, which shows that the coupling strength is a free parameter of the Standard Model Lagrangian. In general only the first few orders of β are calculable, thereafter the physical observables become μ_R dependent, but remain finite. A typical choice for μ_R is the momentum transfer Q of the interaction, such that the coupling constant is expressed as $\alpha(Q^2)$. Taking the electromagnetic interaction as an example, the renormalised electromagnetic coupling constant at leading order becomes

$$\alpha_{em}(Q^2) = \frac{\alpha_{em}(\mu^2)}{1 - \frac{\alpha_{em}(\mu^2)}{3\pi} \ln\left(\frac{Q^2}{\mu^2}\right)}. \quad (2.14)$$

The running of α_{em} is shown in Fig. 2.1 (left), extracted from Bhabha scattering measurements at the LEP experiments in three different energy regimes and compared with the theoretical predictions from QED. An increase of the coupling at larger energies is visible, though at a scale such that perturbation theory ($\alpha_{em} \ll 1$) is applicable at all relevant energy levels. The decrease of α_{em} with decreasing energy scale Q can be viewed as a screening of the electromagnetic charge by the vacuum polarisation.

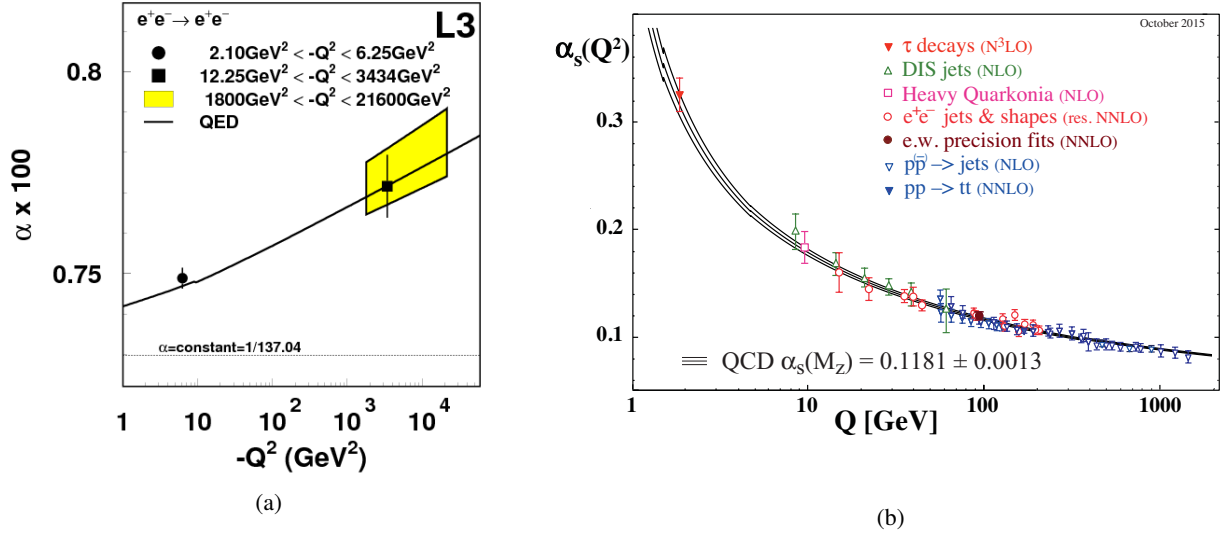


Figure 2.1: Electromagnetic coupling α_{em} as a function of Q^2 determined in measurements and compared with QED predictions, shown as the solid line (a) [40]. Summary of the measurements of the strong coupling α_s as a function of the energy scale Q , extracted at different orders of the QCD perturbation theory, overlaid with the theoretical predictions (solid lines)(b) [27].

The NLO renormalised strong coupling constant, setting $\mu_R = Q$, is

$$\alpha_s(Q^2) = \frac{12\pi}{(33 - 2n_f) \ln\left(\frac{Q^2}{\Lambda_{\text{QCD}}^2}\right)}, \quad \text{with } \Lambda^2 = Q^2 \exp\left(\frac{12\pi}{(33 - n_f)\alpha_s(\mu^2)}\right), \quad (2.15)$$

where n_f is the number of quark flavours, with masses smaller than μ . The positive denominator is the origin of the asymptotic freedom, i.e. the fact that the coupling becomes weaker at high momenta. In contrast, at low momenta the coupling grows strongly, causing gluons and quarks to be strongly bound into hadrons. Thus perturbation theory is only applicable if $\mu \gg \Lambda$, i.e. $\alpha_s(\mu^2) \ll 1$. The regime at which the coupling diverges is often expressed by the constant $\Lambda \rightarrow \Lambda_{\text{QCD}}$, where the scale Λ_{QCD} is of the order of 200 MeV. The running of α_s is measured over a large energy range, from the mass of the τ -lepton to the TeV at the LHC. The values are derived from hadronic τ -lepton decays, deep inelastic scattering data, electron-positron annihilation, lattice QCD calculation and electroweak precision fits. A summary of the measurements is shown in Fig. 2.1. Good consistency between the measured and the predicted values is found. The world average of the strong coupling, evaluated at the scale of the Z boson mass m_Z , is given by $\alpha_s(m_Z) = 0.1181 \pm 0.0013$ [27].

2.1.5 Electroweak Unification

An attempt to describe the weak force was made by Fermi in 1934, describing the β decay as a point-like interaction between four fermions [41]. Although this approach yields a description of weak interactions at low energies, a modification for higher energies is needed, where the exchange of W and Z bosons cannot be ignored. Later the Wu experiment proved the prediction of Lee and Yang [39, 42], that the charged weak interaction does not conserve parity. Actually the charged weak interaction couples only

to left-handed particles, leading to maximal parity violation.

Glashow, Weinberg and Salam were able to describe the weak and electromagnetic interactions in a unified way [43–45]. This electroweak interaction uses a gauge group, with spontaneous symmetry breaking based on the $SU(2)_L \otimes U(1)_Y$ group. The $SU(2)_L$ is the group of the weak isospin transformations and $U(1)_Y$ is the group of the weak hypercharge transformations. The particles are described in terms of massless Dirac spinors $\psi(x)$. They are divided according to their parity into left- and right-handed fermion fields given by $\psi_L = \frac{1}{2}(1 - \gamma_5)\psi$ and $\psi_R = \frac{1}{2}(1 + \gamma_5)\psi$, where $\gamma_5 = \gamma^5 = i\gamma^0\gamma^1\gamma^2\gamma^3$. The invariance of the Lagrangian implies the conservation of certain quantum numbers. These are the weak isospin charges I_W^i ($i = 1, 2, 3$) and the weak hypercharge Y_W . The weak hypercharge is related to the electric charge by the Gell-Mann-Nishijama relation, defined as $Y_W = 2(Q - I_W^3)$, where Q is the electric charge. The left-handed fermions act as doublets, denoted Ψ_L under $SU(2)_L$ transformations and carry weak isospin $I_W^3 = \pm 1/2$, while the right-handed fermions, called ψ_R are singlets with $I_W^3 = 0$. Table 2.3 shows the Standard Model quarks and leptons classified as weak isospin multiplets of identical hypercharge. It should be noted that for the quarks the $SU(2)_L$ gauge group eigenstates differ from the mass eigenstates. These eigenstates are related by the CKM matrix.

Following the principle of the derivation of the QED and QCD Lagrangian, invariance of the Lagrangian under local phase transformations of the $SU(2)_L$ and $U(1)_Y$ group is required:

$$\Psi_L(x) \rightarrow \Psi'_L(x) = e^{\frac{i}{2}g\tau_j w_j(x) + \frac{i}{2}g'Yf(x)}\Psi_L(x), \quad (2.16)$$

$$\psi_R(x) \rightarrow \psi'_R(x) = e^{ig'Yf(x)}\psi_R(x), \quad (2.17)$$

where g and g' are the coupling constants, $w_j(x)$, $j \in \{1, 2, 3\}$ and $f(x)$ are real differentiable functions of x . The generator of the $U(1)_Y$ group is the weak hypercharge Y_W and the three Pauli matrices τ_i are the generators of the $SU(2)_L$ group:

$$\tau_1 = \begin{pmatrix} 0 & 1 \\ 1 & 0 \end{pmatrix}, \quad \tau_2 = \begin{pmatrix} 0 & -i \\ i & 0 \end{pmatrix}, \quad \tau_3 = \begin{pmatrix} 1 & 0 \\ 0 & -1 \end{pmatrix}. \quad (2.18)$$

The particles are described by massless Dirac spinor fields $\Psi(x)$, which are separated into the left- and right-handed components, as described above. Analogously to the interaction of the electromagnetic current with the photon field in QED, an isotriplet of vector gauge bosons W_μ^i , $i \in \{1, 2, 3\}$ with coupling g is introduced to gauge the $SU(2)_L$ and a vector boson B_μ to gauge the $U(1)_Y$ symmetry with coupling g' . The Lagrangian describing the fermion interactions $\mathcal{L}_{\text{Matter}}$ is given by

$$\mathcal{L}_{\text{Matter}} = \sum_{\text{Generations}} i\bar{\Psi}_L \gamma_\mu D^\mu \Psi_L + i\bar{\psi}_{\ell_R} \gamma_\mu D^\mu \psi_{\ell_R} + i\bar{\Psi}_Q \gamma_\mu D^\mu \Psi_Q + i\bar{\psi}_{u_R} \gamma_\mu D^\mu \psi_{u_R} + i\bar{\psi}_{d_R} \gamma_\mu D^\mu \psi_{d_R}, \quad (2.19)$$

where $L = (v_{\ell_L}, \ell_L)^T$ are the left-handed $SU(2)$ lepton doublets, $Q = (u_L, d_L)^T$ are the corresponding up- and down-type quark doublets and ℓ_R, u_R, d_R the corresponding right-handed singlets. The covariant derivatives are formulated to assure gauge invariance

$$D^\mu \Psi_L = \left[\partial^\mu + \frac{1}{2}ig\tau_j W_j^\mu - \frac{1}{2}ig' B^\mu \right] \Psi_L, \quad (2.20)$$

$$D^\mu \psi_R^\ell = [\partial^\mu + ig' B^\mu] \psi_R^\ell. \quad (2.21)$$

Identifying the corresponding conserved charges and neutral currents, the physical gauge fields can be extracted as linear combinations of the W_μ^i and B_μ vector fields

$$W_\mu^\pm = \frac{1}{\sqrt{2}} (W_\mu^1 \mp iW_\mu^2), \quad (2.22)$$

$$\begin{pmatrix} A_\mu \\ Z_\mu \end{pmatrix} = \begin{pmatrix} \cos \theta_W & \sin \theta_W \\ -\sin \theta_W & \cos \theta_W \end{pmatrix} \begin{pmatrix} B_\mu \\ W_\mu^3 \end{pmatrix}, \quad (2.23)$$

where θ_W is the weak mixing angle, W_μ^\pm are identified with the charged W^\pm bosons, A_μ with the photon, and Z_μ with the Z boson. The electric charge is related to the weak mixing angle through the relation

$$e = g' \cos \theta_W = g \sin \theta_W. \quad (2.24)$$

The electroweak Lagrangian is completed by a $SU(2)_L \otimes U(1)_Y$ gauge invariant term describing the dynamics of the gauge fields W_μ^i and B_μ fields:

$$\mathcal{L}_{W,B} = -\frac{1}{4} W_{\mu\nu}^i W^{i,\mu\nu} - \frac{1}{4} B_{\mu\nu} B^{\mu\nu}, \quad (2.25)$$

where the field strength tensors are defined by

$$W_{\mu\nu}^i = \partial_\mu W_\nu^i - \partial_\nu W_\mu^i - g W_\nu^j \times W_\mu^k \quad (2.26)$$

$$W_{\mu\nu}^i = \partial_\mu W_\nu^i - \partial_\nu W_\mu^i - g \epsilon_{ijk} W_\mu^j W_\nu^k \quad i, j, k = 1, 2, 3 \quad (2.27)$$

$$B_{\mu\nu} = \partial_\mu B_\nu - \partial_\nu B_\mu. \quad (2.28)$$

The ϵ_{ijk} in last term in Eq. 2.27 are the structure constants arising from the non-Abelian nature of the underlying $SU(2)_L$ gauge group. This term describes the triple and quartic self-interactions of the gauge bosons.

The complete Lagrangian for the electroweak interaction is expressed by combining the kinetic and the interaction term

$$\mathcal{L}_{EW} = \mathcal{L}_{\text{Matter}} + \mathcal{L}_{W,B} \quad (2.29)$$

The corresponding interaction terms of the QCD Lagrangian can be easily added to the above Lagrangian to complement the Standard Model interactions. Again the invariance of the $SU(2)_L \otimes U(1)_Y$ group under local phase transformations does not allow for a simple mass term of the form $\frac{1}{2} m^2 B_{\mu\nu} B^{\mu\nu}$. The *Higgs mechanism*, through which particles acquire mass in the Standard Model, is introduced in the next section.

2.1.6 Electroweak theory and the Higgs mechanism

The photon is the only massless electroweak gauge boson. Explicit mass terms for the vector boson fields violate the gauge invariance of the Lagrangian. This implies that the $SU(2)_L \otimes U(1)_Y$ gauge symmetry must be broken down to $U(1)_{\text{em}}$. This breaking is accomplished by the *Higgs mechanism*, also named Englert-Brout-Higgs mechanism after its originators, which is furthermore responsible for the generation of fermion masses [46–49]. The *Higgs mechanism* leaves the Lagrangian, but not the vacuum state, invariant under electroweak transformations. This principle is called *spontaneous symmetry breaking*. In its simplest formulation an additional complex scalar $SU(2)_L$ doublet of hypercharge $Y = 1$, with

Fermions			I_W^3	Y
$\begin{pmatrix} u \\ d \end{pmatrix}_L$	$\begin{pmatrix} c \\ s \end{pmatrix}_L$	$\begin{pmatrix} t \\ b \end{pmatrix}_L$	1/2	1/3
u_R	c_R	t_R	-1/2	1/3
d_R	s_R	b_R	0	4/3
$\begin{pmatrix} \nu_e \\ e^- \end{pmatrix}_L$	$\begin{pmatrix} \nu_\mu \\ \mu^- \end{pmatrix}_L$	$\begin{pmatrix} \nu_\tau \\ \tau^- \end{pmatrix}_L$	0	-2/3
e_R	μ_R	τ_R	1/2	-1
			-1/2	-1
			0	-2

Table 2.3: Representation of the Standard Model fermion content according to their weak isospin. The left-handed fermions appear as doublets, while the right-handed fermions are singlets. The right-handed neutrinos do not interact in according to the Standard Model, and are thus neglected.

an electrically charged component ϕ^+ and an electrically neutral component ϕ^0 is introduced

$$\phi = \begin{pmatrix} \phi^+ \\ \phi^0 \end{pmatrix}. \quad (2.30)$$

The contribution to the Standard Model Lagrangian is invariant under $SU(2)_L \otimes U(1)_Y$ transformations and given by

$$\mathcal{L}_{\text{Higgs}} = (D_\mu \phi)^\dagger (D^\mu \phi) - V(\phi), \quad (2.31)$$

where D^μ is the covariant derivative. The *Higgs potential* $V(\phi)$ describes the self-interactions of the ϕ and has the form

$$V(\phi) = \mu^2 (\phi^\dagger \phi) + \lambda (\phi^\dagger \phi)^2. \quad (2.32)$$

The formula has two real free parameters μ^2 and λ , where λ must be positive to comply with vacuum stability. If μ^2 is chosen to be positive, the Higgs potential has a minimum at $\langle \phi \rangle = 0$. However, conventionally one chooses $\mu^2 < 0$, such that the potential is minimised at $|\langle \phi \rangle| = 2\mu^2/\lambda \equiv v^2/2$, where v is the vacuum expectation value. The choice of any particular minimum (*vacuum state*), breaks the $SU(2)_L \otimes U(1)_Y$ symmetry. The vacuum state is chosen to be electrically neutral:

$$\phi = \frac{1}{\sqrt{2}} \begin{pmatrix} 0 \\ v \end{pmatrix}. \quad (2.33)$$

It is quantised by the expansion around the minimum resulting in one massive and three massless bosons, the latter being the *Goldstone bosons*. By choice of a suitable gauge, the massless Goldstone boson fields are eliminated and the Higgs field becomes

$$\phi = \frac{1}{\sqrt{2}} \begin{pmatrix} 0 \\ v + H(x) \end{pmatrix}. \quad (2.34)$$

with the massive Higgs boson H . The Lagrangian from Eq. 2.31 now reads

$$\mathcal{L}_{\text{Higgs}} = \frac{1}{2} (\partial_\mu H) (\partial^\mu H) + \frac{g^2}{4} (v+H)^2 W_\mu^+ W^{-\mu} + \frac{g^2}{8(\cos\theta_W)^2} (v+H)^2 Z_\mu Z^\mu + \frac{\mu^2}{2} (v+H)^2 - \frac{\lambda}{16} (v+H)^4. \quad (2.35)$$

By virtue of the chosen neutral vacuum state, the photon does not acquire mass. In addition, there are also terms describing interactions between the H and the W^\pm and Z bosons with couplings proportional

to the vector boson masses, as well as self-coupling terms of the H . This leads to the following mass terms

$$m_H = \sqrt{2}\mu \quad (2.36)$$

$$m_W = \frac{1}{2}gv \quad (2.37)$$

$$m_Z = \frac{m_W}{\cos\theta_W}. \quad (2.38)$$

The vev v follows from the known value of m_W to be 246 GeV.

Fermion masses can be generated via the coupling of the Higgs SU(2) doublet to the left-handed fermion SU(2) doublets and the right-handed fermion singlets, called *Yukawa coupling*. The corresponding term in the Lagrangian has the form

$$\mathcal{L}_{\text{Yukawa}} = -\bar{\Psi}_L G_\ell \Psi_{\ell_R} \phi - \bar{\Psi}_Q G_u \Psi_{u_R} \phi^C - \bar{\Psi}_Q G_d \Psi_{d_R} \phi + h.c., \quad (2.39)$$

where h.c. is the hermitian conjugate and $\phi^C = i\tau_2\phi^*$ the charge conjugated Higgs doublet. $\Psi_L, \Psi_Q, \Psi_{\ell_R}, \Psi_{u_R}$ and Ψ_{d_R} are 3-component vectors in generational space. G_ℓ, G_u and G_d are 3×3 Yukawa coupling matrices, allowing for cross-generation mixing. Replacing the Higgs field by its vacuum expectation value, one finds the fermion mass matrix

$$\mathbf{m}_f = \frac{v}{\sqrt{2}} \mathbf{y}_f. \quad (2.40)$$

The mass eigenstates of the quarks are obtained by unitary transformations of the quark fields; the diagonalised mass matrices for up- and down-type quarks are

$$\mathbf{m}_u = \frac{v}{\sqrt{2}} (U_L^u)^\dagger G_u U_R^u, \quad \mathbf{m}_d = \frac{v}{\sqrt{2}} (U_L^d)^\dagger G_d U_R^d. \quad (2.41)$$

The product

$$V_{CKM} = (U_L^u)^\dagger U_L^d \quad (2.42)$$

is the aforementioned CKM matrix, describing the quark mixing. A standard representation of CKM matrix is the Wolfenstein parametrisation, utilising three angles and a CP-violating phase.

Neutrino masses cannot be generated through the coupling to the Higgs, as right-handed neutrinos are not incorporated into the Standard Model. It is further not possible for neutrino masses to arise from perturbative corrections. This would destroy the $B - L$ symmetry, where B is the baryon number and L the lepton number, which arises as an accidental symmetry of the Standard Model Lagrangian. Hence a neutrino mass term requires the extension of the Standard Model by new physics. In the simplest extension a heavy right-handed neutrino is added to the Standard Model. Neutrino masses can then be generated using the Higgs mechanism. However due to the very tiny expected neutrino masses this leads to extremely small couplings of the right-handed neutrinos to the Higgs field and SU(2)_L doublets. By abandoning lepton number conservation, neutrino masses can thereafter be generated via a Seesaw mechanism, which is elaborated on in Section 2.2.1.

2.1.7 Limitations of the Standard Model

Albeit the Standard Model being extremely successful in explaining most of the experimental measurements to a high precision, there are some observations and theoretical indications, that call for a more

complete theory (Grand Unified Theory (GUT)), into which the Standard Model can be embedded. A brief summary of the most important shortcomings of the Standard Model is given in the following.

Quantum Gravity : One of the most obvious shortcomings is the lack of incorporating the *gravitational force*, which is described by general relativity. For consistency, a renormalisable quantum field theory should exist. Current attempts are made in the field using String Theory [50] or loop quantum gravity [51], even though quantum gravitational effects only become apparent at the Planck Scale ($\Lambda_{\text{Planck}} = 10^{19}$ GeV), and thus the effect on particle physics is negligible. This indicates that the Standard Model is only an effective theory with validity up to a cutoff scale Λ , beyond which new physics appears.

Dark Matter and Dark Energy : Astronomical observations indicate that the baryonic matter described by the Standard Model only accounts for a small fraction of the gravitationally interacting matter of the universe. Recent measurements of the cosmic microwave background reveal that the baryonic matter constitutes 4.9 % of the universe, while dark energy accounts for 68.3 % and dark matter for 26.8 % of the universe [52]. Neither dark energy nor dark matter can be explained by the Standard Model.

Baryon asymmetry and CP Violation : The observation of the baryon asymmetry in the universe [53] cannot be explained by the CP-violating phase from the CKM of the Standard Model. To generate an unequal amount of baryonic matter and anti-matter in the universe the three Sakharov conditions [54] must be fulfilled: 1. violation of baryon number B , 2. microscopic C and CP violation, and 3. loss of thermal equilibrium. Otherwise the rate of creation of baryons equals the destruction rate, resulting in no asymmetry. In the Standard Model, however, the baryon number is conserved in the perturbative regime and the allowed CP violation through the complex phase of the CKM matrix is insufficiently small to explain the observed asymmetry. One solution is found in leptogenesis scenarios, where the baryon asymmetry arises through a previously existing lepton asymmetry, generated by the decays of sterile neutrinos [55].

Fine-tuning and Hierarchy : The Higgs boson mass can be expanded using perturbation theory as

$$m_H^2(p^2) = m_{0,H}^2 + Cg^2 \int_p^{\Lambda^2} \Lambda^2 dk^2 + \dots, \quad (2.43)$$

where $m_{0,H}^2$ is the tree-level Higgs boson mass, g is the coupling constant, C a model-dependent constant and Λ is the scale up to which the SM is assumed to be valid. The integral includes divergent contributions at loop level. If no new physics appears, the reference scale is at the Planck scale $\Lambda_{\text{Planck}} \sim 10^{19}$ GeV. The Higgs mass of ~ 126 GeV is a result of an immense cancellation of the loop corrections and the bare Higgs mass of 30 orders of magnitudes. This can be regarded as unnatural, and is known as the *hierarchy problem*.

Free Parameters of the Standard Model: The minimal version of the Standard Model, contains 19 arbitrary parameters: three gauge coupling parameters, usually chosen as the strong coupling constant α_S , the weak mixing angle θ_W and the fine structure constant α_{em} , two parameters to specify the Higgs potential λ and μ^2 , six quark masses, three angles and one phase that specify the CKM matrix, three charged lepton masses, and an additional phase θ_{QCD} to allow for non-perturbative CP violation in QCD. Moreover the mere fact that neutrinos have mass adds at least another three neutrino masses, three mixing angles and a CP-violating phase. This is further expanded if neutrinos are Majorana particles. The origin of these parameters, and the large scale

between them, for instance in the mass range, is unknown. But it is a common belief that a fundamental theory of nature should have fewer free parameters.

Unification of the Forces : The evolution of the coupling constants of the strong, the weak and the electromagnetic force as a function of the energy scale Q , shows that there is no convergence to a common value. This can be interpreted as a further hint to new physics.

Neutrino Oscillations : See next Section.

2.2 Neutrino Mass

Neutrinos were first postulated by Wolfgang Pauli in 1930 to explain the continuous electron energy spectrum in β decays. Within the Standard Model they are described by a chiral, left-handed neutrino field $\nu_{\ell,L}$ with $\ell = e, \mu, \tau$ together with their corresponding leptons or as right-handed sterile singlets ν_R . Since neutrinos are electrically neutral and do not carry colour, they interact only via the charged and neutral current weak interaction. The Standard Model neutrinos are massless, which is in clear contradiction to the compelling experimental evidence of neutrino oscillations. Oscillations imply that transitions between the different neutrino flavours occur due to non-vanishing neutrino masses leading to mixing between the flavours, which was first proposed by Pontecorvo in 1957 [56]. The first hints of neutrino oscillations date back to the Homestake experiment [28], which started in the 1960s, where the measured electron neutrino flux accounted only for 1/3 of the expected flux from the sun. These findings were confirmed by further solar neutrino experiments such as GALLEX [57], SAGE [58] or SNO [59]. The disappearance of atmospheric ν_μ and $\bar{\nu}_\mu$ was discovered in the Japanese experiment Super-Kamiokande [31], while this effect was first shown for reactor $\bar{\nu}_e$ at KamLAND [29]. Oscillations of ν_μ were also found in accelerator-based experiments such as MINOS [60] and T2K [61], which also lead to the first evidence for the appearance of ν_τ as a result from a $\nu_\mu \rightarrow \nu_\tau$ transition by the OPERA [62] and Super-Kamiokande [63] experiments.

Hence the neutrinos exist as three different flavour eigenstates $|\nu_\alpha\rangle$ ($i = \alpha, \beta, \gamma$) and three independent mass eigenstates $|\nu_i\rangle$ ($i = 1, 2, 3$)¹. The flavour eigenstates can now be expressed as a linear superposition of the mass eigenstates and vice versa,

$$|\nu_i\rangle = \sum_{\alpha=1}^3 U_{i,\alpha} |\nu_\alpha\rangle, \quad (2.44)$$

where the matrix U is referred to as the Pontecorvo-Maki-Nakgawa-Sakata mixing matrix [56, 64]. The neutrino oscillations depend on the mass-squared difference, $\Delta m_{ij}^2 \equiv m_i^2 - m_j^2$, between neutrino masses. Since all three neutrinos oscillate, there are two mass-squared differences, Δm_{21}^2 and Δm_{32}^2 . There are two possible hierarchies for the neutrino mass spectrum, the normal hierarchy, where $m1 < m2 < m3$, and the inverted hierarchy, where $m3 < m1 < m2$. In general Δm_{21}^2 and the mixing angle θ_{12} are responsible for the oscillation of the solar ν_e neutrinos while Δm_{31}^2 and θ_{23} are associated with the atmospheric ν_μ and $\bar{\nu}_\mu$ oscillations. Thus these values are often referred to as *solar* and *atmospheric* mass differences (angles). While much can be said about the neutrino mass-squared differences, the absolute neutrino masses are yet to be measured. Because the neutrino masses are many orders of magnitude smaller than the quark and lepton masses, so far only mass limits exist. This upper mass scale can be extracted from the larger of the two mass-squared differences measured in neutrino oscillation

¹ In general Greek indices indicate the flavour eigenstates and Latin indices are used for mass eigenstates

experiments [65]

$$\Delta m_{atm}^2 \sim 2.4 \times 10^{-3} \text{ eV}^2, \quad (2.45)$$

by taking the square root, one gets

$$\Delta m_{\nu}^{osc} \leq 0.05 \text{ eV}. \quad (2.46)$$

Direct measurements of the neutrino mass exploit the endpoint spectrum of the tritium β -decay [66], using the kinematical mass

$$m_{\beta} = \sqrt{\sum_i |U_{ei}|^2 m_i^2}, \quad (2.47)$$

where U_{ei} are the elements in the first column of the PNMS matrix. The most stringent limits on the electron neutrino mass are extracted from the Troitzk and the Mainz experiments with $m_{\nu_e} < 2.05 \text{ eV}$ and $m_{\nu_e} < 2.3 \text{ eV}$, respectively, at 95 % confidence level [67, 68]. The upcoming KATRIN experiment in Karlsruhe aims to decrease this limit to $m_{\nu_e} = 0.2 \text{ eV}$ in five years of running [69]. Further information on neutrino masses can be extracted from fits to cosmological data using the Cosmic Microwave Background data from Planck in conjunction with supernovae data and data from galaxy clustering. These are used to constrain the sum of the light neutrino masses $\sum_{i=1}^3 m_i \leq 0.23$ [70]. However, this limit is model and analysis dependent.

2.2.1 The Seesaw Mechanism

A simple solution to generate neutrino masses is the addition of right-handed neutrinos ν_R to the Standard Model. The mere fact that neutrinos are the only fermions with no electric charge in the Standard Model, allows the construction of both Dirac or Majorana type mass terms. A Dirac mass term for neutrinos has the form

$$\mathcal{L}_{\text{mass}}^D = -\bar{\nu}_L M^D \nu_R + h.c., \quad (2.48)$$

where M^D is a complex 3×3 matrix and $\nu = (\nu_{e,L} \quad \nu_{\mu,L} \quad \nu_{\tau,L})$. The neutrinos are Majorana particles, if their spinor field ψ satisfies the condition of being self-charge-conjugate $\psi = \psi^c \equiv C\bar{\psi}^T$, where C is the charge conjugation operator. This constraint leads to a reduction of the independent components in the spinor by a factor of two, as the particle is its own antiparticle. Hence the right-handed component can be simply expressed by $\nu_L^C = C\bar{\nu}_L^T$, such that a Majorana mass can be defined as

$$\mathcal{L}_{\text{mass}}^L = \frac{1}{2} \bar{\nu}_L^C M_L^M \nu_L + h.c., \quad (2.49)$$

$$\mathcal{L}_{\text{mass}}^R = \frac{1}{2} \bar{\nu}_R^C M_R^M \nu_R + h.c., \quad (2.50)$$

where M_L^M and M_R^M are complex, non-diagonal symmetric 3×3 matrices. The most general mass term that can be found for neutrinos thus combines all above terms,

$$\mathcal{L}_{\text{mass}} = \mathcal{L}_{\text{mass}}^D + \mathcal{L}_{\text{mass}}^L + \mathcal{L}_{\text{mass}}^R + h.c.. \quad (2.51)$$

By diagonalising the Dirac and Majorana mass terms, $\mathcal{L}_{\text{mass}}$ can be expressed in matrix form as

$$\mathcal{L}_{\text{mass}} = -\frac{1}{2} \bar{n}_L M^{D+M} (n_L)^c + h.c.. \quad (2.52)$$

where

$$n_L = \begin{pmatrix} \nu_L & (\nu_R)^C \end{pmatrix} \quad (2.53)$$

and

$$M^{D+M} = \begin{pmatrix} M_L^M & M_D \\ M_D^T & M_R^M \end{pmatrix}, \quad (2.54)$$

a symmetrical 6×6 matrix. Presenting the matrix in the form $M^{D+M} = UmU^T$, where U is an unitary 6×6 matrix and $m_{ik} = m_i \delta_{ik}$ ($i, k = 1, \dots, 6$), the mass term of the Lagrangian becomes

$$\mathcal{L}_{\text{mass}} = -\frac{1}{2} \overline{U^\dagger n_L} m (U^\dagger n_L)^C + h.c. = -\frac{1}{2} \sum_{i=1}^6 m_i \bar{\nu}_i \nu_i. \quad (2.55)$$

In the special case of only one neutrino generation the matrix equation is reduced to

$$\mathcal{L}_{\text{mass}} = \begin{pmatrix} \bar{\nu}_L^C & \bar{\nu}_R \end{pmatrix} \begin{pmatrix} m_L & m_D \\ m_D & m_R \end{pmatrix} \begin{pmatrix} \nu_L \\ \nu_R^C \end{pmatrix}, \quad (2.56)$$

with the mass matrix M

$$M = \begin{pmatrix} m_L & m_D \\ m_D & m_R \end{pmatrix}, \quad (2.57)$$

where the parameters m_L , m_D and m_R characterise the left-handed Majorana, Dirac and right-handed Majorana mass terms. Since the chiral fields ν_R and ν_L are no mass eigenstates, due to the existence of the off-diagonal terms m_D , the flavour eigenstates partaking in the weak interaction are superpositions of the different mass eigenstates. The positive mass eigenstates for this matrix are

$$m_{1,2} = \frac{1}{2} \left[m_L + m_R \pm \sqrt{(m_L - m_R)^2 + 4m_D^2} \right]. \quad (2.58)$$

Without loss of generality the right-handed neutrino fields ν_R are taken to be fields with a heavy mass, since the term violates the lepton number, and thus should be beyond the electroweak scale. On the other hand, m_D is set to the electroweak scale as the Dirac mass is supposed to be generated via the Higgs mechanism, hence $m_D \ll m_R$. Since the left-handed neutrino fields ν_L have non-zero isospin and hypercharge, the left-handed Majorana term is explicitly forbidden within this extension of the Standard Model ($m_L = 0$).

With these choices the mass eigenstates m_1 and m_2 can be expressed by

$$m_1 \approx \frac{m_D^2}{m_R} \quad (2.59)$$

$$m_2 \approx m_R \left(1 + \frac{m_D^2}{m_R^2} \right) \approx m_R. \quad (2.60)$$

As a consequence there is one neutrino with mass m_2 , at a mass scale $\Lambda_N = m_R$ of new physics, while the mass m_1 is very light, since it is suppressed by the factor m_D/m_R . This mechanism is the *seesaw mechanism*, which provides a solution for the comparably small size of the neutrino masses. In the general case of three families, m_D and m_R are 3×3 matrices.

The neutrino masses can be introduced, through extending the Standard Model Lagrangian with massless neutrinos by an non-renormalisable effective Lagrangian including a dimension-five operator of the

form

$$(O_5)_{ij} = \overline{L_{iL}^c} \tilde{\phi}^* \tilde{\phi}^\dagger L_{jL} \quad (2.61)$$

with

$$L_{iL} = \begin{pmatrix} \nu_{iL} \\ \ell_{iL} \end{pmatrix}, \quad i = 1, 2, 3 \quad (2.62)$$

being the left-handed lepton doublets, ϕ the Higgs field and $\tilde{\phi} = i\tau_2\phi^*$, with τ_i denoting the Pauli matrices. The dimension-five operator can be realised by three different interaction mechanisms beyond the Standard Model: 1. by the exchange of a heavy Majorana singlet fermion N_R , 2. by the introduction of a scalar triplet Δ with hypercharge $Y = 1$ and 3. by the exchange of a heavy Majorana triplet fermion Σ_R with $Y = 0$. Commonly these models are referred to as type-I, type-II and type-III seesaw models.

2.2.2 Type-I Seesaw Model

The type-I seesaw mechanism [71–75] is realised by extending the Standard Model particle content by right-handed fermionic singlets ν_R^α , of which, in the most general case, an arbitrary number can be introduced². Since these transform as singlets under the Standard Model gauge group, they are defined by the following $SU(3)_C \otimes SU(2)_L \otimes U(1)_Y$ quantum numbers

$$\nu_R^\alpha \sim (\mathbf{1}, \mathbf{1}, 0). \quad (2.63)$$

The Lagrangian now contains both a Yukawa interaction for the neutrinos to the Higgs field and a Majorana mass term for the neutrinos,

$$-\mathcal{L}_{\text{type-I}} \supset \mathcal{L}_Y + \mathcal{L}_M = -Y^v \tilde{\phi} \overline{L_{iL}} \nu_{jR} - \frac{1}{2} M_{ij} \overline{\nu_{iL}} \nu_{jR} + h.c., \quad (2.64)$$

where Y^v is a 3×3 matrix of couplings, $\tilde{\phi} = i\tau_2\phi^*$ as above, and M_{ij} is a 3×3 symmetric matrix. After spontaneous symmetry breaking, Dirac masses are generated for the neutrinos through the Yukawa term. A Feynman diagram of the type-I seesaw mass term is shown in Figure 2.4. Hence the full neutrino mass term after spontaneous symmetry breaking is given by

$$\mathcal{L}_{\text{type-I}} \supset -\frac{1}{2} \overline{(v_L \ v_R)^c} \begin{pmatrix} 0 & M_D \\ M_D^T & M_M \end{pmatrix} \begin{pmatrix} (v_L)^c \\ v_R \end{pmatrix} + h.c., \quad (2.65)$$

where M_M is the Majorana mass and

$$M_D = \frac{v}{\sqrt{2}} Y^v. \quad (2.66)$$

While the Dirac mass term connects the left-handed neutrino component from the doublet to the right-handed singlet neutrino, the Majorana mass term connects the right-handed neutrinos with their charge conjugates and thus violates lepton number by two units. The neutrino gauge interactions are not altered by the addition of the fermionic singlets.

For the general type-I seesaw mechanism, the Yukawa couplings are taken to be of the order of one. Therefore the values of M_D are of the order of the electroweak scale, such that the singlets would have a mass smaller than

$$M_M \leq 10^{14} \text{ GeV}, \quad (2.67)$$

² Though it should be noted that at least two singlets are required to explain the neutrino oscillation experiments.

if we have sub-eV light neutrinos. However, if the Yukawa couplings are much smaller, and assuming $M_D \approx m_e$, one gets

$$M_M \leq 1 \text{ TeV}, \quad (2.68)$$

which is in the reach of the LHC. Unfortunately, these neutrinos are singlets, and can only partake in electroweak processes through their mixing with the light neutrinos. Hence these processes are suppressed by a factor

$$|V_{\nu_L \nu_R}|^2 = \frac{M_D^2}{M_M^2}. \quad (2.69)$$

Therefore the observation of type-I seesaw neutrinos is experimentally very unlikely, unless the type-I seesaw mechanism is included in some further gauge extension of the Standard Model [76].

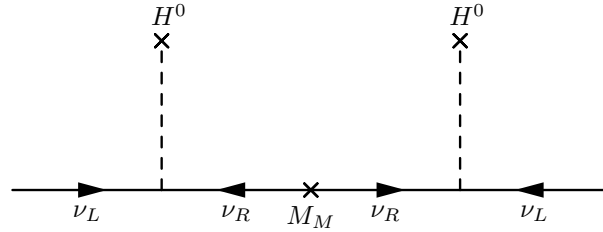


Figure 2.2: Feynman diagram of the Majorana neutrino mass term in the type-I seesaw mechanism, which introduces right-handed neutrinos ν_R , with a Majorana mass M_M .

2.2.3 Type-II Seesaw Model

The type-II seesaw mechanism neutrinos acquire mass through the Yukawa interaction between the neutrino doublets and a scalar triplet Δ added the Standard Model, with the following quantum numbers describing the Standard Model interaction

$$\Delta \sim (\mathbf{1}, \mathbf{3}, 1). \quad (2.70)$$

The relevant mass terms in the Lagrangian are thus expressed by

$$\mathcal{L}_{\text{type-II}} \supset \frac{1}{\sqrt{2}} Y_\Delta \bar{L}_{iL} i\tau_2 \Delta L_{iL} + h.c. - V(\phi, \Delta), \quad (2.71)$$

where

$$V(\phi, \Delta) = -M_\phi^2 \phi^\dagger \phi - M_\Delta^2 \text{Tr}(\Delta^\dagger \Delta) + (\mu \phi^T i\tau_2 \Delta^\dagger \phi + h.c.) + \text{quartic terms}. \quad (2.72)$$

A Feynman diagram of the type-II seesaw Majorana mass term is shown in Figure 2.3. The type-II seesaw mechanism can be tested directly at the LHC, if the mass scale of the triplet is within the reach of the LHC. Interesting signatures include the lepton number violating decay of the hypothesised doubly charged Higgs boson to same-sign leptons,

$$\Delta^{\pm\pm} \rightarrow e_i^\pm e_j^\pm, \quad (2.73)$$

which is the dominant channel if the triplet vev $v_\Delta < 10^{-4} \text{ GeV}$ [77]. Current constraints from the ATLAS experiment are 550 GeV [78]. For $v_\Delta < 10^{-4} \text{ GeV}$, the dominant decay channel is $\Delta^{\pm\pm} \rightarrow$

$W^\pm W^\pm$. The prospects of LHC searches are strongly related with the triplet mass splittings and the actual size of v_Δ . Further discussions on LHC search strategies can for instance be found in Refs. [77, 79].

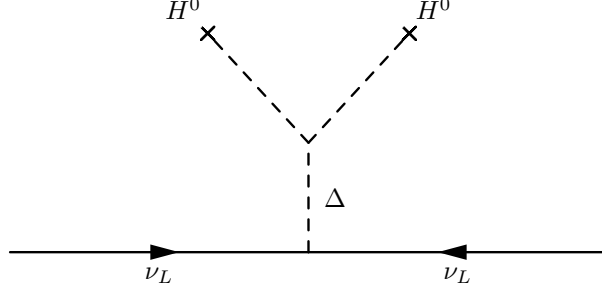


Figure 2.3: Feynman diagram of the Majorana neutrino mass term in the type-II seesaw mechanism, which introduces a scalar triplet Δ . The vacuum expectation value of the scalar triplet is induced by the vacuum expectation values of the neutral component of the Standard Model Higgs.

2.2.4 Type-III Seesaw Model

The type-III seesaw mechanism [10] is generally realised by the addition of three fermionic triplets Σ_j , each composed by three Weyl spinors of zero weak hypercharge. Utilising the four-component notation leads to Lagrangian terms for the mass and Yukawa coupling of the form

$$\mathcal{L}_{\text{type-III}} \supset \mathcal{L}_Y + \mathcal{L}_{\text{mass}} = -Y_{ij} \overline{L_{iL}} (\vec{\Sigma}_j \vec{\tau}) \tilde{\psi} - \frac{1}{2} M_{ij} \overline{\vec{\Sigma}_j^C} \vec{\Sigma}_j + h.c. \quad (2.74)$$

where Y is a 3×3 matrix of the Yukawa couplings and M is a symmetric 3×3 mass matrix. Additionally, all components of $\vec{\Sigma}_j$ have the same mass term. The charge eigenstates of the triplet are given by

$$\Sigma_j^+ = \frac{1}{\sqrt{2}} (\Sigma_j^1 - i\Sigma_j^2), \quad \Sigma_j^0 = \Sigma_j^3, \quad \Sigma_j^- = \frac{1}{\sqrt{2}} (\Sigma_j^1 + i\Sigma_j^2) \quad (2.75)$$

The physical particles are the charged Dirac fermions L_j and the neutral Majorana fermions N_j

$$L_j = \Sigma_j^- + \Sigma_j^{+c}, \quad N_j = \Sigma_j^0 + \Sigma_j^{0c}. \quad (2.76)$$

The right-handed neutrinos then are

$$L_{jL} = \Sigma_j^{+c}, \quad L_{jR} = \Sigma_j^-, \quad N_{jL} = \Sigma_j^{0c}, \quad N_{jR} = \Sigma_j^0. \quad (2.77)$$

After spontaneous symmetry breaking the neutrino mass term is given by

$$\mathcal{L}_{\nu, \text{mass}} = -\frac{1}{2} \overline{\begin{pmatrix} \nu_L & N_L \end{pmatrix}} \begin{pmatrix} 0 & v/\sqrt{2}Y \\ v/\sqrt{2}Y^T & M \end{pmatrix} \begin{pmatrix} \nu_R \\ N_R \end{pmatrix} + h.c. \quad (2.78)$$

The lepton masses include the 3×3 Yukawa matrix Y^ℓ and are defined by

$$\mathcal{L}_{\ell, \text{mass}} = -\overline{\begin{pmatrix} \ell_L & E_L \end{pmatrix}} \begin{pmatrix} v/\sqrt{2}Y^\ell & vY \\ 0 & M \end{pmatrix} \cdot \begin{pmatrix} \ell_R \\ E_R \end{pmatrix} + h.c.. \quad (2.79)$$

The kinetic term of the Lagrangian has the form

$$\mathcal{L}_{kin} = i\overline{\vec{\Sigma}}_j \gamma^\mu D_\mu \vec{\Sigma} \quad \text{with } j = 1, 2, 3 \quad (2.80)$$

and the covariant derivative is given by $D_\mu = \partial_\mu + ig\vec{T}\vec{W}_\mu$, where \vec{T} are 3×3 matrices and \vec{W}_μ are the SU(2) gauge fields. Since the triplets have zero hypercharge, no coupling to the B_μ term is present.

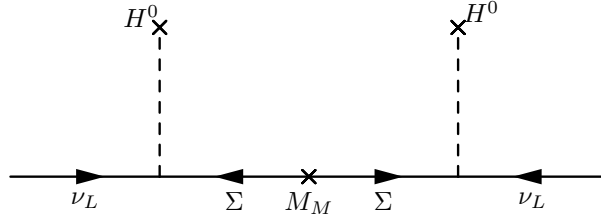


Figure 2.4: Feynman diagram of the Majorana neutrino mass term in the type-III seesaw mechanism, which introduces fermion triplets Σ with a Majorana mass M_Σ .

2.3 Phenomenological Overview of Heavy Lepton Production and Decay at the LHC

Within this thesis a search for heavy leptons giving rise to three-lepton final states is presented. High-mass trilepton resonances are motivated by several extensions of the Standard Model (SM). One of these is the type-III seesaw mechanism [10], introduced in the previous section, which explains the origin of small neutrino masses through the introduction of heavy SU(2) triplets with zero hypercharge. Moreover heavy leptons also arise in vector-like lepton (VLL) models. Vector-like fermions are fermions which couple non-chirally to the electroweak gauge group $SU(2)_L \times U(1)$. Vector-like leptons are invoked to explain the mass hierarchy between the different lepton generations [11]. They arise in various models beyond the Standard Model, such as in Little Higgs models [80] or composite Higgs models [12, 13] and models of warped extra dimensions [14, 15]. The model considered here introduces six $\mathbf{10}$ and $\overline{\mathbf{10}}$ SU(5) supermultiplets in a gauge-mediated supersymmetry framework [81]. The VLL have masses much larger than those of the SM leptons, and are defined as colourless, spin-1/2 fermions whose left- and right-handed chiral components have the same transformation properties under the weak-isospin SU(2) gauge group.

While Section 2.2 gives a general introduction to the theory of the seesaw mechanism this section provides an overview on the main phenomenological aspects of a simplified type-III seesaw model, used for the analysis, and the VLL model at the LHC. A brief overview of the current experimental status of related searches complements this section.

2.3.1 Simplified Type-III Seesaw Model

The type-III seesaw model used in this thesis applies a few restrictions to the more generic model presented in the previous section. The simplified model is derived in Ref. [16], and is based on the generic seesaw model presented in Ref. [82], which includes a generic number of triplets. Since the production cross section of the triplet scales with mass, it is valid to assume that the lightest triplet will

be produced most abundantly at the LHC and thus be the first to be discovered. Hence the simplified type-III seesaw model extends the Standard Model by adding a single fermionic triplet. This reduces the mass matrix M_Σ to a scalar and the new Yukawa couplings from a 3×3 matrix to a vector:

$$Y_\Sigma = (Y_{\Sigma_e} \quad Y_{\Sigma_\mu} \quad Y_{\Sigma_\tau}). \quad (2.81)$$

In addition the simplified model assumes all parameters to be real, consequently neither the phases of the Yukawa coupling nor the phases of the PNMS matrix are taken into account. This changes $\epsilon = v^2/2Y_\Sigma^\dagger M_\Sigma^{-2} Y_\Sigma$ to a 3×3 matrix with the elements

$$\epsilon_{\alpha\beta} = \frac{v^2}{2} M_\Sigma^{-2} Y_{\Sigma_\alpha} Y_{\Sigma_\beta} \quad (2.82)$$

and the corresponding ϵ' is a scalar with

$$\epsilon' = \frac{v^2}{2} M_\Sigma^{-2} (Y_{\Sigma_e}^2 + Y_{\Sigma_\mu}^2 + Y_{\Sigma_\tau}^2). \quad (2.83)$$

At last the couplings are expressed in terms of the mixing parameters, $V_\alpha = v/\sqrt{2}M_{\Sigma-1}Y_{\Sigma_\alpha}$. It is important to note that these simplifications are only meaningful in the context of searches for type-III seesaw neutrinos, as the model only accounts for a single neutrino mass, albeit oscillation experiments have proven the existence of different neutrino masses. Therefore this model has to be extended with at least a further triplet to accommodate several light neutrino masses.

2.3.2 Production and Cross Section

Type-III seesaw fermion triplets at the LHC are predominantly produced in pairs via Drell–Yan processes:

$$q\bar{q}' \rightarrow Z^*/\gamma^* \rightarrow L^+L^- \quad (2.84)$$

$$q\bar{q} \rightarrow W^\pm \rightarrow L^\pm N^0. \quad (2.85)$$

In this model, neutral lepton pairs are forbidden, as both the weak isospin I_W^3 and the hypercharge Y are zero for N^0 , and thus no coupling to the Z boson exists.

The production cross section depends solely on the mass of the L^\pm and N^0 , since the triplet interactions are fixed by the gauge symmetry. The production cross section at 8 TeV is shown in Fig. 2.5 was evaluated by generating the pairs L^+N^0 , L^-N^0 and L^+L^- at mass hypotheses ranging from 100 GeV to 500 GeV in steps of 5 GeV. The cross section of the mode $pp \rightarrow L^+N^0$, is somewhat larger than for $pp \rightarrow L^+L^-$ which in turn is larger than for $pp \rightarrow L^-N^0$. The total expected cross section for heavy lepton pairs ranges from 12.63 pb at 100 GeV to 13 fb at 500 GeV. While the cross sections decrease with higher masses, the selection efficiency is rather small at low masses. This is attributed to the larger backgrounds from Standard Model processes, but also to the limited phase space available to the final state particles, which in turn are fairly soft and thus hard to detect.

Also vector-like leptons can be produced at the LHC through the s-channel Z^*/γ^* process

$$q\bar{q}' \rightarrow Z^*/\gamma^* \rightarrow \tau^+\tau^-. \quad (2.86)$$

The production cross section for vector-like leptons is shown in Fig. 2.6. It is significantly smaller than that of the type-III seesaw model. This is attributed both to the lack of a neutral heavy lepton candidate

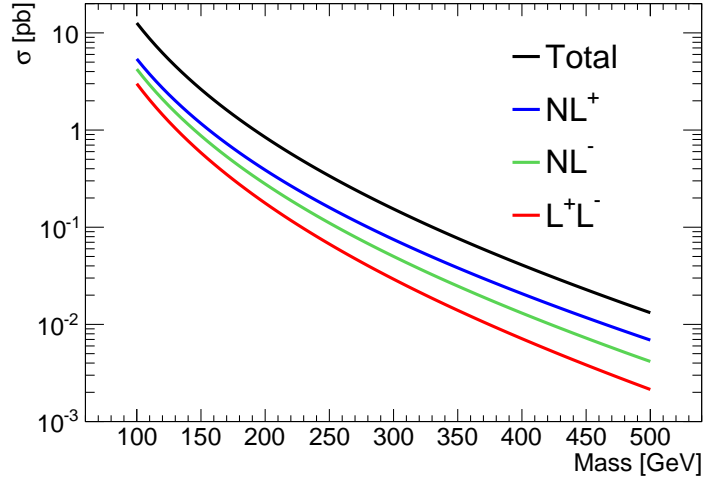


Figure 2.5: Cross sections for $pp \rightarrow L^\pm L^\mp$, $pp \rightarrow N^0 L^\mp$ and $pp \rightarrow N^0 L^\mp$ in the type-III seesaw model.

and the different gauge couplings arising from the SU(5) multiplet (1, -1).

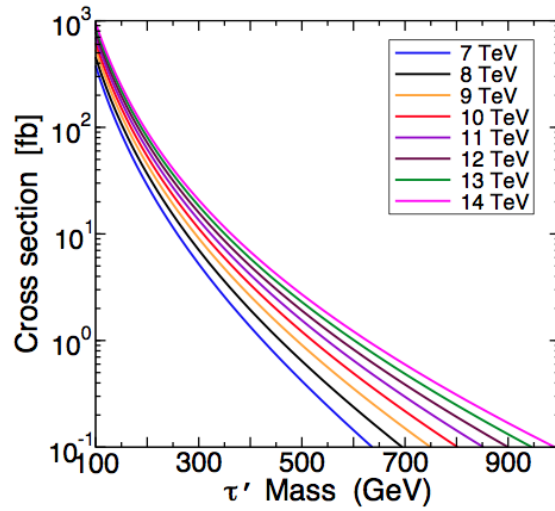


Figure 2.6: Cross sections for $pp \rightarrow L^\pm L^\mp$ in the vector-like lepton model, from [81]. The τ' particle in the figure corresponds to the heavy fermion L^\pm in this analysis.

2.3.3 Triplet Decays

In both models the heavy lepton decays arise from the same underlying mixing to the Standard Model leptons. Hence the decays and branching fractions are common to both models considered in this analysis. The heavy leptons are made unstable by introducing mixing terms with the Standard Model leptons. For instance, one can consider a single extra generation of fermions transforming in the adjoint

representation of $SU(2)_L$, as in the type-III seesaw model [16, 82] (see Section 2.2.4):

$$\Sigma \equiv \begin{pmatrix} N^0/\sqrt{2} & \Sigma^+ \\ \Sigma^- & -N^0/\sqrt{2} \end{pmatrix} \quad (2.87)$$

The Lagrangian contains Yukawa terms mixing the heavy leptons with Standard Model leptons:

$$-\mathcal{L} \ni \sum_{\ell=e,\mu,\tau} \sqrt{2}\phi^0 \bar{\Psi} Y_{L^\pm \ell} \ell_L + \text{h.c.}, \quad (2.88)$$

where $\Psi \equiv \Sigma_R^{+c} + \Sigma_R^-$ is a Dirac spinor representing the four charged degrees of freedom, $\phi \equiv (\phi^+, \phi^0)^T$ is the Higgs doublet, $Y_{L^\pm \ell}$ are Yukawa couplings, and ℓ_L is a Standard Model lepton. After electroweak symmetry breaking, the mass matrices take the form

$$-\mathcal{L} \ni \sum_{\ell=e,\mu,\tau} \begin{pmatrix} \bar{\ell}_R & \bar{\Psi}_R \end{pmatrix} \begin{pmatrix} m_\ell & 0 \\ Y_{L^\pm \ell} v & M_{L^\pm} \end{pmatrix} \begin{pmatrix} \ell_L \\ \Psi_L \end{pmatrix} + \begin{pmatrix} \bar{\ell}_L & \bar{\Psi}_L \end{pmatrix} \begin{pmatrix} m_\ell & Y_{L^\pm \ell}^\dagger v \\ 0 & M_{L^\pm} \end{pmatrix} \begin{pmatrix} \ell_R \\ \Psi_R \end{pmatrix}. \quad (2.89)$$

Diagonalising the mass matrices leads to off-diagonal terms in the gauge interactions, with couplings proportional to the mixing parameters $V_{\alpha\Sigma} = \frac{v}{\sqrt{2}} M_{L^\pm}^{-1} Y_{\alpha\Sigma}$. These couplings enable the decay of the heavy leptons to a boson (W , Z , or h) and a Standard Model charged lepton or neutrino, with partial widths given by:

$$\Gamma(N^0 \rightarrow \ell_\alpha^- W^+) = \Gamma(N^0 \rightarrow \ell_\alpha^+ W^-) = \frac{g^2}{64\pi} |V_{\alpha\Sigma}|^2 \frac{M_{L^\pm}^3}{M_W^2} \left(1 - \frac{M_W^2}{M_{L^\pm}^2}\right)^2 \left(1 + 2 \frac{M_W^2}{M_{L^\pm}^2}\right), \quad (2.90)$$

$$\sum_\ell \Gamma(N^0 \rightarrow \nu_\ell Z) = \frac{g^2}{64\pi c_W^2} \sum_\alpha |V_{\alpha\Sigma}|^2 \frac{M_{L^\pm}^3}{M_Z^2} \left(1 - \frac{M_Z^2}{M_{L^\pm}^2}\right)^2 \left(1 + 2 \frac{M_Z^2}{M_{L^\pm}^2}\right), \quad (2.91)$$

$$\sum_\ell \Gamma(N^0 \rightarrow \nu_\ell H) = \frac{g^2}{64\pi} \sum_\alpha |V_{\alpha\Sigma}|^2 \frac{M_{L^\pm}^3}{M_W^2} \left(1 - \frac{M_H^2}{M_{L^\pm}^2}\right)^2, \quad (2.92)$$

$$\sum_\ell \Gamma(\Sigma^+ \rightarrow \nu_\ell W^+) = \frac{g^2}{32\pi} \sum_\alpha |V_{\alpha\Sigma}|^2 \frac{M_{L^\pm}^3}{M_W^2} \left(1 - \frac{M_W^2}{M_{L^\pm}^2}\right)^2 \left(1 + 2 \frac{M_W^2}{M_{L^\pm}^2}\right), \quad (2.93)$$

$$\Gamma(\Sigma^+ \rightarrow \ell_\alpha^+ Z) = \frac{g^2}{64\pi c_W^2} |V_{\alpha\Sigma}|^2 \frac{M_{L^\pm}^3}{M_Z^2} \left(1 - \frac{M_Z^2}{M_{L^\pm}^2}\right)^2 \left(1 + 2 \frac{M_Z^2}{M_{L^\pm}^2}\right), \quad (2.94)$$

$$\Gamma(\Sigma^+ \rightarrow \ell_\alpha^+ H) = \frac{g^2}{64\pi} |V_{\alpha\Sigma}|^2 \frac{M_{L^\pm}^3}{M_W^2} \left(1 - \frac{M_H^2}{M_{L^\pm}^2}\right)^2. \quad (2.95)$$

here α denotes a given Standard Model lepton generation. The masses m_N , m_W , m_Z and m_H are the masses of the heavy lepton N , the W , Z bosons and the Higgs boson, g is the weak coupling and c_W is the cosine of the weak mixing angle. The branching fractions to each mode are shown as a function of the heavy lepton mass in Fig. 2.7(a) for the charged heavy leptons and in Fig. 2.7(b) for the neutral heavy lepton. At heavy lepton masses of 100 GeV the heavy leptons almost exclusively decay to W bosons. However, the branching fraction to W rapidly decreases, in favour of a sharp turn-on of the branching fraction to Z and H if kinematically accessible. In case of full coupling to only one lepton

generation, the N^+ and N^0 decay widths are the same. For example $\Gamma(N^0 \rightarrow \nu_e Z) = \Gamma(N^+ \rightarrow e^+ Z)$ if $\Gamma(N^0 \rightarrow \nu_\mu Z) = \Gamma(N^0 \rightarrow \nu_\tau Z) = 0$. The observability of the N^0 and L^\pm is quite dependent on their couplings to the Standard Model leptons. Strong couplings to electrons and muons result in final states with highly energetic electrons and muons, which benefit from a high reconstruction efficiency and are thus easily observable. In contrast strong couplings to the τ lead to rather unfavourable final states for a discovery, as the τ is subject to further decays and, the reconstruction of the various decay products significantly reduces the sensitivity for a discovery. After the heavy leptons have decayed into leptons and gauge bosons, these intermediate states are subject to further decays of the gauge bosons. Their decays involve charged leptons, neutrinos, indirectly detected as missing transverse energy, and hadrons, forming jets. Hence a plethora of final states arise from the decay of the heavy leptons, which can for instance be classified by their lepton multiplicity. Final states with five or six leptons in the final states have too small cross sections to be valuable discovery channels, while final states involving three or two leptons are considered more promising channels. Another distinct search channel includes same-sign leptons.

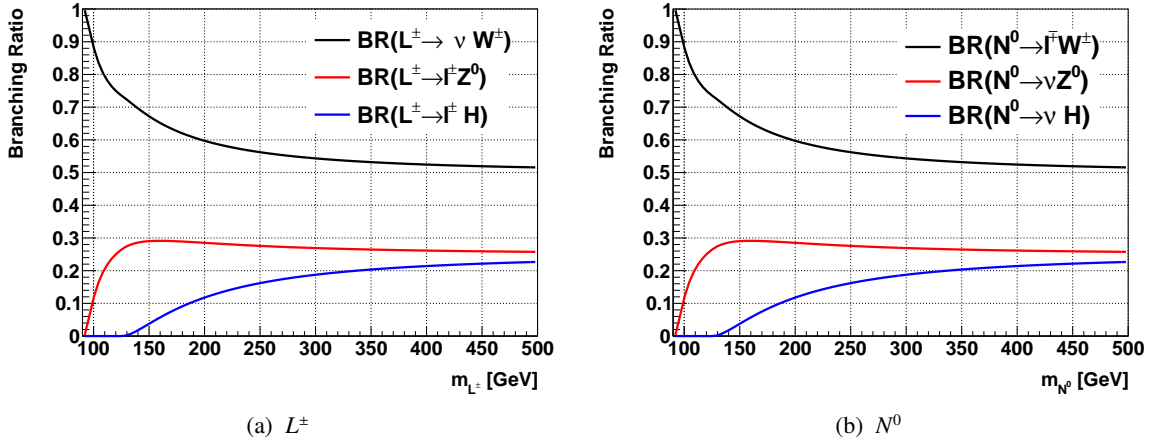


Figure 2.7: Branching ratios of a heavy lepton decaying via mixing with Standard Model leptons.

2.3.4 Bounds on the Mixing Angles

As the decay width depends on the mixing angles, special care should be taken in the choice of mixing scenarios for the signal production. The mixing angles of the type-III seesaw neutrinos are defined by

$$V_\alpha = \frac{v}{\sqrt{2}} \frac{Y_\alpha}{m}, \quad (2.96)$$

where α is the lepton flavour and Y_α the corresponding Yukawa coupling (see Sec. 2.2.4). The triplet mass is denoted as m and v is the Higgs vacuum expectation value. The bounds on the mixing angles are derived from electroweak precision data and decays such as $\mu \rightarrow e\gamma$. The constraints at 90 % confidence

level (CL) on these mixing angles are found in Refs. [83–85]. They are as follows:

$$|V_e| < 5.5 \times 10^{-2} \quad (2.97)$$

$$|V_\mu| < 6.3 \times 10^{-2} \quad (2.98)$$

$$|V_\tau| < 6.3 \times 10^{-2} \quad (2.99)$$

$$|V_e V_\mu| < 1.7 \times 10^{-7} \quad (2.100)$$

$$|V_e V_\tau| < 4.2 \times 10^{-4} \quad (2.101)$$

$$|V_\mu V_\tau| < 4.9 \times 10^{-4}. \quad (2.102)$$

As long as the mixing angles are greater than $\sim 10^{-4}$, the decays of the L^\pm are considered as prompt.

Experimental Status

Searches for heavy leptons date back to the LEP era. The most stringent exclusion limit was set by the L3 experiment with a search for charged and neutral heavy leptons in the $L^\pm \rightarrow W^\pm \nu$ decay mode [86]. The search was performed at centre-of-mass energies between $\sqrt{s} = 133 \text{ GeV}$ to 189 GeV . The analysis included both the search for pair-produced heavy leptons in final states with two leptons and two W , as well as a search for charged heavy leptons. Since no deviation from the Standard Model expectations was found, exclusion limits were set, excluding VLL with masses below $m_{L^\pm} = 101.2 \text{ GeV}$ at 95 % confidence level.

A search for type-III seesaw heavy leptons was performed by the CMS collaboration in proton–proton collision data at $\sqrt{s} = 7 \text{ TeV}$, using non-resonant three lepton signatures. Seesaw fermions with masses below $m_{L^\pm} = 100 \text{ GeV}$ to 210 GeV , depending on the branching fractions assumed [87].

In parallel to this analysis a search for type-III seesaw neutrinos was performed by the ATLAS collaboration using the 2012 dataset corresponding to 20.3 fb^{-1} of proton–proton collisions at $\sqrt{s} = 8 \text{ TeV}$. The analysis was based on the process $pp \rightarrow N^0 L^\pm \rightarrow W^\pm \ell^\mp W^\pm \nu$, where one W boson decays leptonically while the other decays to hadrons. Hence two leptons arise in the final state, which can either be same-sign or opposite-sign. Due to the lack of evidence for heavy lepton pair-production, this analysis excludes heavy leptons with masses below $325 - 540 \text{ GeV}$ at 95 % confidence level, depending on the mixing scenario considered.

2.4 Physics of Proton Proton Collisions

In perturbative QCD the cross section for a hard scattering process is evaluated using the factorisation theorem. It allows one to separate the cross section of the process of interest into different regimes, according to the scale of the momentum transfer involved. At the highest scales, the *hard subprocess*, the partons of the incoming hadron beams interact with a high momentum transfer resulting in the production of new particles. The corresponding *matrix elements* are calculated using perturbative QCD. At the lowest scales of about 1 GeV , the *soft regime*, the incoming partons are confined in the beams and the outgoing partons interact non-perturbatively to form the observed final-state hadrons [88]. These soft processes can so far not be calculated from first principles and are generally modelled. The two regimes are connected by an evolutionary process, which can be calculated with perturbative QCD. As a consequence of the scale evolution many additional partons are produced, forming the initial and final-state parton showers. The cross section for a hard scattering process at hadron-hadron colliders

($ab \rightarrow n$) can be expressed using the factorisation theorem [89, 90]:

$$\sigma_{ab \rightarrow n} = \sum_{a,b} \int_0^1 dx_a dx_b \int f_{a,h_1}(x_a, \mu_F) f_{b,h_2}(x_b, \mu_F) \times \hat{\sigma}_{ab \rightarrow n}(x_1 P_1, x_2 P_2, \alpha_s(\mu_R), \frac{Q}{\mu_F}), \quad (2.103)$$

where the sum includes all contributing initial-state partons ($a, b \in \{q, \bar{q}, g\}$). Assuming that the scale associated with the hard interaction, Q , is much larger than Λ_{QCD} , the delimiting scale of the QCD, binding effects of the partons in the initial-state hadron can be neglected. Therefore, the cross section can be factorised into a product of parton distribution functions (PDFs) $f_{a/b,h_{1/2}}(x_a, \mu_F)$ convoluted with the partonic cross section of all partonic subprocesses ($ab \rightarrow n$). The parton-level cross section for the production of the final state n produced by the initial-state partons a and b , are denoted by $\hat{\sigma}_{ab \rightarrow n}$, which is a function of the matrix element and the available phase space. The matrix element squared is usually evaluated as a power series of the coupling constant α_s , using Feynman diagrams. Most calculations are LO, NLO or NNLO. The partonic cross section furthermore depends on the momenta given by the final-state phase space Φ_n , the factorisation scale μ_F and the renormalisation scale μ_R .

The PDFs give the probability to find a parton of flavour i in the incoming hadron with the momentum fraction x of the momentum P of the hadron. The emission of further partons by i , after the extraction from the hadron and before the hard interaction takes place, modifies x . By convention this effect is included in the proton structure, up to the factorisation scale μ_F , which defines the separation between the soft interactions and the hard scattering process. The choice of μ_F is arbitrary and the scaling behaviour of the PDFs with the momentum transfer scale Q^2 ensures the independence of physical observables. In general the values for μ_F and μ_R , which is the renormalisation scale for the QCD running coupling, are chosen to be on the order of the typical momentum scales of the hard scattering process, such that $\mu_R = \mu_F = Q$. The dependence of the PDFs on the choice of μ_F is expressed by the Dokshitzer-Gribov-Lipatov-Altarelli-Parisi (DGLAP) equation [91–93]. PDFs can so far not be calculated perturbatively (there are some efforts to compute PDFs using lattice QCD), but are determined by global fits to experimental data. In general the results from deep inelastic ep scattering (DIS) at the HERA collider are combined with Drell-Yan and jet production measurements. The fits are performed by several independent collaborations, using different extraction techniques. The two major groups are CTEQ [94] and MSTW [95]. The most frequently used PDF set in the process of generating simulated events within this thesis, is the LO CTEQ6L1[96] set, provided by the CTEQ collaboration. The results for $x \cdot f$ are shown in Fig. 2.8 for two different values of Q^2 . The gluon distribution is dominant at values of $x < 0.2$, whereas the valence quarks are dominant at large values of x , in a regime only probed in cases of large $Q^2 \sim 1$ TeV. Due to the high gluon flux, many processes at the LHC are gluon-induced. It should be noted that the parton distribution functions used should match the level of accuracy of the partonic cross section.

2.4.1 Monte Carlo Generation

Simulated event samples using the Monte Carlo method are an essential tool not only for the analysis and interpretation of experimental data from high energy colliders, but also for predictions of future experiments and new physics signatures beyond the Standard Model. The complete simulation of proton-proton interactions at the LHC consists of several distinct steps, which are illustrated in Fig. 2.9. In the centre of each collision is the *hard scattering* (in this case a $t\bar{t}$ [97]) event shown as a red blob and defined as the interaction with the largest momentum transfer in the event. The subsequent decays of the top quark and the Higgs bosons are represented by the smaller red blobs. The involved partons radiate gluons, which in turn can emit further gluons, or produce quark-antiquark pairs, ultimately lead-

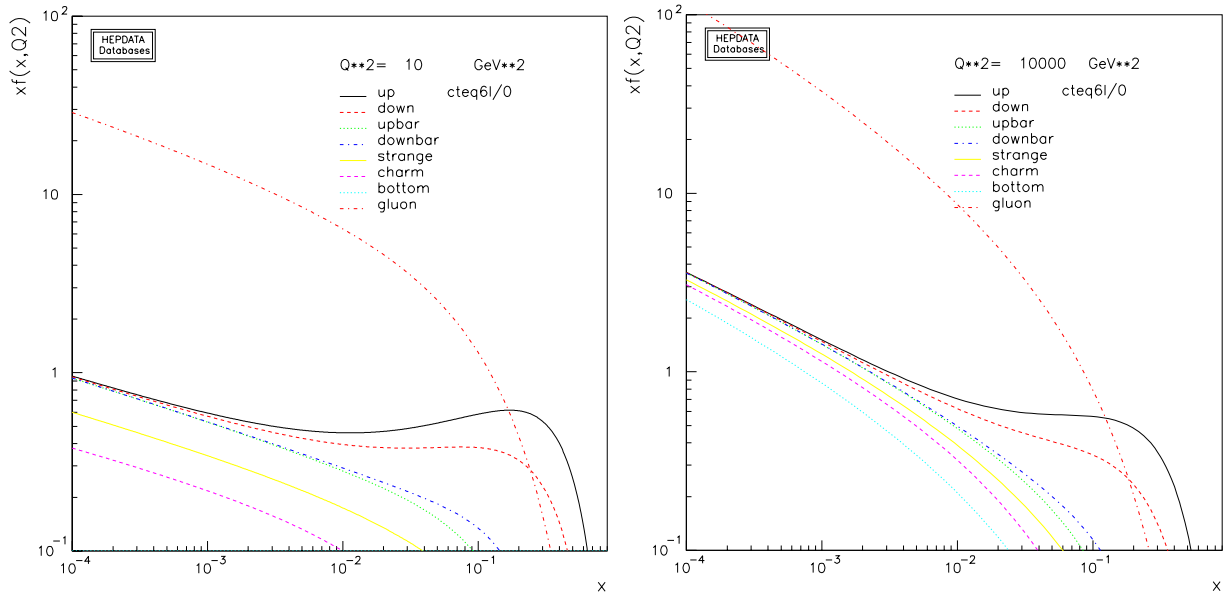


Figure 2.8: CTEQ6L parton-distribution functions as a function of x for $Q^2 = 10 \text{ GeV}^2$ (left) and $Q^2 = 10^4 \text{ GeV}^2$ (right) for the various partons. The figures were generated using <http://hepdata.cedar.ac.uk/pdf/pdf3.html>.

ing to the formation of parton showers. After the parton shower has terminated, colour-neutral hadrons are formed from the partons in a process called *hadronisation*. These hadrons are in general unstable and decay. Due to the structure of the proton-proton interaction the hard process is accompanied by additional activity in the event, arising from the interaction of the remaining constituents of the proton, which form the underlying event.

Most event generators rely on the previously introduced factorisation theorem, which allows to separate the kinematic regimes in the event. The hard scattering is the central piece in the generation and is calculated with perturbation theory at fixed-order of the coupling constants. The evolution of the colour charged partons in the interaction to the hadronisation scale is provided by parton shower algorithms. The transition of the partons into colourless hadrons at the scale of Λ_{QCD} is based on phenomenological fragmentation models, which are tuned to data. Thereafter the resulting hadrons are decayed using effective theories or simple symmetry arguments. Finally, the modelling of the underlying event is simulated, based on phenomenological models with many adjustable parameters in their description. In the following section an overview of these distinct steps in the generation of Monte Carlo simulated events is given. A more complete introduction to the Monte Carlo generation is found for instance given in Ref. [88].

Hard Scattering process

The generation of simulated event samples generally evolves around the hard scattering process, which is initiated by a highly energetic collision of constituents of the colliding particle beams. At the LHC this can either be the collision of a quark-antiquark pair, a quark gluon pair or two gluons from the proton beams. The momenta of the colliding particles is selected by sampling the parton distribution functions at the energy scale of the subprocess. The integration over the phase space and its convolution with the differential cross section of the subprocess is based on the Monte Carlo method.

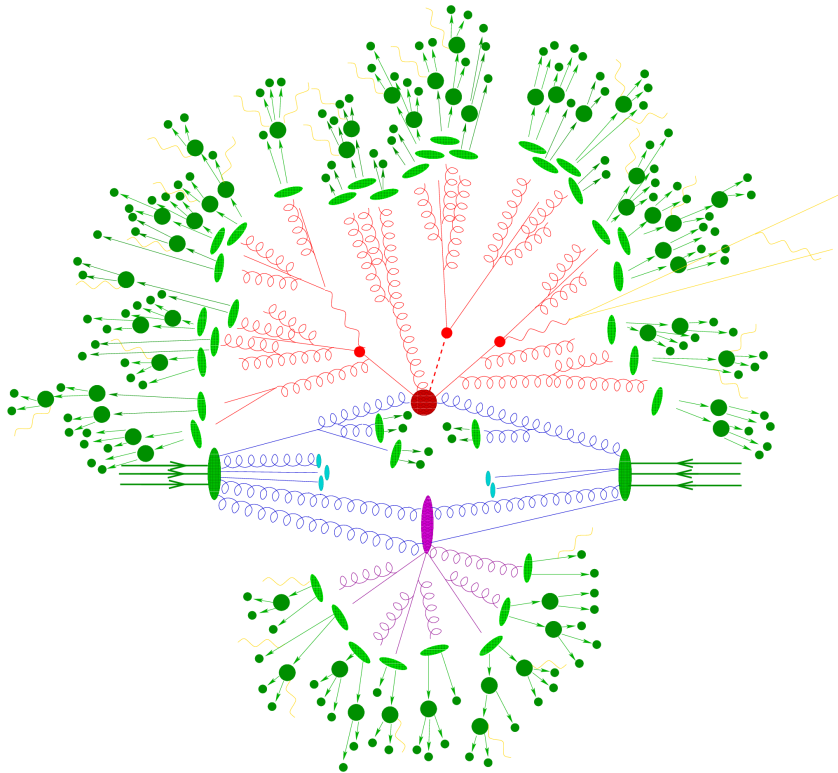


Figure 2.9: Schematic representation of a $t\bar{t}h$ event from simulated proton-proton collisions. The central red blob represents the hard interaction, with the subsequent decays of the top quarks and the Higgs boson shown as small red blobs. Accompanying hard QCD radiation is shown in red. The purple blob represents a secondary hard scattering event. The transition of a parton to hadrons is depicted by light green blobs, while the dark green blobs represent the hadron decays, Photon radiation can occur at any time and is shown as yellow lines. From [97]

Parton Shower

A matrix element Monte Carlo of the hard scattering process provides a powerful tool to describe the kinematics of the outgoing particles. But they can only offer an incomplete picture as the internal structure is not well described at fixed order. The high energetic partons radiate gluons, which in turn produce quark-antiquark pairs, and thus lead to a shower of partons. These showers represent higher-order corrections to the hard subprocess and are described by an approximation scheme, in which the contributions at each order are associated with collinear parton splittings or soft (low-energetic) gluon emissions. Hence parton showers offer a process-independent formulation of an evolution in momentum transfer from higher orders, at the interaction scale, down to low scales of the order of 1 GeV (i.e. the confinement regime).

The emission of an additional parton j with momentum fraction z in a LO hard process that produces partons of any flavour i , is given by [88, 90]

$$d\sigma \approx \sigma_0 \sum_{\text{partons}} \frac{\alpha_s}{2\pi} \frac{d\theta^2}{\theta^2} dz P_{i \rightarrow j,k}(z, \phi) d\phi, \quad (2.104)$$

where $P_{i \rightarrow j,k}$ is a set of universal *splitting functions*, which coincide with the DGLAP evolution functions, describing the probability of parton i to split into partons j and k , and z is the momentum fraction carried away by the emitted parton j . The opening angles with respect to the emitting parton are given by θ and ϕ . The above formula holds for any other evolution variable proportional to θ , therefore different generators evolve around different variables. PYTHIA [98] versions 6.2 and earlier are based on the virtuality of the off-shell parton propagator $q = z(1-z)\theta^2 E^2$, HERWIG [99] uses $E^2(1 - \cos(\theta))$ and PYTHIA 6.4 [100] uses the gluon's transverse momentum $k_T^2 = z^2(1-z)^2\theta^2 E^2$. In all cases the evolutions lead to the same result in the collinear limit.

The emission of partons in the collinear and soft approach leads to two types of divergencies, appearing either, if the emitted parton is collinear with its parent (collinear divergency) or if the energy of the emitted parton goes to zero (infrared divergency). This is circumvented by introducing a cutoff scale Q_0 , which is generally chosen as the relative transverse momentum at which two partons are still resolvable. Furthermore the solutions of the DGLAP equations are rewritten by applying a *Sudakov form factor* $\Delta_i(q_1^2, q_2^2)$, which describes the probability that no splitting occurs for parton i , during the evolution from scale q_1^2 to q_2^2 . Through the introduction of the Sudakov factor all effects attributed to soft and collinear gluon emissions are resummed and a well-defined prediction for the corresponding region is found.

Using the above ingredients, the general parton shower algorithm proceeds in the following way. Starting at the initial scale Q^2 the equation $\Delta_i(Q^2, q^2) = \rho_1$, where ρ_1 is a random number drawn from the interval between 0 and 1, is solved for q^2 . If the found solution is above the cutoff scale Q_0^2 , a splitting $i \rightarrow j, k$ is generated at the scale q^2 and the procedure is repeated for the partons j and k , until all attempted splitting are below the cutoff scale Q_0 . For each resolvable branching values of z and ϕ are chosen according to the distribution $P_{i \rightarrow j,k}(z)$ using the Monte Carlo method. In general the starting scale is of the order of the scale of the hard interaction, although the exact implementation differs for the various generators.

Parton shower algorithms are based on the soft and collinear approximation, which leads to inaccuracies in the description of hard and large angle emissions. In contrast fixed-order matrix element calculations provide an accurate description of the hard scattering process, while failing to describe the soft and collinear limit. In order to combine both descriptions, special care must be taken to avoid double counting in regions where the two approaches overlap. Different merging algorithms exist, leading to

a fully inclusive sample with no double counting at correct leading logarithmic accuracy. Common to all merging algorithms is the division of the phase space into two regions: the high-energy/large-angles region, using the matrix element description of parton branching, and the small-angle/low-energy region employing the parton shower description. The most accepted merging schemes are the CKKW-(L) [101, 102] scheme, used for instance by SHERPA [97] and HERWIG++ [103], and the MLM [104] matching adopted amongst others by ALPGEN [105] and PYTHIA [100]. Algorithms that match NLO calculations with Parton Shower Monte Carlo must include the radiation of an additional parton at tree-level accuracy and must also include NLO virtual corrections. Both MC@NLO [106] and POWHEG-BOX [107, 108] are widely used for this purpose.

Hadronisation

Due to the colour confinement quarks and gluons cannot exist freely but form colour-neutral hadrons. This process in which the outgoing partons end up confined inside hadrons typically at a mass scale of 1 GeV, is called hadronisation. Due to the confinement an explicit calculation of the hadronisation is beyond the means of perturbation theory. Therefore complex phenomenological models are implemented to describe the hadronisation process. The most frequently used descriptions are the Lund string model [109], as implemented in PYTHIA, and the cluster model [110], used by SHERPA and HERWIG. The Lund string model is based on the assumption of linear confinement, the quark-antiquark pairs are treated as being connected by field lines which are attracted by the gluon self-interaction. This forms a colour-string between the particles. These strings linearly increase their potential energy as they drift apart. If the potential energy in the string is large enough the string might break up to form two new $q\bar{q}$ pairs. This proceeds until only on-mass-shell hadrons remain. Each hadron is thus described as a small string piece. Gluons are represented as a kink on the string, carrying energy and momentum.

In the cluster model, the gluons are split non-perturbatively into quark-antiquark pairs. Clusters are formed along the colour lines from the colour-singlet $q\bar{q}$ combinations. These can be regarded as massive colour-neutral particles which decay into hadrons, depending on the density of states with appropriate quantum numbers.

Further information on these models is found in Refs. [88, 100].

Underlying Event

The *Underlying Event* is the collection of mostly low-energy (soft) particles produced in a hadron-hadron collision not attributed to the hard interaction. The origin of the particles arises from phenomena like Initial or Final State Radiation (ISR/FSR), Multiple-Partonic Interactions (MPI) or diffraction. Also the treatment of the underlying event is beyond the scope of perturbative QCD, therefore different phenomenological models are developed and implemented into the various Monte Carlo generators. However, the modelling of the underlying event is of great importance as it can affect the missing transverse momentum resolution, the lepton identification and the jet resolution. Generally these models are based on a set of parameters, which can be tuned to match experimental observables [111, 112]. Two strategies exist to measure the underlying event [113]: In the first strategy, data events are collected using minimalistic trigger conditions, so-called minimum-bias triggers. It is assumed that events selected by these triggers are dominated by underlying event physics. In the second strategy, interactions occurring with a high production rate, such as dijet events, are selected and the hard-scattering process is separated.

2.4.2 Pile-up

At the LHC each proton bunch holds up to 10^{11} protons and has a transverse size of about $16\ \mu\text{m}$. This leads to additional proton–proton interactions in the same bunch crossing referred to as *pile-up*. The pile-up interactions can either originate from the same bunch crossing as the interaction of interest, called *in-time pile-up*, or from additional proton-proton collisions occurring in bunch-crossings before or after the collision of interest (*out-of-time pile-up*). The latter are recorded, because several subsystems have readout windows larger than the 25 ns bunch crossing time. Their exact number depends on the specific run conditions. Activity in the event arising from *cavern background*, *beam halo* and *beam gas events* are included in the pile-up contribution.

During 2012 data-taking the number of pile-up interactions increased from 10 to almost 35 with an average of about 20 additional interactions. Therefore an understanding and modelling of this background is critical for performing analyses in ATLAS. Each component of the pile-up is simulated individually. In case of the in-time pile up additional minimum-bias events are generated using PYTHIA8. The various pile-up sources are then combined and overlaid to the simulated event samples at configurable rates. The simulated samples are reweighted to match the distribution of the number of interactions per bunch crossing in data.

2.4.3 Monte Carlo Generators

General-purpose generators such as PYTHIA, HERWIG and SHERPA produce complete events starting from the proton–proton collisions. They can either be used standalone or in conjunction with more specialised initial-state generators. The complexity of hadron–hadron collisions has led to a diversification of the separate simulation steps, such that specialised generators are developed for individual tasks. The combined effort of the community has led to common file formats like the Les Houches Format [114] or UFO (Universal FeynRules Output) [115] files or common interfaces like LHAPDF [116], which offer the user a large versatility in the combination of the different generators.

Pythia is a LO multi-purpose event generator, which has been extensively used in all high energy particle collision experiments over the past 30 years. It contains an extensive list of matrix-elements of more than 200 hard-coded processes including both Standard Model and beyond. These are restricted to multiplicities of $2 \rightarrow 1$, $2 \rightarrow 2$ and $2 \rightarrow 2$. Additional QED and QCD radiation is added to the hard scattering process using a shower approach. A dedicated model for hard and soft scattering processes is implemented to model the underlying event activity [117]. The showering model combines the multiple scattering events from the underlying event with the parton shower according to the hard scale of the scattering process. The showering process is followed by the phenomenological Lund hadronisation model, which is tuned to ATLAS data. Additionally, hard scattering processes, generated in external programs, can be fed into PYTHIA for parton showering and hadronisation. PYTHIA is chosen as one of the default generators in ATLAS [117], due to its simplicity to use and its speed and robustness. There are two versions of PYTHIA that are used within this thesis, the Fortran based PYTHIA6.4 version and the new PYTHIA8 version, which is a migration of the Fortran code to C++.

Herwig is the second multi-purpose generator used in ATLAS. It is based on Fortran and contains a large library of $2 \rightarrow n$ processes both from Standard Model, supersymmetric extensions and other exotic processes. It offers full spin correlations of the processes. Additional QCD radiation is generated using a coherent branching algorithm, for both initial- and final-state particles. The parton shower model used is based on an angular ordering of the parton shower emissions, which

ensures that colour coherence effects are taken into account. In contrast to PYTHIA the hadronisation is based on the cluster model. Even though HERWIG offers additional hard and soft multiple partonic interactions to model the underlying event, an interface to JIMMY [118], which applies a multiple scattering model, is generally used for this purpose.

Herwig++ Is the succeeding generator for HERWIG based on C++. Besides the library for hard scattering processes HERWIG++ offers a great versatility to add new models by encoding the Feynman rules of the model. A parton shower approach is used for the modelling of the initial- and final- state radiation. The parton shower model is angular-ordered and includes colour coherence effects, with special emphasis on the correct description of radiation from heavy particles. The hadronisation is based on an advanced clustering scheme. Moreover hadron decays are simulated using matrix elements, where possible including spin correlations and off-shell effects.

Sherpa is the newest multi-purpose generator used in ATLAS and offers both LO and NLO event generation. Hard scattering processes can be either generated by SHERPA's two built-in matrix-element generators or fed into SHERPA using a generic interface. Furthermore it is equipped with an automated phase-space generator, automatically calculating and integrating tree-level amplitudes for the implemented models. Since additional partons are included in the calculation of the hard scattering process, by allowing LO contributions to the $2 \rightarrow n$ process, it is expected to give better approximations for final states with high jet multiplicities. The parton showering algorithm implemented in SHERPA corresponds to a sequential splitting approach based on the Catani-Seymour dipole factorisation formalism. One of the key features of SHERPA is the merging of matrix elements and parton showers, based on the CKKW technique. The hadronisation is based on a cluster model.

In addition to the multi-purpose generators, many specialised event generators exist, which provide an improved simulation of dedicated final states or new physics models. Generally they do not provide complete events, but are run in conjunction with one of the above mentioned general-purpose generators. The specialised generators used within this thesis are described in the following:

Alpgen is designed to perform the exact calculation of the matrix element at LO in QCD and EW targeted at processes with many well separated hadronic jets in the final state. It provides parton-level events with the full information on their colour and flavour structure, with the inclusion of b and t quark masses, allowing for the evolution of the partons into fully hadronised final states. In ATLAS it has been used to model W and Z final states with high jet multiplicities. The output of ALPGEN is fed into PYTHIA or HERWIG for hadronisation and the simulation of the initial- and final-state radiation. A dedicated procedure to avoid double counting between ALPGEN and the general purpose generator (MLM) is implemented.

Madgraph5 is a dedicated tool for the automated generation of matrix elements of $2 \rightarrow n$ processes. It can generate any matrix element at tree-level for Lagrangian-based models implemented in FEYNRULES using the UFO interface. Furthermore it offers NLO QCD calculations for Standard Model processes. The events are stored in the Les Houches format and can thus be interfaced to shower Monte Carlo programs, like PYTHIA.

MC@NLO is a generator that evaluates fundamental hard scattering processes at NLO in QCD perturbation theory. This leads to improved cross section predictions and a more sophisticated description of kinematic distributions. Since one-loop corrections with virtual contributions are included,

events appear with positive or negative weights, which must be taken into account in the weighting of the MC events. In general `MC@NLO` is interfaced to `HERWIG` for further processing of the events.

Powheg is a method to interface parton-shower Monte Carlo to fixed NLO QCD calculations.

FeynRules is a Mathematica package, designed for the versatile implementation of new physics models [119]. The user provides the Lagrangian and a model card, which contains the particle content and the parameters. The `FEYNRULES` package uses this input to derive the Feynman rules and stores them into a generic output file format, which can be translated by Feynman diagram calculators, as implemented for instance in `MADGRAPH`, `MADEVENT` or `SHERPA`.

The Large Hadron Collider and the ATLAS Detector

The LHC [120] is a proton-proton collider, designed to collide beams at a centre-of-mass energy of 14 TeV. During Run 1 the collision energy was $\sqrt{s} = 7$ TeV in 2010 and 2011 and $\sqrt{s} = 8$ TeV and has been increased to (13 ± 14) TeV for Run 2. An outstanding success of the Large Hadron Collider (LHC) was the discovery of a Higgs-like particle by the ATLAS (A Toroidal LHC ApparatuS) [121] and CMS (Compact Muon Solenoid) [122] collaborations in 2012 and therewith an advanced understanding of the sources of electroweak symmetry breaking and the generation of boson and fermion masses. At the four interaction points, the experiments ATLAS, CMS, LHCb [123] and ALICE (A Large Ion Collider) [124] are installed. ATLAS and CMS are multi-purpose experiments, which investigate a multitude of research topics, such as the investigation of the Higgs Boson properties, Standard Model measurements in the strong and electroweak sector, top quark physics, B-physics, heavy Ion physics and physics beyond the Standard Model e.g. the search for Supersymmetry or dark matter candidates. LHCb is a collider experiment with a single-spectrometer setup, optimised for measurements of b hadrons and studies of CP violation. ALICE was designed to investigate heavy ion physics and the quark gluon plasma. In this chapter a brief overview of the Large Hadron Collider and the ATLAS detector design.

3.1 An Introduction to the LHC

The LHC (Fig. 3.1) is a proton-proton collider ¹ at the European Organisation for Nuclear Research (CERN) in Geneva, Switzerland. It is built in the same tunnel as the former LEP accelerator, about 100 meters underground. The LHC accelerates two beams of protons in opposite direction inside a ring of 27 km circumference up to a beam energy of 7 TeV and collides them at a total centre-of-mass energy of up to 14 TeV.

During Run 1 the centre-of-mass energy was chosen to be 7 TeV in 2010 - 2011 and 8 TeV in 2012. The beams, designed to contain 3×10^{14} protons, are brought to collision at four interaction points. The design luminosity is $10^{34} \text{ cm}^{-2} \text{ s}^{-1}$. The LHC has provided collision energies and luminosities greater than any previous hadron collider. It builds on the existing accelerator chain at CERN, namely the Linac2, the Booster, the Proton Synchrotron (PS), and the Super Proton Synchrotron (SPS) as shown in the schematic in Fig. 3.1.

¹ The LHC collides heavy ions as well

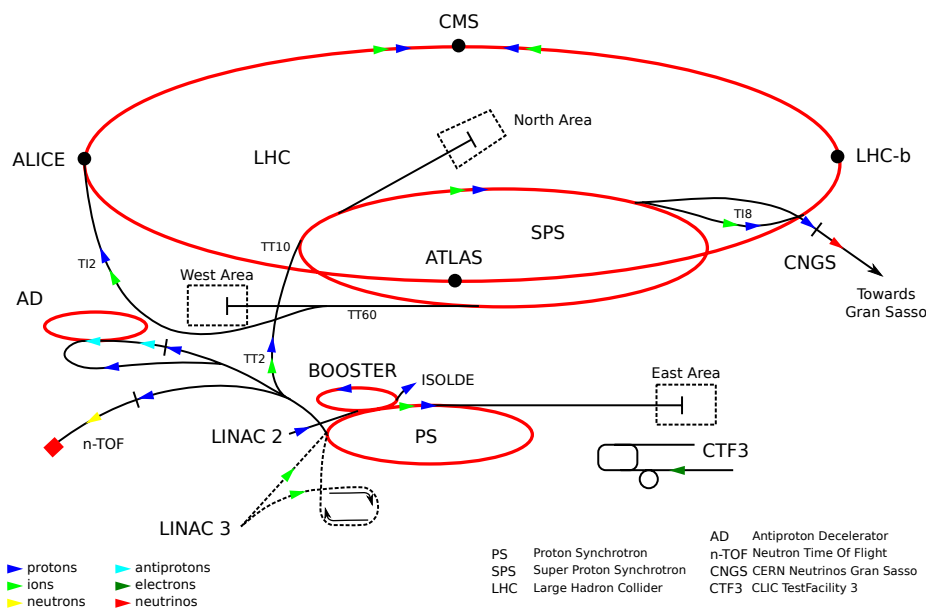


Figure 3.1: Schematic of the LHC accelerator complex. The injection chain consists of the accelerators Linac2, Booster, PS and SPS. The beams are finally injected into the LHC accelerator and storage ring [125].

The protons are obtained by heating hydrogen to form a plasma, thereby removing the orbiting electrons. These are pre-accelerated in the Linac to energies of 50 MeV. Thereafter they enter the Booster, which increases their energy to 1.4 GeV. Further acceleration takes place in the PS leading to 25 GeV protons that are accelerated to 450 GeV in the SPS, before being injected into the LHC. In the SPS they are further accelerated using an RF system operating at a temperature of 4.5 K and at 400.8 MHz, the second harmonic of the SPS frequency. The RF system has 16 MV per beam, providing an average bunch length of 7.5 cm and a bunch spacing of 25 ns. This leads to a bunch crossing rate of 40 MHz.

To keep the particles on track, the LHC is equipped with superconducting Niobium-Titanium (NbTi) dipole magnets, which are cooled by superfluid Helium. The maximum beam energy is limited by the magnetic field available to bend the beam. The LHC uses the most powerful superconducting magnets ever installed in an accelerator, which can produce a maximum field of 8.37 T.

Since two beams of particles with the same charge are accelerated in opposite directions, two independent magnet channels are needed. The twin dipole magnets are arranged such that the return field from one ring provides the field to the other. They are housed in the same yoke and cryostat system. The magnet coils are made of copper-clad NbTi cables. They are operated at 1.9 K with a current of 15 000 A, and have to withstand forces of some hundred tons per meter during the ramping of the magnetic field. The LHC uses 1232 main dipoles and 392 main quadrupoles, the latter producing gradients of 233 T/m. In case of quenches², the stored energy must be safely released from the magnets. Hence resistors are used that can be switched into the circuit, heating eight tons of steel to about 600 K.

3.1.1 Accelerator Parameters

The main parameters that determine the LHC performance are the Luminosity, L , and the centre-of-mass energy, \sqrt{s} . Due to the composite nature of protons, only a fraction of the centre-of-mass energy is available for the interaction between the proton constituents. The LHC will still lead to energies that are almost an order of magnitude larger than at the predecessor Tevatron. The total luminosity of two colliding beams is given by

$$L = f \frac{n_1 n_2}{4\pi\sigma_x\sigma_y}, \quad (3.1)$$

where n_1 and n_2 are the numbers of particles in the two colliding beams, f is the frequency of collisions and σ_x and σ_y characterise the root-mean-square beam sizes of the horizontal and vertical direction. The average number of events produced per second is then given by

$$\langle n \rangle = \frac{L\sigma_{int}t}{F}, \quad (3.2)$$

where σ_{int} is the interaction cross section, t the time interval between bunches and F the fraction of bunches containing protons. The rate, R , of any given particle interaction is determined by the luminosity of the collider and the cross section of the process:

$$R = L\sigma_{int}. \quad (3.3)$$

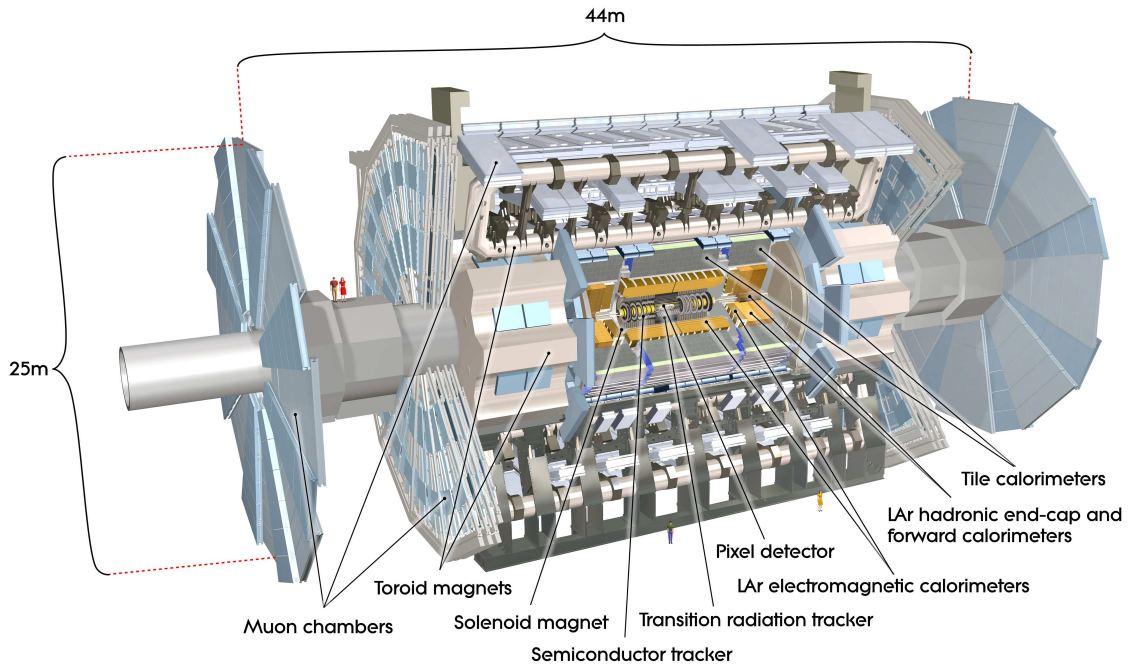


Figure 3.2: The ATLAS detector. The dimensions of the detector are 46 m in length and 25 m in diameter. The detector weighs about 7000 t [121].

3.2 The ATLAS Experiment

ATLAS (A Toroidal LHC Apparatus) is a multi-purpose detector designed to provide accurate measurements of the wide range of physics processes occurring at the LHC. In the following, a brief summary of the principal detector components is given, based on a more detailed description of the detector given in Refs.[121, 126]. The design of ATLAS was driven by the desire to maximise the discovery potential for new phenomena, while retaining the ability for high precision measurements of known processes. One of the main priorities of the experiment was the search for the Higgs boson, and the measurement of its properties. Due to the large luminosity another fundamental physics topic of the ATLAS experiment is the precision measurement of Standard Model processes involving vector bosons, B-mesons and top quarks, as well as detailed studies in the field of QCD, CP-violation and top quark properties. The theoretically well motivated search for supersymmetric particles as a possible extension of the Standard Model belongs to key measurements in the ATLAS physics program. However to keep the potential to observe unexpected phenomena, a flexible design, not utterly tied to any specific physics model was envisaged for the ATLAS experiment. Thus, the basic design criteria, as laid out in the Technical Design Report [126], are:

- Good electromagnetic calorimetry for electron and photon identification and energy measurement, complemented by full-coverage hadronic calorimetry for accurate jet and missing transverse energy (E_T^{miss}) measurements.
- High-precision muon momentum measurements, with the capability to guarantee accurate meas-

² A quench is an abnormal termination of magnet operation occurring when part of the superconducting coil enters the resistive state, resulting in heating of the magnet.

measurements at the highest luminosity using an external muon spectrometer.

- Efficient tracking at high luminosities for high transverse lepton momentum measurement, electron and photon identification, τ -lepton and heavy-flavour identification.
- Large acceptance in the pseudo-rapidity η (see 3.2.1) with almost full azimuthal angle ϕ (see 3.2.1) coverage.
- Triggering and measurements of particles at low transverse momenta, providing high efficiencies for most physics processes of interest at the LHC.

The ATLAS detector has a length of 46 m, a diameter of 22 m and weighs about 7000 t. The design is shown in Fig. 3.2 and follows the usual onion-like configuration of tracking detectors enclosed by calorimeters and finally muon chambers, as present in most multi-purpose detectors. The large size of the ATLAS experiment is primarily driven by the magnet system. It consists of a superconducting solenoid magnet surrounding the inner detector and three superconducting air-core toroids, one barrel and two end-caps, arranged with an eight-fold azimuthal symmetry around the calorimeters. These provide a magnetic field for the muon system.

3.2.1 The ATLAS Coordinate System

Due to its cylindrical shape, ATLAS has adopted a polar coordinate system. The z direction is defined along the beam direction, with the $x - y$ plane perpendicular to the beam direction. The positive x direction points from the interaction point to the centre of the LHC ring, the positive y direction points upward. An alternative coordinate system is defined by the azimuthal angle $\phi = \arctan(y/x)$, which is measured around the beam axis, the polar angle $\theta = \arctan(r/z)$, which is the angle with respect to the beam direction and $r = \sqrt{x^2 + y^2}$. Since rapidity differences δy are Lorentz-invariant, the pseudorapidity, η , provides a physically better suited measure of the polar angle. The Lorentz invariant rapidity y is given through:

$$y = \frac{1}{2} \log \frac{E + p_L}{E - p_L} \quad (3.4)$$

where E is the energy of the particle and p_L is the longitudinal momentum of the particle. As rapidities vary for a given θ with the rest mass of the particle, the pseudorapidity, η , is defined as

$$\eta = -\ln \tan\left(\frac{\theta}{2}\right). \quad (3.5)$$

The $x - y$ plane is called the transverse plane. The energy and momentum of particles are often projected onto the transverse plane; the transverse energy and momentum are defined as $E_T = \sqrt{E_x^2 + E_y^2}$ and $p_T = \sqrt{p_x^2 + p_y^2}$ respectively. The transverse plane is preferred as the initial transverse energy and momentum of the partons is close to zero. In contrast, the initial energy and momentum in the z direction is a priori unknown for hadron colliders. The opening angle between two particles in the $\eta - \phi$ space is given by $R_{ij} = \sqrt{\Delta\phi_{ij}^2 + \Delta\eta_{ij}^2}$. Another important measure is the missing transverse energy, E_T^{miss} , of the event, which is defined as $E_T^{\text{miss}} = \sqrt{(\sum_{\text{Deposits}} E_x)^2 + (\sum_{\text{Deposits}} E_y)^2}$.

3.2.2 The Inner Detector

The Inner Detector (ID), shown in Fig. 3.3, is contained within a cylinder of 7.0 m length and a radius of 1.15 m. It comprises three subsystems: the pixel detector (PD) closest to the beam line, a silicon strip detector called the Semi-Conductor Tracker (SCT) and furthest away from the beam line, a transition radiation tracker (TRT). The inner detector is placed inside a superconducting magnet, within a homogeneous 2 T field in the central region. The solenoid is shorter than both the SCT and TRT, which leads to a significant deviation in the uniformity of the magnetic field, dropping to about 0.8 T at the ends of the inner detector region ($z = 3$). Charged particles are bent by the magnetic field and detected as they pass through these three detectors. The PD, the SCT and the TRT provide space point measurements from which the particle trajectory can be reconstructed. The TRT provides additional information from transition radiation allowing for identification of the type of particles. A schematic view of the cross section of the inner detector in the barrel region is shown in Fig. 3.4. The power dissipated by the various subsystems of the inner detector must be removed by suitable cooling systems. The PD and the SCT use a coolant circulating through a series of aluminum pipes, reducing their temperature to 7 °C. To prevent condensation forming on the detectors, they are enclosed in a cold dry nitrogen environment. The TRT operates at ambient temperature and pressure and sits outside this enclosure. Since the cooling need is less stringent this is achieved through the circulation of CO₂ in the end-caps and by water cooled pipes running through the barrel.

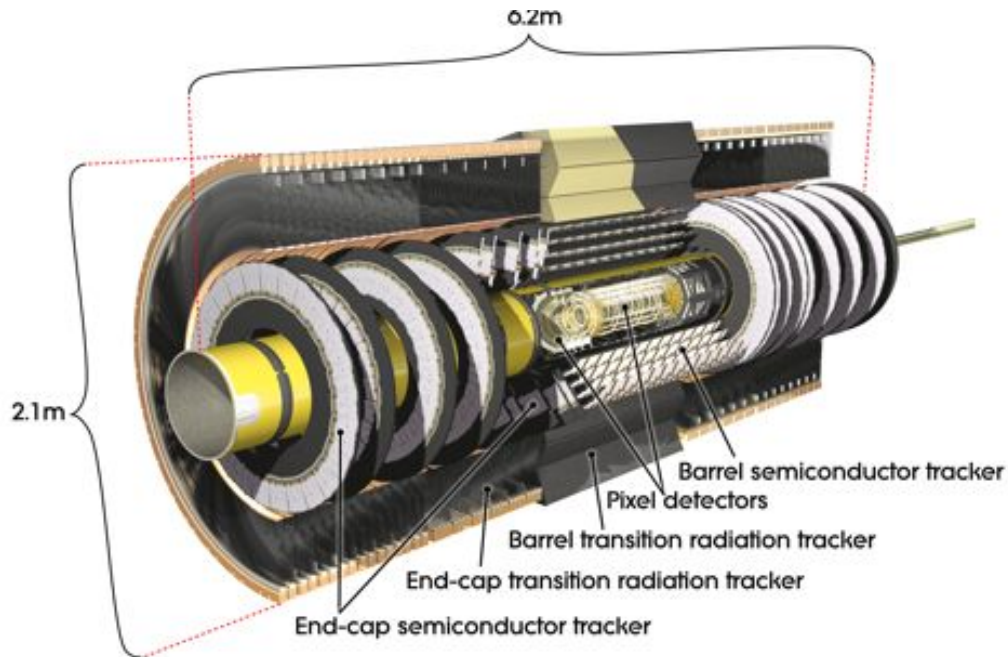


Figure 3.3: The ATLAS inner detector, consisting of the Pixel Detector (PD), the Semiconductor Tracker (SCT) and the Transition Radiation Tracker (TRT). [121]

Pixel Detector

The pixel detector is the innermost detector component and aims to provide high-granularity precision tracking as close to the interaction point as possible. The detector is made up of three barrels at radii of 5.05 cm, 8.85 cm and 12.25 cm from the beam line, together with five end-cap disks of radii from 11 cm to 20 cm. This leads to an angular coverage of $|\eta| < 2.5$ for the innermost barrel layer, the 'B layer' which covers $|\eta| < 1.7$ for the other barrel layers, while the end-caps cover a range of $1.7 < |\eta| < 2.5$ end caps respectively. The PD consists of a total of 140 million detector elements, each of $50\ \mu\text{m}$ in $(R - \phi)$ and $300\ \mu\text{m}$ in z . These are spread over 1500 barrel and 700 disk modules providing a spatial resolution of $12\ \mu\text{m}$ in $(R - \phi)$ and $66\text{--}77\ \mu\text{m}$ in z . Three precision measurements help to determine the impact parameter of short lived particles such as b hadron and τ lepton decays and allow for their identification.

The Semiconductor Tracker

The SCT system consists of silicon microstrip detectors providing four precision measurements per track. The detector is arranged into four barrels and nine end-cap wheels. The barrels have radii of 299, 371, 443, 514 mm with the radii of the end-cap wheel being varied to ensure coverage up to $|\eta| < 2.5$. In total the detector contains $61\ \text{m}^2$ of silicon and 6.2 million readout channels. Each of the 4088 barrel and end-cap modules consists of four p-in-n microstrip detectors. The barrel detectors have a size of $6.36 \times 6.40\ \text{cm}^2$ and contain 768 readout strips of $80\ \mu\text{m}$ pitch. These are wire bonded together in pairs forming a 12.8 cm long section, and glued back-to-back at a stereo angle of $40\ \text{mrad}$. The end-cap modules are similar; the main difference being that the silicon strips are tapered. This gives the detector a spatial resolution of $16\ \mu\text{m}$ in $R - \phi$ and $580\ \mu\text{m}$ in $z(R)$ direction for the barrel(end-cap).

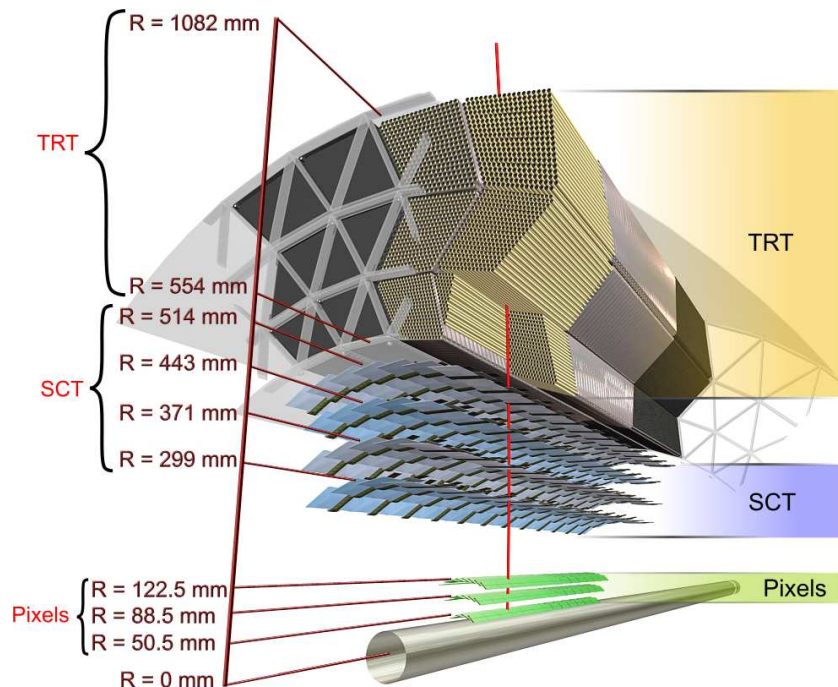


Figure 3.4: Cross section of the ATLAS inner detector. [121]

The TRT Detector

The TRT detector is located in the outer shell of the inner detector. It is based on the drift (straw) tube technology on average 36 hits per track are provided in the region $|\eta| < 2$. Further information on the electron identification is provided by the TRT measuring the so-called transition radiation. The straw tubes have a diameter of 4 mm and are filled with a xenon-based gas mixture. They contain a $30\ \mu\text{m}$ gold-plated tungsten anode wire, such that charged particles ionise the gas-mixture and current is measured. The space between the tubes is filled with polyethylene/polypropylene in order to produce Transition Radiation(TR), which can be used to distinguish for example between electrons and photons. The TRT is made up of a barrel and four end-caps. There are 52 544 axial straws in the barrel, aligned parallel to the beam pipe. Each straw is 148 cm in length and covers radii of 56–107 cm. The 319 488 end-cap straws lie at radii of 64–103 cm for the inner end-caps and 48–103 cm for the outer end-caps. These are arranged in a fan shape, projecting outward from the beam pipe. Each channel gives a drift time measurement, leading to a spatial resolution of $130\ \mu\text{m}$. Two independent energy thresholds are applied during the signal processing. The high thresholds are used to identify photons from the TR process and are used to discriminate electrons from charged particles, such as muons, pions and kaons.

3.2.3 The Calorimeter System

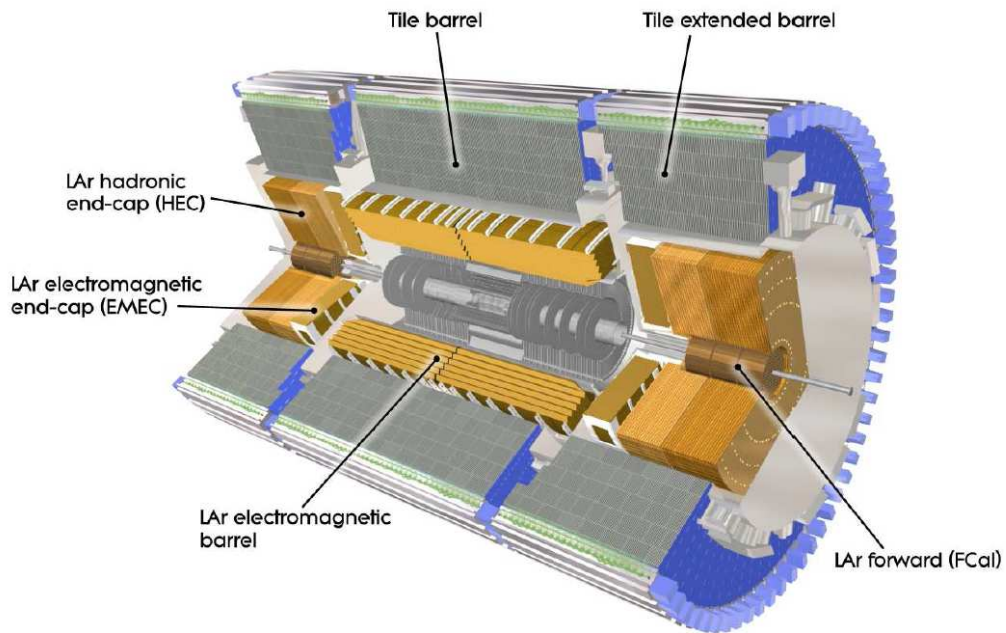


Figure 3.5: The ATLAS calorimeter system [121].

A schematic of the calorimetry system of the ATLAS detector is shown in Fig. 3.5. It covers the range $|\eta| < 4.9$ and consists of the electromagnetic and the hadronic calorimeter. The fine granularity of the electromagnetic calorimeter is well suited for precise electron and photon identification and energy measurement. The electrons and photons interact with the electric fields of the atoms in the detector material. The hadronic calorimeter was designed to identify and measure the energy of jets and E_T^{miss} .

The hadrons interact with the nuclei of the detector material via the strong force. On average they travel further and lead to different shower shapes than electrons and photons. In both cases the energy resolution is of the form:

$$\frac{\sigma_E}{E} = \frac{k}{\sqrt{E}} \otimes \frac{b}{E} \otimes c\% \quad (3.6)$$

where k is a stochastic term representing statistical fluctuations, b is a noise term and c is a constant term which represent uncertainties due to miscalibration, energy losses in calorimeter cracks, etc. which become important at high energies. The calorimeters are also used to provide information on particles which are not absorbed, such as muons or neutrinos. Muons leave an ionizing trace in the calorimeters, while neutrinos do not leave any signal. However they can be indirectly detected by measuring the missing transverse momentum in the event. There are two different calorimeter types installed in the ATLAS detector: The Liquid Argon (LAr) calorimeter and the Tile calorimeter. Both are sampling calorimeters made of more than one substance, an active and a passive medium.

Liquid Argon Calorimeter

The electromagnetic (EM) calorimeter is a lead/liquid-argon sampling calorimeter with accordion structure, using lead as the absorber material and liquid argon as the active medium. It is divided into a barrel part, covering the region $|\eta| < 1.475$ and two end-caps for the region $1.375 < |\eta| < 3.2$ and has a full azimuthal coverage. Energy measurements for electrons and photons are provided in the energy range 5 GeV to 5 TeV. A schematic view of a calorimeter slice in the barrel region is shown in Fig. 3.6, including the granularity of each of the sampling layers. The calorimeter comprises three samplings over its entire η range, with a separate presampler in the range $|\eta| < 1.8$. The presampler information is used in the calibration to estimate the energy lost by the electron or photon in the passive material of the solenoid. The barrel region displays the highest level of granularity and together with the outer end-cap wheels and the corresponding section of the inner detector it is devoted to precision physics. To achieve the desired performance, the amount of material in front of the calorimeter was minimised by having a common vacuum vessel for the LAr calorimeter and the central solenoid. The total thickness of the electromagnetic calorimeter is given in radiation lengths, X_0 , which is a measure of the thickness of the absorber in which the electron or photon energy is on average reduced to $1/e$ of its energy, where e is Eulers number. The thickness of the electromagnetic calorimeter corresponds to at least $22 X_0$. In the barrel region the radiation length increases with η from $22 X_0$ to $33 X_0$ and in the end-cap region from $24 X_0$ to $38 X_0$. The energy resolution of the electromagnetic calorimeter is equal to:

$$\frac{\sigma_E}{E} = \frac{9\%}{\sqrt{E}} \otimes 0.3\%, \quad (3.7)$$

where the energy E is expressed in GeV.

Liquid Argon Hadronic End-Cap Calorimeter

The Hadronic End-cap Calorimeter (HEC) consists of two independent wheels per end-cap using copper of different thicknesses as an absorber material interspersed with 8.5 mm liquid argon gaps as an active medium. The wheels are located directly after the end-cap of the EM and share the same LAr cryostats. The HEC extends out to $|\eta| = 3.2$, overlapping with the forward calorimeter, increasing the material density at the transition between the end-cap and the forward calorimeter (around $|\eta| = 3.1$). Similarly the HEC slightly overlaps with the tile calorimeter, extending to $|\eta| = 1.5$. The wheels are built from 32 identical wedge-shaped modules, assembled with fixtures at the periphery and the central bore. They are

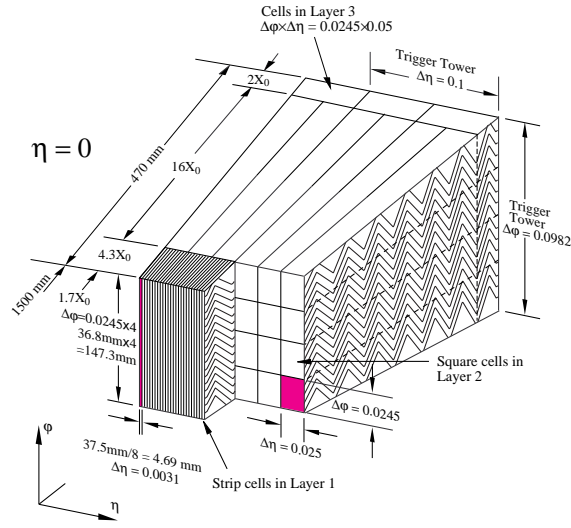


Figure 3.6: Sketch of a LAr barrel module where the different layers are clearly visible with the ganging of electrodes in ϕ . The granularity in η and ϕ of the cells of each of the layers and of the trigger towers is also shown [121].

divided into two longitudinal segments, for a total of four layers per end-cap. The wheels closest to the interaction point are built from 25 mm parallel copper plates, while those further away use 50 mm copper plates (for all wheels the first plate has only half the thickness). The outer radius of the copper plates is 2.03 m, while the inner radius is 0.475 m (except for the overlap region with the forward calorimeter, where the radius is 0.372 m). The energy resolution of the HEC is:

$$\frac{\sigma_E}{E} = \frac{50\%}{\sqrt{E}} \otimes 3\%. \quad (3.8)$$

Liquid Argon Forward Calorimeter

The Forward Calorimeter (FCal) is integrated into the end-cap cryostats. It is approximately ten interaction lengths, λ^3 , deep, and consists of three modules in each end-cap: the first is made of copper and is optimised for electromagnetic measurements. The other two consist of tungsten and mainly measure the energy of hadronic interactions. The modules consist of a metal matrix, with regularly spaced longitudinal channels filled with an electrode structure consisting of concentric rods and tubes parallel to the beam axis. Liquid argon in the gap between the rod and the tube is used as the active medium. This leads to an energy resolution of:

$$\frac{\sigma_E}{E} = \frac{100\%}{\sqrt{E}} \otimes 10\%, \quad (3.9)$$

Tile Calorimeter

The hadronic barrel calorimeter or hadronic tile calorimeter has a cylindrical design and uses plastic scintillator plates embedded in a steel absorber. The barrel covers the region $|\eta| < 1.0$, and the two

³ The interaction length is defined as the mean path length required to reduce the numbers of relativistic charged particles by the factor $1/e$

extended barrels the range $0.8 < |\eta| < 1.7$. The calorimeter is divided azimuthally into 64 modules, extending from an inner radius of 2.28 m to an outer radius of 4.25 m, and is longitudinally segmented into three layers with interaction lengths corresponding to $\sim 1.5 \lambda$, 4.1λ and 1.8λ in the barrel region and 1.5λ , 2.6λ and 3.3λ for the extended barrel. The total detector thickness at the outer edge of the tile-instrumented region is 9.7λ at $\eta = 0$. The tiles have a thickness of 3 mm and the steel plates have a total thickness of 14 mm. The scintillating tiles are read out on two sides by wavelength shifting fibres and two separate photomultiplier tubes. The configuration of the tile calorimeter leads to the same energy resolution as the HEC.

3.2.4 The Muon Spectrometer

The muon spectrometer is the outermost layer of the ATLAS detector. It is designed to efficiently identify and measure the momentum and position of muons up to $|\eta| < 2.7$. The design goal of the muon spectrometer is to measure the momentum of a 1 TeV muon to within 10% accuracy, which corresponds to a precision of at least $50 \mu\text{m}$.

The muon spectrometer is arranged in a barrel and two end-caps, each equipped with three layers of detector stations, as shown in Fig. 3.7. In the barrel region, tracks are measured in chambers arranged in three cylindrical layers around the beam axis positioned at radii of 5, 7.5 and 10 m. In the end-cap regions, the chambers are installed vertically, in three wheels at a distance z from the interaction point of 7.4, 14 and 21.5 m. Different types of subdetectors, optimised for precision measurements of the muon track or triggering, are installed alongside with the three superconducting air-core toroids, providing the magnetic field to bend the muon tracks. The precision measurements of the track coordinates, in the principal bending direction of the magnetic field, in the region $|\eta| < 2.4$, is provided by Monitored Drift Tubes (MDTs). Cathode Strip Chambers (CSCs) with higher granularity are used in the innermost plane and at large pseudorapidities, to withstand the demanding high rate and background conditions. Resistive Plate Chambers (RPCs) serve as trigger detectors in the barrel region, whereas Thin Gap Chambers (TGCs) provide trigger measurements in the end-cap.

MDTs are drift chambers formed by aluminium tubes with 3 cm diameter and length ranging from 0.9 to 6.2 m. In each chamber the tubes are arranged in two multi-layers, each formed by three or four layers of tubes. The MDT chambers use a mixture of Ar/CO₂ (93%/7%), kept at 3 bar absolute pressure. The electrons generated in the ionisation process are collected by a rhenium-tungsten wire with a diameter of $50 \mu\text{m}$, which is held at a potential of 3080 V. The resolution of individual tubes is around $80 \mu\text{m}$ and they have a maximum drift time of ~ 700 ns. In order to achieve $50 \mu\text{m}$ position resolution over the entire muon track, the position of individual tubes, relative to each other, must be known to $30 \mu\text{m}$ accuracy over the whole spectrometer. This alignment task is performed by an optical laser alignment system.

In the region of $2 < |\eta| < 2.7$ particle rates of over 150 kHz/cm^2 are expected in the inner wheel of the end-caps. These rates can not be handled by MDTs, thus CSCs are installed in this region for precision measurements. CSCs are multi-wire proportional chambers, with anode wires oriented radially and cathode strips oriented perpendicular to them, segmented in either η or ϕ . Interpolation of the charge picked up by the strips provides a position measurement. Each crossing muon gives four measurements in both η and ϕ planes, making it possible to resolve multiple particles per station. The chambers are filled with a gas mixture (Ar/CO₂ (80%/20%)) and provide small drift times resulting in a time resolution of 7 ns and achieve a typical resolution of $40 \mu\text{m}$.

A total of 606 RPC layers and 3588 TGCs are installed for triggering. Each RPC chamber is made from two detector layers, providing two ϕ measurements and two η measurements per chamber. Two sets of RPC chambers sandwich the MDT chambers in the middle station of the spectrometer, and a third

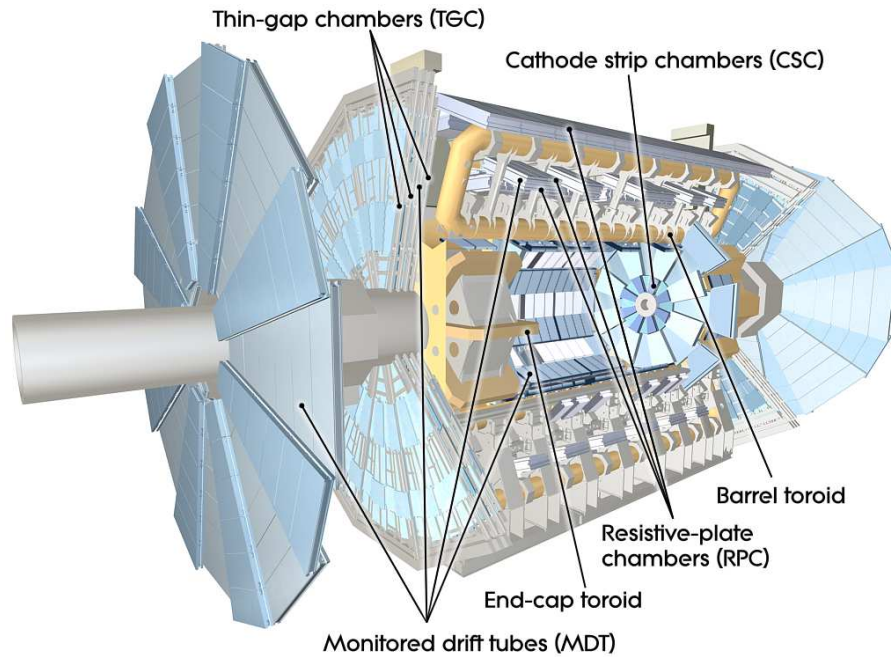


Figure 3.7: The ATLAS muon system [121].

layer of RPC chambers rests against the inside of the MDT outer station chambers. The ϕ measurements provide the second coordinate for the MDT precision measurements. Typical resolutions of the RPC measurements are 10 mm in both the bending and the non-bending plane. The RPCs are gaseous parallel electrode-plate detectors. RPCs are made up of pairs of large area bakelite sheets separated by a 2 mm gas region, filled with tetrafluorethane, in an electric field of 4.5 kV/mm. Discharges initiated by primary ionisation electrons from tracks are read out through capacitive coupling on orthogonal read-out strips on the two sides of the detector.

TGCs are made of effectively the same technology as the CSCs and provide the trigger measurement in the region $1.05 < |\eta| < 2.4$. They have gold-plated tungsten wires at 3100 V in a CO_2 (55%) and n-pentane (45%) mixture, providing a gas amplification of 106. In the TGCs, both the strips and the wires are used for readout. The system is 99% efficient to trigger in one bunch-crossing.

3.2.5 The Magnet System

A schematic of the ATLAS superconducting magnet system can be seen in Fig. 3.8. It comprises a central solenoid (CS) providing the inner detector magnetic field, a set of eight larger air-core toroids generating the field of the muon spectrometer and the two end-cap toroids. The CS extends over a length of 5.3 m and has a bore of 2.4 m. The overall dimensions of the magnet system are 26 m in length and 20 m in diameter. The CS provides a field of 2 T with a peak of 2.6 T at the super conductor itself. The peak magnetic fields for the super conductors in the barrel toroid (BT) and at the end-cap toroid (ECT) are 3.9 T and 4.1 T, respectively. The CS and the electro magnetic calorimeter share a common vacuum vessel in order to minimise the passive material in the detector. The CS coil is a mixture of NbTi, Cu and Al, and its design is a compromise between operational safety and reliability. Each of the toroids consists of eight coils assembled radially and symmetrically (for mechanical stability) around the beam

axis. The ECT coil system is rotated by 25° with respect to the BT coil system in order to provide radial overlap and to optimise the bending power in the interface region of both coil systems.

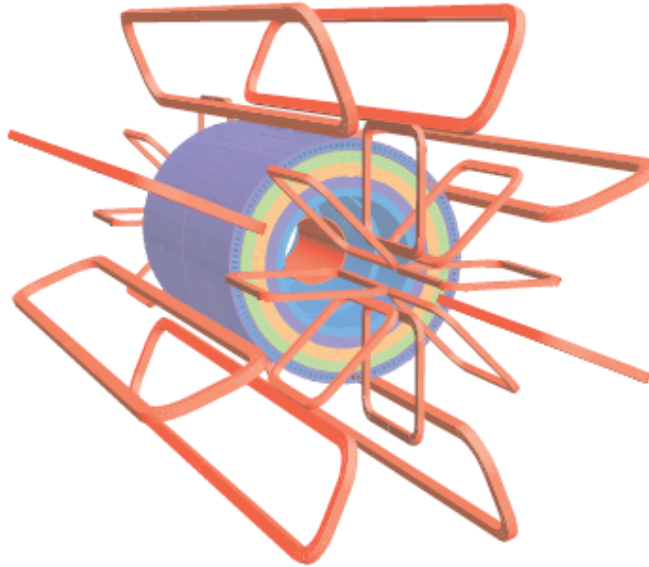


Figure 3.8: The ATLAS magnet system [121]

3.2.6 Forward detectors

Three smaller detector systems cover the ATLAS forward region, namely LUCID (LUMinosity measurement using Cerenkov Integration Detector) at ± 17 m from the interaction point, detecting inelastic $p - p$ scattering in the forward direction. It is used as the main online relative-luminosity monitor for ATLAS. The second luminosity detector is ALFA (Absolute Luminosity For ATLAS). It is located at ± 240 m from the interaction point and consists of scintillating fiber trackers located inside Roman pots designed to approach 1 mm to the beam. The third detector is the Zero-Degree Calorimeter (ZDC), plays a key role in determining the centrality of heavy-ion collisions. It is located at ± 140 m from the interaction point, just beyond the point where the common straight-section vacuum pipe divides back into two independent beam pipes. The ZDC modules consist of layers of alternating quartz rods and tungsten plates, which measure neutral particles at pseudorapidities $|\eta| > 8.2$.

3.3 The ATLAS Trigger System

With a total bunch crossing rate of 40 MHz at nominal luminosity, the ATLAS trigger system is facing the challenge of reducing the amount of data by a factor of 2×10^5 to the storage capacity, while efficiently selecting interesting physics events. The ATLAS trigger and data-acquisition system is based on a three-level online event selection detailed in Fig. 3.9. The Level-1 Trigger (LVL1) is based on custom-made hardware processors that select events containing high- $E_T(p_T)$ objects (electrons, muons, taus, photons, jets), and also missing energy and total energy, using reduced-granularity information from a subset of detectors. Events passing the LVL1 trigger, at the rate of < 75 kHz (upgradable to

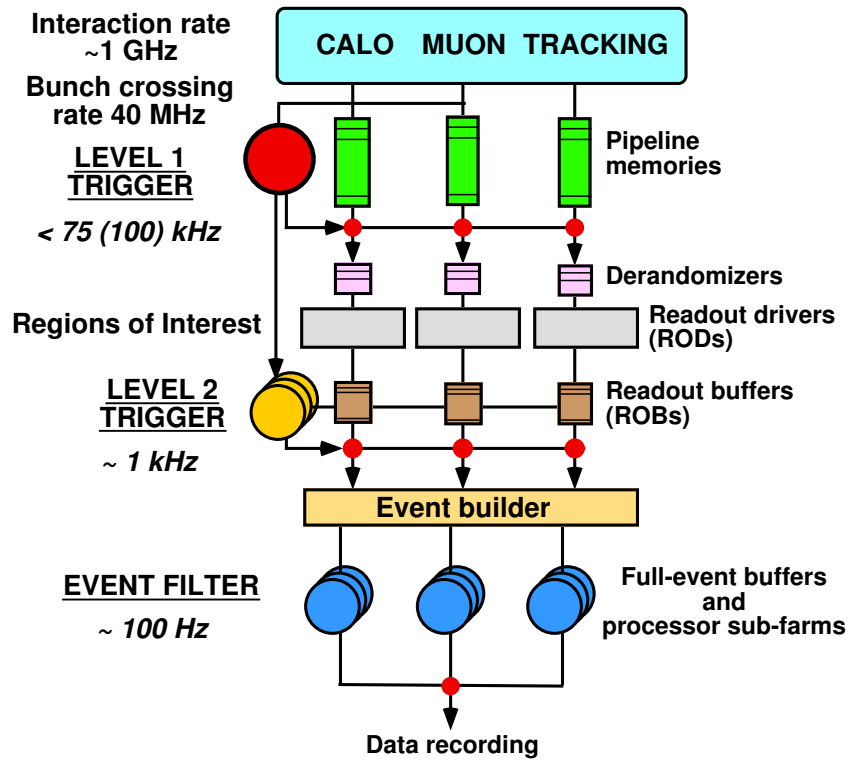


Figure 3.9: Block diagram of the ATLAS trigger [121].

100 kHz), are passed to the software-based High Level Trigger (HLT) system, which consists of the Level-2 (LVL2) and the Event Filter (EF).

The LVL1 trigger uses information based on relatively coarse data from the calorimeter sub-systems, which are used to identify electromagnetic clusters, jets, τ leptons, E_T^{miss} and large total transverse energy. Muons are triggered using the Resistive-Plate-Chambers (RPC) in the muon barrel region and Thin-Gap Chambers (TGC) in the end-cap region, these provide rough measurements of the p_T , η and ϕ of the muons candidate. All components of LVL1 trigger system are synchronised with the 40 MHz LHC clock, and the system architecture makes full use of parallel processing, to reduce processing time. The LVL1 decision has to reach the front-end electronics within a latency of $2.5 \mu\text{s}$. The LVL1 calorimeter trigger uses the information from roughly 7000 projective regions, called *trigger towers*. The energy read out in these trigger towers is normalised to the full expected transverse energy using a dedicated calibration. The trigger towers have a granularity of $\Delta\eta \times \Delta\phi = 0.1 \times 0.1$ in the central region, and are larger and less regular in the forward region of the detector. The electron and photon trigger algorithm identifies Regions of Interest (ROI) as a 2×2 trigger tower cluster in the electromagnetic calorimeter, in which at least one of the pairs of nearest neighbour towers exceeds a pre-defined threshold. Furthermore an isolation veto can be set for the 12 surrounding trigger towers in the electromagnetic calorimeter, as well as for the hadronic tower sums behind the cluster and the isolation ring. Similarly the jet trigger algorithm is based on the excess of pre-defined thresholds using the summed transverse energy of the hadronic and the electromagnetic calorimeter within an ROI built from 4×4 , 6×6 or 8×8 trigger towers. LVL1 muons are identified by forming coincidences between the muon trigger chambers, which are arranged in planes for the barrel (TGC) and end-cap (RPC) trigger chambers. In order to form coincidences the hits are required to lie within a parametrised geometrical muon *road*. These roads represent an envelope containing trajectories, from the nominal interaction point, of muons of either charge with a transverse momentum above a given pre-defined threshold. The data collected from the muon and calorimeter trigger is processed and forwarded to the Central Trigger Processor, which takes the trigger decision based on logical expressions stored in look-up tables. The trigger items can be further penalised by a *prescale* p , which reduces the acceptance rate of this trigger by a factor of p . LVL2 is running in a seeded mode, using local informations from the detectors in ROI identified by LVL1. These ROIs usually contain 1% to 2% of the full event data. LVL2 has access to fragments of detector data, from detector subsystem readout buffers. The LVL2 is optimised for speed and runs fast algorithms to refine the LVL1 selection using the full granularity, reducing the rate to 1 kHz. The latency time of the LVL2 trigger is between 1 and 10 ms, with an accept rate of about 1 kHz. The Event Filter (EF) works on the output events of LVL2. In contrast to LVL2 it has access to the full event to make a decision. In principle, the EF is more properly defined as a filter as it is not limited by response time but rather by storage specifications or input considerations. The full event is stored on disk and is reconstructed with offline-like algorithms. Accepted events are written to mass storage, rejected events are deleted. The EF has an output rate at 100 Hz to 200 Hz that are written to mass storage.

3.4 LHC Operation and ATLAS Data-Taking

This section gives an overview of the LHC conditions during Run 1 data taking following the information given in [127, 128]. The first successful proton–proton collisions at the LHC were recorded in November 2009 at a centre-of mass energy of 900 GeV. Within only one week these energies were increased to 2.36 TeV, surpassing the existing world record energy. The LHC was then commissioned at a beam energy of 1.2 TeV. In March 2010 the energy was increased to a centre-of-mass energy of 7 TeV, and data was collected at a rather low luminosity throughout 2010. The full 2010 dataset accumulated

3 The Experimental Setup

	Nominal	2010	2011	2012
Circumference		26.7 km		
Injection energy per proton [TeV]		450 GeV		
\sqrt{s} [TeV]	14	7	7	8
Peak Luminosity [$\text{cm}^{-2}\text{s}^{-1}$]	10^{34}	2×10^{32}	3.5×10^{33}	7.5×10^{33}
Bunches per beam k	2808	368	1380	1380
Protons per bunch N ($\times 10^{11}$)	1.15	1.2	1.45	1.7
Bunch separation Δt [ns]	25	150	50	50
Bunch length (along z) [mm]	56	56	56	48
Transverse dimension at the interaction point [μm]		25 to 12		

Table 3.1: Summary of the run conditions during the proton-proton data taking during Run 1, separated for the years 2010, 2011 and 2012. Based on the information given in [127].

to 48.1 pb^{-1} of proton-proton collisions delivered to the ATLAS experiment, of which 45.0 pb^{-1} were recorded by ATLAS. This data allowed the 'rediscovery' of the known Standard Model processes and the first iteration of many searches for new physics at the LHC. The proton-proton run was succeeded by the first lead-lead collisions at the LHC. In the beginning of 2011, proton-proton data taking was resumed and the luminosity delivered to ATLAS increased dramatically, resulting in a total integrated luminosity of 5.61 fb^{-1} delivered, and 5.25 fb^{-1} recorded by the ATLAS experiment at $\sqrt{s} = 7 \text{ TeV}$. After another lead-lead run in November and December 2011, the proton beam energies were increased to 4 TeV for the 2012 run, leading to a centre-of-mass energy of $\sqrt{s} = 8 \text{ TeV}$. The LHC delivered an accumulated luminosity of 23.3 fb^{-1} of which 21.7 fb^{-1} were recorded by the ATLAS experiment. In total 1.8 proton-proton collisions were recorded during Run 1 by the ATLAS detector. The Run 1 data taking was concluded by a final proton-lead run in January and February 2013, before the machine was shut down for upgrades to necessary to reach the design energies in Run 2, which has recently started. The cumulative progression of the integrated luminosity delivered to ATLAS, along with the fraction of successfully recorded data, passing quality requirements, is shown in Fig. 3.10. The highest luminosity, with $7.73 \times 10^{34} \text{ cm}^{-2}\text{s}^{-1}$, was achieved by the LHC in 2012, which is close to the design value of $10^{34} \text{ cm}^{-2}\text{s}^{-1}$. This was achieved by halving the proton bunch crossing rate to 50 ns, which was compensated by a higher number of protons in each bunch; 1380 bunches with 1.7×10^{11} protons were accelerated instead of originally 2808 bunches with 1.15×10^{11} protons each. This change lead to a larger number of simultaneously occurring proton-proton collisions, so called *in-time* pile-up events, while the greater separation lead to a lower number *out-of-time* pile-up events. The distribution of the observed number of interactions per bunch crossing for $\sqrt{s} = 7 \text{ TeV}$ and 8 TeV is shown in Fig. 3.10. The average number of pile-up events recorded in 2012 is 20.7. The analysis presented here is based on proton-proton collisions recorded with the ATLAS detector at $\sqrt{s} = 8 \text{ TeV}$ in 2012.

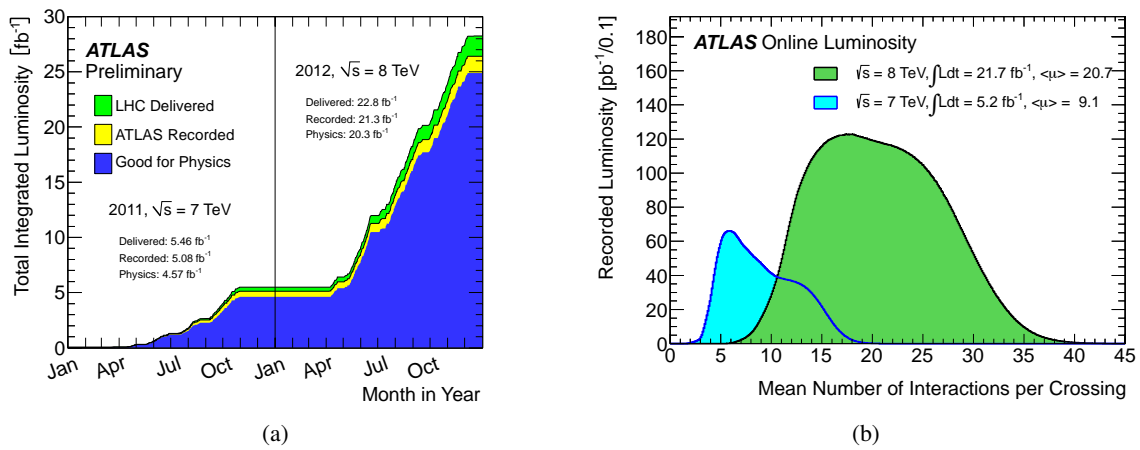


Figure 3.10: Cumulative luminosity versus time delivered by the LHC (green), recorded by ATLAS (yellow), and flagged to be good quality data (blue) during stable beams at proton-proton collision for the Run 1 data taking period (a). Luminosity weighted distribution of the mean number of interactions per bunch crossing for the dataset collected in 2011 and 2012 (b) [128].

Object Reconstruction

The event reconstruction at modern high energy physics experiments is a complex task. Object reconstruction is the process in which physics objects, such as electrons, muons and jets are built from detector information. The information from the sub-detectors of each triggered event is collected and combined into basic quantities such as energy deposits in the calorimeter and hits in the tracker and muon system. These are combined by dedicated reconstruction algorithms for each physics object within the ATHENA software framework [129]. Events generated by Monte Carlo (MC) simulation undergo the same reconstruction algorithms as collision data. A short description of the Monte Carlo simulation and production in ATLAS is presented in 4.1.

This Chapter summarises the reconstruction and identification of the relevant physics objects and their performance, along with a brief outline of the respective systematic uncertainties. The track reconstruction is described in Section 4.2, which is the basis for an efficient primary vertex reconstruction described in Section 4.3. A main focus is set on the description of electrons and muons, as they are indispensable for the reconstruction of the heavy three-lepton resonance described in this thesis and are elaborated on in Section 4.4.2 and Section 4.4.5. Finally a brief description of the jet algorithm in Section 4.5 and the E_T^{miss} reconstruction in Section 4.6 is given.

4.1 ATLAS Simulation

The main objective of simulated event samples in ATLAS is the evaluation of the collected data in the light of our current physics understanding. A realistic detector simulation is needed to simulate the detector effects, allowing for a direct comparison between simulated and collision data [117]. An overview of the steps involved in the simulation process is shown in Fig. 4.1. In this figure, algorithms and applications to be run for the simulation are surrounded by square-cornered boxes. The resulting data objects are depicted in round-cornered boxes, while optional steps and their data format are shown as dashed boxes.

A number of different event generators are used to generate events for the various physics processes, as described in 2.4.1, and form the basis for the simulated event samples. These events are interfaced with the ATLAS simulation software using the standard HepMC [130] output format. Each generated particle is propagated through the full GEANT4 [131] description of the ATLAS detector, producing so-called GEANT4 hits. They are a record of the spatial and timing information of each particle traversing the detector and how much energy it deposited. GEANT4 provides an exact description of the material

distribution in the ATLAS detector, allowing for a detailed description of the detector response and an accurate physics model for the interactions of the different particles with the multiple detector materials. The information in the GEANT4 output file includes the information from the hard scattering process, minimum bias, beam halo, beam gas, and cavern background events. During runtime the user is able to set the desired detector conditions, including extra material, misalignments, distortions of any detector material and known defects. The full simulation step is a very computing intensive step using up to several minutes per event. A truth record, which contains the parton level information of all particles generated and the event information, is kept both in the generation and the simulation step, allowing to track the origin of each final state particle. The truth information of each particle given in the common les houches format [114]¹ is especially helpful to quantify the success of the reconstruction software.

In the digitization step the hits from the simulation are translated into digits, such as times and voltages, comparable to those produced from the raw data in actual collisions. The electronic noise and the expected pile-up are added at this stage, in order to save computation time at the simulation step. Furthermore, the LVL1 trigger simulation is run using the specified trigger menu. In the final simulation step, the reconstruction step, the raw data digits, such as times and voltages are processed and tracks and energy deposits are reconstructed, which form the so-called event summary data (ESD). These ESD are further processed and transformed into more user-friendly data formats.

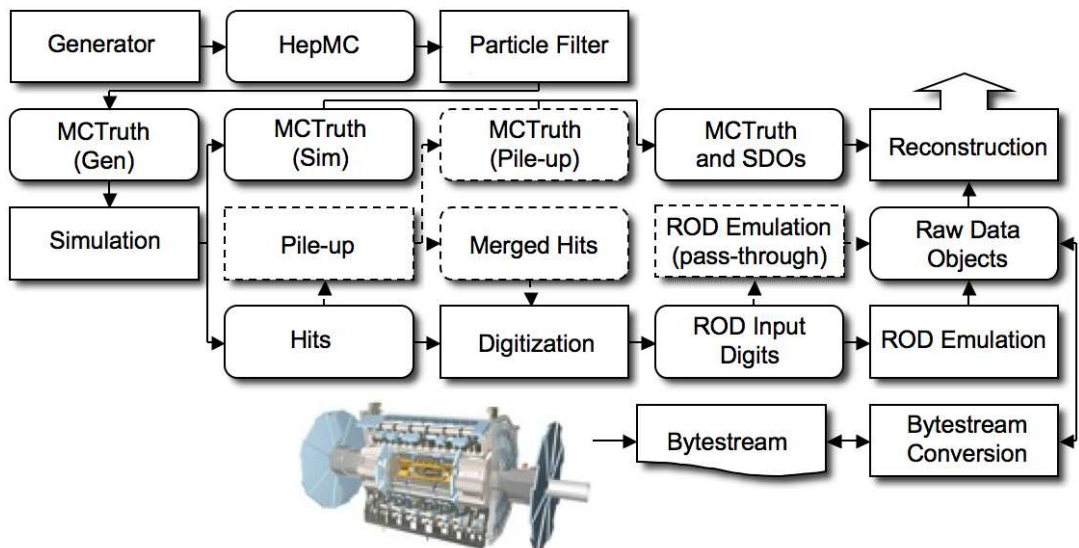


Figure 4.1: The flow of the ATLAS simulation software, from event generation (top left) to reconstruction (top right). Algorithms are placed in square-cornered boxes and persistent data objects are placed in round cornered boxes. The optional pile-up portion of the chain, used only when events are overlaid, is dashed. Generators are used to produce data in HepMC format. MC truth is saved in addition to energy depositions in the detector (hits). This truth is merged into Simulated Data Objects (SDOs) during the digitization. During the digitization stage also the Read Out Driver (ROD) electronics are simulated. [117]

4.2 Track Reconstruction

In the track reconstruction process, charged-particle tracks are reconstructed based on the information from the ATLAS tracking detectors. Tracks are reconstructed within the inner detector coverage of

¹ A standard file format, that stores process and event information, primarily output from parton-level event generators

$|\eta| \leq 2.5$ and a full ϕ acceptance.

Two reconstruction sequences are implemented in the track reconstruction software, the primary *inside-out* track reconstruction and a consecutive *outside-in* algorithm, mainly targeted at secondary particles [132, 133]. The primary step in both tracking algorithms is the formation of three-dimensional space points in the three tracking detectors. In case of the pixel sensors, the two-dimensional measurement is transformed in a local-to-global transformation, using the constraint of the surface representation. For the SCT detector the transformation of the one-dimensional point is performed by utilising the stereo angle from the two sensors of the model, which are glued together back-to-back, and the beam-spot position.

Within the *inside-out* approach, track candidates are built from a seed of three silicon space points, compatible with the preliminary primary vertex found, by applying a window search given by the seed direction. Further hits are added to the track of the particle moving away from centre, using a combinatorial Kalman filter [134]. In the TRT the timing information is converted into calibrated drift circles. The seeds are required to have a minimum transverse momentum of $p_T > 400$ MeV. The fraction of seeds resulting in a track candidate is on the order of 10%. The ambiguity between tracks is solved depending both on the fit quality of the track candidate and different characteristics of a track, which are combined into a so-called *track scoring* [132]. Tracks that pass the ambiguity solving are extended into the TRT using an extension algorithm that searches for the seed candidates, and a mother algorithm, which processes and evaluates the extensions.

Although the *inside-out* approach is very efficient, an *outside-in* approach is needed to account for both tracks coming from secondary vertices, such as from K_S decays or photon conversions, and ambiguous hits that can shadow the track seed in the silicon detectors. In this approach, track segments found in the TRT are extended inwards to the silicon detectors, ignoring hits that have already been assigned in the *inside-out* approach. TRT tracks without an extension to the silicon detectors are called TRT *stand-alone*.

The track reconstruction efficiency is calculated as the fraction of primary particles with $|\eta| < 2.5$ and $p_T > 400$ MeV matched to a reconstructed track [133]. The reconstruction efficiency was only evaluated for the leading *inside-out* algorithm. However, it is expected that both the *outside-in* and the TRT *stand-alone* tracks will have a significant impact from increased pile-up. The track reconstruction efficiency is measured as a function of p_T , shown in Fig.4.2(a), and η shown in Fig.4.2(b), using simulated minimum bias events at three different pile-up scenarios ($\mu = 1, 21, \text{ and } 41$). The solid lines show the reconstruction efficiencies for the *robust requirement*, while the dashed lines show the looser default requirements of seven hits. In both cases the increased pile-up results in a track reconstruction efficiency change of less than 1 %, whereas the tighter robust requirements lead to an efficiency reduction of about 5 %.

4.3 Vertex Reconstruction

Primary vertices in ATLAS are reconstructed by an iterative vertex finding algorithm [133]. It associates the reconstructed tracks to vertex candidates and is extended by a fitting algorithm to reconstruct the vertex position, including the corresponding error matrix. The tracks used in the primary vertex reconstruction are selected to fulfill a number of additional quality criteria. These criteria are based on the number of silicon hits, the transverse momenta and the transverse and longitudinal impact parameters of the track, along with their uncertainties. The quality criteria are targeted at removing a large fraction of tracks originating from secondary interactions. The track finding algorithm is seeded by the global

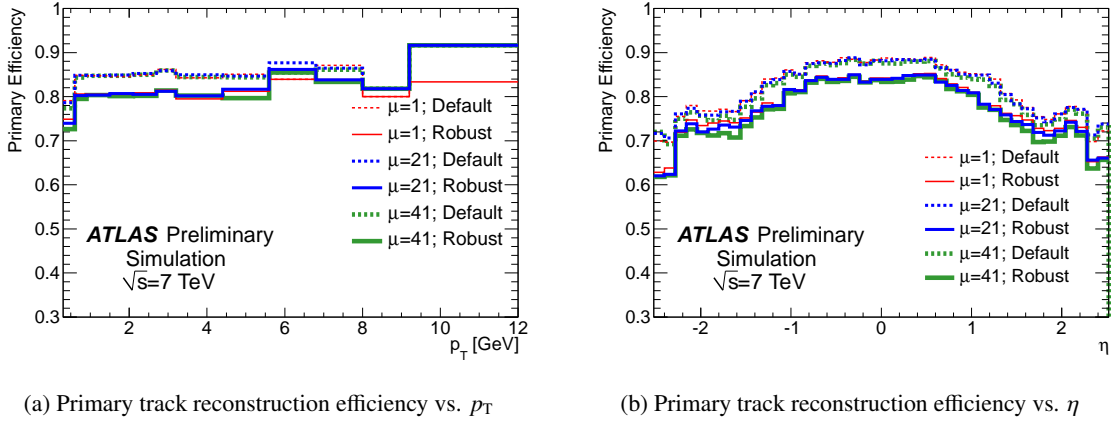


Figure 4.2: The primary track reconstruction efficiency in minimum-bias Monte Carlo samples containing exactly one or on average 21 or 41 interactions, respectively. The distributions are shown for tracks passing the default (dashed) and robust (solid) requirements. Statistical uncertainties are not shown, but they are significant as there are only few secondary particles at higher p_T [133].

maximum in the distribution of z -coordinates of the tracks, computed at the point of closest approach to the beam-spot centre. The vertex fitting algorithm is based on a χ^2 fit, starting from the seed and the nearby tracks. Each track is weighted according to its compatibility with the vertex, depending on the χ^2 of the fit. Tracks that are incompatible with the previous vertex candidate by more than 7σ (have a $\chi^2 > 49$) seed a new vertex. This procedure is repeated until no unassociated tracks are left in the event, or no further vertex is found. The loose χ^2 requirement reduces the number of single vertices, which are discarded. In general the track with the highest sum of track p_T^2 is assumed to be the primary vertex of the event, corresponding to the hardest interaction.

The vertex reconstruction efficiency as a function of the average number of interactions in simulated minimum-bias events is shown in Fig. 4.3(a) [133]. Vertices from interactions with at least two primary charged particles with $|\eta| < 2.5$ and $p_T > 400$ MeV, denoted robust (reconstructible interactions), have a $\sim 90\%$ reconstruction efficiency, for single interactions. The reconstruction efficiency decreases with higher pile-up to $\sim 60\%$. Another important measure is the fake-vertex reconstruction probability, shown in Fig. 4.3(b). While the default reconstruction is very sensitive to the amount of pile-up, increasing from 0.1% for $\mu = 1$ to 7% for $\mu = 7$, the robust reconstruction only exhibits a mild pile-up dependence.

4.4 Leptons

Electrons and muons play an important role in the final states analysed in this thesis. Final states with τ leptons are not included in this thesis, and are thus not reconstructed specifically. Due to their various decay topologies, τ leptons will be identified as isolated electrons, muons or narrow jets. In this section, an overview of the trigger, reconstruction, identification, calibration and efficiency of the reconstruction of electrons and muons is given.

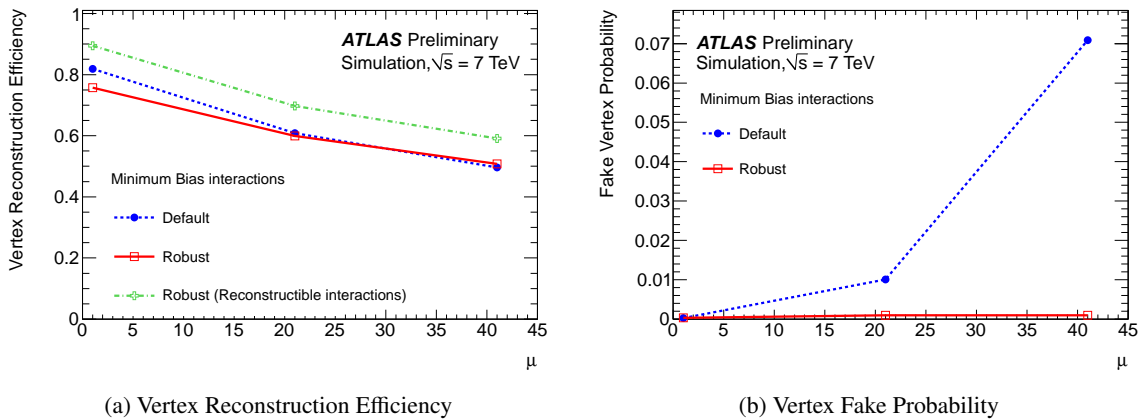


Figure 4.3: The vertex reconstruction efficiency (a) and fake probability (b) as a function of the average number of interactions in minimum bias simulated event samples. The default vertex selection is shown in blue, while the robust selection is shown in red. The green line in (a) shows the vertex reconstruction efficiency for interactions with at least two stable charged primary particles with $p_T > 400$ MeV and $|\eta| > 2.5$. These are defined as reconstructible interactions [133].

4.4.1 Electron Trigger

The ATLAS trigger is a three tiered trigger system, as laid out in Section 3.3. At LVL1 the electron trigger decision is based on Regions of Interest using only calorimeter information, which doesn't allow for a differentiation between electrons and photons. The trigger towers have a granularity of $\Delta\eta \times \Delta\phi = 0.1 \times 0.1$. Events are accepted if the signal within a sliding window of 4×4 trigger towers 3.3 passes a configurable energy threshold in at least one ROI. The second trigger level uses a fast calorimeter reconstruction of the full calorimeter granularity, and uses a fast track reconstruction. The tracks and clusters are matched to find electron trigger candidates. The Event Filter utilises slightly reduced offline reconstruction algorithms. Hence the electron and photon selection depends on the same set of selection criteria as used by the offline particle identification described in Section 4.4.2. This implementation has been adopted in order to minimise potential sources of trigger inefficiencies on events selected by the offline analyses, while retaining a high selection efficiency.

The electron triggers chosen for the analysis are the EF_e24vhi_medium1 and EF_e60_medium1 triggers, which were the lowest unprecaled single electron triggers available during the whole 2012 data taking [135]. In the trigger names the numbers reflect the threshold applied on the online transverse momentum. The medium1 refers to the set of identification criteria applied to the cluster and track of the trigger candidate, and vh indicates the veto on activity in the hadronic calorimeter behind the electron cluster, which further reduces the trigger acceptance of misidentified jets. The hadronic shower leakage requirement consists of a veto on hadronic energy of more than 1 GeV deposited in the hadronic layers of the calorimeter within a region of 0.2×0.2 in $\eta \times \phi$ behind the electromagnetic cluster. Finally, the i indicates that the electron track candidate is required to pass an isolation criteria. In case of the EF_e24vhi_medium1 trigger this is a relative track isolation cut of $\Sigma p_T / p_T(e) < 0.1$, where Σp_T refers to the sum of the transverse momenta of tracks with $p_T > 1$ GeV found in the ID in a cone of $\Delta R = 0.2$ around the electron track after subtracting the transverse momentum of the electron track. This track isolation is looser than the isolation required for the offline reconstructed electron candidates.

The trigger efficiency in data is evaluated with a *tag-and-probe* method using $Z \rightarrow e^+e^-$ events in data. A *tag-electron* is selected to trigger the event and must pass tight identification criteria. For the

second electron, denoted *probe-electron*, no further identification criteria are required. Thus the trigger efficiency is determined from a high-purity sample of electrons, obtained from selected events with two electrons with an invariant mass consistent with the Z -boson mass. The trigger efficiency of the logical OR combination of the EF_e24vhi_medium1 and e60_medium1 triggers is shown as a function of the reconstructed electron E_T in Fig. 4.4(a) and as a function of the pseudorapidity in Fig. 4.4(b), with respect to the medium offline electron identification. These two triggers are combined with a logical OR to improve the high- E_T efficiency, visible in the plot as the abrupt increase in efficiency at 60 GeV. The efficiencies measured in data are compared with those determined from simulated event samples. Scale factors are applied to correct the efficiencies found in simulated events to those observed in data. Systematic uncertainties arising from these corrections are in the order of 2% at low transverse energies and large pseudorapidities and $\sim 2\%$ for transverse energies above 28 GeV in the central detector region.

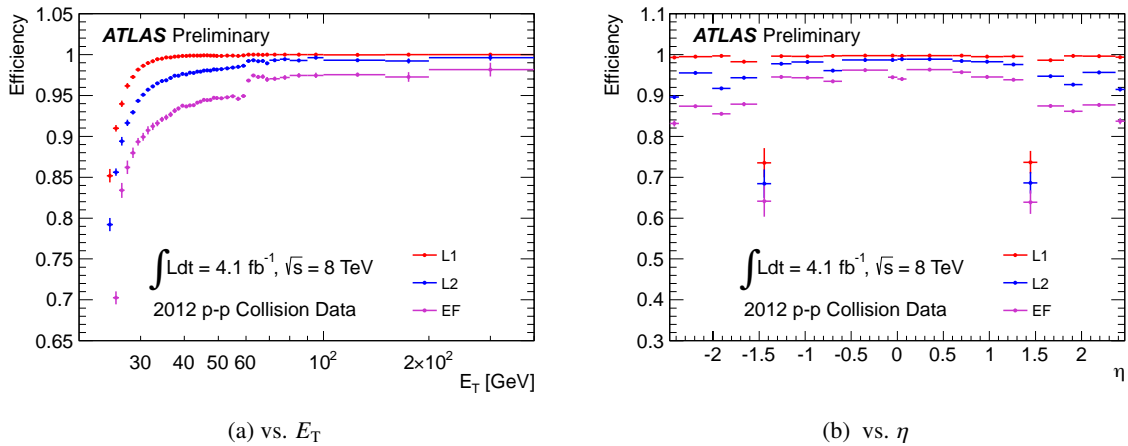


Figure 4.4: Trigger efficiency measured in data for the logical OR of the EF_e24vhi_medium1 and EF_e60_medium1 single electron triggers, as a function of E_T in (a) and η in (b) of the reconstructed electron. The cumulative trigger efficiencies for each level are shown, obtained from a *tag-and-probe* measurement in $Z \rightarrow ee$ events [135].

4.4.2 Electron Reconstruction

Electrons are reconstructed in the central region, up to $|\eta| < 2.47$, from an energy deposit in the electromagnetic calorimeter which is matched to an ID track. Electrons with pseudorapidities in the range $2.47 < |\eta| < 4.9$, so called forward-electrons, can be reconstructed and identified from three-dimensional topological calorimeter clusters as described in Ref. [136].

For the central electron reconstruction a sliding window approach is implemented with a window size of 3×5 calorimeter cells. Each cell corresponds to a size of 0.025×0.025 in $\eta \times \phi$ space. The cluster reconstruction is seeded when the energy forms a local maximum with a transverse energy $E_T > 2.5$ GeV in the second layer of the electromagnetic (EM) calorimeter. The cluster reconstruction efficiency is approximately 100% for electrons with $E_T > 15$ GeV. In contrast to photon candidates, which are reconstructed with the same clustering strategy, electron track candidates are extended by a track-to-cluster matching. Tracks are extrapolated to the middle EM layer from their last measurement point, if their transverse momentum is greater than 0.5 GeV. The matching is successful, if the distance between the track impact point and the EM cluster barycenter is $|\Delta\eta| < 0.05$. For the matching it is required that $|\Delta\eta| < 0.1$ and an asymmetric $\Delta\phi$ requirement is applied, which accounts for bremsstrahlung losses

when the trajectory of the charged particle is bent in the magnetic field of the ID. At least one track is needed to reconstruct the electron candidate. However, if several track candidates are matched to the same cluster, priority is given to the track with the highest number of silicon hits and the closeness in ΔR . The cluster is then rebuilt using 3×7 cells in the barrel region and 5×5 cells in the end-cap. Its energy is computed accounting for energy losses in the material in front of the EM calorimeter, energy leakage outside the cluster and energy deposits beyond the EM calorimeter. Candidates passing the described selection are added to the list of electron candidates.

Typically a significant fraction of electron candidates arise from background objects, like hadronic jets, or secondary electrons originating from photon conversions, Dalitz decays or semileptonic heavy flavour decays. To obtain a high electron purity while keeping a high electron efficiency, several discriminating variables are defined. For electrons selected in this thesis a cut-based identification approach is used. In addition a multivariate analysis approach has been implemented. The variables used for the identification are defined in Table 4.1, which also summarises the application of each of the variables at the three working points (`loose`, `medium`, `tight`). The discriminating variables describe the longitudinal and transverse shower shapes in the calorimeter, the track properties in the ID and the matching between the tracks and the energy clusters. The `loose`, `medium` and `tight` working points are optimised in ten bins of η and eleven bins of E_T . This allows to account for differences in the electromagnetic shower shape due to specific detector responses at different electron energies. The `tight` selection, used in this thesis, has an electron efficiency of $\sim 80\%$ and a hadronic jet rejection rate of 10^6 for electrons from simulated Z decays.

Two optional isolation requirements aim for a further rejection of misidentified electrons. The first isolation is calorimeter-based and uses the variable $E_T^{\text{cone}\Delta R}$, which is the sum of the transverse energy deposited in the calorimeter cells in a cone of ΔR around the electron direction. The reconstructed energy deposited by the electron itself is subtracted. Additionally, this variable is corrected for energy leakage and pile-up. Secondly, a track-based isolation is used based on the variable $p_T^{\text{cone}\Delta R}$, defined as the sum of the transverse momenta of the tracks within a cone of radius ΔR around the electron direction, excluding the track associated with the electron itself. The tracks are required to be of good quality and matched to the primary vertex.

Electron reconstruction and identification efficiency

The total electron efficiency in ATLAS is calculated from the product of the trigger, the reconstruction, the identification and the so-called additional efficiency accounting for additional analysis criteria, like for instance isolation [137]. All these efficiencies are determined using *tag-and-probe* methods. While the determination of the identification efficiency is based on $J/\psi \rightarrow e^+e^-$, $Z \rightarrow e^+e^-\gamma$ and $Z \rightarrow e^+e^-$ events the determination of the reconstruction efficiency uses only the latter decay, which results in the purest probe electron selection. Since the electrons in the heavy lepton analysis are expected to have large transverse momenta, a focus is set on the efficiencies from $Z \rightarrow e^+e^-$ events.

For the $Z \rightarrow e^+e^-$ selection, the tag electron is required to pass the `tight` electron selection, have a $p_T > 25$ GeV and be trigger matched. Electrons in the transition region between barrel and end-cap, $1.37 < |\eta| < 1.52$, are omitted. Probe electrons are selected if they have $p_T > 10$ GeV, a track of good quality and are isolated, based on the requirements defined above. The dielectron invariant mass is required to be within 15 GeV of the Z -pole mass. The expected background is derived using data-driven methods.

The identification and reconstruction efficiency is determined in bins of η and E_T . The measured electron identification efficiency is depicted as a function of E_T in Fig. 4.5(a) and η in Fig. 4.5(b) for the various cut-based and likelihood selections. Tighter cuts on more variables leads to a decrease of

Type	Name	Description	Loose	Medium	Tight
Hadronic leakage	R_{had1}	Ratio of E_T in the first layer of the hadronic calorimeter to E_T of the EM cluster	√	√	√
Middle layer of EM calorimeter	R_η	Ratio of the energy in 3×7 cells over the energy in 7×7 cells centred at the electron cluster position	√	√	√
	$w_{\eta 2}$	Lateral shower width: RMS of the energy weighted η position of all the cells in the second calorimeter layer of the cluster	√	√	√
Strip layer of EM calorimeter	w_{stot}	Lateral shower width, $\sqrt{(\sum E_i (i - i_{\text{max}})^2) / (\sum E_i)}$, where i runs over all strips in a window of $\Delta\eta \times \Delta\phi \approx 0.0625 \times 0.2$ and i_{max} is the index of the highest-energy strip	√	√	√
	E_{ratio}	Ratio of the energy difference between the largest and second largest energy deposits in the cluster over the sum of these energies	√	√	√
3 rd layer of EM calorimeter	f_3	fraction of energy in the 3 rd layer of the EM calorimeter		√	√
Track quality	n_{pixel}	Number of hits in the pixel detector	√	√	√
	n_{Si}	Number of total hits in the pixel and SCT detectors	√	√	√
	d_0	Transverse impact parameter		√	√
TRT	n_{TRT}	Total number of hits in the TRT		√	√
	f_{HT}	Ratio of the number of high-threshold hits to the total number of hits in the TRT		√	√
Conversions	n_{BL}	Number of hits in the b-layer		√	√
		Veto electron candidates matched to reconstructed photon conversions			√
Track-cluster matching	$\Delta\eta$	$\Delta\eta$ between the cluster position in the strip layer and the extrapolated track		√	√
	$\Delta\phi$	$\Delta\phi$ between the cluster position in the middle layer and the extrapolated track			√
	E/p	Ratio of the cluster energy to the track momentum			√

Table 4.1: Definition of variables used for loose, medium and tight electron identification in the central region of the detector ($|\eta| < 2.47$).

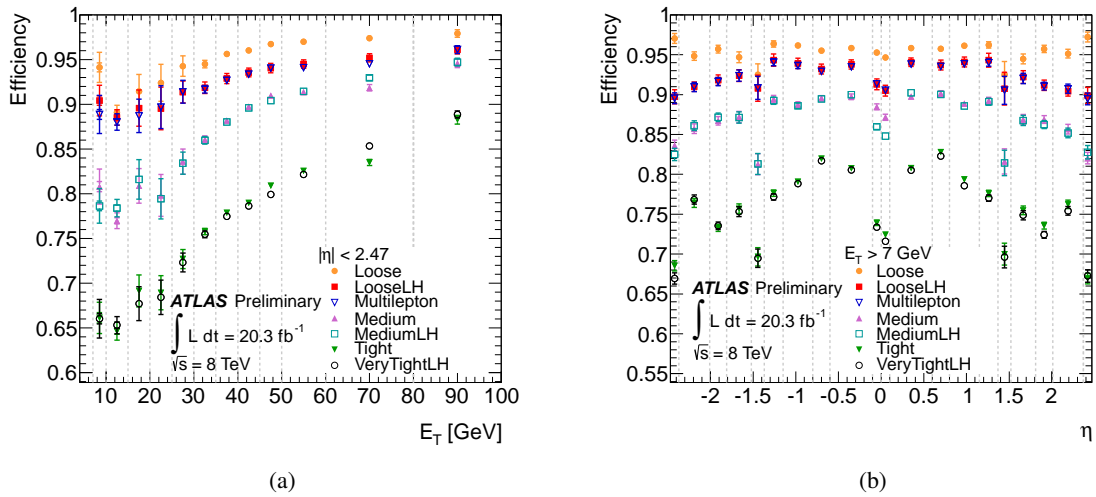


Figure 4.5: Measured electron identification efficiency for the various cut-based and likelihood selections as a function of E_T in (a) and η in (b). The data efficiency is derived from the measured data-to-MC efficiency ratios and the MC prediction from $Z \rightarrow e^+e^-$ decays. The uncertainties are statistical (inner error bars) and statistical+systematic (outer error bars). The dashed lines indicate the bins in which the efficiencies are calculated [136].

the identification efficiency, whereas the E_T and η dependencies increase. As a result of the higher background separation in many variables for high E_T electrons, the identification efficiency increases as a function of E_T . The dependence of the identification efficiency on η originates primarily from geometric features of the detector, which are in general well modelled in the simulation. The observed differences between simulated event samples and data are corrected by applying scale factors to the simulated samples, which are on the few percent level.

The reconstruction efficiency of electrons is displayed as a function of E_T in in Fig. 4.6(a) and η in in Fig. 4.6(b). The reconstruction efficiency is defined as the ratio of the number of electrons reconstructed as a cluster matched to a track passing the quality criteria to the numbers of all clusters. The reconstruction efficiency varies from 95 % to more than 99 %. Scale factors are derived to account for the differences between simulated event samples and data.

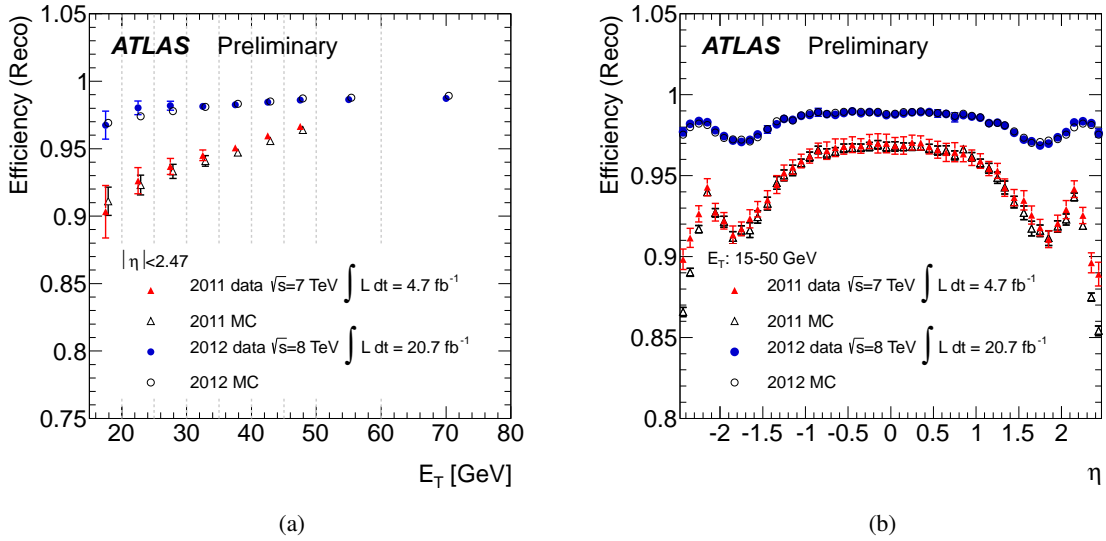


Figure 4.6: Measured reconstruction efficiencies as a function of E_T integrated over the full pseudorapidity range (a) and as a function of η for $15 \text{ GeV} < E_T < 50 \text{ GeV}$ (b) for the 2011 (triangles) and the 2012 (circles) datasets. For illustration purposes a finer η binning is used. The dashed lines in the left plot indicate the bins in which the efficiencies are calculated. [136]

4.4.3 Electron Energy Scale and Resolution

A precise calibration of the energy response in the calorimeter layers and a good knowledge of the energy scale and resolution is vital for physics analyses. The absolute energy scale is derived from collision data using $Z \rightarrow e^+e^-$ events and is described together with the calibration procedure in [137]. The purpose of the calibration is to equalise the calorimeter response between simulated event samples and data. The energy miscalibration is defined as the difference between the response in data and

simulated event samples and is defined as

$$E_{\text{data}} = E_{\text{MC}}(1 + \alpha_i), \quad (4.1)$$

where E_{data} and E_{MC} are the energies in data and simulated event samples, and α_i represents the deviation from the optimal calibration within a given pseudorapidity bin i . This is performed in several independent steps. Firstly the particle energy is calibrated using a multivariate algorithm on cluster level. This energy is corrected for non-uniformities stemming from detector inhomogeneities and time-dependencies using a calibration, based on the single energy deposits in the calorimeter cells as tracked by the simulated event samples using so-called calibration hits. To obtain an absolute energy scale, response differences between the detector layers are corrected using an intercalibration scheme, derived from muons from Z decays. The absolute energy scale of the EM calorimeter, α_i , is set by comparing $Z \rightarrow e^+e^-$ events from simulated event samples and data and aligning the M_Z peak obtained in data to the one from simulated event samples. The energy resolution obtained from data is thereafter used to smear the energies in simulated event samples. The results of the energy scale and smearing are cross-checked using $J/\psi \rightarrow e^+e^-$ and $Z \rightarrow e^+e^-\gamma$ events. The total uncertainty on the described calibration is less than 1% for central electrons. The distribution of the electron pair invariant mass distribution for $Z \rightarrow e^+e^-$ decays in data and improved simulation is shown in Fig. 4.7(a). The energy scale corrections as a function of η are shown in Fig. 4.7(b).

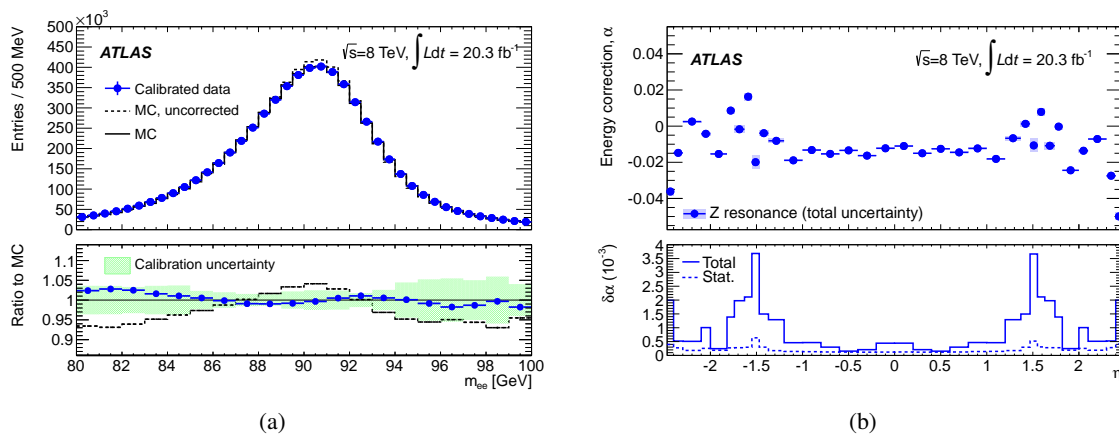


Figure 4.7: The distribution of the electron pair invariant mass distribution for $Z \rightarrow e^+e^-$ decays in data and improved simulation is shown in (a). The energy scale corrections are applied to the data. The lower panel shows the ratio of the data and uncorrected MC distributions to the corrected MC distribution with the calibration uncertainty band. The energy scale corrections as a function of η are shown in distribution (b). The corrections are defined with respect to the 2010 calibration scheme, and after uniformity and layer calibration corrections. The error bands include statistical and systematic uncertainties. the lower panel shows the statistical and total energy scale uncertainties, $\delta\alpha$ as a function of η [137].

4.4.4 Muon Trigger

The muon trigger at LVL1 relies on the timing of coincident signals from the muon trigger chambers to build muon trigger candidates. Namely the resistive plate chambers (RPC) covering the region $|\eta| < 1.05$ and the thin gap chambers in the region $1.05 < |\eta| < 2.4$. ROIs are formed around the hit pattern, using parametrised geometrical muon roads in order to limit the output to LVL2. A muon road is an

envelope of trajectories, from the nominal interaction point, of muons with a transverse momentum above a certain programmable threshold and either charge. While the geometrical acceptance of the LVL1 trigger in the end-cap region is $\sim 99\%$ it is only $\sim 80\%$ in the barrel region attributed to the support structure of ATLAS at $\eta = 0$. The LVL2 trigger is entirely software based and uses fast reconstruction algorithms adding precision tracking information from the monitoring drift tubes (MDT). A rough track fit is performed using the information within the ROI, applying fast lookup tables to assign transverse momenta based on the fit result. An improved background rejection is achieved from the computation of energy deposits in the calorimeter around muon track and additional tracks around the muon candidate. At EF the full detector information is available and algorithms similar to the final offline algorithms are used.

The analysis presented in this thesis selects events using the lowest unrescaled single muon triggers, namely the `EF_mu24i_tight` and `EF_mu36_tight`. As in the electron case the number refers to the online transverse momentum threshold applied, while the `tight` refers to a tight muon selection, and the `i` indicates an isolation requirement that is applied. The relative track isolation cut applied on the `EF_mu24i_tight` trigger is, $\Sigma p_T / p_T(\mu) < 0.12$, where Σp_T is the sum over all tracks with $p_T > 1$ GeV found within $\Delta R < 0.2$ of the muon. The muon track is excluded from the sum. The analysis requires logical OR of the two trigger chains.

The trigger efficiency with respect to the offline muon selection is presented in Fig. 4.8(a) for the central region and in Fig. 4.8(b) for the end-cap region. It has been measured in data using $Z \rightarrow \mu\mu$ events, applying a *tag-and-probe* method [138]. The tag muons is required to trigger the event and be isolated. A second isolated muon of opposite charge is selected as the probe muon. Since the mass of the dimuon system is required to be close to the Z boson mass, the resulting event sample is very pure. Figure 4.8 shows not only the trigger efficiency in data during 2012, but also the trigger efficiency from simulated event samples as a function of the reconstructed transverse momentum. Both curves exhibit a sharp turn-on at $p_T \sim 25$ GeV, and the expected lower overall efficiency within the barrel region. The difference between the efficiency measurement in data and simulation is of the order of $\pm 5\%$. These are used to correct the simulated samples used in the analysis.

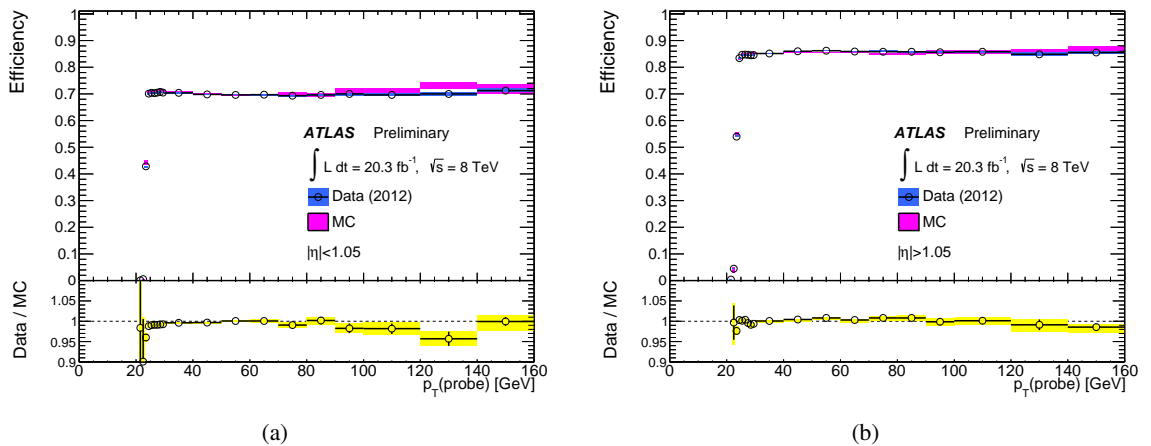


Figure 4.8: Single muon trigger efficiency measured in data for the logical OR of the `mu24i_tight` and `mu36_tight`, measured in $Z \rightarrow \mu\mu$ events using a *tag-and-probe* method in the central region (a) $|\eta| < 1.05$ and the end-cap $|\eta| > 1.05$ (b). A sharp turn-on is shown around 25 GeV leading to plateau of around 70% in (a) and to around 86% in (b). The ratio of the measured efficiency and the one measured in data is found in the lower panel, and shows a good agreement over the full range of momenta [138].

4.4.5 Muon Reconstruction

Muons are the only charged particles which traverse the calorimeter without losing most of their energy. This unique characteristic is used to detect them in the muon chambers. There are various strategies available to reconstruct and identify muons in the ATLAS detector. Four different muon reconstruction strategies are implemented, differing in the information used from the detector subsystems [139]. These mainly depend on the particle track measurements, independently performed in the Muon Spectrometer (MS) and the ID, and to a lesser extent on the information from the calorimeters. The MS allows to reconstruct tracks up to $|\eta| < 2.7$. In a first step all muon chambers intersecting with regions of activity found by the trigger chambers in the $\eta - \phi$ plane, are selected for muon track reconstruction. Local track segments are formed independently in each muon layer, which are combined further into full MS tracks. A segment is valid if at least one hit in each of two multilayers is found.

- In the **Stand-Alone (SA)** muon reconstruction only muon candidates found in the MS are used. To obtain the muon track parameters at the interaction point, the MS track is extrapolated back to the point of closest approach to the beam line, taking the estimated energy loss in the calorimeters into account. The methods used to estimate these energy losses are explained in detail in Ref. [140]. This algorithm is mainly used to extend the muon acceptance in the range $2.5 < \eta < 2.7$, which exceeds the ID tracking range. At least two muon layers have to be transversed by the muon to form an SA muon.
- The most commonly used algorithm is the **Combined (CB)** algorithm. In this case muon candidates are built by successfully matching independently formed MS and ID tracks. Due to the use of ID information the reconstruction is limited to the ID acceptance of $|\eta| < 2.5$.
- **Segmented Tagged (ST)** muons are defined by an algorithm which extends the ID track to a local track in the MS. This algorithm is mainly dedicated to increase the acceptance for muon candidates that passed only one MS layer, i.e. of low- p_T muons.
- The last algorithm is the **Calorimeter Tagged (CaloTag)** algorithm. This reconstruction matches ID tracks to an energy deposit in the calorimeters compatible with minimum ionising particle.

Both the ST and the CaloTag algorithms are targeted at analyses which depend on a high acceptance rather than a high purity. The reconstruction of the SA, CB and ST muons is performed by two different algorithms. One of them, named STACO or Chain 1, performs a statistical combination of the standalone and ID muon track parameters using the covariance matrices of the track parameter measurements from each subsystem. The second, called MUID or Chain 2, obtains combined muons by performing a global refit from the hits measured in both the ID and the MS. The analysis presented in this thesis selects CB muons reconstructed with the STACO algorithm.

Several additional track quality requirements, beyond those described in Section 4.2, are imposed on the tracks used for the CB, ST and CaloTag muons. Among these are: At least one Pixel hit, at least five SCT hits, not more than two active Pixel or SCT sensors, traversed by the track, but without a hit, and at least nine hits in the full TRT acceptance.

Muon Reconstruction Efficiency

The muon reconstruction efficiency was evaluated on the 2012 dataset, using 20.3 fb^{-1} of $\sqrt{s} = 8 \text{ TeV}$ pp collisions, based on a *tag-and-probe* method [139]. For high- p_T muons $Z/\gamma^* \rightarrow \mu^+\mu^-$ events were selected using a single lepton trigger, two muons of transverse momenta $p_{T,1} > 25 \text{ GeV}$ and $p_{T,2} >$

10 GeV, with an invariant dimuon mass of 10 GeV within the Z pole-mass. To extend the efficiency measurement to low- p_T muons, $J/\psi \rightarrow \mu^+\mu^-$ and $\Upsilon \rightarrow \mu^+\mu^-$ events are selected, allowing an efficiency determination down to a few GeV.

The tag muon is required to pass the CB selection, and the trigger requirement, while the probe muon track is selected with looser requirements. When measuring the reconstruction efficiency in the ID, the probe muon is required to be a SA muon, while ID tracks or CaloTag muons can be used as probes when measuring the efficiency in the MS.

The efficiency is defined as the fraction of probe muons successfully matched geometrically to a reconstructed muon of the respective kind. Figure 4.9(a) shows the muon reconstruction efficiency ϵ , for the different muon types as a function of η for muons with $p_T > 10$ GeV. The combination of all different muon types leads to a very uniform efficiency of 99% over the full η region. The efficiency losses for the CB muon in the region $1.1 < \eta < 1.3$ is a consequence of the missing MS chambers.

A good agreement is found between simulated MC events and data, the minor disagreement found stems mainly from imperfections in the modelling of the detector conditions, and is less than 1%. The CB muon efficiency as a function of the transverse momentum p_T is shown in Fig. 4.9(b). The step efficiency increase for rising transverse momenta results from the minimum momentum of at least 3 GeV needed for the muon to cross both the calorimeter material and traverse at least two MS layers. Above 20 GeV the muon reconstruction efficiency is nearly independent of the momentum. Scale factors binned in $\eta - \phi$ are applied to simulated event samples to account for the observed differences in the reconstruction efficiency between simulation and data.

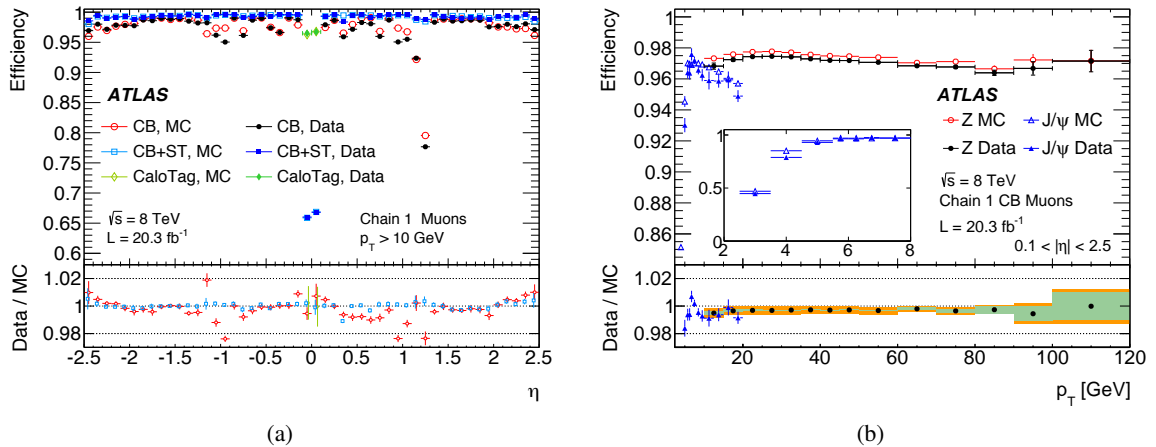


Figure 4.9: Muon reconstruction efficiency as a function of η measured in $Z \rightarrow \mu\mu$ events for muons with $p_T > 10$ GeV and for different muon reconstruction types (a). The panel at the bottom shows the ratio between the measured and predicted efficiencies. The reconstruction efficiency for CB+ST muons as a function of the p_T of the muon, for muons with $0.1 < |\eta| < 2.5$ is shown in (b). The results are obtained with $Z \rightarrow \mu\mu$ and $J/\psi \rightarrow \mu\mu$ events. The panel at the bottom shows the ratio between the measured and predicted efficiencies. The green areas show the pure statistical uncertainty, while the orange areas also include systematic uncertainties [139].

Momentum Resolution

Both the momentum resolution and the scale are important parameters for the muon reconstruction performance, and need to be compared between simulated event samples and data. High statistics dimuon decays from J/Ψ , Υ and Z resonances allow for a very precise determination of the muon momentum

scale and resolution. The corrections are evaluated separately for the ID and MS, and defined in $\eta - \phi$ regions, to keep the corrections small. The muon momentum resolution is parametrised as

$$\frac{\sigma(p)}{p} = \frac{r_0}{p_T} \oplus r_1 \oplus r_2 \cdot p_T, \quad (4.2)$$

where \oplus denotes a sum in quadrature. The first term accounts for fluctuations in the energy loss of the transversed material. The second term represents multiple scatterings, local magnetic field inhomogeneities and local radial displacements, whereas the third term describes the intrinsic resolution effects of the individual track points. Additionally the imperfect knowledge of the magnetic field and the radial distributions as well as local misalignments between sub-detectors are taken into account. The separate evaluation for ID and MS allows for a direct understanding of the sources of corrections, these are further propagated to the CB muon momentum resolution using the weighted average.

The muon momentum scale corrections using $Z/\gamma^* \rightarrow \mu^+\mu^-$ events, are shown for the ID in Fig. 4.10(a) and for the MS in Fig. 4.10(c), along with their systematic uncertainties in yellow. The resulting scales and uncertainties are at the few per mille level. The collected resonance data was further used to study the dimuon mass scale, by fitting the width of the invariant mass peaks. The result for $Z/\gamma^* \rightarrow \mu^+\mu^-$ is displayed in Fig. 4.10(c), along with the uncorrected and corrected simulated event samples. The correction leads to an excellent agreement between data and simulated event samples.

4.5 Jet Reconstruction

A jet is made up of a set of hadrons produced in the hadronisation process of a quark or gluon. The jet reconstruction aims at recombining these objects to obtain a physics object with characteristics close to the one of the initial parton.

Jets are reconstructed in ATLAS based on energy deposits in the calorimeters, called topoclusters [142]. These are reconstructed from topologically connected cells in an iterative noise-suppressing process, seeded by cells with significantly larger energy deposits than the noise threshold $E_{cell} > 4 \cdot \sigma_{noise}$. Cells are added to the cluster, as long as the energy is above a certain noise threshold that depends on their location with respect to the seed. The energy of these topoclusters is calibrated using the Local Cluster Weighting scheme, LCW scheme [143]. The LCW scheme classifies each cluster as hadronic or electromagnetic, depending on its energy density and depth, and applies a correction scheme for the different electron and pion response. Energy loss due to detector effects and noise suppression are also taken into account. These weighted topoclusters now serve as an input to the jet reconstruction, based on the anti- k_T algorithm [144] with a distance parameter of $R = 0.4$. The anti- k_T algorithm is a sequential recombination algorithm clustering particles into jets one at a time until the boundary condition, based on a two-particle distance measure, is met:

$$d_{ij} = \min(k_{ii}^{-2}, k_{ij}^{-2}) \frac{(y_i - y_j)^2 + (\phi_i - \phi_j)^2}{R^2} \quad (4.3)$$

$$d_{iB} = k_{ii}^2, \quad (4.4)$$

where d_{ij} is the distance, between the two particles, and d_{iB} is the distance between the entity i and the beam. The parameters k_{ii} , y_i and ϕ_i are the transverse energy, the rapidity and the azimuthal angle of the entity i . The anti- k_T algorithm was chosen as a baseline algorithm for ATLAS because of its theoretical properties of collinear and infrared safety and because it gives rise to rather circular jets in the $\eta - \phi$ plane and is efficient in terms of computing needs.

After the reconstruction the jet energy scale corrections are applied on the reconstructed jets, as sev-

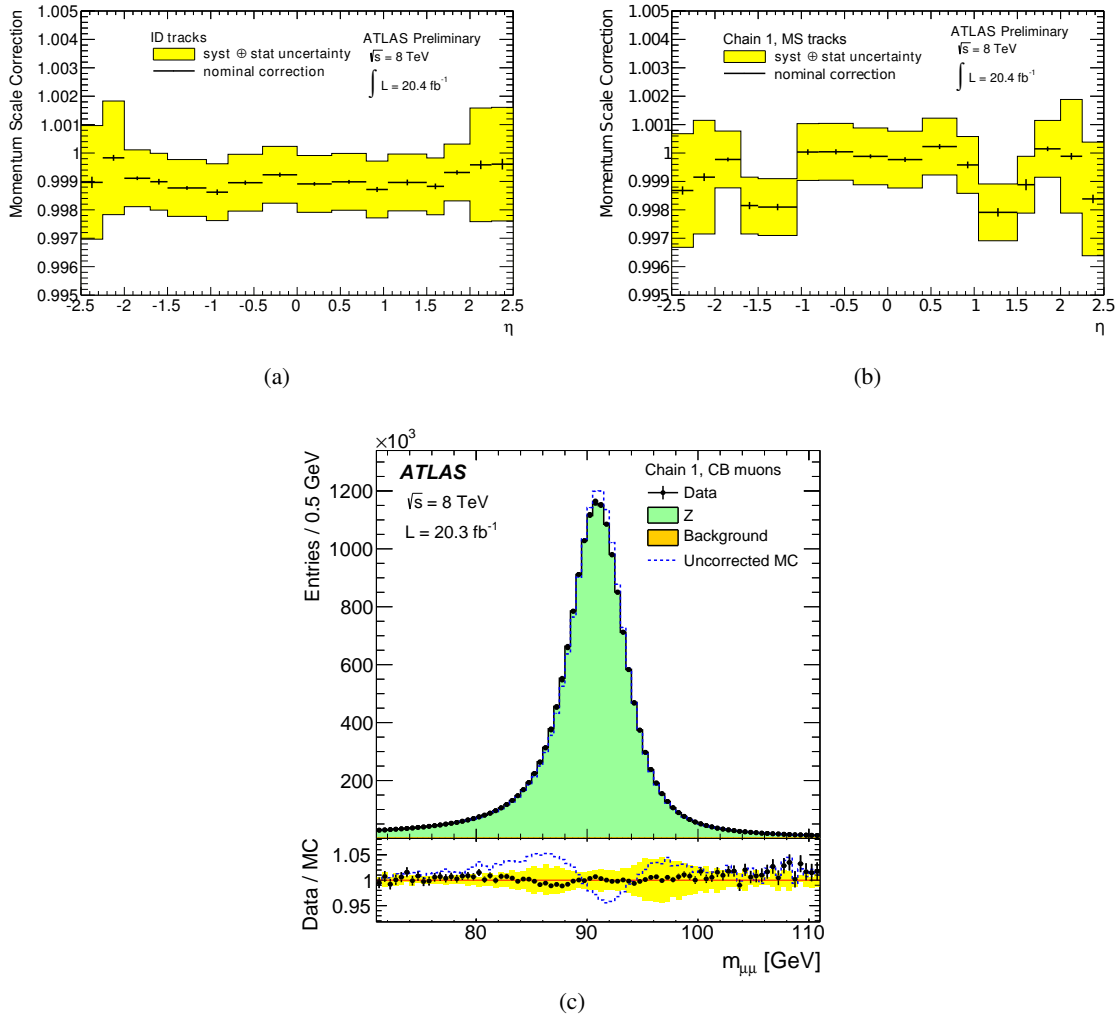


Figure 4.10: The ID momentum scale correction, for MC, derived from $Z/\gamma^* \rightarrow \mu\mu$ data is shown in (a). The systematic uncertainty on the correction is shown in yellow [141]. (b) Shows the MS momentum scale correction, for MC, derived from $Z/\gamma^* \rightarrow \mu\mu$ data for the Chain 1 reconstruction. The systematic uncertainty on the correction is shown in yellow [141]. Finally the dimuon invariant mass distribution of $Z/\gamma^* \rightarrow \mu\mu$ candidate events reconstructed with CB muons is shown in (c). The upper panel shows the invariant mass distribution for data and for the signal simulated event samples and the background estimate. The lower panel shows the Data/MC ratios, where the band represents the effect of the systematic uncertainties on the MC momentum corrections [139].

eral detector effects have an impact on the measured jet energy. The main effect is that only part of the hadronic energy is measured, due to the non-compensational nature of the calorimeter. Further sources of energy mismeasurements are energy leakages outside of the calorimeter, losses due to contributions not clustered to the reconstructed jet, losses due to the thresholds applied in the clustering and reconstruction algorithm. These inefficiencies are corrected for in the jet energy calibration using inclusive jet simulated event samples [145]. The average energy response at the LCW scale is shown in Fig 4.11(a). The inverse of the response shown in each bin is equal to the average jet energy scale correction. Further corrections to the reconstructed jet energy are implemented for the 2012 data and MC samples, including a jet area based pile-up correction and a jet origin correction [146]. The effect of the improved pile-up correction is shown in Fig 4.11(b).

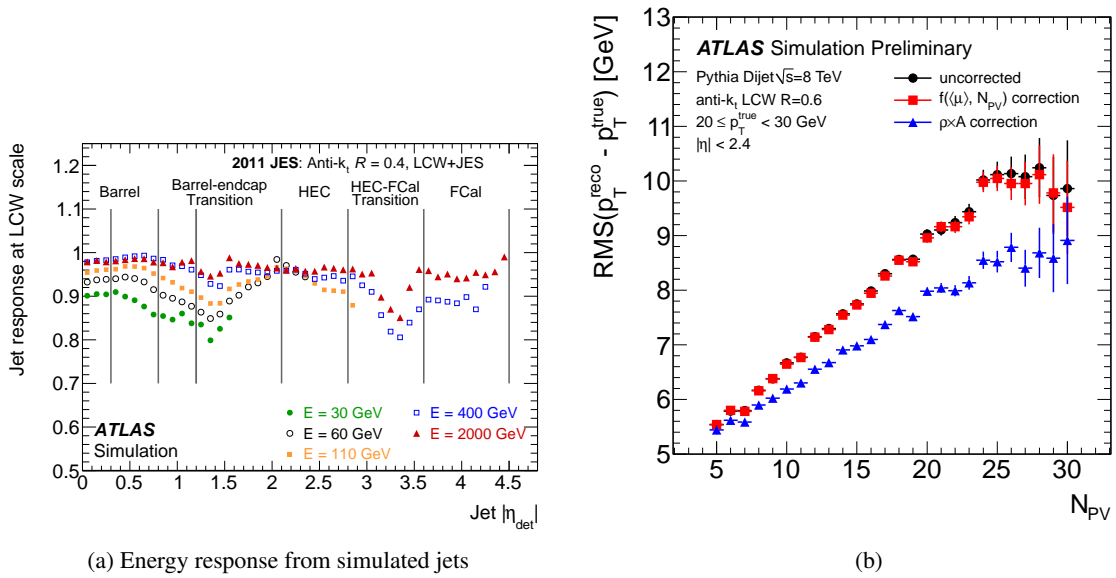


Figure 4.11: The average energy of simulated jets formed from topoclusters at the LCW scale with respect to the truth jet energy ($E_{jet}^{LCW}/E_{jet}^{truth}$) as a function of the jet pseudorapidity is shown in a). The response is shown separately for various truth-jet energies as function of the uncorrected (detector) jet pseudorapidity. The inverse of the response shown in each bin is equal to the average jet energy scale correction. [145]. The RMS width of the $(p_T^{reco} - p_T^{true})$ distribution versus N_{PV} for $anti - k, R = 0.6$ jets at the LCW scale matched to truth particle jets satisfying $20 < p_T^{true} < 30$ GeV, in simulated dijet events is shown in (b). The advantage of the new correction over the previous subtraction method is clearly visible [146].

4.6 Missing Transverse Momentum Reconstruction

Particles that only undergo weak interactions, such as neutrinos or other more exotic particles, do not directly interact with the ATLAS detector. This leads to a momentum imbalance in the transverse plane to the beam axis defined as the missing transverse momentum \mathbf{E}_T^{miss} . The \mathbf{E}_T^{miss} is obtained from the negative vector sum of the momenta of all detected particles in the proton–proton collision, whose absolute value is denoted as E_T^{miss} . The E_T^{miss} reconstruction in ATLAS depends on energy deposits in the calorimeters and muons reconstructed in the muon system [147, 148]. Additionally tracks are added to recover low- p_T particles that are missed by the calorimeters. To ensure an optimal calibration of the calorimeter cells, the calibration is depending on the associated physics objects. These are evaluated

in the following order: electrons, photons, hadronically decaying τ -leptons, jets and muons. Cells with energy deposits not associated with the aforementioned objects are accounted for in the CellOut term. This leads to the following computation of the E_T^{miss} in the two transverse directions

$$E_{x(y)}^{\text{miss}} = E_{x(y)}^{\text{miss,e}} + E_{x(y)}^{\text{miss,\gamma}} + E_{x(y)}^{\text{miss,\tau}} + E_{x(y)}^{\text{miss,jets}} + E_{x(y)}^{\text{miss,softjets}} + (E_{x(y)}^{\text{miss,calo,\mu}}) + E_{x(y)}^{\text{miss,CellOut}} + E_{x(y)}^{\text{miss,\mu}}, \quad (4.5)$$

where each term is the negative sum of the calibrated reconstructed objects, projected onto the x- and y-directions, within the acceptance of the calorimeter ($|\eta| < 4.9$) and for the muons within ($|\eta| < 2.7$). It should be noted that the $E_{x(y)}^{\text{miss,calo,\mu}}$ is only added where applicable. The magnitude, E_T^{miss} , is then given by

$$E_T^{\text{miss}} = \sqrt{(E_x^{\text{miss}})^2 + (E_y^{\text{miss}})^2}. \quad (4.6)$$

The terms $E_{x(y)}^{\text{miss,e}}$ and $E_{x(y)}^{\text{miss,\gamma}}$ are obtained from cells with medium electrons or tight photons with $p_T > 10$ GeV, where the electrons are calibrated using the standard electron calibration, while the photons are calibrated at the electromagnetic scale. The τ contribution, $E_{x(y)}^{\text{miss,\tau}}$, is based on a τ -reconstruction with $p_T > 10$ GeV. Similarly the two jet terms which are reconstructed from clusters associated to anti- k_t jets of a radius of 0.4 and $7 \text{ GeV} < p_T < 20 \text{ GeV}$ for $E_{x(y)}^{\text{miss,softjets}}$ and $p_T > 20 \text{ GeV}$ for $E_{x(y)}^{\text{miss,jets}}$, are also calibrated with the LCW scheme. The $E_{x(y)}^{\text{miss,jets}}$ is additionally calibrated with the jet energy scale and corrected for pile-up. The CellOut term, $E_{x(y)}^{\text{miss,CellOut}}$, is calibrated with the LCW scheme combined with tracking information.

For additional robustness of the E_T^{miss} performance in the high pile-up environment of the 2012 data, additional pile-up suppression methods for the jet and soft jet term were introduced.

The performance of the E_T^{miss} in the 2012 proton-proton collision data is evaluated using $Z/\gamma^* \rightarrow \ell^+ \ell^-$ and $W \rightarrow \ell \nu$ events [148]. The distribution of E_T^{miss} as measured in data samples of $Z/\gamma^* \rightarrow \mu^+ \mu^-$ is shown in Fig. 4.12(a), and of $W \rightarrow e \nu$ is shown in Fig. 4.12(b), after pile-up suppression with the soft vertex term fraction is shown. The expectation from simulated event samples is superimposed and normalised to data.

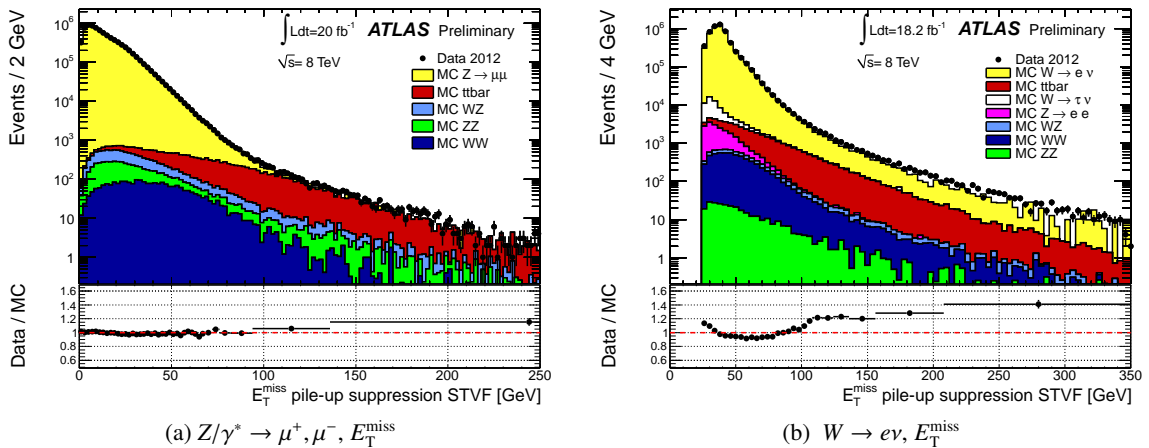


Figure 4.12: The E_T^{miss} distribution in data, compared with weighted simulated event samples, after pile-up suppression in $Z/\gamma^* \rightarrow \mu^+ \mu^-$ (a) and $W \rightarrow e \nu$ (b), using the soft term vertex fraction. While the source of E_T^{miss} in $Z/\gamma^* \rightarrow \mu^+ \mu^-$ events is primarily due to energy mismeasurements and missing objects, the E_T^{miss} in $W \rightarrow e \nu$ stems from the neutrino which leaves the detector undetected. The lower plot shows the corresponding ratio between data and simulated event samples [148].

Search for a Narrow Heavy Lepton Resonance

This chapter presents the search for a heavy lepton resonance, decaying to a three-lepton final state via an intermediate Z decay, using the entire 2012 dataset. This search has been published in Ref. [149].

The existence of such resonances is predicted by several extensions to the Standard Model. Two distinct benchmark models, namely the type-III seesaw mechanism and the vector-like lepton (VLL) model are used in this analysis. Even though the branching ratio to the $Z(\ell\ell) + \ell$ final state is small, it has the advantage of a full mass reconstruction of the resonance, and only a small number of Standard Model processes are expected to contribute to the signal region. Besides the model dependent search this analysis facilitates the search for a generic narrow resonance decaying to $Z(\ell\ell) + \ell$.

The unprecedented centre-of-mass energy at the LHC provides a unique opportunity to search for resonances with masses above the electroweak gauge boson masses. Searches for new particles often employ final states with electrons or muons largely to profit from a full four-momentum reconstruction with a mass resolution better than that achievable using hadronic or semileptonic decay modes. Furthermore searches for resonances benefit significantly from additional mass constraints which can be used, if the leptons originate from a resonance decay. There exists a fruitful history of dilepton resonance searches which have led to the discovery of the J/ψ [3, 4], the Υ [5], and the Z boson [6, 7]. Resonance searches have been utilised at the CERN Large Hadron Collider (LHC) to place strong constraints on a variety of new particles such as additional gauge bosons [8, 9] and doubly-charged scalar particles [150]. Previous searches for low-mass three-lepton resonances include the constraint of lepton flavour violation in muon and tau lepton decays [151, 152].

This chapter commences with an introduction to the type-III seesaw and the vector-like leptons model in Section 5.1 and the generation of signal events in Section 5.2 with an emphasis on the type-III seesaw model. An overview on the contributing background processes is given in Section 5.3 and the analysed data sample is described in Section 5.4. Further analysis specific object selections are detailed in Section 5.5. A brief summary of a preliminary search result for a type-III seesaw resonance in the four lepton channel is given in Section 5.6. This chapter is concluded by a summary of the selection and reconstruction strategy of the heavy lepton candidate in Section 5.7.

5.1 Signal Models

The type-III seesaw mechanism [10] explains the origin of small neutrino masses through the introduction of heavy $SU(2)$ triplets with zero hypercharge. Vector-like leptons are invoked to explain the mass

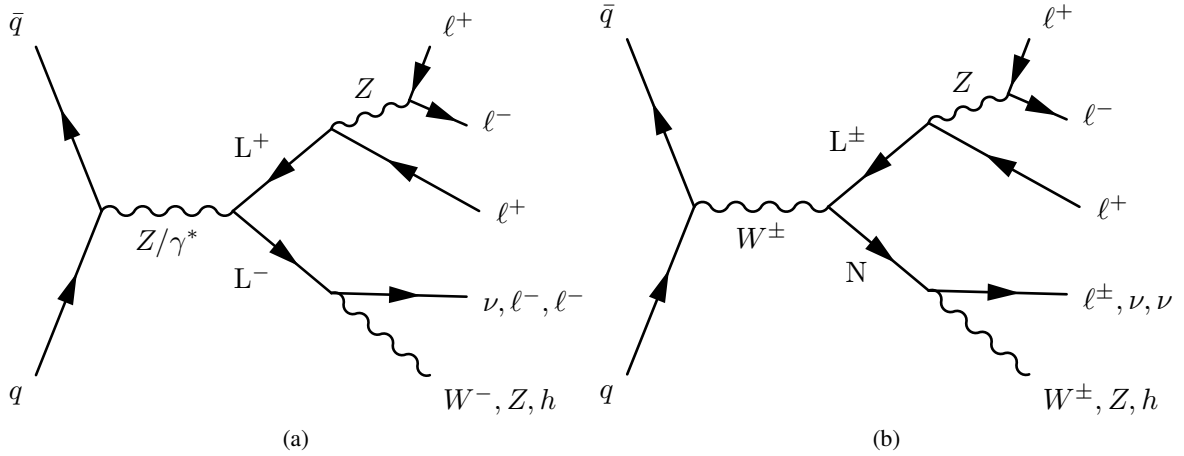


Figure 5.1: Feynman diagrams for the production of new heavy leptons (L^\pm , N^0) and their decays to a three-leptons. Diagram (a) shows the pair production of two charged heavy leptons, and (b) shows the associated production of a charged and a neutral heavy lepton.

hierarchy between the different lepton generations [11]. Vector-like leptons arise in composite Higgs models [12, 13], models of warped extra dimensions [14, 15] and other models of new physics. Such leptons have masses much larger than those of the Standard Model leptons, and are defined as colourless, spin-1/2 fermions whose left- and right-handed chiral components have the same transformation properties under the weak-isospin $SU(2)$ gauge group. A Feynman diagram of the production of the new heavy leptons L^\pm and N^0 and their decays to three leptons is shown in Fig. 5.1.

5.2 Signal Monte Carlo Samples

5.2.1 Type-III Seesaw

Generation

The Monte Carlo input samples for the type-III seesaw mechanism are generated using the input provided by the authors of Ref. [16], for further details see Section 2.3.1. The implemented FEYNRULES [119] model considers the simplest extension to the Standard Model by adding a single triplet, assuming no large degeneracy between the generations. The fermionic triplet is realised by the addition of charged Dirac lepton, L^\pm , and a Majorana neutral lepton, N^0 , to the existing Standard Model leptons. The Lagrangian of Ref. [16] is implemented using the mixing angles for heavy leptons and the Standard Model leptons listed in Table 5.1. The mixing with taus, $V_{L\tau}$, is set to zero. Hence the decays yield final states with a mix of ee , $e\mu$ and $\mu\mu$. For the final analysis the events are reweighted to correspond to either electron-only or muon-only mixing scenarios. The charged and the neutral heavy leptons are generated with identical mass.

The decay widths of the new heavy fermions are calculated with MADGRAPH5 [153]. The values were compared to previous results obtained using BRIDGE (branching ratio inquiry decay generated events) [154] and are shown in Fig. 5.2. They range from 1.5 eV at 100 GeV to 1.1 GeV at a heavy lepton mass of 500 GeV. MADGRAPH5 is used to calculate the matrix elements for each process while MadEvent [155] is used to simulate the initial state parton scattering and decay of the new heavy fermions. PYTHIA8 is used to simulate the underlying physics by adding initial/final state radiation (ISR/FSR)

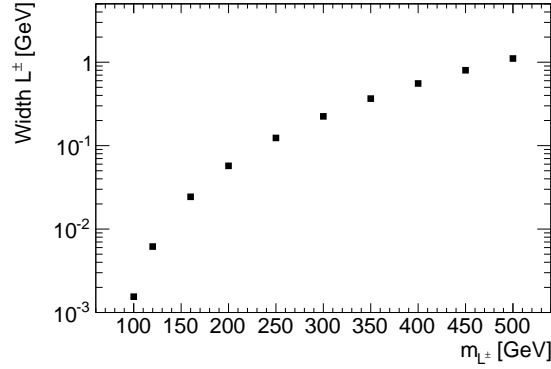


Figure 5.2: Generated width for type-III seesaw heavy leptons as a function of their mass.

and the decays of the W and Z bosons. For this analysis, all possible decay modes that give rise to three or more leptons in the final state are generated

- $pp \rightarrow N^0 L^+ \rightarrow \ell^+ W^- \ell^+ Z$
- $pp \rightarrow N^0 L^+ \rightarrow \ell^- W^+ \ell^+ Z$
- $pp \rightarrow N^0 L^+ \rightarrow \nu_\ell Z \ell^+ Z$
- $pp \rightarrow N^0 L^+ \rightarrow \nu_\ell H \ell^+ Z$
- $pp \rightarrow N^0 L^- \rightarrow \ell^- W^+ \ell^- Z$
- $pp \rightarrow N^0 L^- \rightarrow \ell^+ W^- \ell^- Z$
- $pp \rightarrow N^0 L^- \rightarrow \nu_\ell Z \ell^- Z$
- $pp \rightarrow N^0 L^- \rightarrow \nu_\ell H \ell^- Z$
- $pp \rightarrow L^- L^+ \rightarrow \ell^- Z \ell^+ Z$
- $pp \rightarrow L^- L^+ \rightarrow \nu_\ell W^- \ell^+ Z$
- $pp \rightarrow L^- L^+ \rightarrow \ell^- H \ell^+ Z$
- $pp \rightarrow L^- L^+ \rightarrow \ell^- Z \nu_\ell W^+$
- $pp \rightarrow L^- L^+ \rightarrow \ell^- Z \ell^+ H$

To ensure at least three leptons in the event a generator filter is applied in `PYTHIA`, requiring that each event contains three true electrons or muons with $p_T > 4$ GeV and $\eta < 3.0$. The efficiencies of this 3-lepton filter are listed in Table 5.2 and range from $\sim 10\%$ at 100 GeV to $\sim 25\%$ at 500 GeV. The cross sections for the generated processes are shown in Table 5.2. The largest cross section is at $m_{L^\pm, N} \approx 120$ GeV. At low masses, the trilepton decay is suppressed by the reduced phase space of the $L^\pm \rightarrow Z\ell$ decay, while at higher masses, the cross section is suppressed by the PDF and pair production phase space.

Particle	V_e	V_μ	V_τ
N^0	0.055	0.063	0
L^\pm	0.055	0.063	0

Table 5.1: Type III seesaw model couplings used in the generation.

L^\pm Mass [GeV]	Dataset ID	Cross Section [fb]	Filter Efficiency	Number of Events
100	191030	1.273	10.18	100k
120	191031	2.138	16.28	100k
160	191032	0.853	18.08	100k
200	191033	0.346	20.12	100k
250	191034	0.135	20.96	100k
300	191035	0.0604	21.78	100k
350	191036	0.02969	23.37	100k
400	191037	0.01566	24.09	100k
450	191038	0.00873	24.56	100k
500	191039	0.00504	24.93	100k

Table 5.2: Type-III seesaw model signal Monte Carlo samples. The generator is MADGRAPH5+PYTHIA8, and the PDF is CTEQ6L1 with AU2 tune. The filter applied is a two lepton filter.

Validation

Each step in the generation of the Signal Monte Carlo simulated samples was accompanied by validating basic distributions. The production cross section for heavy lepton pairs at a centre-of-mass energy of 14 TeV was established in previous studies published in Refs. [82, 156]. These were cross checked in Ref. [16]. To validate the setup for the Monte Carlo event generation, the production cross section at two different heavy lepton masses generated at 14 TeV were compared with both the ones obtained by Ref. [16] and Refs. [82, 156]. These were found to be in good agreement.

In this thesis, data collected at a centre-of-mass energy of 8 TeV are analysed. Exemplary the validation of PYTHIA output is shown in Fig. 5.3 for a mass $m_{L^\pm, N} = 120$ GeV and in Fig. 5.4 for a mass $m_{L^\pm, N} = 500$ GeV. Most of the samples were produced using the ATLAS fast simulation package ATLAS-FAST2 [157]. A summary between the samples generated with either simulation approach is found in Ref. [158].

5.2.2 Vector-Like Lepton

The signal model for the vector-like leptons samples is taken from Ref. [81]. The samples were generated with MADGRAPH4.5.2 using the CTEQ6L1 [159] parton distribution functions (PDF) and the AU2 underlying event tune [111]. Parton showering is performed with PYTHIA8 [160]. The decay of the bosons are handled with BRIDGE [154]. Eleven samples are generated with masses ranging between 100 and 400 GeV. Three vector-like leptons, corresponding to vector-like electrons, vector-like muons, and vector-like taus are simulated. Each event contains a same-flavour, opposite-sign pair of vector-like leptons, and thus both vector-like leptons decay to the same flavour Standard Model lepton. The resulting samples have a mix of each of the three flavours, and at least one vector-like lepton is forced to decay via $L^\pm \rightarrow Z\ell^\pm$ with $Z \rightarrow ee, \mu\mu, \tau\tau$. The production cross sections, branching fractions to $Z\ell$, and total filter efficiencies are shown in Table 5.3. The filter requires that one of the two vector-like leptons decays as $L^\pm \rightarrow Z\ell^\pm \rightarrow \ell'^\pm \ell'^\mp \ell^\pm$, where $\ell, \ell' = e, \mu, \text{ or } \tau$.

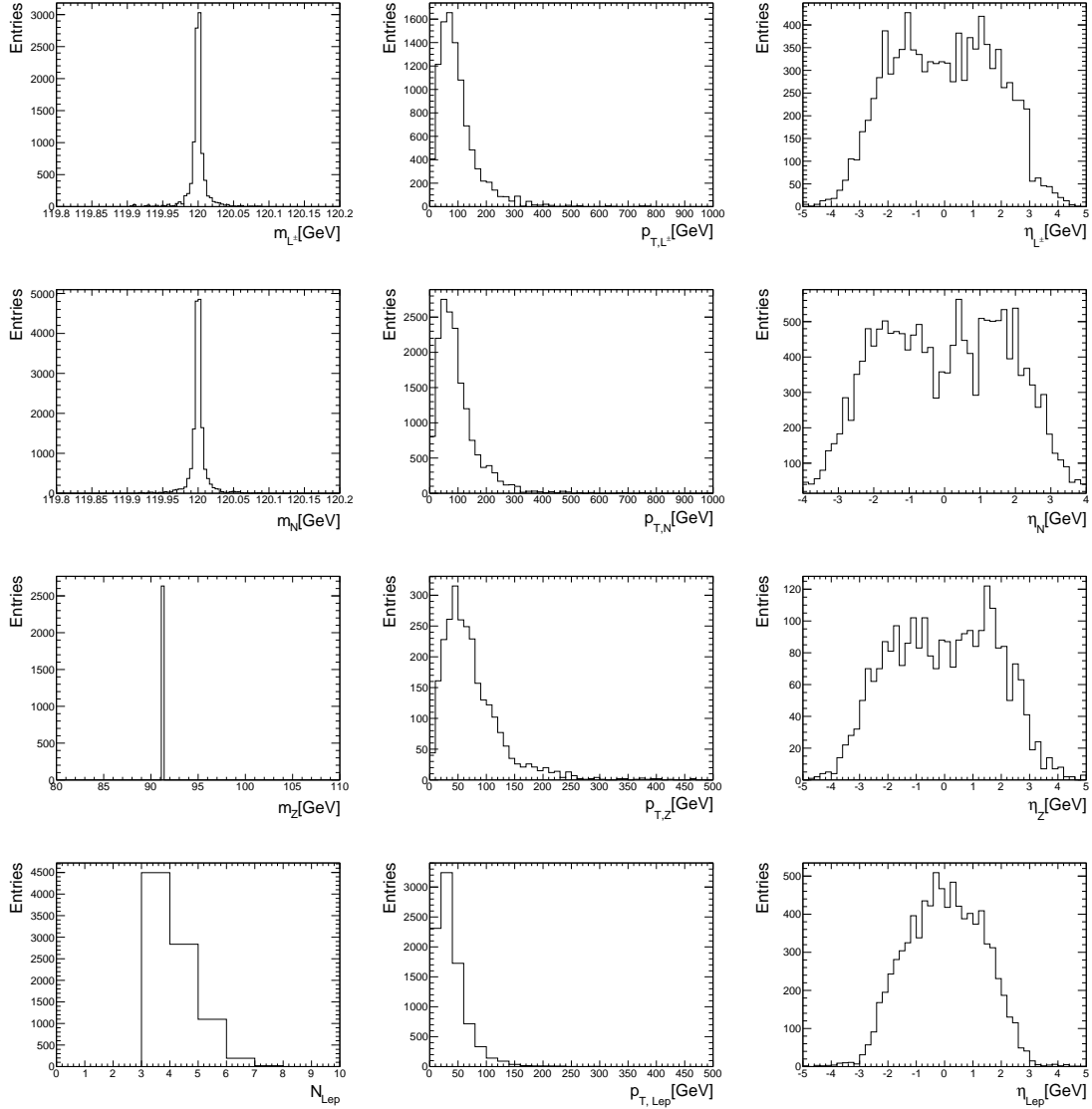


Figure 5.3: Validation plots of the PYTHIA truth output for a mass of $m_{L,N} = 120$ GeV. The columns show the mass (left), the transverse momentum p_T (middle) and the pseudorapidity η (right). The first row shows the distributions for the charged heavy leptons m_{L^\pm} , the upper middle row the neutral heavy lepton m_N , the lower middle row the Z boson, as a decay product and the last row the distributions for the leptons in the event. The missing generated width of the Z boson, due to the large number of final states, is clearly visible.

5 Search for a Narrow Heavy Lepton Resonance

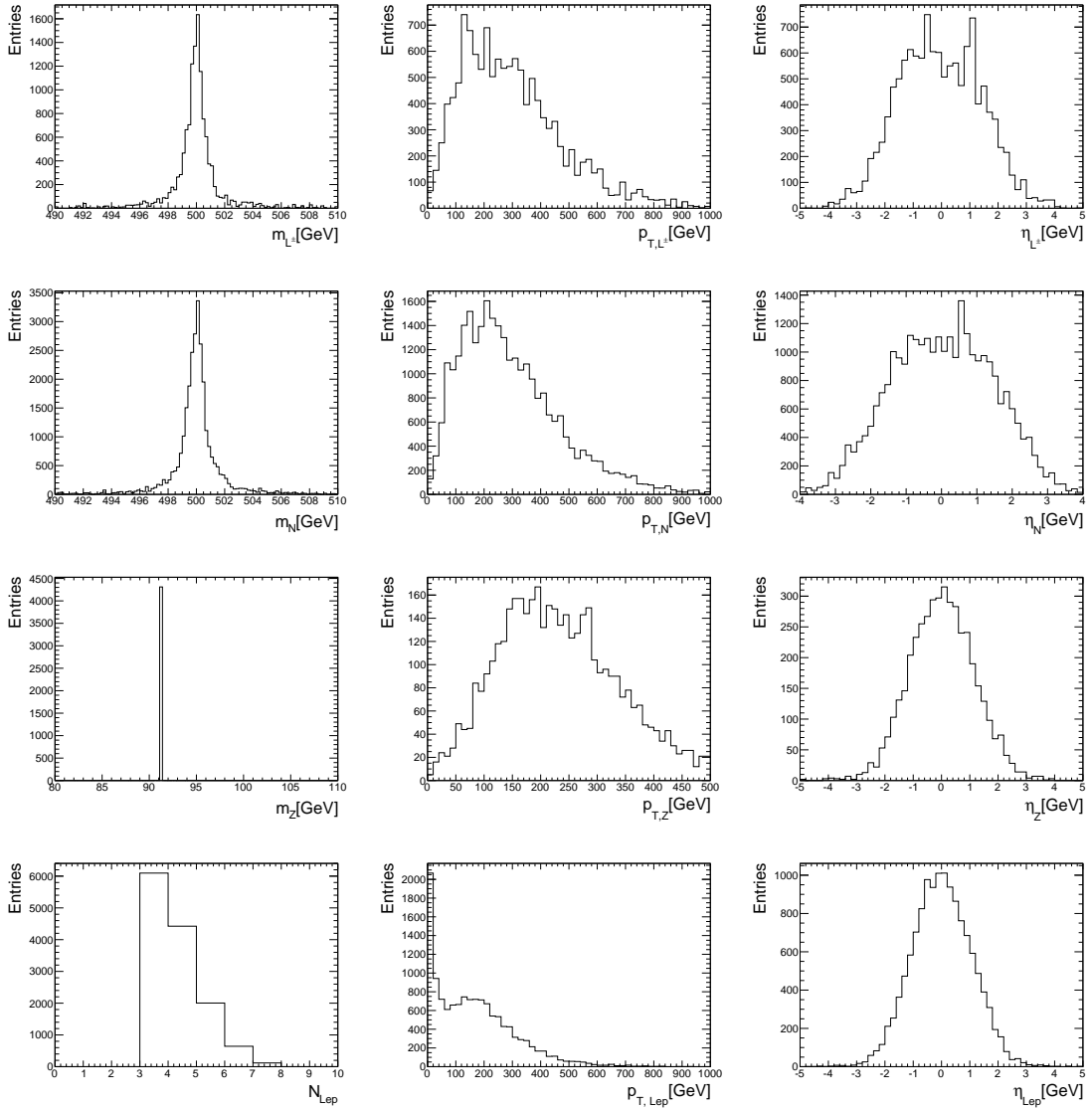


Figure 5.4: Validation figures of the PYTHIA truth output at a mass of $m_{L,N} = 500$ GeV. The columns show the mass (left), the transverse momentum p_T (middle) and the pseudorapidity η (right). The first row shows the distributions for the charged heavy leptons m_{L^\pm} , the upper middle row the neutral heavy lepton m_N , the lower middle row the Z boson, as a decay product and the last row the distributions for the leptons in the event. The missing generated width of the Z boson, due to the large number of final states, is clearly visible.

L^\pm Mass [GeV]	Cross Section [pb]	BR(Zl)	Filter Efficiency	FastSim	FullSim
100	0.378	0.116	0.0233	100,000	-
110	0.264	0.206	0.0412	100,000	-
120	0.193	0.25	0.0498	100,000	100,000
130	0.142	0.275	0.0548	100,000	-
140	0.106	0.286	0.0569	100,000	-
160	0.0645	0.291	0.0579	100,000	-
180	0.0407	0.289	0.0575	100,000	-
200	0.0265	0.285	0.0567	100,000	100,000
250	0.0104	0.275	0.0548	100,000	-
300	0.00457	0.269	0.0536	100,000	100,000
400	0.00115	0.261	0.0520	100,000	-

Table 5.3: Vector-like lepton sample details. The filter requires that one of the two vector-like leptons decays as $L^\pm \rightarrow Zl^\pm \rightarrow l'^\pm l'^\mp l^\pm$, where $l, l' = e, \mu$, or τ . FastSim samples are generated using a dedicated ATLAS detector simulation called ATLFAST2 [157, 161].

5.3 Background Processes and Event Samples

This analysis selects final states with three leptons (e or μ), two of which are consistent with originating from a Z boson decay. There are very few Standard Model processes with three or more real leptons, that potentially populate the signal region. These background processes are classified as reducible or irreducible backgrounds. The irreducible background is a collection of events with three prompt leptons, dominated by the continuum WZ and ZZ production, with smaller contributions from $t\bar{t} + W/Z$ and triboson production. These background contributions are estimated using Monte Carlo simulated events. The validity of this background estimate is confirmed in dedicated validation regions in Section 6.2.

The reducible background comprises events with three leptons, where at least one of the leptons originates from a non-prompt source such as semileptonic b - and c - hadron decays and in-flight decays of pions and kaons or jets that are misidentified as leptons. This reducible background contribution can be largely suppressed using tight lepton identification criteria, as described in Section 5.5. The reducible background is determined using data-driven techniques. These are based on extrapolating the reducible background contribution in the signal region from data-based control samples, with altered lepton selections. The reducible background consists mainly of $Z + \text{jet}$ and $Z + \gamma$ production, with smaller contributions from $t\bar{t}$ production.

The cross sections of important Standard Model physics processes as a function of the centre-of-mass energy of the collider are shown in Fig. 5.5. The vertical solid line indicates the 8 TeV centre-of-mass energy at the LHC Run-1 data taking in 2012, used in this analyses. The surrounding dotted lines indicate the respective centre-of-mass energies of 7 and 14 TeV at the LHC. Multijet processes are the dominant processes, followed by W and Z production on the order of 1 nb to 10 nb. The diboson production cross section, by far the dominating background in this analysis, is more than four magnitudes smaller.

5.3.1 Diboson Background

The productions of WZ/γ^* and ZZ/γ^* are the most important backgrounds contributing to the signal region. WZ/γ^* production is the largest source of Standard Model events with three prompt, isolated,

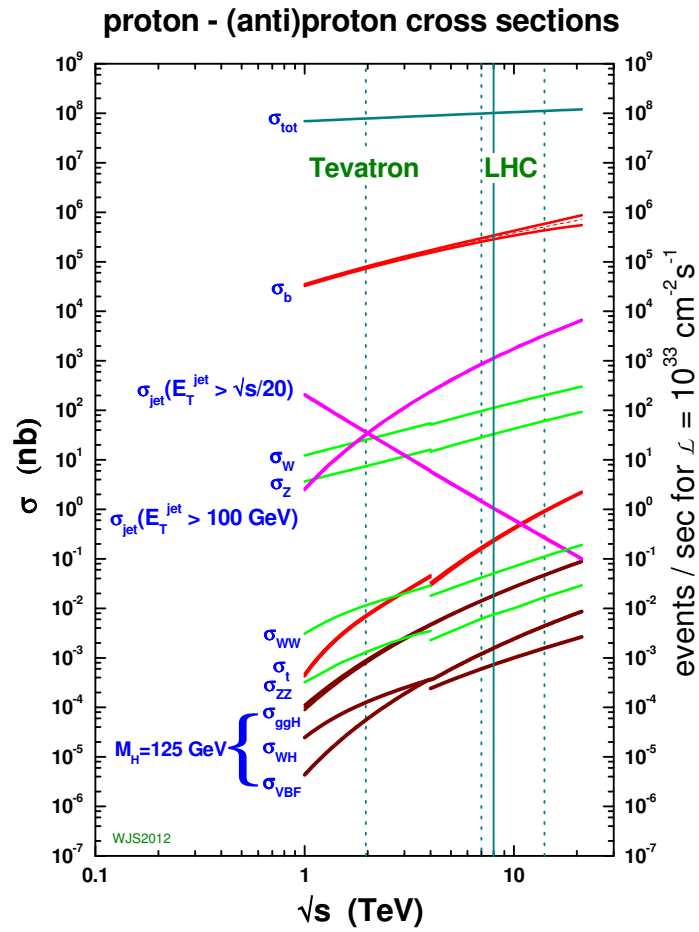


Figure 5.5: Standard Model cross sections for various important physics processes in $p\bar{p}$ and pp collisions as a function of the collider's centre-of-mass energy. The vertical solid line indicates the 8 TeV centre-of-mass energy at the LHC, used in this analysis. The dotted lines indicate the respective centre-of-mass energies of 7 and 14 TeV at the LHC, while the leftmost vertical dotted line indicates the centre-of-mass energy at the Tevatron [89].

high- p_T leptons, followed by ZZ/γ^* production. At the LHC the dominant diboson production mechanism is from quark–antiquark initial states, and to a lesser extent from gluon–gluon fusion. The leading order Feynman diagrams are shown in Fig. 5.6. The branching ratio of $WZ/\gamma^* \rightarrow \ell\nu\ell\ell$ is 1.5% (with $\ell = e, \mu$), while the branching fraction of the ZZ/γ^* pair to a four lepton final states accounts for only 0.4% of the produced ZZ/γ^* pairs. SHERPA [97] is used as the default generator for diboson yield predictions. Since the SHERPA samples used are generated with up to three additional parton emissions in the matrix element, they are expected to exhibit a similar accuracy as NLO generators [162]. The WZ/γ^* and ZZ/γ^* production processes and subsequent pure leptonic decays are modelled by SHERPA version 1.4.3 (1.4.5), and the showering is handled by the internal SHERPA showering algorithm [163–165]. The CT10 [166] parton density function (PDF) set is used and the samples are normalised to the next-to-leading-order (NLO) cross-section prediction from vBFNLO-2.6.2 [167]. No requirement is applied to the invariant mass of same-flavour, opposite-sign leptons, allowing for modelling of $W\gamma^*$ and $Z\gamma^*$ at very low γ^* masses. Samples simulated by the next-to-leading-order generator POWHEG-BOX [168] are used to derive systematic uncertainties. These samples also use the CT10 PDF set. The diboson samples are showered with PYTHIA8 and use the AU2 underlying event tune. For this POWHEG-BOX+PYTHIA event simulated sample, a generator-level filter is applied, which requires all same-flavour opposite-sign pairs to have an invariant mass of $m(\ell\ell) > 5$ GeV as well as at least two leptons with $p_T > 5$ GeV. The cross sections and integrated luminosities of these samples are listed in Table 5.4.

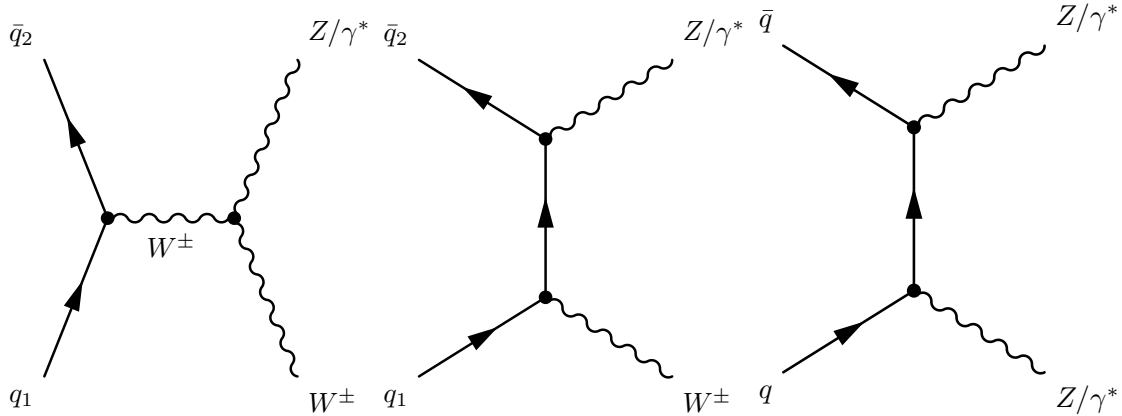


Figure 5.6: Leading order Feynman diagrams for WZ/γ^* and ZZ pair production processes. Higher-order gluon-induced diagrams are not displayed.

5.3.2 Triboson Background

A minor source of backgrounds are events originating from triboson processes $pp \rightarrow WWW \rightarrow \ell\nu\ell\nu\ell\nu$, $pp \rightarrow ZWW \rightarrow \ell\ell\nu\ell\nu$, $pp \rightarrow ZZZ \rightarrow \ell\ell\ell q q$ and $pp \rightarrow ZZZ \rightarrow \ell\ell\ell\ell\ell$, though the latter having a negligible cross section. The sample describing these processes are generated with MADGRAPH at leading order in QCD. PYTHIA8 [169] is used for the showering. CTEQ6L1 is used as the PDF set. The cross sections and integrated luminosities for these samples are shown in Table 5.5, with K -factors to obtain a NLO normalisation taken from [167].

5 Search for a Narrow Heavy Lepton Resonance

Process (ID)	σ [pb]	K -factor	filter efficiency	$\int Ldt$ [fb $^{-1}$]	Events Simulated
WZ ($3e\mu$) SHERPA	9.757	1	0.274	2,244	5,998,980
ZZ ($4e\mu$) SHERPA	8.6551	1.1	1	367	3,497,893
ZZ ($4e$) POWHEG-BOX	0.077	1	0.91	15,768	1,099,997
ZZ ($2e2\mu$) POWHEG-BOX	0.18	1	0.83	11,019	1,599,696
ZZ ($2e2\tau$) POWHEG-BOX	0.18	1	0.58	10,759	1,099,798
ZZ (4μ) POWHEG-BOX	0.077	1	0.91	15,681	1,099,798
ZZ ($2\mu2\tau$) POWHEG-BOX	0.18	1	0.59	10,670	1,098,999
ZZ (4τ) POWHEG-BOX	0.077	1	0.11	36,814	300,000
WZ ($e^- \bar{\nu}_e e^+ e^-$) POWHEG-BOX	1.41	1.122	0.29	1,462	680,000
WZ ($e^- \bar{\nu}_e \mu^+ \mu^-$) POWHEG-BOX	0.94	1.122	0.35	2,158	799,999
WZ ($e^- \bar{\nu}_e \tau^+ \tau^-$) POWHEG-BOX	0.17	1.122	0.17	9,486	310,000
WZ ($\mu^- \bar{\nu}_\mu e^+ e^-$) POWHEG-BOX	1.40	1.122	0.29	1,726	795,000
WZ ($\mu^- \bar{\nu}_\mu \mu^+ \mu^-$) POWHEG-BOX	0.95	1.122	0.35	2,128	800,000
WZ ($\mu^- \bar{\nu}_\mu \tau^+ \tau^-$) POWHEG-BOX	0.17	1.122	0.17	9,384	310,000
WZ ($\tau^- \bar{\nu}_\tau e^+ e^-$) POWHEG-BOX	1.40	1.122	0.14	1,382	310,000
WZ ($\tau^- \bar{\nu}_\tau \mu^+ \mu^-$) POWHEG-BOX	0.94	1.122	0.18	1,613	310,000
WZ ($\tau^- \bar{\nu}_\tau \tau^+ \tau^-$) POWHEG-BOX	0.17	1.122	0.06	7,088	80,000
WZ ($e^+ \nu_e e^+ e^-$) POWHEG-BOX	0.98	1.144	0.30	2,389	795,000
WZ ($e^+ \nu_e \mu^+ \mu^-$) POWHEG-BOX	0.64	1.144	0.35	3,100	799,999
WZ ($e^+ \nu_e \tau^+ \tau^-$) POWHEG-BOX	0.11	1.144	0.16	15,083	310,000
WZ ($\mu^+ \nu_\mu e^+ e^-$) POWHEG-BOX	0.94	1.144	0.30	2,493	794,499
WZ ($\mu^+ \nu_\mu \mu^+ \mu^-$) POWHEG-BOX	0.65	1.144	0.35	3,044	800,000
WZ ($\mu^+ \nu_\mu \tau^+ \tau^-$) POWHEG-BOX	0.11	1.144	0.16	15,033	309,999
WZ ($\tau^+ \nu_\tau e^+ e^-$) POWHEG-BOX	0.94	1.144	0.15	1,956	309,998
WZ ($\tau^+ \nu_\tau \mu^+ \mu^-$) POWHEG-BOX	0.64	1.144	0.19	2,273	310,000
WZ ($\tau^+ \nu_\tau \tau^+ \tau^-$) POWHEG-BOX	0.11	1.144	0.06	11,151	80,000

Table 5.4: Diboson event samples used for the analyses. The LO cross section, K -factors (for NLO normalisation) and filter efficiencies are reported. The integrated luminosities corresponding to the total numbers of events in each sample are also given.

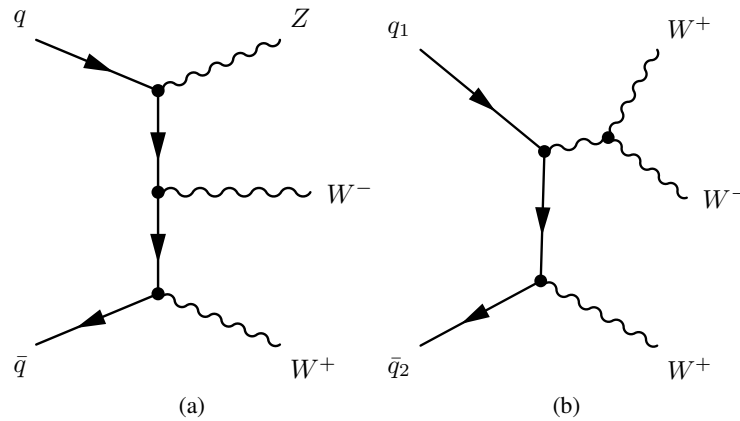


Figure 5.7: Feynman diagrams for the dominant triboson production processes.

5.3.3 $t\bar{t} + V$ Background

The associated production of $t\bar{t}$ and a vector boson ($V = Z$ or W) can lead to final states with up to four leptons. Due to its small cross section it is a finite, but non negligible, background to the final state discussed in this analysis. The main diagrams for the associated production are found in Fig. 5.8. The contribution of this background to the analysed final state is estimated from simulation.

The $t\bar{t} + Z/\gamma^*$ and $t\bar{t} + W$ samples are generated using the LO generator ALPGEN and interfaced to HERWIG for the fragmentation and hadronisation process, with JIMMY [118] modelling the underlying event. The $t\bar{t} + WW$, tWZ and tZ samples are generated using MADGRAPH, with PYTHIA6 or PYTHIA8 used for the parton shower. All above mentioned samples are generated with the NLO PDF set CTEQ6L1. The cross sections are normalised to NLO using Ref. [170]. The LO cross sections, K -factors for NLO normalisation, and sample luminosities are listed in Table 5.6. The systematic uncertainties of the $t\bar{t} + Z/\gamma^*$ and $t\bar{t} + W$ processes are evaluated by comparison with additional samples generated with MADGRAPH.

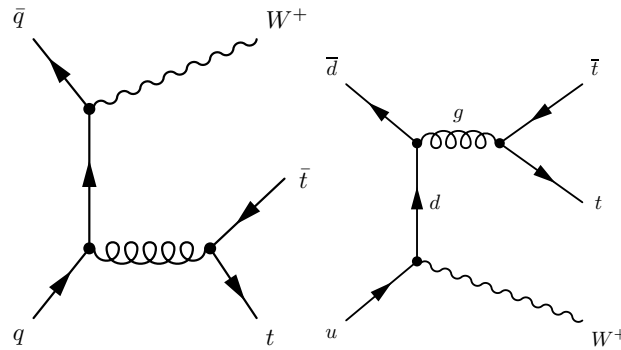


Figure 5.8: Most important leading-order Feynman diagrams for $t\bar{t} + W$ and $t\bar{t} + Z/\gamma^*$ production in proton–proton collisions.

5.3.4 $Z + \text{jets}$ Background

The direct production of Z bosons with associated jets is an important process containing two prompt leptons from the Z decay. These events can enter the signal selection if an additional third lepton candidate is reconstructed, which can originate from misidentified jets, heavy quark decays, or in-flight pion or kaon decays.

Leptons arising from the associated production of $Z + b\bar{b}/c\bar{c}$ succeeded by semileptonic heavy flavour decays are also considered in the *fake* lepton category, although being in fact real leptons. In general the relatively large lifetime of the b and c hadrons means they will travel some distance before decaying, and will give rise to leptons that do not appear to originate from the primary vertex. In addition, leptons from heavy flavour decays will, in the majority of cases, not be well isolated from other particles. Although the event selection criteria listed in Section 5.5, are chosen to reject $Z + \text{jets}$ events, specifically the impact parameter and isolation requirements, the large cross section means some events may inevitably pass the selection. The contribution of the $Z + \text{jets}$ events is derived directly from data, applying the *fake-factor* method detailed in Section 6.1. Simulated samples were used for comparison and validation purposes. Samples of Z/γ^* production in association with jets are produced with ALPGEN interfaced to PYTHIA6.1. The underlying event is modelled using the Perugia 2011C tune [112] and the PDF set CTEQ6L1. Samples were generated with up to 5 additional patrons in the matrix element and parton shower, and are further split into light flavour (LF) and heavy flavour (HF) samples, the latter referring to

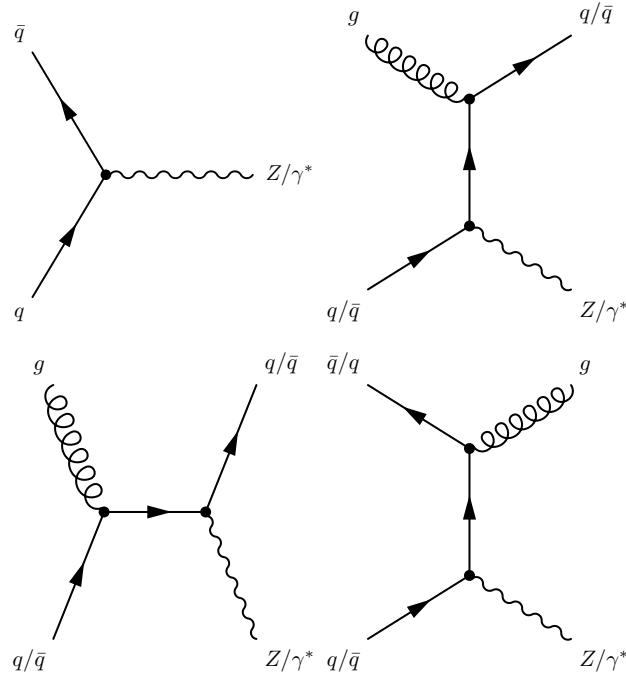


Figure 5.9: Leading- and next-to-leading order Feynman diagrams for Z-boson production in proton–proton collisions.

b and c quarks. The Z/γ^* +LF jets (+HF jets) samples have been generated with a dilepton invariant mass range of $60 \text{ GeV} < M_{\ell\ell} < 2 \text{ TeV}$ ($30 \text{ GeV} < M_{\ell\ell} < 2 \text{ TeV}$) and taking into account the Z/γ^* interference. Additional Z/γ^* + LF jets samples with dilepton invariant mass in the range of $10 \text{ GeV} < M_{\ell\ell} < 60 \text{ GeV}$ were generated using ALPGEN+HERWIG.

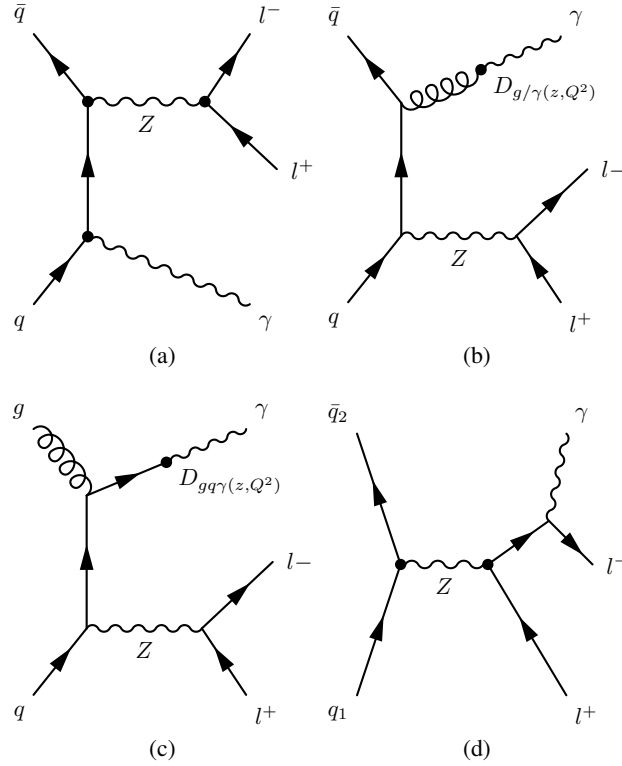
5.3.5 Photon Conversion

Another non-negligible background source to final states with three isolated leptons is due to $Z + \gamma$ production, where two leptons arise from the Z decay and the photon converts and is selected as an electron. Two production mechanisms give rise to $Z + \gamma \rightarrow \ell^+ \ell^- \gamma + X$ final states. Either processes where the photon emerges from bremsstrahlung of leptons in Z -boson decays, or processes with the Z and photon produced in association with one another. In those events photons arise from initial-state radiation of the quarks, or from the fragmentation of quarks and gluons. The corresponding Feynman diagrams are shown in Fig. 5.10.

The $Z + \gamma$ processes are simulated with SHERPA. The samples are produced with up to three additional partons, and require the photon to have transverse momentum of $p_T > 10 \text{ GeV}$. The samples are generated using the next-to-leading order PDF set CT10 The leading order cross sections, K -factors for NLO normalisation, and integrated luminosities are shown in Table 5.7.

5.3.6 $t\bar{t}$ Background

Events from top quark pair production almost exclusively decays via $t\bar{t} \rightarrow bW^+ \bar{b}W^-$. These events can pass the signal selection in the occasion, that both W bosons decay leptonically (this accounts for 5%

Figure 5.10: Feynman diagrams for the production and decay of the $Z + \gamma$ production.

of the $t\bar{t}$ decays [27]) and at least one lepton is reconstructed from a semileptonic b -hadron decay. This leads to final states with three or more leptons.

Events with top quark pairs are the only contribution to the signal region which do not contain a true Z boson. However, due to the rather large production of $t\bar{t}$ events at the LHC, with a cross section of $\sigma = 245.8_{-8.4}^{+6.2} (\text{scale})_{-6.4}^{+6.2} (\text{pdf}) \text{ pb}$ [171], their contribution to the three-lepton final state is not negligible. The contribution of $t\bar{t}$ events to the signal region is determined by taking advantage of the non-prompt nature of the leptons selected from the b -quark jet in these events, and relies on the calculation of so called *fake-factors*. An alternative for estimating this background was explored previously by the author of this thesis. This approach was based on requiring the leptons that have $m_{\ell\ell} \sim m_Z$ to have same charge, rather than the expected opposite charge. This leads to a sample dominated by top quark events with three reconstructed leptons, sharing the kinematics expected for the signal region. The ratio of the total number of data events to the number of top events predicted by simulation, after subtracting from the data the number of expected events from other processes as predicted by simulation, could then be taken as a data-derived scale factor, used to normalise the $t\bar{t}$ contribution predicted by simulation in the signal region.

5.3.7 Pile-up Reweighting

The Monte Carlo samples described above are generated with additional minimum bias interactions overlaid to the hard scatter event. The minimum bias interactions account for the significant number of multiple interactions per bunch crossing, which produce a considerable number of additional tracks and energy deposits in the calorimeter. Therefore an accurate modelling of the additional pile-up events

5 Search for a Narrow Heavy Lepton Resonance

Process	σ [pb]	K -factor	$\int Ldt$ [fb ⁻¹]	Simulated Events
$WWW \rightarrow 3l3\nu$ MADGRAPH	5.10×10^{-3}	1.5	9,800	50,000
$ZWW \rightarrow 4l2\nu$ MADGRAPH	1.55×10^{-3}	1.5	32,260	50,000
$ZZZ \rightarrow 4l2\nu$ MADGRAPH	0.33×10^{-3}	1.5	151,500	50,000

Table 5.5: The triboson samples used for this analyses. The LO cross section and K -factors (for NLO normalisation) are reported. The integrated luminosities corresponding to the total number of events in each sample are also given.

Process	σ [pb]	K -factor	$\int Ldt$ [fb ⁻¹]	Simulated Events
$t\bar{t} + W$ MADGRAPH	0.104100	1.17	3,284	399,997
$t\bar{t} + Wj$ MADGRAPH	0.093317	1.17	3,663	399,896
$t\bar{t} + Z$ MADGRAPH	0.067690	1.35	4,377	399,996
$t\bar{t} + Zj$ MADGRAPH	0.087339	1.35	3,392	399,895
$t\bar{t} + WW$ MADGRAPH	0.000920	1.00	10,870	10,000

Table 5.6: The $t\bar{t}$ +boson samples used for this analyses. The LO cross section and K -factors (for NLO normalisation) are reported. The integrated luminosities corresponding to the total number of events in each sample are also given.

Process	σ [pb]	K -factor	$\int Ldt$ [fb ⁻¹]	Simulated Events
$ee + \gamma$ SHERPA	32.260	1.0	274	8,849,673
$\mu\mu + \gamma$ SHERPA	32.317	1.0	278	8,978,579

Table 5.7: The $V+\gamma$ samples used for background estimation. The LO cross section and K -factors (for NLO normalisation) are reported. The integrated luminosities corresponding to the total number of events in each sample are also given.

in Monte Carlo is crucial for a reliable investigation of the physics processes. Since the distribution of the mean number of interactions per bunch crossing, $\langle \mu \rangle$, (see Fig.3.10) is not well reflected in the simulated samples, the generated $\langle \mu \rangle$ is reweighted to follow the distribution in data.

5.4 Data Sample

The data sample analysed in this search was recorded, by the ATLAS experiment in 2012 at a centre-of-mass energy of $\sqrt{s} = 8$ TeV. The data sample corresponds to a total integrated luminosity of 20.3 fb⁻¹. The luminosity calibration is performed in van der Meer scans to an uncertainty of $\pm 2.8\%$ [172]. A general overview of the run conditions of the LHC during Run-1 data taking is summarised in 3.1.1. A Good-Runs-List (GRL) is used to make sure when the detector was fully operational, at the granularity of certain time intervals. This analysis uses only data present in the standard ATLAS ALL Good GRL, meaning that all detector subsystems were fully operational.

Events are selected using the lowest unscaled single electron and muon triggers available during the full 2012 data-taking period. For electrons this is the EF_e24vhi_medium1 which is combined with the EF_e60_medium to recover for efficiency losses at higher transverse momenta (see Section 4.4.1). The muon triggers used in this analyses are EF_mu24i_tight complemented by EF_mu36_tight (see Section 4.4.4). Thus the lowest online threshold for electrons or muons is 24 GeV at Event Filter level. The selection criteria applied to the electron and muon candidates in the analysis are denoted as offline

criteria. The offline transverse momentum is chosen such that the trigger efficiency is in a stable plateau region.

5.4.1 Data Quality Cuts

The quality of the recorded data can be compromised by detector malfunctions and defects or the selection of non- pp collision interactions, originating from cosmic muons or beam backgrounds. Therefore events that fail one of the following requirements are excluded.

The aforementioned GRL is split up into time intervals, covering run periods of about 60 seconds each. To avoid losing a full time interval, due to corrupted data, malfunctions and problems occurring on a shorter timescale events are marked by so-called event-level flags. These flagged events are removed, when timing problems, noise bursts or data integrity problems have appeared.

In order to reject events originating from non-collision backgrounds, the reconstructed primary vertex of the event is required to have at least three associated tracks with $p_T > 400$ MeV associated to it.

Furthermore events with jets potentially originating from instrumental effects, cosmic events or non-collision background are rejected. So-called bad jets are reconstructed jets. They originate not from collisions but from e.g. noise bursts. Bad jets are detected by a set of criteria, based on energy fractions deposited in the different calorimeter layers, the fit qualities of the calorimeter pulse shapes, the negative energy contribution to the jet, the calorimeter timing in respect to the bunch crossing and the jet charge fraction. Events are rejected if a reconstructed jet with $p_T > 20$ GeV passes the bad jet criteria.

Jet energy mis-measurements due to e.g. non-operational cells in the calorimeter, can lead to fake E_T^{miss} , hence these jets are rejected. This applies to any jet candidate with a transverse momentum of $p_T > 40$ GeV, $BCH_{\text{Corr}}^{\text{jet}} > 0.05$ and $\Delta\phi(E_T^{\text{miss}}, \text{jet}) < 0.3$. Lastly, events with a jet pointing to a noisy, but not masked, cell in the tile calorimeter ($-0.2 < \eta < -0.1$ and $2.65 < \phi < 2.75$), during that run, are rejected, both in simulation and data.

5.5 Object Selection

For events that pass the aforementioned trigger and data quality requirements, analysis-specific physics objects criteria are defined. These are based on the object identification criteria outlined in Chapter 4 and are extended to meet the particular needs for the three-lepton final state. In the following sections, the selection criteria for electron and muon candidates are summarised. Since tracking detector hits and calorimeter deposits can be associated with several physics objects, ambiguities between these objects need to be resolved. Therefore overlap removal criteria are employed.

5.5.1 Electrons

Electron candidates are selected within the geometrical acceptance of $|\eta| < 2.47$, excluding the transition region between the barrel and the end-cap calorimeters $1.37 < |\eta| < 1.52$. Selected electrons must have a transverse energy larger than 15 GeV and are reconstructed using algorithms specifically optimised for high- E_T electrons (`e1_author == 1` or `3`). Candidates affected by the presence of a dead front-end board in the first or second sampling layer, a dead high voltage supply or a masked cell in the core, are excluded. Electron candidates that are matched to an object that passed the above mentioned electron triggers, are required to have a transverse energy momentum of $E_T > 26$ GeV. This ensures that the trigger efficiency for the `EF_e1_EF_e24vhi_medium1` trigger, has reached a stable plateau region in the electron E_T . In this plateau region, systematic uncertainties on the simulated trigger efficiency

are typically smaller than in the turn-on region, where the efficiency strongly depends on the lepton transverse momentum.

Since this analysis is largely dependent on a pure electron selection, stringent selection criteria are set on the isolation. Electron candidates are required to satisfy the `tight++` identification criteria (see Section 4.4) which are optimised for the increased number of multiple interactions per bunch crossing in the 2012 dataset. To reduce the contributions from non-prompt or *fake* electrons the transverse and longitudinal impact parameters of the tracks with respect to the primary vertex and the isolation of the electron candidates from nearby hadronic activity are used. The transverse impact parameter significance, defined as $|d_0/\sigma_{d_0}|$, must be less than 3.0, where d_0 is the transverse impact parameter of the reconstructed track with respect to the primary vertex and σ_{d_0} is the estimated uncertainty on d_0 . The longitudinal impact parameter z_0 must satisfy $|z_0 \sin \theta| < 0.5$ mm. The isolation of the electron candidate is defined by two variables. The first, $p_{T,\text{track}}^{\text{iso}}$, is the scalar sum of the transverse momenta of all tracks, with a transverse momentum $p_T > 1$ GeV within a cone of $\Delta R = 0.3$ around the electron axis. The track associated with the electron candidate is excluded from the sum, as well as tracks inconsistent with originating from the primary vertex. The second variable is the calorimeter based isolation, $E_{T,\text{calo}}^{\text{iso}}$, which is the sum of transverse energy of topological calorimeter clusters in the electromagnetic and hadronic calorimeters in a cone of $\Delta R = 0.3$ around the electron axis, excluding a rectangular region around the candidate axis of 0.125×0.175 , i.e. 5×7 cells in the main sampling layer of the electromagnetic calorimeter, in $\eta \times \phi$. The variable is additionally corrected for the incomplete containment of the electron transverse energy within the excluded region, as well as for the expected effects due to pile-up interactions. Electron candidates are selected if $p_{T,\text{track}}^{\text{iso}}/p_T < 0.1$ and $E_{T,\text{calo}}^{\text{iso}}/p_T < 0.1$. These values are tightened for high energetic electron candidates above $p_T > 100$ GeV to $p_{T,\text{track}}^{\text{iso}} < (10 \text{ GeV} + 0.01 \times p_T)$ and $E_{T,\text{calo}}^{\text{iso}} < (10 \text{ GeV} + 0.01 \times p_T)$. The tighter cut for high- p_T electron candidates actually reduces non-prompt backgrounds to negligible levels.

5.5.2 Muons

Muon candidates are reconstructed within their geometrical acceptance of $|\eta| < 2.5$, reduced to $|\eta| < 2.4$ if the muon candidate is used for trigger matching. For muon candidates which triggered the event a transverse momentum of $p_T > 26$ GeV is required. The remaining muon candidates pass the selection with a transverse momentum of $p_T > 15$ GeV. Muon candidates are reconstructed with the STACO (STATistical COMbination) algorithm, and are required to pass the combined selection, which associates hits in the ID and muon spectrometer [141]. To reduce misidentification and improve the muon momentum resolution, quality requirements on the muon track are applied. Muon candidate tracks are required to have at least one hit in the pixel detector, and four or more hits in the SCT. Tracks are vetoed, if they have more than two holes¹ in the SCT and pixel detectors, as well as tracks with an excessive amount of outlier hits in the TRT². It should be noted, that the detector conditions are included in these requirements by adding hits for inactive modules, if the track is expected to have passed this module.

To ensure, that the muon candidate track is consistent with originating from the primary event vertex, the ID track is required to satisfy $|d_0/\sigma_{d_0}| < 3$ and $|z_0 \sin \theta| < 0.5$ mm, where d_0 and z_0 are the transverse and longitudinal impact parameters of the track with respect to the primary vertex, respectively, and σ_{d_0} is the uncertainty on the transverse impact parameter. As for the electron candidates, tight isolation criteria are used to further reject non-prompt and *fake* leptons by limiting the amount of nearby activity as measured by ID tracks and calorimeter energy deposits. Requirements on $p_{T,\text{track}}^{\text{iso}}$, the scalar sum of

¹ A hole is defined as a missing hit, where one is expected.

² For tracks with $0.1 < |\eta| < 1.9$ the requirement is $n_{\text{TRT}}^{\text{hits}} + n_{\text{TRT}}^{\text{outliers}} > 5$ and $n_{\text{TRT}}^{\text{outliers}} < 0.9 \times (n_{\text{TRT}}^{\text{hits}} + n_{\text{TRT}}^{\text{outliers}})$.

the transverse momenta of all tracks with a transverse momentum $p_T > 1$ GeV within a cone of $\Delta R = 0.3$ around the muon axis excluding the muon track itself and the calorimeter based isolation $E_{T,\text{calo}}^{\text{iso}}$ ³. For muons, the sum only includes cells above a certain threshold in order to suppress noise, and does not include cells with energy deposits from the muon candidate. Both isolation variables are required to be less than 10% of the lepton transverse momentum for muon candidates with $p_T < 100$ GeV, and less than $10 \text{ GeV} + 0.01 \times p_T$ for leptons with $p_T \geq 100$ GeV.

Cut	Electrons
Object ID	tight++
Leading (trigger) E_T	$E_T > 26 \text{ GeV}$
Subleading E_T	$E_T > 15 \text{ GeV}$
Acceptance	$(\eta < 2.47) \ \&\& \ !(1.37 < \eta < 1.52)$
Calo. Isolation	$\text{TopoEtcone30} < \begin{cases} 0.1 \times E_T & : E_T < 100 \text{ GeV} \\ 10 \text{ GeV} + 0.01 \times E_T & : E_T > 100 \text{ GeV} \end{cases}$
Track Isolation	$\text{ptcone30} < \begin{cases} 0.1 \times E_T & : E_T < 100 \text{ GeV} \\ 10 \text{ GeV} + 0.01 \times E_T & : E_T > 100 \text{ GeV} \end{cases}$
Track d_0	$\frac{d_0}{\sigma_{d_0}} < 3$
Track z_0	$z_0 \sin \theta < 0.5 \text{ mm}$
Cut	Muons
Object ID	Combined Tight
Leading (trigger) p_T	$p_T > 26 \text{ GeV}$
Subleading p_T	$p_T > 15 \text{ GeV}$
Trigger Acceptance	$ \eta < 2.4$
Acceptance	$ \eta < 2.5$
Calo. Isolation	$\text{Etcone30} < \begin{cases} 0.1 \times p_T & : p_T < 100 \text{ GeV} \\ 10 \text{ GeV} + 0.01 \times p_T & : p_T > 100 \text{ GeV} \end{cases}$
Track Isolation	$\text{ptcone30} < \begin{cases} 0.1 \times p_T & : p_T < 100 \text{ GeV} \\ 10 \text{ GeV} + 0.01 \times p_T & : p_T > 100 \text{ GeV} \end{cases}$
Track d_0	$\frac{d_0}{\sigma_{d_0}} < 3$
Track z_0	$z_0 \sin \theta < 0.5 \text{ mm}$
Cut	Jets
Object ID	LC TopoClusters
Acceptance	Anti- k_t , $R = 0.4$
E_T	$E_T > 30 \text{ GeV}$
Jet Vertex fraction	JVF > 0.5

Table 5.8: Overview of the object selection criteria used to select the signal candidates.

5.5.3 Jet Definition

Jets are reconstructed from topological clusters using the anti- k_t jet algorithm [144] with a distance parameter of $R = 0.4$ and full four-momentum recombination. The cluster energies are calibrated with

³ This is the the scalar sum of transverse energies of calorimeter cells in a cone of size $\Delta R = 0.3$ around the muon candidate track, already corrected for pile-up

a local cluster weighting (LCW) algorithm (AntiKt4LCTopoJets) [173]. Jets are required to have $p_T > 30$ GeV, in order to limit the number of pile-up jets. For the geometrical acceptance, jets must lie in the range $|\eta| < 4.5$, so that the jet falls within the instrumented regions of the detector. Pile-up jets are additionally suppressed with a cut on the jet vertex fraction.

5.5.4 Resolving Overlapping Objects

Leptons and jets can be reconstructed as multiple objects. The overlap between these ambiguous objects is resolved by applying the following procedure, based on the reconstruction purities. Firstly, the ambiguity between two electron candidates is resolved, by discarding the electron with the lower transverse momentum p_T , if two electrons are reconstructed within $\Delta R(e, e) < 0.1$.

The jet algorithm uses all energy deposits in the calorimeter, therefore electrons are present in both the electron and jet collections. A jet is removed, if an electron and a jet are separated by $\Delta R(\text{jet}, e) < 0.2$. Jets may also contain leptons from semileptonic b - or c -hadron decays, therefore if a jet and an electron satisfy the condition $0.2 < \Delta R(\text{jet}, e) < 0.4$ and $p_T(\text{jet}) > 30 \text{ GeV} + 0.05 \cdot p_T(e)$ the electron is removed. To address cases where a muon undergoes bremsstrahlung and radiates off a hard photon, which is further identified as an electron, electrons are removed if $\Delta R(\mu, e) < 0.1$. Targeted at the efficiency loss from jets induced by muons at high muon p_T , jets are removed if a muon and a jet are separated by $\Delta R < 0.1$ and if the jet transverse momentum satisfies $p_{T,\text{jet}} < 0.5 p_{T,\mu}$ for $p_{T,\mu} < 200$ GeV, or $p_{T,\text{jet}} < 100$ GeV if $p_{T,\mu} > 200$ GeV. The final step in the overlap removal is aimed at decreasing the reducible muon backgrounds by removing muons that satisfy $\Delta R(\text{jet}, \mu) < 0.3$.

5.6 Preliminary Result of the Type-III Seesaw Analysis

A preliminary result of a search for the type-III seesaw model heavy leptons in the four-lepton final state was conducted in 2012. This search is summarised in Refs. [174, 175]. The main contributions by the author of this thesis were: defining the analysis strategy, the optimisation of the signal selection for a heavy three lepton resonance, detailed cutflow comparisons on $\sqrt{s} = 7$ TeV simulated Monte Carlo samples, preparation of the signal Monte Carlo simulation production infrastructure and production of simulated signal event samples, truth matching studies and fits to the resonance width of the $\sqrt{s} = 8$ TeV simulated signal samples as well as providing cross-checks for the exclusion limit, by implementing the results in an alternative limit setting code. The search is performed in a data sample corresponding to 5.8 fb^{-1} of integrated luminosity collected in 2012 at $\sqrt{s} = 8$ TeV by the ATLAS detector at the LHC.

This analysis aims at the direct reconstruction of final states with decays $L^\pm \rightarrow \ell^\pm Z$ ($\ell = e \mu$), in which the Z decays leptonically. The analysis requires at least four leptons, three attributed to the resonance and a fourth from the opposite side of the event to further discriminate the background. While the transverse momentum of the lepton attributed to the trigger needs to pass $p_T > 25$ GeV the remaining ones are selected with a $p_T > 10$ GeV. The resonance $L^\pm \rightarrow Z\ell^\pm$ is reconstructed by selecting a same-flavour opposite-charge lepton-pair with an invariant mass within 10 GeV of the Z pole mass. The third lepton is chosen as the closet in the transverse plane to the Z candidate. Events with a second Z candidate are rejected, which efficiently reduces the ZZ background. The resulting cutflow is shown in Table 5.9. With four leptons in the final state the main background is from ZZ production, followed by minor contributions from Z +jets, $t\bar{t}+W/Z$, ZZZ and ZWW . All background estimations depend on Monte Carlo simulation. The dominating ZZ background is normalised using a dedicated control region, defined by reverting the veto on the second Z candidate in the event. The invariant mass distribution of the $Z(\ell\ell)\ell$ system forming the L^\pm candidate in the signal region is shown in Fig. 5.11. Since no significant excess above the expected Standard Model background was observed, limits on the product of the cross section

	Signal [120 GeV]	ZZ	Z+jets	VVV	$t\bar{t}V$	Total Bkg.	Data
Four or more leptons	115.0 ± 3.0	61.9 ± 0.3	$1.3^{+2.1}_{-0.8}$	0.53 ± 0.01	1.05 ± 0.11	$64.9^{+2.1}_{-0.8}$	58
Z reconstruction	103.4 ± 2.8	57.1 ± 0.3	$1.3^{+2.1}_{-0.8}$	0.45 ± 0.01	0.99 ± 0.04	$59.9^{+2.1}_{-0.8}$	55
Second Z Veto	88.6 ± 2.6	17.2 ± 0.2	$1.3^{+2.1}_{-0.8}$	0.38 ± 0.01	0.85 ± 0.04	$19.8^{+2.1}_{-0.8}$	19
Third μ	50.5 ± 2.0	9.2 ± 0.1	$1.3^{+2.1}_{-0.8}$	0.20 ± 0.01	0.46 ± 0.03	$11.2^{+2.1}_{-0.8}$	8
Third e	38.1 ± 1.7	8.0 ± 0.1	–	0.18 ± 0.01	0.40 ± 0.02	8.6 ± 0.1	11

Table 5.9: Cut flow table with the number of expected events for the signal with a mass of $m_N = 120$ GeV, SM backgrounds, and data. The uncertainties shown are the statistical ones of the MC samples. In this table, $t\bar{t}$ and $t\bar{t}V$ events are considered together. Processes with expected number of events less than 0.1 are neglected. The last two rows are a decomposition of the third row. Reproduced from [175]

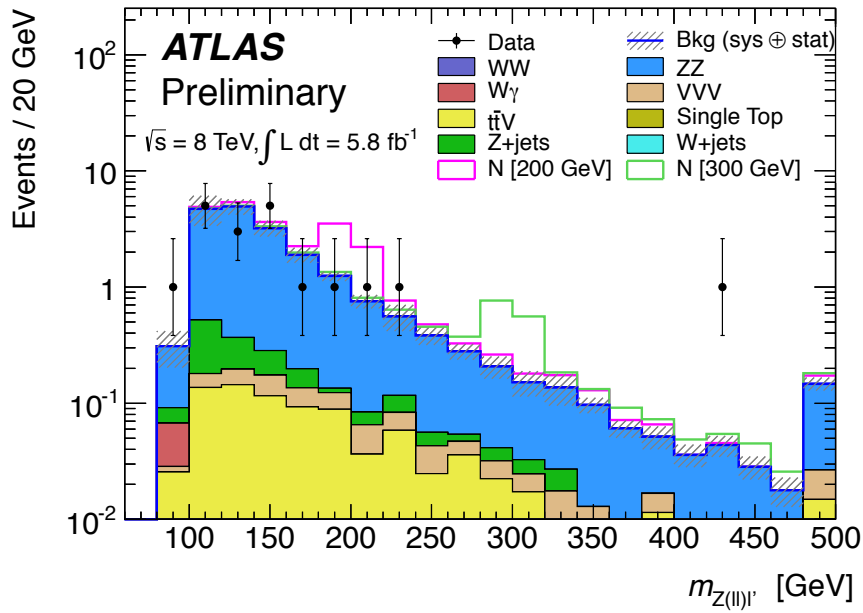


Figure 5.11: Distribution of the $Z(\ell\ell)\ell$ invariant mass distribution, of the L^\pm candidates in the signal region, for data (black points) and the expected total background (solid histograms). The rightmost bin in the histogram is the overflow bin. Here the charged heavy lepton is denoted N^\pm instead of L^\pm . Taken from [175]

times the branching fractions for the process, $\sigma(pp \rightarrow L^\pm N^0) \times BF(N^\pm \rightarrow Z \ell^\pm) \times BF(N^0 \rightarrow W^\pm \ell^\mp)$, were placed as a function of m_N . The upper limits at the 95% CL are shown in Fig.5.12. With the branching ratio set to the nominal value (magenta curve) the expected limit is $m_N > 240.3^{+6.0}_{-5.6}$ GeV and the observed limit is $m_N > 229.3 \pm 6.2$ GeV.

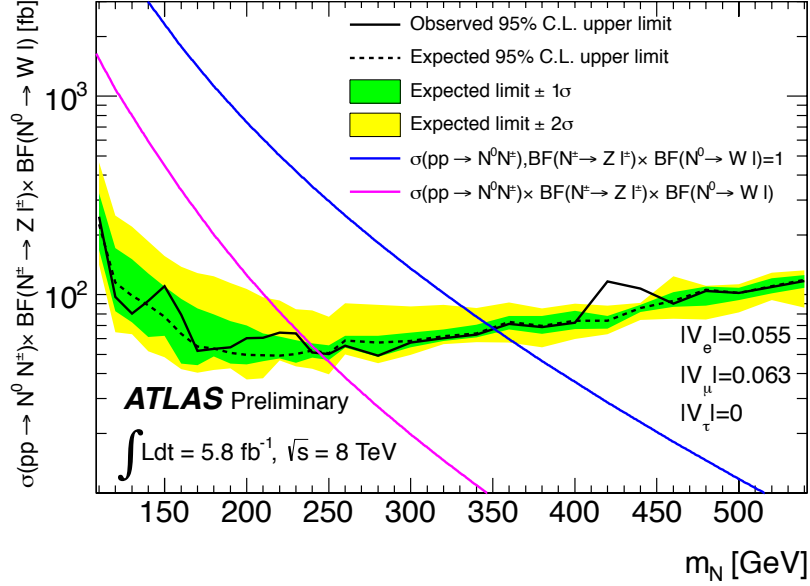


Figure 5.12: Distribution of the expected (dashed line) and observed (solid line) exclusion limit at 95 % CL on the cross section times branching fraction as a function of the heavy fermion mass m_N . For two different branching ratio scenarios. Taken from [175]

5.7 Signal Selection and Heavy Lepton Resonance Reconstruction

This analysis presents the search for a heavy lepton resonance reconstructed from three isolated leptons with an intermediate Z -boson decay, motivated by the type-III seesaw model and the vector-like leptons model. In both benchmark models the heavy leptons are pair produced, so in addition to the reconstructed $L^\pm \rightarrow Z + \ell$ decay, the signal contains either a second charged heavy lepton, L^\pm , or in case of the type-III seesaw an additional neutral heavy lepton, N^0 . The sensitivity of the analysis can be improved by further categorising the events into signal categories, based on the decay topologies from the second heavy lepton in the event. The heavy lepton resonance reconstruction is divided into preselection criteria and the selection of heavy lepton resonance candidate. The two preselection criteria are:

- Events are required to have at least three isolated electrons or muons (eee , $ee\mu$, $\mu\mu e$ or $\mu\mu\mu$), that pass the above defined selection criteria.
- Events need to contain at least one same-flavour opposite-sign lepton pair with invariant mass $m_{\ell^+\ell^-} > 15$ GeV.

Events containing a heavy lepton candidate are selected by the following criteria:

- Require a Z -boson candidate, given by a same-flavour, opposite-sign pair of electrons or muons with an invariant mass consistent with $|m_{\ell^+\ell^-} - m_Z| < 10$ GeV. The Z mass is taken to be 91.1876 GeV [27].
- Reject four lepton events, that contain two leptonic Z candidates. This suppresses background events arising from Standard Model ZZ production. The efficiency loss due to this selection on the signal is on the order of $\sim 4\%$.
- If an event contains more than three leptons a unique trilepton candidate is chosen as follows:
 - Choose the same-flavour, opposite-sign (SFOS) pair with invariant mass closest to m_Z .
 - Select the third lepton as the one closest in ΔR to the reconstructed Z four-momentum. This lepton is called “bachelor” lepton in the remainder of this thesis. The trilepton resonance mass $m_{3\ell}$ is given by the invariant mass of these three leptons.

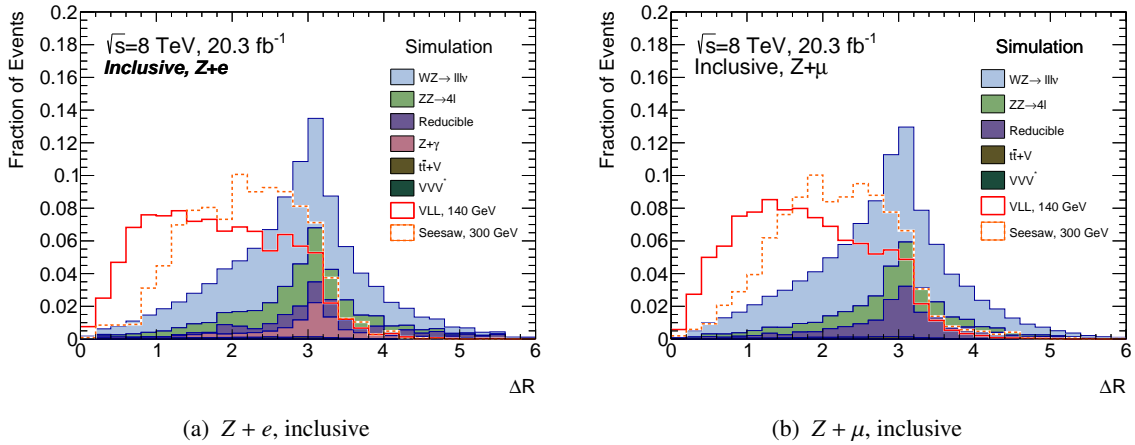


Figure 5.13: Distributions of the separation ΔR between the Z candidate and the bachelor lepton for signal and background in the $Z + e$ (left) and $Z + \mu$ (right) flavour channels. All of the event selection requirements except for the one on ΔR are applied.

For heavy lepton masses $m_{L^\pm} \leq 200$ GeV, the Z candidate and the bachelor lepton tend to be colimated. This is shown in Fig. 5.13, which shows the distance $\Delta R(Z, \ell_3)$, between the Z candidate and the bachelor lepton. To enhance the signal over background ratio, especially at low masses, events are selected if $\Delta R(Z, \ell_3) < 3.0$. This threshold was optimised running a simplified limit setting procedure on the inclusive region using the cut-and-count MCLIMITS code [176] and cross-checked by evaluating the signal-to-background ratio. This selection additionally allows for the construction of a background validation region, using the inverted $\Delta R(Z, \ell_3) > 3.0$ condition.

After identifying the trilepton candidates the events are categorised depending on the decay of the second heavy lepton in the event. Through their decays the final states contain additional neutrinos, leptons or jets from the W/Z or H boson decay. The further categorisation is based on the fraction of events that contain either an additional lepton, a neutrino or a dijet pair from the W/Z and H boson decays. Figure 5.14 shows these categories as a function of the mass of the charged heavy lepton (left) and the neutral heavy lepton (right). An additional dijet pair from the second heavy lepton arises in $2/3$ of the decays. In case of the charged heavy lepton with masses below 200 GeV, many events have an additional neutrino, whereas in the neutral case a fourth lepton is more likely. For masses above

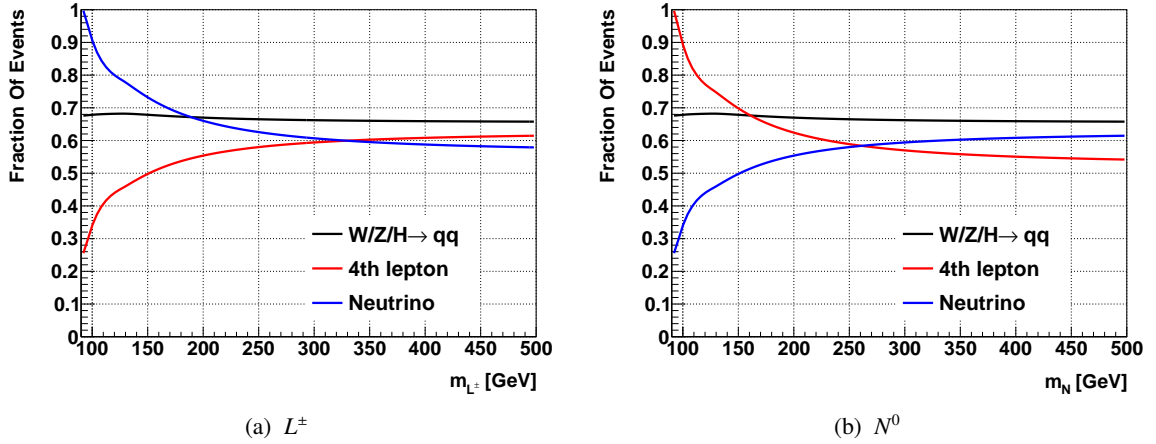


Figure 5.14: Fraction of events with various activity from the second pair-produced heavy lepton, for events with two charged heavy leptons $L^\pm L^\mp$ (left), and events with one charged and one neutral heavy lepton, $L^\pm N^0$ on the right. The left plot, showing the decay of the second charged heavy lepton, is identical for the type-III seesaw and vector-like lepton model. The neutral heavy lepton exists only in the type-III seesaw model.

300 GeV an additional fourth charged lepton is found in $\sim 60\%$ and an additional neutrino is present in $\sim 55\%$ of the cases for the charged heavy lepton. The opposite is true for the neutral heavy lepton. In this case $\sim 50\%$ have an additional charged lepton and $\sim 60\%$ an additional neutrino contributing to the final state topology. At particle level, requiring either a fourth lepton or a hadronically decaying boson is very efficient on the signal:

- if the second heavy fermion is charged, then every decay satisfies this requirement, except for $L^\pm \rightarrow W^\pm(\tau^\pm\nu)\nu$, where the τ decays hadronically;
- if the second heavy fermion is neutral, then every decay except for $N^0 \rightarrow Z\nu \rightarrow \nu\nu\nu$ and a small fraction of Higgs decays ($N^0 \rightarrow H\nu$) satisfies this requirement.

Any categorisation targeting the additional neutrino in the event has proven less effective in separating the signal from the dominant WZ background. Hence the sample is separated by defining three mutually exclusive categories based on:

4 ℓ : Event contains at least four isolated leptons, passing the nominal lepton selection criteria.

3 ℓ + jj : Exactly three leptons and a dijet pair with an invariant mass satisfying with $m_W - 20 \text{ GeV} < m_{jj} < m_H + 20 \text{ GeV}$.

3 ℓ – only : All remaining 3 ℓ signal events, failing the requirements for the 4 ℓ or 3 ℓ +jj categories.

The dijet mass window was not optimised, but was simply chosen to be widely inclusive of dijet boson decays. Finally, events are separated into two channels based on whether the bachelor lepton is an electron or a muon, into the $Z+e$ and $Z+\mu$ flavour channel. This classification leads to in six independent signal regions. In addition the inclusive $Z+e$ and $Z+\mu$ flavour channel, with no categorisation applied, are used for a model independent evaluation of the results (see Section 9.4.3).

The variable of interest in this search is the mass difference $\Delta m \equiv m_{3\ell} - m_{\ell^+\ell^-}$, where $m_{3\ell}$ is the invariant mass of the trilepton candidate and $m_{\ell^+\ell^-}$ invariant mass of the Z candidate. By constructing

the search around this variable, the impact of the lepton momentum in the resolution is reduced, thus leading to a narrower reconstructed resonance of the signal. The distribution of the tripleton mass, $m_{3\ell}$, and the mass difference, Δm , for the inclusive region is found in Fig. 5.15. The selection requirements for the heavy lepton resonance are additionally summarised in Table 5.10.

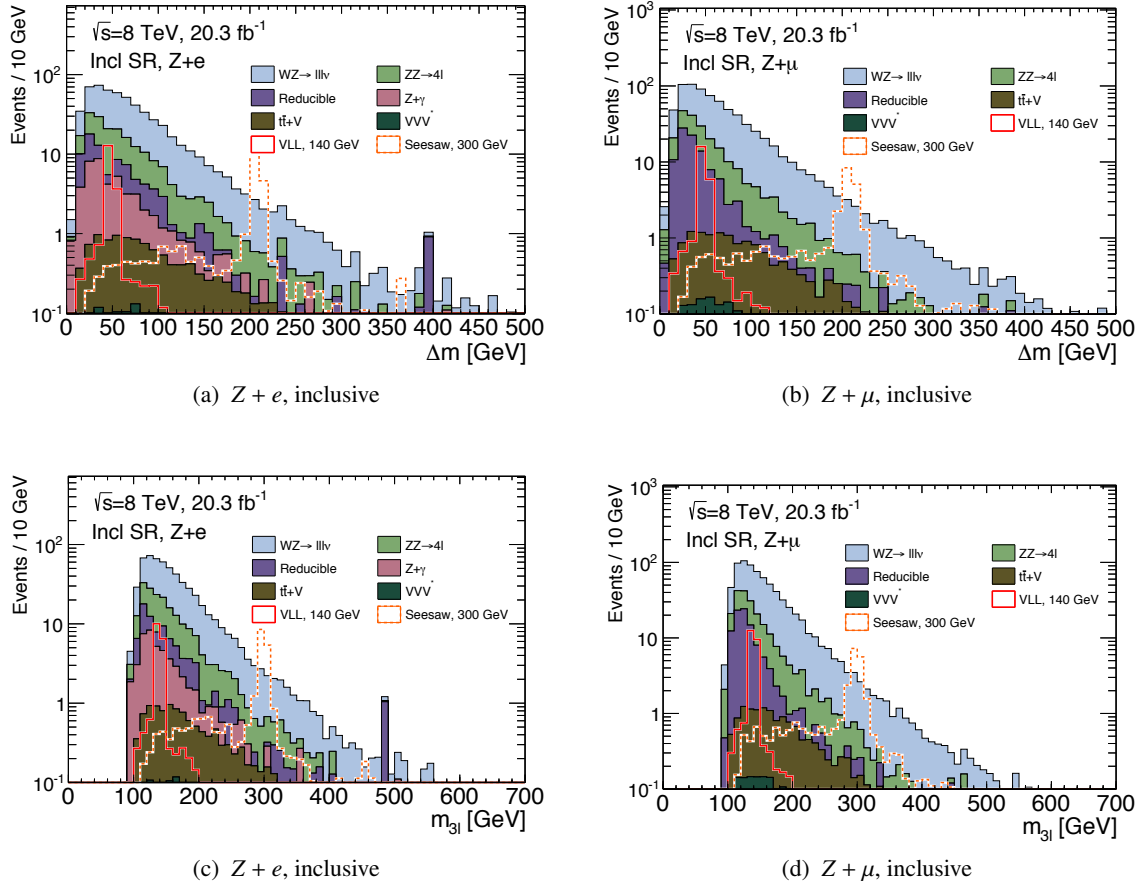


Figure 5.15: Distributions of the Δm (top) and the $m_{3\ell}$ (bottom) signal and background in the inclusive $Z + e$ (left) and $Z + \mu$ (right) flavour channels. All of the event selection requirements are applied.

5.7.1 Performance on Fiducial Signal Events

The performance of the heavy lepton candidate selection is shown in Table 5.11 for $Z + e$ final states and in Table 5.12 for $Z + \mu$ final states in terms of the acceptance of fiducial events. The fiducial event selection is performed separately for the $Z + e$ and $Z + \mu$ flavour channels. The fiducial events are required to have three truth-level leptons with $p_T > 15$ GeV and $|\eta| < 2.5$. Two of these form a Z candidate consistent with $|m_{\ell^+\ell^-} - m_Z| < 10$ GeV. Furthermore, the bachelor lepton is of the correct flavour, and the tripleton mass satisfies $|m_{3\ell} - m_{L^\pm}| < 5$ GeV. For the vector-like leptons and type-III seesaw models used in this analysis, the acceptance of events containing an $L^\pm \rightarrow Z(\ell\ell)\ell$ decay to fall within the fiducial volume is in the ranges from $\sim 30\%/ \sim 45\%$ for a heavy lepton mass of 100 GeV for the $Z + e/Z + \mu$ channel to $\sim 55\%$ for heavy lepton masses of 400 GeV for both channels. It should be noted that the flavour requirement on the reconstructed bachelor lepton has a different efficiency

5 Search for a Narrow Heavy Lepton Resonance

Selection Requirement	
Bachelor Lepton Flavour	Divide sample by flavour of third lepton
Z-Candidate	Same flavour opposite sign lepton pair, with $ m_{\ell^+\ell^-} - m_Z < 10 \text{ GeV}$
Second Z Veto	Reject events with second independent Z candidate
ΔR	$\Delta R(Z, \ell_3) < 3.0$
Categorisation	
4ℓ	4th lepton passing the object selection
$3\ell+jj$	Additional dijet pair, satisfying $m_W - 20 \text{ GeV} < m_{jj} < m_H + 20 \text{ GeV}$, where m_W is the W boson mass and m_H is the Higgs boson mass [27]
3ℓ -only	Remaining signal events not satisfying the 4ℓ or $3\ell+jj$ category

Table 5.10: Signal event selection and candidate reconstruction criteria, including the categorisation of the signal events, based on the activity on the opposite side of the event.

between the vector-like leptons sample and the type-III seesaw sample. This is a consequence of the initial flavour content of the samples: the vector-like leptons samples are divided into two samples with 100% branching fraction to either bachelor electron or bachelor muon, while the seesaw samples are single mixed samples containing both electron and muon decays. The total efficiency of the event selection for the $Z + e$ decay channel ranges from 20% at $m_{L^\pm} = 100 \text{ GeV}$ to 35% at $m_{L^\pm} = 400 \text{ GeV}$. Correspondingly the total efficiency of the event selection for the $Z + \mu$ decay channel ranges from 36% at $m_{L^\pm} = 100 \text{ GeV}$ to 38% at $m_{L^\pm} = 400 \text{ GeV}$. More details on the selection efficiency found in Section 9.4.4.

Process	Requirements					Categories		
	Preselection	Bachelor e	$ m_{\ell^+ \ell^-} - m_Z < 10 \text{ GeV}$	ZZ veto	$\Delta R < 3.0$	4ℓ	$3\ell+jj$	3ℓ -only
VLL, 100 GeV	0.348 ± 0.008	0.318 ± 0.008	0.306 ± 0.008	0.303 ± 0.008	0.298 ± 0.008	0.054 ± 0.004	0.096 ± 0.005	0.147 ± 0.006
VLL, 110 GeV	0.478 ± 0.006	0.435 ± 0.006	0.421 ± 0.006	0.417 ± 0.006	0.401 ± 0.006	0.076 ± 0.003	0.11 ± 0.004	0.215 ± 0.005
VLL, 120 GeV	0.535 ± 0.006	0.491 ± 0.006	0.467 ± 0.006	0.457 ± 0.006	0.424 ± 0.006	0.104 ± 0.004	0.117 ± 0.004	0.204 ± 0.005
VLL, 130 GeV	0.604 ± 0.006	0.539 ± 0.006	0.509 ± 0.006	0.494 ± 0.006	0.445 ± 0.006	0.125 ± 0.004	0.127 ± 0.004	0.194 ± 0.005
VLL, 140 GeV	0.643 ± 0.006	0.578 ± 0.006	0.559 ± 0.006	0.538 ± 0.006	0.491 ± 0.006	0.153 ± 0.004	0.164 ± 0.004	0.174 ± 0.005
VLL, 160 GeV	0.663 ± 0.006	0.593 ± 0.006	0.572 ± 0.006	0.552 ± 0.006	0.499 ± 0.006	0.175 ± 0.005	0.148 ± 0.004	0.176 ± 0.005
VLL, 180 GeV	0.698 ± 0.006	0.62 ± 0.006	0.594 ± 0.006	0.573 ± 0.007	0.505 ± 0.007	0.197 ± 0.005	0.163 ± 0.005	0.144 ± 0.005
VLL, 200 GeV	0.707 ± 0.006	0.624 ± 0.007	0.596 ± 0.007	0.577 ± 0.007	0.52 ± 0.007	0.209 ± 0.006	0.167 ± 0.005	0.145 ± 0.005
VLL, 250 GeV	0.751 ± 0.007	0.654 ± 0.007	0.626 ± 0.007	0.615 ± 0.007	0.548 ± 0.008	0.245 ± 0.007	0.152 ± 0.005	0.151 ± 0.005
VLL, 300 GeV	0.771 ± 0.007	0.662 ± 0.008	0.63 ± 0.008	0.625 ± 0.008	0.547 ± 0.008	0.258 ± 0.007	0.169 ± 0.006	0.121 ± 0.005
VLL, 400 GeV	0.776 ± 0.007	0.669 ± 0.008	0.642 ± 0.008	0.641 ± 0.008	0.562 ± 0.008	0.277 ± 0.007	0.181 ± 0.006	0.103 ± 0.005
Seesaw, 100 GeV	0.381 ± 0.006	0.351 ± 0.005	0.336 ± 0.005	0.334 ± 0.005	0.308 ± 0.005	0.08 ± 0.003	0.096 ± 0.003	0.131 ± 0.004
Seesaw, 120 GeV	0.517 ± 0.004	0.474 ± 0.004	0.45 ± 0.004	0.44 ± 0.004	0.403 ± 0.004	0.128 ± 0.003	0.128 ± 0.003	0.148 ± 0.003
Seesaw, 160 GeV	0.611 ± 0.005	0.548 ± 0.005	0.532 ± 0.005	0.516 ± 0.005	0.464 ± 0.005	0.167 ± 0.004	0.141 ± 0.003	0.157 ± 0.003
Seesaw, 200 GeV	0.657 ± 0.005	0.591 ± 0.005	0.574 ± 0.005	0.559 ± 0.005	0.5 ± 0.005	0.203 ± 0.004	0.146 ± 0.003	0.152 ± 0.004
Seesaw, 250 GeV	0.671 ± 0.007	0.605 ± 0.007	0.592 ± 0.007	0.582 ± 0.007	0.505 ± 0.007	0.221 ± 0.006	0.14 ± 0.005	0.144 ± 0.005
Seesaw, 300 GeV	0.729 ± 0.007	0.649 ± 0.007	0.633 ± 0.007	0.626 ± 0.007	0.541 ± 0.008	0.23 ± 0.006	0.167 ± 0.006	0.144 ± 0.005
Seesaw, 350 GeV	0.72 ± 0.007	0.651 ± 0.008	0.638 ± 0.008	0.635 ± 0.008	0.553 ± 0.008	0.251 ± 0.007	0.157 ± 0.006	0.146 ± 0.006
Seesaw, 400 GeV	0.717 ± 0.007	0.641 ± 0.008	0.627 ± 0.008	0.623 ± 0.008	0.529 ± 0.008	0.243 ± 0.007	0.15 ± 0.006	0.136 ± 0.005
Seesaw, 450 GeV	0.762 ± 0.008	0.67 ± 0.009	0.66 ± 0.009	0.657 ± 0.009	0.554 ± 0.009	0.267 ± 0.008	0.184 ± 0.007	0.103 ± 0.006
Seesaw, 500 GeV	0.72 ± 0.007	0.636 ± 0.008	0.611 ± 0.008	0.608 ± 0.008	0.525 ± 0.008	0.24 ± 0.007	0.151 ± 0.006	0.134 ± 0.005

Table 5.11: Selection efficiencies for fiducial events after each requirement for the $Z + e$ flavour channel. Only statistical uncertainties due to finite Monte Carlo statistics are shown. The preselection cut requires three selected leptons, with one same-flavour opposite-sign pair, as well as the general event selection cuts listed above.

Process	Requirements					Categories		
	Preselection	Bachelor μ	$ m_{\ell^+ \ell^-} - m_Z < 10 \text{ GeV}$	ZZ veto	$\Delta R < 3.0$	4ℓ	$3\ell+jj$	$3\ell\text{-only}$
VLL, 100 GeV	0.52 ± 0.007	0.508 ± 0.007	0.472 ± 0.007	0.461 ± 0.007	0.456 ± 0.007	0.064 ± 0.004	0.14 ± 0.005	0.252 ± 0.006
VLL, 110 GeV	0.61 ± 0.004	0.593 ± 0.004	0.568 ± 0.004	0.554 ± 0.004	0.536 ± 0.004	0.119 ± 0.003	0.142 ± 0.003	0.275 ± 0.004
VLL, 120 GeV	0.67 ± 0.003	0.648 ± 0.004	0.617 ± 0.004	0.596 ± 0.004	0.561 ± 0.004	0.149 ± 0.003	0.139 ± 0.003	0.273 ± 0.003
VLL, 130 GeV	0.702 ± 0.003	0.676 ± 0.003	0.642 ± 0.003	0.614 ± 0.003	0.569 ± 0.003	0.163 ± 0.003	0.143 ± 0.002	0.263 ± 0.003
VLL, 140 GeV	0.723 ± 0.003	0.701 ± 0.003	0.667 ± 0.003	0.634 ± 0.003	0.585 ± 0.003	0.173 ± 0.003	0.156 ± 0.002	0.256 ± 0.003
VLL, 160 GeV	0.752 ± 0.003	0.727 ± 0.003	0.685 ± 0.003	0.65 ± 0.003	0.592 ± 0.003	0.212 ± 0.003	0.156 ± 0.002	0.223 ± 0.003
VLL, 180 GeV	0.77 ± 0.003	0.746 ± 0.003	0.69 ± 0.003	0.659 ± 0.003	0.593 ± 0.003	0.227 ± 0.003	0.161 ± 0.002	0.205 ± 0.003
VLL, 200 GeV	0.779 ± 0.003	0.751 ± 0.003	0.69 ± 0.003	0.66 ± 0.003	0.584 ± 0.003	0.239 ± 0.003	0.161 ± 0.002	0.184 ± 0.002
VLL, 250 GeV	0.786 ± 0.003	0.752 ± 0.003	0.676 ± 0.003	0.657 ± 0.003	0.579 ± 0.003	0.268 ± 0.003	0.162 ± 0.002	0.149 ± 0.002
VLL, 300 GeV	0.789 ± 0.002	0.76 ± 0.003	0.68 ± 0.003	0.667 ± 0.003	0.578 ± 0.003	0.288 ± 0.003	0.163 ± 0.002	0.127 ± 0.002
VLL, 400 GeV	0.787 ± 0.002	0.753 ± 0.003	0.665 ± 0.003	0.656 ± 0.003	0.563 ± 0.003	0.292 ± 0.003	0.166 ± 0.002	0.106 ± 0.002
Seesaw, 100 GeV	0.535 ± 0.006	0.521 ± 0.006	0.484 ± 0.006	0.471 ± 0.006	0.46 ± 0.006	0.192 ± 0.005	0.121 ± 0.004	0.147 ± 0.004
Seesaw, 120 GeV	0.677 ± 0.004	0.66 ± 0.004	0.613 ± 0.004	0.589 ± 0.004	0.546 ± 0.004	0.212 ± 0.004	0.119 ± 0.003	0.215 ± 0.004
Seesaw, 160 GeV	0.745 ± 0.004	0.723 ± 0.004	0.685 ± 0.004	0.658 ± 0.004	0.595 ± 0.005	0.252 ± 0.004	0.14 ± 0.003	0.202 ± 0.004
Seesaw, 200 GeV	0.743 ± 0.004	0.717 ± 0.005	0.668 ± 0.005	0.651 ± 0.005	0.588 ± 0.005	0.263 ± 0.004	0.152 ± 0.004	0.173 ± 0.004
Seesaw, 250 GeV	0.761 ± 0.006	0.735 ± 0.006	0.673 ± 0.007	0.662 ± 0.007	0.585 ± 0.007	0.284 ± 0.006	0.144 ± 0.005	0.157 ± 0.005
Seesaw, 300 GeV	0.785 ± 0.006	0.764 ± 0.006	0.695 ± 0.007	0.688 ± 0.007	0.601 ± 0.007	0.295 ± 0.007	0.171 ± 0.006	0.135 ± 0.005
Seesaw, 350 GeV	0.78 ± 0.006	0.757 ± 0.007	0.688 ± 0.007	0.681 ± 0.007	0.59 ± 0.008	0.294 ± 0.007	0.155 ± 0.006	0.141 ± 0.005
Seesaw, 400 GeV	0.753 ± 0.007	0.727 ± 0.007	0.642 ± 0.008	0.634 ± 0.008	0.544 ± 0.008	0.277 ± 0.007	0.15 ± 0.006	0.118 ± 0.005
Seesaw, 450 GeV	0.762 ± 0.008	0.732 ± 0.008	0.658 ± 0.008	0.653 ± 0.009	0.555 ± 0.009	0.285 ± 0.008	0.152 ± 0.006	0.119 ± 0.006
Seesaw, 500 GeV	0.755 ± 0.007	0.729 ± 0.007	0.654 ± 0.008	0.65 ± 0.008	0.551 ± 0.008	0.275 ± 0.007	0.155 ± 0.006	0.122 ± 0.005

Table 5.12: Selection efficiencies for fiducial events after each requirement for the $Z + \mu$ flavour channel. Only statistical uncertainties due to finite Monte Carlo statistics are shown. The preselection cut requires three selected leptons, with one same-flavour opposite-sign pair, as well as the general event selection cuts listed above.

Background Estimation and Validation Regions

Standard Model processes contributing as background to the signal region, are broadly categorised into irreducible and reducible backgrounds. The irreducible background contains processes with at least three isolated prompt leptons in the final state. Based on the lepton identification criteria, it is therefore indistinguishable from the signal events. These events arise mainly from WZ/γ^* and ZZ/γ^* production and are described using Monte Carlo simulation.

The reducible background is a collection of events with three reconstructed leptons, where one of the leptons originates from non-prompt sources or is misidentified as a lepton. The collection includes semileptonic b - and c -hadron decays (heavy-flavour decays), in-flight-decays of pions and kaons (light flavour) or photon conversions. This non-prompt background contribution can be largely suppressed using tight lepton identification criteria. The reducible background is determined using data-driven techniques. They extrapolate the contribution of the reducible background from control samples in data with altered lepton selection to the signal region. The implementation of these techniques is described in Section 6.1. The background estimation technique for events arising from photon conversions is detailed in Section 6.1.3. The consistency of the background estimation is evaluated using four different validation regions described in Section 6.2.

6.1 Reducible Background Estimation

The reducible background consists of several Standard Model processes with dominant contributions from Z + jets, with associated $b\bar{b}$ and $c\bar{c}$ production, and $t\bar{t}$ production. Despite the tight object selection criteria imposed on the lepton candidates in this analysis, non-prompt and *fake* leptons pose an important background to the signal region. Non-prompt leptons are predominantly real leptons, originating from semileptonic b - or c - hadron decays, in-flight-decays of pions or kaons and photon conversions. Furthermore lepton candidates may also arise from sources such as misidentified jets or hadronic showers, that reach the muon spectrometer and are incorrectly matched to a reconstructed track in the Inner Detector. These are called *fake* leptons and are generally not well described by Monte Carlo simulation, as the misidentification rate of leptons is difficult to model. Within this thesis non-prompt leptons and fake leptons are regarded as reducible background. There are significant theoretical uncertainties associated with heavy-flavour production and their kinematic properties. Furthermore relying on simulation for the non-prompt background also poses a computational difficulty since the production cross sections for relevant processes such as QCD multi-jet and Z + jets production are too large, to produce Monte Carlo

samples of the appropriate size. Therefore the reducible background is estimated by a fully data-driven approach.

Method Overview

The non-prompt background estimate is based on defining a control region in data with an enhanced fraction of non-prompt leptons achieved by inverting certain selection criteria. The background contribution to each signal category is then derived by extrapolating from this region into the specified signal region. The extrapolation relies on measuring the ratio of the number of leptons passing all analysis-level selection cuts, denoted numerator leptons, N , to the number of leptons failing some of these cuts and instead fulfilling a less stringent set of criteria, called denominator leptons, D . The fake factor, f , is defined as the ratio between N and D :

$$f = \frac{N}{D}. \quad (6.1)$$

The quantity measured in the signal region is a collection of all events containing three numerator objects, $n_{\ell_1^N \ell_2^N \ell_3^N}$, from which the number of three real leptons, $n_{\ell_1^R \ell_2^R \ell_3^R}$, needs to be extracted. From the selected events any of the three numerator leptons, labelled $\ell_1^N \ell_2^N \ell_3^N$ could either be a real, ℓ_i^R , or a fake, ℓ_i^F , lepton. Thus the 3-lepton sample can be decomposed into

$$n_{\ell_1^N \ell_2^N \ell_3^N} = n_{\ell_1^R \ell_2^R \ell_3^R} + n_{\ell_1^R \ell_2^R \ell_3^F} + n_{\ell_1^R \ell_2^F \ell_3^R} + n_{\ell_1^R \ell_2^F \ell_3^F} + \quad (6.2)$$

$$+ n_{\ell_1^F \ell_2^R \ell_3^R} + n_{\ell_1^F \ell_2^R \ell_3^F} + n_{\ell_1^F \ell_2^F \ell_3^R} + n_{\ell_1^F \ell_2^F \ell_3^F}, \quad (6.3)$$

where ℓ_1 (ℓ_2) are the positively (negatively) charged leptons associated with the Z candidate, and ℓ_3 is the bachelor lepton. The reducible background prediction is thus given by the number of signal events where at least one lepton is fake, i.e. $n_{\ell_1^N \ell_2^N \ell_3^N} - n_{\ell_1^R \ell_2^R \ell_3^R}$. The remaining terms can be deduced by using events with one or more denominator leptons. Assuming an event where the first lepton is a denominator lepton, which is assumed to be a fake lepton, then this can be expressed by $n_{\ell_1^D \ell_2^N \ell_3^N} f_1$.

$$n_{\ell_1^D \ell_2^N \ell_3^N} f_1 = n_{\ell_1^F \ell_2^R \ell_3^R} + n_{\ell_1^F \ell_2^R \ell_3^F} + n_{\ell_1^F \ell_2^F \ell_3^R} + n_{\ell_1^F \ell_2^F \ell_3^F}, \quad (6.4)$$

where f_1 is the fake factor corresponding to the denominator lepton, which equals the number $n_{\ell_1^N \ell_2^N \ell_3^N}$, where the first lepton is fake. Applying the same method the remaining permutations are expressed by

$$n_{\ell_1^N \ell_2^D \ell_3^N} f_2 = n_{\ell_1^R \ell_2^F \ell_3^R} + n_{\ell_1^R \ell_2^F \ell_3^F} + n_{\ell_1^F \ell_2^R \ell_3^R} + n_{\ell_1^F \ell_2^R \ell_3^F} \quad (6.5)$$

$$n_{\ell_1^N \ell_2^N \ell_3^D} f_3 = n_{\ell_1^R \ell_2^R \ell_3^F} + n_{\ell_1^R \ell_2^F \ell_3^F} + n_{\ell_1^F \ell_2^R \ell_3^F} + n_{\ell_1^F \ell_2^F \ell_3^F} \quad (6.6)$$

$$n_{\ell_1^D \ell_2^D \ell_3^N} f_1 f_2 = n_{\ell_1^F \ell_2^F \ell_3^R} + n_{\ell_1^F \ell_2^F \ell_3^F} \quad (6.7)$$

$$n_{\ell_1^D \ell_2^D \ell_3^D} f_1 f_3 = n_{\ell_1^F \ell_2^F \ell_3^F} + n_{\ell_1^F \ell_2^F \ell_3^F} \quad (6.8)$$

$$n_{\ell_1^N \ell_2^D \ell_3^D} f_2 f_3 = n_{\ell_1^R \ell_2^F \ell_3^F} + n_{\ell_1^F \ell_2^F \ell_3^F} \quad (6.9)$$

$$n_{\ell_1^D \ell_2^D \ell_3^D} f_1 f_2 f_3 = n_{\ell_1^F \ell_2^F \ell_3^F}. \quad (6.10)$$

yielding eight equations and eight unknowns. Hence the system can be solved for the reducible background prediction:

$$\begin{aligned} \ell_1^N \ell_2^N \ell_3^N - \ell_1^R \ell_2^R \ell_3^R = & (\ell_1^N \ell_2^N \ell_3^D f_3 + \ell_1^N \ell_2^D \ell_3^N f_2 + \ell_1^D \ell_2^N \ell_3^N f_1) \\ & - (\ell_1^N \ell_2^D \ell_3^D f_2 f_3 + \ell_1^D \ell_2^N \ell_3^D f_1 f_3 + \ell_1^D \ell_2^D \ell_3^N f_1 f_2) \\ & + \ell_1^D \ell_2^D \ell_3^D f_1 f_2 f_3. \end{aligned} \quad (6.11)$$

The implementation of this fake-factor method was transferred to this analysis from the ATLAS model-independent trilepton analysis [177], and a detailed description can be found in Ref. [178]

6.1.1 Electron Fake Factors

The electron fake factors [158, 177] are calculated using a single electron sample, based on the full 20.3 fb^{-1} 2012 dataset and are binned two-dimensionally in η and p_T . The denominator electrons are defined by inverting the electron identification criteria and the track impact parameter. Additionally, denominator objects must pass the tight requirement on the $\Delta\eta$ and $\Delta\phi$ between the track and the cluster as summarised in Table 6.1.

Criteria	Numerator	Denominator
Electron ID	tight++	!medium++ && loose++
Impact Parameter Significance	$\frac{ d_0 }{\sigma_{d_0}} < 3$	$3 < \frac{ d_0 }{\sigma_{d_0}} < 10$

Table 6.1: Denominator and numerator electron definitions. The denominators are taken to be an exclusive OR combination of the two selection inversions. Additionally, denominator objects must pass the tight requirement on the $\Delta\eta$ and $\Delta\phi$ between the track and the cluster. The structure in the regions $1.37 < |\eta| < 1.52$, arises from the transition region between the barrel and the end-cap calorimeters, which is excluded in the electron candidate selection.

The sample is selected using several electron and photon triggers, depending on the desired transverse momentum bin, in which the reconstructed electron is successfully matched to the trigger object. Besides the basic data quality cuts, as described in Section 5.5, several requirements are imposed to reduce the magnitude of the prompt contamination mainly originating from W and Z decays. Events are vetoed, if they contain more than one electron to reduce the impact of $Z \rightarrow \ell\ell$ decays. Furthermore, events are selected with a transverse mass $m_T < 40 \text{ GeV}$ and $E_T^{\text{miss}} < 40 \text{ GeV}$, which efficiently suppresses the W contamination¹. The remaining prompt contamination is subtracted, using Monte Carlo simulated event samples, and stems mainly from W and Z production as well as Drell-Yan, $t\bar{t}$ and single- t events. Especially for the numerator objects, the prompt contamination can reach up to 60%. The resulting central values of the fake factors are shown in Fig. 6.1 a) along with the relative statistical uncertainty shown in Fig. 6.1 b). The structure in the region $1.37 < |\eta| < 1.52$, arises from the transition region between the barrel and the end-cap calorimeters, which is excluded in the electron candidate selection.

6.1.2 Muon Fake Factors

The muon fake factors [158] follow the approach established in the same-sign dilepton search with the 2011 data set [179, 180]. Herein the denominator muons are selected by loosening the impact parameter

¹ The transverse mass is defined as $m_T = \sqrt{2p_T E_T^{\text{miss}}(1 - \cos(\phi^e - \phi^{\text{miss}}))}$.

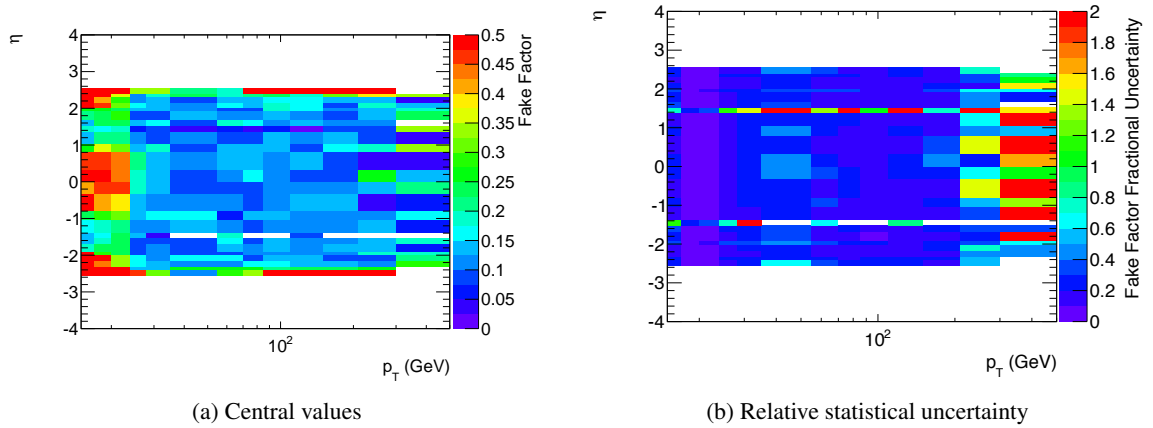


Figure 6.1: Central value and relative statistical uncertainty of the electron fake factors, which are parametrised in p_T and η . [158]

requirements and the inverted isolation criterion, as detailed in Table 6.2, while the numerator muons are selected according to the nominal selection criteria in Table 6.2. For muons with $p_T > 40$ GeV the overlap criteria between muons and jets is removed for the benefit of statistical power at the cost of an additional systematic uncertainty.

Criteria	Denominator
Calo. Isolation	$E_{T,\text{calo}}^{\text{cone30}} > \begin{cases} 0.15 \times p_T & : p_T < 100 \text{ GeV} \\ 15 \text{ GeV} + 0.01 \times p_T & : p_T < 100 \text{ GeV} \end{cases} \& E_{T,\text{calo}}^{\text{cone30}}/p_T < 2.0$
Track Isolation	$p_{T,\text{calo}}^{\text{cone30}} > \begin{cases} 0.15 \times p_T & : p_T < 100 \text{ GeV} \\ 15 \text{ GeV} + 0.01 \times p_T & : p_T > 100 \text{ GeV} \end{cases} \& p_{T,\text{calo}}^{\text{cone30}}/p_T < 2.0$
Track d_0	$\frac{ d_0 }{\sigma_{d_0}} > 3 \& \frac{ d_0 }{\sigma_{d_0}} < 10$

Table 6.2: Denominator muon definitions. The denominators are defined by inverting both specified requirements. [158]

The muon fake factor is measured in a sample of same-sign dimuon events, selected from the entire 2012 dataset, using a dimuon trigger with a p_T threshold of 13 GeV. The two leading- p_T muons are required to have same charge, to efficiently suppresses the prompt contamination from Z events. Each of these two muons in the event, failing the nominal impact parameter requirement, is used to measure the fake factor. An extrapolation factor from the high- $\frac{|d_0|}{\sigma_{d_0}}$ fake-factor measurement region, to the low- $\frac{|d_0|}{\sigma_{d_0}}$ signal region is derived. This extrapolation factor is simply the ratio between the Monte Carlo estimate for the two regions, based on POWHEG-BOX $t\bar{t}$ samples.

In dependence on the jet activity in the event two sets of fake factors are measured called *inclusive* and *two-jets* fake-factor. The jets are selected with a transverse momentum of $p_T > 30$ GeV and a separation from muons of at least $\Delta R(\mu, jet) > 0.3$. The two fake-factor sets are defined as:

Inclusive: The measurement is based on entire same-sign dimuon sample. These fake-factors are applied to events with zero jets.

Two-Jets: The measurement uses same-sign dimuon events with at least two jets. These are applied to events with one or more jets.

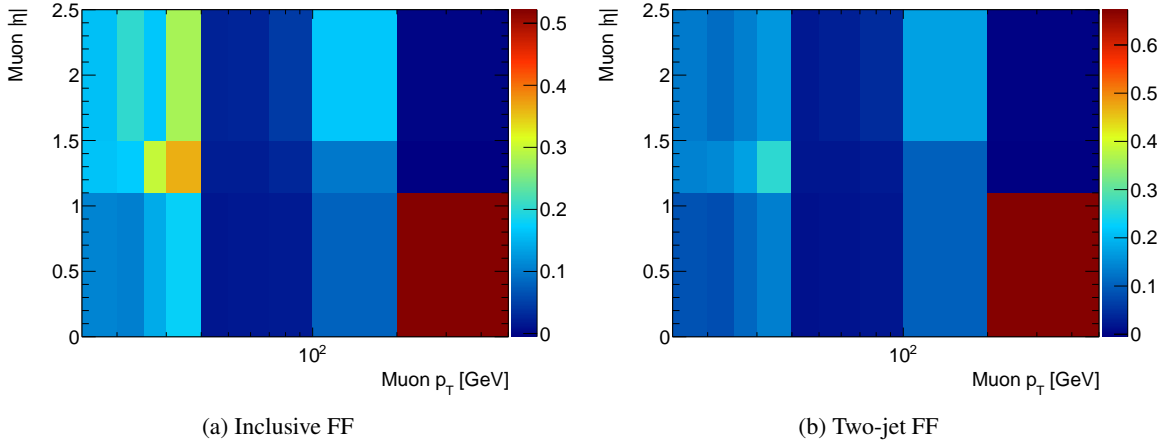


Figure 6.2: Muon fake factors as a function of p_T and $|\eta|$. The left plot shows fake factors measured in the inclusive control sample and applied to events with zero jets. The right plot shows fake factors measured in events with two jets, and applied to events with at least one jet. [158]

Contributions to the two-jet fake-factor are expected to arise from W +jet and $t\bar{t}$ events. The samples are corrected for prompt contamination stemming mainly from $t\bar{t}$ events, using Monte Carlo simulated events. Figure 6.2 shows the muon fake factors as a function of p_T and $|\eta|$. The left plot shows fake factors measured in the inclusive control sample and the right plot shows fake factors measured in events with two jets.

6.1.3 $Z + \gamma$ Background

A further source of reducible background arises from $Z + \gamma$ events [158, 177], where the photon shows up either in the matrix element or through bremsstrahlung. This background is estimated using SHERPA Monte Carlo samples (see Section 5.3) and is thus treated as a prompt contamination in the fake-factor method. Events in which the photon produces an electron-positron pair with an unbalanced momentum are often reconstructed as a single electron candidate. The rate of these events is overestimated in the simulated event samples, especially for denominator electrons. This results in a net deficit in the background prediction, due to the large subtraction of the prompt contamination in the reducible background estimate. Therefore scale factors are derived to account for this mismodelling.

The scale factors are derived following a method for *charge-flipped* electrons, i.e. electrons that are reconstructed with the wrong charge. In general charge flipped events arise in processes, where an electron emits a photon which in turn converts asymmetrically and is reconstructed as an electron of wrong charge. Scale factors for numerator and denominator electrons are derived from a Z -enriched region, requiring dielectron events with an invariant mass between 80 GeV and 100 GeV. The electrons can be either numerator or denominator electrons, as described above. Events with same-sign electrons are expected to entirely arise from $Z \rightarrow ee$ events, in which one electron flipped the charge. Events with opposite-sign electrons are considered as not-charge-flipped. Events with two-charge-flips are neglected, as the charge-flip rate is below the percent level.

The scale factors, to correct for this mismodelling, are evaluated in bins of η and summarised in Table 6.3. While the scale factors for the numerators are close to one, the corresponding scale factors for the denominators deviate significantly. The scale factors are then applied to each $Z + \gamma$ event, depending on the classification of the reconstructed lepton closest to the truth photon, within $\Delta R(\gamma, e) < 0.2$.

Systematic uncertainties on the mismodeling of the scale factors are around 30 %, based both on the statistical uncertainties in data and Monte Carlo simulation and the variations observed in the scale factors when running on different generated samples.

	$ \eta < 2.2$	$2.2 < \eta < 2.37$	$2.37 < \eta < 2.47$
Numerators	1.02	0.95	0.95
Denominators	0.82	0.66	0.40

Table 6.3: Data-to-MC scale factors for photon conversions. [158]

6.2 Validation Regions

A thorough understanding of the different background processes is essential for the interpretation of the observations in the signal regions. Therefore the combined background model is validated in four dedicated control regions, targeted at the different background contributions.

6.2.1 High- ΔR Validation Region

The high- ΔR region closely follows the selection of the signal region with two modifications. It is defined by inverting the signal selection cut on the angular separation between the Z candidate and the bachelor lepton to $\Delta R(Z, \ell_3) > 3.0$. An additional criteria on the lepton invariant mass, $m_{3\ell} < 200$ GeV, is imposed, to limit the signal contamination from the type-III seesaw signal in this region. Since the VLL have a significantly smaller production cross section, no signal contribution is expected in the above mass range.

Due to its similarity to the signal region this control region is expected to have a similar overall background composition. Therefore this region allows a validation of the combined background model. Since the majority of events contributing to the reducible background arise from Z + jet events, where a jet is misidentified as a lepton, a large separation between the Z candidate and the additional jet, which balances the event, is expected. Therefore this region is also used to validate the reducible fake-factor estimate.

The high- ΔR region is evaluated separately for the bachelor electron and bachelor muon final state. On top of that no further classification of the the events is done, based on the opposite side of the event. The distributions of the most relevant variables are found in Fig. 6.3. These show the invariant mass of the resonance candidate, $m_{3\ell}$, the Δm , and the angle between the reconstructed Z and the bachelor lepton, $\Delta R(Z, \ell_3)$, for both bachelor lepton flavours. The dominating contribution arises from diboson production followed equally by the reducible contribution and the $Z + \gamma$ production for the $Z + e$ final state and solely the reducible background for the $Z + \mu$ final state.

A good agreement between data and background expectations is seen in all distributions. An excellent agreement between the predicted background of 239 ± 15.47 (stat) ± 13.66 (syst) events and 239 events in data is found for the $Z + e$ channel. The same is true for events with a bachelor muon, where 301 ± 17.35 (stat) ± 12.33 (syst) are expected and 302 events are observed.

6.2.2 Off- Z Validation Region

The off- Z region consists of events with exactly three leptons and an inverted Z selection, such that events are rejected, if they contain a same-flavour opposite sign pair with $|m_{\ell^+\ell^-} - m_Z| < 20$ GeV.

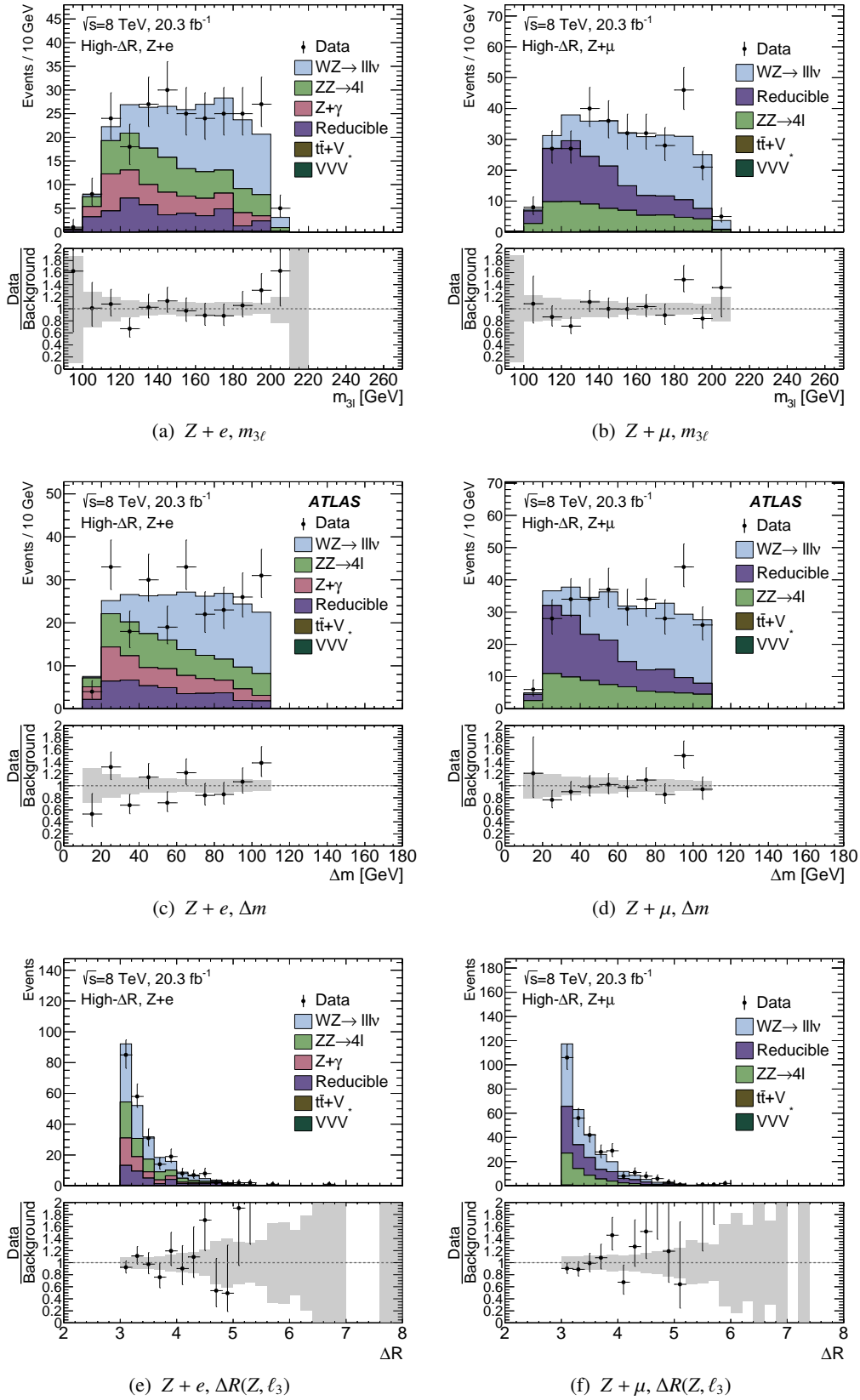


Figure 6.3: High $\Delta R(Z, \ell_3)$ validation region: $m_{3\ell}$ (top), Δm (middle), and ΔR (bottom) for $Z + e$ final states (left) and $Z + \mu$ final states (right). Figures (c) and (d) have previously been published in [149].

Additionally a looser Z window cut is applied, requiring that $|m_{\ell^+\ell^-} - m_Z| < 50$ GeV. The bachelor lepton in this validation region is defined as the remaining lepton which is not part of the same-flavour opposite-sign pair with the highest invariant mass.

The background composition in this region differs significantly for the two lepton flavours. While the final state with a bachelor electron is dominated by $Z + \gamma$ production, followed by diboson production and the reducible background estimate, $Z + \gamma$ production does not play a role for $Z + \mu$ final states. Good agreement between the expected background and the data is observed for final states with a bachelor electron. The largest discrepancy of any control region is found for the muon final states, with $200.25 \pm 14.16(\text{stat}) \pm 7.77(\text{syst})$ expected events and 163 observed data events, corresponding to a significance of -2.3σ based on the combined statistical and systematic uncertainty. Figure 6.4 shows the $m_{3\ell}$, the Δm , and $\Delta R(Z, \ell_3)$ distributions for both bachelor lepton flavours. The good agreement for the $Z + e$ final state is seen in all three corresponding distributions. In contrast, both the $m_{3\ell}$ and the Δm distributions of the $Z + \mu$ final state reveal that the discrepancy between simulation and data arises mainly from an overestimate around a reconstructed 3-lepton mass corresponding to the Z pole mass. This region is mainly populated by ZZ events. Since the signal selection requires the Z candidate to have a mass within 10 GeV of the Z pole mass, this observed deviation will not have an influence on the signal region.

6.2.3 ZZ Validation Region

ZZ pair production is one of the leading backgrounds in this analysis, especially the only significant background contributing to the 4ℓ category. Therefore a detailed validation of the Monte Carlo simulated events in data is of great importance. The ZZ validation region is targeted at selecting on-shell ZZ pairs. This is achieved by requiring two same-flavour opposite-sign pairs, with $|m_{\ell^+\ell^-} - m_Z| < 10$ GeV. These events are rejected in the signal region, to limit the contribution of ZZ production. A summary of the event counts in the selection is given in Tables A.5 and A.6 for the $Z+e$ and $Z+\mu$ final state, respectively. An excellent agreement is found, with 39 events observed and $37.29 \pm 6.11(\text{stat}) \pm 2.14(\text{syst})$ events expected in the $Z + e$ final state. The $Z + \mu$ final state has a slightly worse agreement between simulation and observed data with a total of 74 observed and $63.4 \pm 7.97(\text{stat}) \pm 3.43(\text{syst})$ expected. This leads to a factor of 1.22 in the ratio of the difference between data and simulated background divided by the combined statistical and systematic error. The distributions of $m_{3\ell}$, Δm and $\Delta R(Z, \ell_3)$ are shown in Fig.6.5. The largest disagreement is seen in the $m_{3\ell}$ distribution of the $Z+\mu$ final state, in the mass region between 110 GeV to 140 GeV, however the disagreement is much less pronounced in the corresponding Δm distribution. In contrast to the off- Z region with a bachelor muon, no region with a significant disagreement is found.

6.2.4 WZ Validation Region

WZ pair production is the dominating irreducible background contributing to the inclusive signal region. It is also the main background in the $3\ell+\text{jj}$ and 3ℓ -only category. Since the shape of this background is estimated from Monte Carlo simulation, a detailed understanding of any systematic deviation between data and simulated events is vital for the interpretation of the results. The WZ validation region is designed to select a clean WZ sample while efficiently rejecting signal events contributing to this region, as it is impossible to build an orthogonal selection to the signal region.

This validation region consists of events with exactly three leptons and one Z candidate, i.e. one same-flavour opposite-sign lepton pair with an invariant mass of $|m_{\ell^+\ell^-} - m_Z| < 20$ GeV. To target the decay of the W , events are selected, if the third lepton has a transverse mass within $40 \text{ GeV} < m_{\text{T}}^W < 90 \text{ GeV}$,

and the event has a missing transverse energy satisfying $40 \text{ GeV} < E_T^{\text{miss}} < 100 \text{ GeV}$. Additionally, events are required to have no jets to further suppress signal contamination.

The predicted number of events for the $Z + e$ final state are $133.47 \pm 11.56 \text{ (stat)} \pm 10.29 \text{ (syst)}$, which is in reasonable agreement to 140 $Z + e$ events observed in data. In final states with a bachelor muon $192.96 \pm 13.90 \text{ (stat)} \pm 14.42 \text{ (syst)}$ were expected and 222 were events observed in data. The distributions of $m_{3\ell}$, Δm and $\Delta R(Z, \ell_3)$ are shown in Fig. 6.6 for the $Z + e$ and $Z + \mu$ final states. Since the region almost exclusively selects WZ events, the good agreement between data and Monte Carlo simulation confirms the validity of the use of simulated samples for the WZ background estimate.

6.2.5 Summary of the Validation Regions

The expected and observed numbers of events are summarised in Table. 6.4 for the $Z + e$ and $Z + \mu$ channel. The largest discrepancy is found for the Off- Z region in the $Z + \mu$ channel, where there is a deficit in the data corresponding to 2.3σ . This region is dominated by contributions from ZZ , where only three leptons pass the selection requirements and no 2same-flavour, opposite-sign lepton pair is reconstructed with invariant mass within the Z mass window of 20 GeV. All other regions show an agreement better than 1.5σ . Additional information on the four validation regions is found in Appendix A

Flavour Channel	Control Region	Data	Background Prediction	$\frac{\text{Data-Bkgd}}{\sigma_{\text{bkgd}}}$
$Z + e$	High- ΔR	239	$239.16 \pm 15.47^{\text{(stat)}} \pm 13.66^{\text{(syst)}}$	-0.01
$Z + e$	Off- Z	360	$348.81 \pm 18.68^{\text{(stat)}} \pm 44.21^{\text{(syst)}}$	0.23
$Z + e$	ZZ	39	$37.29 \pm 6.11^{\text{(stat)}} \pm 2.14^{\text{(syst)}}$	0.26
$Z + e$	WZ	140	$133.47 \pm 11.56^{\text{(stat)}} \pm 10.29^{\text{(syst)}}$	0.42
$Z + \mu$	High- ΔR	302	$301.00 \pm 17.35^{\text{(stat)}} \pm 12.33^{\text{(syst)}}$	0.05
$Z + \mu$	Off- Z	163	$200.25 \pm 14.16^{\text{(stat)}} \pm 7.77^{\text{(syst)}}$	-2.31
$Z + \mu$	ZZ	74	$63.4 \pm 7.97^{\text{(stat)}} \pm 3.43^{\text{(syst)}}$	1.22
$Z + \mu$	WZ	222	$192.96 \pm 13.90^{\text{(stat)}} \pm 14.42^{\text{(syst)}}$	1.45

Table 6.4: Summary of the number of events observed and predicted for each validation region. The uncertainty on the background prediction is the total systematic uncertainty. The difference between the observed and predicted number of events divided by the combined statistical and systematic uncertainty on the prediction is also shown.

6 Background Estimation and Validation Regions

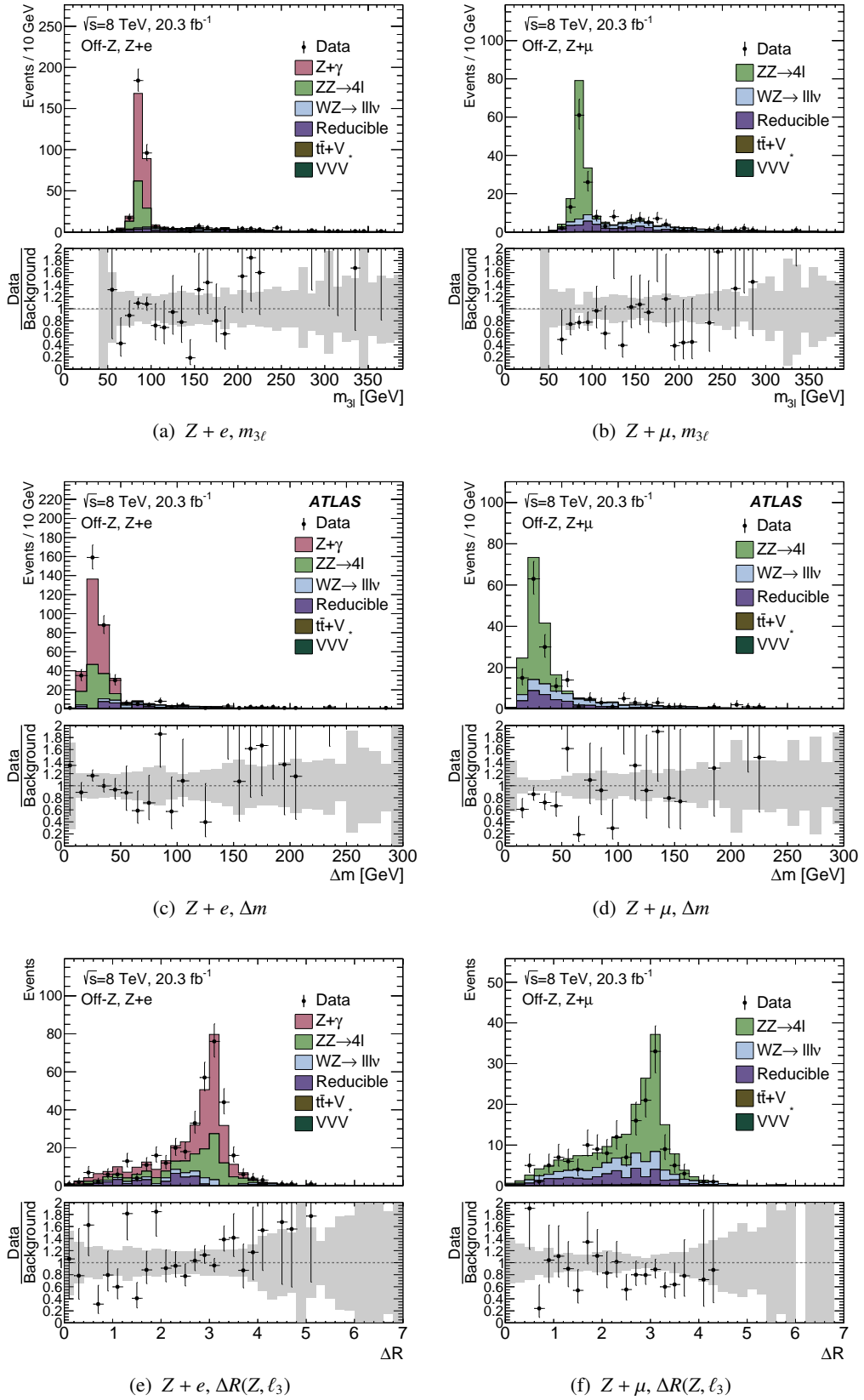


Figure 6.4: Off- Z validation region: $m_{3\ell}$ (top), Δm (middle), and ΔR (bottom) for $Z + e$ final states (left) and $Z + \mu$ final states (right). Figures (c) and (d) have previously been published in [149].

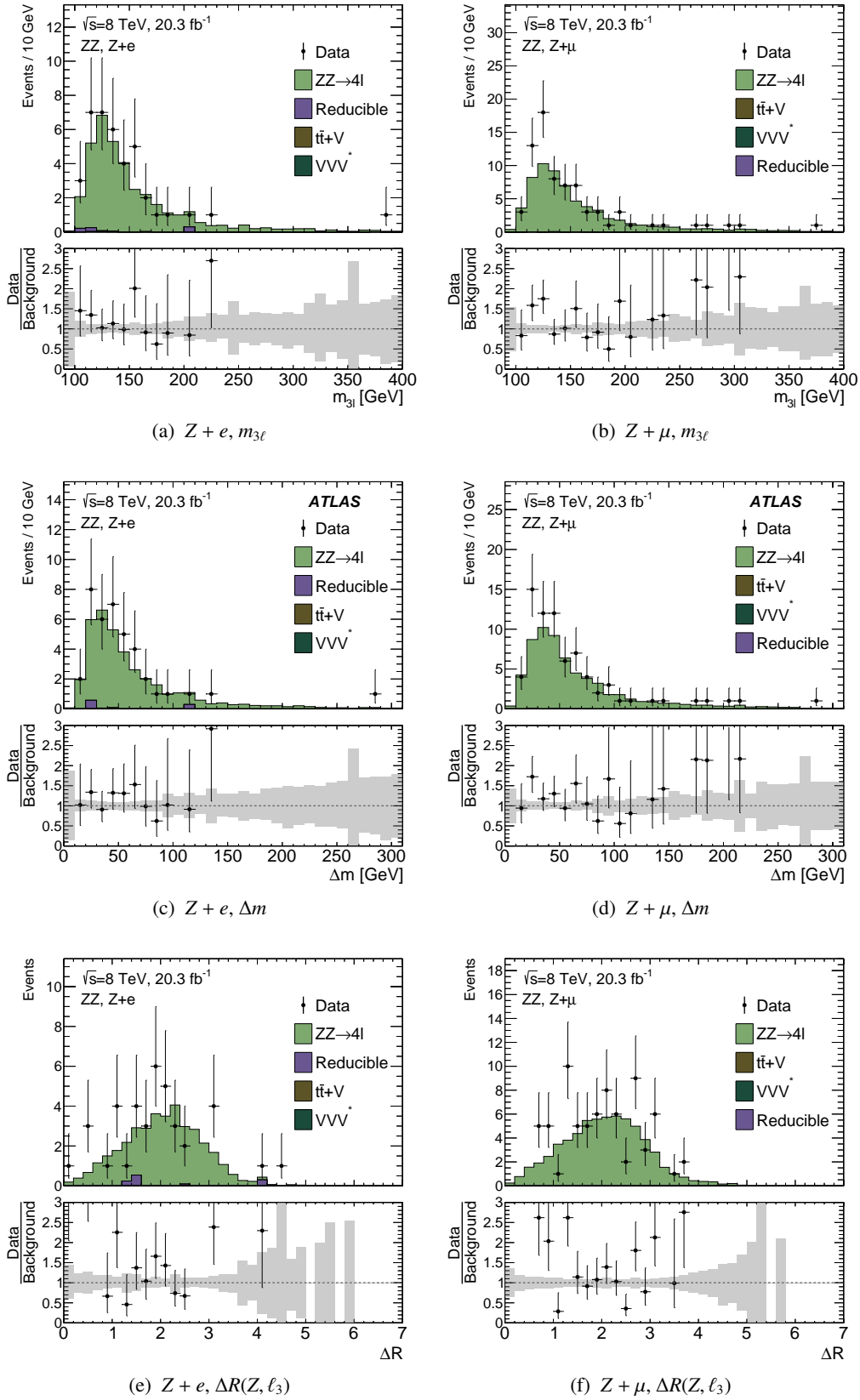


Figure 6.5: ZZ validation region: $m_{3\ell}$ (top), Δm (middle), and ΔR (bottom) for $Z + e$ final states (left) and $Z + \mu$ final states (right). Figures (c) and (d) have previously been published in [149].

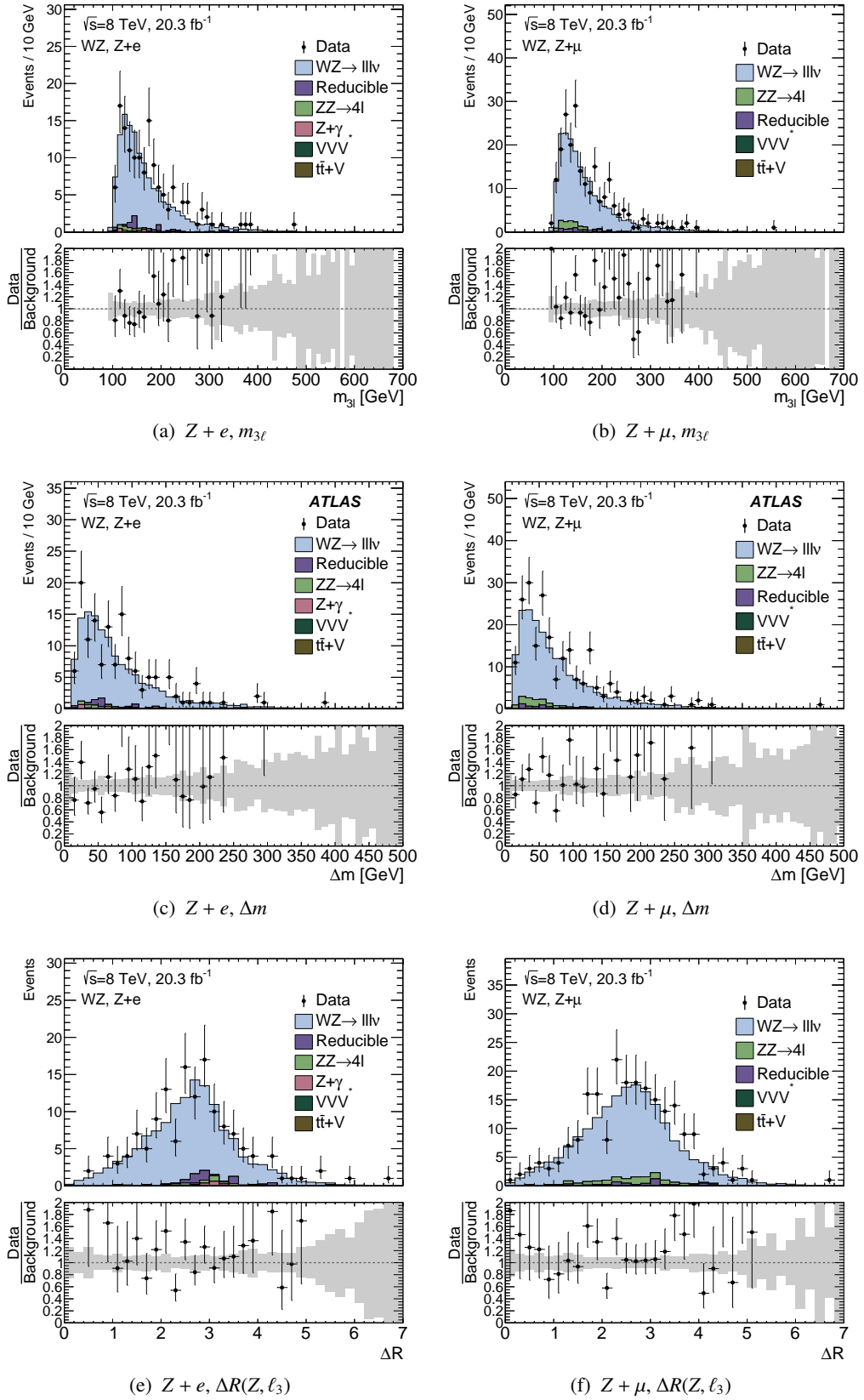


Figure 6.6: WZ validation region: $m_{3\ell}$ (top), Δm (middle), and ΔR (bottom) for $Z + e$ final states (left) and $Z + \mu$ final states (right). Figures (c) and (d) have previously been published in [149].

Systematic Uncertainties

This chapter summarises the evaluation of systematic uncertainties affecting the heavy lepton analysis. *Experimental systematic uncertainties* arise from imperfections in the description between real data and simulation. Such mismodellings, of e.g. energy scales, resolutions or object identifications, trigger efficiencies and pile-up conditions, are generally evaluated using subsidiary measurements and the resulting corrections are applied to the simulated event samples. The uncertainties on these measurements are included as systematic uncertainties to the heavy lepton analysis and are evaluated by varying the corresponding parameters in the event reconstruction and repeating the full analysis. The effect of the systematic uncertainty is hence estimated by comparing the yield and shape between the nominal and varied settings. These uncertainties only affect simulated event samples. A second source of experimental uncertainties arises from the limitations in the data-driven background estimate, mainly attributed to the low data statistics in the data control regions. In the data-driven fake-factor derivation, for the reducible background estimate, systematic uncertainties arise from limited statistics available in the data control regions and uncertainties in their compositions. *Theoretical systematic uncertainties* are due to limitations or approximations in the theoretical model, used to generate simulated event samples. Among these uncertainties are: missing higher-order corrections in the cross-section calculations, precision of the parton distribution functions, the choice of the Monte Carlo generator or the modelling of the underlying event.

A systematic uncertainty generally impacts the analysis, both by affecting the *normalisation* of the signal and background events and the *shape* of the observables in the signal region. Uncertainties affecting the signal and background event yields arise from a number of different sources. The number of events predicted by simulation are subject to uncertainties arising from the mismodelling of reconstruction-level observables resulting in differences in the selection efficiencies between simulated events and data, which can bias the measurement. Moreover, uncertainties on the collected luminosity and the cross sections of the simulated event samples impact the normalisation. Uncertainties primarily affecting the shape are the lepton energy scales and the jet energy scales. The treatment of the systematic uncertainties in the signal extraction using a fit and their impact on the interpretation of the results are detailed in Chapter 9.

7.1 Luminosity

An accurate measurement of the total luminosity depends on the luminosity calibrations performed during beam separation scans in November 2012, similar to those documented in Ref. [172]. The uncertainty in the luminosity determination arises from jitters in the beam during scans, a degradation of the beam size during a scan, uncertainties in handling multiple interactions, and uncertainties in the ability to measure the lengths, using the inner detector. Additionally, the long term stability of this calibration is limited and these calibrations can only be performed a few times per year. The luminosity uncertainty for the data taken during the 2012 run is 2.8 %. The luminosity uncertainty is applied to the signal and all background event yields, derived from simulated event samples.

7.2 Trigger Efficiency

The electron and muon trigger efficiencies are corrected to match the observed trigger efficiency in data. This is measured in $Z \rightarrow ll$ events, using a *tag-and-probe* method. The correction is applied, using an event-by-event scale-factor, SF, based on the lepton trigger efficiencies:

$$\text{SF} = \frac{\epsilon_{\text{data}}(\eta, \phi)}{\epsilon_{\text{MC}}(\eta, \phi)}, \quad (7.1)$$

where $\epsilon_{\text{data}}(\eta, \phi)$ and $\epsilon_{\text{MC}}(\eta, \phi)$ are the lepton trigger efficiencies in bins of (η, ϕ) , obtained from data and simulated events, respectively. Due to the presence of multiple high- p_T leptons in the final state a trigger efficiency of more than 99 % is obtained for the analysis. Variations of the resulting correction factor are applied for each lepton and propagated through the full analysis. The effect of the variation on the signal and background acceptance is found to be less than 1 % in all channels.

7.3 Cross sections

The theoretical cross-section predictions are subject to systematic uncertainties due to the choice of PDF and QCD renormalisation and factorisation scales and are thus dependent on the choice of generator. The Monte Carlo simulated samples used to determine the irreducible background prediction are normalised using these theoretical cross sections. The uncertainties on the cross sections for WZ , ZZ , $t\bar{t} + V$ and $VVV^{(*)}$ are listed in table 7.1. Since diboson events constitute the most prominent background to this analysis, a dedicated study was performed in Ref.[181], following the approach in Reference [182]. The systematic uncertainty is derived by comparing the standard SHERPA WZ and ZZ samples, which include up to three hard jets in the final state, to predictions from vBFNLO . Predictions from vBFNLO are produced with vBFNLO version 2.5.0, with patches provided by the authors of Ref. [182] to provide results in the standardised file format, called LHE (Les Houches Events) format, for events at NLO with more than one jet. Generator options such as the choice of PDF are set (or varied) according to the prescriptions in Ref. [182]. LOOPSIM version 1.0beta3 [183] is used to analyse the LHE outputs. A good agreement between the SHERPA diboson samples and the NNLO predictions from vBFNLO and LOOPSIM was found. The total cross section uncertainty is taken as the scale uncertainty from the LOOPSIM calculation. This leads to a cross section uncertainty of 7.6 % for the WZ production and 4.3 % for the ZZ production.

Process	Cross Section Uncertainty
WZ	7.6%
ZZ	4.3%
$t\bar{t} + V$	22%
$VVV^{(*)}$	22%

Table 7.1: Cross sections and uncertainties for the Monte Carlo samples used for irreducible background estimation. The uncertainties from the WZ and ZZ samples are found in Ref. [181]. While the uncertainty for $t\bar{t} + V$ is established in Refs. [184, 185].

7.4 Signal PDF

The systematic uncertainties on the type-III seesaw signal CTEQ PDF set were evaluated in Ref. [186], using the method described in Ref. [89]. This method applies 40 eigenvectors, corresponding to the positive and negative variations of 20 uncorrelated parameters, that affect the PDF value. The resulting systematic uncertainty on the signal cross section was found to be below 0.4%. Due to its small contribution this uncertainty is neglected. The same holds for PDF uncertainties on the vector-like lepton samples.

7.5 Lepton Efficiencies

Systematic uncertainties arising from differences in the electron identification, reconstruction and isolation efficiencies are evaluated using the results of Z *tag-and-probe* studies described in Reference [136] (see Section 4.4). These studies provide scale factors for the electron efficiency and uncertainties for those scale factors. Systematic uncertainties in the electron efficiencies are a result of subtracting uncertain backgrounds and the limited selection efficiency for signal events. The resulting uncertainties are binned in p_T and η . The effect of the variations in the isolation, identification, and reconstruction efficiency are on the order of 1 – 2% depending on the signal category.

The muon scale factors, correcting the differences between simulated events and observed data, are extracted from Z *tag-and-probe* studies. Systematic uncertainties for the muon identification and isolation efficiencies are described in Ref. [139] (see Section 4.4). Scale factors are applied to the muon identification and isolation efficiencies. Uncertainties in these scale factors, binned in the lepton kinematics, are propagated through the analysis. The ratio of the measured efficiencies in data and simulated events are close to unity, resulting in systematic uncertainties on the muon reconstruction efficiency at the per mille level. Systematic uncertainties for the isolation and impact parameter significance requirements are on the same order.

The electron and muon scale factor uncertainties are combined into the lepton efficiency uncertainty in Table 7.2. The resulting systematic uncertainties on the lepton efficiency are driven by the electron systematic scale uncertainties, resulting in an uncertainty of less than 2% of the signal yield in all categories.

7.6 Lepton Energy Scale and Resolution

Energy scale and resolution corrections are measured in $Z \rightarrow ee$ events [136, 137], as described in Section 4.4, and are used to correct the electron performance. The corresponding uncertainties are derived in bins of η and ϕ , and are applied by weighting the simulated events with the corresponding

scale factors. The weighted events are propagated through the full analysis. Uncertainties on the electron energy are a result of uncertainties of the material model in the inner detector, variations of the fit model used to measure the energy scale, and variations of the energy correction of the pre-sampler. Energy scale and resolution tend to have a larger effect on the shape of the final distribution shape than the sample acceptance. The shape-dependent effects were evaluated by comparing the results of the parametrisation between the nominal and the varied distributions and were found to be negligible with respect to the fit uncertainty arising from the statistical uncertainty. The systematic uncertainties are calculated by first modifying the energy/momentum of the reconstructed electrons by a scale factor prior to the event selection, allowing for changes in the event acceptance due to threshold effects. This can change the event yield due to events containing leptons near the p_T thresholds. Variation of the electron energy resolution or the electron energy scale have an effect up to 1% on the signal acceptance and background normalisation, depending on the lepton flavour of the channel. Muon momentum scale and resolution corrections are derived from $Z \rightarrow \mu\mu$ events [139]. Uncertainties associated with these corrections are derived from these data in bins of p_T and η . The uncertainty in muon momenta is the result of the uncertainty in the inner detector material and the uncertainty in the muon system alignment. Muon momentum resolution uncertainties are derived separately for the inner detector and the muon system, and are varied independently. The effects of the muon momentum uncertainties on the Δm shape are propagated through the full analysis. These were found to be negligible on the final parametrisation of the background models. The effect of muon momentum scale and resolution variations on the signal and background acceptance is much smaller than 1% in all signal categories.

In Table 7.2 the electron and muon energy scale and resolution uncertainties are combined and denoted as Lepton Energy Scale (LES) and Lepton Energy Resolution (LER). The energy of the electrons and muons are precisely measured, thus leading to uncertainties close to unity for both signal and background samples, in all signal categories.

7.7 Jet Energy Scale and Resolution

Studies of systematic uncertainties in the jet energy scale and resolution were performed in Ref. [187] for the 7 TeV data. Preliminary results using the same methods have been produced for the 8 TeV data. The jet-energy scale uncertainty (JES) is derived separately for different components, such as detector uniformity (η -intercalibration), jet flavour composition, topology, pile-up correction method and others. The JES scale determination is obtained by checking the jet response using simulated samples with varied conditions (i.e. hadronic shower model or detector material) and in-situ calibration using γ + jet, Z + jet and multijet events.

The jet energy resolution (JER) is measured in dijet events with uncertainties well below $\pm 10\%$. To propagate the uncertainty in the description of the jet energy resolution, the energy response is smeared by an additional Gaussian term. Since the simulated resolution cannot be reduced easily, the uncertainty, corresponding to a larger resolution is symmetrised to estimate the full uncertainty due to the jet energy resolution.

The jet energy uncertainties have a small impact on this analysis. They only affect the normalisation in the $3\ell+jj$ signal region when the dijet mass moves into or out of the window $m_W - 20 \text{ GeV} < m_{jj} < m_h + 25 \text{ GeV}$. In this region the jet related uncertainties are on the order of 3% on the background prediction.

7.8 Reducible Background Estimate

Various systematic effects may influence the measured fake factors and the predicted non-prompt background, thus influencing the reducible background estimate. In the following a summary on the systematic uncertainties associated with the reducible background estimate is given for both electrons and muons.

7.8.1 Electrons

Systematic uncertainties for the following effects are taken into account in the derivation of the electron fake factors:

- **Prompt subtraction:** The presence of real, prompt leptons from Standard Model processes in the sample, used to measure the fake factors, is accounted for using Monte Carlo simulation. Uncertainties on the simulated samples include luminosity, cross-section uncertainty, reconstruction, trigger and identification efficiency scale factors. These lead to a maximum uncertainty of about 20%, of which the prompt subtraction is the largest contribution.
- **Trigger efficiency correction:** An inefficiency is observed in the loose electron triggers for offline loose++ electrons. For the fake factor derivation, this affects electrons in the range $15 \text{ GeV} < p_T < 24 \text{ GeV}$, where photon triggers are not available. Imposing the tight++ cut on the track-cluster matching (the $\Delta\eta$ and $\Delta\phi$ between the electron track and calorimeter cluster) mitigates most, but not all, of the inefficiency by cutting out electrons with large amounts of bremsstrahlung whose track are not reconstructed in the trigger. Based on a comparison of loose electron and photon triggers in the range $24 \text{ GeV} < p_T < 85 \text{ GeV}$, a correction of about 8% is applied to loose electron-trigger events, and this value is taken as systematic uncertainty.
- **Extrapolation to signal region:** Two systematic uncertainties are assigned to account for bias due to the extrapolation of fake factors from the control region to the signal region. First, the cuts on m_T and E_T^{miss} are varied from $< 40 \text{ GeV}$ to $< 25 \text{ GeV}$ and $< 55 \text{ GeV}$. A p_T -dependent systematic uncertainty of up to 15% is assigned. Second, Monte Carlo-based truth studies indicate that the fake factor values are quite different for heavy- and light-flavour jets, so a difference in heavy flavour fraction between the control and signal regions will bias the fake factors. The effect of this is estimated using a $t\bar{t}$ Monte Carlo simulated sample, and a flat systematic uncertainty of 20% is assigned.

The resulting fake-factor systematic uncertainties are shown in Figure 7.1. Due to the limited statistics available the systematic uncertainties are not binned in two dimensions, but are derived as a function of p_T only.

7.8.2 Muons

Several sources of systematic uncertainty are considered and are described in detail below. The effects of the uncertainties on the fake factor as a function of p_T are shown in Fig. 7.2.

- **Prompt subtraction:** The prompt muon contamination in the region, where the fake factors are derived, is determined using simulated events. The size of this contamination is varied by $\pm 10\%$, leading to a systematic uncertainty of less than 1% at low p_T up to 6% at high p_T .

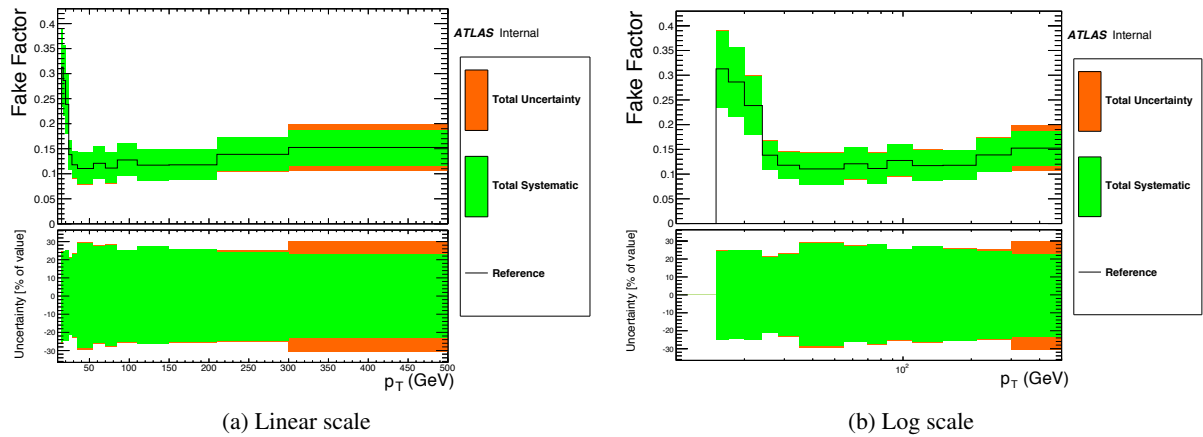


Figure 7.1: Electron fake factors vs. p_T with systematic and total uncertainties. The statistical uncertainty includes both the data and prompt subtraction Monte Carlo simulated events statistics.

- **Topological dependence:** The fake factors are derived both for the inclusive region and the two-jet region. The difference between the inclusive and two-jet fake factors is taken as a systematic uncertainty. The uncertainty is symmetrised, using the full difference as both upward and downward uncertainty, and ranges from 3% to 36%.
- **Dependence on d_0 significance:** An extrapolation factor is applied to the fake factor, to account for the fact that it is derived for muons with a high $d_0/\sigma(d_0)$. This extrapolation factor is derived in a number of different Monte Carlo samples. The largest deviation of 24% is taken as a systematic uncertainty.
- **Light flavour fraction:** As with the electron fake factors, the fake factor values are quite different for muons originating from light flavour (LF) sources (π/K decay or punch-through) compared to heavy flavour (HF) decays. The systematic uncertainty is described in detail in [177]; in brief, it uses the difference in momenta measured by the inner detector and muon spectrometer as a discriminant between HF and LF fakes, estimates the difference in the HF/LF fraction between the control and signal regions, and finally uses HF and LF fake factors measured in Monte Carlo to estimate the effect of the discrepancy in the HF/LF fraction. A systematic uncertainty in the range 2% – 21% is assigned depending on the signal category.

7.9 Charge-Flip Scale Factors

The rate of trilepton events from $Z + \gamma$ production, where the photon converts asymmetrically and is reconstructed as an electron, is observed to be overestimated in the simulated event samples as detailed in Section 6.1.3. Scale factors are applied following the charge-flip likelihood-estimation method from the same-sign dilepton analysis [181]. The uncertainty on these charge-flip rates is 30%. These uncertainties arise both from the variations observed in the scale factors, when running on different simulated samples and from statistical uncertainties in data and simulation. The systematic uncertainty due to the uncertainties in the charge flip only impact events with a bachelor electron. While the impact is 2% in the inclusive region, systematic uncertainties of 1.2% and 2.1% are measured for the 3ℓ -only and $3\ell+jj$ category, respectively. No impact is found in the 4ℓ category.

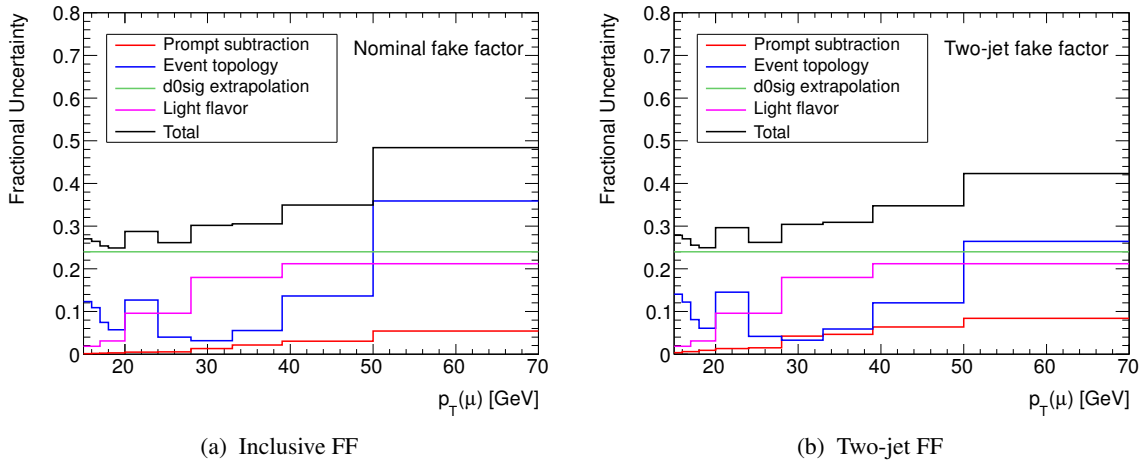


Figure 7.2: Systematic uncertainties on muon fake factor as a function of $p_T(\mu)$. The left plot shows the uncertainties for the inclusive fake factor, while the right one shows the uncertainty for the two-jet fake factor.

7.10 Diboson Shape Uncertainty

A systematic uncertainty is assigned to the modelling of the diboson backgrounds, derived from the differences in the simulated samples from SHERPA and POWHEG-BOX. The central value is taken from the fits to the samples generated with SHERPA and the uncertainty is given by the symmetric difference between SHERPA and POWHEG-BOX. The shapes of the 4ℓ and 3ℓ -only are derived from the fits to the inclusive region, while a separate parametrisation is obtained for the $3\ell+jj$ region. Figures 7.3 shows the comparison of the shapes of the two WZ samples for the inclusive (top) and the $3\ell+jj$ (bottom) category in the $Z + e$ (left) and $Z + \mu$ (right) flavour channel, along with the ratio of the two histograms. The corresponding figures for ZZ are shown in Fig. 7.4

7.11 Summary of Systematic Effects

The impact of each uncertainty in each signal category, in terms of fractional uncertainty on the total normalisation, is summarised for the total background prediction in Table 7.2. The leading uncertainty is due to the limited statistics of simulated events, followed by cross section uncertainties on the diboson production and the luminosity. Even though the systematic uncertainties attributed to the fake-factor method and the charge flip are at the order of 30%, these do not impact the analysis significantly, due to the almost negligible amounts of reducible background and photon conversion events in the signal region.

The total systematic uncertainty for the inclusive signal region is 6.9% for final states with a bachelor electron and 7% for bachelor muon final states. The largest total systematic uncertainties are found in the $3\ell+jj$ categories, with 8.4% (8.7%) for $Z + e$ ($Z + \mu$) events. The systematic uncertainty of some example signal points from type-III seesaw signal are summarised in Tables 7.3 – 7.5. The vector-like lepton signal is affected similarly at the corresponding masses. The total systematic uncertainty increases slightly with mass and rises from 3.9% for the inclusive $Z + e$ flavour channel at a mass hypothesis of 160 GeV to 4.5% for the inclusive $Z + e$ flavour channel for the 500 GeV sample. The corresponding values from the bachelor muon inclusive region rise from 3.3% at 160 V to 3.9% at 500 V. The difference between the bachelor electron and muon final state is driven by the larger electron

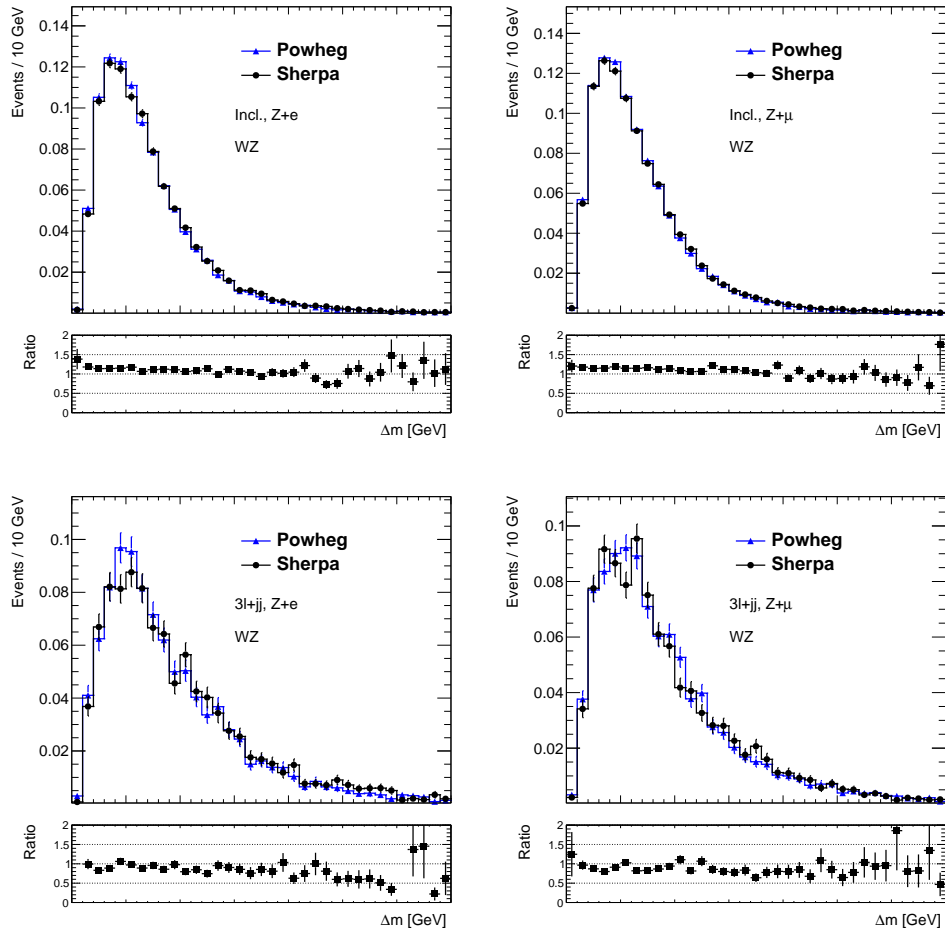


Figure 7.3: Comparison of WZ Δm shapes between the WZ samples generated by SHERPA and POWHEG-BOX. The upper figures show the inclusive signal region, and the lower show the $3\ell+jj$. Final states with a bachelor electron are on the left and with a bachelor muon are on the right.

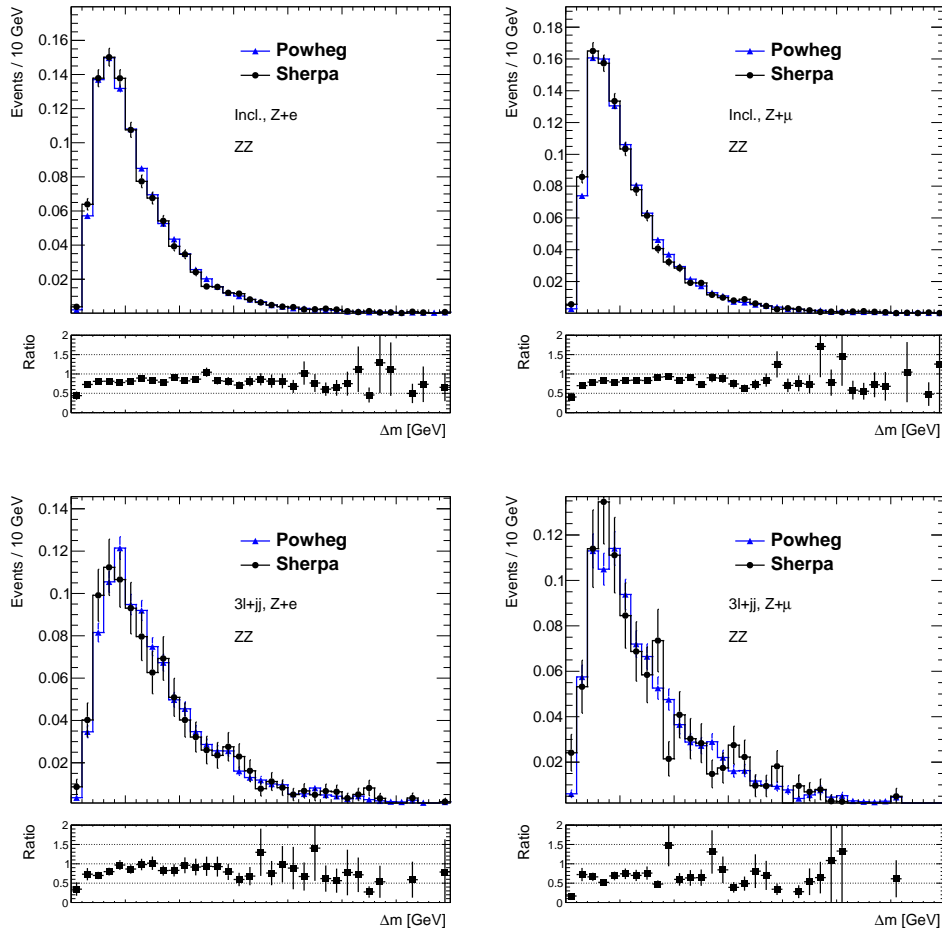


Figure 7.4: Comparison of ZZ Δm shapes between the ZZ samples generated by SHERPA and POWHEG-BOX. The upper figures show the inclusive signal region, and the lower show the $3\ell+jj$. Final states with a bachelor electron are on the left and with a bachelor muon are on the right.

7 Systematic Uncertainties

scale uncertainties. The dominating systematic uncertainty arises from the limited statistics in simulated events, followed by the lepton scale factors. A sizeable effect of the systematic uncertainty due to the jet energy scale, is seen in events belonging to the $3\ell+jj$ category. Slight changes in the energy scale lead to migrations of events in or out of the signal region, due to the selection criteria applied to the jets. In summary systematic effects on the yield of the events in the signal region play a minor role compared to the limited data statistics. The dominant shape uncertainty is attributed to the difference between the modelling of the diboson Δm spectra between events generated with SHERPA and POWHEG-BOX. The implementation of this uncertainty into the signal extraction is described in Chapter 9.

	$Z + e$				$Z + \mu$			
	Incl SR	4ℓ SR	$3\ell + jj$ SR	3ℓ -only SR	Incl SR	4ℓ SR	$3\ell + jj$ SR	3ℓ -only SR
σ_{ZZ}	0.9	3.9	0.9	0.8	0.7	3.8	0.4	0.6
σ_{WZ}	4.9	0.1	4.6	5.1	5.3	–	4.9	5.6
σ_{ttV}	0.4	1.5	2.9	0.1	0.4	0.9	2.9	0.1
Luminosity	2.6	2.8	2.7	2.6	2.5	2.6	2.4	2.5
γ conv. SFs	2.0	–	1.2	2.1	–	–	–	–
ℓ efficiency	1.6	1.8	1.6	1.6	0.9	0.9	1.0	0.9
e reducible SFs	1.7	–	0.5	1.9	0.1	0.9	0.1	0.1
μ reducible SFs	0.3	–	0.3	0.3	3.4	0.6	4.3	3.5
JES/JER	0.1	$^{+0.2}_{-0.0}$	3.3	0.4	0.1	0.2	3.2	0.5
LES/LER	0.6	$^{+1.0}_{-0.3}$	$^{+0.3}_{-1.2}$	$^{+0.7}_{-0.4}$	0.1	0.1	0.2	0.1
MC Statistics	2.4	5.0	4.3	2.6	1.2	3.5	2.8	1.2
Total	6.9	7.4	8.4	7.1	7.0	6.0	8.7	7.2

Table 7.2: Significant sources of uncertainty on the background prediction in each signal region, in terms of percent of the total background normalisation.

	$Z + e$				$Z + \mu$			
	Incl SR	4ℓ SR	$3\ell + jj$ SR	3ℓ -only SR	Incl SR	4ℓ SR	$3\ell + jj$ SR	3ℓ -only SR
Luminosity	2.8	2.8	2.8	2.8	2.8	2.8	2.8	2.8
ℓ scale factors	1.7	1.7	1.7	1.6	1.1	1.1	1.1	1.0
MC Statistics	2.1	4.5	3.7	3.0	1.4	2.7	2.7	2.2
JES/JER	0.0	0.2	3.6	3.0	0.2	0.3	3.0	2.2
LES/LER	0.1	0.4	0.1	0.1	0.1	0.2	0.2	0.2
Total	3.9	5.6	6.1	5.3	3.3	4.0	5.1	4.3

Table 7.3: The impact of different sources of systematic uncertainty on the signal prediction for the type-III seesaw model with $m_{L^\pm} = 160$ GeV, in percent of the total signal normalisation.

	$Z + e$				$Z + \mu$			
	Incl SR	4ℓ SR	$3\ell + jj$ SR	3ℓ -only SR	Incl SR	4ℓ SR	$3\ell + jj$ SR	3ℓ -only SR
Luminosity	2.8	2.8	2.8	2.8	2.8	2.8	2.8	2.8
ℓ scale factors	1.8	1.7	1.8	1.9	1.2	1.2	1.2	1.2
MC Statistics	3.0	5.7	4.9	4.7	2.2	3.7	3.8	3.6
JES/JER	0.1	–	1.6	1.7	0.2	0.3	2.0	2.3
LES/LER	0.4	0.1	1.0	0.4	0.3	0.0	0.9	0.3
Total	4.5	6.5	6.2	6.0	3.8	4.8	5.3	5.3

Table 7.4: The impact of different sources of systematic uncertainty on the signal prediction for the type-III seesaw model with $m_{L^\pm} = 300$ GeV, in percent of the total signal normalisation.

	$Z + e$				$Z + \mu$			
	Incl SR	4ℓ SR	$3\ell + jj$ SR	3ℓ -only SR	Incl SR	4ℓ SR	$3\ell + jj$ SR	3ℓ -only SR
Luminosity	2.8	2.8	2.8	2.8	2.8	2.8	2.8	2.8
ℓ scale factors	1.8	1.8	1.8	2.0	1.3	1.4	1.3	1.3
MC Statistics	3.0	5.5	4.8	4.8	2.4	4.0	3.9	4.1
JES/JER	–	–	1.7	1.9	0.3	0.5	1.8	2.5
LES/LER	0.4	0.5	2.1	1.7	0.4	1.6	2.8	2.2
Total	4.5	6.4	6.4	6.4	3.9	5.4	6.0	6.1

Table 7.5: The impact of different sources of systematic uncertainty on the signal prediction for the type-III seesaw model with $m_{L^\pm} = 500$ GeV, in percent of the total signal normalisation.

Results of the Heavy Lepton Resonance Search

This chapter presents the results from the three lepton heavy resonance search in the $Z + e$ and $Z + \mu$ flavour channel. The observed yield in data is compared to the background expectations, and a detailed comparison of different distributions is shown for both bachelor lepton flavours and their corresponding subcategories.

8.1 Comparison of Data and expected Background Yield

The observed events in data and the expected background yield, along with expected signal yields for different mass hypotheses, are shown in Table 8.1 for $Z + e$ final states and in Table 8.2 for $Z + \mu$ final states, at different stages of the heavy resonance selection. The quoted uncertainties correspond to the statistical uncertainties only.

The background composition in the inclusive region is dominated by WZ/γ^* followed by ZZ/γ^* production for both lepton flavours. Together they account for roughly 80 % of the expected background events in the inclusive signal region. The non-prompt background is the third largest background component for both lepton flavours, while $Z + \gamma$ events only play a significant role in final states with a bachelor electron. The production of $t\bar{t} + V$ and especially VVV^* only plays a minor role in the background composition. In this context, the significant reduction of the reducible and $Z + \gamma$ background component, attributed to the cut on the opening angle between the Z candidate and the bachelor lepton ($\Delta R(Z, \ell_3)$), should be noted.

While $575.0 \pm 6.3(\text{stat}) \pm 39.6(\text{syst})$ events are expected from the combined background estimate in the $Z + e$ final state, 653 events are observed in data. A good agreement between the observed and expected background events are found for the $Z + \mu$ final state, where $743.6 \pm 4.9(\text{stat}) \pm 52.0(\text{syst})$ are expected and 762 events are observed. The distributions of Δm , $m_{3\ell}$ and ΔR can be found in Fig. 8.1 for the $Z + e$ (left) and $Z + \mu$ (right) flavour channel. The distributions of the type-III seesaw model with $m_{L^\pm} = 300 \text{ GeV}$ and the vector-like leptons model with $m_{L^\pm} = 140 \text{ GeV}$ are superimposed on the expected Standard Model backgrounds. The fine binning is chosen, to reflect the search for a narrow resonance. Additionally the distribution of Δm with a wider binning in the tail is shown in Fig. 8.5(a) for $Z + e$ and in Fig. 8.5(b) for $Z + \mu$ final states. No obvious deviation, hinting at a narrow resonance, is observed in any of the distributions.

The three different categories, 4ℓ , $3\ell + \text{jj}$ and 3ℓ -only contain very different background compositions and expected signal fractions. A significant improvement in the signal-to-background ratio is found in

the 4ℓ category, since only 2%/3% of the estimated background events in the $Z+e/Z+\mu$ contain a fourth lepton, whereas 30% of the signal events have a fourth lepton in the final state. Thus the background in the 4ℓ category is almost solely attributed to ZZ/γ^* events. The distributions of Δm , $m_{3\ell}$ and ΔR are shown in Fig. 8.2. A not localised deviation from the expected background in the $Z+e$ region is observed, with $11.96 \pm 0.55(\text{stat}) \pm 0.88(\text{syst})$ and 16 observed events. An excellent agreement is found for the $Z+\mu$ final states, with $24.45 \pm 1.04(\text{stat})1.46 \pm (\text{syst})$ expected and 25 observed events. No data events are found beyond 300 GeV.

The $3\ell+\text{jj}$ category is populated with roughly 10% of the background yield expected in the inclusive region, and is dominated by WZ/γ^* and ZZ/γ^* background and a non negligible $t\bar{t}+V$ contribution. About one third of the signal events are contained in this category as well. In the $Z+e$ flavour channel $58.7 \pm 1.5(\text{stat}) \pm 5.1(\text{syst})$ events are observed while 64 events are expected which is in good agreement. The $Z+\mu$ channel however, contains $72.1 \pm 1.4(\text{stat}) \pm 6.3(\text{syst})$ events, while 86 events are observed in data. Figure 8.3 shows the distributions of Δm , $m_{3\ell}$ and ΔR . No significant deviation from the expected Standard Model background is seen in any of the distributions for the $Z+e$ on the left hand side and the less well agreeing $Z+\mu$ distributions on the right hand side.

The remaining more than 85% of the inclusive background events do not fall into the aforementioned categories and are attributed to the 3ℓ -only category. Therefore this category has the worst signal-to-background ratio after the dividing the events into the orthogonal categories. While the background composition is similar to the inclusive signal region, only $\sim 30\%$ of the signal events fall into this category. An excellent agreement between the expected ($647.1 \pm 4.5(\text{stat}) \pm 46.6(\text{syst})$) and observed 651 events is found for final states with a bachelor muon. A small overshoot at the 2σ level between the observed and expected number of events is evident in the $Z+e$ final state, with $504.3 \pm 6.1(\text{stat}) \pm 36.2(\text{syst})$ expected and 573 observed events. The distributions of the main variables are shown in Fig. 8.4.

The statistics for the reducible background prediction are particularly low in the 4ℓ and $3\ell+\text{jj}$ categories. To mitigate the effect of the low statistics, the shape is taken from the inclusive combination of all three categories, and the normalisation is set to the integrated background prediction in the categories.

In cases where the background normalisation for the reducible background is observed to be negative and consistent with zero within the statistical uncertainty, the normalisation is set to zero. This is an effect from the subtraction of the contamination from real leptons reconstructed as denominator leptons (see Section 6.1), the so-called prompt contamination.

No significant excess above the Standard Model background expectations was found in the Δm distribution in any of the signal regions. For the individual categories this is also seen in Fig. 8.6, which shows the Δm distribution for the 4ℓ (top) the $3\ell+\text{jj}$ (middle) and 3ℓ -only (bottom) with a wider binning in the tails. The observed and expected event yields agree at a reasonable value considering both the statistical and the systematic uncertainties. However, since this analysis is targeted at the reconstruction of a narrow resonance, the signal region is further scrutinised for any deviation from the Standard Model background, using a dedicated unbinned mass fitter, which is described in Chapter 9.

Process	Requirements						Categories		
	Preselection	Bachelor e	$ m_{\ell^+\ell^-} - m_Z < 10$ GeV	ZZ veto	$\Delta R < 3.0$	4ℓ	$3\ell+ij$	3ℓ -only	
$ZZ \rightarrow 4\ell$	890.6 ± 4.1	414.2 ± 2.8	247.1 ± 2.1	210.5 ± 2.0	113.9 ± 1.5	10.92 ± 0.45	11.70 ± 0.47	91.27 ± 1.30	
$WZ \rightarrow \ell\ell\nu$	1753.91 ± 4.76	746.02 ± 3.09	622.44 ± 2.82	622.44 ± 2.82	372.72 ± 2.18	0.08 ± 0.03	35.3 ± 0.67	337.34 ± 2.07	
$\bar{t}t + V$	39.92 ± 0.56	18.12 ± 0.38	13.01 ± 0.32	12.94 ± 0.32	10.12 ± 0.28	0.85 ± 0.08	7.72 ± 0.25	1.54 ± 0.11	
$Z + \gamma$	342.09 ± 5.97	342.09 ± 5.97	93.16 ± 3.10	93.16 ± 3.10	37.46 ± 1.96	0.00 ± 0.00	2.26 ± 0.48	35.20 ± 1.91	
Reducible	447.37 ± 15.28	158.13 ± 13.52	99.58 ± 8.17	98.98 ± 8.15	39.57 ± 5.33	-0.2 ± 0.3	1.64 ± 1.1	38.13 ± 5.2	
VVV*	11.15 ± 0.15	5.30 ± 0.11	1.88 ± 0.05	1.84 ± 0.05	1.24 ± 0.04	0.31 ± 0.02	0.08 ± 0.01	0.85 ± 0.04	
Σ Backgrounds	3485.04 ± 17.57	1683.86 ± 15.35	1077.18 ± 9.43	1039.89 ± 9.38	575.0 ± 6.26	11.96 ± 0.55	58.71 ± 1.47	504.33 ± 6.06	
Data	3597	1805	1163	1124	653	16	64	573	
VLL, 160 GeV	21.75 ± 0.27	18.84 ± 0.25	16.09 ± 0.23	15.69 ± 0.23	13.83 ± 0.22	3.76 ± 0.11	4.52 ± 0.12	5.56 ± 0.14	
VLL, 200 GeV	10.19 ± 0.12	8.66 ± 0.11	7.09 ± 0.10	6.93 ± 0.10	6.11 ± 0.09	1.89 ± 0.05	2.13 ± 0.05	2.08 ± 0.05	
VLL, 250 GeV	4.27 ± 0.05	3.64 ± 0.04	2.94 ± 0.04	2.89 ± 0.04	2.52 ± 0.04	0.93 ± 0.02	0.86 ± 0.02	0.74 ± 0.02	
Seesaw, 160 GeV	688.97 ± 10.41	535.95 ± 9.07	402.72 ± 7.55	393.19 ± 7.43	337.80 ± 6.89	98.63 ± 4.21	104.02 ± 3.73	135.15 ± 3.97	
Seesaw, 200 GeV	322.60 ± 4.80	254.73 ± 4.22	180.03 ± 3.38	176.25 ± 3.33	152.20 ± 3.11	50.04 ± 2.03	49.01 ± 1.71	53.15 ± 1.63	
Seesaw, 300 GeV	61.78 ± 1.27	47.67 ± 1.10	31.92 ± 0.85	31.61 ± 0.85	26.87 ± 0.79	9.93 ± 0.55	8.41 ± 0.41	8.54 ± 0.39	

 Table 8.1: Number of events at various stages in the selection of the $Z + e$ signal regions. Only statistical uncertainties of the Monte Carlo samples are shown.

Process	Requirements					Categories		
	Preselection	Bachelor μ	$ m_{\ell^+\ell^-} - m_Z < 10$ GeV	ZZ veto	$\Delta R < 3.0$	4ℓ	$3\ell+ji$	3ℓ -only
$ZZ \rightarrow 4\ell$	890.60 ± 4.07	476.42 ± 2.99	279.71 ± 2.3	216.41 ± 2.02	119.33 ± 1.5	21.43 ± 0.64	7.46 ± 0.38	90.45 ± 1.31
$WZ \rightarrow \ell\ell\nu$	1753.91 ± 4.76	1007.89 ± 3.62	855.80 ± 3.34	855.80 ± 3.34	521.22 ± 2.6	0.02 ± 0.02	46.34 ± 0.78	474.87 ± 2.49
$\bar{t}t + V$	39.92 ± 0.56	21.80 ± 0.41	16.38 ± 0.36	16.28 ± 0.36	12.59 ± 0.31	1.00 ± 0.09	9.39 ± 0.27	2.20 ± 0.13
$Z + \gamma$	342.09 ± 5.97	0.00 ± 0.00	0.00 ± 0.00	0.00 ± 0.00	0.00 ± 0.00	0.00 ± 0.00	0.00 ± 0.00	0.00 ± 0.00
Reducible	447.37 ± 15.28	289.23 ± 7.13	200.66 ± 5.79	200.66 ± 5.79	88.85 ± 3.81	1.54 ± 0.82	8.81 ± 1.04	78.5 ± 3.57
VVV*	11.15 ± 0.15	5.85 ± 0.11	2.41 ± 0.06	2.35 ± 0.06	1.64 ± 0.05	0.45 ± 0.02	0.08 ± 0.01	1.11 ± 0.04
Σ Backgrounds	3485.04 ± 17.57	1801.18 ± 8.55	1354.89 ± 7.07	1291.49 ± 6.99	743.64 ± 4.86	24.45 ± 1.04	72.08 ± 1.37	647.12 ± 4.54
Data	3597	1792	1414	1340	762	25	86	651
VLL, 160 GeV	26.76 ± 0.29	22.36 ± 0.27	19.11 ± 0.25	18.31 ± 0.24	16.44 ± 0.23	5.70 ± 0.14	4.42 ± 0.12	6.33 ± 0.14
VLL, 200 GeV	12.58 ± 0.13	10.28 ± 0.12	8.51 ± 0.11	8.22 ± 0.1	7.33 ± 0.1	2.90 ± 0.06	1.99 ± 0.05	2.44 ± 0.06
VLL, 250 GeV	5.13 ± 0.05	4.20 ± 0.05	3.41 ± 0.04	3.32 ± 0.04	2.92 ± 0.04	1.30 ± 0.03	0.85 ± 0.02	0.77 ± 0.02
Seesaw, 160 GeV	934.08 ± 9.5	748.59 ± 8.4	516.55 ± 6.72	500.83 ± 6.59	435.14 ± 6.16	147.62 ± 3.95	110.42 ± 2.95	177.1 ± 3.69
Seesaw, 200 GeV	411.01 ± 4.22	323.95 ± 3.7	209.4 ± 2.85	205.45 ± 2.81	178.9 ± 2.64	65.18 ± 1.78	50.82 ± 1.34	62.90 ± 1.43
Seesaw, 300 GeV	72.57 ± 1.07	57.4 ± 0.94	35.36 ± 0.71	35.0 ± 0.7	30.36 ± 0.66	12.53 ± 0.47	9.46 ± 0.34	8.37 ± 0.31

Table 8.2: Number of events at various stages in the selection of the $Z + \mu$ signal regions. Only statistical uncertainties on the Monte Carlo samples are shown.

8.1 Comparison of Data and expected Background Yield

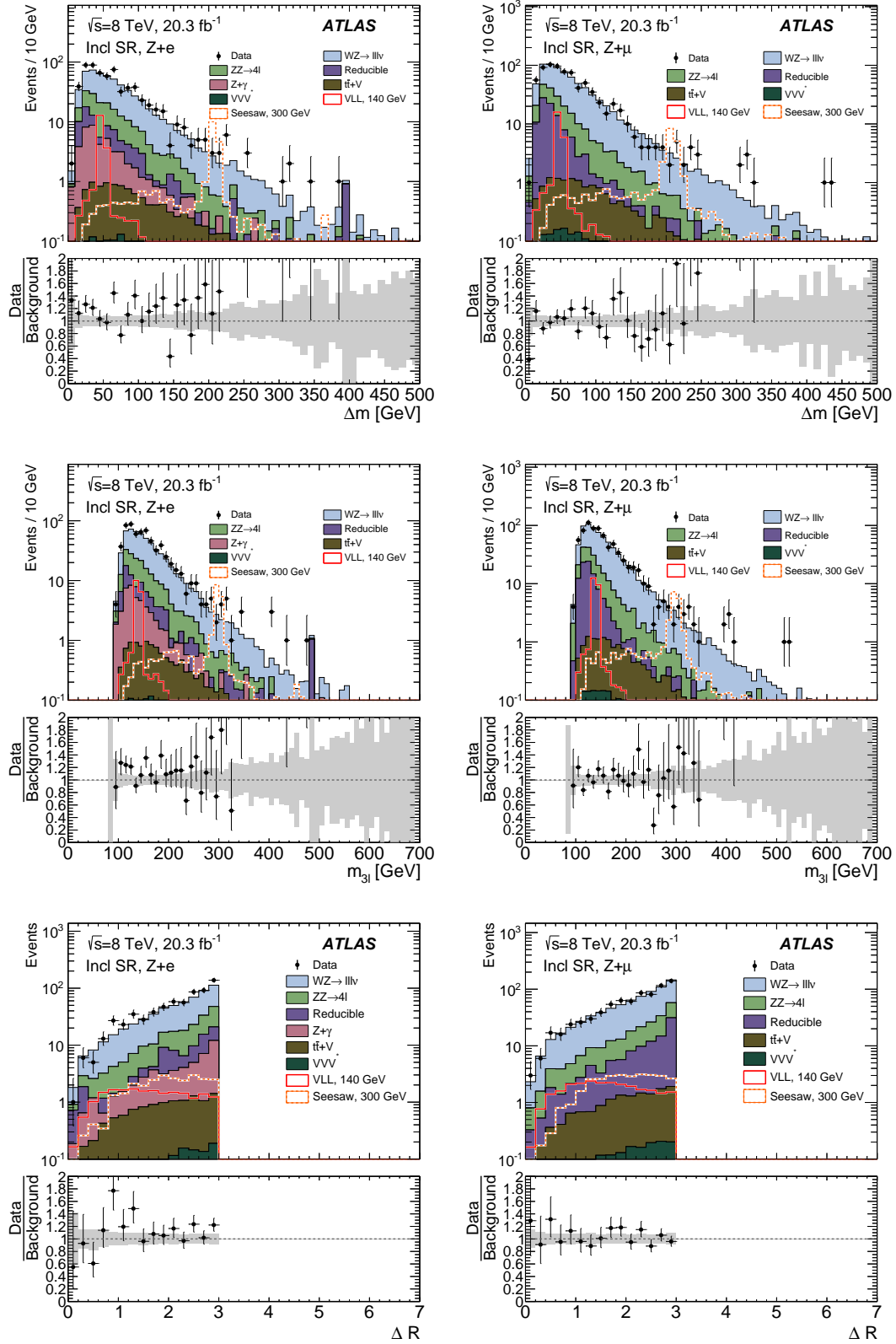


Figure 8.1: Distributions of Δm (top), $m_{3\ell}$ (middle) and $\Delta R(Z, \ell_3)$ (bottom) for the $Z + e$ (left) and $Z + \mu$ (right) candidates are shown for the inclusive signal regions. The figures in the top and bottom row have previously been published in [149].

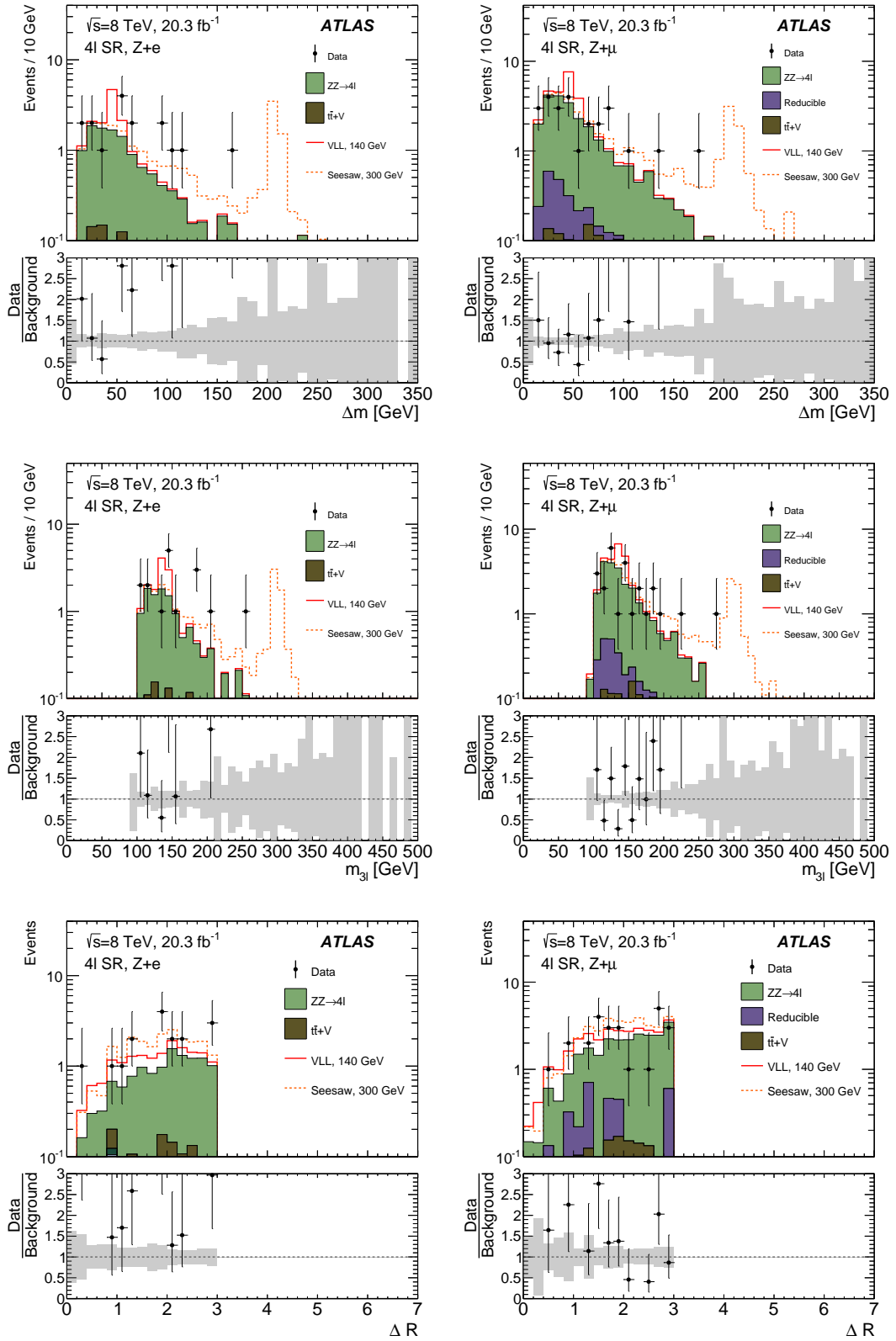


Figure 8.2: Distributions of Δm (top), $m_{3\ell}$ (middle) and $\Delta R(Z, \ell_3)$ (bottom) for $Z + e$ (left) and $Z + \mu$ (right) heavy lepton candidates are shown for the 4ℓ category. The figures in the top and bottom row have previously been published in [149].

8.1 Comparison of Data and expected Background Yield

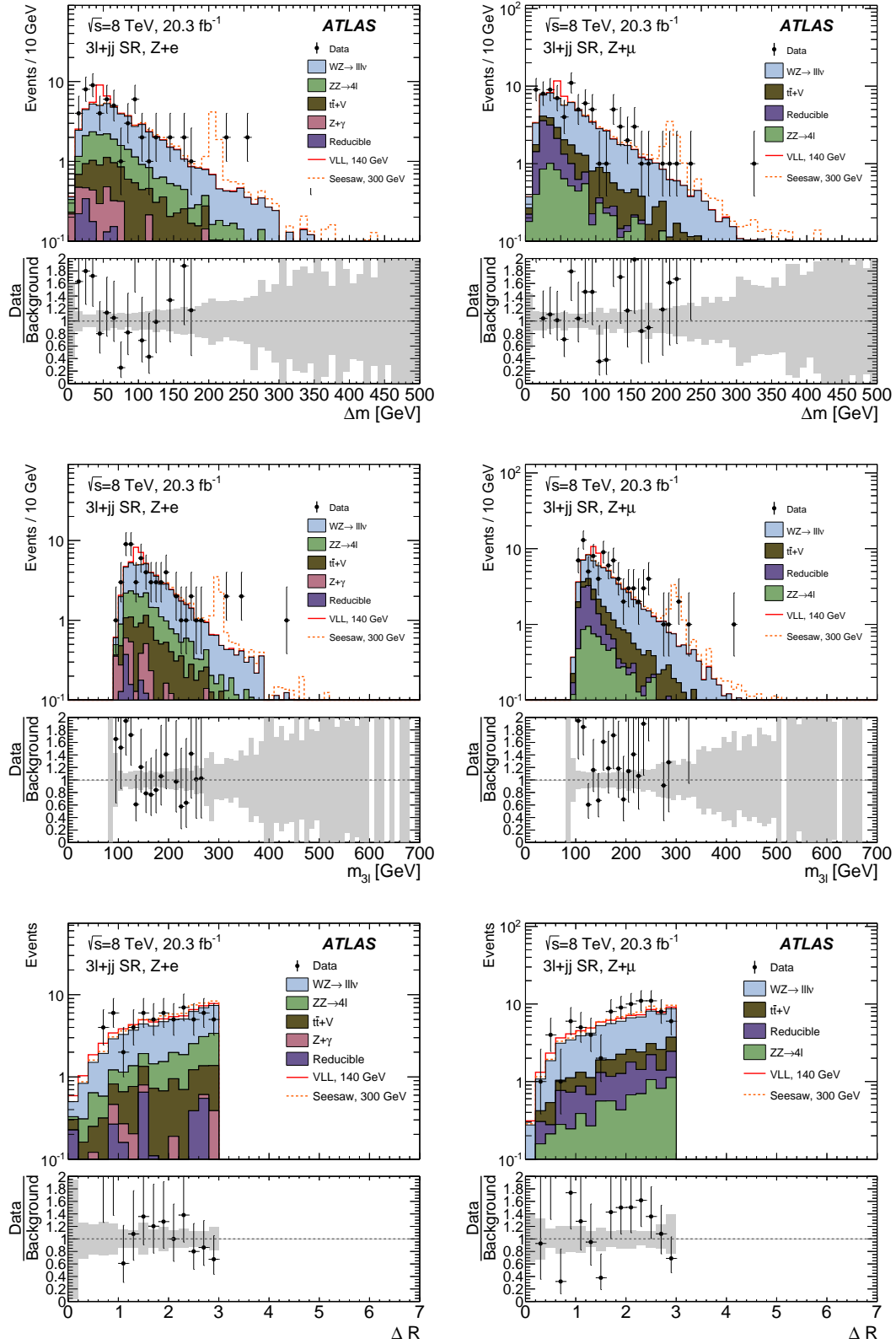


Figure 8.3: Distributions of Δm (top), $m_{3\ell}$ (middle) and $\Delta R(Z, \ell_3)$ (bottom) for $Z + e$ (left) and $Z + \mu$ (right) candidates are shown for the $3\ell+jj$ category. The figures in the top and bottom row have previously been published in [149].

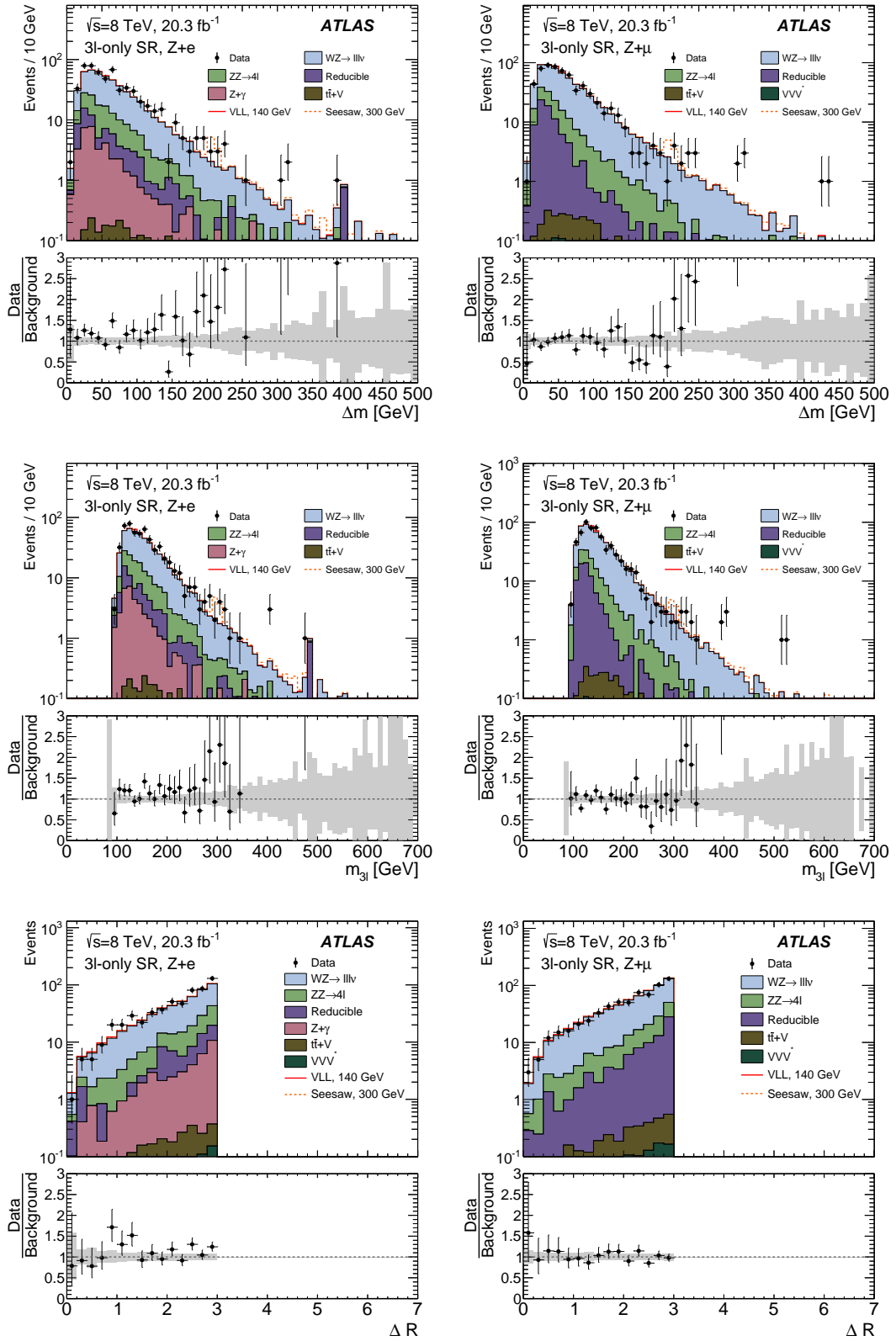


Figure 8.4: Distributions of Δm (top), $m_{3\ell}$ (middle) and $\Delta R(Z, \ell_3)$ (bottom) for $Z + e$ (left) and $Z + \mu$ (right) candidates are shown for the 3ℓ -only category. The figures in the top and bottom row have previously been published in [149].

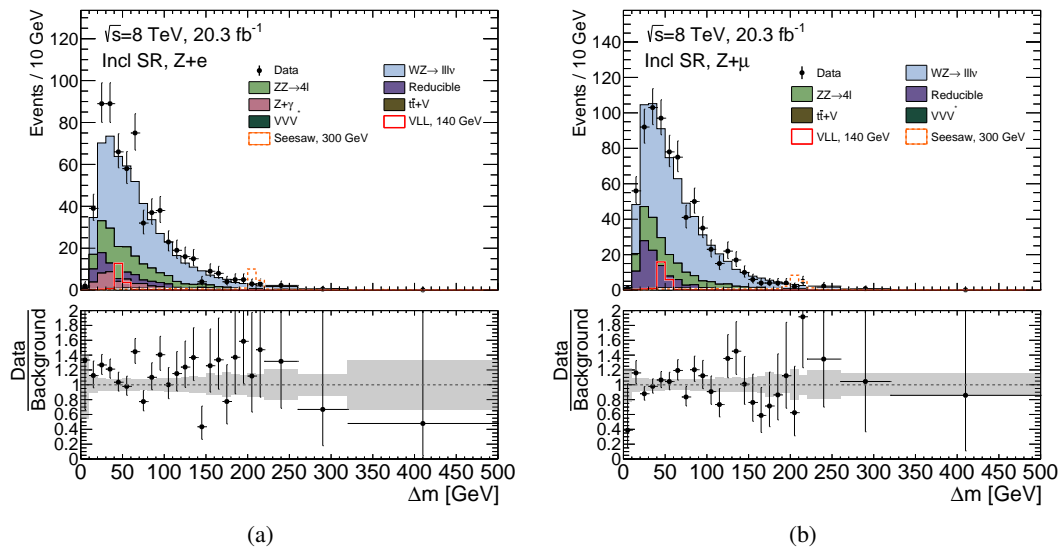


Figure 8.5: Distributions of Δm for $Z + e$ (a) and $Z + \mu$ (b) inclusive signal region with a wider binning in the tails of the distribution.

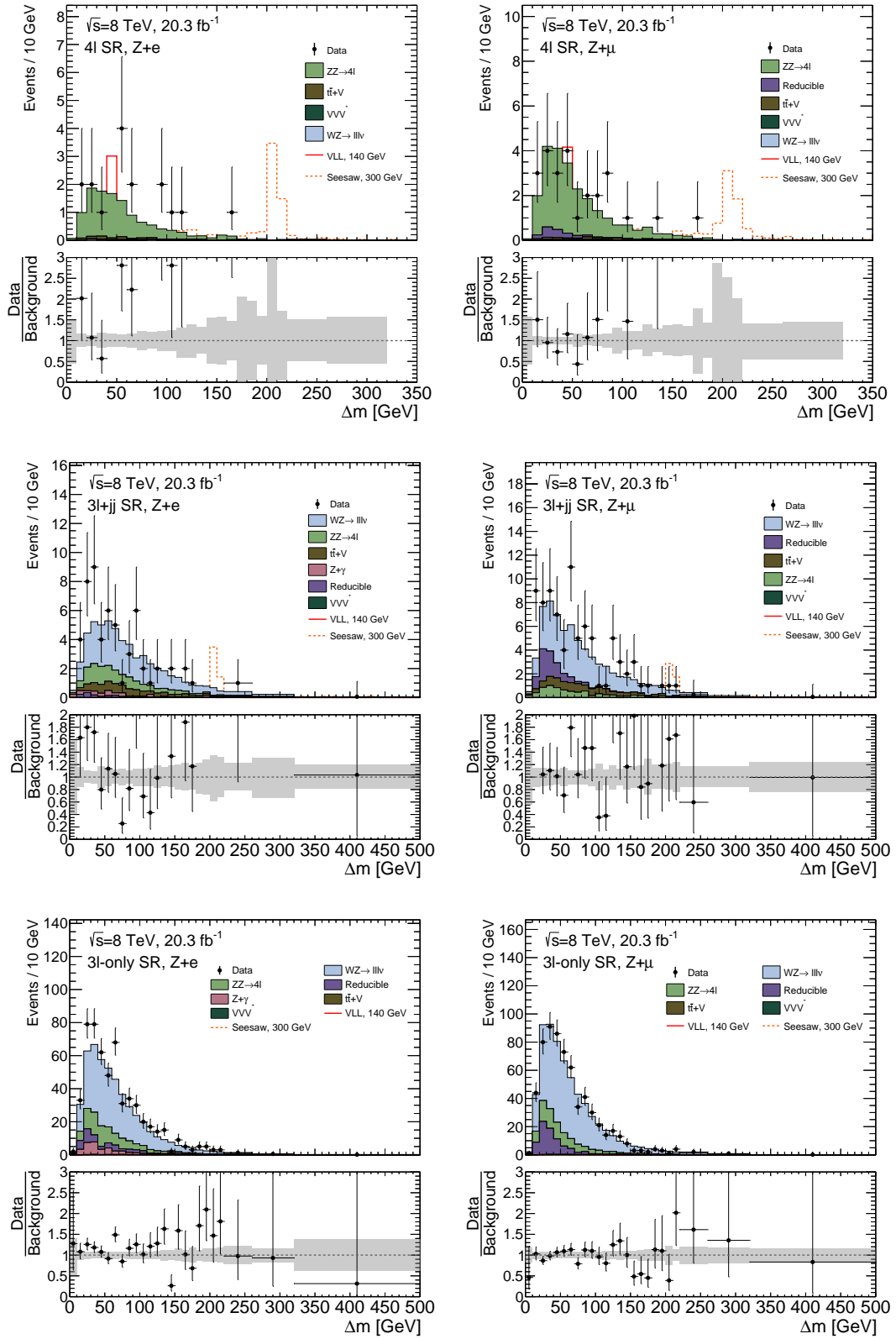


Figure 8.6: Distributions Δm for $Z + e$ (left) and $Z + \mu$ (right) signal regions with a wider binning for the three categories: 4ℓ (top), $3\ell+jj$ (middle) and 3ℓ -only (bottom).

Statistical Analysis of the Results of the Heavy Lepton Search

This chapter describes the results of the heavy lepton search including their statistical interpretation. In order to fully exploit the narrow resonance structure of the signal, the number of signal candidate events is determined from an unbinned maximum-likelihood fit of the combined signal and background model to the data. An introduction to the theory behind the likelihood model and the statistical interpretation of the results is given in Section 9.1. The probability density functions (p.d.f.s) for the signal and various background components are detailed in Section 9.2. The combined signal and background model and its validation is described in Section 9.3. This chapter is concluded by the statistical interpretation of the results in Section 9.4.

9.1 Likelihood Fit Model

An unbinned extended maximum-likelihood fit to the observed data is used to estimate the parameters of the combined signal and background model, including the signal strength parameter μ . The signal strength μ is defined as the ratio between the measured cross section and the theoretically expected cross section: $\mu = \sigma_{\text{meas}}/\sigma_{\text{theo}}$. A value of $\mu = 0$ thus represents the background-only hypothesis, with no presence of the new physics model. A value of $\mu = 1$ corresponds to the theoretically expected signal production. The probability density functions (p.d.f.s) describing the signal and different background components are denoted as $f_S(x; \theta)$ and $f_B(x; \theta)$. These are functions of the observable x , in this case Δm , and are normalised to unity. They can depend on additional parameters θ , called nuisance parameters, which affect the outcome of the result, but are not of primary interest to the measurement. In this case nuisance parameters are used to account for the effect of systematic uncertainties and for background normalisations.

The probability to observe N events, where S and B are the expected number of signal and background events can thus be written as

$$\mathcal{P}(x, \mu, \theta) = \frac{(\mu S + B)^N \cdot e^{-\mu S + B}}{N!} \left[\prod_{i=1}^N \frac{\mu S f_S(x_i; \theta) + B f_B(x_i; \theta)}{\mu S + B} \right]. \quad (9.1)$$

The first term gives the Poisson probability to observe N events, while expecting $\mu S + B$. The second term describes the probability to observe N events at the measured values x_i of the observable x , given

the combined signal and background p.d.f.. This accounts for the relative background and signal contributions, at a signal strength of μ . The function is normalised by the term $\mu S + B$ in the denominator.

The likelihood function, $L(\mu, \theta|\mathbf{x})$, is defined as the probability distribution function, evaluated at the observed outcome of the experiment. A maximum-likelihood fit estimates the parameter values of the model, by maximising the likelihood function, given the observed data. This likelihood can be extended to a combined fit to multiple categories, by multiplying the individual likelihood functions of each category.

A common approach is the minimisation of the negative logarithm of the likelihood function instead of maximising the likelihood function itself, as both are minimal or maximal for the same set of parameters. Often one actually uses the $-2 \ln L$ as one can then use the same error definitions as for a χ^2 fit (i.e. $\min +1$ to get the one sigma errors, etc.). For practical use the negative logarithm of the likelihood function (NLL) is used as dedicated fast computing algorithms, such as MINUIT[188], exist to handle minimisations. The negative logarithmic likelihood function is

$$\min\{-\ln L(\mu, \theta)\} = -\ln L(\hat{\mu}, \hat{\theta}), \quad (9.2)$$

where $\hat{\mu}$ and $\hat{\theta}$ are the best-fit values, called estimators. These minimise the NLL. For a hypothesised value of μ a probability can be assigned using the profile likelihood ratio

$$\lambda(\mu) = \frac{L(\mu, \hat{\theta})}{L(\hat{\mu}, \hat{\theta})}. \quad (9.3)$$

The numerator is the profile likelihood function, $\hat{\theta}$ is the conditional maximum likelihood estimator of θ for a specified value of μ . The denominator is the unconditional maximum likelihood function. The profile likelihood ratio $\lambda(\mu)$ has values between 0 and 1, where a value of 1 is obtained when the tested value of μ corresponds to $\hat{\mu}$ and thus a good agreement is found between data and the tested value of μ . The signal and background expectations depend on nuisance parameters θ .

9.1.1 Nuisance Parameters

There are two kinds of nuisance parameters incorporated into the final likelihood function. The first is arising from unconstrained background normalisations, whose values are constrained by the observed data events. The second source is due to systematic uncertainties, affecting the shape and normalisation of the signal and background components. Systematic uncertainties, such as the luminosity uncertainty and the lepton scale factors, affect the signal and background expectations as described in Chapter 7. For every relevant systematic a nuisance parameter is introduced, which influences the model, but is not of primary interest to the measurement. Systematic uncertainties are determined in auxiliary measurements, i.e. on the calibration of physics objects, which are performed independently of the analysis. Hence the likelihood function needs to be extended with terms expressing the knowledge on these so-called subsidiary measurements. In principle the full likelihood expressing the auxiliary measurement should be added, to account for possible correlations, however a more practical approach is the implementation as an effective likelihood, depending solely on one nuisance parameter θ_i . By convention the value $\theta_i = 0$ is set as the nominal value nominal value of the external parameter (e.g. the lumi) and values of $\theta_i = \pm 1$ correspond to 1σ variations of the external parameter. The likelihood function,

including the systematic uncertainties, is thus defined as:

$$L(\mu, \theta) = L_{\text{main}}(\mu, \theta) \times \prod_{i=1}^{n_{\text{sys}}} \text{Gaussian}(\theta_i|0, 1), \quad (9.4)$$

where $\text{Gaussian}(\theta_i|0, 1)$ is the effective likelihood function for the measurement of the nuisance parameters θ_i .

9.1.2 Hypothesis Test

This section follows the nomenclature of Ref. [189]. The results of an analysis are usually interpreted by evaluating the compatibility of the of the observed data, with either the background-only or the signal-plus-background hypothesis. According to the Neyman-Pearson lemma [190], the optimal test statistic in the absence of any nuisance parameters is given by the likelihood ratio of the corresponding hypotheses. A test statistic, t_μ , is used to define a measure of the compatibility between data and the expected event yields at a signal strength hypothesis of μ . The definition of the likelihood ratio $\lambda(\mu)$ implies, that a good agreement between the data and the hypothesised value of $\lambda(\mu)$ is found for values near unity. The test statistic t_μ is given by

$$t_\mu = -2 \ln \lambda(\mu). \quad (9.5)$$

Large values of t_μ indicate a bad agreement between the observed data and the tested μ . The level of agreement between the observed data under a certain hypothesis, is given by computing the probability under the assumption of the hypothesised value of μ , of finding data of equal or greater incompatibility given the predictions of μ . This p -value is defined as:

$$p = \int_{t_{\mu, \text{obs}}}^{\infty} f(t_\mu|\mu) dt_\mu. \quad (9.6)$$

In this case $f(t_\mu|\mu)$ is the p.d.f. of the test statistic, given the hypothesised value of μ . The obtained p -value can be translated into an equivalent significance Z in terms of Gaussian standard deviations

$$Z = \Phi^{-1}(1 - p), \quad (9.7)$$

where Φ^{-1} the inverse cumulative distribution of the standard Gaussian distribution. If no excess in data is found a signal hypothesis is commonly excluded at a threshold p -value of 0.05 ($Z_\mu > 1.64$). A background-only hypothesis on the other hand, is rejected at a p -value of 2.87×10^{-7} , corresponding to a significance of 5σ .

In this analysis values of $\hat{\mu} < 0$ are non-physical, so that t_μ , as defined in Eq. (9.5) is modified. Under the assumption that the presence of a new signal leads to an increase of the observed event rate, i.e. a positive signal strength of $\mu \geq 0$, the redefined test statistic $\tilde{\lambda}(\mu)$, is given by the likelihood ratio defined as:

$$\tilde{\lambda}(\mu) = \begin{cases} \frac{L(\mu; \hat{\theta})}{L(0; \hat{\theta})} & \hat{\mu} < 0, \\ \frac{L(\mu; \hat{\theta})}{L(\hat{\mu}; \hat{\theta})} & 0 \leq \hat{\mu} \end{cases} \quad (9.8)$$

A special case of the test statistic \tilde{t}_μ is defined for the discovery of a new signal, i.e. rejecting the $\mu = 0$ hypothesis. With $q_0 = \tilde{t}_0$ and $\mu = 0$ Eq. (9.8) can be written as:

$$q_0 = \begin{cases} 0 & \hat{\mu} < 0, \\ -2 \ln \lambda(0) & 0 \leq \hat{\mu}, \end{cases} \quad (9.9)$$

where $\lambda(0)$ is the profile likelihood ratio under the assumption $\mu = 0$. The p -value under this background only hypothesis is defined in the same manner as in Eq (9.6):

$$p_0 = \int_{q_{0,\text{obs}}}^{\infty} f(q_0|0) dq_0. \quad (9.10)$$

Here $f(q_0|0)$ describes the p.d.f. under the background only hypothesis.

A slightly modified test statistic \tilde{q}_μ is implemented for the derivation of upper limits, i.e. rejecting the signal-plus-background hypothesis, given by:

$$\tilde{q}_\mu = \begin{cases} -2 \ln \frac{L(\mu, \hat{\theta})}{L(0, \hat{\theta})} & \hat{\mu} < 0, \\ -2 \ln \frac{L(\mu, \hat{\theta})}{L(\hat{\mu}, \hat{\theta})} & 0 \leq \hat{\mu} \leq \mu, \\ 0 & \hat{\mu} > \mu \end{cases} \quad (9.11)$$

where μ is the signal strength parameter, $\hat{\mu}$ is the best-fit μ value, $\hat{\theta}$ is the collective denotation of the fit favoured nuisance parameters values when μ is kept constant in the fit. $\hat{\theta}$ is the collective notation of the fit favoured nuisance parameters' values, when μ is a free parameter in the fit. The idea behind the modification is, that in Eq. (9.8), an upward fluctuation of the data with $\hat{\mu} > \mu$, could result in a rejection of the hypothesised μ value, while an upward fluctuation in this case should not be regarded as incompatible with the tested μ value. The resulting signal-plus-background hypothesis test can be written as

$$p_\mu = \int_{\tilde{q}_{\mu,\text{obs}}}^{\infty} f(\tilde{q}_\mu|\mu) d\tilde{q}_\mu. \quad (9.12)$$

The p.d.f. of the above defined test-statistics can be either obtained by using pseudo-experiments (toys) or by exploiting asymptotic formulae. A pseudo-experiment consists of generating a dataset according to the expected model, whose nuisance parameters are fitted to the observed model. To obtain the desired distribution of the test statistic q_μ , the parameter of interest μ is fixed to the hypothesised value of μ' . The parameters of the p.d.f.s are fixed to their nominal values. The number of expected events are randomly drawn from the Poissonian distributed number of expected signal, μS , and background events, B . The systematic uncertainties, constrained by auxiliary measurements, are incorporated by drawing a random value for each toy, to shift the mean of the Gaussian, used to constrain the nuisance parameter. This changes the estimation of the systematic uncertainty for each generated pseudo-experiment. The value of the test statistic q_μ is then computed for each generated pseudo-experiment. The number of pseudo-experiments needed, to precisely determine the p.d.f.s in the tails of the distribution, is very large, to allow for a precision of the p -values on the order of 10^{-7} . However, an analytic implementation of the test statistic can be used, given a large enough sample size. These asymptotic formulas are derived using Wald's approximation [191] and Wilk's theorem [192]. The resulting Asimov dataset is a single representative in which all statistical fluctuations are suppressed. Asimov datasets are used to determine the statistical interpretation of the results presented within this thesis.

9.1.3 Calculation of Exclusion Limit

In general upper limits on a given signal model are evaluated by requiring that the p -value for the combined signal-plus-background hypothesis is smaller than a certain value α , i.e. $p_{s+b} < \alpha$, which is usually set to 0.05 in particle physics. The signal-plus-background p -value is defined as

$$p_{s+b} = P(\tilde{q} \geq \tilde{q}_{obs} | s + b) = \int_{\tilde{q}_{\mu, obs}}^{\infty} f(\tilde{q}_{\mu} | \mu S + B) d\tilde{q}_{\mu}. \quad (9.13)$$

This is generally referred to as the CL_{s+b} limit.

To prevent the exclusion of models to which no, or little sensitivity is given, a penalty term, given by the background-only hypothesis, $p_b = 1 - p_0$, is introduced. The exclusion is then defined as

$$CL_s = \frac{p_{s+b}}{1 - p_b} = \frac{CL_{s+b}}{CL_b} < \alpha. \quad (9.14)$$

This is to say that for $\mu = 1$ and $CL_s \leq \alpha$, the hypothesis would be excluded at $(1 - \alpha) CL_s$ confidence level. A 95 % confidence level upper limit on μ is reached, when μ is adjusted such that $CL_s = 0.05$. In cases where the test statistics under the signal-plus-background and under the background-only hypotheses are widely separated the $1 - p_b$ value is close to unity. In this case the above ratio leads to only a slight penalty. If only little or no sensitivity is given the $1 - p_b$ becomes small, efficiently preventing the exclusion. In general the results obtained by the CL_s method are slightly weaker than those obtained by the CL_{s+b} , and therefore regarded as more conservative. An illustration of the ingredients for the CL_s limit is shown in Fig. 9.1.

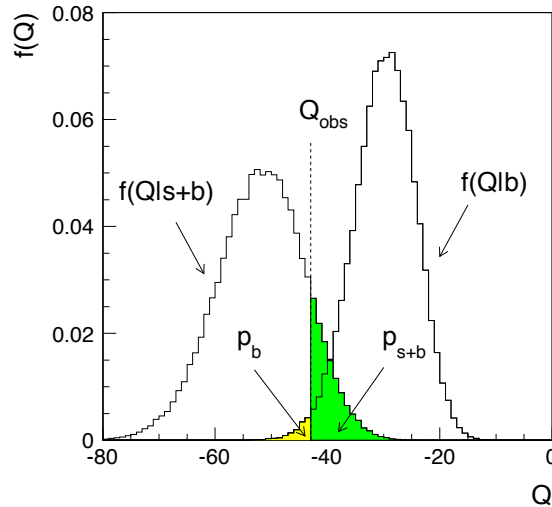


Figure 9.1: Illustration of the ingredients needed for the CL_s based limit [193].

9.2 Signal and Background Parametrisation

The success of an unbinned extended maximum-likelihood fit depends on a precise analytical description of the different signal and background constituents in the signal regions. Probability density functions (p.d.f.s) are defined for the signal and background distributions. Their parameters are determined

from fits to the simulated background processes, or in case of the reducible background from the fake-factor estimate, in each signal region.

9.2.1 Signal Parametrisation

The signal shape for the type-III seesaw and the vector-like leptons models consist of two distinct pieces: A narrow resonance, arising from the correct reconstruction of the $L^\pm \rightarrow Z(\ell^+\ell^-)\ell^\pm$ resonance, and a broad combinatorial background, where the three leptons do not originate from the resonance decay. These events originate mainly from a $Z \rightarrow \ell^+\ell^-$ decay and a lepton originating from the opposite side of the decay.

The Δm distribution is thus described by a combination of two analytical functions: The peak is modelled by a Voigtian, F_V , which is a Breit-Wigner function convolved with a Gaussian smearing term¹, while the combinatorial part is modelled using a Landau function, F_L . This leads to the following analytical description of the signal parametrisation, where f_V denotes the fraction of events in the Voigtian

$$f_{\text{Sig}}(m_{L^\pm}) = f_V F_V(\Delta m; \Gamma_V, m_V, \sigma_V) + (1 - f_V) F_L(\Delta m; \sigma_L, m_L). \quad (9.15)$$

Γ_V , m_V and σ_V , are the width, mean and Gaussian smearing term of the Voigtian, while σ_L and m_L are the width and mean associated to the combinatorial Landau part.

The Δm distributions at each simulated mass point for both the type-III seesaw and the vector-like lepton (VLL) models are fitted with f_{Sig} , separately for each flavour and signal category. An exemplary fit of the 300 GeV mass point from the vector-like lepton model to the inclusive $Z + e$ channel is shown in Fig. 9.2(a) and to the inclusive $Z + \mu$ flavour channel in Fig. 9.2(b). Tables 9.1 and 9.2 summarise the fitted parameters for the inclusive signal regions of the vector-like leptons model. The corresponding values for the type-III seesaw model are given in Table 9.3 for $Z + e$ and in Table 9.4 for $Z + \mu$ flavour channel. Additional fit distributions of the various vector-like leptons mass points are found in C, together with distributions of the fit parameters.

For masses below 200 GeV the width of the resonance is mainly dominated by the Z width. At higher masses the resonance width is mainly driven by the resolution of the bachelor lepton. This leads to a significant deviation between the width expected for bachelor electrons and muons attributed to their difference in the momentum resolution behaviour. While the momentum resolution for muons increases with the energy of the muon, the relative resolution of the electrons decreases with rising energy. This leads to differences of more than a factor of two at $m_{L^\pm} = 400$ GeV. The fraction f_V corresponds to the fraction of events in the Voigtian part and serves as an estimate for the fraction of event that arise from the resonant decay. These are at the level of $\sim 60\%$ ($\sim 75\%$) for type-III seesaw (vector-like leptons) at $m_{L^\pm} = 120$ GeV and $\sim 55\%$ for both models at 400 GeV.

Due to the large number of subchannels generated for the type-III seesaw model, Madgraph was unable to handle the decay of the Z boson intrinsically. Therefore the type-III seesaw samples are modelled without an intrinsic width of the Z bosons. This leads to significantly underestimated values of the width of the resonance at small Δm as seen in Tables 9.3 and 9.4 compared to the corresponding values of the vector-like leptons model in Table 9.1 and 9.2. As the invariant mass of the two leptons associated with the Z decay is subtracted from the trilepton mass to form Δm , the intrinsic width of the Z directly enters the width in Δm . Consequently, the Δm peaks are too narrow for small signal mass hypotheses. For higher values of m_{L^\pm} , the error is less impactful, as the intrinsic width of the Z is much smaller than the resolution on the bachelor lepton. A detailed investigation was done, including the simulation of a subset of decays, to model the correct width and a posterior smearing of the Δm . It was found that

¹ This smearing term is established to account for detector resolution effects.

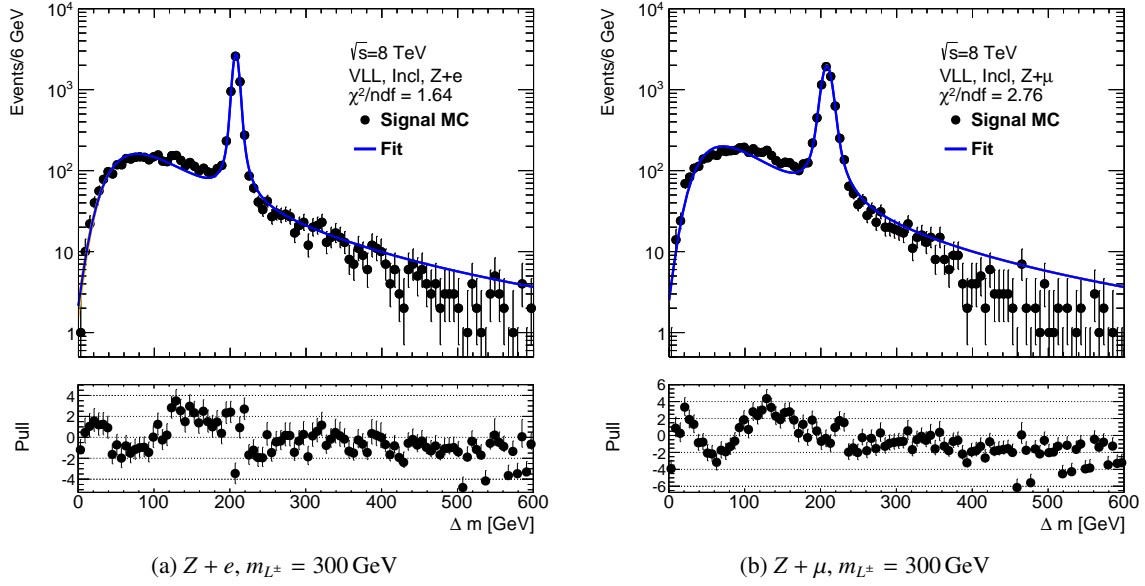


Figure 9.2: Fit of a Landau and a Voigtian to the inclusive distribution of the Δm at 300 GeV of the vector-like leptons model for $Z + e$ flavour channel (a) and $Z + \mu$ flavour channel (b).

the resonant part of the type-III seesaw signal is well described by the Voigtian parametrisation of the vector-like leptons model. Hence the vector-like leptons model Voigtian parametrisation was adapted for the type-III seesaw sample, while the parameters obtained for the Landau and the resonance fraction are derived from the signal model fit to the type-III seesaw simulated samples. An additional systematic uncertainty was applied to the resonance width accounting for the difference observed between the width of the vector-like leptons sample and the width of the additionally generated type-III seesaw samples. The difference at high masses between the two width is on the order of 0.5 GeV to 1.0 GeV.

Mass [GeV]	m_V [GeV]	σ_V [GeV]	Γ_V [GeV]	m_L [GeV]	σ_L [GeV]	f_V
100	10.77 ± 0.18	0.1 ± 0.1	2.5 ± 0.2	34.3 ± 1.5	12.12 ± 0.47	0.37
110	18.54 ± 0.04	1.9 ± 0.2	1.0 ± 0.1	34.1 ± 1.8	10.08 ± 0.51	0.69
120	28.25 ± 0.04	2.7 ± 0.4	0.7 ± 0.2	35.8 ± 3.0	10.95 ± 1.02	0.75
130	38.18 ± 0.04	2.2 ± 0.2	1.2 ± 0.1	31.0 ± 0.6	9.40 ± 0.32	0.71
140	48.07 ± 0.04	2.2 ± 0.2	1.5 ± 0.1	33.4 ± 0.6	10.29 ± 0.28	0.69
160	68.00 ± 0.04	3.0 ± 0.2	1.4 ± 0.1	37.0 ± 0.7	11.52 ± 0.32	0.70
180	87.97 ± 0.05	3.2 ± 0.2	1.6 ± 0.1	43.8 ± 0.7	14.05 ± 0.35	0.67
200	107.89 ± 0.05	3.0 ± 0.2	2.0 ± 0.1	49.7 ± 0.8	16.38 ± 0.39	0.65
250	157.75 ± 0.06	3.2 ± 0.2	2.6 ± 0.2	66.2 ± 0.9	22.76 ± 0.47	0.59
300	207.57 ± 0.07	3.4 ± 0.3	3.3 ± 0.2	83.9 ± 1.1	29.64 ± 0.58	0.57
400	307.53 ± 0.09	4.2 ± 0.3	4.4 ± 0.2	118.9 ± 1.7	46.42 ± 0.93	0.53

Table 9.1: Fit parameters for the vector-like leptons model in the $Z + e$ flavour channel and inclusive category.

Signal Model Validation

To fully exploit the advantages of the unbinned fit method, the signal model must be able to scan continuously over the full Δm range, using the analytical functions derived at the generated mass points.

9 Statistical Analysis of the Results of the Heavy Lepton Search

Mass [GeV]	m_V [GeV]	σ_V [GeV]	Γ_V [GeV]	m_L [GeV]	σ_L [GeV]	f_V
100	10.9 ± 0.13	0.1 ± 0.05	2.85 ± 0.10	35.63 ± 1.21	11.98 ± 0.40	0.44
110	18.7 ± 0.03	2.13 ± 0.16	0.73 ± 0.11	32.88 ± 1.55	9.47 ± 0.46	0.74
120	28.5 ± 0.03	2.26 ± 0.19	0.78 ± 0.11	30.72 ± 1.17	9.44 ± 0.59	0.75
130	38.4 ± 0.03	2.23 ± 0.16	1.07 ± 0.09	29.40 ± 0.48	8.83 ± 0.26	0.73
140	48.5 ± 0.03	2.38 ± 0.16	1.26 ± 0.09	30.57 ± 0.50	9.31 ± 0.25	0.73
160	68.5 ± 0.05	2.71 ± 0.19	1.74 ± 0.10	33.97 ± 0.55	10.45 ± 0.27	0.71
180	88.3 ± 0.05	2.73 ± 0.21	2.19 ± 0.11	40.06 ± 0.62	12.76 ± 0.30	0.68
200	108.4 ± 0.1	3.34 ± 0.26	2.81 ± 0.14	45.44 ± 0.65	14.28 ± 0.32	0.66
250	158.2 ± 0.1	4.45 ± 0.34	3.89 ± 0.17	61.10 ± 0.85	20.71 ± 0.42	0.62
300	208.0 ± 0.1	6.21 ± 0.48	5.26 ± 0.25	76.50 ± 1.01	26.62 ± 0.51	0.58
400	307.9 ± 0.2	9.12 ± 0.84	8.63 ± 0.40	114.84 ± 1.60	42.99 ± 0.85	0.53

Table 9.2: Fit parameters for the vector-like leptons model in the $Z + \mu$ flavour channel and inclusive category.

Mass [GeV]	m_V [GeV]	σ_V [GeV]	Γ_V [GeV]	m_L [GeV]	σ_L [GeV]	f_V
100	8.7222 ± 0.015	0.131 ± 0.04	0.32 ± 0.03	36.1 ± 0.7	10.9 ± 0.355118	0.34
120	28.5035 ± 0.024	0.594 ± 0.12	0.72 ± 0.06	34.1 ± 0.8	10.2 ± 0.391391	0.59
160	68.3224 ± 0.037	1.34 ± 0.15	1.13 ± 0.08	45.9 ± 0.7	15.3 ± 0.392333	0.57
200	108.294 ± 0.052	1.86 ± 0.20	1.59 ± 0.10	59.1 ± 1.1	21.3 ± 0.568737	0.58
250	158.039 ± 0.090	3.08 ± 0.37	1.48 ± 0.26	75.6 ± 2.1	27.6 ± 1.10452	0.59
300	207.856 ± 0.129	2.96 ± 0.45	2.75 ± 0.23	92.3 ± 2.6	35.7 ± 1.39974	0.55
350	257.775 ± 0.169	4.52 ± 0.63	3.21 ± 0.33	106.8 ± 3.4	41.6 ± 1.85383	0.57
400	308.066 ± 0.198	6.84 ± 0.77	2.77 ± 0.48	129.7 ± 4.2	51.3 ± 2.34715	0.55
450	357.463 ± 0.277	7.37 ± 1.05	3.91 ± 0.61	142.1 ± 5.3	58.3 ± 3.06396	0.54
500	407.731 ± 0.262	5.39 ± 1.02	5.26 ± 0.53	179.9 ± 6.1	71.5 ± 3.65063	0.52

Table 9.3: Fit parameters for the type-III seesaw model in the $Z + e$ flavour channel and inclusive category. Note that the absence of the intrinsic width of the Z boson in the simulation leads to smaller values than expected for the width of the Voigtian peak for masses below ~ 250 GeV.

Mass [GeV]	m_V [GeV]	σ_V [GeV]	Γ_V [GeV]	m_L [GeV]	σ_L [GeV]	f_V
100	8.78 ± 0.01	0.13 ± 0.05	0.176 ± 0.01	35.6 ± 0.5	10.6 ± 0.3	0.45
120	28.71 ± 0.01	0.28 ± 0.057	0.62 ± 0.02	31.2 ± 0.5	8.7 ± 0.2	0.60
160	68.56 ± 0.03	1.86 ± 0.14	1.18 ± 0.08	44.7 ± 0.6	15.3 ± 0.3	0.60
200	108.3 ± 0.05	3.10 ± 0.25	1.99 ± 0.13	56.6 ± 0.9	19.4 ± 0.5	0.61
250	158.1 ± 0.1	4.36 ± 0.61	3.64 ± 0.31	73.6 ± 1.9	27.0 ± 1.0	0.61
300	207.7 ± 0.1	8.17 ± 0.84	3.87 ± 0.46	86.2 ± 2.4	32.3 ± 1.3	0.61
350	258.3 ± 0.2	10.04 ± 1.44	6.15 ± 0.75	103.1 ± 3.2	40.2 ± 1.7	0.59
400	307.2 ± 0.3	13.09 ± 1.69	6.39 ± 0.98	120.9 ± 4.2	50.2 ± 2.3	0.58
450	357.4 ± 0.5	18.08 ± 3.05	8.86 ± 1.64	137.7 ± 5.9	57.9 ± 3.4	0.56
500	407.6 ± 0.5	14.20 ± 3.10	12.2 ± 1.44	166.7 ± 6.1	67.9 ± 3.6	0.53

Table 9.4: Fit parameters for the type-III seesaw model in the $Z + \mu$ flavour channel and inclusive category. Note that the absence of the intrinsic width of the Z boson in the simulation leads to smaller values than expected for the width of the Voigtian peak for masses below ~ 250 GeV.

Therefore a morphing scheme was implemented. The parameters at the intermediate mass points are obtained by linearly interpolating the fit parameters, as well as the mass dependent systematic uncertainties, determined at the nearest simulated points above and below. To validate the interpolation method, a closure test was performed comparing the fit parameters determined at a simulated mass point with the values obtained from a linear interpolation between the adjacent simulated points, the results of the interpolation are summarised in Table 9.5. The values agree reasonably well.

Mass [GeV]	m_V [GeV]	σ_V [GeV]	Γ_V [GeV]	m_L [GeV]	σ_L [GeV]	f_V
VLL 120 GeV norm	32.89 ± 1.5	10.224 ± 0.66	28.4355 ± 0.02	2.4767 ± 0.2	0.73 ± 0.12	0.75
VLL 120 GeV morph	31.96 ± 0.47	9.511 ± 0.71	28.49 ± 0.02	2.13 ± 0.02	0.98 ± 0.21	0.73
VLL 160 GeV norm	35.43 ± 0.46	11.018 ± 0.21	68.2511 ± 0.03	2.85 ± 0.14	1.59 ± 0.08	0.70
VLL 160 GeV morph	36.97 ± 0.5	11.68 ± 0.24	68.22 ± 0.03	2.65 ± 0.13	1.641 ± 0.07	0.69

Table 9.5: Comparison of morphed and directly fitted parameters for the signal parametrisation the vector-like leptons at signal masses of 120 GeV and 160 GeV.

Figure 9.3 demonstrates the implemented morphing scheme for the type-III seesaw model, by interpreting the model every 20 GeV. The shapes of the generated mass points are shown in orange, while the interpolated mass points are shown in blue. A smooth transition between generated and interpolated functions is visible. This is crucial to avoid any discontinuities in the final likelihood function. The increasing difference with higher masses in the resonance width between $Z + e$ and $Z + \mu$ is clearly visible.

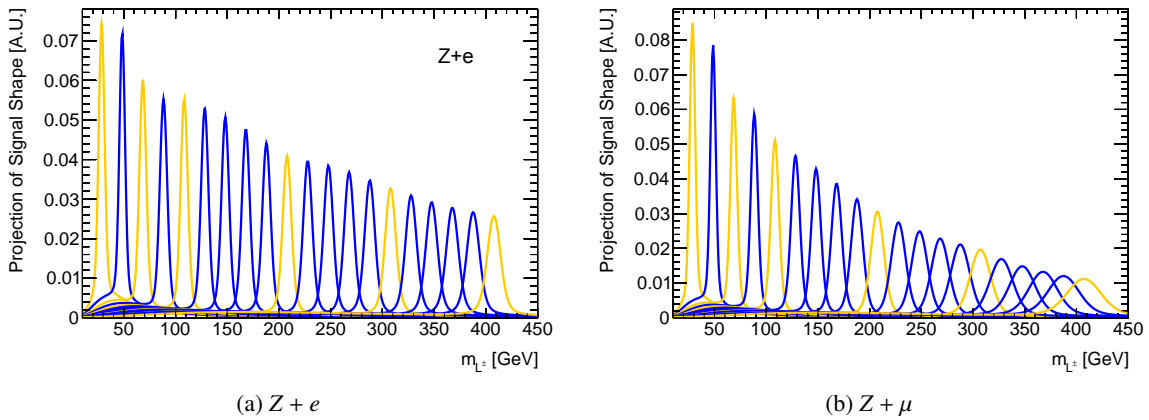


Figure 9.3: Signal model at every 20 GeV, the functions at generated mass points are shown in orange, the functions derived from the interpolation scheme are shown in blue. A smooth transition between the points is visible.

9.2.2 Background Parametrisation

The combined background model consists of five different p.d.f.s. These are the WZ and ZZ Diboson backgrounds, the reducible background estimate (called reducible), the $Z + \gamma$ and the combined $t\bar{t}V$ and triboson background. The statistical uncertainties arising from the limited simulated event statistics, are propagated to the resulting analytical functions through the uncertainties on the fit parameters, where applicable. In the following paragraphs a detailed overview of the different components and their analytical description is given.

Diboson

The shape of the WZ and ZZ continuum background is defined by a sharp turn-on behavior in the Δm region smaller than 30 GeV, arising from the kinematic object selection criteria, and a peak at 40 GeV evolving into an exponential tail at high masses. These backgrounds are modelled by a Bukin function [194]. This five-parameter² function was specifically designed to model asymmetric peaks, utilising a convolution of a gaussian and an exponential with dedicated boundary conditions. The Bukin function is described by:

$$\mathcal{P}(x; x_p, \sigma_p, \xi, \rho) = A_p \exp \left[\frac{\xi \sqrt{\xi^2 + 1} (x - x_1) \sqrt{2 \log 2}}{\sigma_p (\sqrt{\xi^2 + 1} - \xi)^2 \log(\sqrt{\xi^2 + 1} + \xi)} + \rho \left(\frac{x - x_i}{p_p - x_i} \right)^2 - \log 2 \right], \quad (9.16)$$

with the following boundary conditions: $\rho = \rho_1$ and $x_i = x_1$ for $x < x_1$, $\rho = \rho_2$, $x_i = x_2$ for $x \leq x_2$. While the five-parameter Bukin function is well suited to model the asymmetric peak of the turn-on region for WZ and ZZ , the introduction of five parameters leads to large correlations between the individual parameters with some pairs exceeding 99% correlation. To reduce the number of free parameters, 100 toy datasets were generated from the fitted five parameter Bukin function and the Bukin function fit was repeated on each generated dataset. Each pair of parameters were drawn in a two dimensional plane. A linear correlation was found for both, σ_p and ξ as functions of x_p , these are shown in the scatter plots in Fig. 9.4 for the WZ final state and in Fig. 9.5 for ZZ . To improve the performance of the fit, σ_p and ξ were constrained as linear functions of x_p , using the values from the fit to the results of the 100 pseudo experiments. This efficiently reduced the number of free fit parameters from five to three.

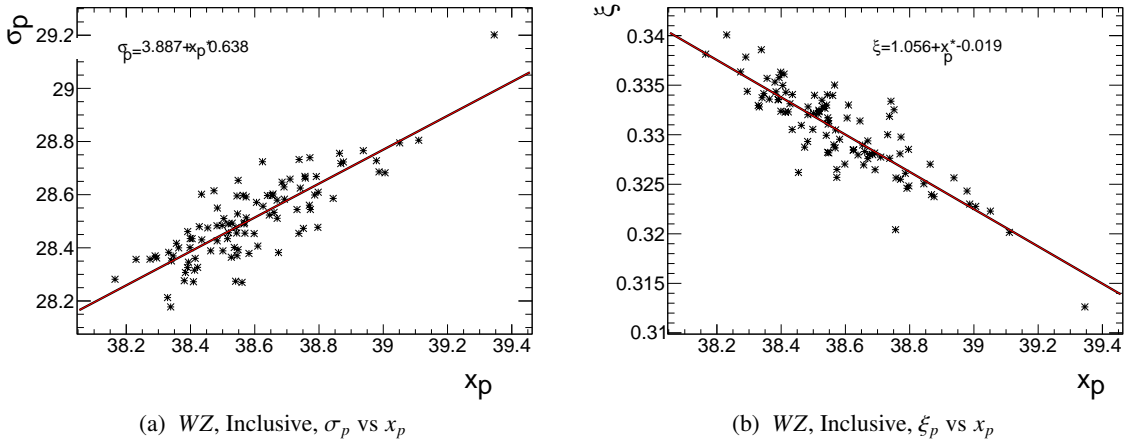


Figure 9.4: Parameter correlation for 100 toy experiments for the inclusive WZ background. The line indicates the linear least squares fit used to constrain the parameter on the y-axis.

To reduce the complexity of the fit it is desirable and to benefit from the higher statistics of the inclusive regions, the shape of the WZ/γ^* and ZZ/γ^* distributions of the individual categories are compared to the inclusive $Z + e$ and $Z + \mu$ categories. The similarity is evaluated using a Kolmogorov-Smirnov test. The results are shown in Fig. 9.6 for WZ/γ^* and in Fig. 9.7 for the ZZ/γ^* backgrounds. While the shapes for the 4ℓ and 3ℓ -only are consistent with the inclusive category for both WZ/γ^* and ZZ/γ^* , the shape for the $3\ell + jj$ categories differs significantly in both. The difference is attributed to the the invariant mass

² σ_p , x_p , ρ_1 , ρ_2 , and ξ

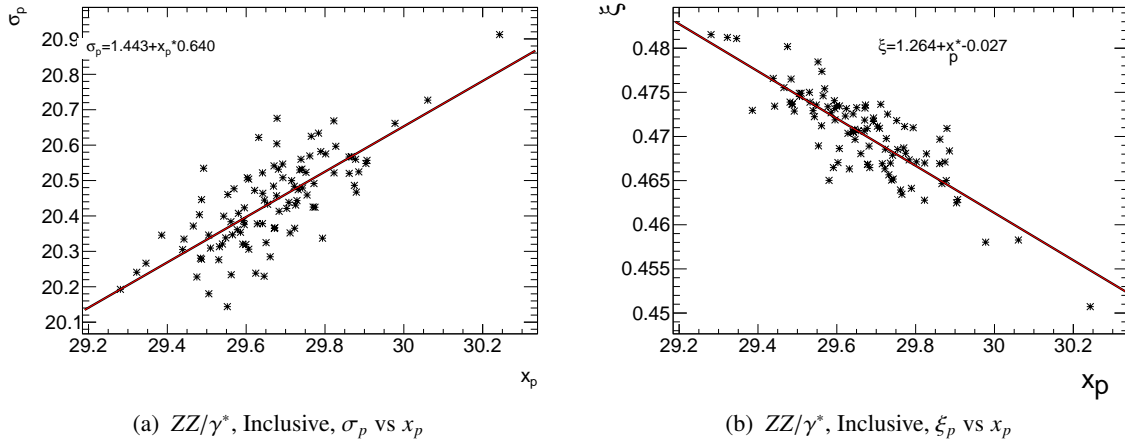


Figure 9.5: Parameter correlation for 100 toy experiments for the inclusive ZZ background. The line indicates the linear least squares fit used to constrain the parameter on the y -axis.

cut on the dijet pair from the opposite side of the event. Therefore the inclusive parametrisation is used in the 4ℓ and 3ℓ -only category, while a separate parametrisation is used for the $3\ell+jj$ categories.

The results of the three-parameter fits are shown in Fig. 9.8 for WZ and 9.9 for ZZ in the upper figures for the inclusive region and in the lower region for the $3\ell+jj$ category. The final states with a bachelor electron are on the left, those with a muon are shown in the distributions in the right-hand-side. The shape uncertainty arising from the statistical uncertainty on the simulated samples is directly accounted for by the uncertainties on the fit parameters. An additional shape uncertainty is added to the Diboson samples, arising from the observed modelling differences between SHERPA and POWHEG-BOX. The SHERPA simulated samples are used as the central values, and the uncertainty is defined by the symmetric difference of the central fit parameters obtained from the fit to two generator samples. These uncertainties are then combined with the fit parameter uncertainties. A comparison of the Δm shapes between SHERPA and POWHEG-BOX is found in Section 7.10.

The ZZ/γ^* contribution is the only significant contribution to the 4ℓ region and the normalisation of this background is a free parameter of the fit model in this region, whereas the WZ/γ^* contribution is almost negligible and thus fixed to the simulated event expectations. For the inclusive, the $3\ell+jj$ and the 3ℓ -only region a large correlation between the shape of the WZ/γ^* and ZZ/γ^* processes, arising from the similar underlying kinematics in the WZ/γ^* and ZZ/γ^* production processes was observed. Therefore the ratio of the WZ/ZZ expectation is therefore fixed to the expectations estimated from simulation, while the overall normalisation is a free parameter of the fit. A systematic uncertainty based on the cross-section uncertainty of the ZZ/γ^* sample as well as the difference in the ratios between SHERPA and POWHEG-BOX generated samples is included onto the normalisation in the fit.

Reducible Background

Reducible processes pose another important background. Given the limited statistics from the fake-factor estimate, the individual categories are summed for $Z + e$ and $Z + \mu$ in final states. The reducible backgrounds are fitted with a Landau distribution, as shown for $Z + e$ final states in Fig. 9.10(a) and for $Z + \mu$ final states in Fig. 9.10(b). The individual regions are then normalised to the expectations from the individual categories. In categories where the overall normalisation of the reducible background is

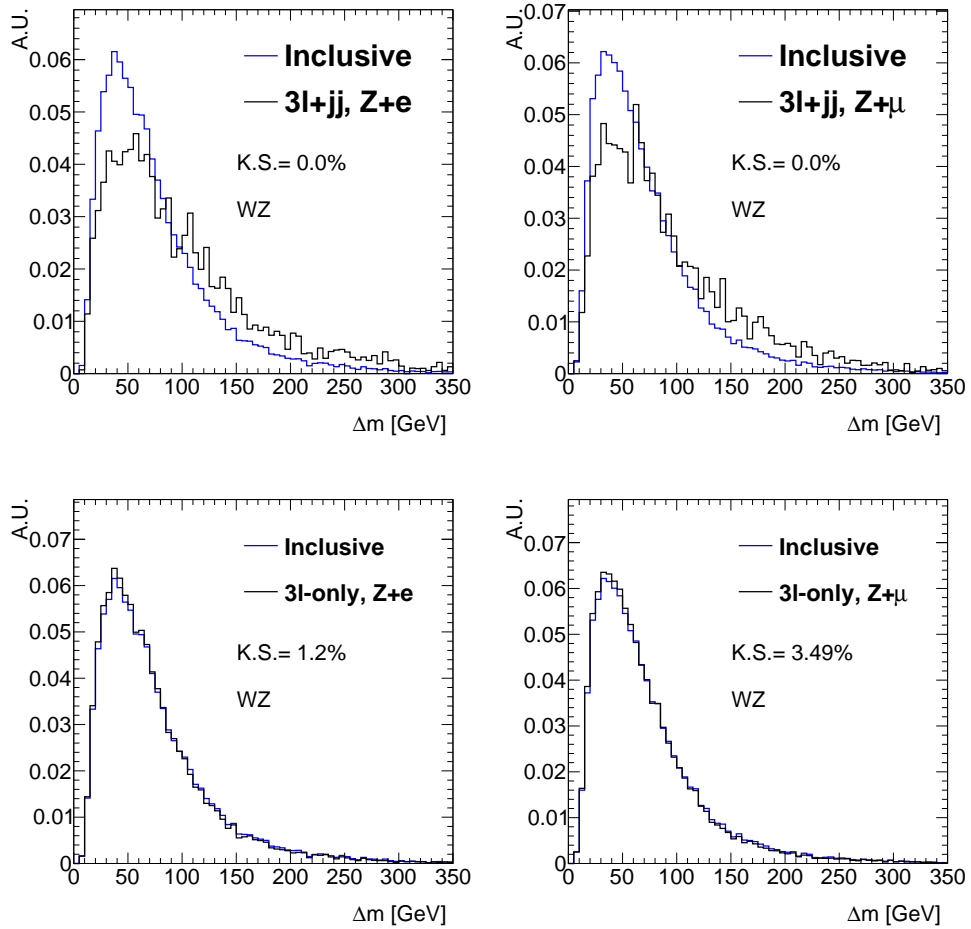


Figure 9.6: Comparison of WZ Δm shapes between the inclusive and the categorised signal regions, $3l+jj$ (top) and $3l\text{-only}$ (bottom) for bachelor electrons (left) and bachelor muon final states (right). Due to the lack of WZ/γ^* events contributing to the $4l$ region, this region is omitted.

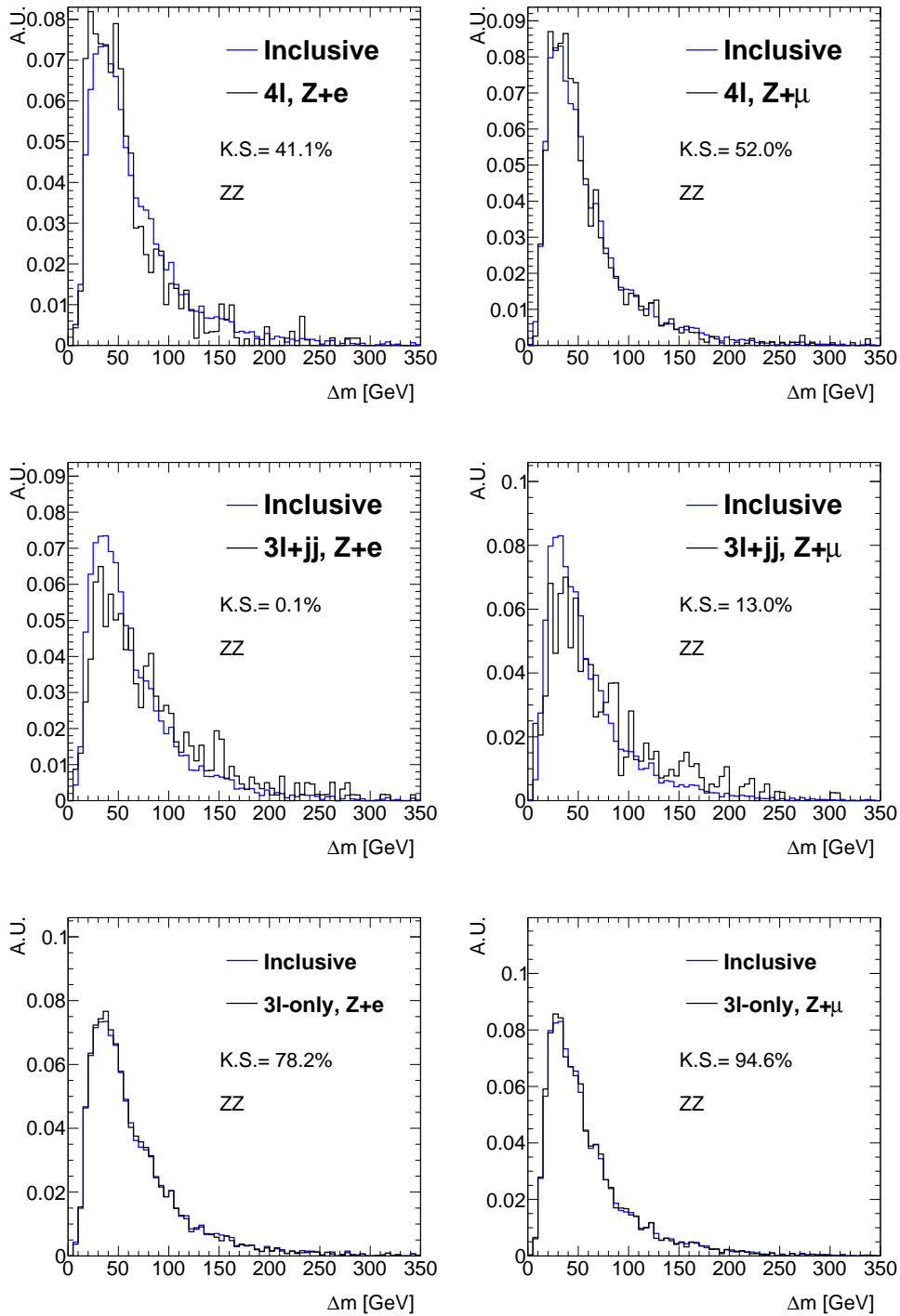


Figure 9.7: Comparison of ZZ Δm shapes between the inclusive and the categorised signal regions, 4ℓ (top), $3\ell+jj$ (middle) and $3\ell\text{-only}$ (bottom) for $Z + e$ final states (left) and $Z + \mu$ final states (right).

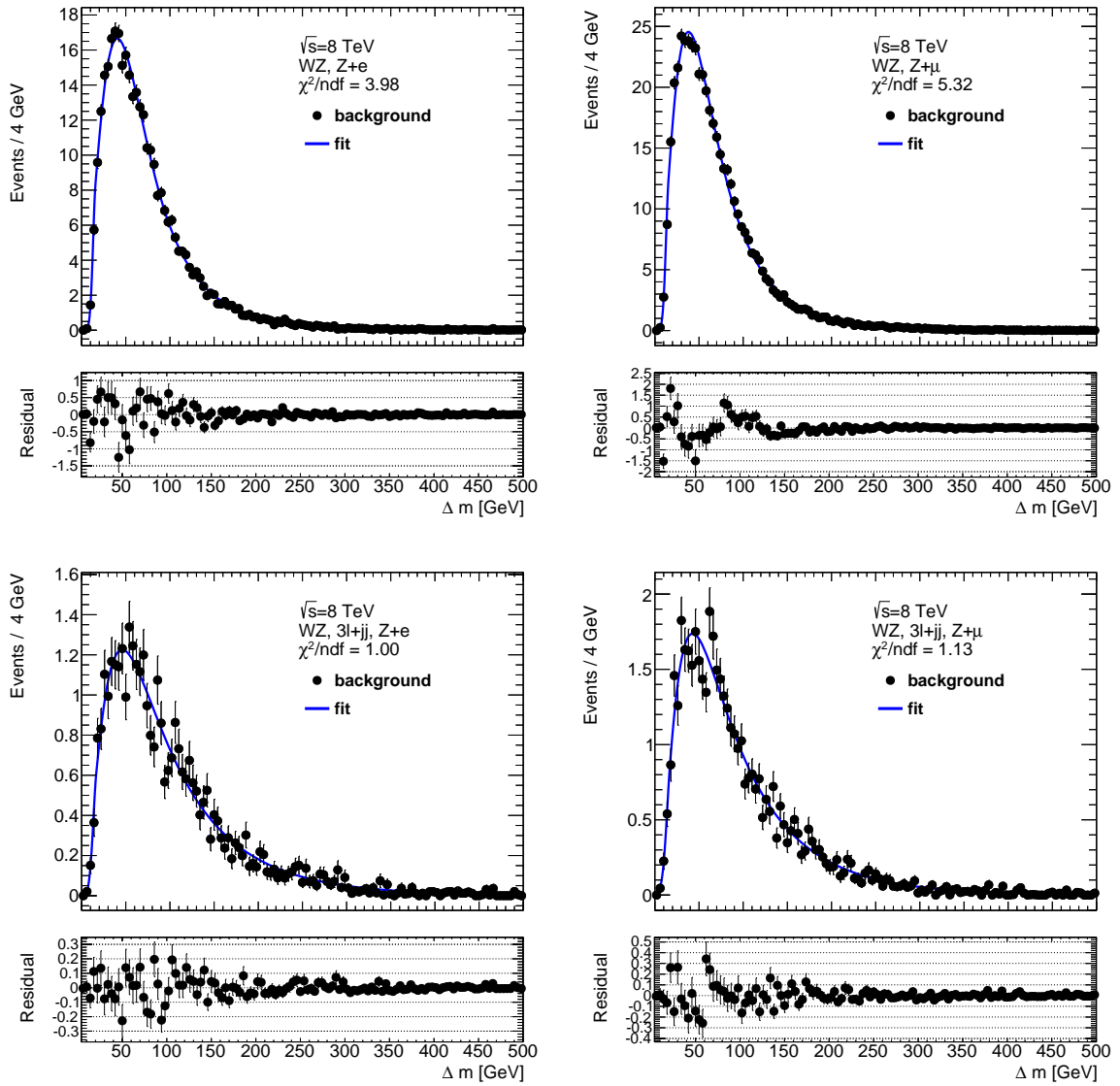


Figure 9.8: Distributions of Δm for WZ/γ^* and Bukin function fits for the inclusive (top) and the $3\ell+jj$ (bottom) signal regions for $Z + e$ final states (left) and $Z + \mu$ final states (right).

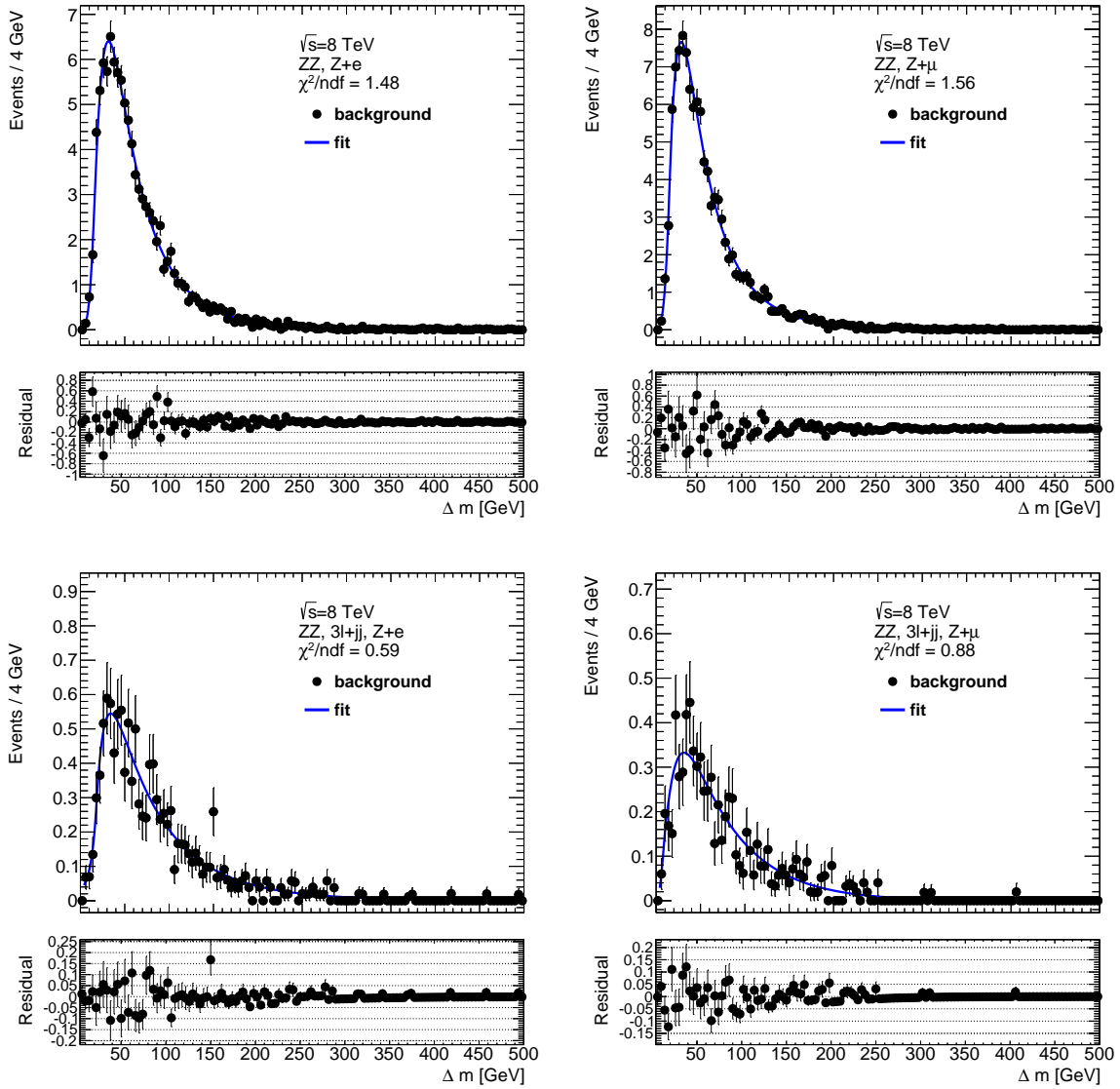


Figure 9.9: Final distributions of Δm for ZZ/γ^* and Bukin function fits for the inclusive (top) and the $3\ell+jj$ (bottom) signal regions for $Z + e$ final states (left) and $Z + \mu$ final states (right).

negative due to the prompt subtraction, the normalisation is set to zero. The limited statistics results also in large uncertainties on the fit parameters. Due to the small number of expected events for the reducible background, the normalisation is fixed and a 30% uncertainty is added, as derived from the fake-factor estimate uncertainty (see Sec. 7.8).

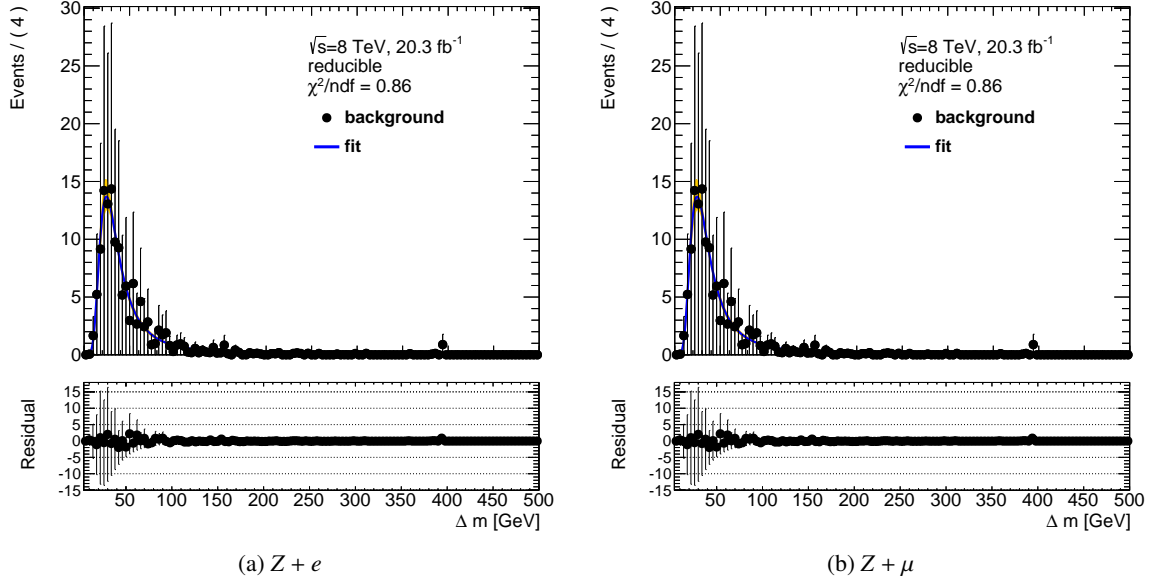


Figure 9.10: The shape of the reducible background is taken from the estimates performed with the fake-factor method. The distribution is parametrised with a Landau function for both bachelor lepton flavours. Due to the limited statistics in the categorised signal regions, the shape is determined from the inclusive $Z + e$ and $Z + \mu$ flavour channel, and only the normalisation varies in the categorised signal regions.

Photon Conversion

The $Z(\ell\ell) + \gamma$ background is only relevant to the inclusive and 3ℓ -only signal region in events with a bachelor electron. This contribution is modelled with the sum of a Landau function and a Gaussian function. These are attributed to the different origins of $Z + \gamma$ production as detailed in Section 5.3. Figure 9.11 shows the resulting $Z(\ell\ell) + \gamma$ fitted function, the uncertainty on the normalisation for this background is 30% (see Sec 7.9). The normalisation is fixed in the fit and a nuisance parameter accounts for the normalisation uncertainty.

Triboson and $t\bar{t} + V$

The remaining contributions are the VVV^* and $t\bar{t} + V$ backgrounds. These are also modelled with Landau functions. Due to the very similar resulting analytic parametrisation of both backgrounds, they are combined into a single background p.d.f.. Because of their small overall contributions, the normalisations are set to the predictions from the simulated event samples for the various regions and a systematic uncertainty of 20% is applied on the normalisation arising from the systematic uncertainty in the production cross-sections. The resulting parametrisation is shown in Fig. 9.12.

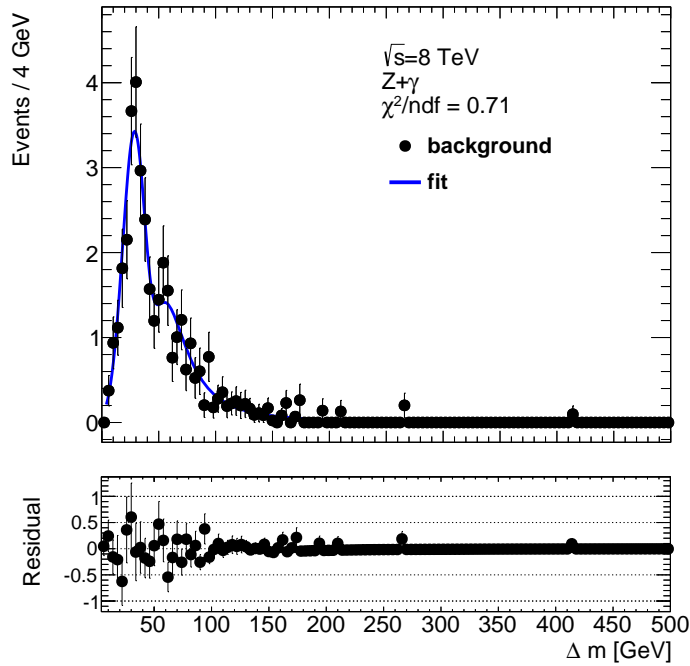


Figure 9.11: Distribution of Δm for $Z + \gamma$ background, fitted with the sum of a Landau function and a Gaussian function. This background contributes only to final states with a bachelor electron.

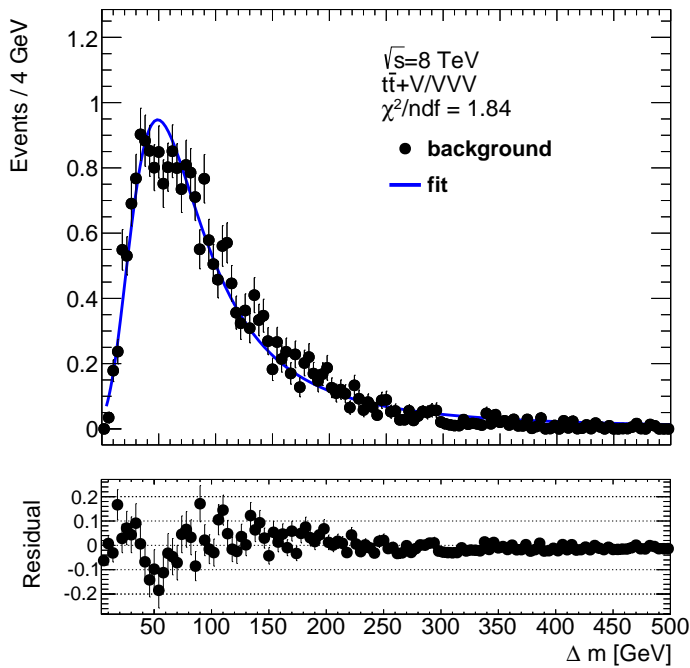


Figure 9.12: Distribution of Δm for the combined $t\bar{t} + V, VVV^{(*)}$ background, fitted with the sum of a Landau function and a Gaussian function. This background is significant for final states with a bachelor electron.

9.3 Combined Fit Model

A combined fit model is built from the individual p.d.f. components describing the signal and four background components. The parameter of interest in the likelihood is the signal strength μ . Additionally several nuisance parameters are included, to describe the background contributions and systematic uncertainties. The individual categories are described independently and a simultaneous fit to each of the signal regions is performed to extract the result. The full likelihood can thus be expressed by:

$$L(\mu, \boldsymbol{\theta} = \cup_{c=1}^{n_{\text{cat}}} \boldsymbol{\theta}_c) = \prod_{c=1}^{n_{\text{cat}}} L_c(\mu, \boldsymbol{\theta}_c), \quad (9.17)$$

where n_{cat} is the number of categories, in this case three for each flavour, and $\boldsymbol{\theta}_c$ is a vector of nuisance parameters used to describe the model in category c . L_c is the likelihood function in category c , described by

$$L_c(\mu, \boldsymbol{\theta}_c) = \frac{e^{-N_{S,c} + \sum_k N_c^{\text{bkg},k}} (N_{S,c} + \sum_k N_c^{\text{bkg},k})^{N_c}}{N_c!} \prod_{k=1}^{N_c} \mathcal{L}_c(\Delta m(k); \mu, \boldsymbol{\theta}_c), \quad (9.18)$$

where N_c is the number of events in category c , the index k runs over the events and $\Delta m(k)$ is the mass difference of event k . \mathcal{L}_c is the likelihood per event, which is of the form

$$\mathcal{L}_c(\Delta m; \mu, \boldsymbol{\theta}_c) = \frac{N_{S,c}(\mu, \boldsymbol{\theta}^{\text{Norm}}) f_{\text{Sig},c}(\Delta m; \boldsymbol{\theta}_c^{\text{shape}}) + \sum_k N_c^{\text{bkg},k} f_c^{\text{bkg},k}(\Delta m; \boldsymbol{\theta}_c^{\text{bkg}})}{N_{S,c} + \sum_k N_c^{\text{bkg},k}}, \quad (9.19)$$

where $N_{S,c}$ and $N_{\text{bkg},k,c}$ are the fitted numbers of signal and background events in data in category c . $f_{\text{Sig},c}$ is the signal p.d.f for category c . The different background p.d.f.s are summed separately, where each background $f_c^{\text{bkg},k}(\Delta m; \boldsymbol{\theta}_c^{\text{bkg}})$, is a function of a vector of nuisance parameters $\boldsymbol{\theta}_c^{\text{bkg}}$. Several sources of systematic uncertainties are included in the fit. The dominant systematic uncertainty arises from the limited statistics in the simulated event samples and are reflected in the uncertainties of the parameters describing the various p.d.f. components. Further uncertainties arise from the theoretical cross-section uncertainties given by $\delta\sigma_i$, and the luminosity uncertainty δL . These are associated to nuisance parameters denoted θ_L and θ_{σ_i} and the values of the auxiliary measurements α_L , and α_{σ_i} . These are added as Gaussian constraints with the widths equal to the size of the systematic uncertainty. Uncertainties which are correlated across all categories (such as the luminosity uncertainty), are parametrised by a single parameter and are shared among the categories. The heavy lepton mass m_L^\pm and the signal strength μ are common to all categories. This also is true for the cross-section uncertainties for backgrounds which is a fixed parameter in all categories, such as the reducible and the combined Triboson and $\bar{t} + V$ background. An overview over the individual fit components in each category and the associated uncertainties is given in Table. 9.6.

In addition to the combined fit to the three categories an inclusive fit model is built, using the inclusive $Z + e$ and $Z + \mu$ flavour channels without any further categorisation. This allows to accommodate the interpretation of the results in the light of a generic heavy lepton resonance. In this case Eq. (9.19) is built using the parameters obtained from the inclusive category.

Component	p.d.f.	Flavour	Category Parametrisation	Nuisance Parameters	Free parameters
Signal	Landau + Voigt	$Z + e$	inclusive	2 Shape	μ
		$Z + \mu$	inclusive	2 Shape	
ZZ	3-parameter Bukin	$Z + e$	4ℓ and 3ℓ -only use inclusive, separate for $3\ell+jj$	2 Shape, 2 Scale	Ratio N_{WZ}/N_{ZZ} and N_{ZZ} in 4ℓ
		$Z + \mu$	4ℓ and 3ℓ -only use inclusive, separate for $3\ell+jj$	2 Shape, 2 Scale	Ratio N_{WZ}/N_{ZZ} for $3\ell+jj$ and 3ℓ -only, N_{ZZ} in 4ℓ
WZ	3-parameter Bukin	$Z + e$	4ℓ and 3ℓ -only use inclusive, separate for $3\ell+jj$	3 Shape, 2 Scale	Ratio N_{WZ}/N_{ZZ} N_{ZZ} in 4ℓ
		$Z + \mu$	4ℓ and 3ℓ -only use inclusive, separate for $3\ell+jj$	2 Shape, 2 Scale	Ratio N_{WZ}/N_{ZZ} for $3\ell+jj$ and 3ℓ -only, N_{ZZ} in 4ℓ
Reducible	Landau		Combined for $Z + e$ and $Z + \mu$	1 Shape + 1 Scale 30 %	None
$Z + \gamma$	Landau + Gaussian	$Z + e$	inclusive	1 Shape + 1 Scale 30 %	None
		$Z + \mu$	non applicable	None	None
Triboson and $t\bar{t} + V$	Landau	$Z + e$	inclusive	1 Shape + 1 Scale 20 %	None
		$Z + \mu$	inclusive	1 Shape + 1 Scale 30 %	None

Table 9.6: Summary of the fit model, including the number of nuisance parameters arising from the parametrisation and the normalisation of the various backgrounds. Depending on the signal category a different number of normalisations are left floating.

9.3.1 Reduction of free Parameters

The experimental systematic uncertainties (see Chapter 7) are derived by shifting the corresponding parameters in the analysis by one standard deviation and repeating the analysis with the changed settings. The differences between the nominal and the changed settings are interpreted as systematic uncertainties, and are added to the likelihood function as nuisance parameters. The complexity of the likelihood function and resulting from this the time needed for its minimisation is strongly dependent on the number of free parameters. Many of the systematic variations described in Chapter 7 are well compatible with the nominal expectations, as limited sample size prevents to resolve the systematic variation.

To reduce the complexity of the likelihood function, it is desirable to only include systematic uncertainties that have an actual impact on either the shape of the underlying p.d.f. parametrisation or the normalisation and by that to reduce the number of fit parameters. Uncertainties related to the shape of the p.d.f. mainly originate from the limited statistics in the simulated samples. The muon and electron energy scale factors, which are expected to impact the shape of the Δm distribution, are very well measured. The shifts in the parametrisation due to the electron and muon energy scales were at least one order of magnitude smaller than the uncertainties on the fit parameters, originating from the limited statistics in the simulated event samples, and thus omitted.

It was further decided that uncertainties that only impact the normalisation and have an impact on the results of less than 2% are neglected. This applies among others to the uncertainties related to the electron and muon scaling factors, and the trigger scaling factors. Additionally, nuisance parameters that showed a correlation of more than 90% were combined to a single nuisance parameter. For instance the two nuisance parameters arising from two parameters of the Landau function of the reducible background parametrisation were constrained as a single nuisance parameter using this approach. This significantly reduced the number of nuisance parameters related to the p.d.f. shape uncertainties.

The reduction and combination of nuisance parameters process has been verified, by repeating the limit setting procedure for a few selected mass-point. No significant impact on the final result was found.

9.3.2 Validation of Combined Fit Model

A thorough validation of the combined likelihood function is performed to discover any intrinsic problems and to validate the fit procedure. The robustness of the method was evaluated both in ensemble tests and using Monte Carlo generated events. In an ensemble test the measurements are based on pseudo-experiments. These are obtained by randomly generating events from the p.d.f.s of the combined fit model. The obtained events are then in turn fitted with the combined fit model and the results are compared to the input values of the p.d.f.. An important concern in this respect is the introduction of any bias to the result. This is evaluated by measuring the pull of the corresponding parameter of interest, x , given by:

$$\text{pull} = \frac{x_{\text{fitted}} - x_{\text{generated}}}{\sigma_{x,\text{fitted}}}, \quad (9.20)$$

which should follow a Gaussian distribution with mean zero and width one.

An internal RooFit issue was observed during the bias testing in regions which are sparsely populated with background events. This was attributed to the fact the signal strength might become negative, for datasets with no entries within a large mass range. RooFit only evaluates the positiveness of a p.d.f. at mass points given in the dataset, hence the p.d.f. can become negative in the unpopulated region.

This problem was solved by introducing so called ghost events, which are events with a very small weight, which do not have an influence on the likelihood function, but rather force RooFit to test the positiveness of the p.d.f. over the full mass range. To further circumvent any impact of this issue on the hypothesis testing, the range of the signal strength was thereafter limited to positive values, given that the test statistics are set to zero for negative signal strengths.

The bias test was performed generating 500 pseudo experiments at six different signal strength values ($\mu = 0, 0.25, 0.5, 1.0, 2.0, 3.0$). Figure 9.13 shows the result of the bias test of the combined fit to the three categories in the $Z + e$ and $Z + \mu$ final state with a signal strength of $\mu = 1$ and at $m_{L^\pm} = 120$ GeV (left) and $m_{L^\pm} = 300$ GeV (right). Also for the cases not shown here the mean of the pull distribution agree reasonably well with zero, which indicate that the fit is unbiased with respect to the determination of the signal strength parameter μ . The width also agrees well with unity, which indicates that the errors cover what they claim to cover (i.e. 1σ indeed is 68 %).

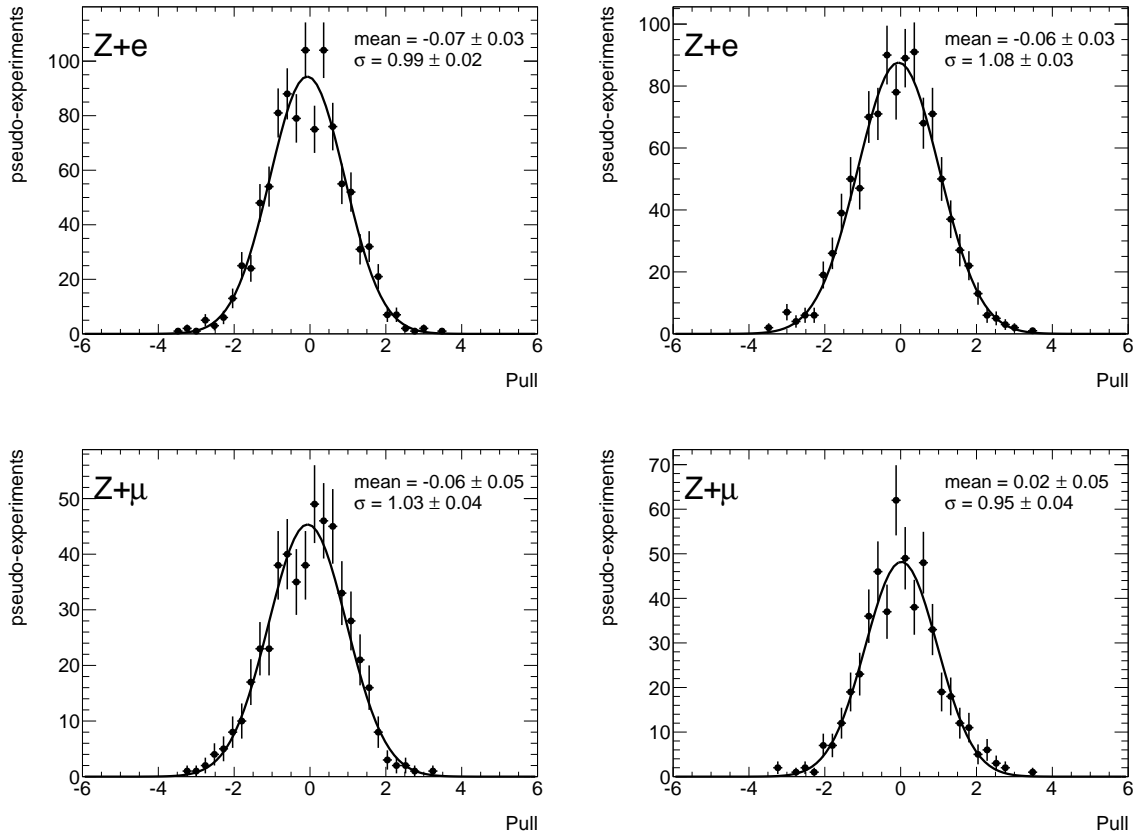


Figure 9.13: Pull distribution at a signal strength of $\mu = 1$ and a type-III seesaw mass hypothesis of $m_{L^\pm} = 120$ GeV (left) and $m_{L^\pm} = 300$ GeV (right), for the $Z + e$ (upper) and $Z + \mu$ (lower) final states.

The pseudo-experiments were also used to validate the linearity of the fit result. The results of the linearity test for assuming a type-III seesaw resonance mass of 300 GeV are shown in Fig. 9.14. An excellent agreement with a first order polynomial with a slope close to unity and no offset is found both for the $Z + e$ flavour channel in Fig. 9.14(a) and the $Z + \mu$ flavour channel in Fig. 9.14(b).

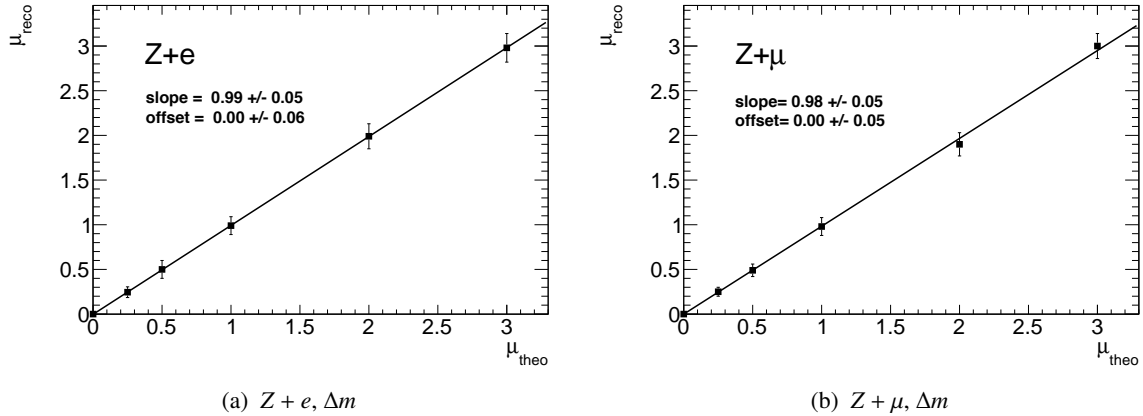


Figure 9.14: Linearity for the reproduction of injected signal at various signal strength μ . The expected linear behaviour is clearly reproduced for $Z + e$ (a) and $Z + \mu$ (b) final state.

9.3.3 Comparison of Results Obtained from Pseudo Experiments

The final results are based on Asimov datasets, which are a single representative dataset generated under the assumption that the maximum likelihood estimators of the parameters are the assumed true values of the parameters. The validity of this approximation for this analysis was verified by comparing the results obtained from Asimov datasets and pseudo experiments at different signal strength parameters. Figure 9.15 shows the Asimov dataset generated under the background-only hypothesis for the two bachelor lepton flavors. The resulting CL_s value are shown in Fig. 9.16. An excellent agreement is found between the CL_s values obtained with the two approaches.

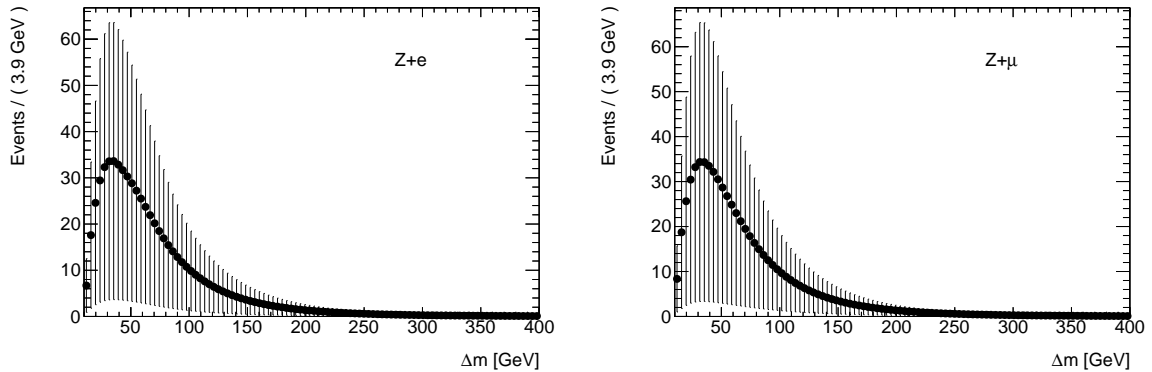


Figure 9.15: Asimov dataset for the background-only hypothesis in the $Z + e$ final state (a) and the $Z + \mu$ final state (b).

9.3.4 Fit to Data

The fit to data using the combined signal and background model is performed simultaneously for the three categories and each of the two flavour channels. The total number of events observed in each signal region is summarised in Table 9.7, along with the estimated background before and after fitting

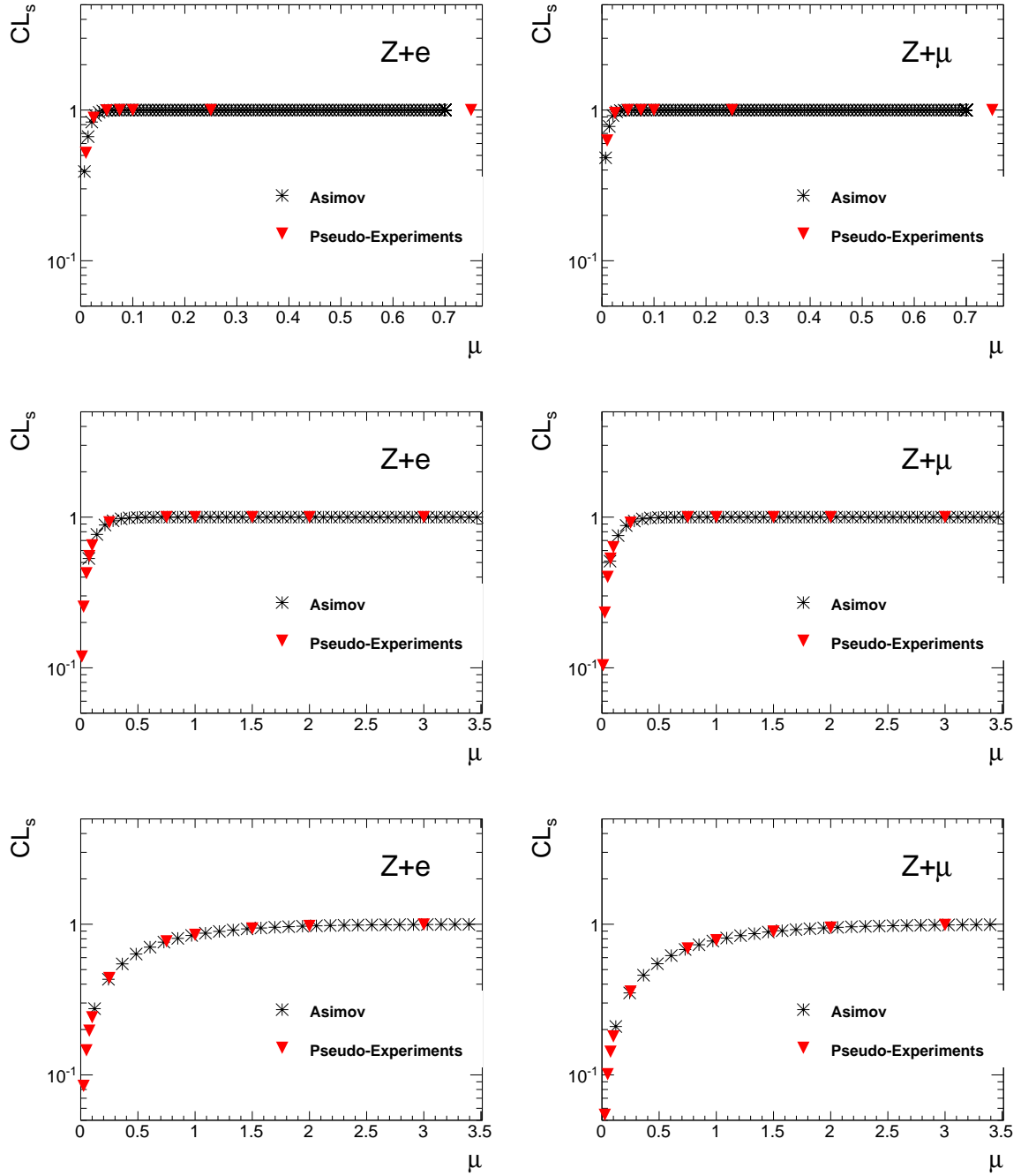


Figure 9.16: Comparison of CL_s results obtained using pseudo-experiments and the asimov approximation for the type-III seesaw model at masses of 120 GeV (top), 300 GeV (middle) and 500 GeV (bottom) for the combined fit to the three subcategories in the $Z + e$ (right) and $Z + \mu$ (left) final state.

the total background model to the data. It should be noted that in every category the normalisation of at least the leading background is determined from the fit, which explains the larger uncertainties on the post-fit normalisations. The projections of the fit results under the background-only hypothesis are shown in Fig. 9.17 for the combination of the three categories in each flavour channel. Good agreement

Process	$Z + e$			$Z + \mu$		
	4ℓ SR	$3\ell + jj$ SR	3ℓ -only SR	4ℓ SR	$3\ell + jj$ SR	3ℓ -only SR
	Before combined background-only fit					
ZZ	10.9 ± 0.6	11.7 ± 0.8	91 ± 5	21.4 ± 1.1	7.5 ± 0.6	90 ± 5
WZ	0.08 ± 0.01	35.3 ± 3.1	337 ± 28	—	46 ± 4	480 ± 40
$Z + \gamma$	—	2.3 ± 0.8	35 ± 11	—	—	—
Reducible	—	1.6 ± 0.5	38 ± 14	1.5 ± 0.3	8.8 ± 3.0	79 ± 22
$\tilde{t}\tilde{t} + V, VVV^{(*)}$	1.2 ± 0.2	7.8 ± 1.7	2.3 ± 0.4	1.5 ± 0.2	9.5 ± 2.1	3.3 ± 0.5
Total Background	12.2 ± 0.7	59 ± 4	504 ± 34	24.4 ± 1.2	72 ± 6	652.3 ± 65.9
	After combined background-only fit					
ZZ	15 ± 4	13.4 ± 2.3	107 ± 9	22 ± 5	10.1 ± 1.6	88 ± 8
WZ	0.08 ± 0.03	39 ± 6	393 ± 28	0.02 ± 0.02	56 ± 9	460 ± 40
$Z + \gamma$	—	2.2 ± 0.8	34 ± 11	—	—	—
Reducible	—	1.8 ± 1.2	37 ± 13	1.8 ± 0.9	10.2 ± 2.8	92 ± 24
$\tilde{t}\tilde{t} + V, VVV^{(*)}$	1.1 ± 0.3	7.5 ± 1.7	2.5 ± 0.6	1.5 ± 0.4	9.1 ± 2.1	3.3 ± 0.8
Total Background	16 ± 4	64 ± 7	574 ± 34	25 ± 5	85 ± 10	643.0 ± 47.3
Data	16	64	573	25	86	651

Table 9.7: Observed and expected number of events in the six signal regions, before and after the combined unbinned maximum-likelihood fit. The pre-fit uncertainties represent the total systematic uncertainties on the background estimates. The post-fit uncertainties are determined by the maximum-likelihood fit.

is observed between the pre-fit and post-fit normalisations for the 4ℓ and $3\ell+jj$ categories in the $Z + \mu$ flavour channel. The largest shift in the normalisation due to the fit is found in the 4ℓ category for the $Z + e$ flavour channel, where the fitted ZZ/γ^* normalisation exceeds the prediction by 35%. The WZ/γ^* and ZZ/γ^* normalisations increase by roughly 15% in the $3\ell+jj$ and 3ℓ -only categories in the $Z + e$ flavour channel, and 30% in the $3\ell+jj$ category in the $Z + \mu$ flavour channel. The projections of the fit result of the combined background fit into the separate categories in the $Z + e$ and $Z + \mu$ channel are shown in Figure 9.18. A good agreement between the fit result and the data is observed in all categories. Figure 9.19 shows the mutual correlation coefficients of the signal strength μ and the nuisance parameters for the $Z + e$ final state in Fig. 9.19(a) and the $Z + \mu$ final state Fig. 9.19(b). No correlation is observed between any of the other fit parameters and the signal strength μ (muSignal) at a type-III seesaw resonance mass of 300 GeV. Some correlations are found, as expected, between the nuisance parameters associated to the shape uncertainties of the WZ/γ^* and ZZ/γ^* background components. The largest correlation is found between the normalisation of the WZ/γ^* and the reducible background in the 3ℓ -only region for both lepton flavors (named "Rest" in the plot), attributed to a very similar shape in the turn on region. The correlation between the two normalisation parameters is reflected in the uncertainty on the fitted value in in Table 9.7. The best-fit values for the nuisance parameters are evalu-

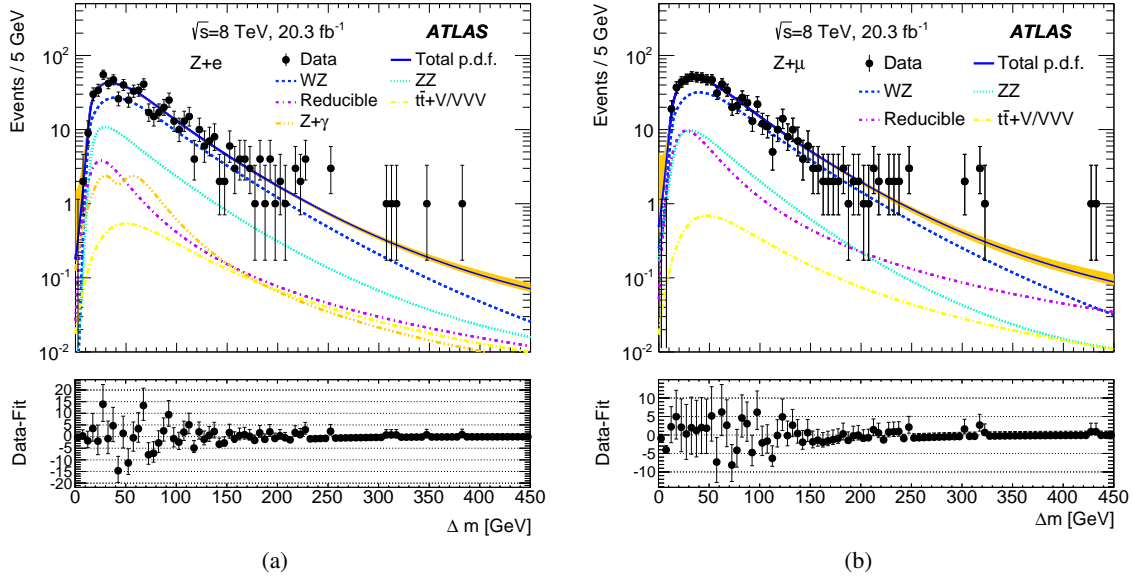


Figure 9.17: Projections onto the Δm variable of the background-only unbinned maximum-likelihood fits, shown superimposed on the data with the three categories in each flavour channel added together. The $Z + e$ flavour channel is shown in (a), and the $Z + \mu$ channel is shown in (b). The contributions of the separate background components to the total background fit are also shown. The error bars on the data points represent statistical uncertainties. The orange error band imposed on the fit is determined from the 1σ variation of the uncertainties on fit parameters. Good agreement is observed between the background model and the data.

ated both for the background-only hypothesis, and a signal-plus-background hypothesis at an arbitrary type-III seesaw resonance mass of 300 GeV. The results for the bachelor electron flavour are shown in Fig. 9.20 and for the bachelor muon flavour in Fig. 9.21. The shifts from the initial values of 0 and their errors are evaluated in units of the pre-fit uncertainty of the given parameter. A full list of the naming convention of the parameters can be found in Appendix C. All nuisance parameters are well contained within one standard deviation. In the $Z + e$ final state no significant deviation is observed between the best-fit values of the nuisance parameters found for the fixed and the floating signal strength μ . In cases where the uncertainty on the nuisance parameter is close to unity, no further constraint on this parameter is given by the fit to the data. This is the case for the nuisance parameters associated to the cross-section uncertainties or the luminosity, denoted as $\theta_{XS_{BKG}}$ and $\theta_{XS_{Lumi}}$. The largest constraints are found for the shape parameter in case of the $Z + \gamma$ and the nuisance parameters associated to the Diboson modelling in the $3\ell+jj$ region. The largest pull of the nuisance parameter is found in case of the ZZ/γ^* shape description and the nuisance parameter associated to the shape of the reducible background denoted, $\theta_{Shape_Zjsigma}$. A similar picture is seen for the best-fit values of the nuisance parameters in the $Z + \mu$ final state. The most significant pull toward higher values is observed for the reducible background denoted as θ_{XS_Zj} , which is also attributed to the correlation observed between the WZ/γ^* and reducible background in the turn-on region.

9.4 Statistical Evaluation of the Results

This section details the different aspects of the statistical evaluation of the results. These include the calculation of the discovery significance, the results from the model dependent limit setting and a more

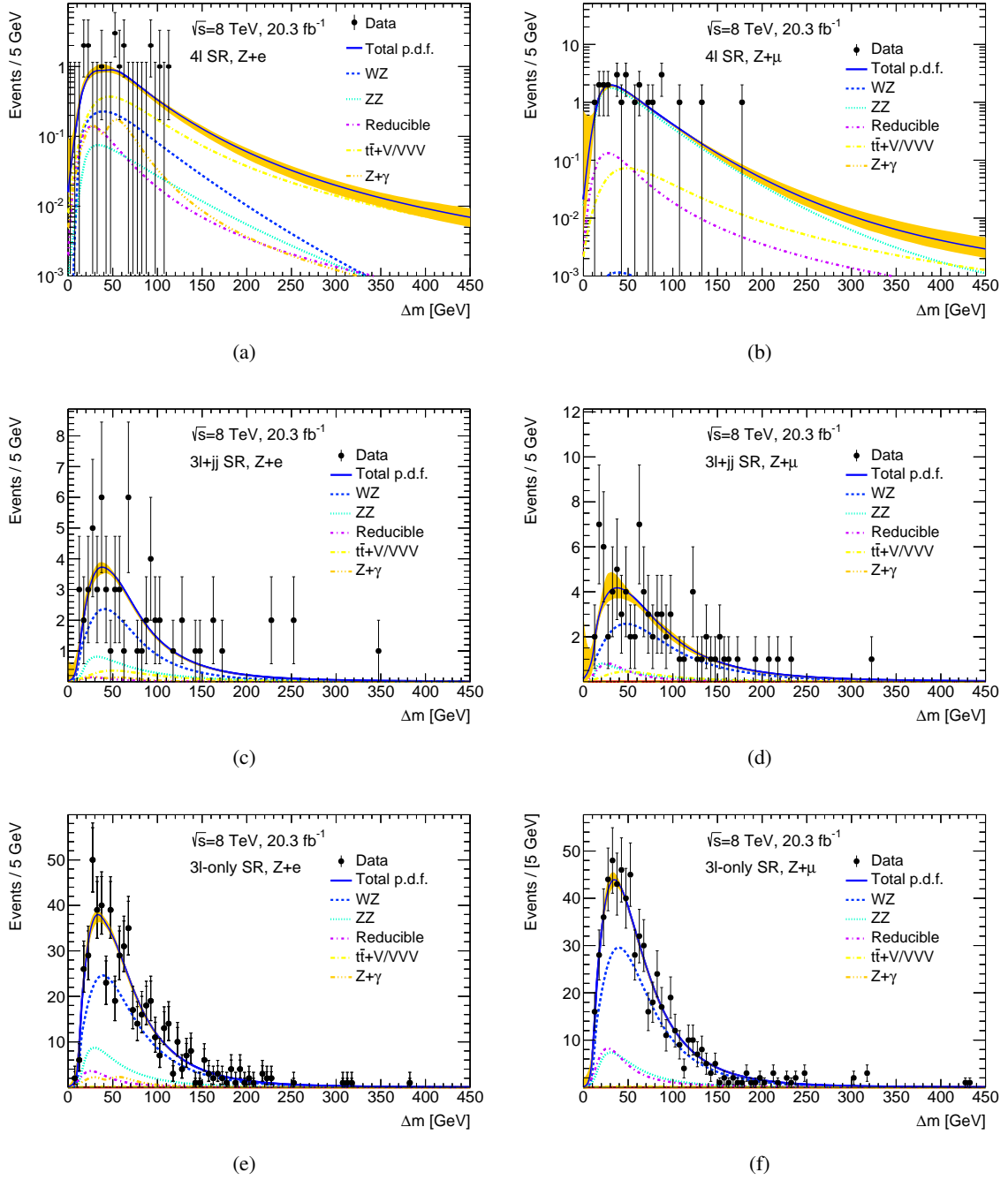
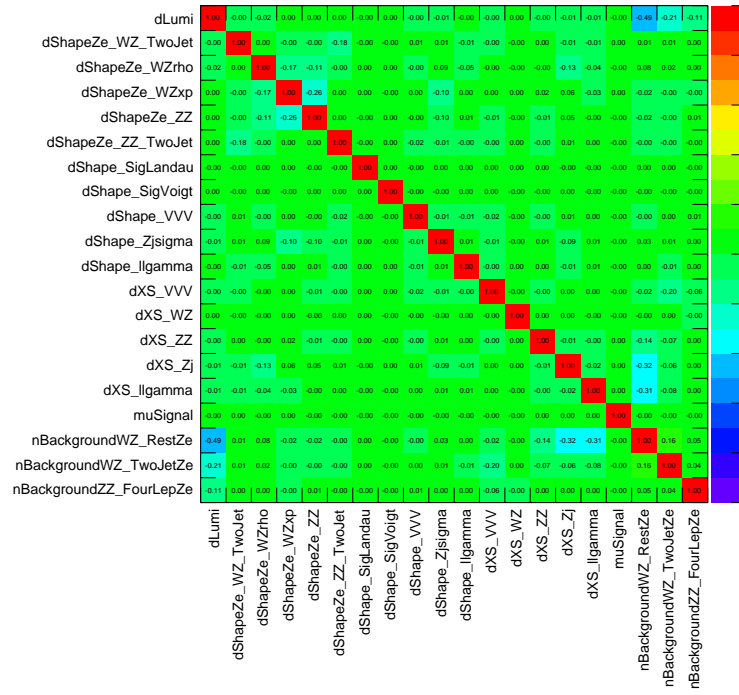
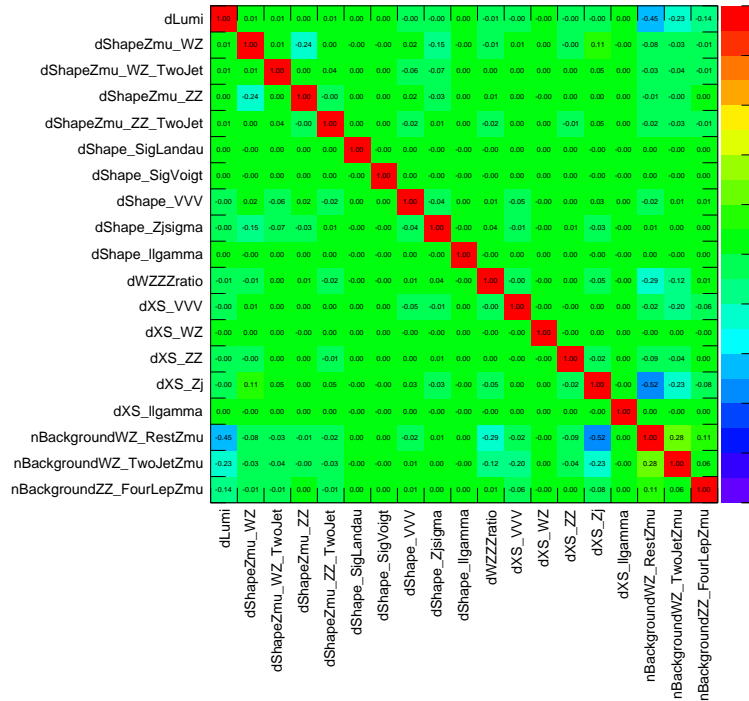


Figure 9.18: Projections onto the Δm variable of the background-only unbinned maximum-likelihood fits, shown superimposed onto the data separately for the three categories in each flavour channel. The $Z+e$ flavour channel is shown on the left-hand side, and the $Z+\mu$ channel is shown on the right-hand side, with the 4ℓ (top), $3\ell+jj$ (middle) and 3ℓ -only (bottom). The contributions of the separate background components to the total background-only fit are also shown. The error bars on the data points represent statistical uncertainties. Good agreement is observed between the background models and the data in all categories.



(a)



(b)

Figure 9.19: Correlation coefficients for the unconstrained fit parameters of the $Z + e$ (a) and $Z + \mu$ (b) flavour channel, some correlations are observed between the normalisations of the different background p.d.f.s if shapes are similar.

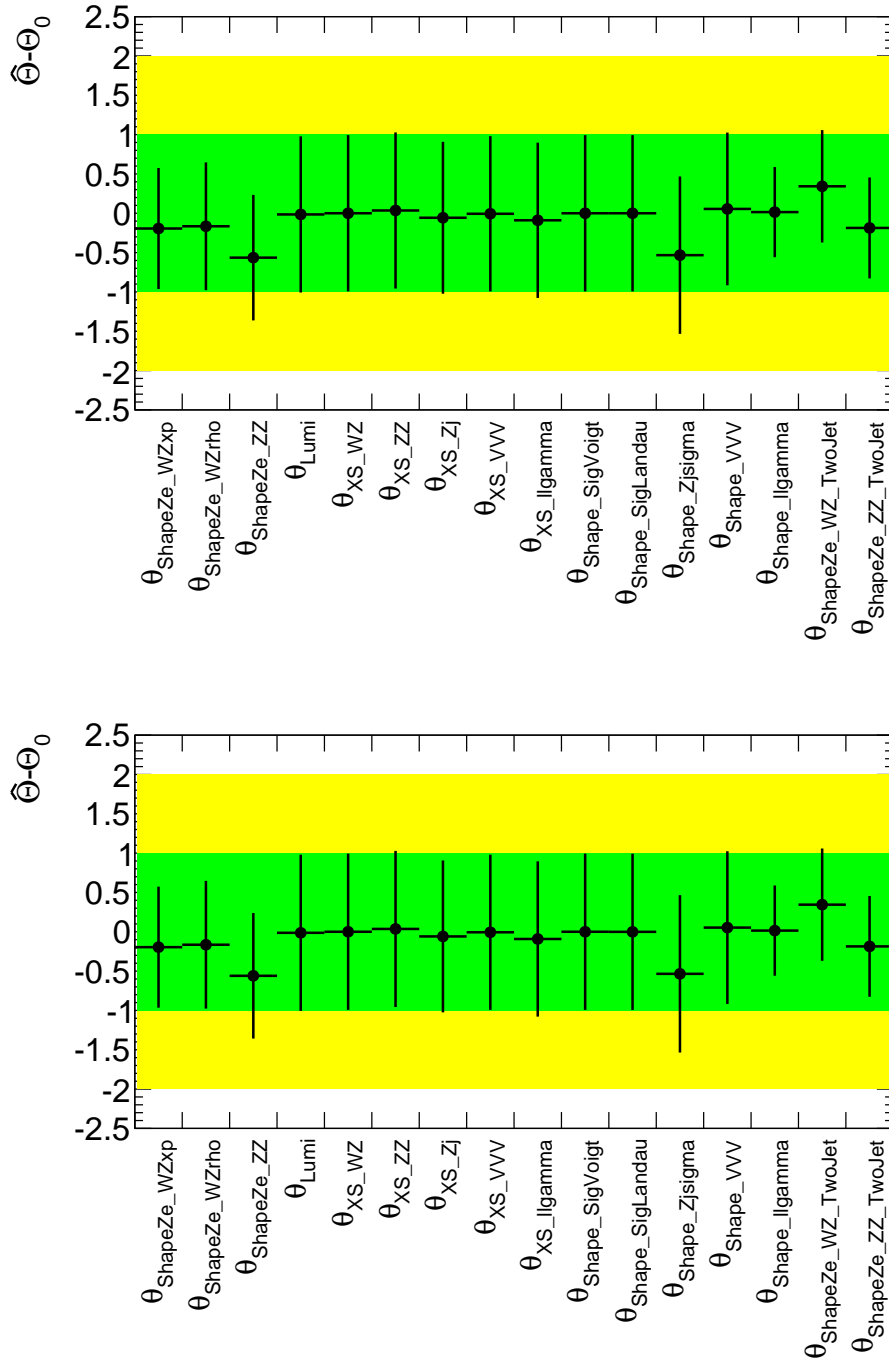


Figure 9.20: Pulls of the Nuisance parameters for the simultaneous fit to the three signal regions in the $Z + e$ final state. Upper plot: background only, i.e. signal strength fixed to 0. Lower plot: floating signal strength for a seesaw model signal hypothesis of 300 GeV.

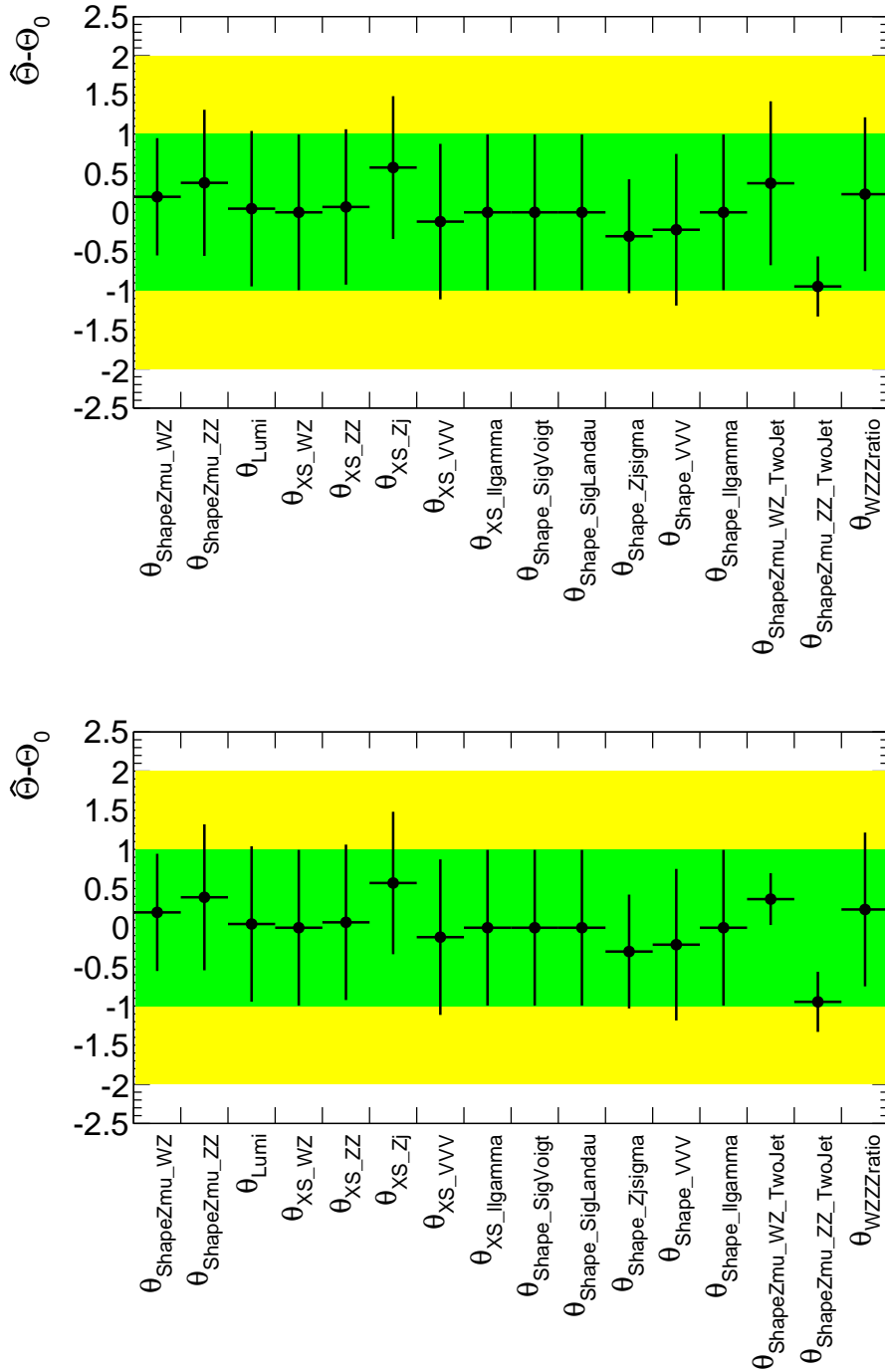


Figure 9.21: Pulls of the Nuisance parameters for the simultaneous fit plot to the three signal regions in the $Z + \mu$ final state. Upper plot: background only, i.e. signal strength fixed to 0. Lower plot: floating signal strength for a seesaw model signal hypothesis of 300 GeV.

general interpretation in the context of a generic heavy resonance within a fiducial region.

9.4.1 Calculation of the Discovery Significance

The discovery significance is calculated by searching for a potential signal and evaluating the compatibility of the data with the background-only hypothesis ($\mu = 0$). This is quantified by the local- p_0 value, i.e. the probability for a dataset generated under the background-only hypothesis to be in same or worse agreement than what is observed in the data. Large p_0 -values correspond to datasets that agree well with the background-only hypothesis, while small p_0 can be interpreted as hints to a positive signal. The local- p_0 value is evaluated every 3 GeV, using the unbinned maximum-likelihood fit, in the range $100 \text{ GeV} \leq m_{L^\pm} \leq 500 \text{ GeV}$. Figure 9.22 shows the expected ($\mu = 1$) and observed local- p_0 values for the vector-like leptons (blue) and the type-III seesaw (red) model for the $Z + e$ flavour channel in Fig. 9.22(a) and the $Z + \mu$ flavour channel in Fig. 9.22(b). The dotted horizontal lines indicate the corresponding significance level. The minimum p_0 -value in the $Z + e$ flavour channel is $p_0 = 0.02$ at a mass of 183 GeV, which corresponds to a local significance of $\sim 2\sigma$. For the $Z + \mu$ flavour channel the minimum $p_0 = 0.05$ value is found at a mass of 109 GeV corresponding to a local significance of $\sim 1.5\sigma$.

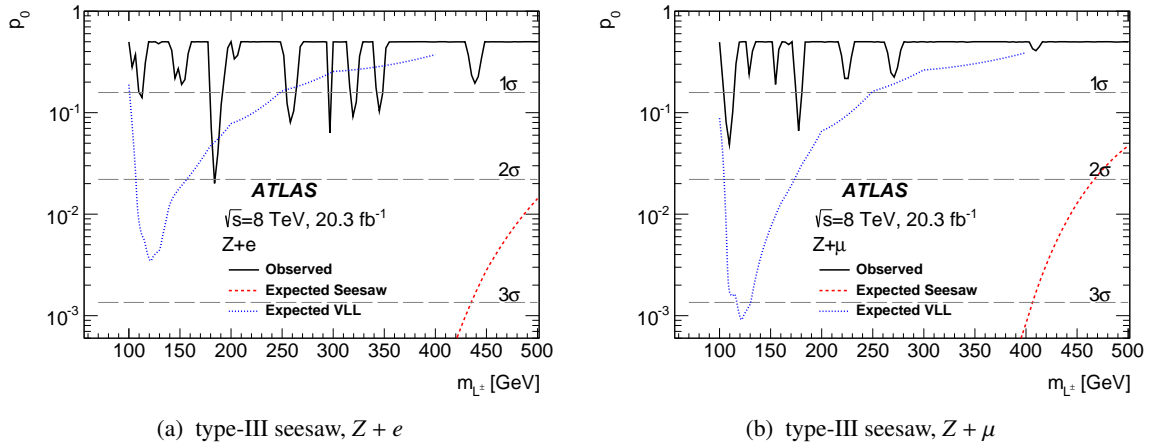


Figure 9.22: p_0 -values for the background-only hypothesis as a function of the heavy lepton mass and the corresponding expected p_0 -values for the vector-like lepton model (blue) and the type-III seesaw model (red). Previously published in [149]

9.4.2 Calculation of the Exclusion Limit on the Production Cross-Section of Type-III Seesaw and Vector-Like Lepton Model

Since no deviation from the Standard Model background expectation is observed in data, exclusion limits at 95 % confidence level are set using the CL_s frequentist method from Eq. (9.14). The limit is obtained by scanning values of the μ hypothesis, computing the CL_s exclusions and identifying the μ_{lim} for which the value equals to 0.05.

The results are interpreted as cross-section limits for the type-III seesaw and the vector-like lepton benchmark model assuming a 100 % branching fraction to either $Z + e$ or $Z + \mu$ final states. The limit is given by the intersection point of the theoretical cross section (red) and the observed limit (closed black dots, connected with black line). The limits are shown for the vector-like lepton model in Figure 9.23,

Model + Final State	Expected	Observed
VLL $Z + e$	[109, 152]	[129, 144] \cup [163, 176] GeV
VLL $Z + \mu$	[105 – 167] GeV	[114, 153] \cup [160, 168] GeV
Seesaw $Z + e$	[100, 436] GeV	[100, 430] GeV
Seesaw $Z + \mu$	[100, 419] GeV	[100, 401] \cup [419, 468] GeV

Table 9.8: Observed 95 % upper limits on the production cross-section. For the combined fits to the three signal regions in the two lepton flavours.

and for the type-III seesaw model in Figure 9.24 and are evaluated in the same 3 GeV intervals as the p_0 -values. The vector-like lepton model is excluded for electron-only the heavy lepton mass ranges of 129–144 GeV and 163–176 GeV, with an expected exclusion in the range of 109–152 GeV. The corresponding observed (expected) exclusion for the muon-only scenario is 114–153 GeV and 160–168 GeV (105–167 GeV). The significantly higher production cross sections for the type-III seesaw model lead to an observed (expected) exclusion in the electron-only scenario in the heavy lepton mass range of 100–430 GeV (100–436 GeV). For the muon-only scenario, the observed exclusion is in the ranges of 100–401 GeV and 419–468 GeV, while the expected exclusion is 100–419 GeV. These numbers are additionally summarised in Table 9.8. The observed and expected exclusion limit split into the separate categories are shown for the $Z + e$ flavour channel in Fig. 9.25(a) and for the $Z + \mu$ flavour channel in Fig. 9.25(b). The highest sensitivity is obtained in the 4ℓ and $3\ell+jj$ category in both channels

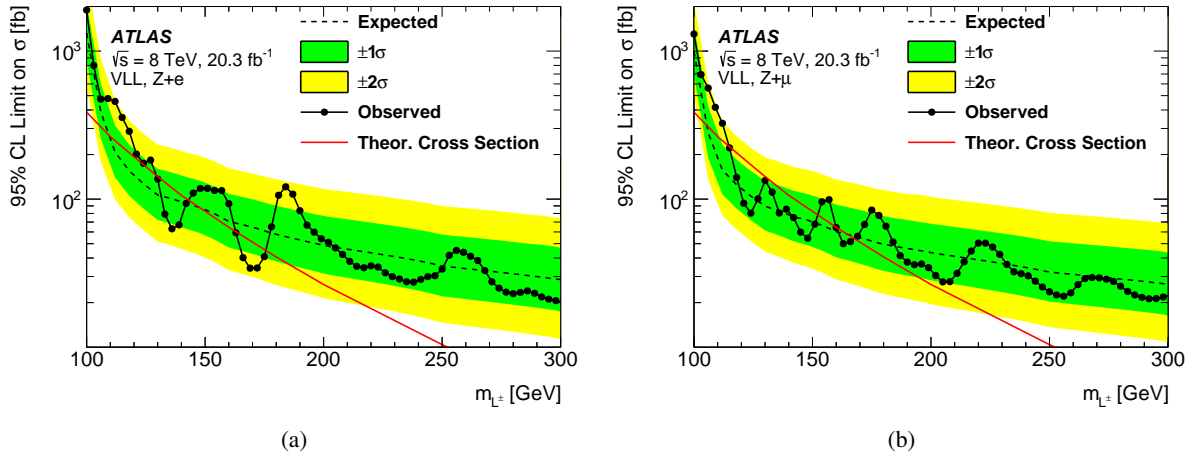


Figure 9.23: 95% CL upper limits on the vector-like lepton production cross section. The left (right) plot shows the limits assuming 100% branching fraction to e/ν_e (μ/ν_μ). The closed circles, connected with a solid line shows the observed limit. The dashed line shows the median expected limit for a background-only hypothesis, with green and yellow bands indicating the expected limits at the $\pm 1\sigma$ and $\pm 2\sigma$ levels. The limit is evaluated in 3 GeV intervals. Previously published in [149].

9.4.3 Calculation of the Exclusion Limit on the Production of a Generic Heavy Lepton Resonance

The above derived model dependent cross-section limits can be extended to other scenarios predicting trilepton resonances with an intermediate Z boson. A more model-independent observable is the *visible*

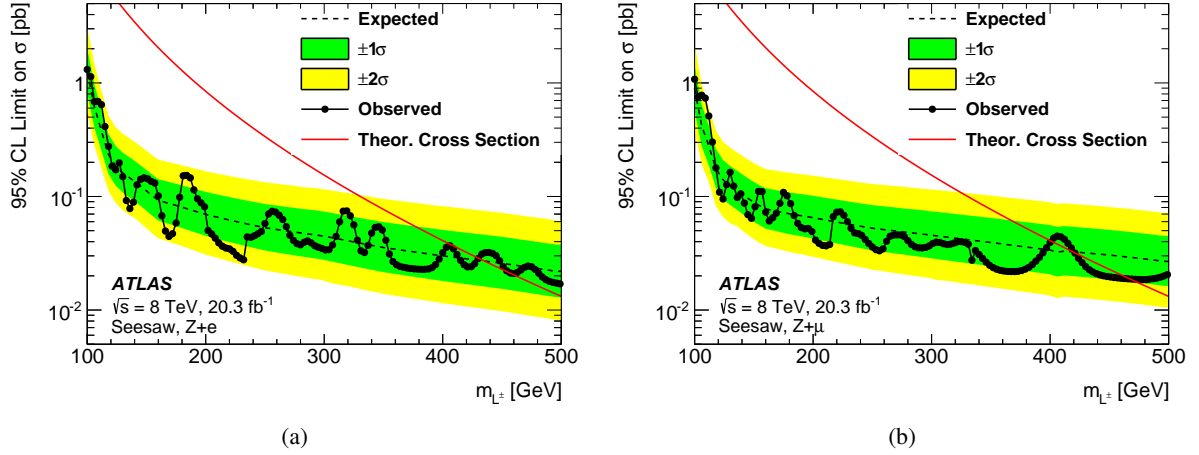


Figure 9.24: 95% CL upper limits on the type-III seesaw production cross section. The left (right) plot shows the limits assuming 100% branching fraction to e/ν_e (μ/ν_μ). The closed circles, connected with a solid line shows the observed limit. The dashed line shows the median expected limit for a background-only hypothesis dataset, with green and yellow bands indicating the expected limits at the $\pm 1\sigma$ and $\pm 2\sigma$ levels. The limit is evaluated in 3 GeV intervals. Previously published in [149].

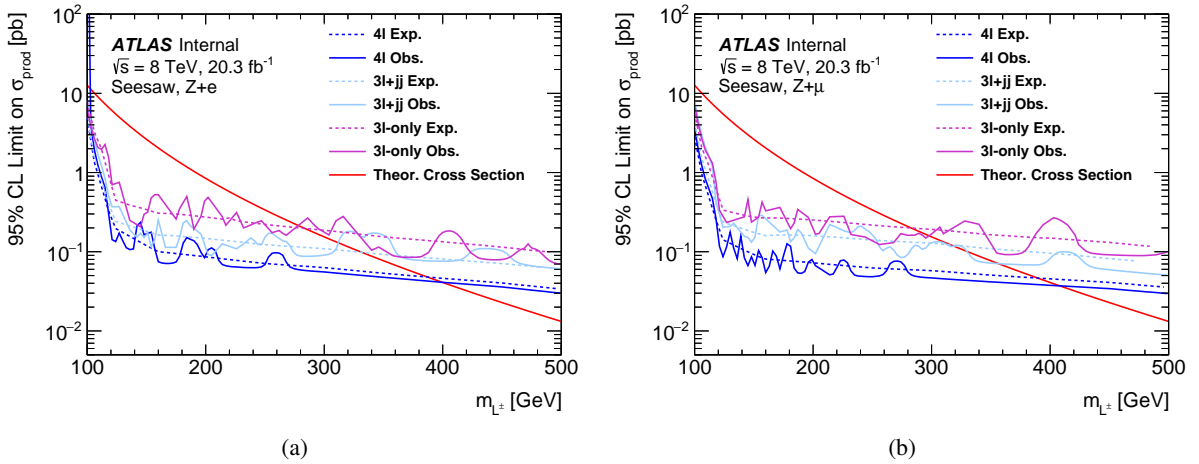


Figure 9.25: 95% CL upper limits on the type-III seesaw production cross section separated into the different categories. The left (right) plot shows the limits assuming 100% branching fraction to e/ν_e (μ/ν_μ). The solid lines show the observed limit. The dashed line shows the median expected limit for a background-only hypothesis dataset. The limit is evaluated in 3 GeV intervals.

cross section, σ_{vis} , defined as the number of observed events with $Z + \ell$ -induced trilepton resonances for a given resonance mass divided by the integrated luminosity of the data sample, 20.3 fb^{-1} . In this generic limit setting approach the signal region in the two flavour channels is not split up into the three categories. This circumvents any dependencies on additional activity in the final states produced by the new heavy lepton resonance. The 95% CL upper limits on σ_{vis} , denoted σ_{95}^{vis} , are derived from a fit to each flavour channel, using only the resonant component of the signal. This is done by setting the fraction of events in the Voigtian part of the signal p.d.f. to $f_V = 1$. The visible cross section limits are also derived every 3 GeV, using the unbinned maximum-likelihood fit, in the range $10 \text{ GeV} \leq \Delta m \leq 450 \text{ GeV}$. The results for the inclusive $Z + e$ and $Z + \mu$ flavour channels, are shown in Figure 9.26. The expected limits on the visible cross section range from roughly 1.5 fb at 100 GeV to approximately 0.2 fb at 500 GeV for the $Z + \ell$ production in both flavours. The observed and expected limits agree well, generally the observed limits are within 1σ of the expected limits.

Visible cross section limits are also derived for the 4ℓ and $3\ell + \text{jj}$ categories, again only using the resonant peak component of the signal. These are shown in Fig. 9.27 and Fig. 9.28. In the 4ℓ category they range from 0.5 fb (0.6 fb) for the $Z + e$ ($Z + \mu$) flavour channel at 100 GeV to 0.1 fb at 500 GeV for both flavours. The expected limits derived in the $3\ell + \text{jj}$ category are slightly stronger with 0.3 fb (0.3 fb) for the $Z + e$ ($Z + \mu$) flavour channel at 100 GeV to 0.1 (0.15 fb) at 500 GeV. In both categories the observed and expected limits agree well.

The limits on σ_{vis} can be used to test specific models after taking into account the models' acceptance with respect to a fiducial volume, \mathcal{A} , and reconstruction and selection efficiency of events within the fiducial volume, ϵ_{fid} . The 95% CL upper limit on the cross section for the model is given by:

$$\sigma_{95} = \frac{\sigma_{95}^{\text{vis}}}{\mathcal{A} \times \epsilon_{\text{fid}}}. \quad (9.21)$$

The acceptance \mathcal{A} is defined as the probability for generated events to lie within a fiducial volume defined by the kinematics of the generated leptons.

Although these limits are derived on the generic fiducial cross sections, they can be translated to a limit on a particular model of new physics. Only the acceptance of the new model to enter the fiducial region must be additionally determined. Since the fiducial region is defined at Monte Carlo generator level, such limits can be obtained without further dependence on any ATLAS detector simulation.

9.4.4 Calculation of Fiducial Acceptance and Fiducial Efficiencies

The fiducial volume is defined to remain independent from the ATLAS detector environment. To facilitate further interpretations of the results presented above, the fiducial acceptance and fiducial efficiencies are calculated.

The fiducial volumes are constructed at *particle level*, i.e. after parton shower and hadronisation, to parallel the definitions of the signal regions at reconstruction level. Only leptons with lifetimes longer than 10^{-11} s are considered at particle level. The prompt charged leptons are *dressed*, i.e. are formed by clustering all photons around the direction of the bare lepton, within a cone of $\Delta R < 0.1$. This leads to a lepton with a partial QED radiation recovery. To fall into the fiducial volume, events are required to contain an L^\pm decaying to a prompt electron or muon and a Z boson, which thereafter decays to electrons or muons. The three leptons from the L^\pm decay are required to have $p_T > 15 \text{ GeV}$ and lie within $|\eta| < 2.5$. At least one lepton must have $p_T > 26 \text{ GeV}$. Two of the leptons must form a same-flavour opposite-charge pair with a mass within 10 GeV of m_Z . The Z boson and the bachelor lepton

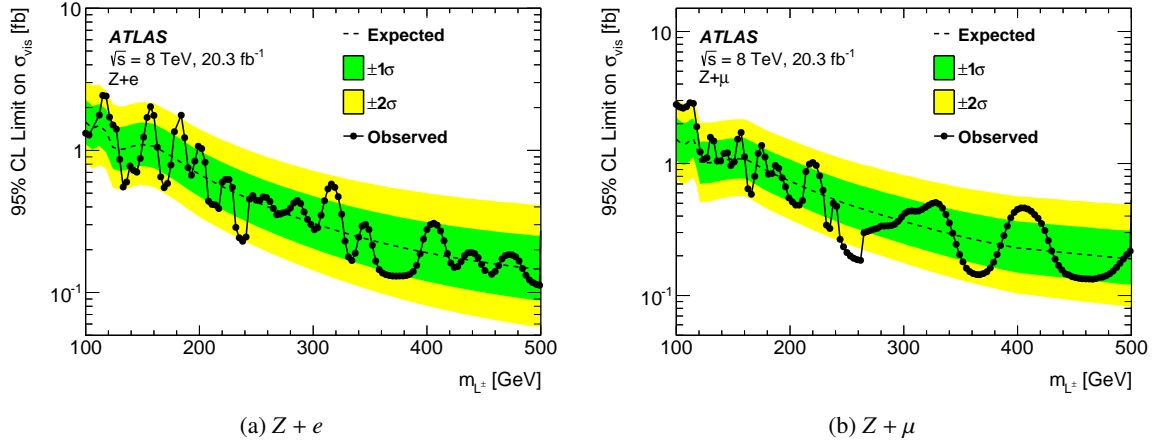


Figure 9.26: Upper limits at 95% CL on σ_{vis} for the $Z+e$ (a) and $Z+\mu$ (b) flavour channels, derived without dividing events into the three categories. The limits are evaluated in 3 GeV intervals. Previously published in [149].

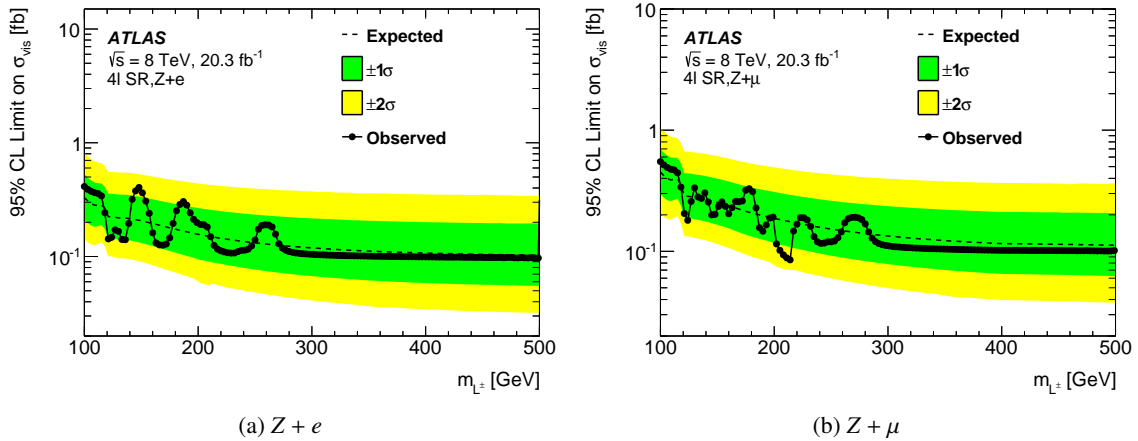


Figure 9.27: Upper limits at 95% CL on σ_{vis} for the (a) $Z + e$ and (b) $Z + \mu$ flavor channels in the 4ℓ category, using only the resonant part of the signal. The limits are evaluated in 3 GeV intervals. The solid line shows the observed limit. The dashed line shows the median expected limit for a background-only hypothesis, with green and yellow bands indicating the expected fluctuations at the $\pm 1\sigma$ and $\pm 2\sigma$ levels. Previously published in [149].

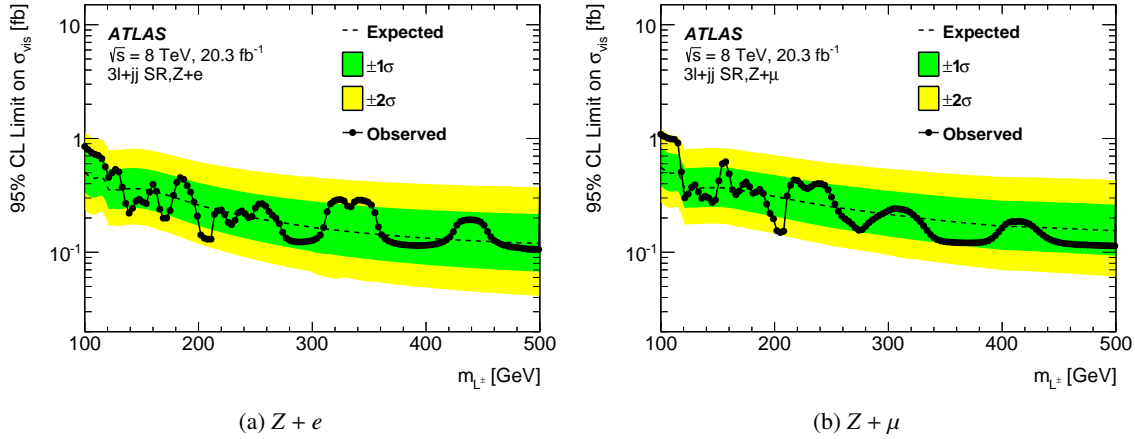


Figure 9.28: Upper limits at 95% CL on σ_{vis} for the (a) $Z + e$ and (b) $Z + \mu$ flavor channels, in the $3\ell+jj$ channel, using only the resonant part of the signal. The limits are evaluated in 3 GeV intervals. The solid line shows the observed limit. The dashed line shows the median expected limit for a background-only hypothesis, with green and yellow bands indicating the expected fluctuations at the $\pm 1\sigma$ and $\pm 2\sigma$ levels. Previously published in [149].

must be separated by $\Delta R < 3$. Also in the fiducial volume the events are divided into flavour channels according to the flavour of the bachelor lepton.

For the type-III seesaw model used in this analysis, the acceptance, \mathcal{A} , of events containing an $L^\pm \rightarrow Z(\ell\ell)\ell$ decay are summarised in table 9.10. They are in the range 60%–65% for most of the generated mass points. The decrease at higher masses is attributed to the cut on the ΔR between the Z boson and the bachelor lepton. The acceptance loss at low masses is due to the lepton p_T requirement, hence the acceptance only reaches 30%–35% at $m_{L^\pm} = 100$ GeV. Similar values are obtained for the vector-like leptons model.

The fiducial efficiencies are calculated for each possible decay of the heavy leptons, and each signal region. Besides the requirement to lie within the fiducial volume, the three identified leptons must be truth-matched to a $L^\pm \rightarrow Z(\ell^+\ell^-)\ell^\pm$ decay, with $\Delta R < 0.2$ between the truth and reconstructed leptons. Figures 9.29-9.32 show the efficiencies as a function of mass for each combination of heavy lepton decays, determined from the type-III seesaw samples. The sharp turn on behaviour between 100 and 200 GeV is present in all figures, for most of the decay channels. For type-III seesaw and vector-like leptons events within the fiducial volume, ϵ_{fid} ranges from 20% to 49% if the other heavy lepton decays to a neutrino and a W , Z , or H boson³. If the other heavy lepton decays to an electron or a muon, the efficiencies range between 25%–35% for most of the mass range. The decrease in efficiency is attributed to the increased probability of incorrectly selecting the bachelor lepton. A slight decrease in the efficiency as a function of mass is seen in final states with a bachelor muon. Here the efficiency for electron and muon final states is around 40% at 120 GeV and roughly 30% at 500 GeV. The event selection efficiencies for the type-III seesaw model in scenarios where the second heavy lepton decays to a W boson are shown in Fig. 9.29 as a function of m_{L^\pm} ; the efficiencies for scenarios where the second heavy lepton decays to a Z or H boson and for the vector-like leptons model are consistent with these efficiencies within the statistical uncertainties. The efficiencies in the 4ℓ region are shown in Fig. 9.30, most of the efficiencies for decay to an additional electron or muon are on the order of 20% for $Z + e$

³ Note that the quoted efficiencies are dependent on the modelling of the polarisation of the Z bosons, due to the requirements imposed on lepton isolation and separation.

final states over most of the mass range. In the $Z + \mu$ final state, again a slight decrease from $\sim 25\%$ at 120 GeV to $\sim 20\%$ at 500 GeV is observed. Final states involving an neutrino and a W , Z , or H boson, are at most 5% for both flavours. A slightly different picture is seen in Fig. 9.31 summarising the $3\ell+jj$ category. Here efficiencies above 10% are only seen for final states in which the other heavy lepton decays to a neutrino and a W , Z , or H boson. These efficiency increase slightly with the mass of the heavy lepton and range between 15%–35%. Figure 9.32 summarises the efficiencies for the 3ℓ -only final state. The efficiencies to neutrinos and an additional W , Z , or H boson are the largest and span between $\sim 15\%$ and $\sim 25\%$ for the $Z + e$ flavour, and $\sim 20\%$ and $\sim 30\%$ for the $Z + \mu$ final state. Final states involving an additional electron or muon are again on the order of 5% for both flavours.

Selection Requirement
at least one L^\pm to decay to three electrons or muons
leptons must have $p_T > 15$ GeV and lie within $ \eta < 2.5$
one lepton with $p_T > 26$ GeV
one same-flavour opposite-charge lepton pair, with $ m_{\ell^+\ell^-} - m_Z < 10$ GeV
require third lepton to satisfy $\Delta R(Z, \ell_3) < 3.0$
separate sample according to flavour of bachelor lepton

Table 9.9: Requirements for events to lie within the fiducial volume.

m_{L^\pm} [GeV]	$Z + e$	$Z + \mu$
100	0.35±0.01	0.31±0.01
120	0.61±0.01	0.60±0.01
160	0.65±0.01	0.65±0.01
200	0.63±0.01	0.65±0.01
250	0.63±0.01	0.62±0.01
300	0.63±0.01	0.65±0.01
350	0.59±0.01	0.62±0.01
400	0.58±0.01	0.60±0.01
450	0.61±0.01	0.60±0.01
500	0.59±0.01	0.59±0.01

Table 9.10: Acceptance \mathcal{A} of type-III seesaw events containing a $L^\pm \rightarrow Z(\ell\ell)\ell$ decay to fall into the fiducial volume ($\ell = e, \mu$). The uncertainties shown arise from the limited statistics in the simulated event samples. The fiducial volume requires the three leptons from the L^\pm decay to have $p_T > 15$ GeV and $|\eta| < 2.5$, and at least one to have $p_T > 26$ GeV. The leptons from the Z decay are required to have invariant mass within 10 GeV of the Z mass, and the Z and the off- Z lepton are required to satisfy $\Delta R < 3$. Previously published in [149].

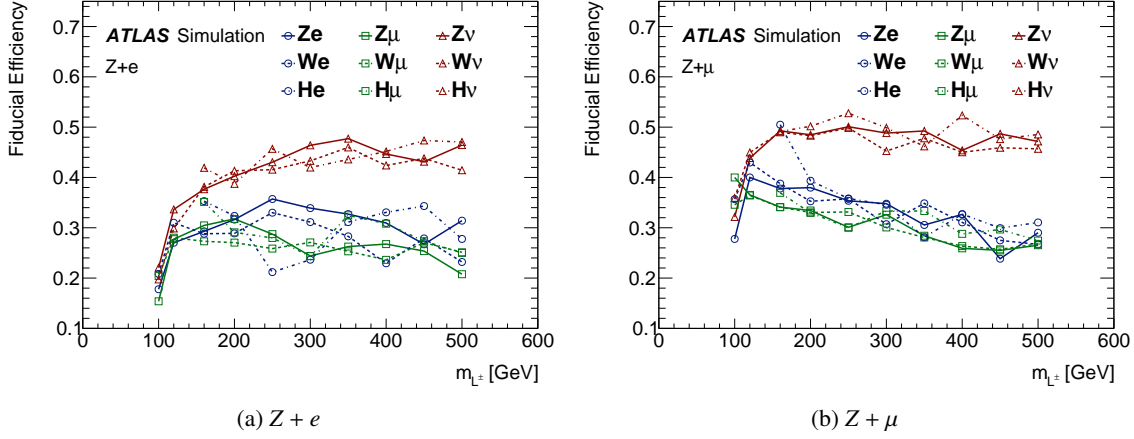


Figure 9.29: Efficiencies for reconstructing and correctly identifying the $L^\pm \rightarrow Z(\ell\ell)\ell^\pm$ decay in events within the fiducial volume for the type-III seesaw model. For $Z + e$ ($Z + \mu$) events, one heavy lepton is required to decay to $Z + e$ ($Z + \mu$), while the second heavy lepton decay is specified in the legend. The fractional statistical uncertainty is of order 10%. Note that decays involving a Higgs boson are forbidden for heavy leptons masses below the Higgs mass. Previously published in [149].

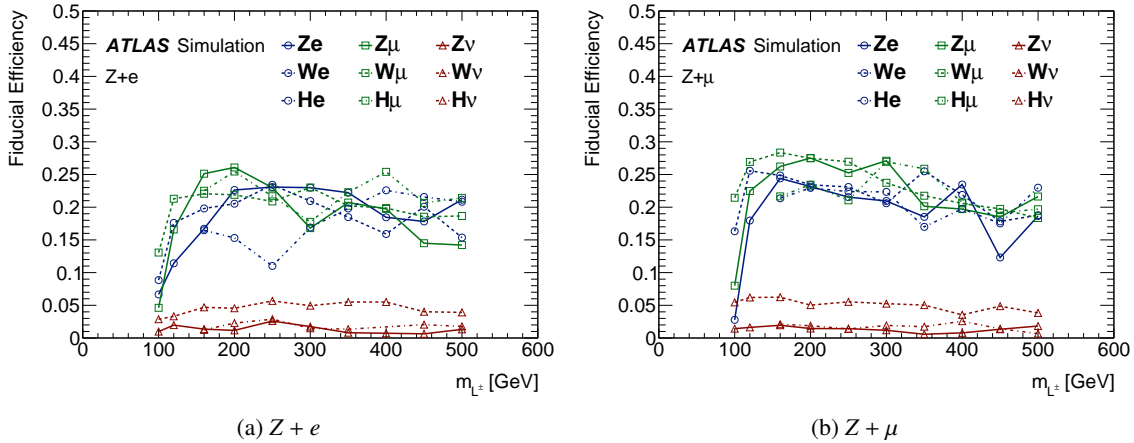


Figure 9.30: Efficiencies for reconstructing and correctly identifying the $L^\pm \rightarrow Z(\ell\ell)\ell^\pm$ decay in the 4ℓ category in events within the fiducial volume for the type-III seesaw model. For $Z + e$ ($Z + \mu$) events, one heavy lepton is required to decay to $Z + e$ ($Z + \mu$), while the second heavy lepton decay is specified in the legend. The fractional statistical uncertainty is of order 10%. Note that decays involving a Higgs boson are forbidden for heavy leptons masses below the Higgs mass. Previously published in [149].

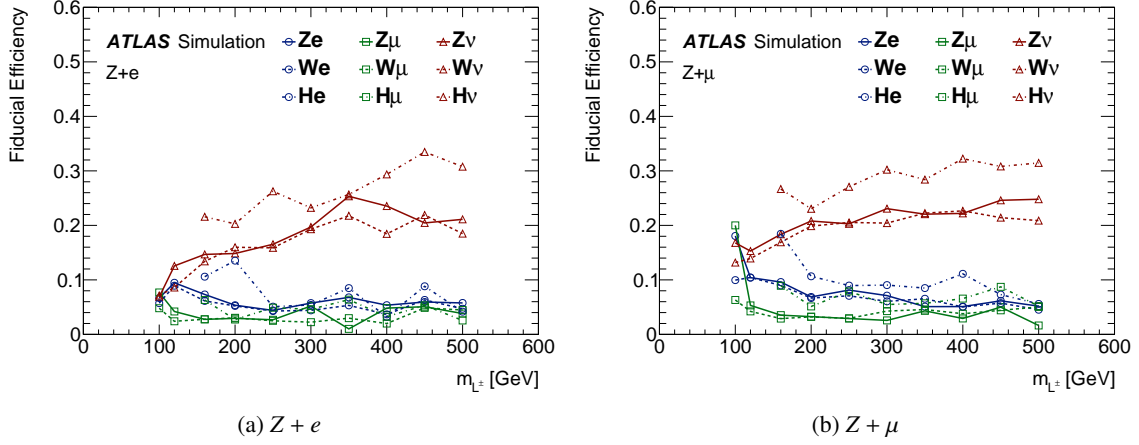


Figure 9.31: Efficiencies for reconstructing and correctly identifying the $L^\pm \rightarrow Z(\ell\ell)\ell^\pm$ decay in the $3\ell+jj$ category in events within the fiducial volume for the type-III seesaw model. For $Z + e$ ($Z + \mu$) events, one heavy lepton is required to decay to $Z + e$ ($Z + \mu$), while the second heavy lepton decay is specified in the legend. The fractional statistical uncertainty is of order 10%. Note that decays involving a Higgs boson are forbidden for heavy leptons masses below the Higgs mass. Previously published in [149].

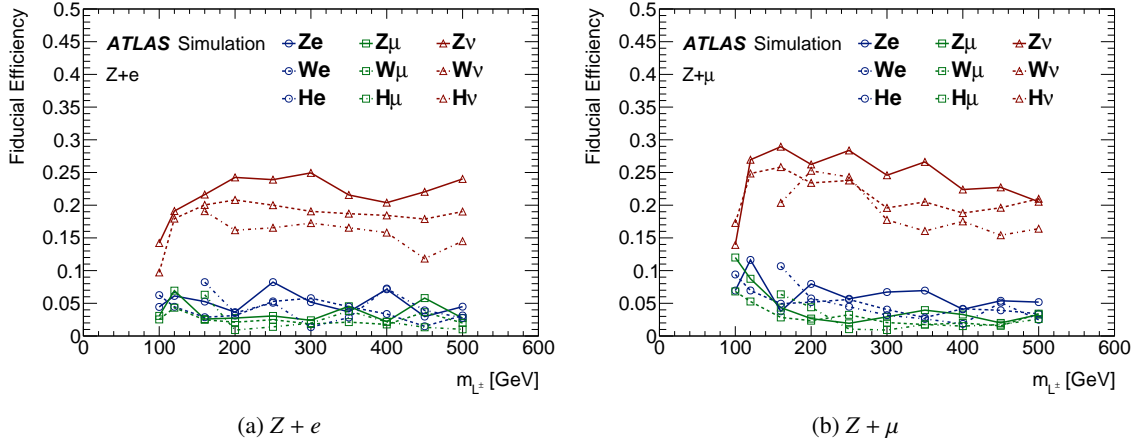


Figure 9.32: Efficiencies for reconstructing and correctly identifying the $L^\pm \rightarrow Z(\ell\ell)\ell^\pm$ decay in the 3ℓ -only category in events within the fiducial volume for the type-III seesaw model. For $Z + e$ ($Z + \mu$) events, one heavy lepton is required to decay to $Z + e$ ($Z + \mu$), while the second heavy lepton decay is specified in the legend. The fractional statistical uncertainty is of order 10%. Note that decays involving a Higgs boson are forbidden for heavy leptons masses below the Higgs mass. Previously published in [149].

Introduction to Silicon Detectors

The following chapters provide a summary of a few selected measurements and projects performed by the author of this thesis, dedicated to R&D projects towards the upgrade of the present ATLAS silicon microstrip detectors. The ATLAS silicon microstrip detector will be one of the two sub-detectors in the upgraded all-silicon Inner Tracker for the running at the High-Luminosity LHC (HL-LHC).

Since the 1980s *semiconductor trackers* have been extensively used as tracking devices in high energy physics experiments. In the range of semiconductors silicon detectors are chosen for high energy physics application, due to their cost efficiency and their availability, as they are easiest to be produced with a high efficiency and resolution. Silicon tracking devices 'act as solid state ionisation chambers' [27] and are to date the most precise tracking devices with spatial resolutions of a few micrometers. Their resolution is up to two orders of magnitude better than in the previously used gaseous chambers. High resolution is crucial for modern particle physics and enables the measurement of secondary vertices, which play a fundamental role in physics involving tau leptons and b quark decays.

Being a solid state detector, silicon detectors have a significantly higher density than gaseous detectors, which results in a larger energy loss for the traversing particle leading to a larger detector signal. The energy deposited by the particles traversing the detector creates electron-hole pairs which move under an applied external electric field toward the respective electrode, where they induce a signal. The mean energy to produce an electron hole pair in silicon is 3.67 eV at room temperature. This is roughly five times smaller than the comparable value for gaseous detectors and facilitates a superior energy resolution. Exploiting the high density of silicon and the small ionisation energy yield, active layers of 100 μm to 300 μm are sufficient to yield adequate signals. This leads to readout times on the order of a few nanoseconds and a typical radiation length of less than 0.5 %. Silicon detectors are employed as the central tracking devices in all LHC experiments and are built to directly surround the beam pipe with distances of a few centimetres from the interaction point. An introduction to the current ATLAS SCT is already given in Section 3.2.2. The upgrade from the LHC to the HL-LHC leads to an increase in the instantaneous luminosity by a factor of five. The radiation will be at a level, demanding the replacement of the current ATLAS inner detector by an all silicon microstrip detector. However the high radiation environment given by the proton-proton interactions at the LHC cause defects in the silicon bulk material, as silicon is a crystalline material. The radiation induced defects in the silicon bulk lead to changes in the *effective doping concentration*, an *increase in the leakage current* and *trapping of single charge carriers*. Especially the latter effect leads to a major degradation of the signal. In addition the radiation induced rise of the noise, significantly impacts the signal-to-noise ratio and thus endangers the

performance and reliability of silicon tracking devices.

This chapter will commence with a general introduction to silicon sensors and their application as tracking devices in high energy physics in Section 10.1. The basic radiation damage mechanisms and radiation induced defects to the silicon bulk are described in Section 10.2, combined with a summary of the irradiation induced effects on the detector operations. This chapter is concluded by an overview on radiation tolerant silicon sensor designs in Section 10.3. For a more thorough introduction to the concepts behind silicon detectors, excellent and comprehensive literature is found in [195–200], upon which the following sections are based.

10.1 Fundamental Properties of Silicon and Silicon Detectors

10.1.1 Intrinsic and Extrinsic Semiconductors

Semiconductors are generally described by their *energy gap* between the *valence* and the *conduction band*, which is at $E_g = 1.12$ eV for silicon at room temperature. Semiconductors are called intrinsic if the concentration of impurities is negligible compared with the thermally generated free electrons and holes pairs, leading to only a few free charge carriers. An *extrinsic* semiconductor is formed by deliberately introducing impurities and defects into the semiconductor lattice. This process is called *doping* and allows to alter conductivity of the semiconductor material. Since silicon is an element of the fourth group of the periodic table, it is generally doped with either elements from the third group (e.g. boron) or the fifth group (e.g. phosphorus, arsenic or antimony). In the latter case four of the five valence electrons will form covalent bonds with the surrounding silicon electrons, while the fifth is loosely bound (~ 45 meV) and thus easily excited into the conduction band at room temperature. These are called *donors*. The effect of donors is described by introducing shallow energy levels into the forbidden energy region close to the conduction band and by that elevating the Fermi level closer to the conduction band. This leads to an increase in the electron concentration and a decrease of the hole concentration. Therefore the electrons are the *majority carries* and holes the *minority carries*. Donor doped silicon is therefore called *n-type* material.

Following the the same argument for doping with elements from the third group (i.e. having a valence electron less), so-called *acceptors*, leads to additional acceptor levels close to the valence band. In this case holes are the majority carries and the acceptor-doped material is called *p-type* material.

10.1.2 Sensor Grade Silicon Material

Currently there are three different production processes for silicon detector material namely: *Czochralski* (Cz), *Float Zone* (FZ) and *epitaxial* silicon. The differences arise due to the growing process involved in their production.

Silicon is the second most prevalent material on the earth, making up more than 25 % of the earth crust. Due to its high reactivity it is either found as an oxide (SiO_2) or as a silicate. To be utilised as a detector material, high purity monocrystalline silicon with a high resistivity (>1 k Ω /cm) and a long minority carrier lifetime is needed.

Starting from SiO_2 (quartz sand) metallurgical grade silicon (95 % to 99 % pure silicon) is fabricated in a series of melting processes. To extract pure silicon, SiO_2 is transformed in chemical reactions to monosilan or trichlorsilan (SiHCl_3). The very-pure silicon is then extracted via hydrogen reduction of the SiHCl_3 at temperatures around 1000 °C. The silicon then grows slowly on ~ 1000 °C hot slimrods.

Most commercially grown silicon is of Cz type, which can be summarised as a pull-from-melt method. The above produced high purity poly-silicon is melted together with additional dopants (re-

quired for the final resistivity) in a rotating quartz crucible. A monocrystalline silicon seed crystal is placed above the melt and drawn upwards whilst being rotated. The silicon at the interface between the melt and the silicon solidifies into a single crystal, sharing the crystal orientation of the seed. The growth is controlled by the pull rate, the rotation speed and the melt temperature. While this method is very cost-effective, it has the drawback of a high amount of impurities, which dissolve for instance from the crucible into the melt. However, by applying an additional magnetic field in the vertical or horizontal direction, convection is prevented and by that a mixing between the contaminated melt near the crucible wall and the pure silicon in the middle is circumvented. Silicon ingots produced within this magnetic field method are called magnetic Czochralski (mCz) ingots.

The second method is the float zone technique, based on a zone-melting principle. Float zone silicon is produced by bringing a high-purity polycrystalline rod face to face to a single crystal silicon seed, that are held in a vertical position and rotated. The process takes place under vacuum or an inert gaseous atmosphere. The zone around the contact is then melted by means of radio-frequency and the seed is brought in contact to the melt formed at the tip of the poly-silicon rod. By gradually shifting the melted zone away from the contact the Si solidifies into a single crystal. Since the impurities tend have a different diffusion constant, they remain in the liquid and a very pure silicon is achieved.

The final method producing detector grade silicon is based on growing a thin layer on a single-crystal substrate and called epitaxial technology. In this method the epitaxial layer adopts the the crystal orientation of the of the substrate and is mono-crystalline.

The final high-purity ingots are then sliced into thin wafers of usually 200 μm to 300 μm thickness which undergo numerous processing steps before being used as a silicon detector. The standard production steps for a silicon microstrip detector follow the routine developed in the 1980s by J. Kemmer [201] and briefly summarised in the following for a standard p-in-n type sensor. The initial lowly doped n-type material is chemically cleaned and heated in an oxygen atmosphere to 1035 $^{\circ}\text{C}$, which results in a uniform oxide coating of the wafer. This oxide wafer is then processed in several photolithographic manufacturing steps. The first step is to apply a photoresist on the junction layer. By masking dedicated areas, the following illumination, development, etching of the SiO_2 and cleaning, will result in a structured wafer front, where in the regions of the negative of the mask the SiO_2 layer remains. The wafer will then undergo p^+ doping, for instance by boron, which will only form in the uncovered regions. The depth of this p^+ layer is controlled by the implantation energy and doping dose. Afterwards the backside is implanted with arsenic, forming the n^+ backside. Thereafter the sensor is annealed by heating it to 600 $^{\circ}\text{C}$ for 30 min. This repairs eventual damages to the silicon lattice and leads proper implantation of the doping atoms in the lattice. The contacts are formed by aluminisation by evaporation on both surfaces. The aluminium on the structured front, provides the electrical connection, whereas the aluminium on the back-side forms the ohmic contact. A further photolithographic step gives further structures to the aluminium electrodes. Finally the sensor is again heated to 420 $^{\circ}\text{C}$ to obtain an excellent connection between the silicon and the aluminium. A schematic of a silicon strip sensor is shown in Fig 10.1. The wafer front is divided into equidistant readout strips, with typical distances of 20 μm to 100 μm .

10.1.3 pn-junction

A reversely biased *pn-junction* is the foundation of silicon detectors. It is formed by the interconnection of a p-doped and an n-doped material, which results in a charge-carrier-concentration gradient between the two materials, schematically represented in Fig. 10.2. Close to the junction majority charge carriers from either side, diffuse into the opposite doped side and recombine with the free charge carriers. This leads to a region without any free charge carries, the so-called *depletion region*. Since the acceptor and donor ions are left without their reversely charged free carriers, an electric field is generated which

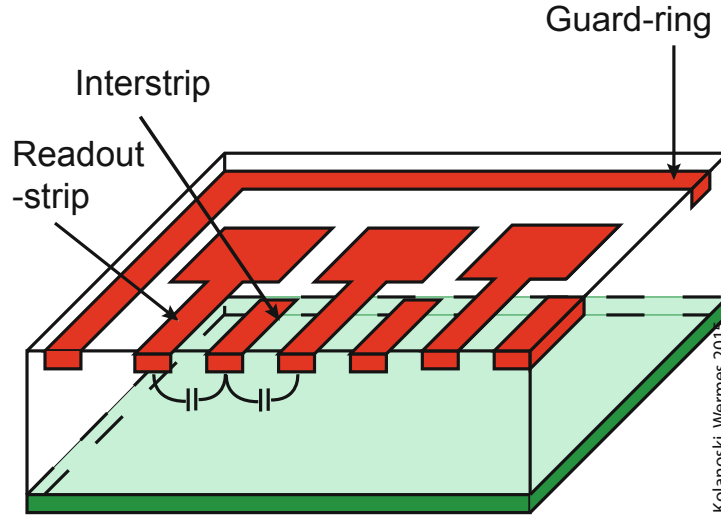


Figure 10.1: Principle design of a planar silicon strip detector. Taken from Ref. [202]

acts against the diffusion. At equilibrium between the diffusion current and the drift current a bipolar space-charge region is built up, surrounding the junction, which is depleted from free charge carriers. The potential difference, corresponding to the difference in the Fermi level E_F^2 on the n-side (E_{F_n}) and the one on the p-side (E_{F_p}), is known as the *built-in voltage* V_{bi} . The electric-field strength E and the electric potential ϕ can be solved using Poisson's equation. Under the assumption that the free charge carrier concentration is zero the Poisson equation in the one-dimensional case is given by

$$-\frac{d^2\phi(x)}{dx^2} = \frac{\rho_{el}}{\epsilon\epsilon_0} = \frac{eN_{\text{eff}}}{\epsilon\epsilon_0}, \quad (10.1)$$

where $\epsilon\epsilon_0$ is the dielectric constant ($\epsilon\epsilon_0 = 11.9$ for Si), e is the electric charge and $N_{\text{eff}} = N_D - N_A$ is the effective doping concentration. The electric field distribution is found by integrating over Eq. (10.1), using the boundary condition $E(x = W) = \frac{d}{dx}\phi(x = W) = 0$, where W is the thickness of the depleted region.

As also seen in Fig. 10.3 is the linear development of the field, for a homogenous space charge density ρ_{el} , inside the space charge region from its maximum absolute value at $x = 0$ to 0 at $x = W$

$$E(x) = \frac{N_{\text{eff}}}{\epsilon\epsilon_0}(x - W), \quad 0 \leq x \leq W \text{ and } W \leq d, \quad (10.2)$$

where d is the thickness of the pn-junction. A further integration with the boundary condition $\phi(x = W) = 0$ gives a parabolic behaviour of the potential

$$\phi(x) = \frac{1}{2} \frac{eN_{\text{eff}}}{\epsilon\epsilon_0}(x - W)^2 \quad 0 \leq x \leq W \text{ and } W \leq d. \quad (10.3)$$

The corresponding electron potential energy $-e\phi$ is also depicted in Fig. 10.3. In case of no external bias voltage, $\phi(x = 0)$ corresponds to V_{bi} . By applying an external voltage the width of the space charge region is modified. An external voltage applied in the same direction as V_{bi} removes further majority

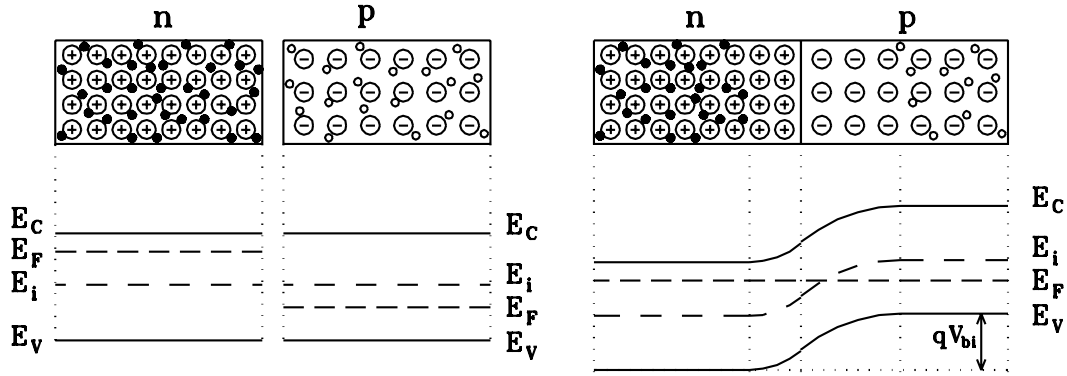


Figure 10.2: Schematic of a pn-junction at thermal equilibrium, with the respective energy levels of the conduction band E_C , the Fermi level E_F , the valence band E_V and the intrinsic level E_i . The left figure shows the separated p- and n-doped sides, while they are brought in contact on the right hand side. Figure taken from Ref. [197]

carriers, thus extending the space charge region. The junction is now reversely biased. After convention this voltage is defined as positive. The width of the space charge region under a reverse bias voltage V is then given by

$$W(U) = \sqrt{\frac{2\epsilon\epsilon_0}{e|N_{\text{eff}}|}(V + V_{\text{bi}})} \quad W \leq d. \quad (10.4)$$

In silicon sensors a pn-junction is generally formed by a highly doped ($N_A > 10 \times 10^{18} \text{ cm}^{-3}$) p⁺-implant in a low doped ($N_D \sim 10 \times 10^{12} \text{ cm}^{-3}$) n-bulk material. Hence the space charge region extends almost solely into the lower doped side of the junction. A sensor is called fully depleted if the space-charge region extends to the backside of the detector, up to which point the maximum of the electric field at the junction increases with $E_{\text{max}} \propto \sqrt{V}$. The depletion voltage V_{dep} can be approximated, given that $V_{\text{dep}} \gg V_{\text{bi}} \sim 0.5 \text{ V}$, to

$$V_{\text{dep}} = \frac{e}{2\epsilon\epsilon_0} N_{\text{eff}} d^2, \quad (10.5)$$

and is proportional to the square of the sensors thickness d . The depletion voltage is one the crucial sensor parameters, as it indicates the minimum operation voltage. If the reverse bias voltage exceeds the depletion voltage the sensor is called over depleted and an additional constant field of $(V - V_{\text{dep}})/d$ is added at each point of the sensor. A second important figure of merit in the operation of silicon detectors is the leakage or reverse current I_{leak} , which has a large effect on the noise and power consumption of a detector. The leakage current arises from several sources, such as diffusion of free charge carriers from the undepleted volume into the sensitive space space charge region, and from the thermal generation of charge carriers through process- and radiation induced defects. The latter arises from defects in the depleted volume, $I_{\text{bulk}} \propto W \propto \sqrt{V}$ for $V \leq V_{\text{dep}}$ and saturates if the applied reverse bias is larger than the depletion voltage

$$I_{\text{leak}} \sim I_{\text{bulk}} \frac{e n_i W V A}{\tau_g}, \quad (10.6)$$

where n_i is the intrinsic carrier concentration, τ_g is the carrier generation lifetime and A is the effective area of the diode. As the reverse current arises mainly due to a temperature dependent process, a strong

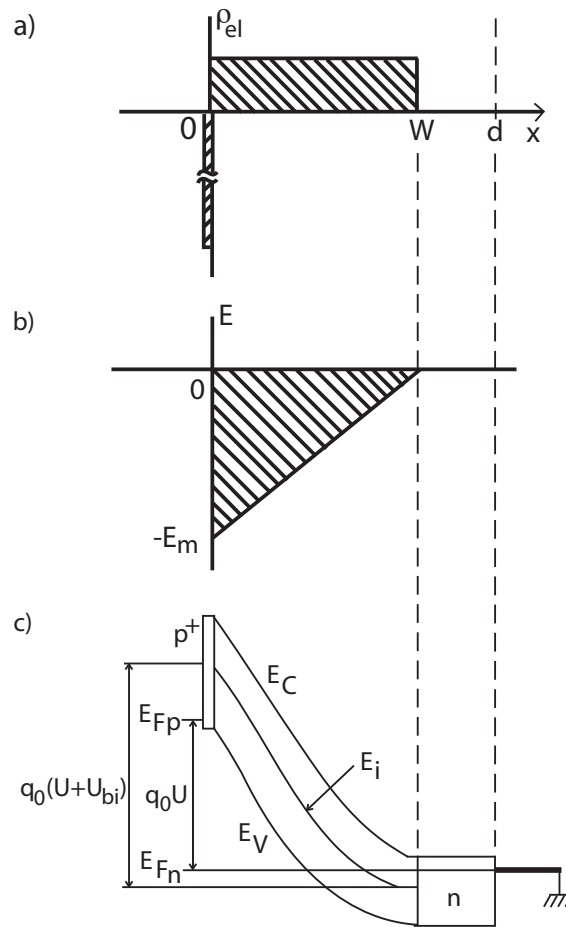


Figure 10.3: Schematic representation of the (a) space charge density, (b) electric field E and (c) electric potential ρ_{el} of a pn-junction with an asymmetric doping concentration.

correlation between the temperature and the current is found

$$I_{\text{leak}}(T) = I_{\text{leak}}(T_R) \cdot \left(\frac{T}{T_R}\right)^2 \exp\left(-\frac{E_{g,\text{eff}}}{k_B} \left[\frac{1}{T} - \frac{1}{T_R}\right]\right), \quad (10.7)$$

where k_B is the Boltzmann's constant, T_R a reference temperature, and $E_{g,\text{eff}}$ an effective energy band gap, which is 1.21 eV [203] As a rule of thumb the effective energy doubles for every temperature increase of 8 °C [198].

10.1.4 Capacitance

Since the depletion layer efficiently separates the electrodes, it shows an insulating behaviour and acts as a capacitor. Hence the capacitance C is a further important detector parameter, as it influences the noise and can be used to determine the depletion voltage. The capacitance is defined as the incremental change of the depletion-layer charge dQ on each side of the junction upon an incremental change of the

applied voltage dV

$$C = \frac{dQ}{dV}. \quad (10.8)$$

In an abrupt pn-junction the space charge Q is expressed as $Q = e|N_{\text{eff}}|AW$, so that the incremental change is given by $dQ = e|N_{\text{eff}}|AdW$. Together with Eq. 10.4 the capacitance C can be written as

$$C = \frac{dQ}{dV} = \frac{dQ}{dW} \frac{dW}{dV} = A \sqrt{\frac{e\epsilon\epsilon_0|N_{\text{eff}}|}{2V}} = \epsilon\epsilon_0 \frac{A}{W(V)}. \quad (10.9)$$

Hence the capacitance decreases with $C \propto 1/\sqrt{V}$ for $V \leq V_{\text{dep}}$. However, as soon as the the applied voltage exceeds the depletion voltage, the capacitance C reaches a constant value

$$C_{\text{end}} = \epsilon\epsilon_0 \frac{A}{d}. \quad (10.10)$$

This capacitance is also referred to as end or geometrical capacitance. With this specific behaviour the depletion voltage from a sensor can be determined from the kink in the doubly logarithmic plot of a C–V measurement.

10.1.5 Charge Motion and Signal Collection

The interaction of a particle with the detection material forms the basis of any detector concept. In silicon sensors, charged particles deposit a fraction of their energy in the interaction through the generation of electron-hole pairs along their paths, whereas photons interact, depending on their energy range, either via Compton scattering, the photoelectric effect or pair production.

The mean energy loss of a charged particles traversing the silicon sensor, through scattering processes with the electrons along the particle track is described by the *Bethe-Bloch formula*

$$-\left\langle \frac{dE}{dx} \right\rangle = Kz^2 \frac{Z}{A} \frac{A}{\beta^2} \left(\frac{1}{2} \ln \frac{2m_e c^2 \beta^2 \gamma^2 T_{\text{max}}}{I^2} - \beta^2 \right) + \dots \quad (10.11)$$

where $\langle dE/dx \rangle$ is the energy loss of a particle given in eV/g/cm^2 , $K \sim 0.307 \text{ MeVcm}^2$ is a constant, z is the charge of the traversing particle in units of the electron charge, Z/A is the atomic number/mass of the absorption medium, $m_e c^2$ is the rest energy of the electron, β is the velocity of the traversing particle in units of the speed of light, γ is the Lorentz factor and I is the mean excitation energy (137 eV for Si). Additional correction terms as discussed for instance in [27] are indicated by the dots. The energy loss $\langle dE/dx \rangle$ is a function of the particles velocity $v = \beta\gamma$ and depends only implicitly on the particle mass. At low $\beta\gamma$ the particles are highly ionising and the $1/\beta^2$ term is dominating. This leads to densely ionised regions, if the particles are stopped in the material. The minimum of the function is reached at $\beta\gamma \sim 4$. At higher energies the logarithmic term dominates such that the energy loss increases slowly. A particle with an energy within this minimum regime is called *minimum ionising particle* (MIP).

Since the actual energy loss of a particle is subject to large fluctuations it is typically described by a *Landau distribution*, with a pronounced tail towards large values. Due to the tail, the average value is much higher than the *most probable value* (MPV) of the distribution. The fluctuations around the maximum of the Landau distribution are more prominent in thinner detectors. The Landau fluctuations are attributed to the occurrence of so-called δ - or knock-on electrons, which gather enough energy in the interaction to become ionising particles themselves. Special care needs to be taken to account for the finite thickness of silicon sensors. Therefore the energy loss is commonly described by the *Landau-*

Vavilov-Bichsel function [204–206], that takes care to describe the most probable energy loss Δ_p in a detector given the finite thickness and statistical fluctuations. A comparison between the Bethe-Bloch mean energy loss and the Landau-Vavilov-Bichsel most probable energy loss in silicon sensors of a finite thickness is seen in Fig. 10.4, while the $\langle -dE/dx \rangle$ rises slowly with the energy of the muon, the most probable energy loss Δ_p/x remains almost constant for values above 0.2 eV. Therefore it is generally accepted to use the term minimum ionising particle for all particles in high-energy physics tracking detectors. In semiconductors, only part of the energy loss is used for the creation of electron-hole pairs. In silicon for instance the average energy needed for the creation of a pair amounts to $w_i = 3.67$ eV, i.e. three times larger than the band gap of 1.12 eV [206]. It should be kept in mind that the average energy to create an electron-hole pair is temperature dependent, and the above value holds for temperatures around 300 K

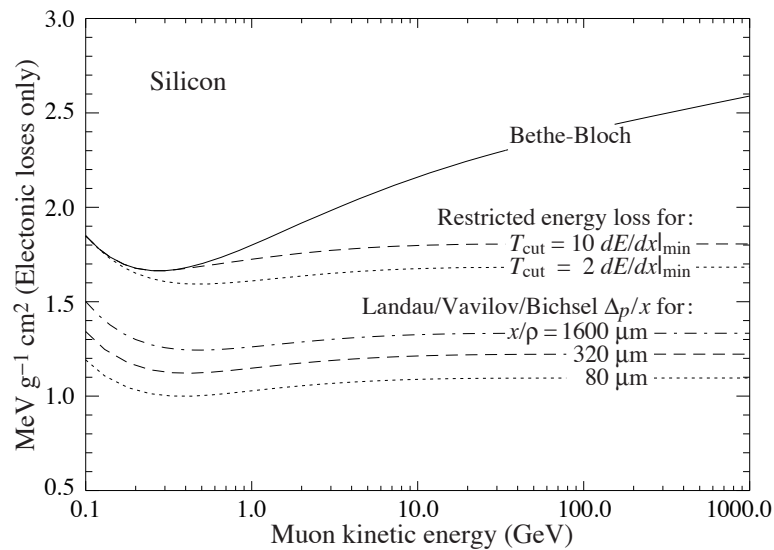


Figure 10.4: A comparison between the Bethe-Bloch $\langle -dE/dx \rangle$ and the Landau-Vasilov-Bichsel Δ_p/x description for muons. [27]

Also electromagnetic radiation are detected by silicon sensors. Photons interact with silicon via three different processes, depending on their energy, namely the Compton effect, the photoelectric effect and pair production. In contrast to charged particles the photon is either absorbed, as given in photoelectric effect and pair production, or scattered by a large angle, as in the Compton effect. Therefore a monochromatic photon beam penetrating the silicon material is not changed in energy, but attenuated in intensity, following

$$I(x) = I_0 e^{-x/\mu}, \quad (10.12)$$

where I_0 is the intensity of the beam before and $I(x)$ after traversing the material of thickness x . The attenuation length μ is a property of the absorption material and is energy dependent. At low photon energies (~ 100 keV in Si) the photoelectric effect is dominating and drops rapidly down while the scattering processes become dominating. Pair production is the most important process for energies exceeding 10 MeV.

10.1.6 Signal Formation and Charge Collection

The signal in a silicon detector is generated on the collecting electrodes through the drift of the charge carriers in the electric field. In a silicon sensor free charge carriers (electron or holes) move randomly with a mean kinetic energy of $3/2k_B T$, where k_B is the Boltzmann constant and T is the temperature. Along their path these free carriers are scattered on the lattice, impurity atoms or other scattering centres, leading to mean free path on the order of $0.1 \mu\text{m}$. In the presence of an external electric field, the free charge carriers are accelerated towards their respective electrodes. The average drift velocity \vec{v} is then given by

$$\vec{v} = \frac{q\tau_c \vec{E}}{m_{e,h}} = \mu_{e,h} \vec{E}, \quad (10.13)$$

where q is the electron (hole) charge, m is the effective electron (hole) mass and \vec{E} is the electric field. The mobility $\mu_{e,h}$ in a low field depends linearly on the mobility of the charges. For high values of the field, $4 \times 10^4 \text{ V/cm}$, the velocity saturates, and becomes constant. In general the transition between the low and the high field region is parametrised [207]. The low field mobility for silicon at room temperature is $\mu_h = (1415 \pm 45) \text{ cm}^2/\text{Vs}$ for holes and $\mu_e = (480 \pm 17) \text{ cm}^2/\text{Vs}$ for electrons [207]. Hence the electrons are three times more mobile, which makes them less prone to effects like trapping.

The drift of a charge q at the position \vec{r} induces a current I in the circuit of a readout electrode i . This is expressed in the Shockley-Ramo theorem [208, 209]

$$I_i(t) = q\vec{v}_{dr} \vec{E}(\vec{r}(t)) \cdot \vec{E}_{i,w}(\vec{r}(t)), \quad (10.14)$$

where $\vec{E}(\vec{r}(t))$ is the electric field at point \vec{r} and $\vec{E}_{i,w}(\vec{r}(t))$ is the weighting field of the i^{th} electrode at the same point. The weighting field is the negative gradient of the weighting potential $\phi_{i,w}(\vec{r})$, which is given by as the solution of the Laplace equation $\Delta\phi_{i,w} = 0$ using the unit potential of the i^{th} electrode and 0 at the other electrodes. The weighting field is strongly influenced by the detector geometry. The weighting potential of a simple pad detector is a linear function given by the inverse of the detector thickness $1/d$. Hence the induced current is the same for any part in the drift path and electrons and holes contribute the same amount to the final signal. The weighting potential in strips however, is much more pronounced in the vicinity of the segmented electrode. Hence a charge close to the strip induces a larger current than a charge far away from the strip. Hence the signal in a strip detector is dominated by the charges drifting towards the segmented readout side.

A further defining figure of interest in silicon sensors is the integral of the induced current, known as the collected charge Q

$$Q = \int_0^{t_{c_e}} I_e(t) dt + \int_0^{t_{c_h}} I_h(t) dt = \int_{x_0}^d \frac{eN_e(t(x))}{d} dx + \int_{x_0}^0 \frac{eN_h(t(x))}{d} dx. \quad (10.15)$$

Under the assumption that all electron-hole pairs are created at position x_0 at time $t = 0$, dt is substituted by dx/v_{dr} . The most probable energy loss of a minimum ionising particle E_{MP} traversing a silicon sensor of finite thickness d can be approximated using a parametrisation by Bichsel [206]

$$E_{MP} = d(190 + 16.9 \cdot \ln d) \quad (10.16)$$

which is valid for sensors with a thickness ranging between $110 \mu\text{m}$ to $3000 \mu\text{m}$. Hence the most probable signal is given by the ratio of Eq. (10.16) and the mean energy needed to create an electron-hole

pair 3.67 eV

$$Q = \frac{E_{MP}}{3.68 \text{ eV}}. \quad (10.17)$$

For a standard silicon detector with a thickness of 300 μm , a minimum ionising particle traversing the detector results in a most probable energy of $E_{MP} = 85 \text{ keV}$ and a signal of 23 ke (3.7 fC). The mean energy loss amounts to 32 000 e(5 fC), with $dE/dx = 0.39 \text{ keV}/\mu\text{m}$.

The charge collection efficiency is thus defined as the ratio between the collected charge and the deposited charge $Q_0 = eN_0$

$$\text{CCE} = \frac{Q}{Q_0}. \quad (10.18)$$

Hence a charge collection efficiency of $\text{CCE} = 1$ is achieved, if the number of charge carries remains constant during the drift time, i.e. $N_e = N_h = N_0$. The number of charge carries, can be altered due to effects like trapping of charges at defects in the silicon band gap (decrease) or charge multiplication due to avalanche effects (increase). The CCE is therefore an important measure in the evaluation of the detector performance.

10.1.7 Position Sensitive Measurement

Silicon detectors on high energy physics experiments are generally employed as position sensitive tracking detectors. The strip- and pixel-geometry of the electrodes, as well as the readout method are the defining factors for the precision of the position measurement. If only digital information is available the resolution, i.e. root-mean-square deviation from the true coordinate, of a silicon strip sensor, with a pitch distance p^1 , assuming that effects arising from track inclination and charge diffusion during charge collection can be neglected, is

$$\sigma_x^2 = \frac{1}{p} \int_{-p/2}^{p/2} x^2 dx = \frac{p^2}{12}. \quad (10.19)$$

The pitch is usually in the range of 20 μm to 100 μm , resulting in a resolution between 6 μm to 29 μm . The resolution can be significantly enhanced, if the signal is distributed over several strips and the centre-of-gravity can be calculated, preferably when using an analogue readout. The drawback of charge sharing is however, the decreased signal per strip, which might degrade the detection efficiency. Hence a compromise between an enhanced resolution due to charge sharing with a smaller pitch and a high signal per strip, i.e. large pitch, must be found. The position coordinate x is then found by interpolation, e.g. by the centre of gravity of the signal.

10.1.8 Detector Readout and Noise

The root mean square (RMS) of statistical fluctuations of electrons and holes measured in the absence of a signal, are defined as noise and arise from a variety of different sources in the sensor and readout chain. The dominant noise contributions arise either from the discrete nature of the charge emissions, called shot noise, or from fluctuations in the velocity of charge carriers in resistors, called thermal or voltage noise. The current spectral density of the shot noise is expressed by $i_{n,sh}^2 = 2eI_{rev}$ and the voltage spectral density of the thermal noise is given by $e_{n,th}^2 = 4k_BTR$. The latter is highly influenced by the detector capacitance, when propagated through the amplifier output.

Together with the signal-to-noise ratio (SNR), the detector noise is an integral parameter for the evaluation of the detector performance. The values of noise are generally expressed using the Equivalent

¹ The pitch is the distance between the centre position of two adjacent strips.

Noise Charge (ENC). To enhance the SNR, the signal after the preamplifier is usually shaped by CR-RC circuit, which further influences the sensor noise. The final noise of a detector readout system is found by folding the spectral densities with the frequency dependent transfer function of the system. Since the different noise sources are uncorrelated the total ENC of the sensor readout system is given by the sum of the quadrature of the individual components

$$ENC = \sqrt{ENC_{C_d}^2 + ENC_{I_L}^2 + ENC_{R_p}^2 + ENC_{R_s}^2}. \quad (10.20)$$

While the latter two terms, i.e. the parallel thermal noise arising from the bias resistance and the serial thermal noise attributed to the metal strip resistance, can safely be ignored, the detector capacity at the input of a charge sensitive amplifier is usually the dominant noise source in the detector system. The corresponding noise term is expressed by

$$ENC_{C_d} = a + \frac{b}{\tau_P} \cdot C_d, \quad (10.21)$$

where the parameters a and b are specific to the design of the (pre-)amplifier and C_d is the load capacitance, which is subject to the interstrip capacitance and the strip to backplane capacitance. The integration time τ_P is crucial, as short integration times generally lead to larger a and b values. To reduce this noise component segmented detectors with short strip or pixel structures are preferred. The shot noise is given by

$$ENC_{I_L} = \sqrt{c I_L \tau_P}, \quad (10.22)$$

where c is also a readout specific parameter. The shot noise is proportional to the leakage current and, in contrast to $ENC_{C_d}^2$, it decreases for increasing τ_P . Since irradiation leads to an increase in the current, the shot noise increases strongly after irradiation. Hence the noise increases only slightly under the LHC fluences [121, 200]. However, the influence of the leakage current can be controlled by operating the sensors at low temperatures, utilising the strong temperature dependence of the leakage current. Typical noise values for silicon sensors at the LHC are at the level of 1000 e for silicon microstrip sensors and 200 e to 300 e for pixel detectors, which profit from their smaller cell size [121, 122, 200].

10.2 Radiation damage in Silicon Sensors

Detectors in high-energy physics experiments are subject to a constant flux of particles. Over the course of time, this leads to severe *radiation damage* in the sensor material, which alter the detector performance. The radiation damage is subdivided into *surface* and *bulk damage*. The surface damage is primarily caused by ionising energy loss and affects the surface, the surface boundaries (i.e. Si – SiO₂) and the readout electronics. It is only of secondary interest at the HL-LHC. The bulk damage in silicon arises through energy deposition in the silicon bulk material, by *non-ionising energy loss (NIEL)*. The interaction between the high-energy particles and the silicon lattice atoms can lead to high energy transfer from the initial incoming particle. These interactions cause a variety of defects in the bulk material. The main effects on the silicon bulk and the detector operations, following the radiation damage, are

- Fluence proportional *increase of the leakage current* I_L , attributed to the creation of generation and recombination centres
- *Change of effective doping concentration*, N_{eff} , leading to alterations in the space charge, causing a severe increase in the operating voltage needed for full depletion

- *Trapping and recombination of charge carriers*, leading to a deterioration in the charge collection efficiency, due to a reduction in the signal height.

An atom from the silicon lattice that is displaced through the interaction with a high-energetic incoming particle is called a primary knock-on atom (PKA). For an incoming particle of kinetic energy T and mass m , the maximal transferable energy T_{\max} is given by

$$T_{\max} = 4T \frac{m_{\text{Si}} \cdot m}{(m_{\text{Si}} + m)^2}, \quad (10.23)$$

where m_{Si} is the silicon mass. To create a PKA with a probability of more than 50 %, requires an energy of at least 25 eV [210]. This leads to the creation of a *vacancy* (V) in the silicon lattice and an *interstitial* (I), together called a *Frenkel pair*. Generally these knocked out atoms have enough recoil energy to knock out further silicon atoms from the lattice, causing a whole cascade of defects along the path. With decreasing kinetic energy of the recoil atom, the cross section for elastic scattering increases, causing a dense accumulation of defects, so called clusters. Many of the created defects are not stable and will recombine, as they are mobile and can move through the silicon.

10.2.1 NIEL Scaling Hypothesis

To compare the radiation damage caused by different particle types at different energies, a scaling hypothesis is provided relating the microscopic damage caused and allows to translate the displacement damage for different particle types and energies. The energy dependent displacement cross-section damage function $D(E)$

$$D(E) = \sum_i \sigma_i(E) \int_{E_d}^{E_R^{\max}} f_i(E, E_R) P(E_R) dE_R, \quad (10.24)$$

where the index i runs over all possible reactions with cross section σ_i , between the impinging particle with energy E and the and Si atom. The function $f_i(E, E_R)$ gives the probability to create a recoil atom with energy E_R in the reaction with index i . The Linhard partition function $P(E_R)$ describes the portion of energy available for displacement damage by a recoil atom with energy E_R and is calculated analytically. The integration extends over all recoil energies ranging from the displacement threshold E_d to the maximum transferable energy E_R^{\max} . The displacement-damage cross-section for Si is shown in Fig. 10.7 for different particle types, as a function of energy, normalised to 1 MeV neutrons.

The energy dependent hardness factor κ converts the damage caused by a certain type of particle with fluence Φ into the neutron equivalent fluence Φ_{eq} caused by 1 MeV neutrons.

$$\kappa = \frac{\int_{E_{\min}}^{E_R^{\max}} D_x(E) \Phi(E) dE}{D(E_n = 1 \text{ MeV}) \int_{E_{\min}}^{E_R^{\max}} \Phi(E) dE} \quad (10.25)$$

The 1 MeV neutron equivalence fluence Φ_{eq} is calculated by

$$\Phi_{\text{eq}} = \kappa \Phi = \kappa \int \Phi(e) dE \quad (10.26)$$

If not explicitly stated otherwise the fluences quoted within his thesis are given as neutron equivalent fluences, with the unit $\text{nl}_{\text{eq}}/\text{cm}^2$. Experimentally the hardness factor is determined using the leakage current.

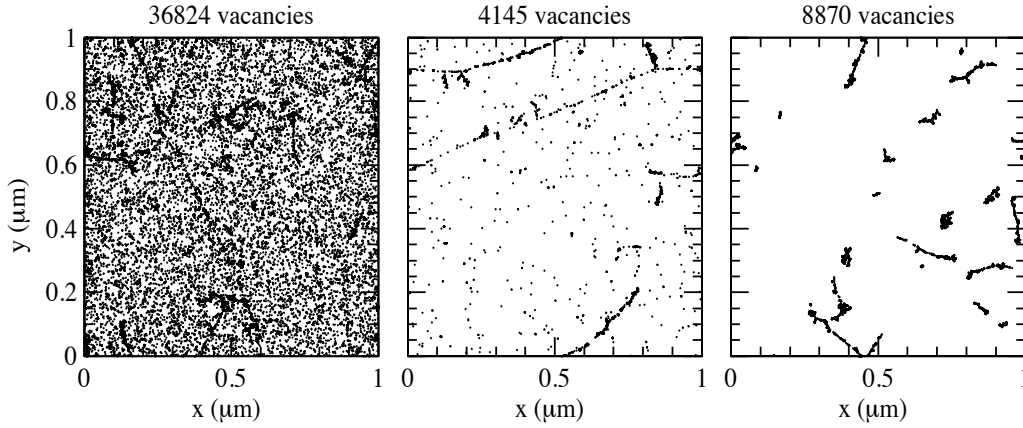


Figure 10.5: Simulation of the number of vacancy defects created at a fluence of $1 \times 10^{14} \text{ cm}^{-2}$ by 10 MeV protons (left), 24 MeV protons (middle) 1 MeV neutrons (right). The figures show the number of vacancies produced by the simulation, projected over $1 \mu\text{m}$ of depth in z -direction. While the left figure shows a relative homogenous distribution of vacancies, the more energetic protons shown in the the middle figure lead to more clustered and discrete defects. Since neutrons only interact via the strong force, their defects caused as seen in the right figure, are more isolated and clustered.

10.2.2 Annealing

The initial defects caused by radiation are very mobile at temperatures above 150 K and generally undergo further developments. In fact around 60 % of the overall Frenkel pairs recombine, especially in the cluster region where the recombination rate is ranging from 75 % to 95 % [211]. Other defect migrations lead to the combination of a *vacancy* and an *interstitial* or to more complex defects through the combination with impurities in the silicon crystal. The most common defects are summarised in Fig. 10.6. This defect evolutionary process is called annealing and is subdivided into a constant part, that does not evolve with time, a beneficial (or short-term) annealing and a reverse (or long-term) annealing. The annealing process is strongly temperature dependent, and some processes can be frozen out at temperatures below 0°C . While the microscopic knowledge on the defect migration and their reactions is still being investigated, a phenomenological parametrisation of the process is found to describe the annealing behaviour. The most widely accepted description is given by the so-called Hamburg model [212]

$$N_{\text{eff}}(\Phi, t_a) = N_{\text{eff},0} - N_{\text{eff}}(\Phi_{\text{eq}}, t_a) = N_A(\Phi_{\text{eq}}, t_a) + N_C(\Phi_{\text{eq}}) + N_Y(\Phi_{\text{eq}}, t_a), \quad (10.27)$$

where t_a denotes the storage temperature after irradiation. The model consists the superposition of three terms: a constant term, N_C , describing the fluence dependence of the effective doping concentration as a function of the received equivalence fluence Φ_{eq} and the short-term, N_A . and long-term, N_Y , annealing components.

The *constant term* N_C describes the stable damage, which is independent of the storage temperature and the annealing time. It is expressed by

$$N_C(\Phi_{\text{eq}}) = N_{C,0}(1 - e^{-C\Phi_{\text{eq}}}) + g_C\Phi_{\text{eq}}, \quad (10.28)$$

where C is the donor removal constant, describing the removal velocity. The first term accounts for the incomplete donor removal, with $N_{C,0} < N_{\text{eff},0}$ being the removable doping concentration, and is comple-

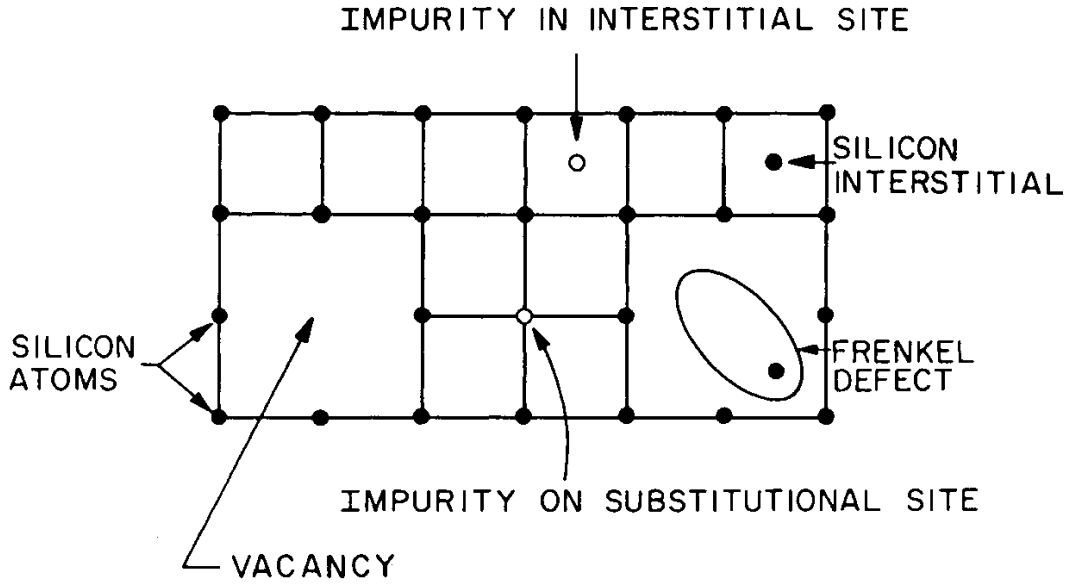


Figure 10.6: Graphic representation of the most common radiation induced point defects in Si sensors. Taken from [197]

mented by a fluence dependent term, accounting for the creation of stable acceptors at an introduction rate g_C .

The *beneficial annealing* term in the *Hamburg model* 10.27, N_A , is given by

$$N_A = g_A \Phi_{\text{eq}} e^{\frac{t}{t_A}}. \quad (10.29)$$

The value of the amplitude g_A of the exponential function is measured to $g_A = (1.81 \pm 0.14) \times 10^{-2} \text{ cm}^{-1}$. The beneficial annealing is related to the generation of donor-like states and the annealing of acceptor-like defect states, resulting in a decrease of the depletion voltage [212]. The reverse annealing is given by the last contribution in Wq 10.27. It accounts for the increase of the full depletion voltage after a certain annealing time, due to the formation of acceptor like states. This leads to an increase of the effective doping concentration, which in turn causes the increase of the full depletion voltage. Models on the reaction kinetics and the experimental data suggest a parametrisation following a first order process

$$N_Y = N_{Y,\infty} \left(1 - e^{-\frac{t}{t_Y}} \right), \quad (10.30)$$

with $N_{Y,\infty} = g_Y \Phi_{\text{eq}}$ and $g_Y = (5.160 \pm 0.009) \times 10^{-2} \text{ cm}^{-1}$.

10.2.3 Leakage Current

Defects in the middle of the Si band gap act as generation and recombination centres. It was found that the number of generation centres increases with the irradiation fluence and are directly proportional to the increase of the leakage current, irrespective of the type and energy of the irradiation. The change in the leakage current is given by

$$\Delta I_L = \alpha \Phi_{\text{eq}} V, \quad (10.31)$$

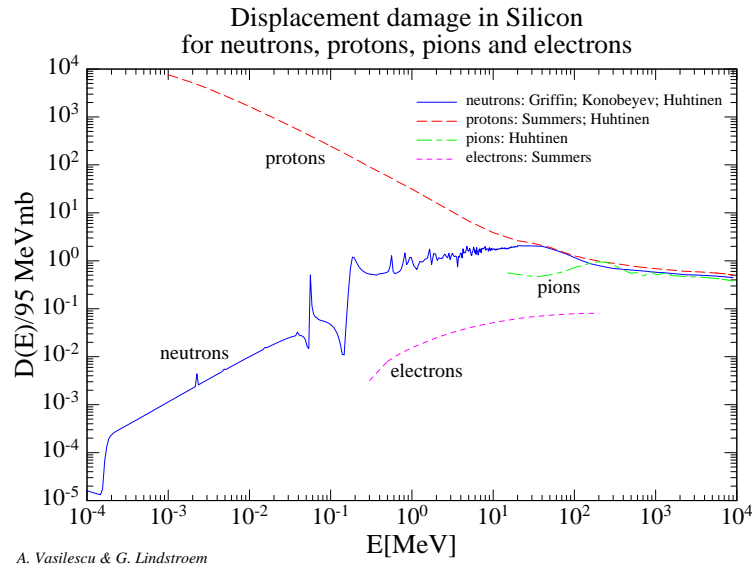


Figure 10.7: Displacement-damage cross section in silicon for neutron, protons, pions and electrons as a function of energy, normalised to 1 MeV neutrons. [213]

where α is the current related damage parameter and V is the sensitive detector volume. For measurements at room temperature a value of $\alpha = 3.99 \times 10^{-17} \text{ Acm}^{-1} (\pm 5\%)$ is found after annealing at 60°C for 80 min. The above relation is often used to determine the fluence of irradiated samples and is shown in Fig. 10.8.

10.2.4 Effective Doping

Radiation damage also changes the effective doping concentration $N_{\text{eff}} = N_D - N_A$, as defects can be electrically active or doping impurities (such as P or B) form new defect complexes. This alters the space-charge and thus impacts the depletion voltage and can go so far to invert the type of the material. An example of the fluence dependence on the effective doping concentration and the depletion voltage is shown in Fig. 10.10. In this case the depletion voltage for the initially n-doped material decreases until the space charge vanishes and the material effectively changes to p-type, due to the dominating acceptor-like defects. This behaviour is known as type-inversion or space charge sign inversion. After type inversion the pn-junction now moves from the p^+ -side to the n^+ -side. Since the effective space charge keeps increasing with further irradiation the full depletion voltage might rise above the maximal possible depletion voltage and the sensors will only be partially depleted, which has an enormous impact both on the charge collection and the resolution, in case that the region around the strips is not depleted.

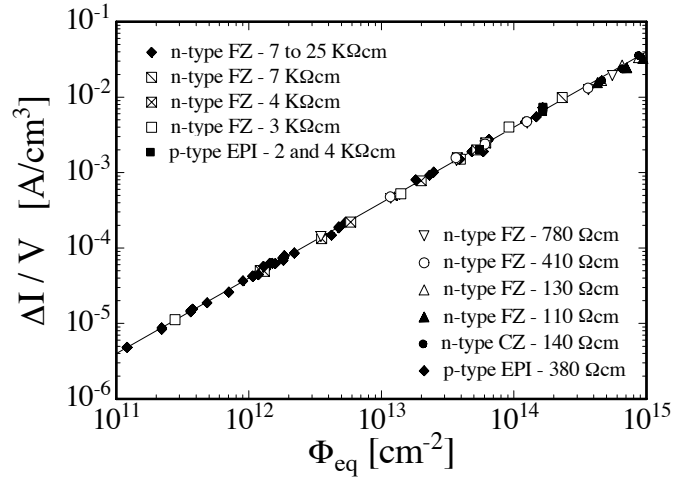


Figure 10.8: Fluence dependence of the leakage current I_L for detectors produced by various process technologies in different silicon materials, after an annealing for 80 min at 60 °C. [212]

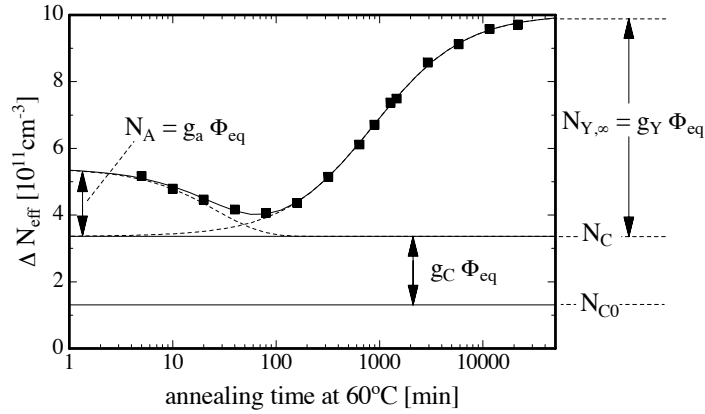


Figure 10.9: Annealing behaviour of the radiation induced change in the effective doping concentration ΔN_{eff} . [212]

10.2.5 Charge Trapping

Radiation-induced defects also act as trapping centres, in which electrons and holes are captured and re-emitted after some time. This leads to a reduction in signal height. A decrease of the charge collection efficiency is found, if the defects have a large trapping cross-section and the detrapping times are longer than the charge collection time of the amplifier. Charge carrier trapping is described by the effective trapping time $\tau_{\text{eff},e,h}$, which is inversely proportional to the concentration of traps and thus the equivalent fluence Φ_{eq} [214]

$$\frac{1}{\tau_{\text{eff},e,h}} = \gamma_{e,h} \Phi_{\text{eq}} \quad (10.32)$$

where $\gamma_{e,h}$ is a trapping-related damage parameter. The trapping constants are measured in FZ material for fluences up to $10 \times 10^{15} \text{ cm}^{-2}$ at -10°C . It was measured at $0.37 \times 10^{-6} \text{ cm}^2/\text{s}$ for electrons and $0.57 \times 10^{-6} \text{ cm}^2/\text{s}$ for holes after neutron irradiation and to $0.54 \times 10^{-6} \text{ cm}^2/\text{s}$ for electrons and $0.66 \times 10^{-6} \text{ cm}^2/\text{s}$ after irradiations with charged hadrons (pions, protons) [215]. The trapping constant

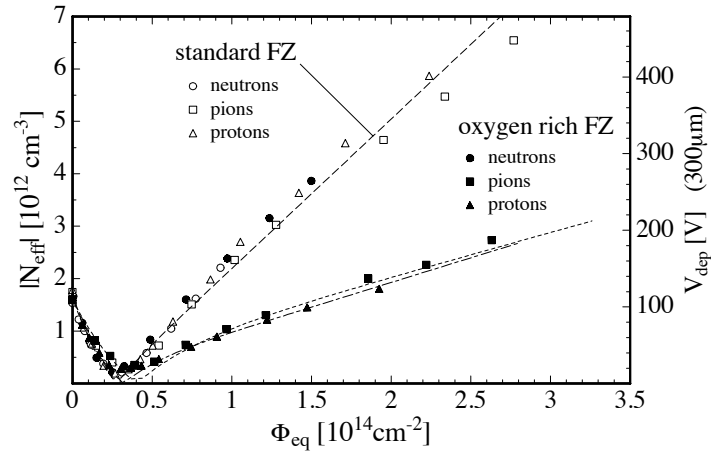


Figure 10.10: Effective doping concentration, N_{eff} as a function of the received fluence, for standard and oxygen rich float-zone material, irradiated with neutrons, pions or protons. []

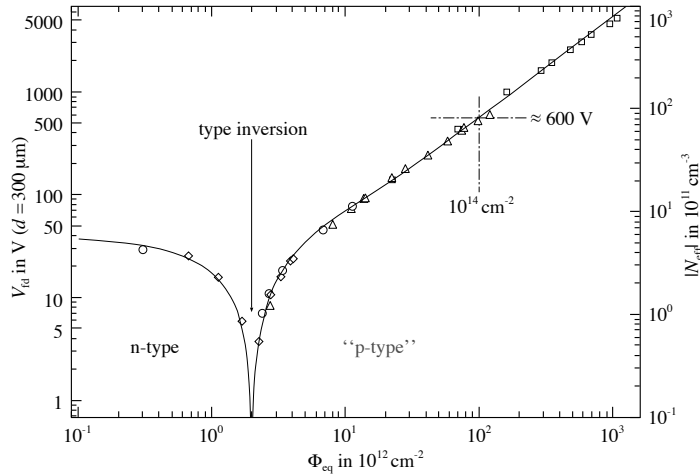


Figure 10.11: Full depletion voltage V_{fd} for a 300 μm thick silicon sensor and corresponding effective doping concentration N_{eff} for initially lightly n-doped silicon as a function of the received fluence.

is slightly temperature dependent and varies with 20% to 30% in the range from 220 to 294 K [216]. Furthermore a contrary annealing behaviour between γ_e and γ_h was found. Whilst γ_e decreases with 30% during annealing, γ_h increases by the same amount under the annealing. So far no clear microscopic mechanism responsible for the trapping has been found [217]. Trapped charges are also subject to recombination with oppositely charged free charges, which leads to an additional charge loss.

Whilst trapping effects have played a secondary role on previous silicon tracking devices, it will become the limiting factor for silicon tracking detector operations at the HL-LHC. The impact can be evaluated using mean drift distance $l_{\text{eff}} = v_{\text{dr}} \tau_{\text{eff}}$ before being trapped, assuming a saturated drift velocity of $v_{\text{dr}} = 10^5$ m/s. At a fluence of 10^{15} $\text{n}_{\text{eq}}\text{cm}^{-2}$ the mean drift distance is $l_{\text{eff}} \sim 200$ μm , which is already less than the standard thickness of 300 μm commonly used in tracking detectors. At the HL-LHC fluences of up to 10^{16} $\text{n}_{\text{eq}}\text{cm}^{-2}$ are expected, which result in drift distances of $l_{\text{eff}} \sim 20$ μm , effectively limiting the use of silicon sensors.

10.2.6 Charge Multiplication

In the presence of a high electric field ($10\ \mu\text{m}$ to $15\ \mu\text{m}$ [195]) in the silicon detector the charge carriers can be accelerated strongly enough to create additional electron hole pairs between the collisions. This can lead to an avalanche effect if the newly created charge carriers themselves might ionise again. Charge multiplication, i.e. the multiplication of the original number of charge carriers N_0 , is a well described process and utilised for instance in gaseous detectors or avalanche photodiodes or silicon photomultipliers. However the occurrence of charge multiplication as a result of high irradiation, has only been observed a few years ago [218–220]. For irradiation fluences above the order of $10^{15}\ \text{n}_{eq}\text{cm}^{-2}$ and high bias voltages more charge carriers are collected within the sensor than expected by the generally accepted trapping model [221, 222]. The charge multiplication in irradiated sensors is attributed to the increase of the effective doping concentration and thus higher electric field strengths. To fully understand the origin of irradiation induced charge multiplication and an eventual exploitation of the multiplied charge in the high radiation environment at the HL-LHC this effect has been subject to intensive studies for instance in silicon strip detectors [223, 224], 3D detectors [225] and pad detectors [226]. However the signal increase comes at the cost of an increased noise, hence detailed studies on the signal-to-noise ratio and long term stability tests are essential.

10.3 Improving Radiation Hardness

The operation of silicon detectors in the high radiation environment of the LHC has been subject to an intensive research and development programme not only from the individual LHC experiments, but also from dedicated collaborations such as the CERN-RD50 [227, 228] programme and its predecessor the ROSE-collaboration [229]. Several strategies have been put forward to allow reliable detector operations even in the harsh HL-LHC environment, which will be briefly summarised in the following sections.

10.3.1 Change of Operating Conditions

Several measures to enhance the lifetime of silicon sensors under harsh radiation environments are connected to the operation conditions. For instance the annealing process described in the previous section is strongly temperature dependent can be almost frozen out at low temperatures. Hence the silicon sensors at the LHC are held at temperatures between $-6\ ^\circ\text{C}$ to $-10\ ^\circ\text{C}$, even during shutdown. Short time intervals without cooling, needed for necessary interventions, are chosen such that the positive effects of the beneficial annealing are exploited. Operating the detectors in a cooled environment also reduces the leakage current, limits the power consumption and reduces the noise. For data-taking at the HL-LHC temperatures down to $-20\ ^\circ\text{C}$ are envisaged by implementing a CO_2 cooling system.

The bias voltage is another parameter to influence the radiation tolerance. There is not only the need to increase the bias voltage in conjunction with the rising full depletion voltage, but also an increased electric field positively influences the radiation tolerance. A high electric field leads to a higher drift velocity and thus an extended effective drift distance due to the lower trapping probability.

10.3.2 Material Engineering

The deliberate addition of impurities to the silicon in order to enhance the radiation tolerance, mainly toward hadron induced damages to the silicon bulk, is known as defect engineering. Especially oxygen enrichment of the silicon bulk, during the manufacturing process, results in a considerable rise of the radiation tolerance [230–232]. Oxygen rich silicon material are known as DOFZ, MCz or EPI. Even

though the microscopic details are yet to be fully understood, it appears that the additional oxygen captures vacancies and neutralises charged defects in a stable configuration thus leading to a superior performance after the exposure to radiation. The enhanced radiation hardness is mainly attributed to the stable damage from Eq. (10.27), through a reduction of the acceptor introduction rate g_C (see Eq. (10.28)), which is reduced by a factor of four compared to the standard FZ material. This leads to a much smaller increase of the irradiation induced type-inversion. Benefits of the oxygen enhancement are also seen in the annealing behaviour. In this case the oxygen leads to a reduction of the reverse annealing by a factor of two, and a double time constant for the reverse annealing.

10.3.3 Device Engineering

A further method to improve the radiation tolerance of silicon sensors is by optimising the geometry of the detector material. One option that is already realised at the current LHC, is the transition from p-in-n material to n-in-n or n-in-p material. While p-in-n sensors are the most cost effective, they suffer strongly from the radiation induced damage. First of all after type inversion the depletion zone will grow from the completely unstructured ohmic side of the sensor and unless full depletion is reached, the readout electrodes remain undepleted, severely affecting the readout of the signal. Secondly holes are three times less mobile than electrons, and thus more prone to trapping, which further deteriorates the signal in p-in-n sensors. In turn n-in-n or n-in-p sensors have the advantage of collecting electrons, which have a higher mobility and are less prone to trapping. Furthermore the depletion zone, will grow from the segmented side and a signal can still be measured, if the sensor is not fully depleted. The current ATLAS [121] and CMS [122] pixel sensors as well as the vertex locator of LHCb [123] use n-in-n technologies, which have the downside of being quite cost extensive due to the need of double sided manufacturing processes. Detectors with n-in-p technology are the desired candidates for large fractions of the HL-LHC upgraded trackers.

A further option is the thinning of the silicon bulk material and operate thin detectors ($d < 300 \mu\text{m}$). Thin detectors can either be achieved by: physical thinning of the processed FZ or MCz wafers down to $50 \mu\text{m}$, deep diffusion of dopants from the backside and epitaxial growing of a thin Si layer on a Cz material [226]. Thin detectors have the advantage of a significantly reduced depletion voltage and a reduced leakage current. Furthermore the smaller drift distance as well as the larger weighting field result in a higher drift velocity, which significantly reduces the trapping probability. However, since the collected charge is proportional to the sensor thickness, thin detectors have the drawback of collecting less charge, which decreases the signal-to-noise ratio in non-irradiated sensors.

A promising option for highly radiation tolerant detectors, which have been extensively studied in Freiburg [225], are so-called 3D-detectors [233, 234]. The basic principle of these detectors is to decouple the sensor thickness from the distance between the electrodes, by etching columnar electrodes perpendicular to the surface into the silicon substrate. These columns are doped to form readout junction electrodes and ohmic electrodes. The enhanced radiation hardness arises from the reduced trapping and a reduced depletion voltage.

From the LHC to the HL-LHC

With the successful running of the LHC at design luminosity at $\sqrt{s} = 13$ TeV, the LHC is able to deliver proton–proton collisions at centre-of-mass energies allowing to go beyond the boundaries set by the Standard Model. The luminosity upgrade of the LHC to the High Luminosity-LHC (HL-LHC) is the most natural extension of the LHC and provides an excellent environment both for precision measurements of discoveries made at the nominal LHC and accessing low cross-section channels. Upgrades to the machine complex and the detectors are foreseen in two stages, called the Phase-I and Phase-II upgrade. The beginning of operation of the HL-LHC is expected for the year 2025.

This chapter commences with an overview on the various upgrades necessary both to the accelerator complex, to achieve the high luminosity, and the ATLAS detector, to efficiently operate at every stage of the LHC and HL-LHC programme in Section 11.1, followed by an introduction to the physics potential of the HL-LHC in Section 11.2. This chapter is concluded by an overview of the Phase-II upgrade for the ATLAS detector, with a strong emphasis on the Inner TracKer (ITK) upgrades in Section 11.3.

11.1 The High-Luminosity Upgrade of the LHC

Several upgrades to the LHC accelerator complex are necessary to achieve a seven-fold increase in instantaneous luminosity as foreseen for the HL-LHC. The roadmap for the next two decades is shown in Fig. 11.1, where extended periods of data-taking are interrupted by long shutdown periods, called Long Shutdown 1 (LS1) and LS2 and LS3. The corresponding upgrades to the experiments are called Phase-I and Phase-II upgrade. The centre-of-mass energy is indicated by the red line, while the green line reflects the foreseen change in luminosity.

The LHC resumed data taking in 2015, after a larger technical shutdown between 2013–2014, which was focussed on consolidation work, mainly of the magnets system [235]. This shutdown permitted the LHC to reach its ultimate centre-of-mass energy of $\sqrt{s} = 14$ TeV. During this shutdown the ATLAS experiment executed extensive detector consolidation works and additionally a fourth pixel layer, the so-called Insertable B-Layer (IBL), was installed [236]. It is expected that the IBL improves the vertex resolution, secondary vertex finding and b-tagging. The IBL encloses the new central beam-pipe and is inserted into the present pixel detector. It is thus placed between the innermost pixel layer, the B-layer, and the beam pipe at a radius of 33 mm, which was only possible due to the installation of a new Be beam pipe with a 4 mm reduced radius ($r = 29$ mm \rightarrow $r = 25$ mm). Further changes included

the restructuring of the ATLAS Higher Level Trigger system into a single stage trigger, by merging the Level-2 and Event Filter step, allowing for a more efficient CPU resource management [237].

The LS2 upgrade is envisaged to commence in 2018 and foresees several changes to the LHC accelerator complex. The main improvements are the integration of the Linac4, the increase of the energy of the PS Booster, which reduces the beam emittance, an upgrade to the LHC injectors and an upgrade of the collider collimation system.

These changes are expected to result in a peak luminosity of $L = 2 \times 10^{34} \text{ cm}^{-2}\text{s}^{-1}$ corresponding to 55 to 80 interactions per crossing. An accumulated luminosity delivered to the experiments by the LHC of 300 fb^{-1} to 400 fb^{-1} is expected for the first 13–15 years of running before the next long shutdown planned for 2022. Further information on the details of these upgrades are found in Reference [238]

The Phase-I upgrade of the ATLAS detector, during the Long Shutdown 2 (LS2), incorporates the installation of new muon Small Wheels and the introduction of a new trigger scheme. The new muon Small Wheels, which replace the first layer of the end-cap muon instrumentation, are designed to cope with the higher number of pile-up events and beam cavern background. The improved design ensures an efficient tracking even at particle rates expected at the HL-LHC and will also be integrated into the ATLAS Level-1 trigger system. The advances in the ATLAS trigger system include the implementation of a Fast Tracker trigger (FTK), topological triggers and an improved L1Calo granularity. The FTK trigger is a hardware based track reconstruction using associative memories to perform the reconstruction of tracks with transverse momenta larger than $p_T > 1 \text{ GeV}$. These are then forwarded to the Event Filter processing farms, which provide high-quality tracking information to allow complex track-based trigger decisions. These changes are established to efficiently handle luminosities beyond the nominal values at the LHC. Further details on the Phase-I upgrade of the ATLAS detector are described in Ref. [239–242]

The LS3 will take place between 2023-2025 and transforms the LHC to the High Luminosity LHC (HL-LHC), its ultimate operation mode. The HL-LHC is designed to run at instantaneous luminosities up to $\sim 5 - 710^{34} \text{ cm}^{-2}\text{s}^{-1}$. With an integrated luminosity of 250 fb^{-1} per year the HL-LHC is expected to collect 3000 fb^{-1} of data during its course of running. This tenfold increase in collected data comes at the cost of a higher track rate, causing severe radiation damage in the tracking detectors. With up to 200 pile-up events at the HL-LHC, the pile-up rate will increase roughly by a factor of ten compared to the current LHC conditions. Therefore tremendous efforts were undertaken to develop the necessary upgrades not only for the inner detector, but for all subsystems of the ATLAS experiment. To reach its ultimate performance goals significant changes to the hardware and beam parameters of the LHC have to be made [243]. Hardware changes include the replacement of the inner triplet and some inner quadrupole magnets, the cryogenics, the collimation systems, some of the highly irradiated electronics and an advanced quench protection system. The ultimate peak luminosity performance of the HL-LHC is constrained both by the requirement of a maximum number of 140 events per bunch crossing in the experimental detectors and the consideration of energy deposition by collision debris in the interaction region magnets. Hence the large integrated luminosity can only be achieved by operating the HL-LHC with the maximum number of bunches and utilising luminosity levelling¹. Important beam parameters to maximise the integrated luminosity include: maximising the fill length, short average machine turnaround time, an average operational fill length that exceeds the luminosity levelling time and good overall machine efficiency. The HL-LHC will run with a standard 25 ns bunch spacing. The novel use of crab cavities is further deciding factor to reach the luminosity goal. At the LHC the proton–proton beams collide under a crossing angle of 0.3 mrad, whose size correlates with the luminosity. The up-

¹ i.e. operating the machine with a constant luminosity at a value below its maximum achievable luminosity

grade of the HL-LHC foresees to include crab cavities, which generate a transverse electric field that rotates each bunch longitudinally, such that the beams effectively collide head-on at the collision point. These crab cavities can furthermore be used to control the bunches direction perpendicular to the plane of the interaction and are thus an additional tool for pile up control and luminosity levelling. The upgrades during LS3 will result in increased technical requirements for the experiments and upgrades to major parts of the detector subsystems will be inevitable for a successful data taking.

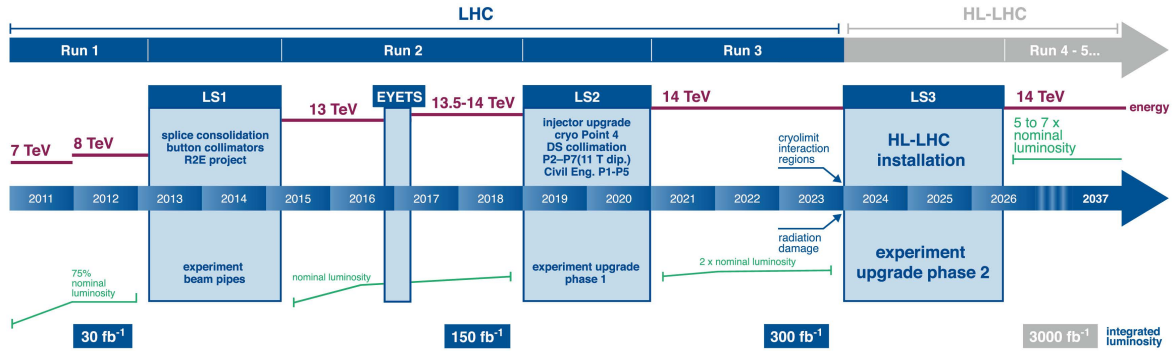


Figure 11.1: Schematic of the baseline plan for the running of the LHC. The upper red line indicates the center-of-mass energy and the green line the luminosity. The first shutdown (LS1) was dedicated to the inevitable alterations needed to achieve the design energy and luminosity parameters. The second shutdown (LS2) will be used to upgrade the LHC injectors and for further consolidation works. Finally the alteration planned for the long shutdown in 2023-2025 will permit the LHC to enter the High Luminosity-LHC phase [238].

11.2 Physics Motivation for the HL-LHC

The HL-LHC is the most natural extension of the LHC physics programme. With 3000 fb^{-1} of accumulated luminosity, the HL-LHC enables both the discovery of very rare processes which are beyond the reach of the LHC and facilitates detailed investigations of particles discovered at the nominal LHC. This section is based on the studies presented in the Letter of Intent for the ATLAS detector upgrade [244] and in Reference [245].

One of the main targets of the HL-LHC physics programme is the investigation of the properties of the 125 GeV Higgs boson discovered by the ATLAS and CMS experiments at the LHC in 2012. With over 100 million Higgs bosons produced in 3000 fb^{-1} , the HL-LHC offers an excellent environment to measure the couplings of the Higgs to elementary fermions and bosons at the level of a few percent accuracy. This is of fundamental importance, as many theories beyond the Standard Model predict deviations in the Higgs couplings. Furthermore there are a number of very rare decay modes of the Higgs such as the WH/ZH , $H \rightarrow \gamma\gamma$ and $t\bar{t}H$, $H \rightarrow \gamma\gamma$ which become accessible at the HL-LHC. Especially the $t\bar{t}H$ channel is of extraordinary interest as it enables a direct measurement of the top-Yukawa coupling. The HL-LHC will also allow to discover the $H \rightarrow \mu\mu$ decay with a significance of more than 6σ . A final confirmation of the Higgs mechanism and the nature of the electroweak symmetry breaking would be the observation and measurement of the Higgs self-interactions. Even though the discovery of the quartic Higgs boson coupling is beyond reach, the observation of the triple Higgs coupling is possible at the HL-LHC.

A major motivation for building the LHC in the first place were the divergencies in the weak boson scattering (WBS) cross-sections at the TeV scale, which are damped by the Higgs in the Standard Model.

The HL-LHC allows further measurements on the energy dependence of the WBS cross-section, and can increase the significance of anomalous WBS signals beyond 5σ for resonance masses at the 1 TeV scale, given that the coupling is strong enough.

Supersymmetry is among the very popular extensions to the Standard Model, hence the search or exclusion of a weak scale supersymmetry is of great importance and extends the physics programme at the HL-LHC. The data recorded at the HL-LHC will not only permit to expand the limits by $\sim 20\%$, but will also provide an environment that enable precision measurements of their properties if supersymmetric particles are to be found.

The HL-LHC will also facilitate valuable insights to Physics beyond Standard Model, as the tenfold increase in data will push the sensitivity into the multi-TeV range, which increases the sensitivity by $\sim 20\%$ to 30% compared with the nominal LHC. Among the benchmark models investigated are high-mass resonances decaying to top quark pairs or lepton pairs. Di-top resonances are for instance predicted by the Randall-Sundrum model [246, 247] or Z' resonances by the topcolour model [248]. In the case of the Randall-Sundrum gluon the boundaries will be pushed from 4.3 TeV at the LHC to 6.7 TeV with the full dataset of the HL-LHC. The projected limit in the search for a $Z' \rightarrow ee(\mu\mu)$ are extended from 6.5 TeV (6.4 TeV) at the LHC to 7.8 TeV (7.6 TeV) after the running of the HL-LHC.

Further searches for deviations from the Standard Model such as Flavour Changing Neutral Currents (FCNC) decays of the top quark benefit from the increased statistics. FCNC are searched for in top pair production, where one top decays via $t \rightarrow Wb$ and the other decays via a FCNC channel such as $t \rightarrow q\gamma$ or $t \rightarrow qZ$. The expected limits on the branching ratio at 95% CL are in the range of 10^{-5} and 10^{-4} .

11.3 ATLAS Upgrade

A reliable performance of the ATLAS detector in the harsh environment set by the HL-LHC is the foundation of any physics analysis. To meet the challenges in operation and performance set by the HL-LHC environment, most of the detector subsystems require major upgrades and consolidation work. The upgrade tasks falls broadly into two categories. The first is related to radiation damage, either caused by 15–20 years of running at the LHC, or that the existing systems are not designed to cope with the radiation damage caused by the accumulated luminosity expected at the HL-LHC. The second category includes necessary upgrades resulting from the increased trigger rates and detector occupancy, arising from the large number of expected interactions per bunch crossing. While the upgrades of the ITK are driven by the need for higher radiation tolerance, fundamental upgrades to the trigger and computing system are necessary to cope with the immense particle flux.

The indispensable upgrade programme for the calorimeters consists of the upgrade of the readout electronics of both the LAr and the Tile calorimeter. The upgrade is mandatory, not only because the radiation tolerance limits are reached, but also since the on-detector front-end electronics cannot operate at the envisaged trigger rates and latencies required for the Phase-II luminosities. Due to the upgrade to a novel trigger architecture, a higher processing speed and finer granularity of EM calorimeter electronics beyond the Phase-I upgrades is needed. The Phase-II calorimeter system will potentially include a new sFCal with higher transverse granularity for improved handling of the large fluctuations in the energy deposition due to the large pile-up expected during operations at the HL-LHC. Special attention is given to an improved high voltage distribution network and an improved cooling, to avoid potential over-heating of the liquid argon and to cope with the large energy deposit expected in the detector due to the large number of pile-up events. It is also foreseen to include a finely segmented precision timing detector in the existing volume of the Minimum Bias Trigger Scintillators, covering the region between

$2.4 < |\eta| < 4.3$, in which the segmentation of the electromagnetic calorimeter is significantly reduced compared with the central region. This is to overcome a degradation in the detector performance, due to pile-up collisions, which lead to energy clusters. These can be identified and rejected by both the fine transverse segmentation and precision time resolution.

Upgrades to the muon system include the replacement of the Muon Spectrometer readout systems, to comply with the high number of muon tracks and triggering. The replaced MDT readout electronics are designed to provide the necessary information for track triggering. A replacement with finer granularity readout electronics is also foreseen for the RPC and TGC trigger chambers.

A major transition is foreseen in the trigger architecture. Both the discovery of a Higgs-like particle with a mass of ~ 125 GeV and the acceptance of key signatures of W, Z or $t\bar{t}$ -pairs require trigger thresholds for single lepton triggers at a p_T -threshold level of 20 GeV. In view of anticipated discoveries the upgraded trigger system should also provide the flexibility to quickly adapt to new physics scenarios. An extrapolation of the current Phase-I trigger rates would lead to Level-1 rates of more than 500 kHz, which is far beyond the scope of the DAQ and trigger systems even after the upgrades performed during LS1 and LS2. To meet these challenges an entirely new trigger layout is implemented for the HL-LHC upgrade. The baseline design for the new architecture is a two staged Level-0/Level-1 hardware trigger with an accept rate of 200 kHz and a total latency of 20 μ s. With a functionality similar to the Phase-II Level-1 trigger, the Level-0 trigger provides an accept rate of 500 kHz within a latency of 6 μ s. As in the current system, the decision is based on coarse information within Regions of Interest (ROI) from the calorimeters and upgraded muon trigger systems. The information is gathered and processed by a central Level-0 trigger system which incorporates topological triggering capability. The Level-1 trigger stage is initiated upon the Level-0 accept, which is broadcasted to the various detector subsystems participating in the Level-1 trigger decision. Within the Level-1 trigger stage the rate is reduced to 200 kHz during an additional latency of 14 μ s. This is achieved by introducing track information within predefined ROI, full calorimeter granularity within the same ROI and a refined muon selection based on the use of the MDT information. This information is again collected by a central Level-1 trigger processor generating the Level-1 trigger signal, which is distributed to all ATLAS detector subsystems. Upon a Level-1 accept signal all data from the subsystems is read out for the HLT processing and subsequent data acquisition. The Phase-II HLT trigger is a software-based single-stage trigger, similar to the Phase-I Level-2 trigger design and is foreseen to operate at an output rate between 5 kHz to 10 kHz using objects at almost full offline precision. This can only be achieved if the software and hardware of the HLT trigger farms are upgraded to comply with the increased bandwidth from Level-1 and the larger event sizes due to large number of simultaneous interactions per bunch crossing.

11.3.1 Inner Detector Upgrade for the HL-LHC

A reliable and well performing ITK builds the fundament to achieve the physics goals set for the HL-LHC. These can only be reached by a complete replacement of the current ATLAS tracker. Despite the harsh environment at the HL-LHC leading to high radiation and occupancy levels, the new ITK is designed to at least maintain and even improve the identification and reconstruction performance performance of the current ATLAS inner detector, despite the tenfold increase in charged particles per interaction. The ITK plays a crucial role in the identification and reconstruction of physics objects such as electrons, photons, muons, tau leptons, but is also important for b-tagging purposes and the reconstruction of certain hadronic decays. Hence the upgraded ITK should be able to provide high precision transverse momentum and direction measurements of isolated particles, such as electrons and muons. In the presence of up to 200 pile-up events it should be able to reconstruct all vertices and identify the

one associated to the hard interaction. Furthermore secondary vertices in b-jets should be identified with high efficiency and purity, even within highly boosted jets, as well as track measurements in the core of a jet, to reduce the rate of misidentified objects. It should also provide the identification of tau-lepton decays and reconstruction of tracks arising from converted photons.

The large number of interactions per bunch crossing poses an extreme challenge to the design of the ITK, as the proton–proton interactions will lead to a drastic increase in radiation damage affecting both the silicon sensors and the electronics. The impact of the radiation on the silicon detectors and the electronics is generally expressed by two quantities: the total ionising dose (TID) measured in Gray ($1 \text{ Gy} = 1 \text{ J/kg}$) and the 1 MeV neutron equivalence. The TID is a measure of the energy loss of high-energetic particles due to direct ionisation processes in the material and is mainly used to quantify surface damage effects from photons, electrons and positrons in the electronic devices. The second quantity measures the non-ionising energy losses (NIEL) that occur through displacements in the atomic lattice and is needed to determine the bulk damage to silicon sensors. It is obtained by weighting the particle spectra with energy dependent damage curves, see Section 10.2. The 1 MeV neutron equivalent dose expected at the HL-LHC after 3000 fb^{-1} is shown in Fig.11.2 and was simulated using FLUKA [249]. Since the current ATLAS detectors are built to withstand to fluences up to $10 \times 10^{15} \text{ n}_{\text{eq}}\text{cm}^{-2}$ (corresponding to 400 fb^{-1} running) for the pixel and $2 \times 10^{14} \text{ n}_{\text{eq}}\text{cm}^{-2}$ in the SCT, the new sensors need to withstand much harsher radiation levels. The maximum 1 MeV $_{\text{neq}}$ fluence predictions for 3000 fb^{-1} in the pixel system is $1.4 \times 10^{16} \text{ n}_{\text{eq}}\text{cm}^{-2}$, seen at the centre of the innermost barrel layer. For the outer pixel barrels, the maximum fluence is $1.7 \times 10^{15} \text{ n}_{\text{eq}}\text{cm}^{-2}$. For the pixel end-cap, the maximum is $1.8 \times 10^{15} \text{ n}_{\text{eq}}\text{cm}^{-2}$ in the most inner layer. The maximum fluence predictions in the strip barrel detectors are $5.3 \times 10^{14} \text{ n}_{\text{eq}}\text{cm}^{-2}$ for layer closest to the interaction point and $2.9 \times 10^{14} \text{ n}_{\text{eq}}\text{cm}^{-2}$ for the outermost strip barrel layer. For the strip end-cap, the maximum fluence of $8.1 \times 10^{14} \text{ n}_{\text{eq}}\text{cm}^{-2}$ is seen in the inner regions of the disk farthest away from the interaction point [249]. The maximum ionising dose predictions for 3000 fb^{-1} in the pixel system is $7.7 \times 10^6 \text{ Gy}$ seen at the end of the innermost barrel layer. For the outer pixel barrels, the maximum dose is $9.0 \times 10^5 \text{ Gy}$ at the end of layer 3. For the pixel end-cap, the maximum is $1.0 \times 10^6 \text{ Gy}$ in the inner regions of disk 4. The maximum dose predictions in the strip barrel detectors are $2.2 \times 10^5 \text{ Gy}$ for short strips (layer 1) and $6.3 \times 10^4 \text{ Gy}$ for long strips (layer 4). For the strip end-cap, the maximum dose of $2.9 \times 10^5 \text{ Gy}$ is seen in the inner regions of disk 7 [249].

In the current inner detector the pixel and SCT front-end electronics were designed for an occupancy level of up to 50 pile-up events. With more than 200 pile-up events expected at the HL-LHC the SCT and pixel detectors will suffer from large occupancy, leading to inefficiencies resulting in major data losses at luminosities above $3 \times 10^{34} \text{ cm}^{-2}\text{sec}^{-1}$, as well as the inability to resolve close-by particles in the SCT. The most dramatic effects due to the expected pile-up are found for the TRT. Being a gaseous detector with readout times much larger than for silicon detectors, the pile-up events, which result in multiplicities beyond > 1000 per rapidity unit, lead to approximately 100% occupancy of the TRT leaving it inoperative under HL-LHC conditions. Hence the current ATLAS inner detector will be replaced by an all silicon inner tracker during the Phase-II upgrade. The new design consists of a pixel detector covering the inner radii surrounded by silicon microstrip sensors. The current baseline layout is shown in Fig. 11.3. However the layout is not yet finalised and discussions on alternative layouts are ongoing and can be found in [244, 250–254]. All layouts have in common that they have a barrel and two end-cap, which are equipped with pixel detectors in the inner and strip detectors of two different strip length in the outer region.

In its current layout the barrel region is arranged in cylinders equipped with four pixel layers, followed by three short strip layers (strip length $\approx 2.4 \text{ cm}$) complemented by two long strip layers (strip length $\approx 4.8 \text{ cm}$ length) covering the current TRT regime. The forward regions are equipped with six pixel discs followed by seven strip discs.

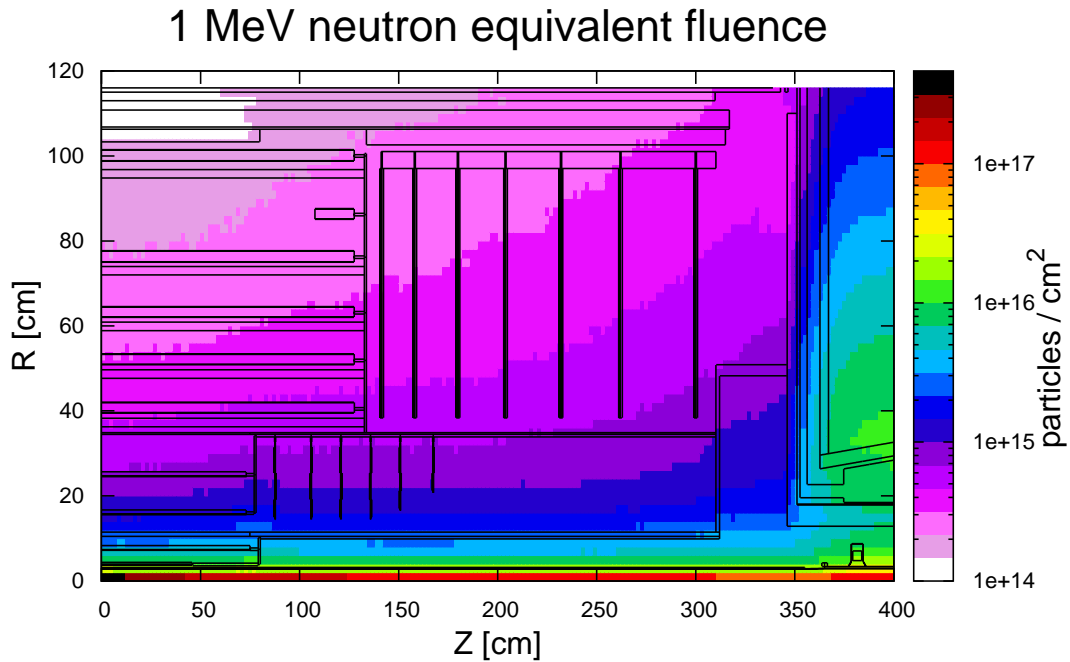


Figure 11.2: Baseline layout of the ATLAS ITK envisaged for the HL-LHC. The graphic shows a projection of one quadrant of the ID in the $r - z$ plane with the active cylinder and disk layers of the pixel (red) and the silicon microstrip detectors (blue). [249]

The barrel pixel layers are arranged at radii $R \sim 39, 78, 155$ and 250 cm from the interaction point. To allow for a higher flexibility and modularity the innermost pixel layer in the barrel region is not integrated to the beam pipe and thus removable without major intervention. This also holds for the barrel and disc layers, which are removable without affecting the silicon microstrip sensors. The size of the pixels is significantly reduced and measures $25 \times 150 \mu\text{m}^2$ for the inner two layers and $50 \times 250 \text{m}^2$ for the outer pixel layers.

This design facilitates robust tracking with at least 14 hits per track for a geometrical acceptance covering a pseudo-rapidity of $|\eta| < 2.5$, at a channel occupancy of less than 1% at a pile-up level up to 200 events. With an overall readout channel number of 638 M for the pixel and 74 M for the silicon microstrip detector. Hence Type-1 services in the ITK require much more channels, and due to the very limited space budget for services per channel, this can only be realised by multiplexing of the different services. The new design also leads to a significantly reduced material budget compared to the current inner detector, which leads to a reduction of tracking inefficiencies arising from hadronic interactions, Bremsstrahlung effects and multiple scattering.

11.4 Silicon Microstrip Detector

The current status of the upgraded silicon microstrip detector plans are the result of more than ten years of extensive research and development, organised in dedicated working groups investigating new

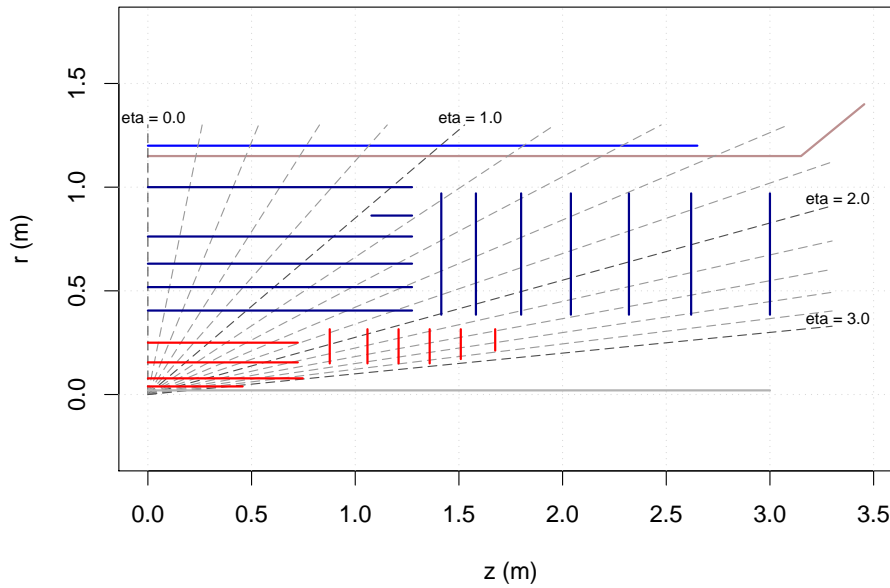


Figure 11.3: Baseline layout of the ATLAS ITK envisaged for the HL-LHC. The graphic shows a projection of one quadrant of the ID in the $r-z$ plane with the barrel and disk layers of the pixel (red) and the silicon microstrip detectors (blue). [244]

technologies and designs for silicon sensors, readout electronics, services and mechanical support. At the moment the design choices in all areas are finalised and are to be published in a Technical Design Report by the end of this year. Besides that the workflow for mass-production and QA strategies are investigated.

The baseline design will incorporate more than 200 m^2 of silicon sensors covering a pseudorapidity area of 2.5 in $|\eta|$. The barrel region consists of five full-length cylinders, organised in three short-strip layers and two long strip layers extending over a region of $\pm 1.3\text{ m}$ parallel to the beam-pipe. The five layers are positioned at $r = 405\text{ mm}$, 519 mm , 762 mm and 1000 mm from the beam-pipe. A so-called stub-layer complements the barrel layout at an radius of $r = 862\text{ mm}$ from the beam-pipe, to cover the loss of acceptance in the transition region between the end-cap and the barrel (see Figure 11.3). On either side of the barrel forward end-caps are installed, each consisting of seven disks. They cover a region of $\pm 1.4\text{ m}$ to $\pm 3\text{ m}$ in z -direction and $\pm 0.4\text{ m}$ to $\pm 1.0\text{ m}$ in radial direction. The whole tracker is encased by a polyethylene moderator, which significantly reduces the energy of neutrons entering from the calorimeter.

The baseline design concept as found in the Letter Of Intent [244] evolves around a common low mass mechanical structure referred to as staves in the barrel and petals in the end-cap region. These structures integrate the modules and house the common electrical, optical and cooling services. They are interfaced via the End-Of-Structure (EOS) card. The barrel region is mounted with 472 of these rectangular staves, each equipped with 28 modules (14 on each side). A schematic view of the stave arrangement in the barrel part in the $r-\phi$ plane is shown in Figure 11.4. The staves are arranged in concentric cylinders centred around the beam-pipe in a turbine-like layout in lengthwise pairs of two units, matched at $z = 0$, and are rotated by a 10° tilt-angle along their long sides, such that they overlap in ϕ -direction. The overlap ensures a hermetic enclosure of the layer down to 1 GeV tracks, while the tilt-

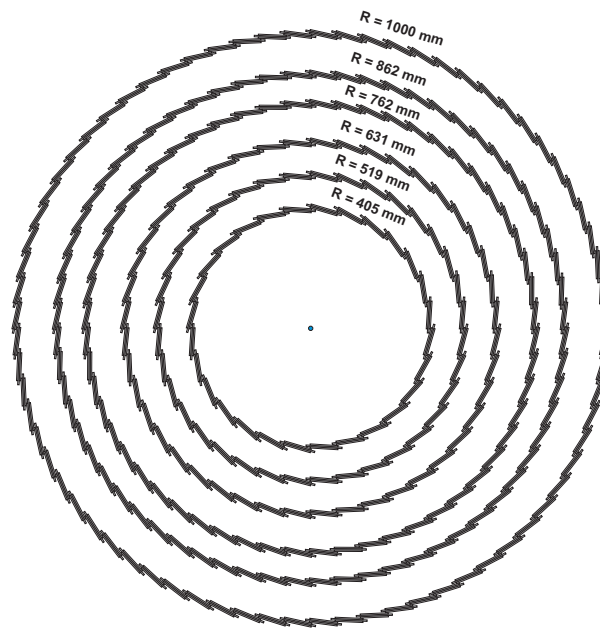


Figure 11.4: Arrangement of staves in barrels. Staves are tilted 10 degrees

angle is chosen to minimise charge distribution between neighbouring strips due to the Lorentz drift of charge carries in the silicon sensor bulk. The layers are inserted into lightweight carbon fibre reinforced plastic cylinders with 2.8 m length and radii matched to the layer radius, which gives torsional stiffness. An advantage of the modular approach of the stave concept is the possibility of an easy replacement of individual staves during the testing stages.

In the end-cap each disk consists of 32 identical wedge-shaped petals. There are two competing concepts for the petal arrangement, shown in Figure 11.5. The upper figure shows the turbine layout, and the lower the two-sided castellated layout, i.e. 16 petals are placed side by side on each side of the disk. Both designs enable to be hermetic down to 1 GeV/c in the end-caps. This highly integrated detector concept reduces the radiation length in the barrel (end-cap) to $1.98 \chi_0$ (1.6) compared with $2.48 \chi_0$ (3.28) for the current SCT.

Stave Concept

Each stave has a length of 1.4 m and is built from a carbon composite structure that provides mechanical support and cooling for 28 modules. The stave core is composed of carbon fibre honeycomb and carbon foam, in which the U-shaped cooling pipes are embedded, as spacing material and carbon fibre facings are glued on either side. Carbon fibre was specifically chosen, due to its high tensile modulus paired with a high thermal conductivity, which is crucial in meeting the thermal requirements to avoid thermal runaway in the silicon sensors. A polyimide bus cable runs along each facing of the stave connecting data input and output lines, low voltage, high voltage and slow control lines to an End of Stave (EoS) card, for all modules of a half stave. All electrical connections are also routed through the EOS card, which contains optical interconnects, buffers and high-voltage (HV) multiplexers for powering and communication with the trigger system and the off detector electronics, as well as a detector control system (DCS) chip. Each stave is equipped with 14 sensors on either side, with a $200 \mu\text{m}$ spacing between the sensors. To enable the second coordinate measurement, the sensors have axial orientation on one side and are rotated by an stereo angle of 40 mrad on the opposite side. The silicon microstrip detectors are

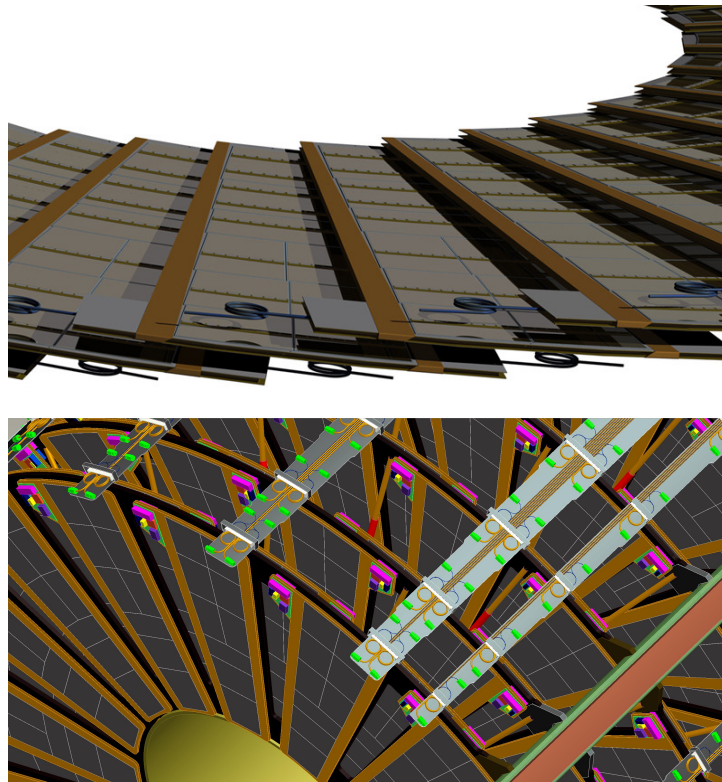


Figure 11.5: Schematic view of different layout considered for the assembly of the petals. The turbine layout is shown in the upper figure and the castellated layout is depicted in the lower figure. [244]

glued on the bus cable and hybrids carrying the front-end electronics are then glued on top of the sensitive side of the detectors. The sensors are made of p-type float zone silicon bulk materials with n-type implants with a thickness of 300 to 320 μm and AC-coupling. To maximally exploit the size of a 6-inch wafer, the barrel sensors will have a size of $97.54 \times 97.54 \text{ mm}^2$. The first three layers are equipped with four rows of 1280 readout strips with a pitch of 75 μm each at a strip length of 23.82 mm and a field-shaping strip at each side across a sensor, while the outer two layers have a strip length of 47.775 mm and two rows. In order to save material and provide an efficient heat transfer, hybrids are glued directly onto the sensitive sensor surface. The hybrids distribute the data in- and output and powering lines to the column of ten readout ASICs, constructed in 130 nm CMOS technology (called ABC130), which are attached to the hybrid. The ABC130 are binary readout chips with 256 channels each, they are connected to the sensor strips using Al wire-bonds. Hence each hybrid is capable of reading out two rows of 2×1280 strips each, providing the hit information for all channels above a certain threshold. These are stored in a pipeline memory and are read out upon a Level-0 trigger signal for further processing. ABC130 incorporates two buffers that permit implementation of a two level trigger scheme anticipated in a Level-0 and Level-1 trigger. The strips can be read out at a rate of 500 kHz at Level-0 and 200 kHz at Level-1. Each hybrid is also equipped with a uniquely addressed Hybrid Controller Chip (HCC). It provides the interface between the ABC130s and the EOS and distributes the information on trigger, timing and control (TTC). The information is sent from the HCC via dedicated links (e-link) to the EOS. Each EOS contains a GigaBit Transceiver (GBT), which connects the HCCs and a Versatile link (Vlink) fibre optic driver.

Intensive R&D effort has been put into the powering of the upgraded strip detector. In the current ATLAS SCT, each module is provided with an individual high and low voltage supply. However with an increase from currently 4,088 to 20,000 modules for the ITk strip detector this is impractical due to the increase of inactive material in the tracking volume and would lead to severe space and routing constraints on the design of the detector. Hence several modules will be grouped together and share the LV and HV supplies. Low-voltage multiplexing for groups of modules can be achieved through serial powering (SP) or point-of-load Direct Current to Direct Current (DC-DC) [255] conversion and due to the comparison of the electrical performance of the stave prototypes DC-DC powering was chosen for the LV powering scheme [256]. Studies for the HV multiplexing are still ongoing and it is envisaged to use one HV supply for several modules which still allows switching of individual modules, such that a single failure does not affect the others. The current prototypes exploit commercial small footprint Gallium Nitride (GaN), Silicon JFET, Silicon MOSFET, and Silicon Carbide (SiC) JFET devices, which are capable of switching voltages up to 1700 V. The HV and LV power are connected to the EOS and are distributed to each hybrid via a power bus.

The total cooling power needed for the strip tracker will increase from currently $\sim 22 \text{ kW}$ for the current SCT to $\sim 75 \text{ kW}$ at the HL-LHC strip tracker. The envisaged cooling power is provided by a novel two-phase CO_2 cooling system, running at coolant temperature of $-35 \text{ }^\circ\text{C}$. Liquid CO_2 has the advantage of a larger heat transfer, than the current fluorocarbon based cooling system of the SCT², which allows the use of smaller Ti cooling tube diameters and hence less inactive material in the tracker volume and easier handling due to its non-toxicity, as well as lower mechanical forces during thermal expansion. The cooling system is designed to optimise the thermal path. Hence the Ti cooling pipes are directly embedded into the carbon foam and the sensors are directly glued onto the staves (petals) bus tape or carbon face sheet, to utilise the full sensor cross-sectional area of the module for heat transfer. The cooling lines itself are multiplexed and connected to one inlet and one outlet per stave or petal. A CO_2 cooling system is currently utilised in the IBL and serves as a prototype for ITk upgrade cooling

² Which is currently considered as a backup option

system. Further information on the cooling system can be found in [257].

11.4.1 Petal Concept

The petal concept is analogous to the stave concept covering the forward region. Each petal consists of a roughly 60 cm long wedge-shaped carbon fibre support structure, with a U-shaped cooling pipe embedded in carbon foam within a carbon fibre honeycomb core. Petals have fewer modules than staves and most have single hybrids, which reduces the power load and servicing needed. The cable bus runs along the outer edge of a petal and each side of the petal has an EOS, which connects the cable bus on that side. Each petal-face houses nine sensors organised in six rings in ϕ direction, which are directly glued onto the carbon fibre facings to reduce thermal impedance. The outer rings are equipped with two modules side by side whilst the inner three rings hold one module each, therefore the inner modules will be cooled by two lengths of cooling pipe, while the outer modules, are cooled by one pipe. Due to the complex geometry the petal is equipped with six different sensor geometries to cover the petal facing and avoiding dead areas or unnecessary overlap in any regions. A total of 13 different flex-circuit hybrid geometries are designed, which hold the readout ASICs and provide the electrical lines for detector control, data transmission and powering. Again the hybrids are directly glued onto the active sensor material using electronics grade epoxy. This does not only reduce the dead material in the tracker, but is also an efficient way to achieve the required heat transport. The various petal sensors are designed with radial strips, pointing to the beam-line, allowing for an accurate measurement of the $r-\phi$ coordinate. To provide a stereo space point measurement the strips are rotated by 20 mrad within the sensor, resulting in a 40 mrad stereo angle between strips on the opposite petal side. In case of the petals, the polyimide bus tape is run along the edge on either side of the petal and are connected to the EOS cards, placed at upper edge of either petal side. Alike the stave, the EOS cards contains optical and electrical connections for DCS, powering and data readout for the three lower sensors and right handed sensors from the upper three rows from the front and backside.

The petal support is given by an inner cylinder and an outer frame, with structural elements connecting the two and is mostly made of carbon fibre. Each of these structures holds 32 petals. The outer cylinder also provides the support for the service infrastructures needed, along the z -direction.

11.4.2 Super-Module Concept

A Super-Module concept [258, 259] has been developed as an alternative to the stave concept, and is currently considered as a fallback option. The Super-Module concept is an advancement of the current SCT modules. Like in the SCT, double-sided modules are attached to a light, stable carbon-fibre local support structure (LS) which in turn is inserted into the overall tracker support structure.

The modules are built by gluing two silicon sensors onto a central thermal pyrolytical graphite (TPG) base-board, which offers the necessary mechanical stability and thermal contact, as shown in Figure 11.7 (a). Flex hybrids, made of a four-layer copper-polyimide, are attached on either side of the module. Each hybrid holds two columns of ABC130 readout ASICs, and host the necessary routing for power and signals. The hybrids are glued onto a carbon-fibre bridge, which is supported by Aluminium-Nitride (AlN) facings at both ends on the TPG base-board. In contrast to the stave concept the hybrids are thus not in direct contact with the sensor surface. A Super-Module is the arrangement of thirteen of these double-sided modules into the lightweight and stiff local support structure, made of a central carbon-fibre tube and supporting carbon-fibre wing-like structures which hold the individual double sided modules as shown in Figure 11.7 (b) and (c). Cooling plates with a high thermal conductivity are attached to the wings, which provide both mechanical and thermal contact for the modules to the cooling pipes, resid-

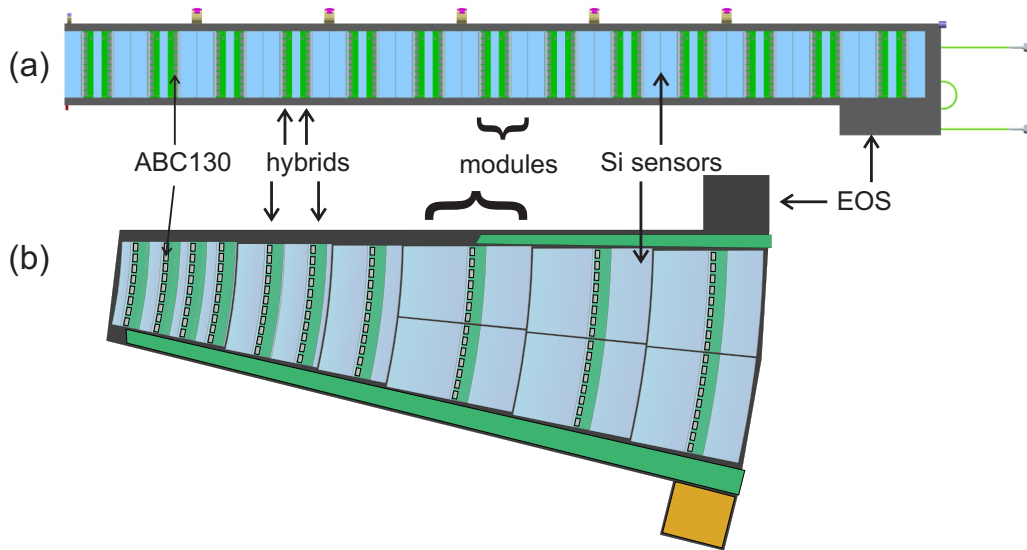


Figure 11.6: Schematic view of the concept of the barrel stave (a) and end-cap petal (b) layout with its different components. [244]

ing at the lateral sides. The highly modular Super-Module approach provides mechanically independent subcomponents aimed at minimising mechanical stress and easing the integration and potential rework of individual components at the latest stages in the assembly and testing process. Current design key issues are the optimisation and further characterisation of the service bus and power distribution, i.e. the choice of DC-DC or serial powering for the super-module. A further aim is to minimise the material budget, currently estimated in the range of $2.15 X_0$ to $2.25 X_0$ while keeping the mechanical and electrical integrity and the long-term operational robustness.

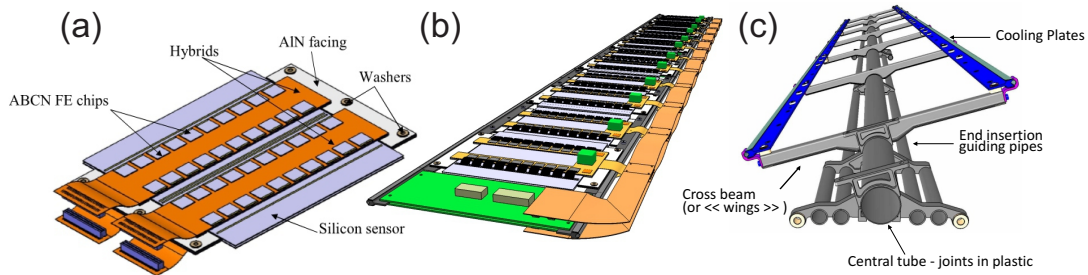


Figure 11.7: Schematic view of the different components of (a) a double-sided short strip detector module, (b) the main components of a fully assembled Supermodule and (c) the local support and cooling structure. Taken from [258].

11.5 ATLAS HPK 07 Sensors

The silicon microstrip detectors for the ATLAS upgrade will be n-in-p type sensors, i.e. using a n-type readout in a p-type bulk material. These sensors are favourable due to their higher radiation tolerance compared with the current ATLAS SCT p-in-n type sensors and reach similar levels as n-in-n type sensors, see Section 10.3. Thorough evaluation of n-in-p sensor properties and different sensor layouts

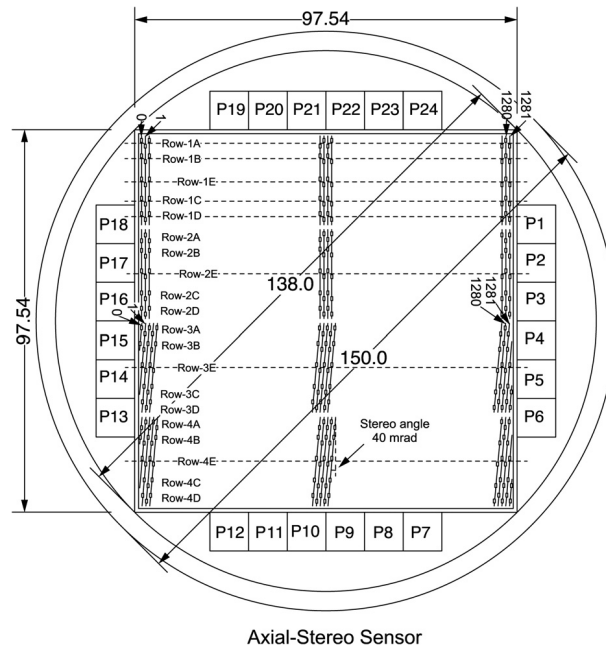


Figure 11.8: Wafer layout of the ATLAS07 p-type sensors. The large-area sensor is placed in the middle and is divided into four rows of 1280 strips each. The large area sensor is surrounded by 24 miniature sensors. Taken from [260].

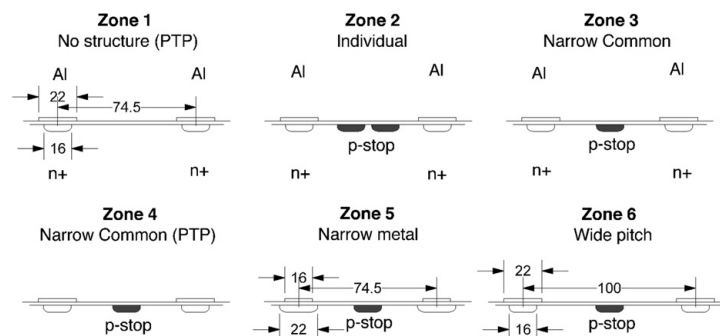


Figure 11.9: Cross-sections of the strip (n+) and the isolation structures (e.g., p-stop) in the surface of the miniature sensors. Six structures, named Zone 1 to Zone 6, are implemented on the miniature sensors. The large-area sensor is designed using the layout of Zone 3. The dimensions are given in mm. Taken from [260]

has been conducted in large scale test campaigns by the ATLAS collaboration. Within this thesis silicon strip sensors from one of these prototype campaigns, called ATLAS07 [260] are evaluated. The ATLAS07 sensors were designed by the collaboration and produced by Hamamatsu Photonics [261] on float-zone silicon substrate with a $\langle 100 \rangle$ crystal orientation and a resistivity of $\sim 6.7 \text{ k}\Omega\text{cm}$. These sensors were produced to study strip isolation schemes, high-voltage performance, punch-through protection, and charge collection as a function of the irradiated fluence. The mask layout of the 6 inch (150 mm) wafer is shown in Fig 11.8. The central piece is the large area strip sensor of $9.75 \times 9.75 \text{ cm}^2$, which is the maximum square size possible. Additionally 24 (P1–P24) $1 \times 1 \text{ cm}^2$ miniature strip sensors are included on each wafer, with various strip and isolation structures. The remaining space on the wafer is equipped with $4 \times 4 \text{ mm}^2$ diodes. All strip sensors have a thickness of $320 \mu\text{m}$.

The large area sensor contains four rows of 1280 strips each, with a pitch of $74.5 \mu\text{m}$. Each strip is 16 mm wide and has a length of 28.82 mm. The upper two rows have an axial strip orientation, i.e. the strip is orientated parallel to the sensor edge, while the lower two rows have stereo strips, that are inclined by 40 mrad with respect to the sensor edge. The n-type strip row is surrounded by a bias-ring, which is connected to each individual strip via a polysilicon resistor, used to bias the strips. The collected charge at each strip is read out via a metallisation on top of each strip. The metallisation layer also provides several DC and AC coupled contact pads for each strip, which can be used for wire bonds to readout ASICs or for testing purposes. To protect the top layer strip implantations and the bias ring from high voltage short cuts at the sensor edges an additional outer floating p-type guard ring surrounds the bias ring. The silicon surface is covered by a silicon oxide layer. Due to the accumulation of built-in defects and radiation damages arising from the ionising dose, electrons are accumulated in the interface layer between the silicon and the silicon oxide, causing potential shortcuts between neighbouring n-implants. To efficiently prevented these shortcuts, additional p-type structures between the n-type implants are introduced, to isolate the n-strip implants from one another. This is done by either by covering the whole readout side with a p^+ layer, referred to as p-spray or by implanting p-doped ions in restricted areas surrounding the n-type implants, called p-stop structures. The different p-stop layouts are presented in Fig. 11.9. In the large area sensors, the n-strips are surrounded by common $6 \mu\text{m}$ wide p-stop implants, corresponding to the layout shown for Zone 3 of Fig.11.9.

Each miniature sensor accommodates 104 8 mm long strips with a pitch of $74.5 \mu\text{m}$. The ATLAS07 miniature sensors were made with an integrated AC-coupling structure, consisting of a sandwich of an insulating layer with aluminium and implant strips. For the sensors used within this thesis the aluminium-metal is wider than the n-strip implant, hence the wider metal functions as a field plate to reduce the electric field strength at the n-strip implant edge in cases where the potential of the metal and the n-strip is the same. Both p-spray and p-stop isolation schemes were used on the sensors. Further details on the design, including strip isolation structures, are given in Ref.[260]. Both the large scale and the miniature sensors have undergone an intensive testing and measuring. A summary of the comparison between the design specifications and the actual measurements, performed at several institutes, is found in Table. 11.1, a reasonable agreement between the measurements of the different characteristics and the design specifications are found. Within this thesis the large scale sensors were measured during the setup of a centralised test facility(see Section 13.3), while miniature sensors evaluated in beam test measurement (see Chapter 12) and in laboratory measurements (see brief summary in Section 11.5.2).

11.5.1 Irradiations

One of the main motivations for the development of the miniature ATLAS07 sensors was a thorough understanding of their performance after the exposure to radiation doses comparable to those expected at the HL-LHC. It was the authors responsibility to prepare and conduct the proton irradiations of the

	ATLAS07 Specification	Measurement
Leakage Current	$< 200 \mu\text{A}$	200 nA
Full Depletion Voltage	$< 500 \text{ V}$	190 V to 245 V
Coupling Capacitance at 1 kHz	$> 20 \text{ pF/cm}$	28 pF/cm
Silicon Bias Resistance	$(1.5 \pm 0.5) \text{ M}\Omega$	1.3 M Ω to 1.6 M Ω
Current through dielectric	$I_{diel} < 10 \text{ nA}$	$< 10 \text{ nA}$
Strip Current	No explicit limit	$< 2 \text{ nA}$
Inter-strip Capacitance	1.1 pF	0.7 pF to 1.8 pF
Inter-strip Resistance per cm	$> 10x R_{bias} \approx 15 \text{ M}\Omega$	$> 150 \text{ G}\Omega$

Table 11.1: Comparison of measured parameter values and with technical specification [262].



Figure 11.10: Picture of the irradiation setup at Karlsruhe. The miniature sensors are mounted on an aluminium frame and inserted into the insulated box.

sensors in collaboration with the Forschungszentrum Karlsruhe.

The sensors were irradiated at the Irradiation Centre Karlsruhe, with a 23 MeV proton beam from a Compact Cyclotron operated by the ZAG Zyclotron AG [263]. A detailed overview on the irradiation facility is found in References [264, 265]. The machine accelerates H_2^+ ions, where the electrons are stripped of by the foil closing the beam pipe, which is also used as an online monitoring measurement of the beam current. The samples are placed in a thermally and electrically insulated box, mounted on a controlled x-y stage, placed 50 cm from the exit window. This allows the irradiation of objects up to an area of $400 \times 200 \text{ mm}^2$ by scanning the sample. To avoid an increased irradiation dose due to the scanning procedure, the scanning area is enlarged by a minimum of 10 mm at either side. A picture of the ATLAS07 miniature sensors mounted in the insulated box is shown in Fig. 11.10. The sensors are fixed on an aluminium frame using kapton tape, which in turn is inserted into an insulated styrodur box. The front window of the box is made of two layers of mylar foil and the back is equipped with a graphite absorber. Due to heating effects typical beam currents are limited to $1.5 \mu\text{A}$, hence the irradiation of an ATLAS07 miniature sensor to $5 \times 10^{15} \text{ n}_{\text{eq}}/\text{cm}^2$ takes about 90 min. During the course of the irradiation the sensors were held at a temperature of $-30 \text{ }^\circ\text{C}$ using cooled nitrogen gas. The irradiation fluence is estimated by [264]

$$F_{\text{est}} \sim \frac{nI}{q_{\text{el}}v_x\Delta z}, \quad (11.1)$$

where n is the number of scans, I is the proton beam current, q_{el} denotes the electric charge, v_x is the horizontal scan velocity and Δz is the step width in vertical direction. A hardness factor of 1.85 is taken for the appropriate NIEL scaling of the proton beam for the samples irradiated within this thesis. The post irradiation dosimetry is done by measuring the activity of ^{57}Ni foils, which are attached to the back of the sensors during the irradiation process. The foil is activated by proton collisions and the electron capture of ^{57}Ni is observed by means of γ spectroscopy, which uses the dominating γ line at 1377.6 keV to determine the specific activity. The fluence is then determined as the ratio between the activity and a calibration factor assigned to the proton current. Additionally the half life of ^{57}Ni , has to be considered, in cases where considerable time has passed between the irradiation process and the measurement of the specific activity.

11.5.2 Measurements performed in the Laboratory

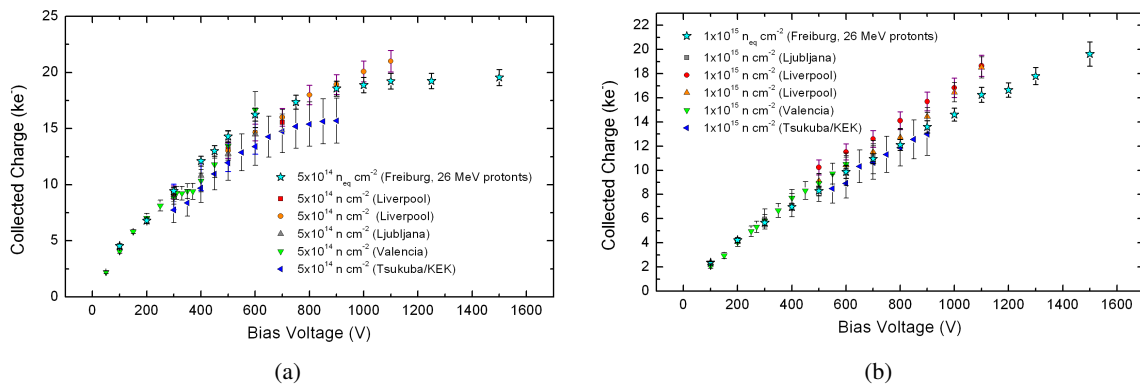


Figure 11.11: Charge collection as a function of the bias voltage measured at different sites. The sensors were irradiated with proton to fluences of $5 \times 10^{14} \text{ n}_{\text{eq}} \text{ cm}^{-2}$ in (a) and $1 \times 10^{15} \text{ n}_{\text{eq}} \text{ cm}^{-2}$ in (b).

Some of the irradiated ministrip sensors were measured by the author of this thesis using laboratory setups in Freiburg and contributed to the large scale test campaign performed together with Liverpool University, Jozef Stefan Institute in Ljubljana, UC-Santa Cruz, Tsukuba University/KEK and IFIC-Valencia. The sensors were irradiated to fluences of $5 \times 10^{14} \text{ n}_{\text{eq}}\text{cm}^{-2}$ and $1 \times 10^{15} \text{ n}_{\text{eq}}\text{cm}^{-2}$. While the lower fluence corresponds to the expected accumulated fluence in the outer region of the inner tracker, the latter corresponds to the expected radiation level at the innermost strip layer of the inner tracker layout.

The sensors performance was evaluated in terms of charge collection efficiency using electrons from a ^{90}Sr source and space resolved measurements using a 1064 nm laser setup, as well as current/voltage and capacitance/voltage measurements. A summary of the charge collection of the proton irradiated ministrip sensors prior to annealing is shown for the sensors irradiated to $5 \times 10^{14} \text{ n}_{\text{eq}}\text{cm}^{-2}$ in Fig. 11.11(a) and those irradiated $1 \times 10^{15} \text{ n}_{\text{eq}}\text{cm}^{-2}$ in Fig. 11.11(b). The measurements taken at the different sites using various readout systems are in good agreement. The expected signal of an unirradiated ATLAS07 sensors given a thickness of $(320 \pm 20) \mu\text{m}$ is $(24.7 \pm 1.6) \text{ ke}$. Hence a degradation of the charge collection arising from the high irradiation fluences is clearly visible. In an unirradiated sensor the maximum signal would be reached with the full depletion voltage of the sensor, at values of less than 200 V. Assuming a voltage limit of 500 V, 10 ke are collected for the sensors irradiated to $5 \times 10^{14} \text{ n}_{\text{eq}}\text{cm}^{-2}$, which decreases to about 8 ke for the higher irradiation dose $1 \times 10^{15} \text{ n}_{\text{eq}}\text{cm}^{-2}$. the collected charge would suffice even with the expected full radiation damage at the HL-LHC.

These and further measurements conducted under participation of the author in Freiburg are also summarised by the author in Ref. [266] or co-authored amongst others in Ref. [267].

Beam Test Measurements of Silicon Sensors Irradiated to HL-LHC Fluences

This chapter reports the results of beam test measurements conducted at the CERN H2 beamline in July 2009. Within this beam test nine different miniature n-in-p silicon sensors, irradiated to fluences up to $3 \times 10^{15} \text{ n}_{\text{eq}}\text{cm}^{-2}$, were measured. The devices under test include three planar silicon microstrip sensors from the ATLAS07 production and six 3D detectors from two different manufacturers. The objectives of the beam test measurements are the measurement of the radiation hardness of n-in-p material at fluences comparable to those expected at the HL-LHC and comparative measurements between sensors in planar and 3D detector geometry. Within this thesis a focus is set on the results from the planar ATLAS07 sensors, while the results of the 3D-detectors are treated in great detail in Ref. [225]. Some of the results quoted here have been previously reported by the author of this thesis in Ref. [268]. Results of the beam test analysis, provided by the author of this thesis, also gave significant contributions to the co-authored publications found in Refs. [267, 269–272].

12.1 Devices under Test

The results described in this section focus on planar miniature sensors from the ATLAS07 production described in Section 11.5. The sensors inserted in the beam test are either Zone 2 or Zone 3 sensors and have strip isolation schemes with high doses of p-stop and p-spray implants as shown in Fig. 11.9. The sensors from Zone 2 have individual p-stop implants encircling each n-strip, while the Z3 sensors have one continuous common p-stop implant in between the n-strips. An additional p-spray layer is found for the sensor W44-BZ2-P5. A summary on the serial numbers and the radiation fluences is found in Table 12.1.

serial number	strip isolation (cm^{-2})	radiation fluence ($\text{n}_{\text{eq}}/\text{cm}^2$)
W33-BZ3-P18	4×10^{12} p-stop	5×10^{13}
W44-BZ2-P5	4×10^{12} p-stop + p-spray	1×10^{15}
W33-BZ3-P15	4×10^{12} p-stop	3×10^{15}

Table 12.1: Radiation fluences of the devices under test.

The beam test also included 3D detectors produced by IMB-CNM (Barcelona, Spain) [273]. They

consist of float-zone silicon with a resistivity of 1 to 5 k Ω cm and are designed in a double-sided processing technology on p-type substrate [274]. The n⁺-doped junction columns are etched into the wafer from the front side and p⁺-doped ohmic columns are etched from the back side. The sensors have a substrate thickness of 285 μ m and both column types have a depth of 250 μ m at a radius of \sim 10 μ m. Hence they do not penetrate the sensor completely. The columns are partially filled with polysilicon. Strips are formed by connecting the junction columns in a row by a metallisation layer. The ohmic columns are connected to a metallisation layer, which in turn is connected to a p⁺-doped polysilicon layer. Each 3D detector contains 50 strips with a pitch of 80 μ m and a length of 4 mm. Each of these strips is connected to an individual channel of the readout chip via a pitch-adaptor with integrated capacitors to achieve AC-coupling. The active area is surrounded by a 3D guard ring consisting of n⁺ and p⁺ columns. To provide isolation of the strips after radiation-induced accumulation of oxide charges, each n⁺ column is surrounded by a p-stop implantation on the front side. The sensors in this beam test were irradiated at the FZK as described in Sec. 11.5.1. The planar detectors were irradiated to fluences of 5×10^{13} n_{eq}cm⁻², 1×10^{15} n_{eq}cm⁻² and 3×10^{15} n_{eq}cm⁻². The sensors irradiated to 5×10^{13} n_{eq}cm⁻² are regarded as lightly irradiated since no significant radiation damage leading to a lower signal is expected at this comparatively low fluence. While one of the 3D detectors was kept unirradiated, the other two received fluences of 1×10^{15} n_{eq}cm⁻² and 2×10^{15} n_{eq}cm⁻². No annealing has been performed on purpose, however the devices under test were stored at room temperature between preparation and the measurements a maximum of three days.

12.2 Experimental Setup

The beam test was performed at the North Area H2 beamline in Juli 2009 using 225 GeV pions. The pion beam is produced by impinging the incoming proton beams of the SPS accelerator onto a Beryllium target. The collisions of the protons with the target provide a variety of particles, such as electrons, positrons, muons, pions, kaons and (anti-)protons, from which the pions are selected and transported to the user areas. The devices under test were inserted into the Silicon Beam Telescope (SiBT) [275, 276],

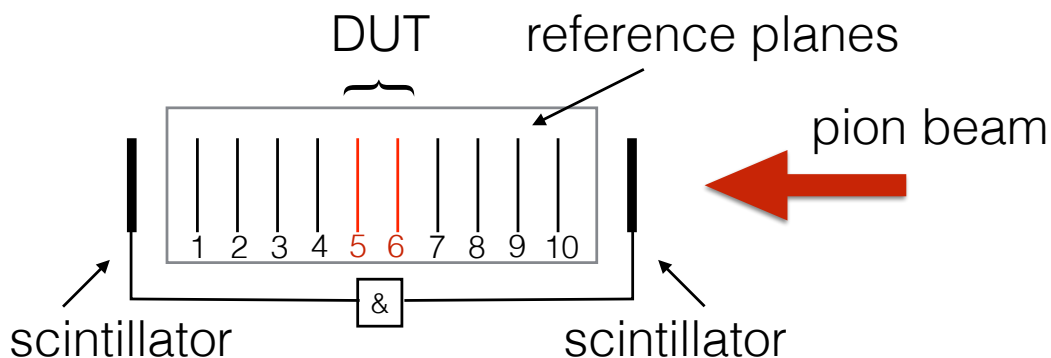


Figure 12.1: Schematic of the silicon beam telescope. The cooled box consists of eight reference planes (1-4 and 7-10) and two planes to insert devices under test (5+6). The telescope is triggered by the coincidence of the two scintillators.

which provides reference tracks with a nominal resolution of up to 3 μ m. The SiBT is consists of 10 slots for modules with a 4 cm separation. Figure 12.1 shows a schematic of the beam telescope. The SiBT is equipped with eight reference silicon microstrip modules, inserted into slots 1 – 4 and 7 – 10 and two

slots (5 and 6) holding the test modules. The beam telescope is installed inside a cold chamber known as Vienna box, which allows cooling down to $-25\text{ }^{\circ}\text{C}$ using two Peltier elements. The Vienna box is placed perpendicular to the beam and is triggered by the coincidence of two scintillators placed on either side of the setup, as shown in the schematic Fig. 12.1. The reference sensors are single sided AC coupled Si strip detectors produced by Hamamatsu Photonics (HPK) [261]. These are made from high resistivity float-zone material with a thickness of $(320 \pm 20)\text{ }\mu\text{m}$ and an active area of $98 \times 38\text{ mm}^2$. Each sensor has 639 strips with a readout pitch of $60\text{ }\mu\text{m}$. Between the readout strips electrically floating strips are installed, which allow to achieve an effective pitch of $30\text{ }\mu\text{m}$. The full depletion voltage of these reference sensors at room temperature is of the order of 100 V . The reference sensors are installed as pairs with alternating rotation of $\pm 45^{\circ}$ relative to the floor of the box. This generates four space-points, and leads to an active area of $38 \times 38\text{ mm}^2$ of the SiBT. The reference tracks are reconstructed using the method described in Ref. [275] and a resolution of $4\text{ }\mu\text{m}$ is achieved. The readout electronics and the data acquisition is based on CMS Tracker prototype components. Hence the reference sensors and the devices under test are connected to the CMS APV hybrid boards via pitch adapters. The hybrid boards are equipped with six APV25 hybrid chips and each chip contains 128 channels. The APV25 chips employ a charge sensitive preamplifier and a CR-RC shaping, which transform the detector signal into a Gaussian pulse. These analogue pulses are sampled at a frequency of 40 MHz and stored in a memory pipeline from where they are retrieved upon a trigger signal. During this beam test, the APV25 chips were operated in peak mode meaning that one pipeline cell is retrieved per channel. The signals are further amplified and transmitted to the front-end driver cards which digitise the signal using analogue-to-digital converters (ADCs). The ADC counts are then stored for further data analysis. Since the pion beam was asynchronous to the local 40 MHz master clock of the SiBT, the signal level was not always at its maximum level upon sampling. The estimated signal loss due to this operation mode is of the order of 10% [275]. Alternatively, it would have been possible to gather only those particles that coincided with the 40 MHz clock. This would have lead to a significant reduction in the trigger rate, and was thus discarded.

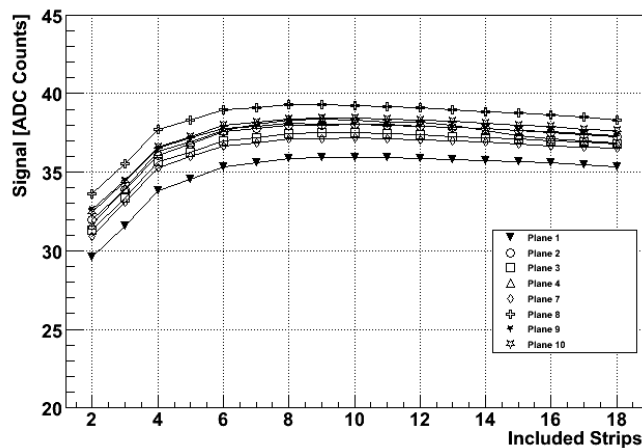


Figure 12.2: The most probable value of the signal of the SiBT reference sensors as a function of the number of strips included in the signal summation.

12.3 Data Preparation

12.3.1 Alignment

A precise knowledge of the impact point of the track on the sensor surface is of fundamental importance for all measurements involving a space resolved signal. The track parameters in the beam test measurements are provided in the reference frame of the SiBT. In order to transform these into the reference frame of the sensor, an alignment procedure based on a χ^2 -minimisation has been put in place. A detailed description of the alignment method is found in Ref. [277]. Figure 12.3 shows a schematic of

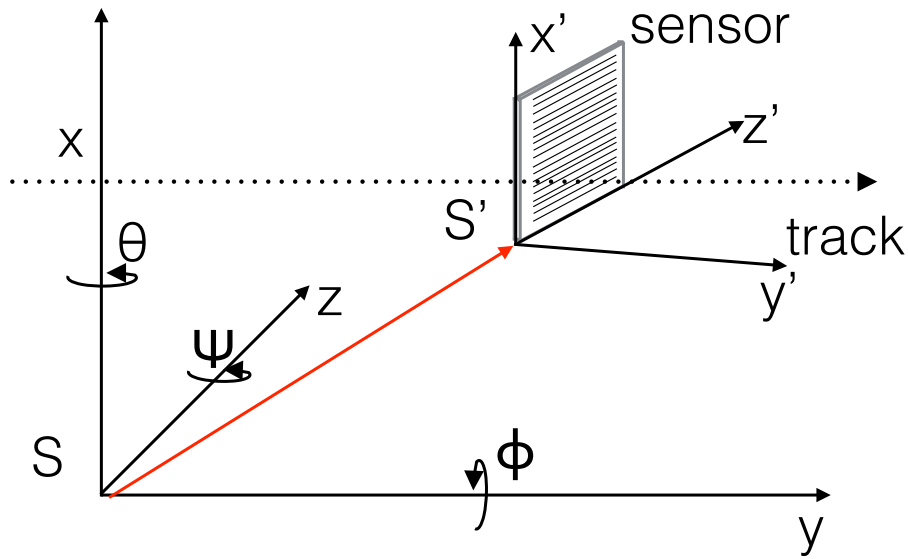


Figure 12.3: Coordinate system of the SiBT reference frame S and the local coordinate system of the sensor S' . The sensor strips run parallel to the z' axis. The origins of both coordinate systems are connected via the translation vector \vec{t} . The rotations of the sensor are given by the rotation matrix $R = R_z(\psi)R_y(\phi)R_x(\theta)$.

the coordinate system of the SiBT reference frame and of the sensor frame. The sensor is positioned in the $x' - z'$ plane in the local coordinate system S' , with the readout strips running parallel to the z' axis. The position \vec{r} of the reference track and the direction $d\vec{r}$ is given in the global system for a fixed y , taken to be at the position of the device under test given by the construction of the SiBT. The goal of the alignment is to find the position of impact \vec{p} on the surface of the sensor under test. Therefore a transformation from the local coordinate system of the device under test S' into the global reference frame of the telescope S is needed. This is achieved by a translation of the origin in the reference frame to the origin in the local frame, given by the vector \vec{t} and a rotation R , including the three rotations around the axis in the global reference frame S , expressed by $R = R_z(\psi)R_y(\phi)R_x(\theta)$, where $R_{x,y,z}$ are rotation matrices. The transformation of the vectors \vec{r} and $d\vec{r}$ into the sensor system S' are then given by

$$\vec{r}' = R^{-1}(\vec{r} - \vec{t}) \quad (12.1)$$

$$d\vec{r}' = R^{-1}d\vec{r}. \quad (12.2)$$

The determination of the point of impact \vec{p} on the sensor surface accounts for an additional tilt or shift within the sensor plane, given by

$$\vec{p} = \vec{r}' - \frac{r'_y}{dr'_y} d\vec{r}' \quad (12.3)$$

The rotation angles ϕ, θ, ψ and the translation vector \vec{t} are determined by a minimisation of the residuals between the predicted position, determined by the beam telescope, and the measured track position, given by the device under test. The χ^2 minimisation is computed using

$$\chi = \sum_{n_{\text{Events}}} \left(\frac{(p_x - x_{\text{dut}})^2}{\sigma_x^2} + \frac{(p_z - z_{\text{dut}})^2}{\sigma_z^2} \right), \quad (12.4)$$

The device under test (DUT) is oriented such that x_{dut} is perpendicular to the readout strips. The coordinate x' is defined as the centre of the readout strip with the highest signal to noise ratio in that event. Since strip detectors are not segmented parallel to the readout strips, the variable z_{dut} is set to the middle of the strips in z' direction for all hits. The coordinates p_x and p_z are measured by the beam telescope and transformed according to Eq. 12.3.1. The uncertainty are given by track extrapolation uncertainties of the telescope σ_{SiBT} , combined with the binary resolution of the strip detectors

$$\sigma_x = \sqrt{\sigma_{\text{SiBT}}^2 \frac{p_{\text{dut}}^2}{12}} \sim \frac{p_{\text{dut}}}{\sqrt{12}} \quad (12.5)$$

$$\sigma_y = \sqrt{\sigma_{\text{SiBT}}^2 \frac{l_{\text{dut}}^2}{12}} \sim \frac{l_{\text{dut}}}{\sqrt{12}}, \quad (12.6)$$

where p_{dut} is the pitch of the device under test and l_{dut} the corresponding strip length. Given that the sensors measured within this beam test have a pitch of $\sim 80 \mu\text{m}$, and a strip length of several millimetres, the resolution of the SiBT of the order of $3 \mu\text{m}$ can be safely neglected.

The track extrapolation uncertainty is a function of the telescope resolution and the alignment uncertainty. It can be approximated by calculating the residuals, given as the difference between the track position measured by the device under test and the track position given by the telescope.

To calculate the residuals, the strip with the highest signal to noise ratio was calculated for each event. Since large charge sharing between neighbouring strips would limit the resolution, only those signal hits with negligible charge sharing are considered. Hence events are discarded in which the neighbouring strips of the highest signal to noise strip have a signal to noise ratio larger than three. Exemplary residual distributions are shown in Fig. 12.4 for the sensor irradiated to $5 \times 10^{13} \text{ n}_{\text{eq}}/\text{cm}^2$ for a single run at a bias voltage of 500 V. Ideally the distribution should follow a rectangular function, however the edges are smeared out due to the track extrapolation uncertainties. The residual distribution along x direction, shown in Fig. 12.4(a), is fitted with a convolution of a Gaussian and a rectangular function. The Gaussian width of the fitted function defines the track extrapolation error. In this case an extrapolation error of $\sigma = (6.7 \pm 0.3) \mu\text{m}$ was extracted from the fit.

For asymmetric beam shapes the distribution of residuals running along the strip length are not centred around zero, but depend strongly on the beam shape in z -direction and is different for runs with different beam shapes. Nevertheless, the residuals along the z direction have to be included in the calculation of χ^2 to use the information for the angle theta, affecting the apparent strip length. As one can see in Fig. 12.4(b) the strip length of 0.8 cm is clearly reproduced. Most of the data taking runs during the beam test collected the signal of about 100 000 triggers. The impact point of the corresponding tracks

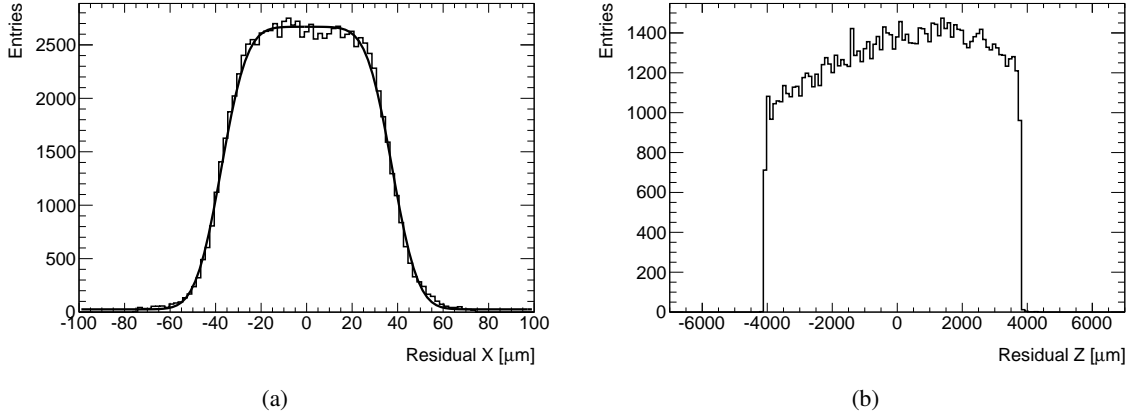


Figure 12.4: Residual perpendicular (a) and transverse (b) to the strip of the sensor irradiated to $5 \times 10^{13} \text{ n}_{\text{eq}}/\text{cm}^2$ at a bias voltage of 500 V.

are subject to the position of the beam spot, its size and the beam luminosity. Since the active area of the device under test is smaller than the active area of the beam telescope, in general runs at the same bias voltage taken under the same run conditions are combined. The alignment is influenced both by interruptions to the beam telescope, due to maintenance work, and changes to the operating temperature. Therefore the alignment procedure must be recomputed after each intervention.

12.3.2 Pedestal and Common Mode Reduction

The ADC values collected from each strip in the measurement are a superposition of pedestal, common mode, noise and a possible signal from a traversing particle. In this beam test the pedestal, noise and common mode are calculated in an iterative procedure outlined in the following.

The pedestal is defined as the read-out value at a strip in the absence of both particle signals and noise and varies from channel to channel. It is generally related to the presence of a digital converter offset at the output in the readout chips. In the beam the initial pedestal and noise values are calculated directly from the unaligned traversing tracks. The pedestal value P_i of the i -th channel is given by the mean of the corresponding ADC values

$$P_i = \frac{1}{n} \sum_{j=1}^n \text{ADC}_{ij}, \quad (12.7)$$

where n is the number of events and ADC_{ij} corresponds to the j -th read-out value of the i -th channel. Besides the noise sources intrinsically related to the sensor and to the front-end electronics, the oscillation at a channel input can be enhanced by environmental origins, like by the pick-up effect of the sensor and by the instability of the reference grounds induced for instance by power supplies or other electromagnetic sources. While the intrinsic noise is characteristic of the single channel and the event-by-event oscillation of its output does not depend on the neighbouring channels, the common mode noise influences coherently a group of neighbouring channels. By taking advantage of the a coherent displacement of all the channels belonging to the same chip, the common mode noise is generally derived by averaging the signal amplitude of all channels connected to a readout chip. However, during this beam test large common mode fluctuations were apparent affecting primarily the 3D sensors after the pedestal subtraction, such that the common mode was corrected by fitting second order polynomials

to the data of each event. The definite cause of the increased common mode could not be identified, but might be connected to wire-bond connections or to the manufacturing process of the sensors.

The corrected signal ADC^{corr} at a given channel i for the event j is given by

$$ADC^{\text{corr}}_{i,j} = ADC_{ij} - CNM_j - P_i, \quad (12.8)$$

where CNM_j is the common mode noise of the j -th event. The noise of each channel, which essentially follows a Gaussian distribution, is then given by the standard deviation of the ADC spectrum. To evaluate the pedestal, common mode and noise in this beam test, the strip closest to point of impact of the traversing track, as well as the two neighbouring are excluded. This ensures that the signals induced by the traversing particles do not affect the pedestal and noise calculation. Channels exhibiting extraordinarily high noise are excluded from the analysis as well, because they can affect the pedestal calculation. Excessive noise can have its origin in the readout strip of the sensor, in a faulty wirebond or fanin connection or in the channel of the readout chip. A preliminary calculation of the pedestal, common mode and noise is done on the unaligned data. The pedestal values are subtracted from the raw ADC counts. Thereafter the common mode was corrected by a second order polynomial fit. Since most of the sensors were connected to more than one chip, the common mode function was calculated independently for the collection of all strips connected to a single chip. This initially corrected data then served as an input to determine the sensor alignment described in the previous section. Whereupon the aligned input data was used for the final iteration of the noise, common mode and pedestal evaluation.

Figure 12.5 shows the distribution of the ADC counts for ten events before (upper) and after (lower) common mode and pedestal correction. The peaks in the upper distribution show the signal hits given by a traversing particle. The sensor is partly bonded to APV chip four and partly to chip number five, with the separation channel being channel 512. The different common mode and pedestal behaviour is clearly visible in the raw data. A separate common mode function was found applied for the strips connected to the different chips. To account for the shape in the common mode, which is clearly visible for the channels connected to chip four, a second order polynomial correction was applied, to improve the common mode subtraction. The common mode is subtracted from the data event by event. During the analysis of the 2009 data, a large number of extremely noisy channels were encountered in the 3D sensors, up to 50%. These were mainly attributed to open wire bond connections between the sensor, the readout chip and the fan-ins but also to the sensor itself. Due to the limited options of intervention during the actual beam test, it was not possible to correct these faults, hence these channels had to be excluded.

12.3.3 Calibration

The signal hits are converted from ADC counts into charge, using the signal yield of the beam telescope reference sensors. Since these sensors have not been irradiated, they are expected to collect the full signal for a given thickness. During the beam test the sensors were biased at 150 V, which is well above the expected full depletion voltage of 100 V. The signal is extracted by summing up the signals of the strips surrounding the track impact point. The most probable value of the signal, extracted by a fit of the signal spectrum with a convolution of a Landau with a Gaussian noise term, as a function of the number of strips included is shown in Fig. 12.2. The highest signal was found including the signal of the strip closest to the hit and four strips on either side, i.e. nine strips in total and is given by

$$S(\text{ADC}) = (37.8 \pm 1.1) \text{ ADC}. \quad (12.9)$$

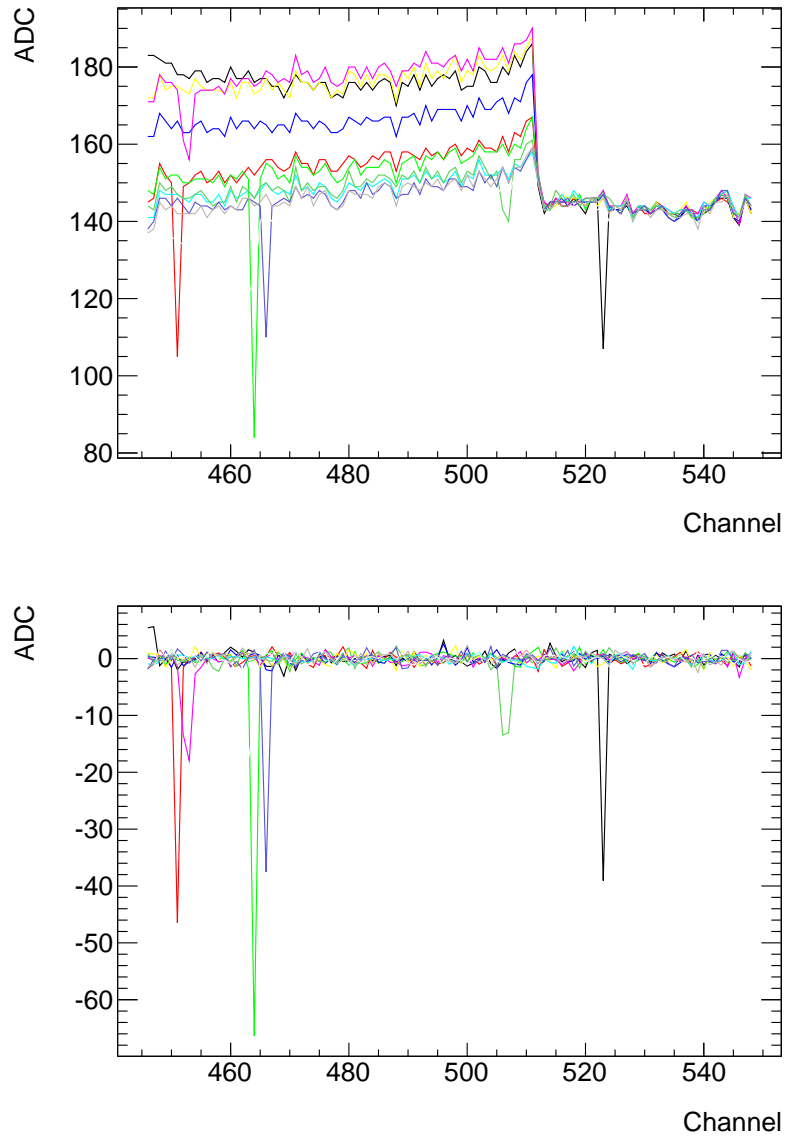


Figure 12.5: The upper figure shows the raw ADC counts for each channel for ten events for the sensor irradiated to $5 \times 10^{13} \text{ n}_{\text{eq}}/\text{cm}^2$. The lower figure shows the same events, with the ADC counts corrected for the pedestal and common mode noise contributions. The large spikes visible in the distributions are hits from muons traversing the detector. The sensor is partly bonded to APV chip four and partly to chip number five. The different common mode and pedestal behaviour is clearly visible in the raw data.

The uncertainty is the standard deviation, accounting for the deviation in the signal measured by the eight reference sensors. These variations are attributed to uncertainties in the sensor thickness, differences in the gains of the APV25 chips and timings. Assuming a sensor thickness t of $(320 \pm 20) \mu\text{m}$ the charge is given by

$$Q(e^-) = \frac{t(190 + 16.2 \ln t)}{3.68} = (24.7 \pm 1.6) \text{ ke}. \quad (12.10)$$

The gain G , i.e. the conversion of the signal measured in ADC counts into ke, is thus given by

$$G = \frac{Q}{S(\text{ADC})} = 0.065 \pm 0.05 \frac{\text{ke}}{\text{ADC}}, \quad (12.11)$$

where the uncertainty follows from

$$\sigma_G = G \sqrt{\left(\frac{\sigma_Q}{Q}\right)^2 + \left(\frac{\sigma_{S(\text{ADC})}}{S(\text{ADC})}\right)^2}. \quad (12.12)$$

The dependence of the gain due to changes in the operation conditions or the sensor capacitance have not been considered in the beam test measurements. The signal measured in ADC counts can now be easily converted into ke using the relation

$$S(\text{ke}) = S(\text{ADC}) \cdot G \quad \text{with} \quad \sigma_{S(\text{ke})} = \sqrt{(G \cdot \sigma_{S(\text{ADC})})^2 + (S(\text{ADC}) \cdot \sigma_G)^2 + (0.03 \cdot S(\text{ke}))}, \quad (12.13)$$

where the 3 % in the last term of the uncertainty is a conservative estimate of the systematic error given by the variations of the different methods applied to generate the signal spectra.

12.3.4 Cluster Finding

A cluster finding algorithm was implemented to determine the signal of the detectors in the beam test. The cluster sums all channels that comply with certain threshold criteria. A single strip is required to have signal-to-noise ratio (SNR) greater than five to be considered as the seed strip. The signals of neighbouring channels are added to the cluster as long as their signal-to-noise ratio exceeds three. Hence the total signal of the cluster is given by

$$S = \sum_{i|w_i < w_{\text{cut}}} w_i \quad (12.14)$$

where w_i is the signal measured on the i -th strip and w_{cut} is the cut value for that strip, determined using the noise of the strip and the SNR cut for this strip (seed/neighbour). The noise of the cluster is defined by

$$N = \sqrt{\sum_{i|w_i < w_{\text{cut}}} n_i^2} \quad (12.15)$$

with n_i being the noise of the i -th channel. The noise sums all channels passing the above cluster criteria. The mean number of channels attributed to a cluster is shown in Fig. 12.6. Most of the clusters, do not contain more than two strips. For the sensor irradiated to $5 \times 10^{13} \text{ n}_{\text{eq}}/\text{cm}^2$, the cluster width increases from an average of one strip per cluster at 100 V to a stable plateau of almost two strips per cluster when the full depletion voltage is reached at 300 V. A clear degradation of the cluster width resulting from the irradiation can be seen for the sensors irradiated to $1 \times 10^{15} \text{ n}_{\text{eq}}/\text{cm}^2$ and $3 \times 10^{15} \text{ n}_{\text{eq}}/\text{cm}^2$. This is generally explained by the decrease of the interstrip resistance with irradiation. Only a slight influence

on the voltage is observed for the sensor irradiated to $3 \times 10^{15} \text{ n}_{\text{eq}}/\text{cm}^2$. No increase in the average cluster width is seen for the sensor irradiated to $1 \times 10^{15} \text{ n}_{\text{eq}}/\text{cm}^2$, even though it was biased with up to 950 V.

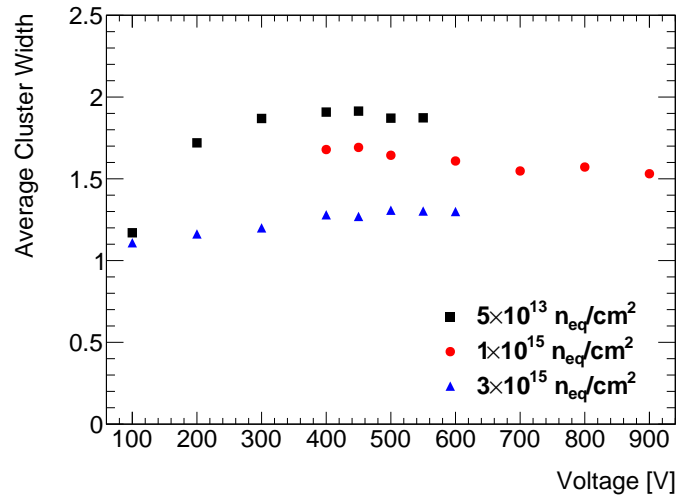


Figure 12.6: Average number of channels included to the cluster of the planar sensors as a function of the bias voltage.

12.4 Results

This section summarises the results of the sensor measurements in the beam test with a focus on the planar sensors, irradiated to fluences expected at the HL-LHC. The results include measurements of the collected charge, space resolved measurements of the charge collection, the resolution and investigations of charge sharing between strips. Where applicable comparative results from the 3D sensors measured in this beam test are quoted.

12.4.1 Measured Signal

The signal is determined from the total cluster signal, which is fitted with a convolution of a Landau and a Gaussian. The MPV of the fit gives the measured signal. Two exemplary signal spectra are shown in Fig. 12.7 in black for the sensor irradiated to $5 \times 10^{13} \text{ n}_{\text{eq}}/\text{cm}^2$ and in blue for the highly irradiated sensor ($3 \times 10^{15} \text{ n}_{\text{eq}}/\text{cm}^2$), measured at a bias voltage of 500 V. Both spectra are well described by the fit function. The lightly irradiated sensor has, as expected, a higher most probable value as the sensor irradiated to $3 \times 10^{15} \text{ n}_{\text{eq}}/\text{cm}^2$. Throughout this beam test analysis, a bias voltage of 500 V is chosen as a reference point for the measurements of the planar sensors as it matches the limit of the existing ATLAS SCT and presumably also the upgraded Silicon Microstrip detector voltage supply. The signal of the planar sensors as a function of the bias voltage is summarised in Fig. 12.8(a) and the corresponding result for the 3D detectors are shown in Fig. 12.8(b). The uncertainties on the signals are dominated by a systematic contribution by the calibration uncertainty. Due to the limited cooling power available the voltages were selected in order to comply with a safe current limit of the detectors. The lightly irradiated sensor yields a maximum signal of $(24.2 \pm 1.8) \text{ ke}$ (i.e. $(3.87 \pm 0.30) \text{ fC}$) at a

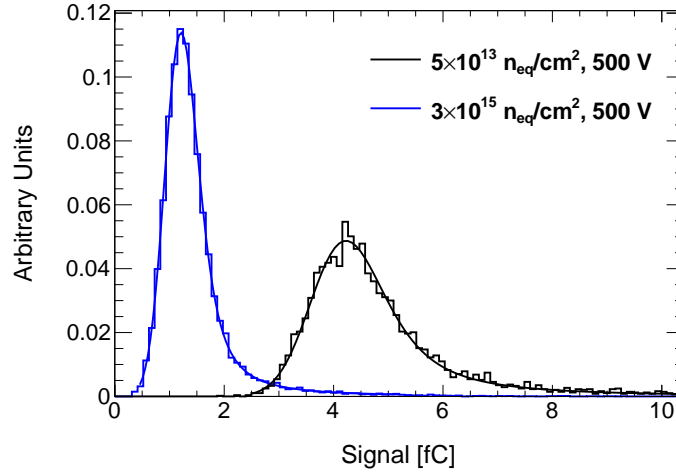


Figure 12.7: Spectra of the measured signals for the sensor irradiated to $5 \times 10^{13} \text{ n}_{\text{eq}}/\text{cm}^2$ (black) and the sensor irradiated to $3 \times 10^{15} \text{ n}_{\text{eq}}/\text{cm}^2$, both measured at a bias voltage of 500 V. The spectra are fitted with a convolution of a Landau and Gaussian function.

bias voltage of 500 V, corresponding to the expected charge liberated by a minimum ionising particle passing through 320 μm of silicon. The plateau of the signal is already measured at 200 V, which is above the full depletion voltage of the sensor. Both irradiated planar sensors show a clear degradation in charge collection. The signal of the sensor irradiated to $1 \times 10^{15} \text{ n}_{\text{eq}}/\text{cm}^2$ rises from $(11.6 \pm 0.9) \text{ ke}$ to $(17.7 \pm 1.4) \text{ ke}$ (i.e. $(1.85 \pm 0.14) \text{ fC}$ to $(2.84 \pm 0.22) \text{ fC}$) between 500 V and 950 V, which is the highest voltage applied for this sensors during the beam test. The sensor irradiated to $3 \times 10^{15} \text{ n}_{\text{eq}}/\text{cm}^2$ collects $(6.8 \pm 0.5) \text{ ke}$ (i.e. $(1.09 \pm 0.08) \text{ fC}$) at a bias voltage of 500 V. The full depletion voltage V_{dep} of the planar sensors can be approximated by [230]

$$V_{\text{dep}} \approx \frac{q_0 d^2}{2\epsilon_0 \epsilon_r} g_C \Phi_{\text{eq}}, \quad (12.16)$$

where q_0 is the elementary charge, d is the detector thickness and ϵ_0 and ϵ_r are the permittivity of vacuum and silicon, respectively and $g_C \Phi_{\text{eq}}$ is the effective doping concentration (see Eq. (10.28)). A linear dependence on the irradiation fluence Φ_{eq} is assumed. With an acceptor introduction rate $g_C = 0.012 \text{ cm}^{-1}$ [278] for protons in p-type float-zone silicon, full depletion voltages of $V_{\text{dep}} \approx 900 \text{ V}$ at $\Phi_{\text{eq}} = 1 \times 10^{15} \text{ n}_{\text{eq}}/\text{cm}^2$ and $V_{\text{dep}} \approx 2800 \text{ V}$ at $\Phi_{\text{eq}} = 3 \times 10^{15} \text{ n}_{\text{eq}}/\text{cm}^2$ are expected. Although Eq. (12.16) is only valid after beneficial annealing, which was not performed for the sensors investigated here, it serves as an estimate. Therefore, the highest bias voltage applied for the sensor irradiated to $1 \times 10^{15} \text{ n}_{\text{eq}}/\text{cm}^2$ is in the order of the estimated full depletion voltage, whereas the full depletion voltage could not be reached for the sensor irradiated to the highest fluence.

In contrast to the degradation in the planar sensors, the irradiated 3D sensors exceed the signal of the unirradiated sensor and show effects of irradiation induced charge multiplication. The signal yield of the unirradiated 3D detector is $(22.8 \pm 1.8) \text{ ke}$ (i.e. $(3.67 \pm 0.29) \text{ fC}$) at 70 V, the highest voltage applied. This agrees well with the expected value given the sensors thickness. The signal of the irradiated 3D detectors surpass this value and increase strongly for voltages above approximately 150 V. They reach almost twice the value of the unirradiated one. These measurements show that a radiation-induced increase of the effective doping concentration leads to electric field strengths high enough for

charge multiplication (See Section 10.2.6). As already mentioned, charge multiplication has also been observed in highly irradiated planar silicon strip detectors [223, 224] as well as in epitaxial silicon pad detectors [279], where much higher voltages due to a larger spacing between the electrodes are needed. The short distance of about $50\ \mu\text{m}$ between junction columns and ohmic columns in the 3D detectors investigated here leads to a high electric field and therefore to strong charge multiplication already at comparatively low voltages. Since the operating voltage was limited in this beam test, onset of charge multiplication effects in the planar strip detectors could not be proved. However, keeping in mind the application of these sensors as tracking devices at the HL-LHC, shows that the planar sensors are radiation hard enough to be inserted in the Silicon Microstrip detector or the medium pixel layers of the ATLAS upgrade. This assumes that a threshold value of $1\ \text{fC}$ ($6.2\ \text{ke}$) as currently used by the ATLAS SCT is kept and that sufficiently high bias voltages can be supplied to the individual sensors.

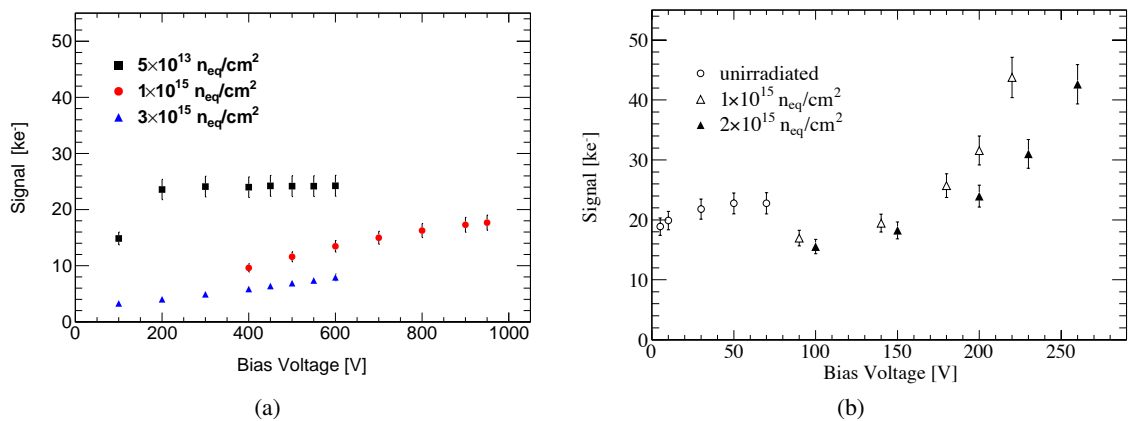


Figure 12.8: Collected charge for the planar (a) and 3D (b) sensors as a function of the bias voltage. While the sensor irradiated to $5 \times 10^{13}\ \text{n}_{\text{eq}}\text{cm}^{-2}$ collects the expected charge of an unirradiated sensor of $320\ \mu\text{m}$, less charge is collected for the highly irradiated sensors. Figure 12.8(b) is taken from Ref. [268]

The signal yield can also be evaluated using alternative signal extraction strategies. The results of the most probable value extracted from a fitted Landau convolved with a Gaussian noise term using eight different strategies are shown in Fig. 12.9. The planar sensor irradiated to $5 \times 10^{13}\ \text{n}_{\text{eq}}/\text{cm}^2$ is shown in Fig. 12.9(a) and the sensor irradiated to $1 \times 10^{15}\ \text{n}_{\text{eq}}/\text{cm}^2$ in Fig. 12.9(b). The clustering algorithms are defined by:

1. Signal contains only the strip closest to the track impact point, i.e. the expected channel.
2. The strip with the highest signal of the three strips closest to the track impact point, named highest ADC.
3. The sum of the signal of the expected channel and first neighbour, i.e. the strips closest to the track impact point.
4. The sum of the signal of the strips with the highest and second highest signal found in a window of the three strips closest to the track impact point.
5. The sum of the signal of the three strips surrounding the track impact point.

6. The sum of the signal of the five strips surrounding the track impact point.
7. The sum of the signal of the seven strips surrounding the track impact point.
8. 'real' clustering algorithm, see Section 12.3.4

For the slightly irradiated sensor, strategies including either only the highest or the expected channel, leads to collected charges that are on the order of 5 % lower than algorithms including several strips, except for the charge collected at 100 V. At this voltage the sensor is not fully depleted. In this case strategies summing the signal of several strips, regardless of a threshold cut, yield a lower signal. At all other voltages, the signal in the remaining strategies increases by accounting for charge sharing between different channels. No significant difference between the signals collected by strategies 5–7 is observed in Fig. 12.11. However, the clustering algorithm eight, which employs a signal to noise cut on the neighbouring channel, leads to a slightly smaller collected charge. For the sensor irradiated to $1 \times 10^{15} \text{ n}_{\text{eq}}/\text{cm}^2$, which only reaches the level of full depletion at the highest bias voltage applied in the beam test (950 V), the differences between the clustering strategies diminish with increasing voltage. This is in agreement with Fig. 12.6, where the average cluster size decreases with increasing radiation of the sensor. The charge collection is highest for the strategies involving more than one strip and the clustering strategy eight. At bias voltages below 600 V the charge collection is smaller the more channels are included, which indicates a negative signal at the strips included in these clustering approaches. A further investigation on the signal as function of the distance to the impact point is found in Section 12.4.4.

12.4.2 Efficiency

A further important figure of merit to define the suitability of sensors as a tracking devices in a high energy physics experiment, is its detection efficiency ϵ . It is determined by the fraction of events, whose signals pass a certain predefined threshold

$$\epsilon = \frac{s}{n}, \quad (12.17)$$

where s is the number of events above threshold and n is the total number of events. The uncertainty is calculated according to Ref. [280]

$$\sigma_{\epsilon} = \frac{(s+1)(s+2)}{(n+1)(n+2)} - \frac{(k+1)^2}{(n+2)^2}, \quad (12.18)$$

which is chosen because it does not lead to unphysical results near 0 % and 100 % efficiency. To mimic the binary readout of the ATLAS SCT system, the efficiency is calculated using clustering strategy two, which defines a hit if at least one of the three strips surrounding the impact point of the impinging track passes the threshold cut of 1 fC. This coincides with the threshold applied in the binary readout of the current ATLAS SCT [121].

The resulting efficiencies as a function of the applied bias voltage for the three planar sensors are shown in Fig. 12.10 . For the sensor irradiated to $5 \times 10^{13} \text{ n}_{\text{eq}}\text{cm}^{-2}$, an efficiency of $(99.96 \pm 0.06) \%$ is found already at a bias voltage of 100 GeV and remains at this level also for the other bias voltages. The sensor irradiated to $1 \times 10^{15} \text{ n}_{\text{eq}}\text{cm}^{-2}$ does already show signs of a deterioration of the efficiency. At a bias voltage of 400 V, the lowest applied for this sensor in the beam test, the efficiency is at (98.41 ± 0.25) and rises to (99.95 ± 0.02) at a bias voltage of 950 V. It is expected that the bias voltage at the HL-LHC will be limited at 500 V, for which the overall efficiency is at (99.70 ± 0.08) A clear

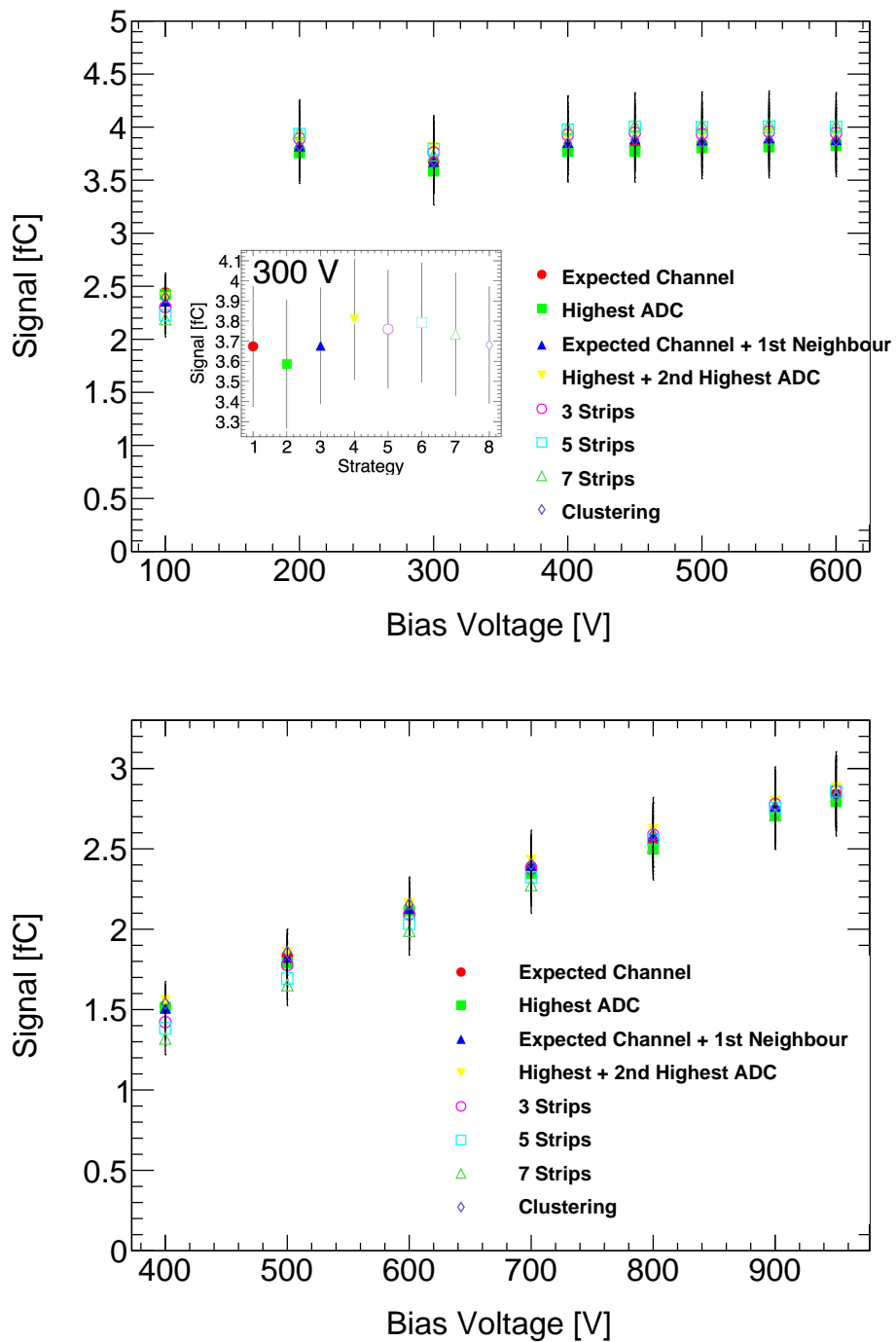


Figure 12.9: Charge collection as a function of the applied bias voltage using eight different clustering strategies. In Fig. (a) for the sensor irradiated to $5 \times 10^{13} \text{ n}_{\text{eq}}/\text{cm}^2$ and in Fig. (b) for the sensor irradiated to $1 \times 10^{15} \text{ n}_{\text{eq}}/\text{cm}^2$.

degradation of the efficiency is found for the sensor with the highest fluence. At 100 V an efficiency of $(2.76 \pm 0.14) \%$ is measured which rises to $(77.35 \pm 0.29) \%$ to 500 V.

For the application as a tracking device an overall detection efficiency of more than 99 % is needed for efficient operation given a limited bias voltage of 500 V. Hence, both for the sensor irradiated to $5 \times 10^{13} \text{ n}_{\text{eq}}\text{cm}^{-2}$ and the sensor irradiated $1 \times 10^{15} \text{ n}_{\text{eq}}\text{cm}^{-2}$ have a high enough operation efficiency to be used in the HL-LHC environment. The sensor irradiated to $3 \times 10^{15} \text{ n}_{\text{eq}}\text{cm}^{-2}$ fails this basic requirement. However, the efficiencies increase considerably for the sensor irradiated to $3 \times 10^{15} \text{ n}_{\text{eq}}\text{cm}^{-2}$ when using clustering scheme eight (see Fig.12.8(a)).

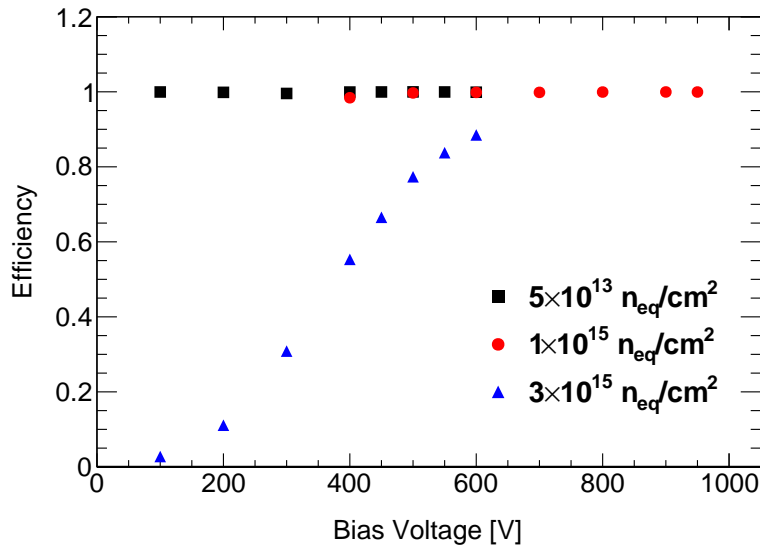


Figure 12.10: Efficiency for the three planar sensors at a threshold of 1 fC.

12.4.3 Charge Sharing

The different detector geometries of planar and 3D detectors have a large impact on the charge sharing probability between neighbouring readout strips. Charge sharing between neighbouring strips can be utilised to increase the resolution of silicon sensors, but it comes at the cost of a decreased signal measured at each strip. This can lead to reduced detection efficiencies when the collected signal per strip decreases, i.e. due to radiation induced trapping of the charge carriers. These arise from the underlying electric field configurations: In planar sensors liberated charge carriers drift parallel to the readout strips and the charge clouds are broadened by transverse diffusion during the drift time, whereas 3D sensors exhibit a strong force perpendicular to the readout strips on the charge carriers. Hence it is expected that the charge sharing between neighbouring strips is much less pronounced in 3D sensors than in planar sensors.

The fraction of events with more than one strip per cluster as a function of the distance to the strip centre of the particle impact point at a bias voltage of 500 V is shown in Fig. 12.11(a) for the three planar sensors and in Fig. 12.11(b) for the unirradiated 3D detector. The measurements of the planar sensors are reported at a bias voltage of 500 V, where only the sensor irradiated to $5 \times 10^{13} \text{ n}_{\text{eq}}\text{cm}^{-2}$ is fully depleted and at a bias voltage of 70 V for the 3D detector, which is well above the depletion voltage in this case. In both technologies the measurement is separable into two distinct regions. One

flat central region for particles impinging close to the middle of the readout strip, which induce a signal predominantly on a single channel. Whereas particles traversing the detector between two strips show a significant charge sharing probability. For planar sensor this region starts at a distance of $20\ \mu\text{m}$ from the strip centre, while this region is clearly reduced for the unirradiated 3D sensor and limited to a region of less than $10\ \mu\text{m}$. It has to be considered that 3D sensors have p type columns at half pitch, which significantly changes the charge movement, due to the geometrically different the weighting field distribution.

The charge collected for particles impinging around the strip centre shows no large differences for the three planar detectors. The fraction of hits with clusters combining more than one strip rises quickly with increasing distance from the strip centre leading to a plateau, such that roughly 100 % of the tracks impinging in between two strips for the sensor irradiated to $5 \times 10^{13}\ \text{n}_{\text{eq}}\text{cm}^{-2}$ and 80 % for the sensor irradiated to $1 \times 10^{15}\ \text{n}_{\text{eq}}\text{cm}^{-2}$ exhibit charge sharing. The most significant change in the charge sharing between strips, due to the radiation induced defects, is seen for the sensor irradiated to $3 \times 10^{15}\ \text{n}_{\text{eq}}\text{cm}^{-2}$. In this case charge sharing is only measured in 40 % of the events. This is again in agreement with Fig. 12.6, and indicates that the average cluster width for the highest fluence is mainly lower because of the lower charge collection for particles impinging between strips and not charge sharing as also shown in Fig. 12.12 and Fig. 12.13 This is partially attributed by charge loss due to trapping, i.e. the higher the trapping probability the lower is the chance for the charge to reach the next strip. For the unirradiated 3D sensor, only around half of the tracks impinging in the region between two strips show charge sharing. Since the noise level of all sensors evaluated in this beam test are at the same level, the signal and noise cut values in the clustering have the same effect on the unirradiated 3D sensor and the planar sensor irradiated to $5 \times 10^{13}\ \text{n}_{\text{eq}}\text{cm}^{-2}$.

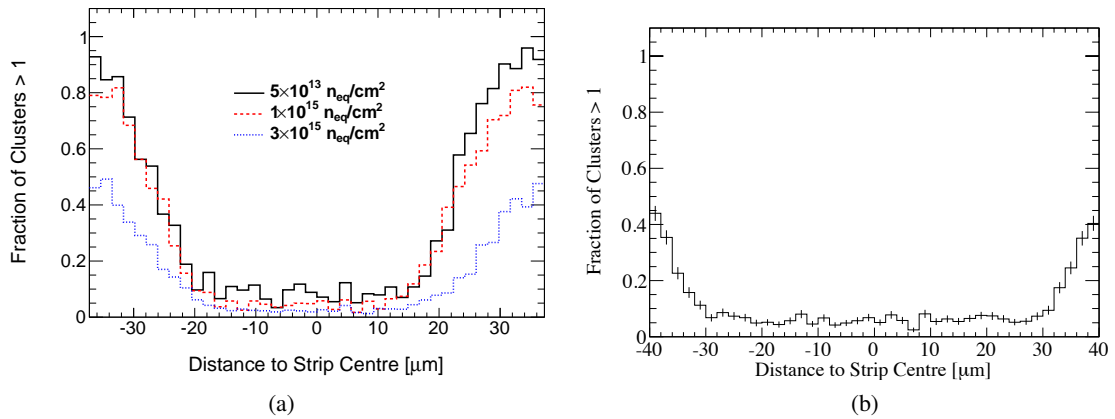


Figure 12.11: Fraction of events with more than one strip per cluster, as a function of the impact point of the particle, for the three planar sensors in (a) and in (b) for the unirradiated 3D sensor (the latter is taken from Ref. [268]).

Further insight into the distribution of charges between strips is found using the quantity η defined by [281]

$$\eta = \frac{w_{\text{right}}}{w_{\text{left}} + w_{\text{right}}}, \quad (12.19)$$

where $w_{\text{right/left}}$ is the pulse height on the left(right) strip according to the following definition: The system is defined as the strip with the maximum signal of the cluster and the highest of its two neighbours. The

left and right strip is then defined by the sensor reference frame. This allows to reconstruct the average impact position using [281]

$$x_0 = p \cdot f(\eta) + x_{\text{left}} \quad (12.20)$$

where p is the pitch of the sensor, and x_{left} is the x coordinate of the left strip according to the definition of η , i.e. the seed strip, or its left neighbour. The function $f(\eta)$ is defined as

$$f(\eta) = \int_0^\eta \frac{dN}{d\eta'} d\eta'. \quad (12.21)$$

under the assumption that the particles are uniformly distributed in x_0 . An example of the η distribution for the planar sensors is shown in Fig. 12.12 taken at a bias voltage of 500 V. The peaks around zero and one are a common feature of silicon sensors without any intermediate floating strips. This means that the charge division between two strips is not a linear function, as this would yield a flat η function. An η distribution with two δ function at zero and one on the other hand would indicate that no charge sharing, no noise, no cross-talk or capacitive coupling between the strips is present. In general the width of the peaks can be associated to the single strip noise and the cross-talk can be evaluated by a displacement of the peaks from zero [282].

The overall shape of the observed η distribution can be described by accounting for the particle impact point and diffusion. A fully depleted silicon sensor with a thickness of 300 μm yields a diffusion cloud of less than 10 μm , which is far less than the readout pitch of 74.5 μm . Hence all particles that impact close enough to one strip, such that the charge spread does not reach the border between two strips, are collected by one readout strip only. This is clearly seen in the distribution of the sensor irradiated to $5 \times 10^{13} \text{ n}_{\text{eq}}\text{cm}^{-2}$, where the charge is mostly collected by one strip, indicated by the flat region extending from $0.1 < \eta < 0.9$ and the peaks centred at zero and one. A strong increase in charge sharing is seen in dependence of the radiation fluence, visible by the increased number of events in the range $0.2 < \eta < 0.8$. This is very much expected as both the sensor irradiated to $1 \times 10^{15} \text{ n}_{\text{eq}}\text{cm}^{-2}$ and the sensor irradiated to $3 \times 10^{15} \text{ n}_{\text{eq}}\text{cm}^{-2}$ are not fully depleted. This leads to a broadening of the charge cloud through diffusion, also indicated by the broadening of the peaks at zero and one.

The average impact point x_0 , normalised to the readout pitch, relates the measured η value to the distance x_0 of the particle from the left readout strip. This is shown for the three sensors in Fig. 12.13. The y-axis represents the impact point x_0 corresponding to the pitch. It is clearly indicated that the increased radiation leads to a flatter curve, and a much earlier onset of charge sharing between the strips a function of x_0 . For all sensors a particle that impacts between the strips leads to the charge being evenly distributed between the two strips ($\eta = 0.5$). A clear change in the shape is found for increasing radiation. While a sharp turn on behaviour, i.e. a region with minimal charge sharing close to the strip centre, is apparent in the sensor irradiated to $5 \times 10^{13} \text{ n}_{\text{eq}}\text{cm}^{-2}$, the slope vanishes for increasing radiation fluence, indicating that charge sharing is found for all tracks close to the strip centre. On the other hand, the slope in the intermediate region increases significantly with the irradiation fluence, due to the increased diffusion of the signal, which results in a larger charge cloud and higher charge sharing.

12.4.4 Space Resolved Signal

The drift path of the free charge carriers towards the electrodes depends heavily on the impact position of the track with respect to the nearest strip. Heavily irradiated sensors are subject to high trapping probabilities, which severely affect the liberated charge carriers collected at the electrodes. With the data taken in this beam test, detailed studies of the charge collection as a function of the track impact point are possible. Considering the results of the charge sharing probabilities in Section 12.4.3, the

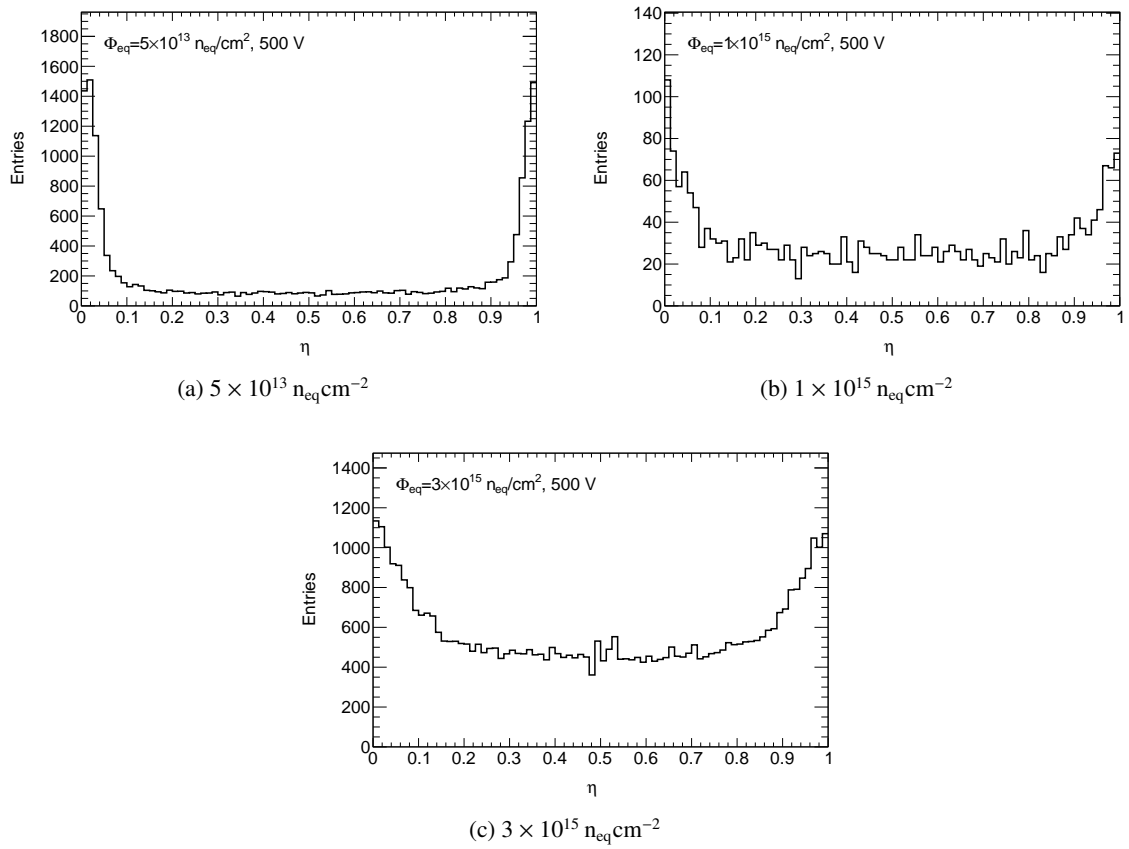


Figure 12.12: η distribution of the three planar sensors at a bias voltage of 500 V.

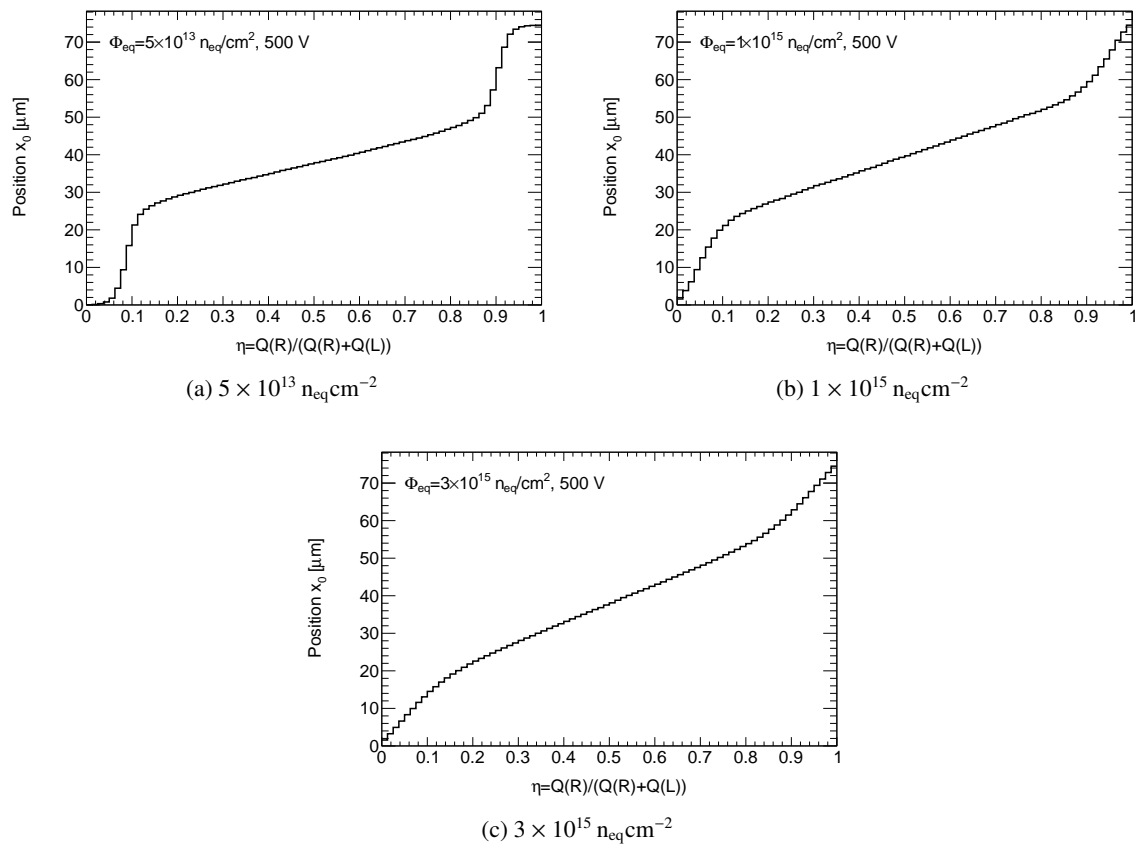


Figure 12.13: The relation between the impact point x_0 of a particle and the η value at a voltage of 500 V for the three planar sensors normalised to the pitch.

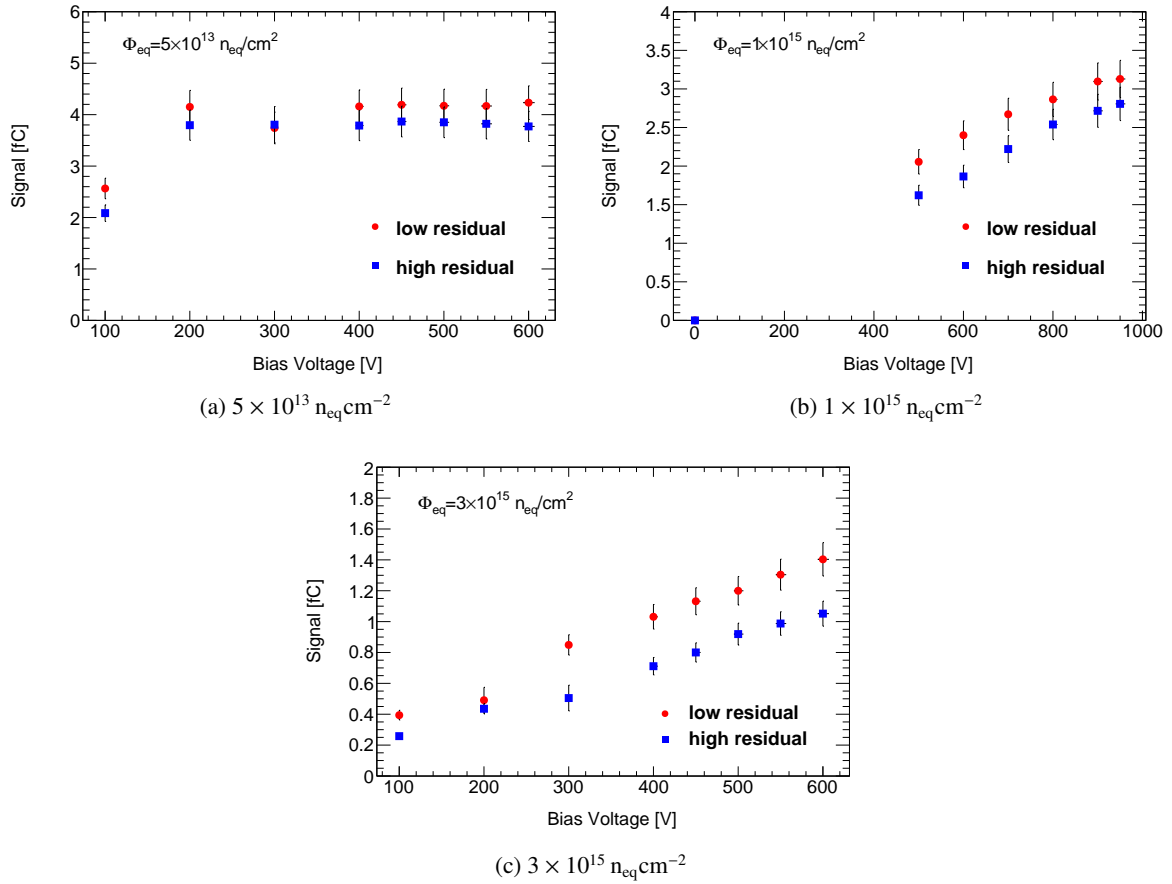


Figure 12.14: Collected charge for all three sensors in the region of the strip centre, low residual (red), and the region in between two strips, high residual (blue).

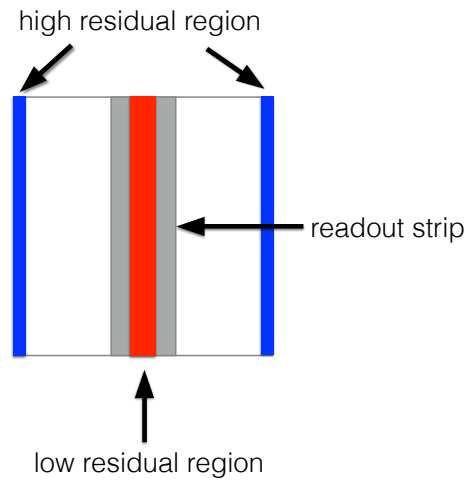


Figure 12.15: Schematic of the high (blue) and low (red) residual region within a unit cell of the silicon strip detector. The readout strip is indicated by the grey area.

sensor is divided into two distinct regions to study the space resolved charge collection as schematically represented in Fig. 12.15. The low residual region shown in red, includes all particles impinging onto a region of $\pm 6 \mu\text{m}$ around the strip centre, and the high residual region, represented in blue, selects all particles impinging within a region of $\pm 6 \mu\text{m}$ in the middle of two strips, corresponding to the region of the lower electric field. The results of the charge collection separated into these two regions is shown in Fig. 12.14 separately for the three sensors. In all three cases the charge collected in the high residual region is significantly smaller than in the low residual region. In both the sensor irradiated to $5 \times 10^{13} \text{ n}_{\text{eq}}\text{cm}^{-2}$ and $1 \times 10^{15} \text{ n}_{\text{eq}}\text{cm}^{-2}$, no significant influence on the depletion voltage is found and a constant difference in charge collection of 0.5 fC to 0.6 fC is found over the full range. The sensor irradiated to the highest fluence also shows a considerable difference between the two regions. At a bias voltage of 100 V, the difference is 0.15 fC and rises to a rather constant value of about 0.35 fC for voltages above 300 V.

Any alterations of the signal and noise thresholds in the clustering algorithm, do not significantly impact the observed difference. All clustering algorithms defined in this beam test lead to a significantly lower signal for the high residual region compared to the low residual region. The peculiarity of the observed difference is, that it neither seems to be a function the irradiated fluence nor the bias voltage.

The difference in the signal between the regions can be attributed to an interplay between charge sharing, the electric field and charge carrier trapping. The difference in charge sharing between the regions is clearly shown in Fig. 12.16, which shows the number of strips included in the clustering scheme separated for the high and low residual region, at a bias voltage of 500 V. Particles impinging onto the high residual region share their charge between at least two strips, which might lead to a deficit in charge collection depending on the clustering scheme. As before, it should be noted that the average number of strips per cluster decreases with increasing radiation, and increases for increasing voltage.

The electric field in a highly irradiated n^+p sensor is the result of an interplay between the initial doping concentration, the changes in the effective doping arising from charged defects and the density of free charge carriers. From measurements of the electric field after pion irradiation, it can be deduced that the sensor irradiated to $1 \times 10^{15} \text{ n}_{\text{eq}}\text{cm}^{-2}$ already has a substantial electric field at a bias voltage of 200 V, and at 500 V a high drift velocity throughout the full silicon bulk should be achieved. The weighting field in a highly segmented sensor is largest close to the sensing strip, and the highest induced signal is found for particles impinging in this region [283]. Furthermore it should be noted that the weighting field has a low field region present between the individual strip implants from which the space charge region grows. Hence charges generated within this region, might not be accelerated to the nearest readout strip, and thus lead to a lower signal for tracks impinging on the border between two strips, i.e. the low residual region. Charge carrier trapping in highly irradiated silicon sensors is the dominating origin of the decrease in the charge collection. Even though these sensors collect electrons, which are less prone to trapping, due to their larger drift velocity and the longer effective trapping times a clear degradation in dependence of the fluence is seen. Attributed to the increased drift distance for particles generated in the middle between two strips these are more prone to trapping, which is in agreement with the lower signal found in the high residual region. However, an increase of the electric field should influence the drift velocity, and thus lead to systematically decreasing differences between the high and low residual regions of the sensor. A full understanding of constant deficit in charge collection observed over the full range of bias voltages needs further detailed studies. Especially space resolved measurements of the sensor irradiated to $1 \times 10^{15} \text{ n}_{\text{eq}}\text{cm}^{-2}$ at lower bias voltages would be desirable, as well as measurements of the impact of the strip isolation schemes.

For the application of a silicon sensor in a high energy physics experiment, a position independent charge collection is desirable. This can be achieved by slightly tilting the sensors and/or applying a sufficient magnetic field. Such conditions also enhance the charge collection due to the longer path

through the sensor. Though it should be kept in mind that the charge sharing is also increased by either of these measures. This is confirming that the lower average cluster size for the highest fluence is due to lower charge collection and not due to lower charge sharing.

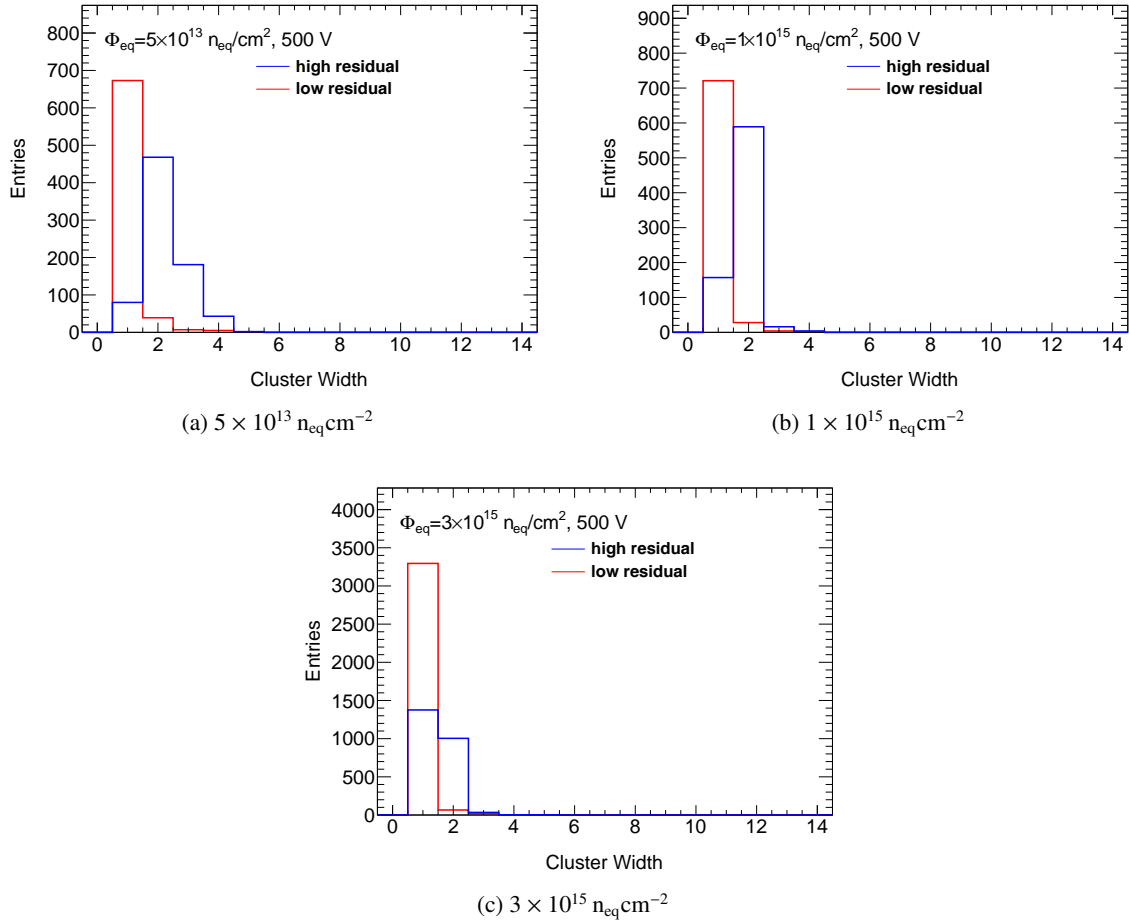


Figure 12.16: Cluster size for the planar sensors for tracks impinging in the low residual region and the high residual region at a bias voltage of 500 V.

12.4.5 Single Strip Signal

To further investigate the impact on the signal as a function of the impact point, the signal measured by a single strip as a function of the impact point is shown in Fig. 12.17 at two different bias voltages. This allows a further investigation of the charge sharing and the extent of signal induced on neighbouring readout strips. The sensor irradiated to $5 \times 10^{13} \text{ n}_{\text{eq}}\text{cm}^{-2}$ is shown in the upper row at bias voltages of 100 V (left) and 500 V (right), the sensor irradiated to $1 \times 10^{15} \text{ n}_{\text{eq}}\text{cm}^{-2}$ is shown in the middle row biased at 500 V (left) and 950 V (right), while the sensor irradiated to $3 \times 10^{15} \text{ n}_{\text{eq}}\text{cm}^{-2}$ is shown in the bottom row at voltages of 100 V (left) and 500 V (right). The lines in the figures indicate the borders between the expected strip, and its left and right neighbours. The middle of the neighbouring strips are found at $\pm 74.5 \mu\text{m}$. All sensors exhibit a pronounced charge sharing for tracks impinging close to the border between two strips at a distance of $37 \mu\text{m}$, indicated by the vertical line and a measurable signal

is still induced if the signal impinges on the border to next but one strip (112 μm).

For the sensor irradiated to $5 \times 10^{13} \text{ n}_{\text{eq}}\text{cm}^{-2}$, a small negative signal is found if the signal impinges on the neighbouring strip and the sensor is biased with 100 V, which is below the full depletion voltage. In the corresponding figure on the right at a bias voltage of 500 V, the shape of the distribution remains, but the induced signal becomes positive.

These observations also hold for the sensors irradiated to $1 \times 10^{15} \text{ n}_{\text{eq}}\text{cm}^{-2}$ shown in the middle. At a bias voltage of 500 V the strip collects negative signal if the track impact point is on of the neighbouring strip, while a signal close to zero is found for strips impinging in between the readout strips. By applying a bias voltage of 950 V, which is on the order of full depletion, the negative signal collected for hits close to the neighbouring readout strip vanishes and the signal for strips impinging between the neighbouring readout strip becomes positive.

A quantitatively similar behaviour is seen for the sensor irradiated to the highest fluence in the bottom plots, with an even more pronounced negative signal at a bias voltage of 100 V (left), which decreases at an increased bias voltage of 500 V as shown in the bottom right figure.

The negative collected charges at the neighbouring strips arise from a ballistic deficit given by the limited integration time of 25 ns which is too small for holes to reach the backplane. Additionally for the highly irradiated sensors, the trapping of charge carriers enhances this effect. It has to be kept in mind that for voltages below the full depletion voltage, the holes in the neutral bulk are not accelerated by an electric field and thus do not reach the p^+ electrode. This explains the negative signals in Fig. 12.17 for all sensors, where the bias voltage is below the full depletion voltage. However, given that the sensors are made from p-type bulk material, the holes are less prone for trapping, due to the lack of donors in the bulk material. Hence the influence on the negative space charge is not a pronounced function of the fluence.

12.5 Spatial Resolution

A focus is set on the spatial resolution of the sensors which is a further figure of merit in the application of the sensor's as tracking devices. Experimentally, the sensor spatial resolution is obtained from the width of the residual distribution, where the residual is defined as the distance between the track intercept point in the reference frame of the telescope and the cluster position. The cluster position x_{rec} is measured by applying the centre-of-gravity method, defined by

$$x_{\text{rec}} = \frac{\sum_{i|w_i > w_{\text{cut}}} w_i \cdot i}{\sum_{i|w_i > w_{\text{cut}}} w_i} \cdot p \quad (12.22)$$

where p is the strip pitch. Accounting for the effects of charge sharing allows to improve the spatial resolution beyond the expected binary resolution of $\sigma_{\text{binary}} = p/\sqrt{12}$. Hence to benefit from charge sharing, events are excluded if either the strip the track is intercepting with or its nearest neighbours are excluded due to exceeding noise or if they are dead.

The resolution as a function of the bias voltage is shown in Fig. 12.18(a) for the planar sensors and in Fig. 12.18(b) for all three planar sensors in the beam test. The track extrapolation uncertainty, which is approximately 4 μm and mainly attributed to the telescope resolution, was not subtracted. The statistical uncertainties are indicated in the figure. Given the limited statistics remaining for the 3D sensor irradiated to $1 \times 10^{15} \text{ n}_{\text{eq}}/\text{cm}^2$, after excluding noisy or dead channels and their neighbours, the interpolation of the track position could not be exploited and the detector was excluded from the spatial resolution study.

A beneficial effect on the resolution resulting from charge sharing between strips is apparent for

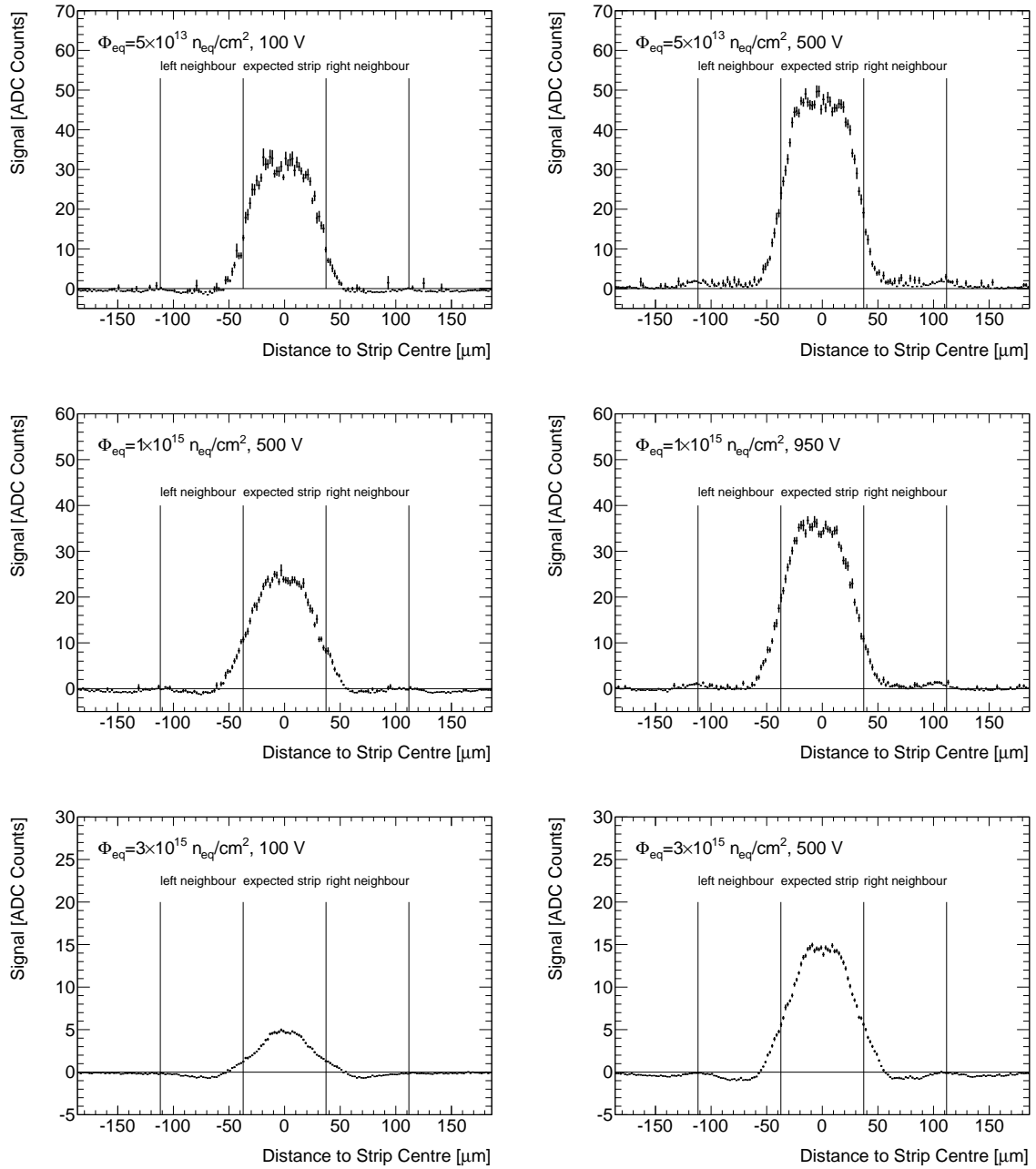


Figure 12.17: Mean Signal as a function of the distance to the readout strip centre for the planar sensor irradiated to $5 \times 10^{13} \text{ n}_{\text{eq}}\text{cm}^{-2}$ at 100 V and 500 V in the upper row, for the sensor irradiated to $1 \times 10^{15} \text{ n}_{\text{eq}}\text{cm}^{-2}$ at voltages of 500 V and 950 V in the middle row and for the sensor irradiated to $3 \times 10^{15} \text{ n}_{\text{eq}}\text{cm}^{-2}$ in the bottom row at bias voltages of 100 V and 500 V.

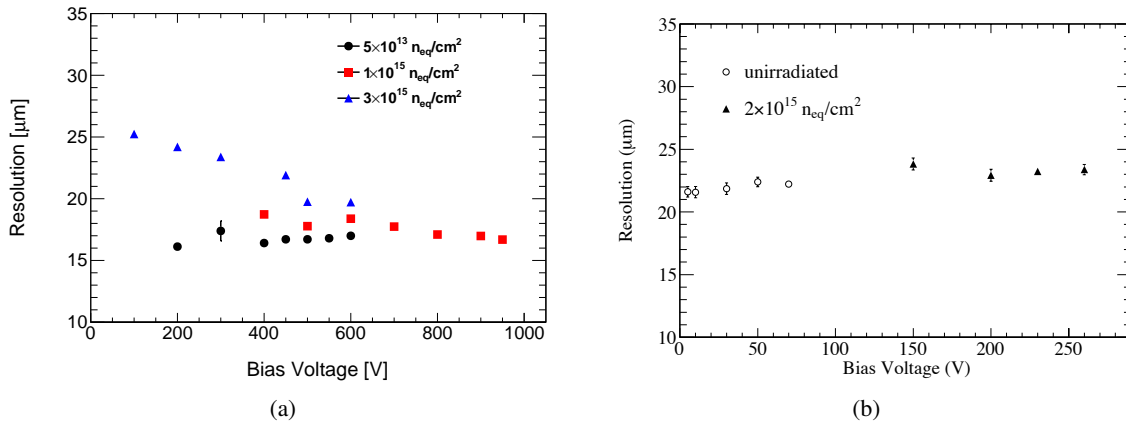


Figure 12.18: Resolution versus applied bias voltage of (a) planar detectors and (b) 3D detectors irradiated to different fluences. Figure 12.18(b) is taken from Ref. [268]

all three planar sensors. Given a pitch of $74.5 \mu\text{m}$, a binary resolution of $21.5 \mu\text{m}$ is expected. The distribution of the resolution for the lightly irradiated sensor as a function of the bias voltage is relatively constant at a value of $(16.7 \pm 0.2) \mu\text{m}$ at 500 V. For the planar sensor irradiated to $1 \times 10^{15} \text{ n}_{\text{eq}}/\text{cm}^2$, a slight improvement of the resolution with increasing bias voltage is apparent, leading to a resolution of $(16.7 \pm 0.2) \mu\text{m}$ at 950 V. This corresponds to the resolution measured for the lightly irradiated sensor. A large impact on the resolution due to of the irradiation is apparent in the highest irradiated sensor, $3 \times 10^{15} \text{ n}_{\text{eq}}/\text{cm}^2$. At a bias voltage of 100 V the resolution is only $(25.2 \pm 0.2) \mu\text{m}$. However increasing the bias voltage to 600 V leads to an improved resolution of $(19.7 \pm 0.1) \mu\text{m}$. As mentioned above, this detector is far from being depleted at these voltages, so a further enhancement of the resolution is expected at a higher bias voltages.

The resolution measured with the unirradiated 3D detector at 70 V yields $(22.2 \pm 0.2) \mu\text{m}$, which is only a slight improvement to the binary resolution of $23.1 \mu\text{m}$ attributed to the limited charge sharing, as seen in Fig. 12.11. The detector irradiated to $2 \times 10^{15} \text{ n}_{\text{eq}}/\text{cm}^2$ has a resolution of $(23.4 \pm 0.4) \mu\text{m}$ at a bias voltage of 260 V, which is somewhat worse than for the unirradiated sensor but still in agreement with the binary resolution. Hence, the resolution degrades slightly after irradiation. However, no influence on the resolution due to charge multiplication for voltages higher than approximately 150 V is seen. Within the error margins, the resolution determined for the 3D detector irradiated to $2 \times 10^{15} \text{ n}_{\text{eq}}/\text{cm}^2$ does not depend on the bias voltage in the voltage range shown.

ATLAS Inner Tracker Upgrade: Infrastructure setup and Measurements

Another part of the studies performed for this thesis was dedicated to the prototyping of the new module design for the strip layers of the new Inner Detector. This included the set up of a centralised infrastructure for large scale testing of hybrids and modules. The test facility was located at CERN in building 180 and included a clean room for measurements and an adjacent bunker intended for measurements with irradiated test devices and radioactive sources. The facilities included electrical test stands for both irradiated and unirradiated staves and modules and preparatory steps in the setup of a laser system.

A short overview of the different test facilities is given in Section 13.1, with a brief introduction to the electrical characterisation procedure for hybrids and modules in Section 13.3. This chapter is concluded by a summary of a comparative measurement between a single DC-DC powered stave module and a double-sided Supermodule in Section 13.4.

13.1 Upgrade Testing Facility B180

The test facilities in B180 were set-up for large scale testing of both irradiated and unirradiated modules, staves, Supermodules and eventually end-cap petals. Figure 13.1 shows the electrical test setup facilities for modules and staves in the cleanroom as of November 2011, which were installed with the help of the author.

Single Module Test Stand The single module test stand is equipped with an HSIO system for data acquisition, controlled by a PC. The modules are placed on top of a purpose-built testing jig providing the necessary mechanical support, connections of the bias voltage to the sensor, cooling loops for the heat transport and vacuum holes to securely attach the module and thus allowing a good thermal contact for heat dissipation. The jig consists of a central isolated aluminium insert which is used to flatly attach the sensor and provides biasing of the sensor backside. The jig also acts as a common ground for the low voltage of the ASICs and/or the high-voltage return for sensor biasing. The aluminium jig is placed inside a light tight freezer which is flushed with dry air to prevent condensation on the module, while testing at low temperatures.

The cooling is provided by a Julabo chiller, which circulates an oil for cooling, allowing for temperatures to -20°C . Several power supplies are available. Generally a Keithley 2410 source meter was

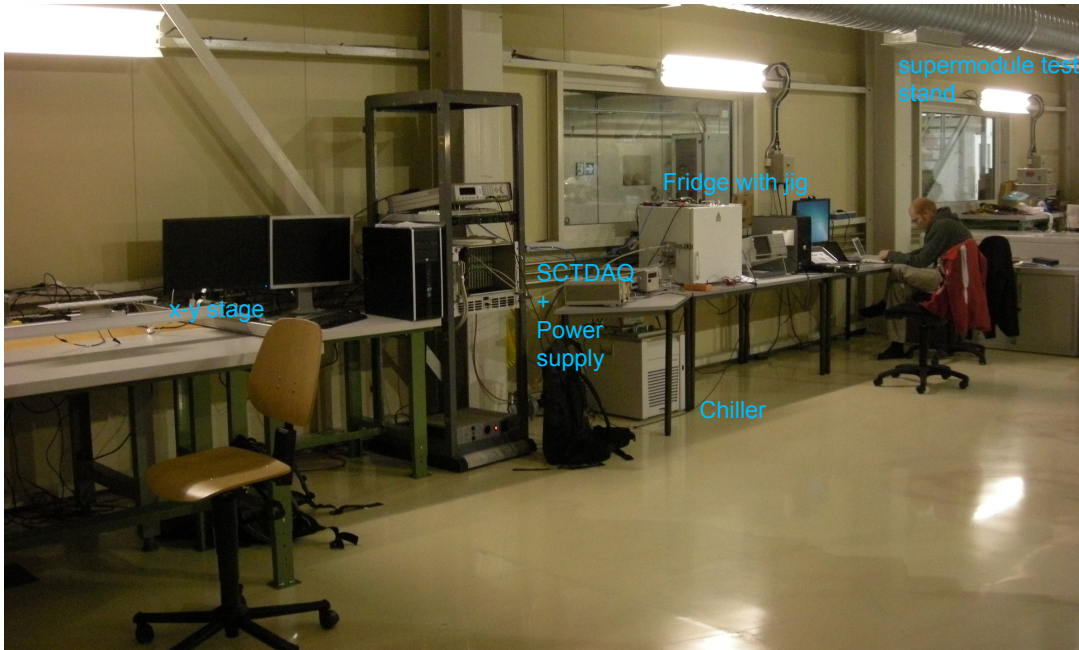


Figure 13.1: Overview of the electrical test setup in B180 used for the measurements.

used for sensor biasing controlled via its general purpose interface bus (GPIB). Further low voltage power supplies by TTI were used to power the HSIO or modules also controlled via the GPIB. The DAQ system was installed and commissioned using a dummy module.

Test Stand for Stavelets The electrical test stand was later extended by a large scale setup to test full staves. For this application an $x - y$ stage, with a travel range of $700 \times 1000 \text{ mm}^2$ was installed and tested. This was later mounted onto a $1.5 \times 1.2 \text{ m}^2$ large optical table produced in Freiburg, equipped with a lattice of M6 holes to fix both staves and modules of various size and shape. This setup has been further extended and is summarised in Ref. [284].

Test Facility for Irradiated Sensors A bunker was installed adjacent to the cleanroom consisting of a concrete roof and walls secured by a controlled access. In fall 2011 the bunker room was equipped with two freezers, one for measurements with irradiated modules and a second one for storage of irradiated module or stave prototypes. Compressed dryair and vacuum outlets were installed as well as power outlets. A cable guide was installed and used to connect the HSIO in the cleanroom via a ten meter long cable to the device under test. First electrical tests with the dummy module were performed in summer 2011. Hence all necessary installations and infrastructure for measurement of irradiated modules were put in place.

Besides the mentioned test stands the cleanroom was also equipped with all necessary tools for basic repairs of the modules. Further it was envisaged to install a laser setup to enable spatial and timing resolved measurements using a Nd:Yag 1066 laser. While the author contributed to the first successful triggering and detection of a laser signal using a DC-DC module prototype, a fully refined setup was never realised.

13.2 Data Acquisition System

The data acquisition (DAQ) and detector control system (DCS) that was set up and commissioned in B180 is a generic DAQ system purpose built at SLAC called High Speed Input Output (HSIO), as shown in Fig 13.2(a). It is designed to provide signal processing for the prototype testing of both the pixel and strip upgrade of the ATLAS experiment. The HSIO is designed as a stand-alone DAQ system and is based on a generic base board using the Advanced Telecommunications Computing Architecture (ACTA) standard as an interface card, containing connectors and buffering to interface the front end electronics.

The central processing unit consists of a Xilinx Virtex-4 Field Programmable Gate Array (FPGA) for data acquisition and processing. The FPGA provides a variety of connections, including the standard network connections (such as RJ45, GigE, SFP and XFP), USB connections and additional connectors for general purpose input and output. The main communication with the DAQ control PC is handled via a small form-factor pluggable (SFP) transceiver module using an Ethernet connection. The network interface uses raw Ethernet protocol without any further network or transport layers on top.

The DAQ control software is based on the SCTDAQ package [285] which dates back to the various tests performed on hybrids and modules in the SCT era. The SCTDAQ software package is a collection of C++ routines and libraries interfaced to the ROOT framework [286]. Hence SCTDAQ provides both the core readout software and the interface to the HSIO board to initiate commands to be send to the front-ends, write data to their registers for configuration, read-back status registers, command responses and the actual sensor hit data send back from the ASICs.

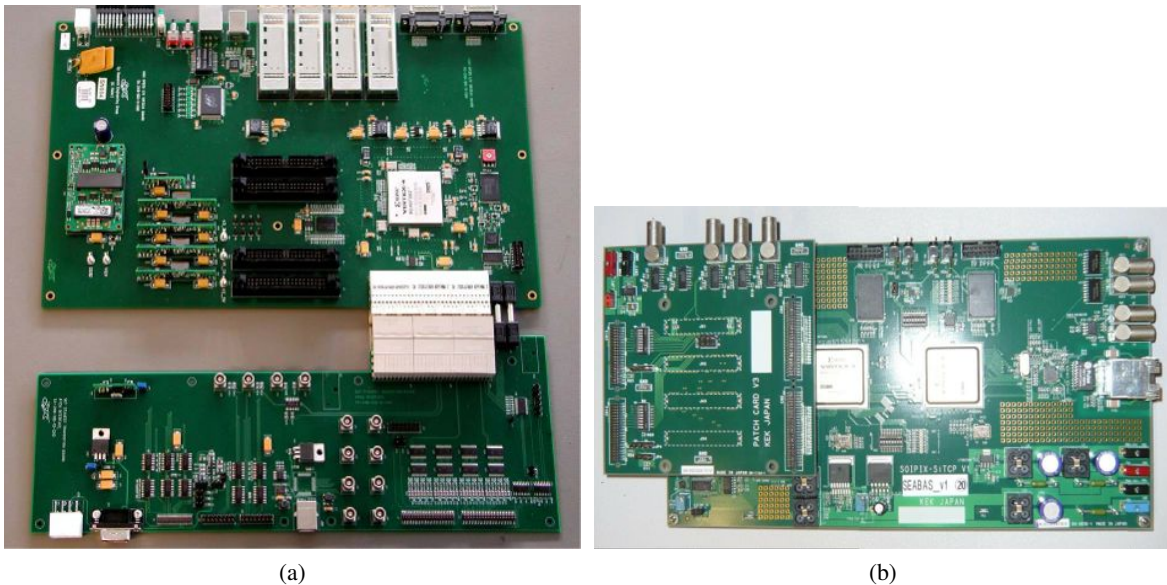


Figure 13.2: HSIO (a) and SEABAS (b) readout system

13.3 Front-end calibration and Electrical Tests

High requirements are set on the electrical performance of the individual modules and staves to comply with the demanding environment set by the HL-LHC. Specifically the noise occupancy level, timing and power consumption are of fundamental importance. Therefore, a thorough testing of both the analogue

and digital electrical performance along the development of modules for the upgrade is vital. The digital tests are performed by injecting an adjustable calibration charge, generated by an internal circuit of the chips into the preamplifier of each channel. Since the readout chips are binary, analogue properties can not be measured directly, but are determined in a parameter scan. A scan evaluates a certain parameter, by varying this parameter according to a defined range and step. The most used scan in the following is the threshold scan, in which the discriminator threshold is varied while a fixed calibration charge is sent multiple times at each threshold. The lower the threshold is set, the lower is the amount of charge required to pass the threshold. The hit occupancy is defined as the fraction of calibration charges exceeding the threshold. In an ideal detector the distribution would follow a step function, however noise sources lead to a smeared distribution. A schematic of a threshold scan is shown in Fig. 13.3. The final distribution follows a rectangular error function known as s-curve, due to its characteristic shape. The vt_{50} point is defined as the threshold corresponding to an occupancy of 50% and the noise at the discriminator output is given by the width of the distribution.

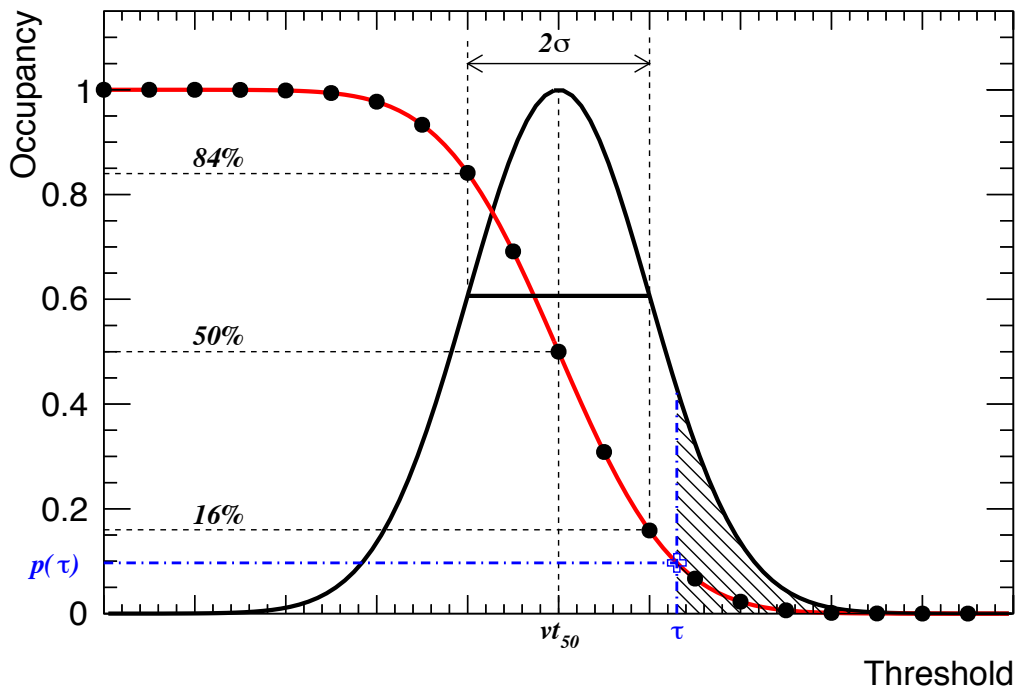


Figure 13.3: Schematic of a threshold scan. A number of fixed calibration pulses is injected at each threshold step. The s-curve (shown in red) follows from a convolution of a step function, describing the calibration pulse and Gaussian distributed noise arising from the electronics. The hit occupancy at a given threshold τ is defined as the fraction of events above threshold. The vt_{50} point is defined as the threshold corresponding to an occupancy of 50%. Figure taken from [287].

In the following paragraphs a summary of the characterisation sequence performed on the modules (or staves) for the ATLAS upgrade is given. The electrical tests are performed using a single-sided DC-DC module prototype, which uses the ABC250 front-end ASICS a 250 nm CMOS successor to the ABCD chip that is used in the ATLAS SCT. In contrast to the final ABC130 readout ASIC this chip has only 128 readout channels and does not yet provide the extended trigger, readout and bandwidth capabilities implemented in the final version. Therefore there are two columns each containing ten chips on each hybrid. The sensor used is a ATLAS07 large area sensor, as described in Section 11.5.

The DC-DC module was inserted on a module testing jig and placed inside an air and light tight thermal enclosure (fridge) that was flushed with liquid nitrogen, as shown in Fig. 13.4.



Figure 13.4: Top view of the single-sided DC-DC module placed on a metal jig contained within the fridge.

Initial Powering Test The general test sequence starts with an initial powering test to ensure the correct initialisation and operation of all ASICs. This test allows to identify potential faults in wire bonds, traces or connectors and thus prevent potential damage to the sensor or front-end ASICs during the test procedure.

Burst Test The burst test consists of a sequence of tests that verify the communication with the front-end electronics. A series of L1A trigger bursts is sent to the front-end ASICs. On their receipt the hit data, which is sampled at the bunch crossing clock from the discriminators and stored in a pipeline memory, is transferred to the buffers for readout.

Strobe Delay Test The strobe delay test varies the phase of the charge injection relative to the L1A trigger command, in order to define the optimal setting of the delay register for each chip and thus assure the accuracy in the threshold calibration. In this test a 4 fC signal is injected while the threshold is set to 2 fC. This should lead to a 100 % hit efficiency, if the timing is set correctly. For too short delays, the signal has not arrived and no hits are registered. With too long delay settings, the signal has decayed below threshold. The strobe delay is set for each ASIC individually and corresponds to a value of either 25 % or 40 % of the functional range determined in the scan. A typical result from the strobe delay test is shown in Fig. 13.5. The optimal setting for each strip is clearly visible.

Threshold scans Threshold scans are performed to measure the gain, offset and linearity of the amplifiers by evaluating its response to different injected charges. The test is often referred to as three-point gain scan when injecting 0.5 fC, 1.0 fC and 1.5 fC. The occupancy versus threshold data is measured for each channel and the resulting occupancy ranges from 0 % (i.e. all injected signals are below threshold) to 100 % (i.e. all injected signals produce a hit). The occupancy distribution is fitted with a complementary error function, known as s-curve. The threshold at which the occupancy is 50 % is called vt_{50} point

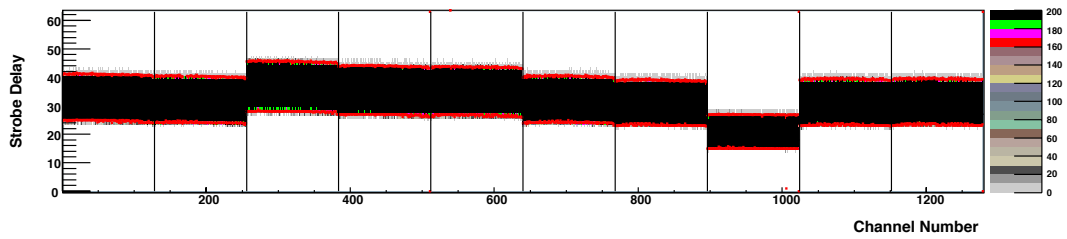


Figure 13.5: Exemplary result of a strobe delay scan for one hybrid column, consisting of ten ASICs. The ideal setting safe clearly visible.

and determines the mean amplifier response to the injected charge. The variance of the complementary error function is a measure of the noise at the amplifier output. A linear fit to each set of vt_{50} values for the three injected charges gives the response curve. From the straight line fit the discriminator offset (response at 0 fC) and the gain at each channel (slope measured in mV/fC) is determined. Figure 13.6 shows an example of the resulting distributions of the vt_{50} , the gain, the extrapolated offset and the noise as a function of the channel number derived from a three-point-gain of a column of ASICs from the DC-DC stave module. Even before adjusting the individual channel feedback, as described in the next section, a rather uniform gain and noise distribution is seen. The average gain is around 110 mV/fC which is in good agreement with the design specifications of the ABC-250 ASICs of >90 mV/fC [288]. The equivalent noise charge (ENC) is given by the quotient of the amplifier output noise (at 1 fC) and the amplifier gain. This value is often used to define the overall noise performance of the charge amplifying system. The input noise matches well the expected ~ 600 ENC(e) derived from the short-strip input capacitance.

Trimming The channel trims must be set in order to assure a unified response of each channel to a given charge by varying the discriminator offset. A trim range scan is performed to adjust the optimal trim value which allows the individual calibration of each channel to an equal target response per hybrid or module with highest possible precision. During the trim range scan a charge of 1 fC is injected and threshold scans are performed using different trim DAC settings. The vt_{50} points are extracted and compared to the target threshold in order to determine the maximum number of channels that can be aligned for each trim range setting. The lowest possible set of trim values that maximises the number of channels is chosen for each chip. Channels that are not trimmable, for instance due to fault wire-bonds or shorts, are masked and stored to a mask file. The determined trim DAC values for all channels of a hybrid or module are instantaneously applied and stored in a trim file for later application. An exemplary result of the optimal trim settings for the front-end ASICs of one of the hybrid columns is shown in Fig.13.7(a). For each channel the optimal trim DAC steps are stored. The results of a threshold scan with the optimal trim settings is shown in Fig. 13.7(b) at an input charge of 1 fC, the reduction in channel to channel spread of the response compared with the results before trimming shown in Fig. 13.6(a) are clearly visible. This sensor shows two excluded channels due to excessive noise.

Response Curve The response curve is an extended threshold scan injecting ten different charges, usually over a range from 0 fC to 8 fC. It is performed on the trimmed channels and gives a precise measurement of gain, discriminator offset and input noise for each channel. Due to the increased number of reference points the vt_{50} points as a function of the injected charge are fitted with a quadratic function to account any non-linearities in the amplifier response. Figure 13.8 shows an exemplary result of an extended threshold scan for one of the chips on the DC-DC module. The non linearity is especially

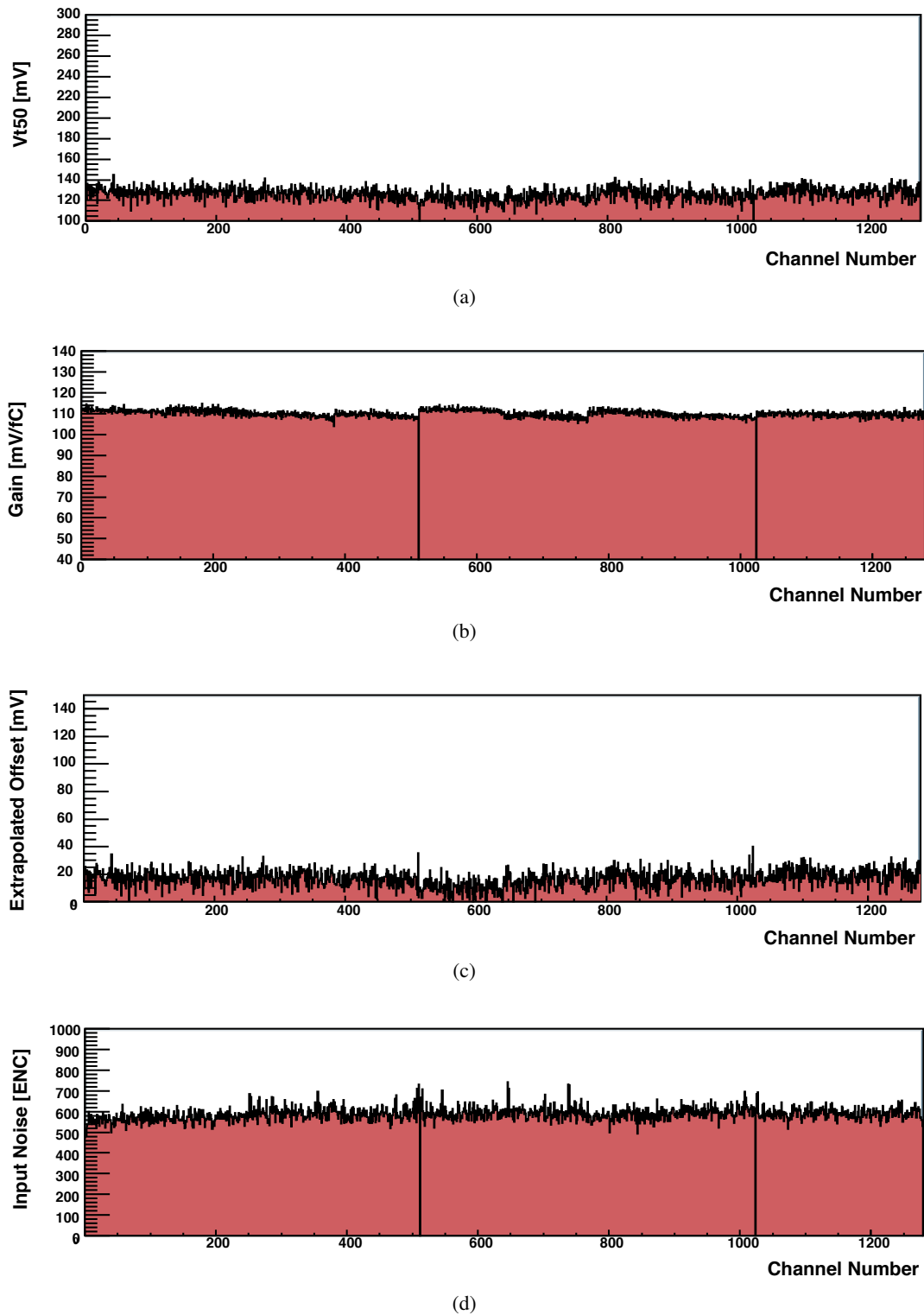


Figure 13.6: Exemplary results from a three point gain scan. From top to bottom: distribution of v_{t50} , gain, extrapolated offset and input noise, obtained from a three-point gain test using 0.5 fC, 1 fC and 1.5 fC input charges. The plots show the distributions as a function of all 1280 channels of a single hybrid column (ten readout ASICs). The sensor was biased at 200 V.

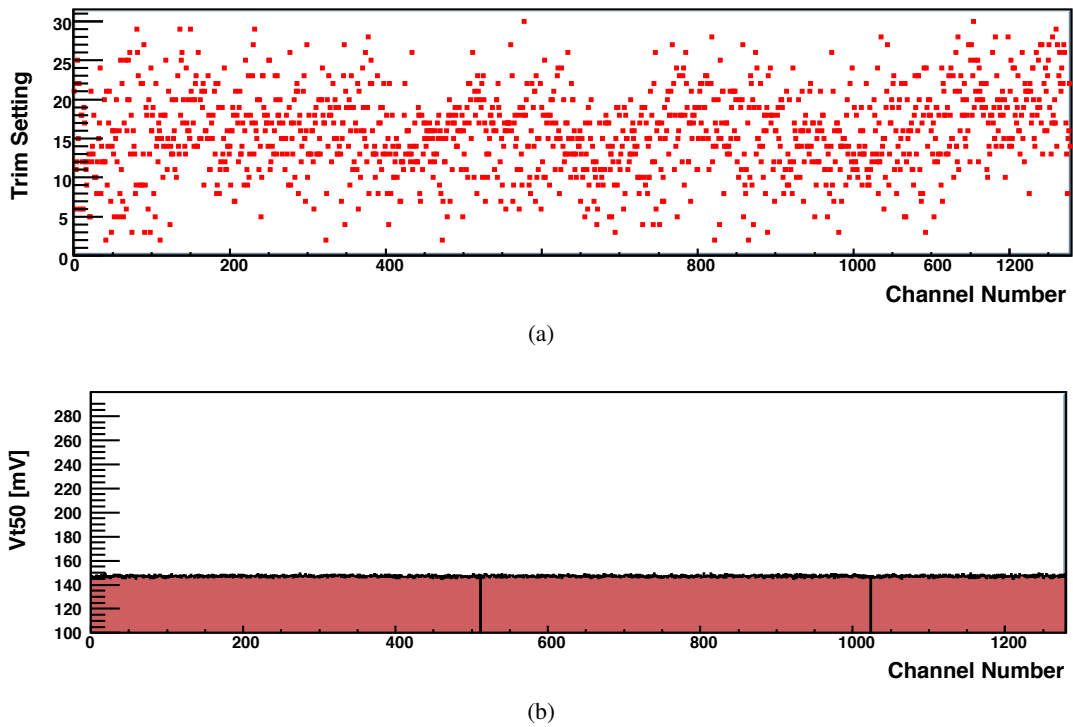


Figure 13.7: Top: Distribution of the trim settings of all 1280 channels of a single hybrid column (ten readout ASICs). The sensor was biased at 200 V.

visible at higher input charges.

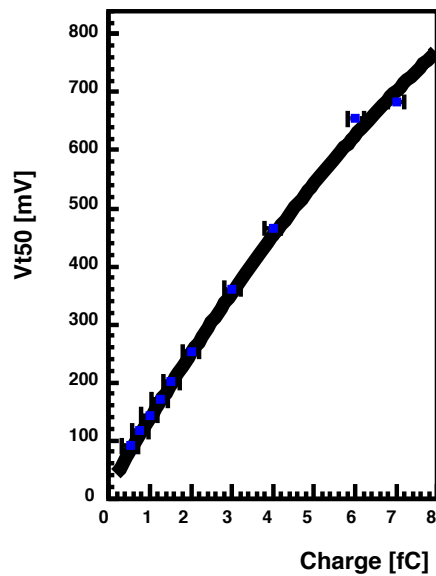


Figure 13.8: Response curve with ten injected charges of an individual chip, fitted with a quadratic function. The values are averaged over the 128 channels of the chip.

Noise Occupancy For efficient detector operations it is crucial that the detector occupancy from noise hits remains below a level of the order of 10^{-5} . The noise occupancy test measures the noise occupancy as a function of threshold. It is determined by the number of hits returned from the front-ends for increasing threshold values without any charge injection. Depending on set threshold number of triggers between 2×10^3 and 10^6 are sent to obtain sufficient statistics even at the highest thresholds. The minimal number of iterations per threshold is chosen such that at least 50 hits are recorded in more than 50 % of the active channels. An exemplary noise occupancy measurement as a function of the discriminator threshold is shown in Fig. 13.9 for all channels of a single hybrid of the DC-DC coupled Stave prototype module.

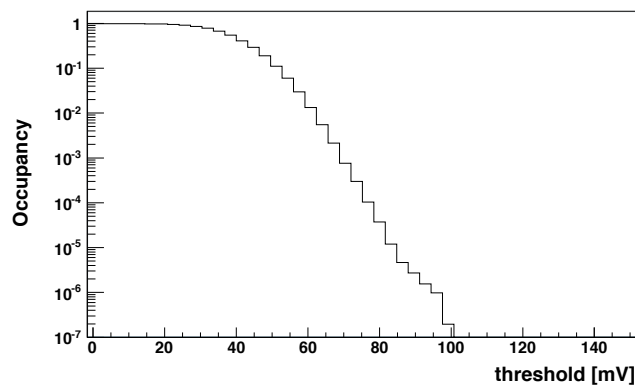


Figure 13.9: The average noise occupancy as a function of the threshold, measured in a threshold scan without injecting a calibration charge.

13.4 Performance Comparisons of Single and Double-sided Modules

This section provides a summary of the first comparison of the electrical performance between the competing stave (see Section 11.4) and Supermodule (see Section 11.4.2) designs performed in summer and fall 2011. The comparison is based on measurements using a single-sided DC-DC coupled stave module and a double-sided Supermodule prototype. The stave design is based on individual single-sided modules, that are glued from both sides on a common support and cooling structure, whereas a Supermodule defines the collection of individual double-sided modules assembled into a common support structure.

The setup of the centralised test facilities in B180 allowed to test the modules with both the HSIO readout system, built by the stave community, and the SEABAS [289] system developed at KEK in Japan by the Supermodule community as shown in Fig. 13.2(b). The SEABAS data acquisition system consists of a 12.4 cm×22.4 cm base board which holds two Virtex-4 FPGAs. These provide connectivity to the front-end electronics, the standard TCP/IP and UDP connections to a controller PC and allow for a customised data processing. The Supermodule was housed in a custom built air and light tight metal container with a cooling liquid running through the pipes as shown in Fig. 13.10.

The motivation for the comparative measurements arose from observed differences on the order of 10 % in the input noise values reported for single- and double-sided modules [290]. Differences in the input noise can be related to different sources, hence the measurements included

- Measurement of both prototype modules with the two readout systems, to review if the differences

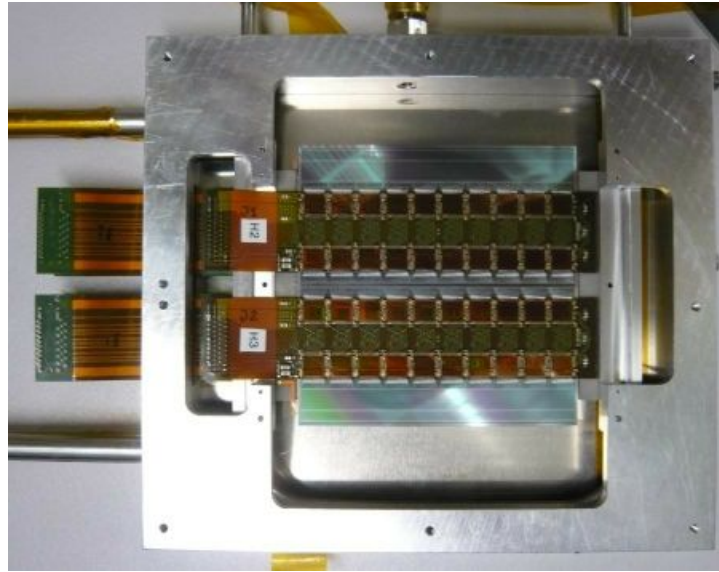


Figure 13.10: Top view of the double-sided Supermodule inside its thermal enclosure, with the cooling pipes are clearly visible

arise from the readout system and are related to the computation of the noise in either system

- Both systems rely on a different housing and cooling infrastructure, which might lead to considerable differences in the temperature of the sensors. To account for the differences in the cooling performances between the two setups, the measurements of the module were performed at different temperatures ranging between 8 °C to 20 °C.
- Measurements of the noise depending on the bias voltage were also included, as the stave prototype has DC-DC powering whereas the supermodule prototype is individually powered.

A voltage current curve of the two modules is shown in Fig. 13.11. Both sensors are fully depleted at voltages beyond 150 V. A difference of roughly 10^3 in the leakage current is found between the DC-DC stave module and a double-sided Supermodule sensor. To account for the temperature dependence in the calibration steps, threshold scans and trim range scans, these were repeated at every temperature step. The scans were taken at a bias voltage of 200 V, to ensure full depletion of the sensors. An exemplary result of the optimal strobe delay settings, as a function of the temperature is shown for column 0 in Fig.13.12(a) and for column 1 in Fig.13.12(b) for hybrid one of the DC-DC coupled stave module. A decrease of the strobe delay related to an increasing temperature only becomes visible at chiller temperatures beyond 17 °C.

The dependence of the measured noise as a function of the bias voltage is shown in Fig. 13.13(a). In general the measurements were repeated five times and the values are the average values extracted from threshold scans performed at 1 fC. A strong increase in the noise is seen in both modules for voltages below 150 V, indicating that the sensors are not yet fully depleted. Thereafter no further dependence of the noise on the bias voltage is seen in either module. The double-sided Supermodule exhibits a higher noise at low bias voltages and a lower noise at bias voltages beyond 150 V.

The noise as a function of the hybrid temperature is shown in Fig. 13.13(b). The actual hybrid temperature is extracted from the negative temperature coefficient thermistors placed on the middle of each hybrid between the two ASIC columns. Again each noise value is extracted as the average of five differ-

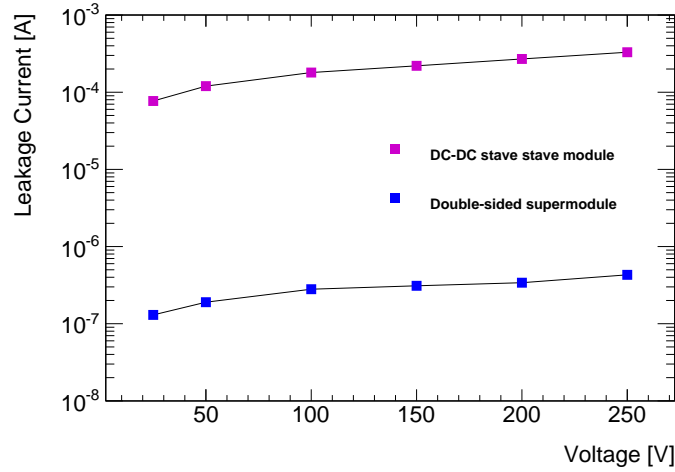


Figure 13.11: Current-voltage measurement of the modules. The blue line shows the Double-sided Supermodule and the purple line shows the measurement of the DC-DC stave module.

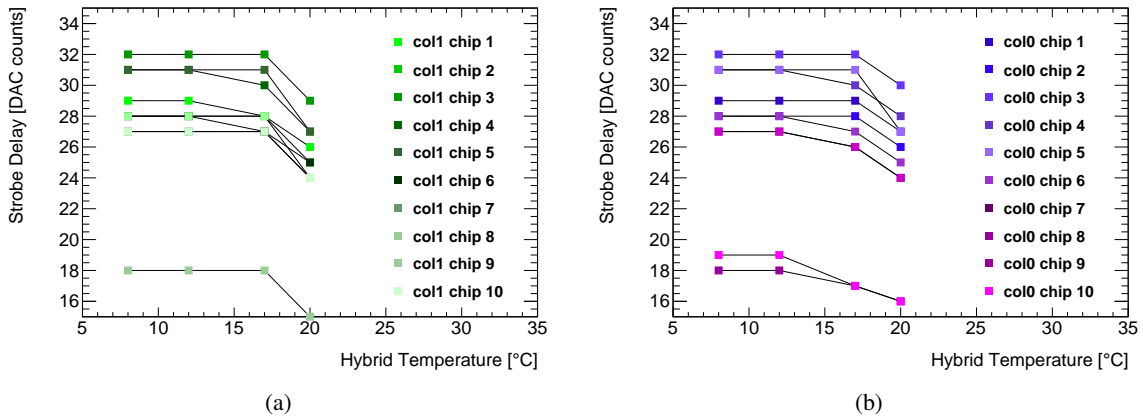


Figure 13.12: Optimal strobe delay setting as a function of the hybrid temperature derived from calibration scans of the DC-DC powered stave module for one of the two hybrids. Column 0 is shown in (a) and column 1 in (b).

ent threshold scans at 1 fC. Although the same temperature was set at the chiller, the hybrid temperature of the Supermodule hybrids range from 24 °C to 37.5 °C, while the hybrid temperature of the DC-DC coupled stave module varies between 22.5 °C to 58 °C. For similar hybrid temperatures the noise of the DC-DC stave module show on average a 5 % higher noise than the double-sided Supermodule. Much of this difference is attributed to an increased load capacitance of $\sim 10 - 20 \%$ at the preamplifier input, arising from the direct gluing of the hybrids to the sensor surface in the DC-DC stave module. Further contributions to this difference stem from the factor 10^3 higher leakage current, which is not easily corrected without a measurement of the individual strip leakage current. A comparison of the noise and

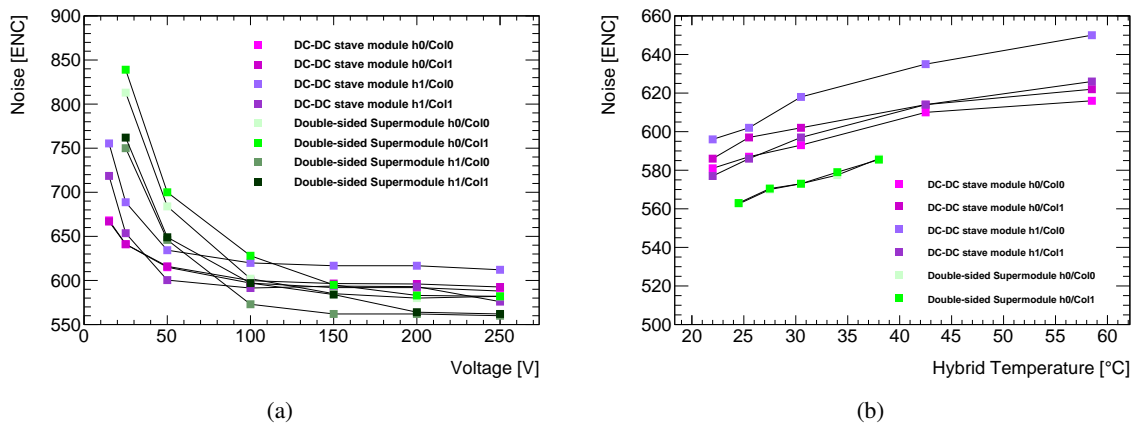


Figure 13.13: The noise as a function of the voltage (a) and the hybrid temperature (b) for the double-sided Supermodule and the DC-DC stave module.

gain values measured by the HSIO and the SEABAS systems is found in Table. 13.1. The noise and gain are measured for a single hybrid on the double-sided Supermodule and the DC-DC module performing threshold scans at 1 fC at a hybrid temperature of 27 °C. Irrespective of the readout system, the input noise of the DC-DC stave module is about 20 ENC to 30 ENC lower, corresponding to $\sim 4 - 5 \%$, than the input noise of the double-sided Supermodule. Furthermore a difference on the order of 3 % is found in the gain of the ASICs between the two designs. The lower gain is found for the double-sided Supermodule and is attributed to the slightly lower voltage supply of the ASICs. It was found in direct measurements, that if the external voltage is set 2.6 V only 2.35 V are measured directly at the hybrid connector. In contrast the 2.6 V are derived by the DC-DC converters placed directly underneath the hybrids on the module testing frame, leading to a smaller voltage loss. In this case the measured voltage at the ASICs was 2.45 V. The higher voltage leads to a higher gain. In an independent measurement an almost linear dependence of the supply voltage on the gain was found.

The comparison between the HSIO and the SEABAS system reveals that the SEABAS systems determines a roughly 9 % higher gain and a lower input noise (up to 4 %), irrespective of the measured module. While a full determination of the is effect could not be identified during the comparative measurements, these deviations can be the result of differences in the algorithms used to determine the gain, i.e. the fitting procedure to extract the response curve and the slope.

		HSIO			SEABAS		
module (hybrid)	column	gain [mV/fC]	input noise [ENC]	output noise [ENC]	gain [mV/fC]	input noise [ENC]	output noise [ENC]
single-sided	0	109.2	589.9	10.32	116.3	571.9	10.66
module	1	109.7	596.0	10.48	116.9	576.9	10.81
double-sided	0	105.9	570.3	9.68	113.6	546.1	9.93
module	1	105.7	570.6	9.66	113.3	546.0	9.91

Table 13.1: Comparison of the average gain, input and output noise values of a single hybrid on a single and double-sided module. The values are derived in threshold scans performed at 1 fC using both the HSIO and the SEABAS readout systems.

Conclusion

Since the 1990s several neutrino oscillation experiments have been able to prove that neutrinos of all three generations oscillate and are indeed massive. However, the origin of their masses is still unknown. A natural mechanism to explain these small neutrino masses is arguably one of the most important topics in modern particle physics.

In so-called seesaw mechanisms the smallness of the neutrino masses is explained by introducing new particles at a high mass scale. This thesis presents a search for type-III seesaw neutrinos. Here the lightest fermionic triplet have two charged heavy leptons denoted L^+ and L^- and one neutral heavy lepton N_0 .

The search for type-III seesaw heavy leptons at the LHC has been put forward as a novel analysis idea in ATLAS, which involved a significant amount of pioneering work. Despite the low production cross section, decays where $L^\pm \rightarrow \ell^\pm Z$ ($\ell = e\mu$) with the Z boson decaying leptonically, have proven to be more sensitive for discoveries of a resonance structure. They benefit from a good signal-to-background ratio and allow for a direct reconstruction of the narrow L^\pm resonance, which is further utilised in constraining the background. Tripletons are not specific to the type-III seesaw models, but also occur in models of vector-like leptons, which appear in several extensions of the Standard Model. The analysis is therefore not only performed in a model dependent way, but also provides a model independent evaluation of the signal regions.

In this thesis the search for a heavy tripleton resonance decaying to an intermediate Z boson and an electron or muon has been presented. The search is based on proton–proton collisions recorded by the ATLAS experiment at the CERN Large Hadron Collider in 2012 at $\sqrt{s} = 8$ TeV, corresponding to an integrated luminosity of 20.3 fb^{-1} . Events are selected if they contain three electrons or muons and two of them form a same-flavour opposite-sign pair consistent with originating from a Z boson. Since both vector-like leptons and type-III seesaw neutrinos are pair produced, the events are further categorised into three mutually exclusive regions based on the decay of the second heavy lepton within the event. The first category includes all events with an additional lepton. The second category selects from the remaining events those that have a dijet pair, which is consistent with the decay products of a second heavy lepton. The third category includes all remaining events. The signal events are further divided based on the flavour of the lepton, which is not associated with the Z boson, and this ultimately leads to six exclusive signal categories. Standard Model background populating the signal region arises mainly from irreducible sources dominated by continuum WZ and ZZ production. Smaller background contributions originate from $t\bar{t} + W/Z$ and triboson production and from reducible sources consisting

mainly of Z +jet and $Z+\gamma$ production, with smaller contributions from $t\bar{t}$ production. While the reducible background is determined using data-driven techniques, the irreducible background is estimated using simulated event samples. Four different validation regions are defined that confirm the validity of the background estimate. Using the difference between the trilepton and the Z boson candidate masses reduces the impact of the lepton momentum measurement in the resolution of the resonance. This improves the sensitivity to very narrow resonances.

The search is performed in each of the defined categories, and the number of signal and background events are determined by using an unbinned maximum-likelihood fit of parameterised signal and background shapes to the data. This approach allows the narrow resonance structure of the signal to be fully exploited. The data is well described by the combined fit of the three categories in both flavour channels, however no significant excess above the Standard Model predictions is observed. Therefore 95% CL limits on the heavy lepton pair-production cross section, σ , using the CL_s method are derived. The results are interpreted in the context of two benchmark models of new heavy leptons decaying to three charged leptons. In case of electron-only case the vector-like leptons model is excluded for heavy lepton mass ranges of 129–144 GeV and 163–176 GeV. The corresponding observed exclusion for the muon-only scenario is 114–153 GeV and 160–168 GeV. The type-III seesaw model has significantly higher production cross sections. Hence, the observed exclusion in the electron-only scenario excludes heavy leptons in the mass range of 100–430 GeV. For the muon-only scenario, the observed exclusion is in the ranges of 100–401 GeV and 419–468 GeV. To accommodate the interpretation of results for generic trilepton searches, limits are also put on the visible cross section of trilepton resonance production. The additional derivation of fiducial efficiencies facilitates model testing beyond those covered here.

This search provides the strongest limits on heavy lepton resonances decaying to a three lepton final state to date. A complementary search in ATLAS used final states that contain two leptons (electrons or muons) and two jets. This analysis allowed to exclude masses below 400 GeV in the case of an exclusive coupling to electrons, and 325 GeV in the case of a muon-only coupling. A search by the CMS experiment excluded type-III seesaw heavy leptons with masses in the range of 100 GeV to 210 GeV, depending on theoretical assumptions. Similar searches have also been done by the L3 experiment, which rule out charged heavy leptons with masses below 100 GeV.

The second part of this thesis is dedicated to the development of radiation hard silicon detectors needed for the ATLAS luminosity upgrade which will commence in about ten years time. Several projects were performed by the author, which contribute to multiple key aspects for a successful upgrade of the ATLAS silicon strip detector.

As the silicon detectors currently installed in ATLAS are not sufficiently radiation tolerant, novel radiation hard silicon sensors had to be identified for the inner tracker upgrade. Promising candidates for radiation hard options are planar sensors with n-type readout on a p-type substrate and silicon sensors in 3D technology. Here columnar electrodes are etched into the silicon substrate.

As part of this thesis, a beam test was performed which provided the first direct comparison between the performance of planar n-in-p sensors and 3D sensors. In this beam test three ATLAS07 ministrip sensors and three 3D sensors by CNM, irradiated up to fluences of $3 \times 10^{15} \text{ n}_{\text{eq}}\text{cm}^{-2}$, were measured. Measurements of the collected charge showed that both detector geometries collected enough charge to equip the silicon microstrip layers at the HL-LHC. It was further found that the signals of the irradiated 3D detectors significantly exceeded the signal measured with the unirradiated 3D detectors at high bias voltages, which points towards the occurrence of charge multiplication caused by impact ionisation. This was the first observation of this novel effect in 3D sensors. Given the limitations in the bias voltage during the beam test, the electric field needed for charge multiplication in planar silicon sensors to occur, could not be reached. Furthermore, the signal of the unirradiated planar detectors could not

be reached with the irradiated planar detectors. Due to lower charge sharing in 3D detectors, a better spatial resolution could be obtained with the planar sensors. A degradation of the spatial resolution after irradiation was measured. Measurements of the collected charge considering the impact point clearly showed a deficit of the collected charge for tracks impinging in between two strips compared with tracks impinging onto the strip centre. This is attributed to a combination of the capacitive coupling, charge sharing, trapping and the electric field distribution. In addition to the beam test measurements, measurements in the laboratory were performed using different setups which contributed to an ATLAS wide sensor test campaign.

Further contributions to the inner tracker upgrade included the installation of the infrastructure and test setups for centralised large scale testing on large structures and tests of irradiated modules at CERN. This infrastructure allowed for the first direct comparison between competing design approaches and readout systems for the inner tracker, called the Supermodule and the Stave approach. The Supermodule prototype showed a slightly lower input noise. However, both tested modules met the quality requirements set for the performance at the HL-LHC with respect to their gain (>105 mV/fC) and noise (<650 ENC) behaviour. The stave concept has hence shown its superiority, given its high integration and thus lower material budget.

In conclusion, both the laboratory measurements and the comparative beam test provided an outstanding contribution for the final conclusion on the sensor technology for the upgrade. The measurements underline that planar detectors with n-side readout exhibit a sufficient radiation hardness for applications in detector layers further outwards from the interaction point. In this region 3D detectors do not offer a significant advantage over planar detectors. Even at fluences in the order of 1×10^{15} n_{eq}cm⁻² planar n-in-p detectors yield a sufficient signal, provided that sufficiently high bias voltages can be supplied to the detectors. Sensors in 3D-technology remain a viable option for the pixel layers for the HL-LHC upgrade, and are successfully installed and perform well in the innermost detector layer of ATLAS.

Auxiliary Information for the Validation Regions

This chapter gives some extended information on the four background validation regions described in Section 6.2. The signal and background composition of each region is detailed for the $Z + e$ and $Z + \mu$ final state. Since the analysis is highly dependent on a good modelling of the transverse lepton momenta, additional histograms on the transverse momenta of the three leptons associated to the resonance in the dedicated control region are given.

A.1 High $\Delta - R$

Process	Preselection	Bachelor e	$ m_{\ell^+\ell^-} - m_Z < 10$ GeV	ZZ Veto	$\Delta m < 200 - m_Z$	MinDeltaR
$ZZ \rightarrow 4\ell$	890.6 ± 4.07	414.2 ± 2.76	247.1 ± 2.13	210.53 ± 1.97	156.92 ± 1.7	58.73 ± 1.04
$WZ \rightarrow \ell\ell\nu$	1753.91 ± 4.76	746.02 ± 3.09	622.44 ± 2.82	622.44 ± 2.82	403.81 ± 2.27	100.41 ± 1.13
$i\bar{i} + V$	39.92 ± 0.56	18.12 ± 0.38	13.01 ± 0.32	12.94 ± 0.32	7.56 ± 0.24	0.91 ± 0.09
$Z + \gamma$	342.09 ± 5.97	342.09 ± 5.97	93.16 ± 3.1	93.16 ± 3.1	74.23 ± 2.78	39.72 ± 2.04
Reducible	447.37 ± 15.28	158.13 ± 13.52	99.58 ± 8.17	98.98 ± 8.15	75.2 ± 7.27	39.23 ± 5.15
VVV*	11.15 ± 0.15	5.3 ± 0.11	1.88 ± 0.05	1.84 ± 0.05	1.03 ± 0.04	0.15 ± 0.02
Σ Backgrounds	3485.04 ± 17.57	1683.86 ± 15.35	1077.18 ± 9.43	1039.89 ± 9.38	718.75 ± 8.28	239.16 ± 5.75
Data	3597	1805	1163	1124	787	239
VLL, 160 GeV	21.75 ± 0.27	18.84 ± 0.25	16.09 ± 0.23	15.69 ± 0.23	14.63 ± 0.22	1.41 ± 0.07
VLL, 200 GeV	10.19 ± 0.12	8.66 ± 0.11	7.09 ± 0.1	6.93 ± 0.1	4.94 ± 0.08	0.5 ± 0.03
VLL, 250 GeV	4.27 ± 0.05	3.64 ± 0.04	2.94 ± 0.04	2.89 ± 0.04	0.36 ± 0.01	0.01 ± 0.0
Seesaw, 160 GeV	688.97 ± 10.41	535.95 ± 9.07	402.72 ± 7.55	393.19 ± 7.43	335.53 ± 6.82	30.92 ± 2.03
Seesaw, 200 GeV	322.6 ± 4.8	254.73 ± 4.22	180.03 ± 3.38	176.25 ± 3.33	117.5 ± 2.71	10.15 ± 0.72
Seesaw, 300 GeV	61.78 ± 1.27	47.67 ± 1.1	31.92 ± 0.85	31.61 ± 0.85	3.89 ± 0.32	0.03 ± 0.01

Table A.1: Event counts at various stages in the cutflow for the $Z + e$ flavour channel, high ΔR validation region. Only statistical uncertainties on the Monte Carlo samples are shown.

A Auxiliary Information for the Validation Regions

Process	Preselection	Bachelor μ	$ m_{\ell^+\ell^-} - m_Z < 10$ GeV	ZZ Veto	$\Delta m < 200 - m_Z$	MinDeltaR
$ZZ \rightarrow 4\ell$	890.6 ± 4.07	476.4 ± 2.99	279.71 ± 2.3	216.4 ± 2.02	170.67 ± 1.79	65.16 ± 1.11
$WZ \rightarrow \ell\ell\nu$	1753.91 ± 4.76	1007.89 ± 3.62	855.8 ± 3.34	855.8 ± 3.34	569.58 ± 2.72	136.22 ± 1.33
$t\bar{t} + V$	39.92 ± 0.56	21.8 ± 0.41	16.38 ± 0.36	16.28 ± 0.36	9.73 ± 0.27	1.2 ± 0.1
$Z + \gamma$	342.09 ± 5.97	0.0 ± 0.0	0.0 ± 0.0	0.0 ± 0.0	0.0 ± 0.0	0.0 ± 0.0
Reducible	447.37 ± 15.28	289.23 ± 7.13	200.6 ± 5.79	200.66 ± 5.79	185.0 ± 5.49	98.2 ± 4.01
VVV*	11.15 ± 0.15	5.85 ± 0.11	2.41 ± 0.06	2.35 ± 0.06	1.44 ± 0.05	0.22 ± 0.02
Σ Backgrounds	3485.04 ± 17.57	1801.18 ± 8.55	1354.89 ± 7.07	1291.49 ± 6.99	936.42 ± 6.4	301.0 ± 4.37
Data	3597	1792	1414	1340	953	302
VLL, 160 GeV	26.76 ± 0.29	22.36 ± 0.27	19.11 ± 0.25	18.31 ± 0.24	17.5 ± 0.24	1.51 ± 0.07
VLL, 200 GeV	12.58 ± 0.13	10.28 ± 0.12	8.51 ± 0.11	8.22 ± 0.1	5.47 ± 0.09	0.53 ± 0.03
VLL, 250 GeV	5.13 ± 0.05	4.2 ± 0.05	3.4 ± 0.04	3.32 ± 0.04	0.43 ± 0.01	0.01 ± 0.0
Seesaw, 160 GeV	934.08 ± 9.5	748.59 ± 8.4	516.55 ± 6.72	500.83 ± 6.59	435.35 ± 6.12	39.23 ± 1.76
Seesaw, 200 GeV	411.01 ± 4.22	323.95 ± 3.7	209.4 ± 2.85	205.45 ± 2.81	130.37 ± 2.24	10.56 ± 0.58
Seesaw, 300 GeV	72.57 ± 1.07	57.4 ± 0.94	35.36 ± 0.71	35.0 ± 0.7	4.82 ± 0.28	0.11 ± 0.04

Table A.2: Event counts at various stages in the cutflow for the $Z + \mu$ flavour channel, high ΔR validation region. Only statistical uncertainties on the Monte Carlo samples are shown.

A.2 Off-Z Validation Region

Process	Preselection	Bachelor e	$= 3 e/\mu$	$\leq 1 Z$	Invert $ m_{\ell^+\ell^-} - m_Z < 10$ GeV	$ m_{\ell^+\ell^-} - m_Z < 10$ GeV
$ZZ \rightarrow 4\ell$	891.04 ± 4.07	413.68 ± 2.76	362.29 ± 2.58	133.06 ± 1.56	133.06 ± 1.56	102.51 ± 1.37
$WZ \rightarrow \ell\ell\nu$	1753.91 ± 4.76	745.91 ± 3.09	745.77 ± 3.09	73.7 ± 0.97	73.7 ± 0.97	33.18 ± 0.65
$t\bar{t} + V$	39.92 ± 0.56	18.26 ± 0.38	17.11 ± 0.37	4.01 ± 0.18	4.01 ± 0.18	1.91 ± 0.12
$Z + \gamma$	342.09 ± 5.97	342.09 ± 5.97	342.09 ± 5.97	202.31 ± 4.59	202.31 ± 4.59	183.69 ± 4.37
Reducible	447.36 ± 15.28	158.04 ± 13.52	157.21 ± 13.5	44.34 ± 9.42	44.34 ± 9.42	26.24 ± 8.85
VVV*	11.15 ± 0.15	5.37 ± 0.11	4.86 ± 0.11	2.69 ± 0.08	2.69 ± 0.08	1.27 ± 0.06
Σ Backgrounds	3485.48 ± 17.57	1683.35 ± 15.35	1629.33 ± 15.3	460.12 ± 10.64	460.12 ± 10.64	348.81 ± 9.99
Data	3597	1816	1742	479	479	360
VLL, 160 GeV	21.77 ± 0.27	17.22 ± 0.24	14.31 ± 0.22	1.41 ± 0.07	1.41 ± 0.07	0.81 ± 0.05
VLL, 200 GeV	10.19 ± 0.12	7.79 ± 0.1	6.38 ± 0.09	0.93 ± 0.04	0.93 ± 0.04	0.37 ± 0.02
VLL, 250 GeV	4.27 ± 0.05	3.2 ± 0.04	2.55 ± 0.04	0.44 ± 0.01	0.44 ± 0.01	0.11 ± 0.01
Seesaw, 160 GeV	689.27 ± 10.41	507.94 ± 8.79	416.75 ± 7.79	77.09 ± 3.84	77.09 ± 3.84	46.99 ± 3.0
Seesaw, 200 GeV	322.64 ± 4.8	237.0 ± 4.03	195.78 ± 3.59	55.2 ± 2.18	55.2 ± 2.18	16.43 ± 1.17
Seesaw, 300 GeV	61.81 ± 1.27	44.31 ± 1.05	36.48 ± 0.93	13.68 ± 0.65	13.68 ± 0.65	1.19 ± 0.19

Table A.3: Event counts at various stages in the cutflow for the $Z + e$ flavour channel, off-Z validation region. Only statistical uncertainties on the Monte Carlo samples are shown.

A.3 ZZ Validation Region

Process	Preselection	Bachelor μ	$=3 e/\mu$	$\leq 1 Z$	Invert $ m_{\ell^+\ell^-} - m_Z < 10 \text{ GeV}$	$ m_{\ell^+\ell^-} - m_Z < 10 \text{ GeV}$
$ZZ \rightarrow 4\ell$	891.04 ± 4.07	477.36 ± 3.0	383.64 ± 2.69	156.11 ± 1.71	156.11 ± 1.71	120.58 ± 1.5
$WZ \rightarrow \ell\ell\nu$	1753.91 ± 4.76	1008.0 ± 3.62	1007.85 ± 3.62	86.5 ± 1.06	86.5 ± 1.06	41.95 ± 0.74
$t\bar{t} + V$	39.92 ± 0.56	21.67 ± 0.41	20.49 ± 0.4	4.22 ± 0.18	4.22 ± 0.18	1.85 ± 0.12
$Z + \gamma$	342.09 ± 5.97	0.0 ± 0.0	0.0 ± 0.0	0.0 ± 0.0	0.0 ± 0.0	0.0 ± 0.0
Reducible	447.36 ± 15.28	289.32 ± 7.12	288.04 ± 7.08	61.73 ± 3.59	61.73 ± 3.59	34.71 ± 2.76
VVV*	11.15 ± 0.15	5.79 ± 0.11	5.22 ± 0.11	2.63 ± 0.08	2.63 ± 0.08	1.16 ± 0.05
Σ Backgrounds	3485.48 ± 17.57	1802.13 ± 8.54	1705.25 ± 8.4	311.18 ± 4.12	311.18 ± 4.12	200.25 ± 3.23
Data	3597	1781	1675	257	257	163
VLL, 160 GeV	26.75 ± 0.29	20.65 ± 0.26	15.34 ± 0.22	1.69 ± 0.07	1.69 ± 0.07	1.06 ± 0.06
VLL, 200 GeV	12.57 ± 0.13	9.33 ± 0.11	6.71 ± 0.09	0.98 ± 0.04	0.98 ± 0.04	0.39 ± 0.02
VLL, 250 GeV	5.12 ± 0.05	3.75 ± 0.04	2.66 ± 0.04	0.5 ± 0.02	0.5 ± 0.02	0.13 ± 0.01
Seesaw, 160 GeV	933.79 ± 9.49	720.87 ± 8.23	573.03 ± 7.21	141.29 ± 3.93	141.29 ± 3.93	89.04 ± 3.12
Seesaw, 200 GeV	410.88 ± 4.22	305.95 ± 3.58	246.83 ± 3.15	83.37 ± 2.02	83.37 ± 2.02	27.44 ± 1.15
Seesaw, 300 GeV	72.51 ± 1.07	53.67 ± 0.9	42.73 ± 0.79	18.44 ± 0.57	18.44 ± 0.57	2.23 ± 0.19

Table A.4: Event counts at various stages in the cutflow for the $Z + \mu$ flavour channel, off- Z validation region. Only statistical uncertainties on the Monte Carlo samples are shown.

A.3 ZZ Validation Region

Process	Preselection	Bachelor e	$ m_{\ell^+\ell^-} - m_Z < 10 \text{ GeV}$	RequireBachelorZ
$ZZ \rightarrow 4\ell$	890.6 ± 4.07	414.2 ± 2.76	247.1 ± 2.13	36.58 ± 0.82
$WZ \rightarrow \ell\ell\nu$	1753.91 ± 4.76	746.02 ± 3.09	622.44 ± 2.82	0.0 ± 0.0
$t\bar{t} + V$	39.92 ± 0.56	18.12 ± 0.38	13.01 ± 0.32	0.07 ± 0.02
$Z + \gamma$	342.09 ± 5.97	342.09 ± 5.97	93.16 ± 3.1	0.0 ± 0.0
Reducible	447.37 ± 15.28	158.13 ± 13.52	99.58 ± 8.17	0.6 ± 0.63
VVV*	11.15 ± 0.15	5.3 ± 0.11	1.88 ± 0.05	0.04 ± 0.01
Σ Backgrounds	3485.04 ± 17.57	1683.86 ± 15.35	1077.18 ± 9.43	37.29 ± 1.04
Data	3597	1805	1163	39
VLL, 160 GeV	21.75 ± 0.27	18.84 ± 0.25	16.09 ± 0.23	0.4 ± 0.04
VLL, 200 GeV	10.19 ± 0.12	8.66 ± 0.11	7.09 ± 0.1	0.16 ± 0.02
VLL, 250 GeV	4.27 ± 0.05	3.64 ± 0.04	2.94 ± 0.04	0.05 ± 0.01
Seesaw, 160 GeV	688.97 ± 10.41	535.95 ± 9.07	402.72 ± 7.55	9.53 ± 1.33
Seesaw, 200 GeV	322.6 ± 4.8	254.73 ± 4.22	180.03 ± 3.38	3.78 ± 0.56
Seesaw, 300 GeV	61.78 ± 1.27	47.67 ± 1.1	31.92 ± 0.85	0.3 ± 0.09

Table A.5: Event counts at various stages in the cutflow for the $Z + e$ flavour channel, two Z validation region. Only statistical uncertainties on the Monte Carlo samples are shown.

A Auxiliary Information for the Validation Regions

Process	Preselection	Bachelor μ	$ m_{\ell^+\ell^-} - m_Z < 10$ GeV	RequireBachelorZ
$ZZ \rightarrow 4\ell$	890.6 ± 4.07	476.4 ± 2.99	279.71 ± 2.3	63.31 ± 1.09
$WZ \rightarrow \ell\ell\nu$	1753.91 ± 4.76	1007.89 ± 3.62	855.8 ± 3.34	0.0 ± 0.0
$t\bar{t} + V$	39.92 ± 0.56	21.8 ± 0.41	16.38 ± 0.36	0.11 ± 0.03
$Z + \gamma$	342.09 ± 5.97	0.0 ± 0.0	0.0 ± 0.0	0.0 ± 0.0
Reducible	447.37 ± 15.28	289.23 ± 7.13	200.6 ± 5.79	-0.07 ± 0.03
VVV*	11.15 ± 0.15	5.85 ± 0.11	2.41 ± 0.06	0.06 ± 0.01
Σ Backgrounds	3485.04 ± 17.57	1801.18 ± 8.55	1354.89 ± 7.07	63.4 ± 1.09
Data	3597	1792	1414	74
VLL, 160 GeV	26.76 ± 0.29	22.36 ± 0.27	19.11 ± 0.25	0.8 ± 0.05
VLL, 200 GeV	12.58 ± 0.13	10.28 ± 0.12	8.51 ± 0.11	0.29 ± 0.02
VLL, 250 GeV	5.13 ± 0.05	4.2 ± 0.05	3.4 ± 0.04	0.07 ± 0.01
Seesaw, 160 GeV	934.08 ± 9.5	748.59 ± 8.4	516.55 ± 6.72	15.72 ± 1.29
Seesaw, 200 GeV	411.01 ± 4.22	323.95 ± 3.7	209.4 ± 2.85	3.95 ± 0.43
Seesaw, 300 GeV	72.57 ± 1.07	57.4 ± 0.94	35.36 ± 0.71	0.37 ± 0.08

Table A.6: Event counts at various stages in the cutflow for the $Z + \mu$ flavour channel, two Z validation region. Only statistical uncertainties on the Monte Carlo samples are shown.

A.3.1 WZ Validation Region

Process	Preselection	Bachelor e	$ m_{\ell^+\ell^-} - m_Z < 10$ GeV	MaxNLeptons	MaxNJets	MinETMiss	MaxETMiss	MinMTW	MaxMTW
$ZZ \rightarrow 4\ell$	890.6 ± 4.07	414.2 ± 2.76	247.1 ± 2.13	197.58 ± 1.91	80.7 ± 1.22	8.94 ± 0.4	8.66 ± 0.4	4.25 ± 0.28	3.25 ± 0.24
$WZ \rightarrow \ell\ell\nu$	1753.91 ± 4.76	746.02 ± 3.09	622.44 ± 2.82	622.36 ± 2.82	365.53 ± 2.16	205.18 ± 1.61	184.52 ± 1.53	160.95 ± 1.43	124.13 ± 1.26
$t\bar{t} + V$	39.92 ± 0.56	18.12 ± 0.38	13.01 ± 0.32	12.05 ± 0.31	0.08 ± 0.02	0.06 ± 0.02	0.04 ± 0.02	0.03 ± 0.02	0.01 ± 0.01
$Z + \gamma$	342.09 ± 5.97	342.09 ± 5.97	93.16 ± 3.1	93.16 ± 3.1	67.41 ± 2.65	4.67 ± 0.66	4.67 ± 0.66	2.46 ± 0.46	1.94 ± 0.41
Reducible	447.37 ± 15.28	158.13 ± 13.52	99.58 ± 8.17	98.88 ± 8.14	67.19 ± 6.89	9.35 ± 2.39	8.55 ± 2.32	5.25 ± 1.76	4.01 ± 1.66
VVV*	11.15 ± 0.15	5.3 ± 0.11	1.88 ± 0.05	1.49 ± 0.05	0.71 ± 0.04	0.55 ± 0.03	0.36 ± 0.03	0.31 ± 0.02	0.13 ± 0.02
Σ Backgrounds	3485.04 ± 17.57	1683.86 ± 15.35	1077.18 ± 9.43	1025.52 ± 9.36	581.62 ± 7.79	228.75 ± 2.98	206.81 ± 2.89	173.24 ± 2.33	133.47 ± 2.13
Data	3597	1805	1163	1104	605	241	226	189	143
VLL, 160 GeV	21.75 ± 0.27	18.84 ± 0.25	16.09 ± 0.23	11.81 ± 0.2	1.13 ± 0.06	0.97 ± 0.06	0.58 ± 0.04	0.5 ± 0.04	0.18 ± 0.03
VLL, 200 GeV	10.19 ± 0.12	8.66 ± 0.11	7.09 ± 0.1	4.97 ± 0.08	0.37 ± 0.02	0.33 ± 0.02	0.15 ± 0.01	0.14 ± 0.01	0.04 ± 0.01
VLL, 250 GeV	4.27 ± 0.05	3.64 ± 0.04	2.94 ± 0.04	1.93 ± 0.03	0.11 ± 0.01	0.1 ± 0.01	0.03 ± 0.0	0.03 ± 0.0	0.0 ± 0.0
Seesaw, 160 GeV	688.97 ± 10.41	535.95 ± 9.07	402.72 ± 7.55	290.2 ± 6.06	36.83 ± 1.88	30.03 ± 1.69	18.15 ± 1.33	15.74 ± 1.25	5.05 ± 0.71
Seesaw, 200 GeV	322.6 ± 4.8	254.73 ± 4.22	180.03 ± 3.38	124.74 ± 2.61	13.48 ± 0.73	11.89 ± 0.68	5.74 ± 0.49	4.96 ± 0.46	1.29 ± 0.22
Seesaw, 300 GeV	61.78 ± 1.27	47.67 ± 1.1	31.92 ± 0.85	21.34 ± 0.64	2.15 ± 0.17	2.09 ± 0.17	0.44 ± 0.07	0.39 ± 0.06	0.06 ± 0.02

Table A.7: Event counts at various stages in the cutflow for the $Z + e$ flavour channel, WZ validation region. Only statistical uncertainties on the Monte Carlo samples are shown.

Process	Preselection	Bachelor μ	$ m_{\ell\ell} - m_Z < 10$ GeV	MaxNLeptons	MaxNJets	MinETMiss	MaxETMiss	MinMTW	MaxMTW
$ZZ \rightarrow 4\ell$	890.6 ± 4.07	476.4 ± 2.99	279.71 ± 2.3	191.26 ± 1.9	128.25 ± 1.55	24.44 ± 0.68	23.02 ± 0.66	16.73 ± 0.56	11.63 ± 0.47
$WZ \rightarrow \ell\ell\nu$	1753.91 ± 4.76	1007.89 ± 3.62	855.8 ± 3.34	855.78 ± 3.34	512.21 ± 2.59	296.62 ± 1.96	267.32 ± 1.86	236.82 ± 1.75	176.19 ± 1.52
$t\bar{t} + V$	39.92 ± 0.56	21.8 ± 0.41	16.38 ± 0.36	15.15 ± 0.34	0.07 ± 0.02	0.07 ± 0.02	0.03 ± 0.02	0.03 ± 0.01	0.0 ± 0.0
$Z + \gamma$	342.09 ± 5.97	0.0 ± 0.0	0.0 ± 0.0	0.0 ± 0.0	0.0 ± 0.0	0.0 ± 0.0	0.0 ± 0.0	0.0 ± 0.0	0.0 ± 0.0
Reducible	447.37 ± 15.28	289.23 ± 7.13	200.6 ± 5.79	199.19 ± 5.73	125.43 ± 4.85	21.25 ± 2.13	21.2 ± 2.11	6.08 ± 1.34	4.91 ± 1.17
VVV*	11.15 ± 0.15	5.85 ± 0.11	2.41 ± 0.06	1.85 ± 0.05	0.96 ± 0.04	0.79 ± 0.04	0.57 ± 0.03	0.48 ± 0.03	0.23 ± 0.02
Σ Backgrounds	3485.04 ± 17.57	1801.18 ± 8.55	1354.89 ± 7.07	1263.23 ± 6.9	766.93 ± 5.71	343.17 ± 2.98	312.14 ± 2.89	260.14 ± 2.28	192.96 ± 1.97
Data	3597	1792	1414	1305	793	363	331	289	223
VLL, 160 GeV	26.76 ± 0.29	22.36 ± 0.27	19.11 ± 0.25	12.44 ± 0.2	1.79 ± 0.08	1.4 ± 0.07	0.8 ± 0.05	0.67 ± 0.05	0.25 ± 0.03
VLL, 200 GeV	12.58 ± 0.13	10.28 ± 0.12	8.51 ± 0.11	5.19 ± 0.08	0.56 ± 0.03	0.51 ± 0.03	0.23 ± 0.02	0.19 ± 0.02	0.06 ± 0.01
VLL, 250 GeV	5.13 ± 0.05	4.2 ± 0.05	3.4 ± 0.04	1.97 ± 0.03	0.17 ± 0.01	0.16 ± 0.01	0.05 ± 0.0	0.04 ± 0.0	0.01 ± 0.0
Seesaw, 160 GeV	934.08 ± 9.5	748.59 ± 8.4	516.55 ± 6.72	349.63 ± 5.24	64.79 ± 2.21	53.33 ± 1.98	34.32 ± 1.62	29.42 ± 1.51	10.83 ± 0.91
Seesaw, 200 GeV	411.01 ± 4.22	323.95 ± 3.7	209.4 ± 2.85	137.71 ± 2.16	20.15 ± 0.79	17.45 ± 0.73	8.15 ± 0.52	7.32 ± 0.49	2.09 ± 0.26
Seesaw, 300 GeV	72.57 ± 1.07	57.4 ± 0.94	35.36 ± 0.71	22.13 ± 0.51	2.3 ± 0.15	2.23 ± 0.15	0.45 ± 0.06	0.4 ± 0.06	0.08 ± 0.03

Table A.8: Event counts at various stages in the cutflow for the $Z + \mu$ flavour channel, WZ validation region. Only statistical uncertainties on the Monte Carlo samples are shown.

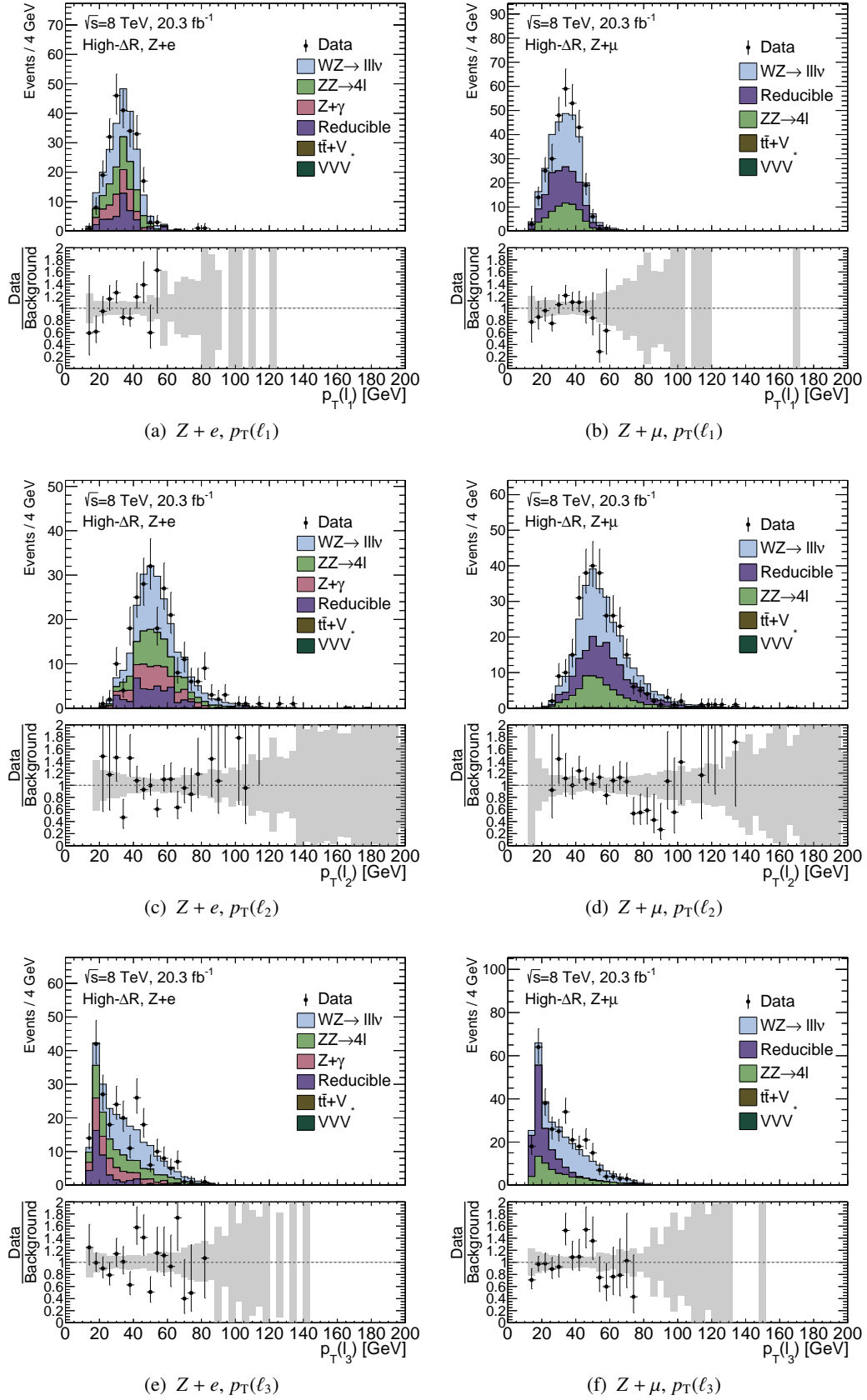


Figure A.1: High ΔR validation region: p_T of leading lepton (top), p_T of second leading lepton (middle), p_T of third lepton. For $Z + e$ final states (left) and $Z + \mu$ final states (right).

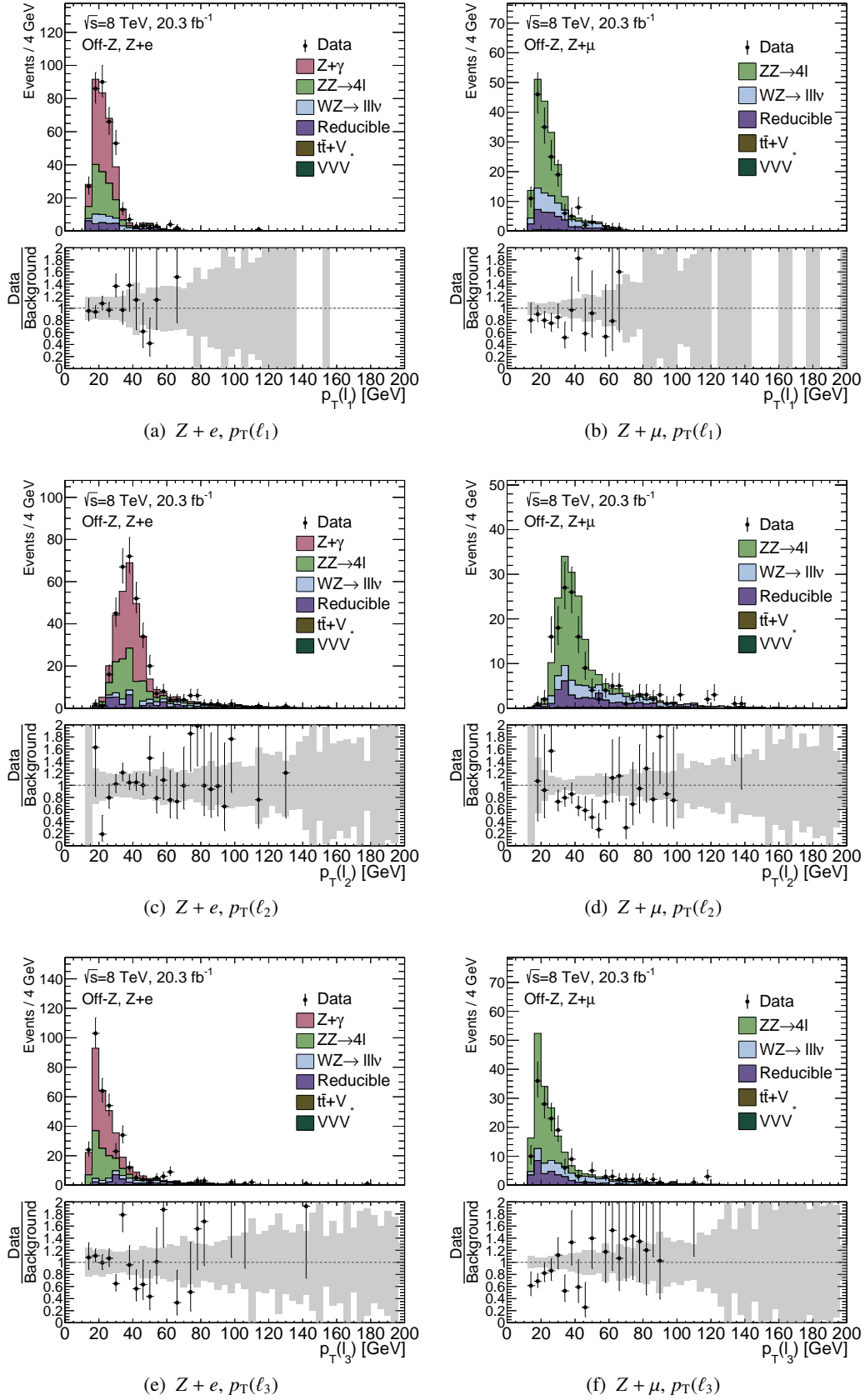


Figure A.2: Off-Z validation region: p_T of leading lepton (top), p_T of second leading lepton (middle), p_T of third lepton. For $Z + e$ final states (left) and $Z + \mu$ final states (right).

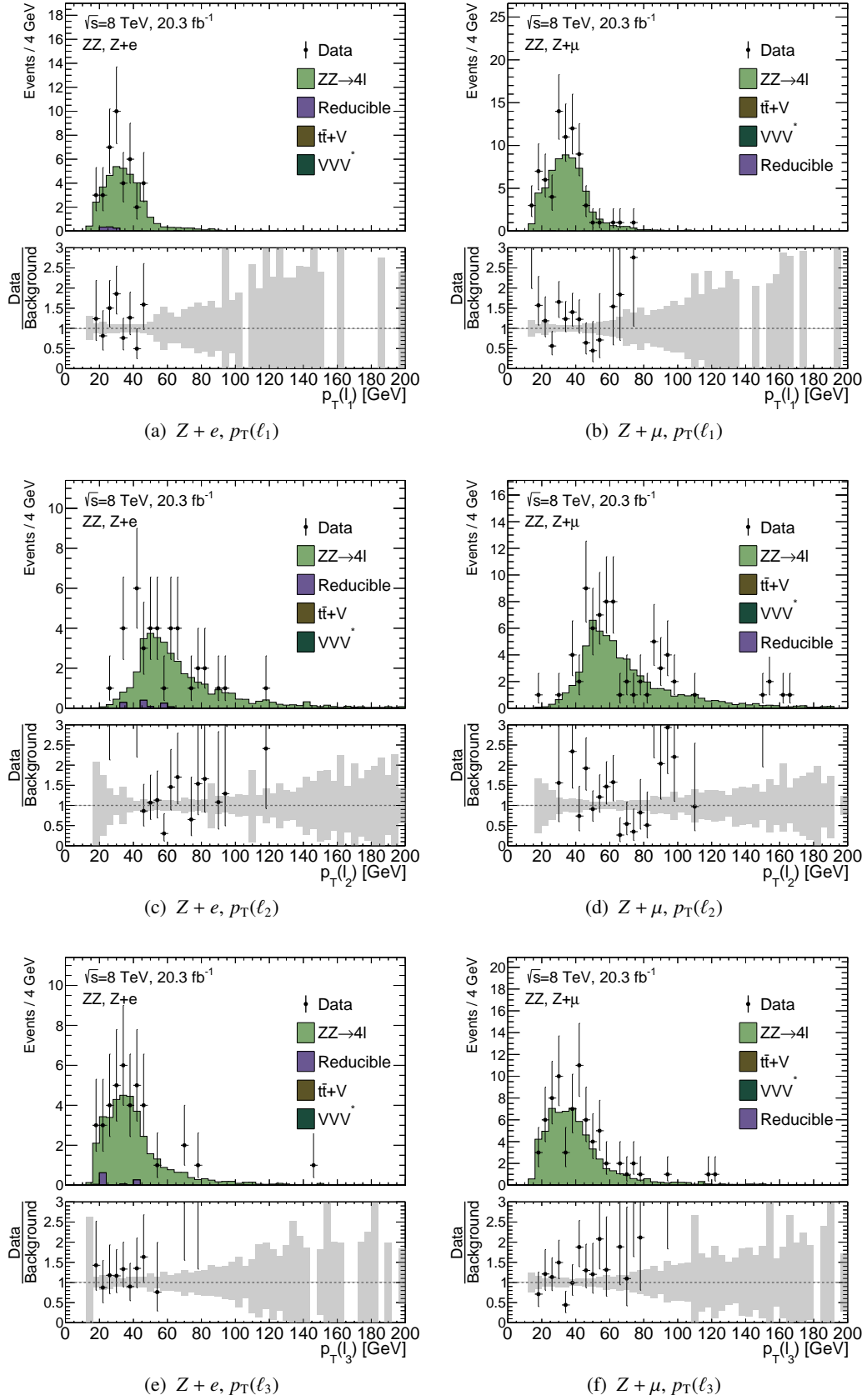


Figure A.3: Two Z validation region: p_T of leading lepton (top), p_T of second leading lepton (middle), p_T of third lepton. For $Z + e$ final states (left) and $Z + \mu$ final states (right).

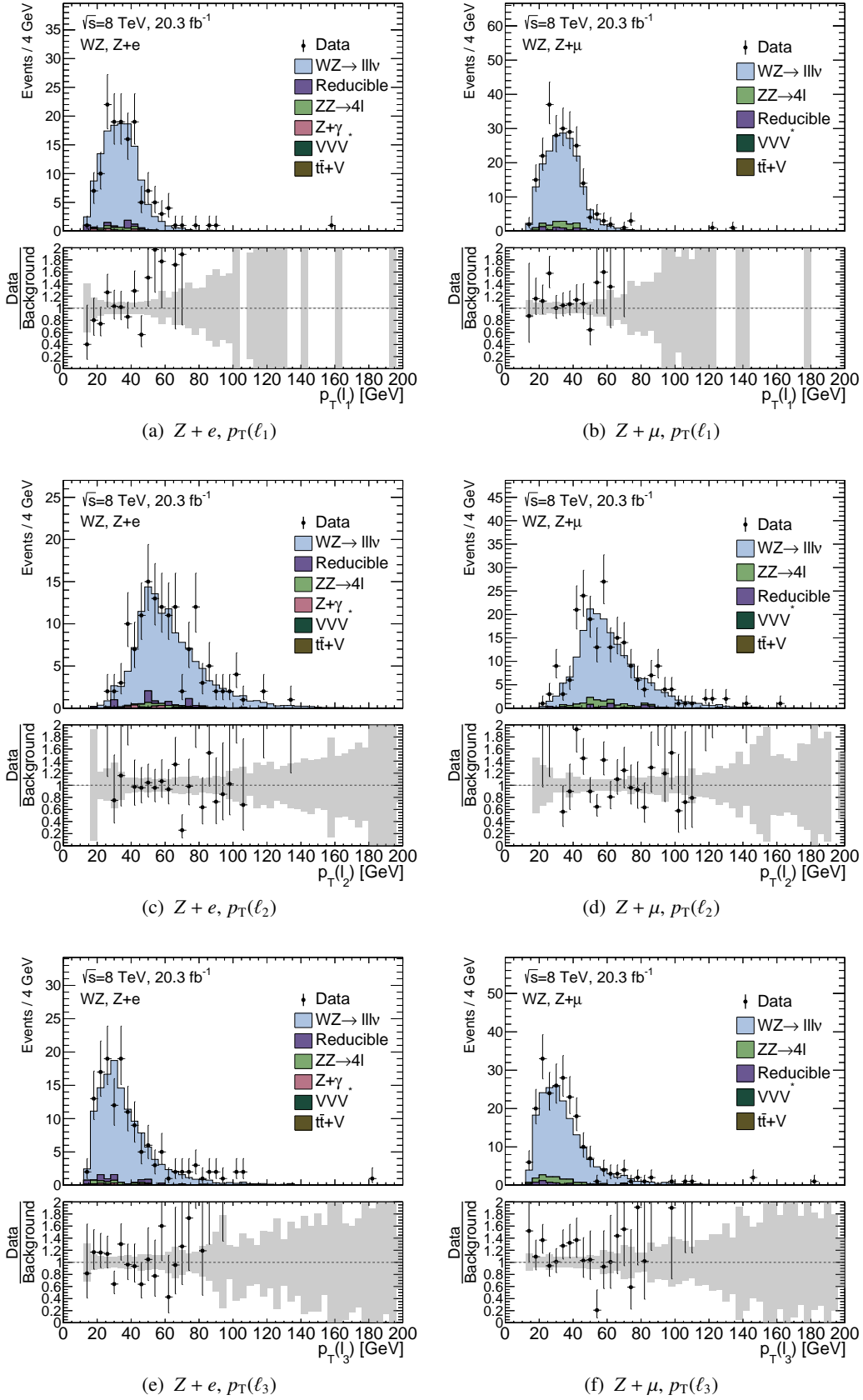


Figure A.4: WZ validation region: p_T of leading lepton (top), p_T of second leading lepton (middle), p_T of third lepton. For $Z + e$ final states (left) and $Z + \mu$ final states (right).

Auxiliary Information for the Signal Region

B Auxiliary Information for the Signal Region

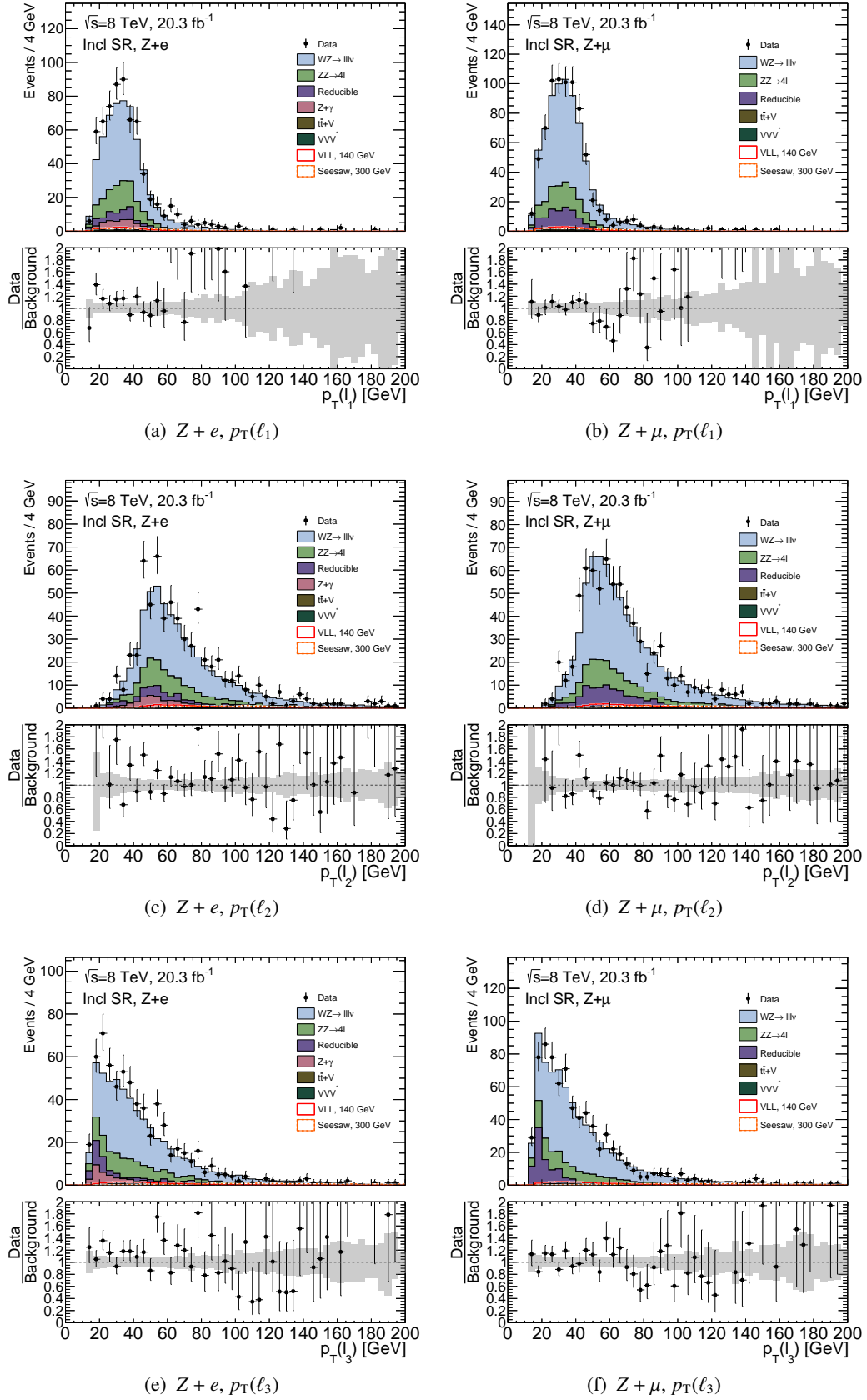


Figure B.1: Inclusive signal region: p_T of leading lepton (top), p_T of second leading lepton (middle), p_T of third lepton. For $Z + e$ final states (left) and $Z + \mu$ final states (right).

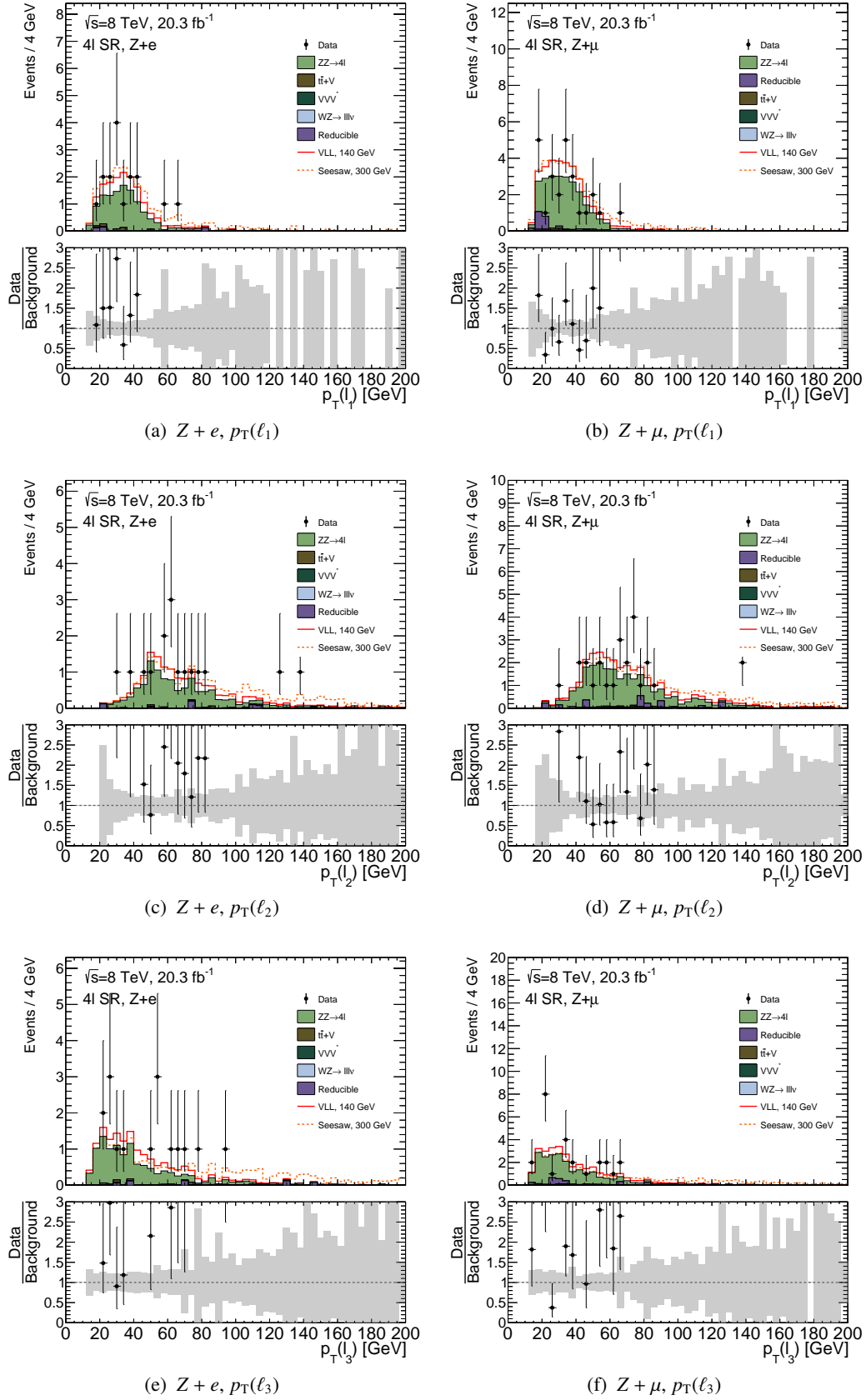


Figure B.2: 4l category: p_T of leading lepton (top), p_T of second leading lepton (middle), p_T of third lepton. For $Z + e$ final states (left) and $Z + \mu$ final states (right).

B Auxiliary Information for the Signal Region

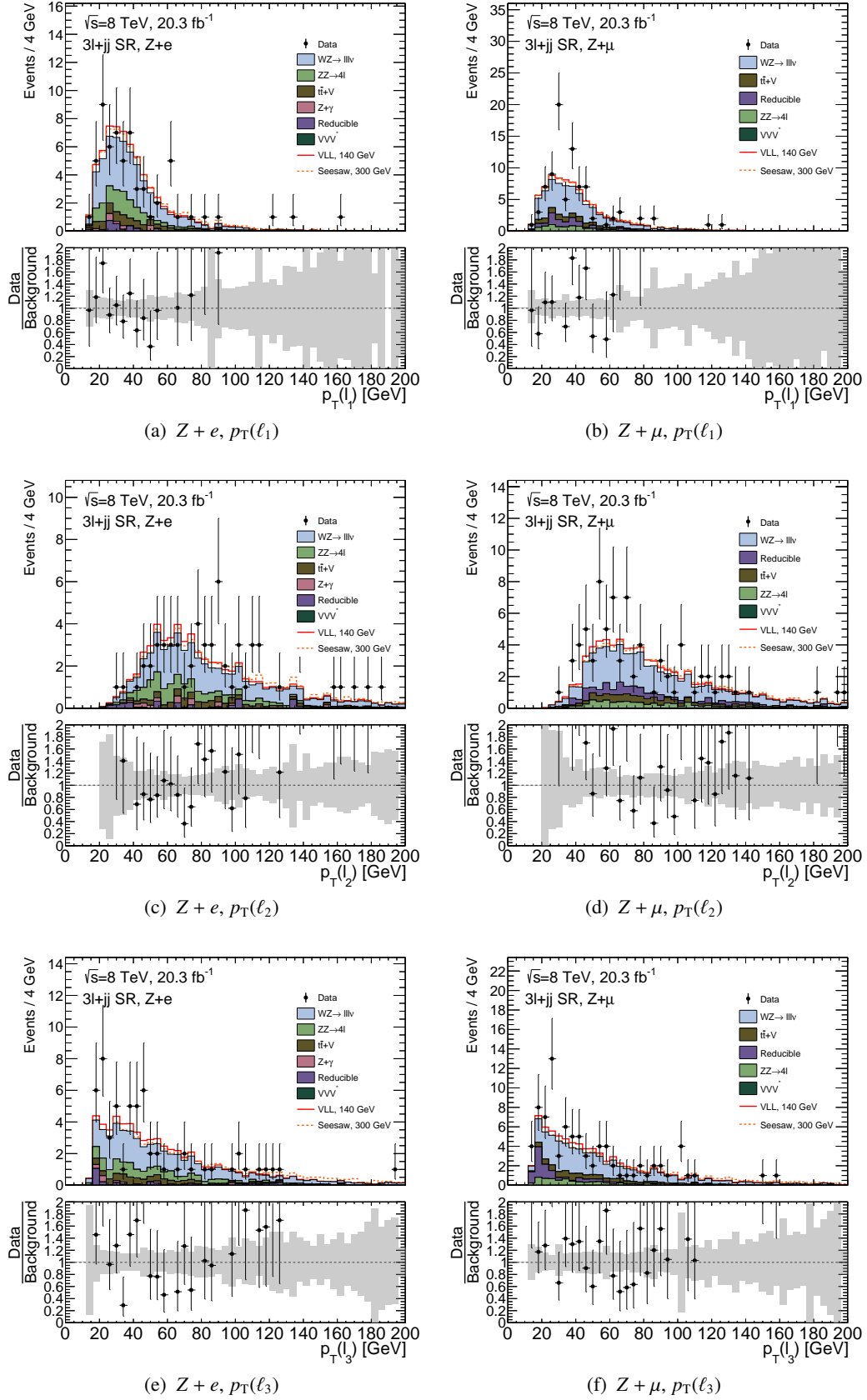


Figure B.3: $3l+jj$ category: p_T of leading lepton (top), p_T of second leading lepton (middle), p_T of third lepton. For $Z + e$ final states (left) and $Z + \mu$ final states (right).

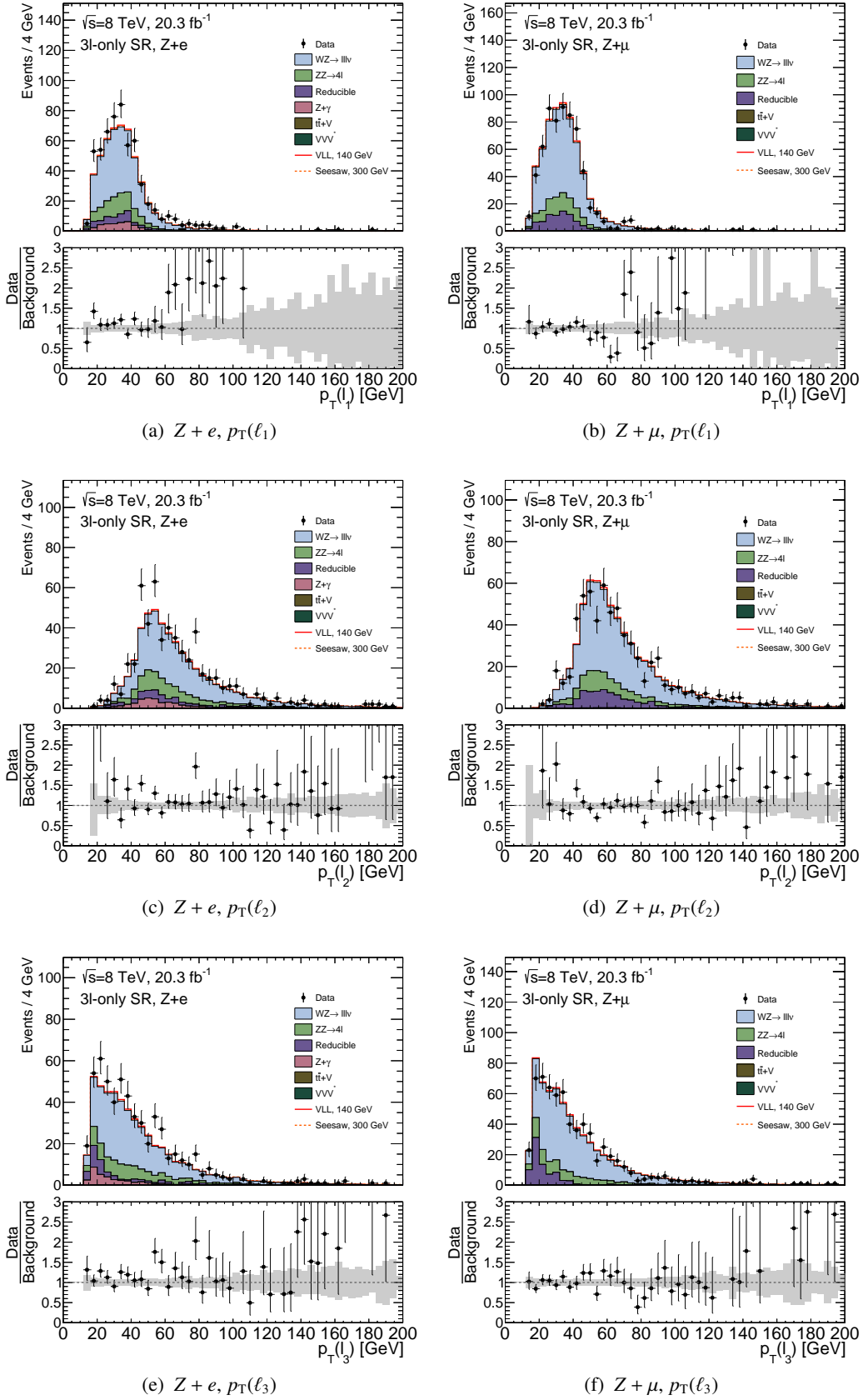


Figure B.4: 3ℓ -only category: p_T of leading lepton (top), p_T of second leading lepton (middle), p_T of third lepton. For $Z + e$ final states (left) and $Z + \mu$ final states (right).

Appendix Interpretation

C.1 Nuisance Parameters

Description of the various nuisance parameters used in the unbinned fit.

Lumi Luminosity uncertainty, a value of the nuisance parameter of 1 corresponds to the nominal luminosity measurement. The luminosity uncertainty is 2.8%.

XS_WZ Theoretical cross-section uncertainty on the production of WZ events.

XS_ZZ Theoretical cross-section uncertainty on the production of ZZ events.

XS_llgamma Uncertainty on the estimate of the production of $ll\gamma$ events.

XS_Zj Uncertainty on the reducible background estimate, calculated from the fake-factor estimate.

XS_VVV Theoretical cross-section uncertainty on the production of VVV events.

Shape_SigVoigt Uncertainty associated to the fit parameters of the Voigtian part of the signal

Shape_SigLandau Uncertainty associated to the fit parameters of the Landau part of the signal

ShapeZmu_WZ Uncertainty associated to the Bukin fit parameters of the WZ parametrization in the 3ℓ -only and Four Lepton region with a bachelor muon.

ShapeZmu_ZZ Uncertainty associated to the Bukin fit parameters of the ZZ parametrization in the 3ℓ -only and Four Lepton region with a bachelor muon.

ShapeZmu_WZ_TwoJet Uncertainty associated to the Bukin fit parameters of the WZ parametrization in the Two Jet region with a bachelor muon.

ShapeZmu_ZZ_TwoJet Uncertainty associated to the Bukin fit parameters of the ZZ parametrization in the Two Jet region with a bachelor muon.

ShapeZe_WZrho Uncertainty associated to the Bukin fit parameter ρ of the WZ parametrization in the 3ℓ -only and Four Lepton region with a bachelor electron.

ShapeZe_WZxp Uncertainty associated to the Bukin fit parameter ξ_p of the WZ parametrization in the 3ℓ -only and Four Lepton region with a bachelor electron.

ShapeZe_ZZ Uncertainty associated to the Bukin fit parameters of the ZZ parametrization in the 3ℓ -only and Four Lepton region with a bachelor electron.

ShapeZe_WZ_TwoJet Uncertainty associated to the Bukin fit parameters of the WZ parametrization in the Two Jet region with a bachelor electron.

ShapeZe_ZZ_TwoJet Uncertainty associated to the Bukin fit parameters of the ZZ parametrization in the Two Jet region with a bachelor electron.

C.2 Signal Fit Model

The Δm distributions at each simulated signal mass point are fitted with a Voigtian plus Landau function. The resulting fits for various mass points of the vector-like leptons model are shown in Fig. C.1 for the inclusive $Z + e$ final state and in Fig. C.2 for the inclusive $Z + \mu$ final state. The corresponding distributions of the fit parameters are shown in Fig. C.3 for $Z + e$ inclusive final states and in Fig. C.3 for $Z + \mu$ inclusive final states.

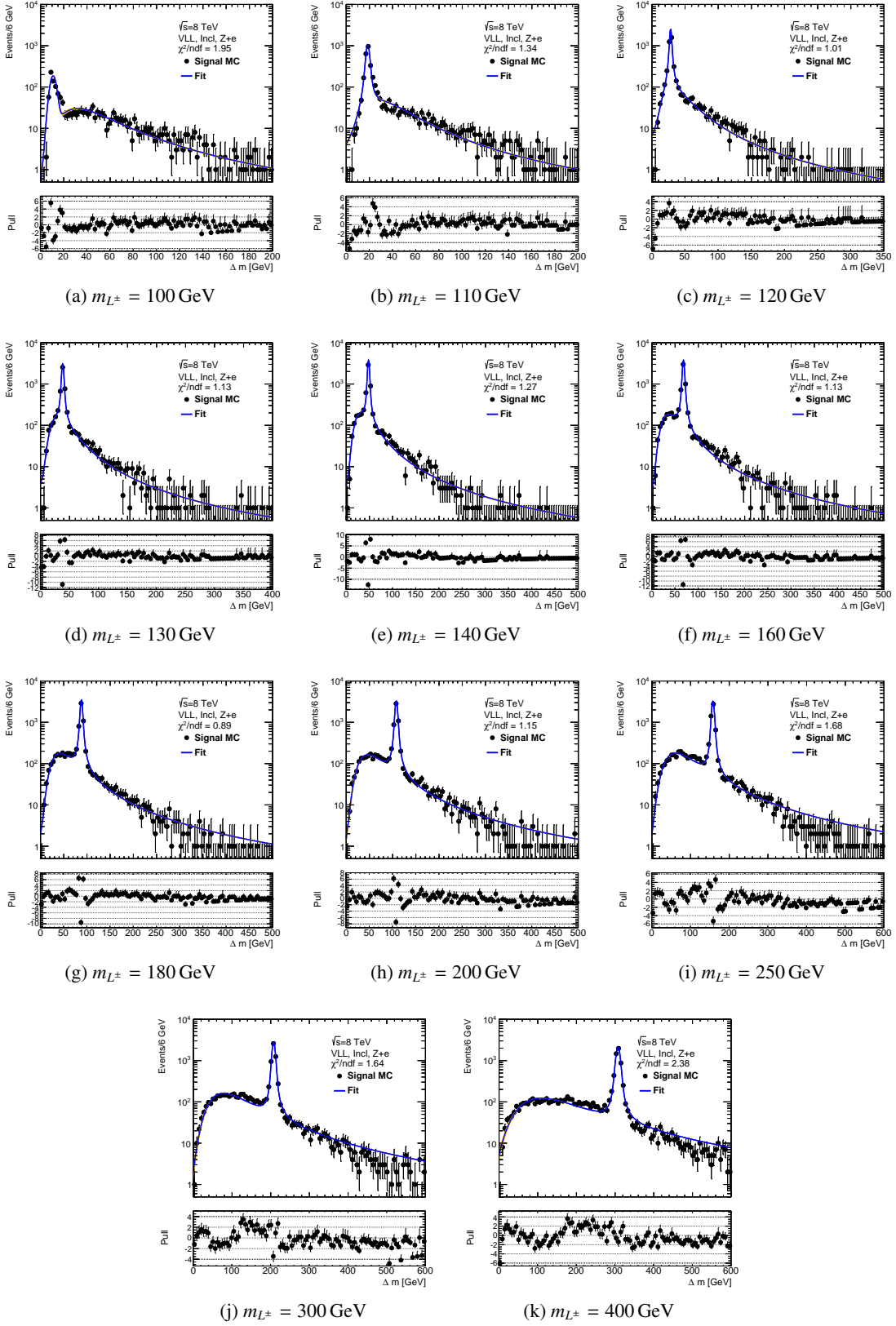


Figure C.1: Fit of a Landau and a Voigtian to the $Z + e$ distribution of the Δm of the VLL model at the various mass points.

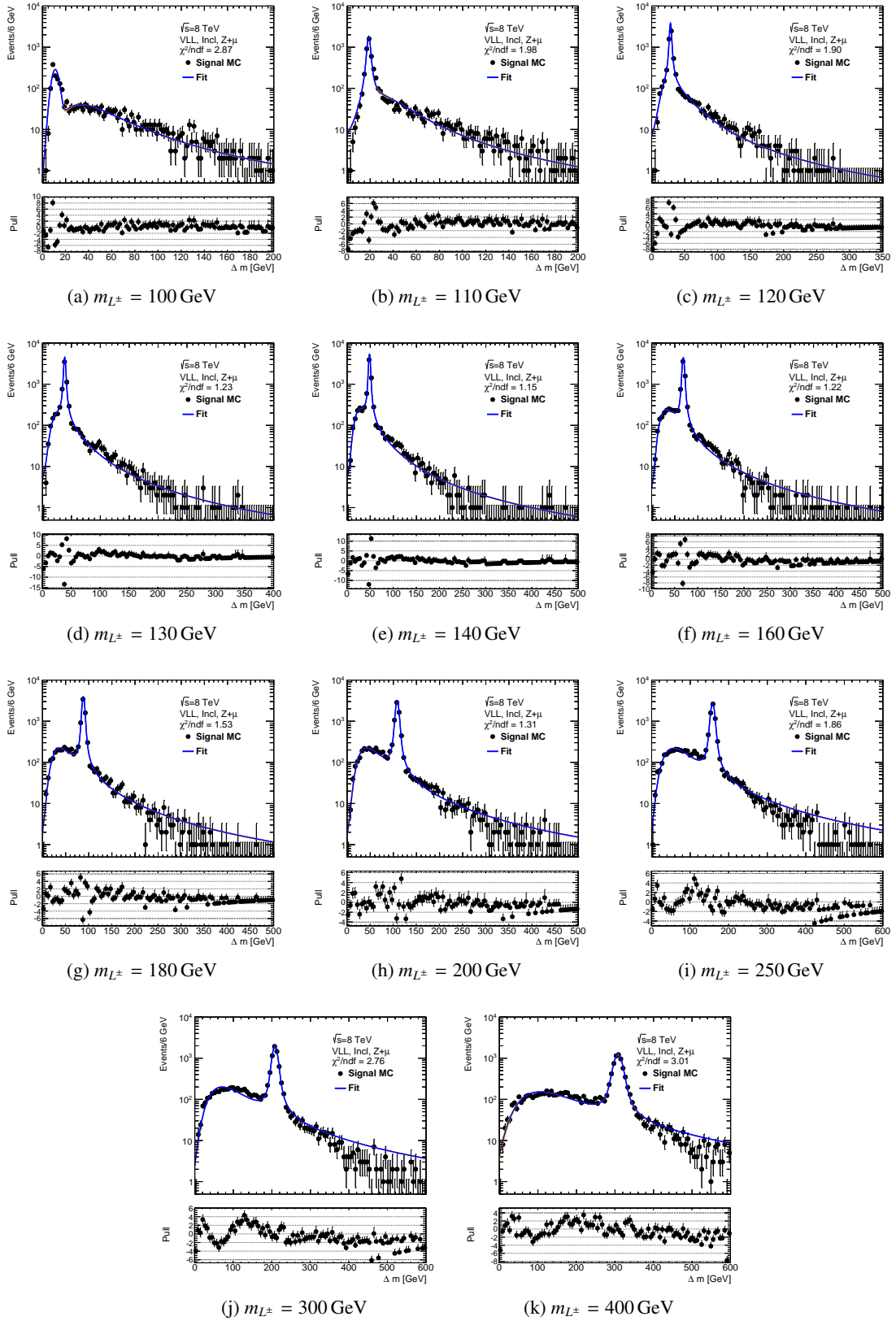


Figure C.2: Fit of a Landau and a Voigtian to the $Z + \mu$ distribution of the Δm of the VLL model at the various mass points.

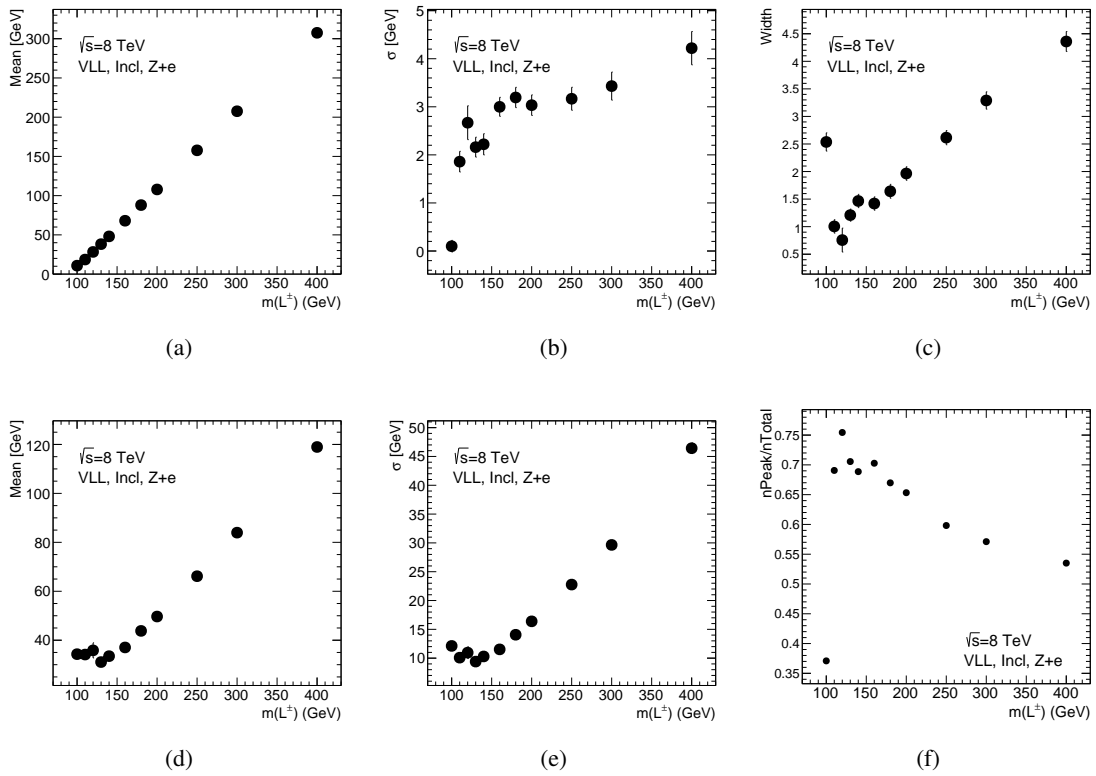


Figure C.3: Fit parameters of the VLL signal model in the Z+e final state. Used in the linear interpolation between the points.

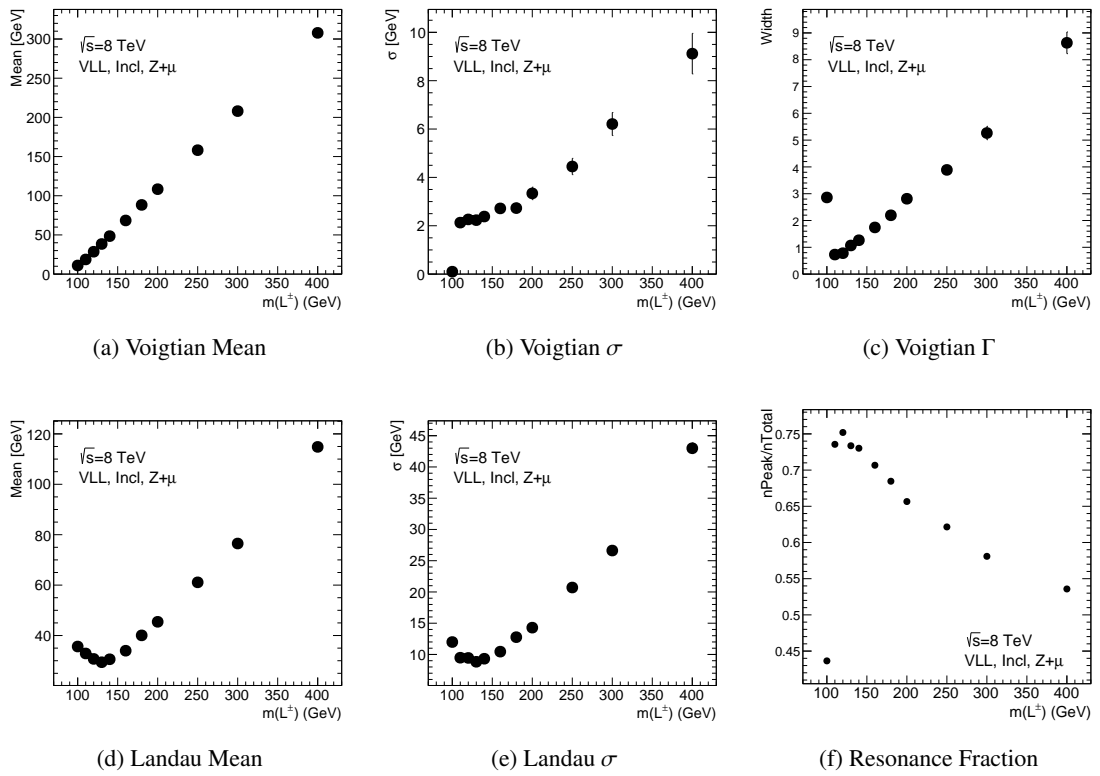


Figure C.4: Fit parameters of the VLL signal model in the $Z + \mu$ final state. Used in the linear interpolation between the points.

Bibliography

- [1] ATLAS Collaboration, “Observation of a new particle in the search for the Standard Model Higgs boson with the ATLAS detector at the LHC”, *Phys. Lett. B* 716 (2012) 1–29, doi: 10.1016/j.physletb.2012.08.020, arXiv: 1207.7214 [hep-ex].
- [2] CMS Collaboration, “Observation of a new boson at a mass of 125 GeV with the CMS experiment at the LHC”, *Phys. Lett. B* 716 (2012) 30–61, doi: 10.1016/j.physletb.2012.08.021, arXiv: 1207.7235 [hep-ex].
- [3] J. J. Aubert et al., “Experimental Observation of a Heavy Particle J ”, *Phys. Rev. Lett.* 33 (23 Dec. 1974) 1404–1406, doi: 10.1103/PhysRevLett.33.1404, URL: <http://link.aps.org/doi/10.1103/PhysRevLett.33.1404>.
- [4] J.-E. Augustin et al., “Discovery of a Narrow Resonance in e^+e^- Annihilation”, *Phys. Rev. Lett.* 33 (23 Dec. 1974) 1406–1408, doi: 10.1103/PhysRevLett.33.1406, URL: <http://link.aps.org/doi/10.1103/PhysRevLett.33.1406>.
- [5] S. W. Herb et al., “Observation of a Dimuon Resonance at 9.5 GeV in 400-GeV Proton-Nucleus Collisions”, *Phys. Rev. Lett.* 39 (1977) 252, doi: 10.1103/PhysRevLett.39.252.
- [6] UA1 Collaboration, “Experimental Observation of Lepton Pairs of Invariant Mass Around 95-GeV/c**2 at the CERN SPS Collider”, *Phys. Lett. B* 126 (1983) 398–410, doi: 10.1016/0370-2693(83)90188-0.
- [7] P. Bagnaia et al., “Evidence for $Z^0 \rightarrow e^+e^-$ at the CERN anti-p p Collider”, *Phys. Lett. B* 129 (1983) 130–140, doi: 10.1016/0370-2693(83)90744-X.
- [8] CMS Collaboration, “Search for physics beyond the standard model in dilepton mass spectra in proton-proton collisions at $\sqrt{s} = 8$ TeV” (2014), arXiv: 1412.6302 [hep-ex].
- [9] ATLAS Collaboration, “Search for high-mass dilepton resonances in pp collisions at $\sqrt{s} = 8$ TeV with the ATLAS detector”, *Phys.Rev. D* 90.5 (2014) 052005, doi: 10.1103/PhysRevD.90.052005, arXiv: 1405.4123 [hep-ex].
- [10] R. Foot et al., “Seesaw Neutrino Masses Induced by a Triplet of Leptons”, *Z.Phys. C* 44 (1989) 441, doi: 10.1007/BF01415558.
- [11] A. Falkowski, D. M. Straub and A. Vicente, “Vector-like leptons: Higgs decays and collider phenomenology”, *JHEP* 1405 (2014) 092, doi: 10.1007/JHEP05(2014)092, arXiv: 1312.5329 [hep-ph].
- [12] K. Fujikawa, “A Vector - like extension of the standard model”, *Prog.Theor.Phys.* 92 (1994) 1149–1160, doi: 10.1143/PTP.92.1149, arXiv: hep-ph/9411258 [hep-ph].

- [13] B. Keren-Zur et al., “On Partial Compositeness and the CP asymmetry in charm decays”, *Nucl.Phys.* B867 (2013) 394–428, doi: 10.1016/j.nuclphysb.2012.10.012, arXiv: 1205.5803 [hep-ph].
- [14] M. Redi, “Leptons in Composite MFV”, *JHEP* 1309 (2013) 060, doi: 10.1007/JHEP09(2013)060, arXiv: 1306.1525 [hep-ph].
- [15] R. Contino et al., “Warped/composite phenomenology simplified”, *JHEP* 0705 (2007) 074, doi: 10.1088/1126-6708/2007/05/074, arXiv: hep-ph/0612180 [hep-ph].
- [16] C. Biggio and F. Bonnet, “Implementation of the Type III Seesaw Model in FeynRules/MadGraph and Prospects for Discovery with Early LHC Data”, *Eur.Phys.J.* C72 (2012) 1899, doi: 10.1140/epjc/s10052-012-1899-z, arXiv: 1107.3463 [hep-ph].
- [17] M. Kobayashi and T. Maskawa, “CP Violation in the Renormalizable Theory of Weak Interaction”, *Prog.Theor.Phys.* 49 (1973) 652–657, doi: 10.1143/PTP.49.652.
- [18] D0 Collaboration, “Search for high mass top quark production in $p\bar{p}$ collisions at $\sqrt{s} = 1.8$ TeV”, *Phys.Rev.Lett.* 74 (1995) 2422–2426, doi: 10.1103/PhysRevLett.74.2422, arXiv: hep-ex/9411001 [hep-ex].
- [19] CDF Collaboration, “Observation of top quark production in $\bar{p}p$ collisions”, *Phys.Rev.Lett.* 74 (1995) 2626–2631, doi: 10.1103/PhysRevLett.74.2626, arXiv: hep-ex/9503002 [hep-ex].
- [20] UA1 Collaboration, “Experimental Observation of Isolated Large Transverse Energy Electrons with Associated Missing Energy at $s^{*(1/2)} = 540$ -GeV”, *Phys.Lett.* B122 (1983) 103–116, doi: 10.1016/0370-2693(83)91177-2.
- [21] UA2 Collaboration, “Observation of Single Isolated Electrons of High Transverse Momentum in Events with Missing Transverse Energy at the CERN anti-p p Collider”, *Phys. Lett.* B122 (1983) 476–485, doi: 10.1016/0370-2693(83)91605-2.
- [22] DONUT Collaboration, “Observation of tau neutrino interactions”, *Phys. Lett.* B504 (2001) 218–224, doi: 10.1016/S0370-2693(01)00307-0, arXiv: hep-ex/0012035 [hep-ex].
- [23] D. Griffiths, *Introduction to Elementary Particles*, Wiley, 2008.
- [24] F. Halzen and A. D. Martin, *Quarks and Leptons: An Introductory Course in Modern Particle Physics*, Wiley, 1984.
- [25] M. E. Peskin and D. V. Schroeder, *An Introduction to Quantum Field Theory*, Westview Press, 1995.
- [26] S. Dittmaier and M. Schumacher, “The Higgs Boson in the Standard Model - From LEP to LHC: Expectations, Searches, and Discovery of a Candidate” (2012), arXiv: 1211.4828 [hep-ph].
- [27] K. Agashe et al., “Review of Particle Physics (RPP)”, *Chin.Phys.* C38 (2014) 090001.
- [28] B. Cleveland et al., “Measurement of the solar electron neutrino flux with the Homestake chlorine detector”, *Astrophys.J.* 496 (1998) 505–526, doi: 10.1086/305343.
- [29] KamLAND Collaboration, “First results from KamLAND: Evidence for reactor anti-neutrino disappearance”, *Phys.Rev.Lett.* 90 (2003) 021802, doi: 10.1103/PhysRevLett.90.021802, arXiv: hep-ex/0212021 [hep-ex].

- [30] GNO Collaboration, “Complete results for five years of GNO solar neutrino observations”, *Phys.Lett.* B616 (2005) 174–190, doi: 10.1016/j.physletb.2005.04.068, arXiv: hep-ex/0504037 [hep-ex].
- [31] Super-Kamiokande Collaboration, “Evidence for oscillation of atmospheric neutrinos”, *Phys.Rev.Lett.* 81 (1998) 1562–1567, doi: 10.1103/PhysRevLett.81.1562, arXiv: hep-ex/9807003 [hep-ex].
- [32] M. Y. Han and Y. Nambu, “Three-Triplet Model with Double SU(3) Symmetry”, *Phys. Rev.* 139 (4B Aug. 1965) B1006–B1010, doi: 10.1103/PhysRev.139.B1006, URL: <http://link.aps.org/doi/10.1103/PhysRev.139.B1006>.
- [33] W. A. Bardeen, H. Fritzsch and M. Gell-Mann, “Light cone current algebra, π^0 decay, and e^+e^- annihilation”, *Topical Meeting on the Outlook for Broken Conformal Symmetry in Elementary Particle Physics Frascati, Italy, May 4-5, 1972*, 1972, arXiv: hep-ph/0211388 [hep-ph], URL: http://tuvalu.santafe.edu/~mgm/Site/Publications_files/MGM%2079.pdf.
- [34] D. J. Gross and F. Wilczek, “Ultraviolet Behavior of Nonabelian Gauge Theories”, *Phys.Rev.Lett.* 30 (1973) 1343–1346, doi: 10.1103/PhysRevLett.30.1343.
- [35] H. D. Politzer, “Reliable Perturbative Results for Strong Interactions?”, *Phys.Rev.Lett.* 30 (1973) 1346–1349, doi: 10.1103/PhysRevLett.30.1346.
- [36] TASSO Collaboration, “Evidence for Planar Events in e^+e^- Annihilation at High-Energies”, *Phys. Lett.* B86 (1979) 243, doi: 10.1016/0370-2693(79)90830-X.
- [37] F. D. Aaron et al., “Combined Measurement and QCD Analysis of the Inclusive e^+e^-p Scattering Cross Sections at HERA”, *JHEP* 01 (2010) 109, doi: 10.1007/JHEP01(2010)109, arXiv: 0911.0884 [hep-ex].
- [38] N. Cabibbo, “Unitary Symmetry and Leptonic Decays”, *Phys. Rev. Lett.* 10 (1963) 531–533, doi: 10.1103/PhysRevLett.10.531.
- [39] C. Wu et al., “Experimental Test of Parity Conservation in Beta Decay”, *Phys. Rev.* 105 (1957) 1413–1414, doi: 10.1103/PhysRev.105.1413.
- [40] P. Achard et al., “Measurement of the running of the electromagnetic coupling at large momentum-transfer at LEP”, *Phys. Lett.* B623 (2005) 26–36, doi: 10.1016/j.physletb.2005.07.052, arXiv: hep-ex/0507078 [hep-ex].
- [41] E. Fermi, “An attempt of a theory of beta radiation. 1.”, *Z. Phys.* 88 (1934) 161–177, doi: 10.1007/BF01351864.
- [42] T. Lee and C.-N. Yang, “Question of Parity Conservation in Weak Interactions”, *Phys.Rev.* 104 (1956) 254–258, doi: 10.1103/PhysRev.104.254.
- [43] S. L. Glashow, “Partial-symmetries of weak interactions”, *Nucl. Phys.* 22 (1961) 579–588, doi: DOI: 10.1016/0029-5582(61)90469-2.
- [44] S. Weinberg, “Implications of Dynamical Symmetry Breaking: An Addendum”, *Phys. Rev. D* 19 (1979) 1277–1280, doi: 10.1103/PhysRevD.19.1277.
- [45] A. Salam, in *Elementary Particle Theory*, p. 367, ed. by N. Svartholm, Stockholm: Almqvist and Wiksell, 1968.
- [46] F. Englert and R. Brout, “Broken Symmetry and the Mass of Gauge Vector Mesons”, *Phys.Rev.Lett.* 13 (1964) 321–323, doi: 10.1103/PhysRevLett.13.321.

- [47] P. W. Higgs, “Broken Symmetries, massless particles and gauge fields”, *Phys.Lett.* 12 (1964) 132–133, doi: 10.1016/0031-9163(64)91136-9.
- [48] P. W. Higgs, “Broken Symmetries and the Masses of Gauge Bosons”, *Phys.Rev.Lett.* 13 (1964) 508–509, doi: 10.1103/PhysRevLett.13.508.
- [49] G. Guralnik, C. Hagen and T. Kibble, “Global Conservation Laws and Massless Particles”, *Phys.Rev.Lett.* 13 (1964) 585–587, doi: 10.1103/PhysRevLett.13.585.
- [50] J. H. Schwarz and N. Seiberg, “String theory, supersymmetry, unification, and all that”, *Rev. Mod. Phys.* 71 (1999) S112–S120, doi: 10.1103/RevModPhys.71.S112, arXiv: hep-th/9803179 [hep-th].
- [51] A. Ashtekar, “An Introduction to Loop Quantum Gravity Through Cosmology”, *Nuovo Cim.* B122 (2007) 135–155, doi: 10.1393/ncb/i2007-10351-5, arXiv: gr-qc/0702030 [gr-qc].
- [52] P. A. R. Ade et al., “Planck Intermediate Results. XI: The gas content of dark matter halos: the Sunyaev-Zeldovich-stellar mass relation for locally brightest galaxies”, *Astron. Astrophys.* 557 (2013) A52, doi: 10.1051/0004-6361/201220941, arXiv: 1212.4131 [astro-ph.CO].
- [53] A. G. Cohen, A. De Rujula and S. L. Glashow, “A Matter - antimatter universe?”, *Astrophys. J.* 495 (1998) 539–549, doi: 10.1086/305328, arXiv: astro-ph/9707087 [astro-ph].
- [54] A. D. Sakharov, “Violation of CP invariance, C asymmetry, and baryon asymmetry of the universe”, *Pis'ma Zh. Eksp. Teor. Fiz.* 5 (1967) 32–35, doi: 10.1070/PU1991v034n05ABEH002497.
- [55] A. Pilaftsis, “The Little Review on Leptogenesis”, *J. Phys. Conf. Ser.* 171 (2009) 012017, doi: 10.1088/1742-6596/171/1/012017, arXiv: 0904.1182 [hep-ph].
- [56] B. Pontecorvo, “Mesonium and anti-mesonium”, *Sov. Phys. JETP* 6 (1957), [*Zh. Eksp. Teor. Fiz.* 33,549(1957)] 429.
- [57] W. Hampel et al., “GALLEX solar neutrino observations: Results for GALLEX IV”, *Phys. Lett.* B447 (1999) 127–133, doi: 10.1016/S0370-2693(98)01579-2.
- [58] J. N. Abdurashitov et al., “Measurement of the solar neutrino capture rate with gallium metal. III: Results for the 2002–2007 data-taking period”, *Phys. Rev.* C80 (2009) 015807, doi: 10.1103/PhysRevC.80.015807, arXiv: 0901.2200 [nucl-ex].
- [59] Q. R. Ahmad et al., “Direct evidence for neutrino flavor transformation from neutral current interactions in the Sudbury Neutrino Observatory”, *Phys. Rev. Lett.* 89 (2002) 011301, doi: 10.1103/PhysRevLett.89.011301, arXiv: nucl-ex/0204008 [nucl-ex].
- [60] MINOS Collaboration, “Improved search for muon-neutrino to electron-neutrino oscillations in MINOS”, *Phys.Rev.Lett.* 107 (2011) 181802, doi: 10.1103/PhysRevLett.107.181802, arXiv: 1108.0015 [hep-ex].
- [61] T2K Collaboration, “Indication of Electron Neutrino Appearance from an Accelerator-produced off-axis Muon Neutrino Beam”, *Phys.Rev.Lett.* 107 (2011) 041801, doi: 10.1103/PhysRevLett.107.041801, arXiv: 1106.2822 [hep-ex].
- [62] N. Agafonova et al., “Discovery of τ Neutrino Appearance in the CNGS Neutrino Beam with the OPERA Experiment”, *Phys. Rev. Lett.* 115.12 (2015) 121802, doi: 10.1103/PhysRevLett.115.121802, arXiv: 1507.01417 [hep-ex].

- [63] Super-Kamiokande Collaboration, “A Measurement of the Appearance of Atmospheric Tau Neutrinos by Super-Kamiokande”, *Phys.Rev.Lett.* 110 (2013) 181802, doi: 10.1103/PhysRevLett.110.181802, arXiv: 1206.0328 [hep-ex].
- [64] Z. Maki, M. Nakagawa and S. Sakata, “Remarks on the unified model of elementary particles”, *Prog. Theor. Phys.* 28 (1962) 870–880, doi: 10.1143/PTP.28.870.
- [65] M. C. Gonzalez-Garcia et al., “Global fit to three neutrino mixing: critical look at present precision”, *JHEP* 12 (2012) 123, doi: 10.1007/JHEP12(2012)123, arXiv: 1209.3023 [hep-ph].
- [66] E. W. Otten and C. Weinheimer, “Neutrino mass limit from tritium beta decay”, *Rept. Prog. Phys.* 71 (2008) 086201, doi: 10.1088/0034-4885/71/8/086201, arXiv: 0909.2104 [hep-ex].
- [67] V. N. Aseev et al., “An upper limit on electron antineutrino mass from Troitsk experiment”, *Phys. Rev. D* 84 (2011) 112003, doi: 10.1103/PhysRevD.84.112003, arXiv: 1108.5034 [hep-ex].
- [68] C. Kraus et al., “Final results from phase II of the Mainz neutrino mass search in tritium beta decay”, *Eur. Phys. J. C* 40 (2005) 447–468, doi: 10.1140/epjc/s2005-02139-7, arXiv: hep-ex/0412056 [hep-ex].
- [69] A. Osipowicz et al., “KATRIN: A Next generation tritium beta decay experiment with sub-eV sensitivity for the electron neutrino mass. Letter of intent” (2001), arXiv: hep-ex/0109033 [hep-ex].
- [70] P. A. R. Ade et al., “Planck 2013 results. XVI. Cosmological parameters”, *Astron. Astrophys.* 571 (2014) A16, doi: 10.1051/0004-6361/201321591, arXiv: 1303.5076 [astro-ph.CO].
- [71] P. Minkowski, “ $\mu \rightarrow e\gamma$ at a Rate of One Out of 10^9 Muon Decays?”, *Phys. Lett.* B67 (1977) 421–428, doi: 10.1016/0370-2693(77)90435-X.
- [72] R. N. Mohapatra and G. Senjanovic, “Neutrino Mass and Spontaneous Parity Nonconservation”, *Phys. Rev. Lett.* 44 (14 Apr. 1980) 912–915, doi: 10.1103/PhysRevLett.44.912, URL: <http://link.aps.org/doi/10.1103/PhysRevLett.44.912>.
- [73] T. Yanagida, “Horizontal Symmetry and Masses of Neutrinos”, *Prog. Theor. Phys.* 64 (1980) 1103, doi: 10.1143/PTP.64.1103.
- [74] M. Gell-Mann, P. Ramond and R. Slansky, “Complex Spinors and Unified Theories”, *Conf. Proc. C790927* (1979) 315–321, arXiv: 1306.4669 [hep-th].
- [75] S. Glashow, “The future of elementary particle physics, in Quarks and leptons”, *Conf. Proc. NATO Sci.Ser.B*,59,687 (1980).
- [76] P. Fileviez Perez, T. Han and T. Li, “Testability of Type I Seesaw at the CERN LHC: Revealing the Existence of the B-L Symmetry”, *Phys. Rev. D* 80 (2009) 073015, doi: 10.1103/PhysRevD.80.073015, arXiv: 0907.4186 [hep-ph].
- [77] P. Fileviez Perez et al., “Neutrino Masses and the CERN LHC: Testing Type II Seesaw”, *Phys. Rev. D* 78 (2008) 015018, doi: 10.1103/PhysRevD.78.015018, arXiv: 0805.3536 [hep-ph].
- [78] ATLAS Collaboration, “Search for anomalous production of prompt same-sign lepton pairs and pair-produced doubly charged Higgs bosons with $\sqrt{s} = 8$ TeV pp collisions using the ATLAS detector”, *JHEP* 03 (2015) 041, doi: 10.1007/JHEP03(2015)041, arXiv: 1412.0237 [hep-ex].

- [79] A. Melfo et al., “Type II Seesaw at LHC: The Roadmap”, *Phys. Rev. D* 85 (2012) 055018, doi: 10.1103/PhysRevD.85.055018, arXiv: 1108.4416 [hep-ph].
- [80] N. Arkani-Hamed, A. G. Cohen and H. Georgi, “Electroweak symmetry breaking from dimensional deconstruction”, *Physics Letters B* 513.1–2 (2001) 232–240, ISSN: 0370-2693, doi: [http://dx.doi.org/10.1016/S0370-2693\(01\)00741-9](http://dx.doi.org/10.1016/S0370-2693(01)00741-9), URL: <http://www.sciencedirect.com/science/article/pii/S0370269301007419>.
- [81] S. P. Martin and J. D. Wells, “Implications of gauge-mediated supersymmetry breaking with vector-like quarks and a 125 GeV Higgs boson”, *Phys.Rev. D* 86 (2012) 035017, doi: 10.1103/PhysRevD.86.035017, arXiv: 1206.2956 [hep-ph].
- [82] A. Abada et al., “ $\mu \rightarrow e\gamma$ and $\tau \rightarrow l\gamma$ decays in the fermion triplet seesaw model”, *Phys. Rev. D* 78 (2008) 033007, doi: 10.1103/PhysRevD.78.033007, arXiv: 0803.0481 [hep-ph].
- [83] F. del Aguila, J. de Blas and M. Perez-Victoria, “Effects of new leptons in Electroweak Precision Data”, *Phys. Rev. D* 78 (2008) 013010, doi: 10.1103/PhysRevD.78.013010, arXiv: 0803.4008 [hep-ph].
- [84] R. Franceschini, T. Hambye and A. Strumia, “Type-III see-saw at LHC”, *Phys.Rev. D* 78 (2008) 033002, doi: 10.1103/PhysRevD.78.033002, arXiv: 0805.1613 [hep-ph].
- [85] A. Abada et al., “Low energy effects of neutrino masses”, *JHEP* 12 (2007) 061, doi: 10.1088/1126-6708/2007/12/061, arXiv: 0707.4058 [hep-ph].
- [86] P. A. et al. (L3 Collaboration), “Search for Heavy Neutral and Charged Leptons in e^+e^- Annihilation at LEP”, *Phys.Lett. B* 517 (2001) 75, doi: 10.1016/S0370-2693(01)01005-X, arXiv: hep-ex/0107015 [hep-ex].
- [87] CMS Collaboration, “Search for heavy lepton partners of neutrinos in proton-proton collisions in the context of the type III seesaw mechanism”, *Phys.Lett. B* 718 (2012) 348–368, doi: 10.1016/j.physletb.2012.10.070, arXiv: 1210.1797 [hep-ex].
- [88] A. Buckley et al., “General-purpose event generators for LHC physics”, *Phys.Rept.* 504 (2011) 145–233, doi: 10.1016/j.physrep.2011.03.005, arXiv: 1101.2599 [hep-ph].
- [89] J. M. Campbell, J. Huston and W. Stirling, “Hard Interactions of Quarks and Gluons: A Primer for LHC Physics”, *Rept.Prog.Phys.* 70 (2007) 89, doi: 10.1088/0034-4885/70/1/R02, arXiv: hep-ph/0611148 [hep-ph].
- [90] R. K. Ellis, W. J. Stirling and B. Webber, “QCD and collider physics”, *Camb.Monogr.Part.Phys.Nucl.Phys.Cosmol.* 8 (1996) 1–435.
- [91] V. N. Gribov and L. N. Lipatov, “Deep inelastic e-p scattering in perturbation theory”, *Sov. J. Nucl. Phys.* 15 (1972) 438–450.
- [92] G. Altarelli and G. Parisi, “Asymptotic Freedom in Parton Language”, *Nucl. Phys.* B126 (1977) 298, doi: 10.1016/0550-3213(77)90384-4.
- [93] Y. L. Dokshitzer, “Calculation of the Structure Functions for Deep Inelastic Scattering and e^+e^- Annihilation by Perturbation Theory in Quantum Chromodynamics.”, *Sov.Phys.JETP* 46 (1977) 641–653.
- [94] Lai, H.-L. et al., “New generation of parton distributions with uncertainties from global QCD analysis”, *Phys. Rev. D* 82 (2010) 074024, arXiv: 1007.2241.
- [95] A. Martin et al., “Parton distributions for the LHC”, *Eur.Phys.J. C* 63 (2009) 189–285, doi: 10.1140/epjc/s10052-009-1072-5, arXiv: 0901.0002 [hep-ph].

-
- [96] J. Pumplin et al., “New generation of parton distributions with uncertainties from global QCD analysis”, *JHEP* 07 (2002) 012, arXiv: 0201195 [hep-ph].
- [97] T. Gleisberg et al., “Event generation with SHERPA 1.1”, *JHEP* 02 (2009) 007, doi: 10.1088/1126-6708/2009/02/007, arXiv: 0811.4622 [hep-ph].
- [98] T. Sjöstrand et al., “High-Energy-Physics Event Generation with PYTHIA 6.1”, *Comput. Phys. Comm.* 135 (2001) 238, doi: 10.1016/S0010-4655(00)00236-8, arXiv: 0010017 [hep-ph].
- [99] G. Corcella et al., “HERWIG 6: An Event generator for hadron emission reactions with interfering gluons (including supersymmetric processes)”, *JHEP* 0101 (2001) 010, doi: 10.1088/1126-6708/2001/01/010, arXiv: hep-ph/0011363 [hep-ph].
- [100] T. Sjöstrand, S. Mrenna and P. Z. Skands, “PYTHIA 6.4 physics and manual”, *JHEP* 0605 (2006) 026, doi: 10.1088/1126-6708/2006/05/026, arXiv: hep-ph/0603175 [hep-ph].
- [101] S. Catani et al., “QCD matrix elements + parton showers”, *JHEP* 0111 (2001) 063, doi: 10.1088/1126-6708/2001/11/063, arXiv: hep-ph/0109231 [hep-ph].
- [102] F. Krauss, “Matrix elements and parton showers in hadronic interactions”, *JHEP* 0208 (2002) 015, arXiv: hep-ph/0205283 [hep-ph].
- [103] M. Bahr et al., “Herwig++ Physics and Manual”, *Eur. Phys. J. C* 58 (2008) 639–707, doi: 10.1140/epjc/s10052-008-0798-9, arXiv: 0803.0883 [hep-ph].
- [104] J. Alwall et al., “Comparative study of various algorithms for the merging of parton showers and matrix elements in hadronic collisions”, *Eur. Phys. J. C* 53 (2008) 473–500, doi: 10.1140/epjc/s10052-007-0490-5, arXiv: 0706.2569 [hep-ph].
- [105] M. L. Mangano et al., “ALPGEN, a generator for hard multiparton processes in hadronic collisions”, *JHEP* 0307 (2003) 001, doi: 10.1088/1126-6708/2003/07/001, arXiv: hep-ph/0206293 [hep-ph].
- [106] S. Frixione and B. R. Webber, “Matching NLO QCD computations and parton shower simulations”, *JHEP* 0206 (2002) 029, doi: 10.1088/1126-6708/2002/06/029, arXiv: hep-ph/0204244 [hep-ph].
- [107] P. Nason, “A new method for combining NLO QCD with shower Monte Carlo algorithms”, *JHEP* 0411 (2004) 040, doi: 10.1088/1126-6708/2004/11/040, arXiv: hep-ph/0409146 [hep-ph].
- [108] S. Frixione, P. Nason and C. Oleari, “Matching NLO QCD computations with Parton Shower simulations: The POWHEG method”, *JHEP* 0711 (2007) 070, doi: 10.1088/1126-6708/2007/11/070, arXiv: 0709.2092 [hep-ph].
- [109] B. Andersson et al., “Parton Fragmentation and String Dynamics”, *Phys.Rept.* 97 (1983) 31–145, doi: 10.1016/0370-1573(83)90080-7.
- [110] J.-C. Winter, F. Krauss and G. Soff, “A Modified cluster hadronization model”, *Eur.Phys.J. C* 36 (2004) 381–395, doi: 10.1140/epjc/s2004-01960-8, arXiv: hep-ph/0311085 [hep-ph].
- [111] ATLAS Collaboration, “ATLAS Run 1 Pythia8 tunes”, ATL-PHYS-PUB-2014-021 (Nov. 2014).
- [112] P. Z. Skands, “Tuning Monte Carlo Generators: The Perugia Tunes”, *Phys.Rev. D* 82 (2010) 074018, doi: 10.1103/PhysRevD.82.074018, arXiv: 1005.3457 [hep-ph].

- [113] G. Aad et al., “Measurements of underlying-event properties using neutral and charged particles in pp collisions at 900 GeV and 7 TeV with the ATLAS detector at the LHC”, *Eur. Phys. J. C* 71 (2011) 1636, doi: [10.1140/epjc/s10052-011-1636-z](https://doi.org/10.1140/epjc/s10052-011-1636-z), arXiv: [1103.1816](https://arxiv.org/abs/1103.1816) [hep-ex].
- [114] J. Alwall et al., “A standard format for Les Houches Event Files”, *Comput. Phys. Commun.* 176.hep-ph/0609017. CERN-LCGAPP-2006-03. 4 (Sept. 2006) 300–304. 8 p, URL: <https://cds.cern.ch/record/981808>.
- [115] C. Degrande et al., “UFO - The Universal FeynRules Output”, *Comput. Phys. Commun.* 183 (2012) 1201–1214, doi: [10.1016/j.cpc.2012.01.022](https://doi.org/10.1016/j.cpc.2012.01.022), arXiv: [1108.2040](https://arxiv.org/abs/1108.2040) [hep-ph].
- [116] A. Buckley et al., “LHAPDF6: parton density access in the LHC precision era”, *Eur. Phys. J. C* 75 (2015) 132, doi: [10.1140/epjc/s10052-015-3318-8](https://doi.org/10.1140/epjc/s10052-015-3318-8), arXiv: [1412.7420](https://arxiv.org/abs/1412.7420) [hep-ph].
- [117] ATLAS Collaboration, “ATLAS Simulation Infrastructure”, *Eur. Phys. J. C* 70 (2010) 823–874, doi: [10.1140/epjc/s10052-010-1429-9](https://doi.org/10.1140/epjc/s10052-010-1429-9), arXiv: [1005.4568](https://arxiv.org/abs/1005.4568) [physics.ins-det].
- [118] J. Butterworth, J. R. Forshaw and M. Seymour, “Multiparton interactions in photoproduction at HERA”, *Z. Phys. C* 72 (1996) 637–646, doi: [10.1007/s002880050286](https://doi.org/10.1007/s002880050286), arXiv: [9601371](https://arxiv.org/abs/9601371) [hep-ph].
- [119] Christensen, N. L. and Duhr, C., “FeynRules - Feynman rules made easy”, *Comput. Phys. Commun.* 180 (2009) 1614.
- [120] L. Evans and P. Bryant, “LHC Machine”, *JINST* 3 (2008), ed. by L. Evans S08001, doi: [10.1088/1748-0221/3/08/S08001](https://doi.org/10.1088/1748-0221/3/08/S08001).
- [121] ATLAS Collaboration, “The ATLAS Experiment at the CERN Large Hadron Collider”, *JINST* 3 (2008) S08003, doi: [10.1088/1748-0221/3/08/S08003](https://doi.org/10.1088/1748-0221/3/08/S08003).
- [122] CMS Collaboration, “The CMS experiment at the CERN LHC”, *JINST* 3 (2008) S08004, doi: [10.1088/1748-0221/3/08/S08004](https://doi.org/10.1088/1748-0221/3/08/S08004).
- [123] LHCb Collaboration, “LHCb Technical Design Report: Reoptimized Detector Design and Performance” (Sept. 2003), URL: <http://cds.cern.ch/record/630827>.
- [124] ALICE Collaboration, “The ALICE experiment at the CERN LHC”, *JINST* 3 (2008) S08002, doi: [10.1088/1748-0221/3/08/S08002](https://doi.org/10.1088/1748-0221/3/08/S08002).
- [125] Wikipedia, *Map of the CERN accelerator complex*, webpage, accessed April-2015, URL: <http://en.wikipedia.org/wiki/File:Cern-accelerator-complex.svg>.
- [126] ATLAS Collaboration, “ATLAS Detector and Physics Performance: Technical Design Report” (1999), URL: <http://cds.cern.ch/record/391176>.
- [127] R. Alemany-Fernandez et al., “Operation and Configuration of the LHC in Run 1” (Nov. 2013), URL: <https://cds.cern.ch/record/1631030>.
- [128] ATLAS Collaboration, *ATLAS Twiki: Luminosity Public Results*, webpage, accessed 20-Februray-2014, URL: <http://twiki.cern.ch/twiki/bin/view/AtlasPublic/LuminosityPublicResults>.
- [129] ATLAS Collaboration, “ATLAS Computing: Technical Design Report” (2005), URL: <http://cds.cern.ch/record/837738>.
- [130] M. Dobbs and J. B. Hansen, “The HepMC C++ Monte Carlo Event Record for High Energy Physics”, tech. rep. ATL-SOFT-2000-001, revised version number 1 submitted on 2001-02-27 09:54:32: CERN, June 2000, URL: <https://cds.cern.ch/record/684090>.

- [131] S. Agostinelli et al., “GEANT4: A Simulation toolkit”, *Nucl. Instrum. Meth.* A506 (2003) 250–303, doi: 10.1016/S0168-9002(03)01368-8.
- [132] T. Cornelissen et al., “Concepts, Design and Implementation of the ATLAS New Tracking (NEWT)” (Mar. 2007), URL: <http://cds.cern.ch/record/1020106>.
- [133] ATLAS Collaboration, “Performance of the ATLAS Inner Detector Track and Vertex Reconstruction in the High Pile-Up LHC Environment” (Mar. 2012), URL: <http://cds.cern.ch/record/1435196>.
- [134] R. Fruhwirth, “Application of Kalman filtering to track and vertex fitting”, *Nucl. Instrum. Meth.* A262 (1987) 444–450, doi: 10.1016/0168-9002(87)90887-4.
- [135] G. Pasztor, D. Damazio and F. Monticelli, “Electron and photon trigger performance plots using 2012 data”, tech. rep. ATL-COM-DAQ-2014-058, CERN, June 2014, URL: <https://cds.cern.ch/record/1706278>.
- [136] “Electron efficiency measurements with the ATLAS detector using the 2012 LHC proton-proton collision data” (June 2014).
- [137] “Electron and photon energy calibration with the ATLAS detector using LHC Run 1 data”, *Eur. Phys. J. C* arXiv:1407.5063. CERN-PH-EP-2014-153 (July 2014) 74. 51 p, URL: <https://cds.cern.ch/record/1744017>.
- [138] ATLAS Collaboration, *ATLAS Twiki: Muon Trigger Public Results*, accessed 10-June-2015, Geneva, 2013, URL: https://twiki.cern.ch/twiki/bin/view/AtlasPublic/MuonTriggerPublicResults#Plots_for_2012_data_8_TeV.
- [139] ATLAS Collaboration, “Measurement of the muon reconstruction performance of the ATLAS detector using 2011 and 2012 LHC proton-proton collision data”, *Eur.Phys.J. C* 74.11 (2014) 3130, doi: 10.1140/epjc/s10052-014-3130-x, arXiv: 1407.3935 [hep-ex].
- [140] K. Nikolopoulos et al., “Muon Energy Loss Upstream of the Muon Spectrometer” (2006).
- [141] “Preliminary results on the muon reconstruction efficiency, momentum resolution, and momentum scale in ATLAS 2012 pp collision data” (Aug. 2013).
- [142] W. Lampl et al., “Calorimeter Clustering Algorithms: Description and Performance” (Apr. 2008), URL: <http://cdsweb.cern.ch/record/1099735>.
- [143] T. Barillari et al., “Local Hadronic Calibration” (June 2008).
- [144] M. Cacciari, G. P. Salam and G. Soyez, “The Anti- k_r jet clustering algorithm”, *JHEP* 0804 (2008) 063, doi: 10.1088/1126-6708/2008/04/063, arXiv: 0802.1189 [hep-ph].
- [145] ATLAS Collaboration, “Performance of pile-up subtraction for jet shapes” (Aug. 2013).
- [146] ATLAS Collaboration, “Pile-up subtraction and suppression for jets in ATLAS” (Aug. 2013).
- [147] S. Hassani et al., “A muon identification and combined reconstruction procedure for the ATLAS detector at the LHC using the (MUONBOY, STACO, MuTag) reconstruction packages”, *Nucl. Instrum. Meth.* A572 (2007) 77–79, doi: 10.1016/j.nima.2006.10.340.
- [148] “Performance of Missing Transverse Momentum Reconstruction in ATLAS studied in Proton-Proton Collisions recorded in 2012 at 8 TeV” (Aug. 2013).
- [149] G. Aad et al., “Search for heavy lepton resonances decaying to a Z boson and a lepton in pp collisions at $\sqrt{s} = 8$ TeV with the ATLAS detector”, *JHEP* 09 (2015) 108, doi: 10.1007/JHEP09(2015)108, arXiv: 1506.01291 [hep-ex].

- [150] ATLAS Collaboration, “Search for anomalous production of prompt same-sign lepton pairs and pair-produced doubly charged Higgs bosons with $\sqrt{s} = 8$ TeV pp collisions using the ATLAS detector”, *JHEP* 1503 (2015) 041, doi: 10.1007/JHEP03(2015)041, arXiv: 1412.0237 [hep-ex].
- [151] U. Bellgardt et al., “Search for the Decay $\mu^+ \rightarrow e^+e^+e^-$ ”, *Nucl.Phys.* B299 (1988) 1, doi: 10.1016/0550-3213(88)90462-2.
- [152] LHCb Collaboration, “Searches for violation of lepton flavour and baryon number in tau lepton decays at LHCb”, *Phys.Lett.* B724 (2013) 36–45, doi: 10.1016/j.physletb.2013.05.063, arXiv: 1304.4518 [hep-ex].
- [153] J. Alwall et al., “MadGraph 5 : Going Beyond”, *JHEP* 06 (2011) 128, doi: 10.1007/JHEP06(2011)128, arXiv: 1106.0522 [hep-ph].
- [154] P. Meade and M. Reece, “BRIDGE: Branching ratio inquiry / decay generated events” (2007), arXiv: hep-ph/0703031 [hep-ph].
- [155] F. Maltoni and T. Stelzer, “MadEvent: automatic event generation with MadGraph”, *Journal of High Energy Physics* 2003.02 (2003) 027, URL: <http://stacks.iop.org/1126-6708/2003/i=02/a=027>.
- [156] F. del Aguila and J. A. Aguilar-Saavedra, “Distinguishing seesaw models at LHC with multi-lepton signals”, *Nucl. Phys.* B813 (2009) 22–90, doi: 10.1016/j.nuclphysb.2008.12.029, arXiv: 0808.2468 [hep-ph].
- [157] “Performance of the Fast ATLAS Tracking Simulation (FATRAS) and the ATLAS Fast Calorimeter Simulation (FastCaloSim) with single particles”, tech. rep. ATL-SOFT-PUB-2014-001, CERN, Mar. 2014, URL: <http://cds.cern.ch/record/1669341>.
- [158] J. Dingfelder et al., “Search for New Phenomena Producing Tripleton Resonances in pp Collisions at $\sqrt{s} = 8$ TeV with the ATLAS Detector”, tech. rep. ATL-COM-PHYS-2014-344, CERN, Apr. 2014, URL: <https://cds.cern.ch/record/1696850>.
- [159] P. M. Nadolsky et al., “Implications of CTEQ global analysis for collider observables”, *Phys. Rev.* D78 (2008) 013004, doi: 10.1103/PhysRevD.78.013004, arXiv: 0802.0007 [hep-ph].
- [160] T. Sjostrand, S. Mrenna and P. Z. Skands, “A Brief Introduction to PYTHIA 8.1”, *Comput. Phys. Commun.* 178 (2008) 852–867, doi: 10.1016/j.cpc.2008.01.036, arXiv: 0710.3820 [hep-ph].
- [161] “The simulation principle and performance of the ATLAS fast calorimeter simulation FastCaloSim”, *ATL-PHYS-PUB-2010-013* (2010), <http://cds.cern.ch/record/1300517>.
- [162] T. Gleisberg et al., “Studying W^+W^- production at the Fermilab Tevatron with SHERPA”, *Phys. Rev.* D72 (2005) 034028, doi: 10.1103/PhysRevD.72.034028, arXiv: hep-ph/0504032 [hep-ph].
- [163] S. Höche et al., “QCD matrix elements and truncated showers”, *JHEP* 0905 (2009) 053, doi: 10.1088/1126-6708/2009/05/053, arXiv: 0903.1219 [hep-ph].
- [164] T. Gleisberg and S. Höche, “Comix, a new matrix element generator”, *JHEP* 0812 (2008) 039, doi: 10.1088/1126-6708/2008/12/039, arXiv: 0808.3674 [hep-ph].
- [165] S. Schumann and F. Krauss, “A Parton shower algorithm based on Catani-Seymour dipole factorisation”, *JHEP* 0803 (2008) 038, doi: 10.1088/1126-6708/2008/03/038, arXiv: 0709.1027 [hep-ph].

- [166] H.-L. Lai et al., “New parton distributions for collider physics”, *Phys. Rev. D* 82 (2010) 074024, doi: 10.1103/PhysRevD.82.074024, arXiv: 1007.2241 [hep-ph].
- [167] K. Arnold et al., “VBFNLO: A Parton level Monte Carlo for processes with electroweak bosons”, *Comput. Phys. Commun.* 180 (2009) 1661–1670, doi: 10.1016/j.cpc.2009.03.006, arXiv: 0811.4559 [hep-ph].
- [168] T. Melia et al., “ W^+W^- , WZ and ZZ production in the POWHEG BOX”, *JHEP* 11 (2011) 078, doi: 10.1007/JHEP11(2011)078, arXiv: 1107.5051 [hep-ph].
- [169] T. Sjöstrand, S. Mrenna and P. Z. Skands, “A Brief Introduction to PYTHIA 8.1”, *Comput. Phys. Commun.* 178 (2008) 852–867, doi: 10.1016/j.cpc.2008.01.036, arXiv: 0710.3820 [hep-ph].
- [170] M. V. Garzelli et al., “ $t\bar{t}W^{+-}$ and $t\bar{t}Z$ Hadroproduction at NLO accuracy in QCD with Parton Shower and Hadronization effects”, *JHEP* 11 (2012) 056, doi: 10.1007/JHEP11(2012)056, arXiv: 1208.2665 [hep-ph].
- [171] M. Czakon, P. Fiedler and A. Mitov, “The total top quark pair production cross-section at hadron colliders through $O(\alpha_s^4)$ ” (2013), arXiv: 1303.6254 [hep-ph].
- [172] ATLAS Collaboration, “Improved luminosity determination in pp collisions at $\sqrt{s} = 7$ TeV using the ATLAS detector at the LHC”, *Eur.Phys.J. C* 73.8 (2013) 2518, doi: 10.1140/epjc/s10052-013-2518-3, arXiv: 1302.4393 [hep-ex].
- [173] ATLAS Collaboration, “Expected Performance of the ATLAS Experiment - Detector, Trigger and Physics” (2009), arXiv: 0901.0512 [hep-ex].
- [174] E. Barberio et al., “Search for Type III seesaw model heavy leptons in events with 4 charged leptons.”, tech. rep. ATL-COM-PHYS-2012-1470, CERN, Oct. 2012, URL: <https://cds.cern.ch/record/1483288>.
- [175] “Search for Type III Seesaw Model Heavy Fermions in Events with Four Charged Leptons using 5.8 fb^{-1} of $\sqrt{s} = 8$ TeV data with the ATLAS Detector”, tech. rep. ATLAS-CONF-2013-019, CERN, Mar. 2013, URL: <https://cds.cern.ch/record/1525526>.
- [176] T. Junk, “Sensitivity, Exclusion and Discovery with Small Signals, Large Backgrounds, and Large Systematic Uncertainties”, tech. rep. CDF/DOC/STATISTICS/PUBLIC/8128, Fermilab, 2007.
- [177] P.-O. DeViveiros et al., “Search for New Physics in Events with Three Charged Leptons”, tech. rep. ATL-COM-PHYS-2014-236, CERN, Mar. 2014.
- [178] D. R.-H. Yu and B. Heinemann, “Searches for new phenomena using events with three or more charged leptons in pp collisions at $\sqrt{s} = 8$ TeV with the ATLAS detector at the LHC”, Presented 2015, PhD thesis: UC, Berkeley, 2015, URL: <https://cds.cern.ch/record/2110749>.
- [179] L. Skinnari, “A Search for Physics Beyond the Standard Model using Like-Sign Muon Pairs in pp Collisions at $\sqrt{s} = 7$ TeV with the ATLAS Detector”, <https://cds.cern.ch/record/1503359/files/CERN-THESIS-2012-217.pdf>, PhD thesis: University of California, Berkeley, 2012.
- [180] J.-F. Arguin et al., “Search for anomalous production of prompt like-sign lepton pairs and constraints on physics beyond the Standard Model”, tech. rep. ATL-COM-PHYS-2012-529, CERN, May 2012.

- [181] ATLAS Collaboration, “Search for new phenomena in events with three or more charged leptons in pp collisions at $\sqrt{s} = 8$ TeV with the ATLAS detector”, *submitted to JHEP* (2014), arXiv: 1411.2921 [hep-ex].
- [182] F. Campanario and S. Sapeta, “WZ production beyond NLO for high- p_T observables”, *Phys. Lett. B* 718 (2012) 100–104, doi: 10.1016/j.physletb.2012.10.013, arXiv: 1209.4595 [hep-ph].
- [183] M. Rubin, G. P. Salam and S. Sapeta, “Giant QCD K-factors beyond NLO”, *JHEP* 09 (2010) 084, doi: 10.1007/JHEP09(2010)084, arXiv: 1006.2144 [hep-ph].
- [184] M. Garzelli et al., “ Z^0 - boson production in association with a top anti-top pair at NLO accuracy with parton shower effects”, *Phys. Rev. D* 85 (2012) 074022, doi: 10.1103/PhysRevD.85.074022, arXiv: 1111.1444 [hep-ph].
- [185] J. M. Campbell and R. K. Ellis, “ $t\bar{t}W^\pm$ production and decay at NLO”, *JHEP* 07 (2012) 052, doi: 10.1007/JHEP07(2012)052, arXiv: 1204.5678 [hep-ph].
- [186] S. Vanini, “Search for Seesaw type III Signals in 2011 LHC CMS Data”, https://cds.cern.ch/record/1483246/files/TS2012_034.pdf, PhD thesis: University of Padua, Italy, 2011.
- [187] “Jet energy scale and its systematic uncertainty in proton-proton collisions at $\sqrt{s} = 7$ TeV with ATLAS 2011 data” (Jan. 2013).
- [188] F. James and M. Roos, “Minuit: A System for Function Minimization and Analysis of the Parameter Errors and Correlations”, *Comput.Phys.Commun.* 10 (1975) 343–367, doi: 10.1016/0010-4655(75)90039-9.
- [189] G. Cowan et al., “Asymptotic formulae for likelihood-based tests of new physics”, *Eur. Phys. J. C* 71 (2011) 1554, doi: 10.1140/epjc/s10052-011-1554-0, arXiv: 1007.1727 [physics.data-an].
- [190] J. Neyman and E. S. Pearson, “On the Problem of the Most Efficient Tests of Statistical Hypotheses”, *Phil. Trans. R. Soc. Lond.* A231 (1933) 289–337, doi: 10.1098/rsta.1933.0009.
- [191] A. Wald, “Tests of Statistical Hypotheses Concerning Several Parameters When the Number of Observations is Large”, English, *Trans. Amer. Math. Soc.* 54 (1943) 426–482, ISSN: 00029947, doi: 10.2307/1990256, URL: <http://www.jstor.org/stable/1990256>.
- [192] S. S. Wilks, “The Large-Sample Distribution of the Likelihood Ratio for Testing Composite Hypotheses”, English, *The Annals of Mathematical Statistics* 9.1 (1938), ISSN: 00034851, doi: 10.1214/aoms/1177732360, URL: <http://www.jstor.org/stable/2957648>.
- [193] G. Cowan, “Statistics for Searches at the LHC” (2013) 321–355, doi: 10.1007/978-3-319-05362-2_9, arXiv: 1307.2487 [hep-ex].
- [194] A. D. Bukin, “Fitting function for asymmetric peaks”, arXiv:0711.4449 (Nov. 2007).
- [195] S. M. Sze and K. K. Ng, *Physics of Semiconductor Devices*, Wiley-Interscience, 2006, ISBN: 0471143235.
- [196] H. Kolanoski and N. Wermes, *Teilchendetektoren: Grundlagen und Anwendungen (German Edition)*, Springer Spektrum, 2016, ISBN: 3662453495.
- [197] G. Lutz, *Semiconductor Radiation Detectors: Device Physics*, Springer, 2008, ISBN: 3540716785.

- [198] H. Spieler, *Semiconductor Detector Systems (Series on Semiconductor Science and Technology)*, Oxford University Press, 2005, ISBN: 0198527845.
- [199] L. Rossi et al., *Pixel Detectors: From Fundamentals to Applications (Particle Acceleration and Detection)*, Springer, 2006, ISBN: 3540283323.
- [200] F. Hartmann, *Evolution of Silicon Sensor Technology in Particle Physics (Springer Tracts in Modern Physics)*, Springer, 2008, ISBN: 3540250948.
- [201] J. Kemmer, “Fabrication of low noise silicon radiation detectors by the planar process”, *Nucl. Instrum. Meth.* 169 (1980) 499–502, DOI: 10.1016/0029-554X(80)90948-9.
- [202] H. Kolanoski and N. Wermes, *Teilchendetektoren - Grundlagen und Anwendungen*, Wiesbaden: Springer Berlin Heidelberg, 2016, ISBN: 978-3-662-45349-0.
- [203] A. Chilingarov, “Temperature dependence of the current generated in Si bulk”, *Journal of Instrumentation* 8.10 (2013) P10003, URL: <http://stacks.iop.org/1748-0221/8/i=10/a=P10003>.
- [204] L. Landau, *J. Exp. Phys.* 8.201 (1944).
- [205] P. Vavilov, *Sov. Phys. JETP* 5.749 (1957).
- [206] H. Bichsel, “Straggling in thin silicon detectors”, *Rev. Mod. Phys.* 60 (3 July 1988) 663–699, DOI: 10.1103/RevModPhys.60.663, URL: <http://link.aps.org/doi/10.1103/RevModPhys.60.663>.
- [207] C. Jacoboni et al., “A review of some charge transport properties of silicon”, *Solid-State Electronics* 20.2 (1977) 77–89, ISSN: 0038-1101, DOI: [http://dx.doi.org/10.1016/0038-1101\(77\)90054-5](http://dx.doi.org/10.1016/0038-1101(77)90054-5), URL: <http://www.sciencedirect.com/science/article/pii/0038110177900545>.
- [208] S. Ramo, “Currents Induced by Electron Motion”, *Proceedings of the IRE* 27.9 (Sept. 1939) 584–585, ISSN: 0096-8390, DOI: 10.1109/JRPROC.1939.228757.
- [209] W. Shockley, “Currents to Conductors Induced by a Moving Point Charge”, *J. Appl. Phys.* 9.10 (1938) 635, DOI: 10.1063/1.1710367, URL: <http://dx.doi.org/10.1063/1.1710367>.
- [210] V. A. J. V. Lint et al., *Mechanisms of Radiation Effects in Electronic Materials (Volume 1)*, Wiley, 1980, ISBN: 0471041068.
- [211] Y. Shi et al., “A numerical study of cluster center formation in neutron-irradiated silicon”, *J. Appl. Phys.* 67.2 (1990) 1116, DOI: 10.1063/1.345799, URL: <http://dx.doi.org/10.1063/1.345799>.
- [212] M. Moll, “Radiation damage in silicon particle detectors: Microscopic defects and macroscopic properties”, PhD thesis: University of Hamburg, Germany, 1999, URL: <http://www-library.desy.de/cgi-bin/showprep.pl?desy-thesis99-040>.
- [213] A. Vasilescu and G. Lindstroem, *Displacement damage in silicon, on-line compilation*, URL: <http://rd50.web.cern.ch/RD50/NIEL/default.html>.
- [214] R. Wunstorf, “Systematische Untersuchung zur Strahlenresistenz von Silizium-Detektoren für die Verwendung in Hochenergiephysik-Experimenten”, PhD thesis: University of Hamburg, Germany, 1992, URL: <http://www-library.desy.de/cgi-bin/showprep.pl?DESY-FH1K-92-01>.

- [215] G. Kramberger et al., “Impact of annealing of trapping times on charge collection in irradiated silicon detectors”, *Nuclear Instruments and Methods in Physics Research Section A: Accelerators, Spectrometers, Detectors and Associated Equipment* 579.2 (2007), Proceedings of the 6th Hiroshima Symposium on the Development and Application of Semiconductor Detectors 762–765, issn: 0168-9002, doi: <http://dx.doi.org/10.1016/j.nima.2007.05.294>, url: <http://www.sciencedirect.com/science/article/pii/S0168900207011795>.
- [216] G. Kramberger, “Signal Development in Irradiated Silicon Detectors”, PhD thesis: University of Ljubljana, Slovenia, 2001.
- [217] A. Junkes, “Influence of Radiation Induced Defect Clusters on Silicon Particle Detectors”, PhD thesis: University of Hamburg, Germany, 2011, url: <http://www-library.desy.de/cgi-bin/showprep.pl?desy-thesis-11-031>.
- [218] G. Casse et al., “Enhanced efficiency of segmented silicon detectors of different thicknesses after proton irradiations up to $1 \times 10^{16} \text{ n(eq) cm}^{-2}$ ”, *Nucl. Instrum. Meth.* A624 (2010) 401–404, doi: [10.1016/j.nima.2010.02.134](https://doi.org/10.1016/j.nima.2010.02.134).
- [219] I. Mandić et al., “Annealing effects in n+-p strip detectors irradiated with high neutron fluences”, *Nucl. Instrum. Meth.* A629 (2011) 101–105, doi: [10.1016/j.nima.2010.11.057](https://doi.org/10.1016/j.nima.2010.11.057).
- [220] M. Milovanovic et al., “Effects of accelerated long term annealing in highly irradiated n + -p strip detector examined by Edge-TCT”, *Journal of Instrumentation* 7.06 (2012) P06007, url: <http://stacks.iop.org/1748-0221/7/i=06/a=P06007>.
- [221] G. Kramberger et al., “Effective trapping time of electrons and holes in different silicon materials irradiated with neutrons, protons and pions”, *Nucl. Instrum. Meth.* A481 (2002) 297–305, doi: [10.1016/S0168-9002\(01\)01263-3](https://doi.org/10.1016/S0168-9002(01)01263-3).
- [222] G. Kramberger et al., “Determination of effective trapping times for electrons and holes in irradiated silicon”, *Nucl. Instrum. Meth.* A476 (2002) 645–651, doi: [10.1016/S0168-9002\(01\)01653-9](https://doi.org/10.1016/S0168-9002(01)01653-9).
- [223] I. Mandić et al., “Observation of full charge collection efficiency in heavily irradiated np strip detectors irradiated up to $3 \times 10^{15} \text{ neq/cm}^2$ ”, *Nuclear Instruments and Methods in Physics Research Section A: Accelerators, Spectrometers, Detectors and Associated Equipment* 612.3 (Jan. 2010) 474–477, doi: [10.1016/j.nima.2009.08.004](https://doi.org/10.1016/j.nima.2009.08.004), url: <http://dx.doi.org/10.1016/j.nima.2009.08.004>.
- [224] G. Casse et al., “Evidence of enhanced signal response at high bias voltages in planar silicon detectors irradiated up to $2.2 \times 10^{16} \text{ neq/cm}^2$ ”, *Nuclear Instruments and Methods in Physics Research Section A: Accelerators, Spectrometers, Detectors and Associated Equipment* 636.1 (Apr. 2011) S56–S61, doi: [10.1016/j.nima.2010.04.085](https://doi.org/10.1016/j.nima.2010.04.085), url: <http://dx.doi.org/10.1016/j.nima.2010.04.085>.
- [225] M. Köhler, “Double-sided 3D silicon detectors for the high-luminosity LHC”, PhD thesis: University of Freiburg, Germany, 2011.
- [226] J. C. Lange, “Differential Top-Quark-Pair Cross Sections in pp Collisions at $\sqrt{s} = 7 \text{ TeV}$ with CMS and Charge Multiplication in Highly-Irradiated Silicon Sensors”, PhD thesis: Hamburg U., 2013, url: <https://cds.cern.ch/record/1602217>.
- [227] RD50 Collaboration, *Development of Radiation Hard Semiconductor Devices for Very High Luminosity Colliders*, Geneva, 2002.
- [228] RD50 Collaboration, url: <http://rd50.web.cern.ch/rd50/>.

- [229] RD48 Collaboration, URL: <http://rd48.web.cern.ch/rd48/links/links.htm>.
- [230] G. L. et. al., “Radiation hard silicon detectors—developments by the RD48 (ROSE) collaboration”, *Nuclear Instruments and Methods in Physics Research Section A: Accelerators, Spectrometers, Detectors and Associated Equipment* 466.2 (July 2001) 308–326, DOI: 10.1016/S0168-9002(01)00560-5, URL: [http://dx.doi.org/10.1016/S0168-9002\(01\)00560-5](http://dx.doi.org/10.1016/S0168-9002(01)00560-5).
- [231] J. Härkönen et al., “Radiation hardness of Czochralski silicon, Float Zone silicon and oxygenated Float Zone silicon studied by low energy protons”, *Nuclear Instruments and Methods in Physics Research Section A: Accelerators, Spectrometers, Detectors and Associated Equipment* 518.1-2 (Feb. 2004) 346–348, DOI: 10.1016/j.nima.2003.11.018, URL: <http://dx.doi.org/10.1016/j.nima.2003.11.018>.
- [232] I. Pintilie et al., “Radiation-induced point- and cluster-related defects with strong impact on damage properties of silicon detectors”, *Nuclear Instruments and Methods in Physics Research Section A: Accelerators, Spectrometers, Detectors and Associated Equipment* 611.1 (Nov. 2009) 52–68, DOI: 10.1016/j.nima.2009.09.065, URL: <http://dx.doi.org/10.1016/j.nima.2009.09.065>.
- [233] C. Kenney et al., “Silicon detectors with 3-D electrode arrays: fabrication and initial test results”, *IEEE Trans. Nucl. Sci.* 46.4 (1999) 1224–1236, DOI: 10.1109/23.785737, URL: <http://dx.doi.org/10.1109/23.785737>.
- [234] C. D. Viá et al., “Radiation hardness properties of full-3D active edge silicon sensors”, *Nuclear Instruments and Methods in Physics Research Section A: Accelerators, Spectrometers, Detectors and Associated Equipment* 587.2-3 (Mar. 2008) 243–249, DOI: 10.1016/j.nima.2007.12.027, URL: <http://dx.doi.org/10.1016/j.nima.2007.12.027>.
- [235] F. Lackner et al., “An Improved Insulation System for the LHC Main 13 kA Interconnection Splices”, tech. rep. CERN-ATS-2013-021, CERN, Feb. 2013, URL: <https://cds.cern.ch/record/1516043>.
- [236] M. Capeans et al., “ATLAS Insertable B-Layer Technical Design Report”, tech. rep. CERN-LHCC-2010-013. ATLAS-TDR-19, CERN, Sept. 2010, URL: <https://cds.cern.ch/record/1291633>.
- [237] “Studies for the development of the Inner Detector trigger algorithms at ATLAS”, tech. rep. ATL-DAQ-PUB-2013-002, CERN, Sept. 2013, URL: <https://cds.cern.ch/record/1602918>.
- [238] G. Apollinari et al., *High-Luminosity Large Hadron Collider (HL-LHC): Preliminary Design Report*, Geneva: CERN, 2015, URL: <http://cds.cern.ch/record/2116337>.
- [239] “Letter of Intent for the Phase-I Upgrade of the ATLAS Experiment”, tech. rep. CERN-LHCC-2011-012. LHCC-I-020, CERN, Nov. 2011, URL: <https://cds.cern.ch/record/1402470>.
- [240] T. Kawamoto et al., “New Small Wheel Technical Design Report”, tech. rep. CERN-LHCC-2013-006. ATLAS-TDR-020, ATLAS New Small Wheel Technical Design Report: CERN, June 2013, URL: <https://cds.cern.ch/record/1552862>.
- [241] M. e. a. Aleksa, “ATLAS Liquid Argon Calorimeter Phase-I Upgrade Technical Design Report”, tech. rep. CERN-LHCC-2013-017. ATLAS-TDR-022, Final version presented to December 2013 LHCC.: CERN, Sept. 2013, URL: <https://cds.cern.ch/record/1602230>.

- [242] ATLAS Collaboration, “Technical Design Report for the Phase-I Upgrade of the ATLAS TDAQ System”, tech. rep. CERN-LHCC-2013-018. ATLAS-TDR-023, Final version presented to December 2013 LHCC.: CERN, Sept. 2013, URL: <https://cds.cern.ch/record/1602235>.
- [243] I. Bejar et al., “The HL-LHC Machine”, *The High Luminosity Large Hadron Collider: the new machine for illuminating the mysteries of Universe*, ed. by O. Brning and L. Rossi, 2015 31–44, doi: 10.1142/9789814675475_0003, URL: <http://inspirehep.net/record/1421704/files/The%20HL-LHC%20Machine.pdf>.
- [244] C. ATLAS, “Letter of Intent for the Phase-II Upgrade of the ATLAS Experiment”, tech. rep. CERN-LHCC-2012-022. LHCC-I-023, Draft version for comments: CERN, Dec. 2012, URL: <https://cds.cern.ch/record/1502664>.
- [245] F. Gianotti et al., “Physics potential and experimental challenges of the LHC luminosity upgrade”, *Eur. Phys. J. C* 39 (2005) 293–333, doi: 10.1140/epjc/s2004-02061-6, arXiv: hep-ph/0204087 [hep-ph].
- [246] B. Lillie, L. Randall and L.-T. Wang, “The Bulk RS KK-gluon at the LHC”, *JHEP* 09 (2007) 074, doi: 10.1088/1126-6708/2007/09/074, arXiv: hep-ph/0701166 [hep-ph].
- [247] B. Lillie, J. Shu and T. M. P. Tait, “Kaluza-Klein Gluons as a Diagnostic of Warped Models”, *Phys. Rev. D* 76 (2007) 115016, doi: 10.1103/PhysRevD.76.115016, arXiv: 0706.3960 [hep-ph].
- [248] R. M. Harris, C. T. Hill and S. J. Parke, “Cross-section for topcolor Z-prime(t) decaying to t anti-t: Version 2.6” (1999), arXiv: hep-ph/9911288 [hep-ph].
- [249] P. S. Miyagawa and I. Dawson, “Radiation background studies for the Phase II inner tracker upgrade”, tech. rep. ATL-UPGRADE-PUB-2013-012, CERN, Feb. 2013, URL: <https://cds.cern.ch/record/1516824>.
- [250] “ATLAS Phase-II Upgrade Scoping Document”, tech. rep. CERN-LHCC-2015-020. LHCC-G-166, CERN, Sept. 2015, URL: <https://cds.cern.ch/record/2055248>.
- [251] P. Delebecque et al., “Alpine Pixel Detector Layout”, tech. rep. ATL-UPGRADE-PUB-2013-009, CERN, Feb. 2013, URL: <https://cds.cern.ch/record/1516529>.
- [252] S. Burdin et al., “Study of Conical Layout for Upgrade Pixel Detector”, tech. rep. ATL-UPGRADE-PUB-2013-003, CERN, Feb. 2013, URL: <https://cds.cern.ch/record/1514670>.
- [253] A. Ludwig, B. Heinemann and M. Garcia-Sciveres, “Studies of Inner Detector Layouts with 5 Pixel layers for the Phase-II Upgrade”, tech. rep. ATL-UPGRADE-PUB-2013-013, CERN, Feb. 2013, URL: <https://cds.cern.ch/record/1516829>.
- [254] A. Clark et al., “Final Report: ATLAS Phase-2 Tracker Upgrade Layout Task Force”, tech. rep. ATL-UPGRADE-PUB-2012-004, CERN, Oct. 2012, URL: <https://cds.cern.ch/record/1482960>.
- [255] A. Affolder et al., “DC-DC converters with reduced mass for trackers at the HL-LHC”, *Journal of Instrumentation* 6.11 (2011) C11035, URL: <http://stacks.iop.org/1748-0221/6/i=11/a=C11035>.

- [256] T. Liu and S. Diez, “Proceedings of the 2nd International Conference on Technology and Instrumentation in Particle Physics (TIPP 2011) System Implications of the Different Powering Distributions for the ATLAS Upgrade Strips Tracker”, *Physics Procedia* 37 (2012) 960–969, ISSN: 1875-3892, DOI: <http://dx.doi.org/10.1016/j.phpro.2012.02.433>, URL: <http://www.sciencedirect.com/science/article/pii/S1875389212017877>.
- [257] J. G. et. al, *ATLAS upgrade tracker integration: Inner Tracker Cooling*, Accessed: 07/07/2016, 2012, URL: <https://edms.cern.ch/document/1262223/1..>
- [258] A. Clark et al., “Development of a silicon-microstrip super module prototype for the high luminosity {LHC}”, *Nuclear Instruments and Methods in Physics Research Section A: Accelerators, Spectrometers, Detectors and Associated Equipment* 699 (2013), Proceedings of the 8th International Hiroshima Symposium on the Development and Application of Semiconductor Tracking Detectors Academia Sinica, Taipei, Taiwan, December 5–8, 2011 97–101, ISSN: 0168-9002, DOI: <http://dx.doi.org/10.1016/j.nima.2012.04.016>.
- [259] S. Gonzalez-Sevilla et al., “Electrical performance of a silicon micro-strip super-module prototype for the High-Luminosity {LHC} collider”, *Nucl. Instr. and Meth. A:* 699 (2013), Proceedings of the 8th International Hiroshima Symposium on the Development and Application of Semiconductor Tracking Detectors Academia Sinica, Taipei, Taiwan, December 5–8, 2011 102–106, ISSN: 0168-9002, DOI: <http://dx.doi.org/10.1016/j.nima.2012.03.025>, URL: <http://www.sciencedirect.com/science/article/pii/S0168900212003063>.
- [260] Y. U. et. al., “Development of n-on-p silicon sensors for very high radiation environments”, *Nuclear Instruments and Methods in Physics Research Section A: Accelerators, Spectrometers, Detectors and Associated Equipment* 636.1 (Apr. 2011) S24–S30, DOI: [10.1016/j.nima.2010.04.080](http://dx.doi.org/10.1016/j.nima.2010.04.080), URL: <http://dx.doi.org/10.1016/j.nima.2010.04.080>.
- [261] H. P. K.K., 1126-1 Ichino-cho, Hamamatsu-shi 435-8558, Japan, 2016, URL: <http://www.hamamatsu.com>.
- [262] S. Lindgren et al., “Testing of surface properties pre-rad and post-rad of n-in-p silicon sensors for very high radiation environment”, *Nuclear Instruments and Methods in Physics Research Section A: Accelerators, Spectrometers, Detectors and Associated Equipment* 636.1 (Apr. 2011) S111–S117, DOI: [10.1016/j.nima.2010.04.094](http://dx.doi.org/10.1016/j.nima.2010.04.094), URL: <http://dx.doi.org/10.1016/j.nima.2010.04.094>.
- [263] Z. Z. AG, Hermann-von-Helmholtz-Platz 1, D-76344 Eggenstein-Leopoldshafen, Germany, 2016, URL: <http://www.zyklotron-ag.de>.
- [264] A. Dierlamm, “Untersuchungen zur Strahlenhärte von Siliziumsensoren”, PhD thesis: University of Karlsruhe, Germany, 2003, URL: <http://www-ekp.physik.uni-karlsruhe.de/~thesis/data/iekp-ka2003-23.pdf>.
- [265] I. C. Karlsruhe, Hermann-von-Helmholtz-Platz 1, D-76344 Eggenstein-Leopoldshafen, Germany, 2016, URL: https://www.ekp.kit.edu/english/irradiation_center.php.
- [266] L. Wiik, “ATLAS Tracker Upgrade: Silicon Strip detectors for the SLHC” (June 2010), URL: <http://cds.cern.ch/record/1269636>.
- [267] A. Affolder et al., “Silicon detectors for the sLHC”, *Nucl. Instrum. Meth.* A658 (2011) 11–16, DOI: [10.1016/j.nima.2011.04.045](http://dx.doi.org/10.1016/j.nima.2011.04.045).

- [268] M. Kohler, L. Wiik et al., “Beam test measurements with planar and 3D silicon strip detectors irradiated to sLHC fluences”, *IEEE Trans. Nucl. Sci.* 58 (2011) 1308–1314, doi: 10.1109/TNS.2011.2126598.
- [269] M. Köhler et al., “Measurements with Irradiated 3D Silicon Strip Detectors”, *Nuclear Physics B - Proceedings Supplements* 215.1 (June 2011) 247–249, doi: 10.1016/j.nuclphysbps.2011.04.021, URL: <http://dx.doi.org/10.1016/j.nuclphysbps.2011.04.021>.
- [270] J. Harkonen et al., “Test beam results of a heavily irradiated Current Injected Detector (CID)”, *Nuclear Instruments and Methods in Physics Research Section A: Accelerators, Spectrometers, Detectors and Associated Equipment* 612.3 (2010), Proceedings of the 7th International Conference on Radiation Effects on Semiconductor materials, Detectors and Devices RESMDD 2008 488–492, ISSN: 0168-9002, doi: <http://dx.doi.org/10.1016/j.nima.2009.08.006>, URL: <http://www.sciencedirect.com/science/article/pii/S0168900209015757>.
- [271] G.-F. D. Betta et al., “Performance evaluation of 3D-DDTC detectors on p-type substrates”, *Nuclear Instruments and Methods in Physics Research Section A: Accelerators, Spectrometers, Detectors and Associated Equipment* 624.2 (Dec. 2010) 459–464, doi: 10.1016/j.nima.2010.03.164, URL: <http://dx.doi.org/10.1016/j.nima.2010.03.164>.
- [272] C. M. Fleta et al., “Laboratory and Testbeam Results on 3D Detectors”, *Proceedings of the 19th International Workshop on Vertex Detectors. June 6-11, 2010, Loch Lomond, Scotland, UK. p.23*, 2010 23.
- [273] I. de Microelectrónica de Barcelona, Centro Nacional de Microelectrónica, 08193 Cerdanyola del Vallès (Bellaterra), Barcelona, Spain.
- [274] G. Pellegrini et al., “First double-sided 3-D detectors fabricated at CNM-IMB”, *Nuclear Instruments and Methods in Physics Research Section A: Accelerators, Spectrometers, Detectors and Associated Equipment* 592.1-2 (July 2008) 38–43, doi: 10.1016/j.nima.2008.03.119, URL: <http://dx.doi.org/10.1016/j.nima.2008.03.119>.
- [275] T. M. et. al., “Silicon beam telescope for {LHC} upgrade tests”, *Nuclear Instruments and Methods in Physics Research Section A: Accelerators, Spectrometers, Detectors and Associated Equipment* 593.3 (2008) 523–529, ISSN: 0168-9002, doi: <http://dx.doi.org/10.1016/j.nima.2008.05.012>, URL: <http://www.sciencedirect.com/science/article/pii/S0168900208007468>.
- [276] M. Kortelainen et al., “Off-line calibration and data analysis for the silicon beam telescope on the CERN H2 beam”, *Nuclear Instruments and Methods in Physics Research Section A: Accelerators, Spectrometers, Detectors and Associated Equipment* 602.2 (Apr. 2009) 600–606, doi: 10.1016/j.nima.2009.01.189, URL: <http://dx.doi.org/10.1016/j.nima.2009.01.189>.
- [277] G. Pahn, *Teststrahlungsmessungen mit 3D-stc Silizium-Streifendetektoren*, 2008.
- [278] V. Cindro et al., “Radiation damage in p-type silicon irradiated with neutrons and protons”, *Nuclear Instruments and Methods in Physics Research Section A: Accelerators, Spectrometers, Detectors and Associated Equipment* 599.1 (Feb. 2009) 60–65, doi: 10.1016/j.nima.2008.11.007, URL: <http://dx.doi.org/10.1016/j.nima.2008.11.007>.
- [279] J. Lange et al., “Charge collection studies of proton-irradiated n- and p-type epitaxial silicon detectors”, *Nuclear Instruments and Methods in Physics Research Section A: Accelerators, Spectrometers, Detectors and Associated Equipment* 624.2 (Dec. 2010) 405–409, doi: 10.1016/j.nima.2009.11.082, URL: <http://dx.doi.org/10.1016/j.nima.2009.11.082>.

-
- [280] T. Ullrich and Z. Xu, *Treatment of Errors in Efficiency Calculations*, 2007, eprint: arXiv: physics/0701199.
- [281] E. Belau et al., “Charge collection in silicon strip detectors”, *Nuclear Instruments and Methods in Physics Research* 214.2-3 (Sept. 1983) 253–260, DOI: 10.1016/0167-5087(83)90591-4, URL: [http://dx.doi.org/10.1016/0167-5087\(83\)90591-4](http://dx.doi.org/10.1016/0167-5087(83)90591-4).
- [282] R. Turchetta, “Spatial resolution of silicon microstrip detectors”, *Nuclear Instruments and Methods in Physics Research Section A: Accelerators, Spectrometers, Detectors and Associated Equipment* 335.1 (1993) 44–58, ISSN: 0168-9002, DOI: [http://dx.doi.org/10.1016/0168-9002\(93\)90255-G](http://dx.doi.org/10.1016/0168-9002(93)90255-G), URL: <http://www.sciencedirect.com/science/article/pii/016890029390255G>.
- [283] G. Kramberger et al., “Influence of trapping on silicon microstrip detector design and performance”, *IEEE Trans. Nucl. Sci.* 49 (2002) 1717–1723, DOI: 10.1109/TNS.2002.801517.
- [284] C. Garca-Argos, C. Lacasta Licer and S. J. McMahon, “A Silicon Strip Detector for the Phase II High Luminosity Upgrade of the ATLAS Detector at the Large Hadron Collider”, Presented 08 Jan 2015, PhD thesis: Valencia U., Nov. 2015, URL: <https://cds.cern.ch/record/1980680>.
- [285] *SCTDAQ online documentation*, webpage, accessed November-2016, URL: <http://sct-testdaq.home.cern.ch/sct-testdaq/sctdaq/sctdaq.html>.
- [286] R. Brun and F. Rademakers, “ROOT: An object oriented data analysis framework”, *Nucl.Instrum.Meth.* A389 (1997) 81–86, DOI: 10.1016/S0168-9002(97)00048-X.
- [287] S. Gonzalez-Sevilla et al., “A double-sided silicon micro-strip Super-Module for the ATLAS Inner Detector upgrade in the High-Luminosity LHC”, *Journal of Instrumentation* 9.02 (2014) P02003, URL: <http://stacks.iop.org/1748-0221/9/i=02/a=P02003>.
- [288] F. Anghinolfi, *ABC-N ASIC specifications v1.3*. webpage, accessed November-2016, URL: http://dpnc.unige.ch/atlas/upgrade/Upgrade/ABCN/abcn_V1.3.doc.
- [289] Y. Takubo et al., “Development of SiTCP based DAQ system of double-sided silicon strip super-module”, *Nuclear Instruments and Methods in Physics Research Section A: Accelerators, Spectrometers, Detectors and Associated Equipment* 699 (Jan. 2013) 116–119, DOI: 10.1016/j.nima.2012.04.032, URL: <http://dx.doi.org/10.1016/j.nima.2012.04.032>.
- [290] S. Gonzales-Sevilla, private communication.